Targeting the mystery of extragalactic neutrino sources

- A Multi-Messenger Window to the Extreme Universe -

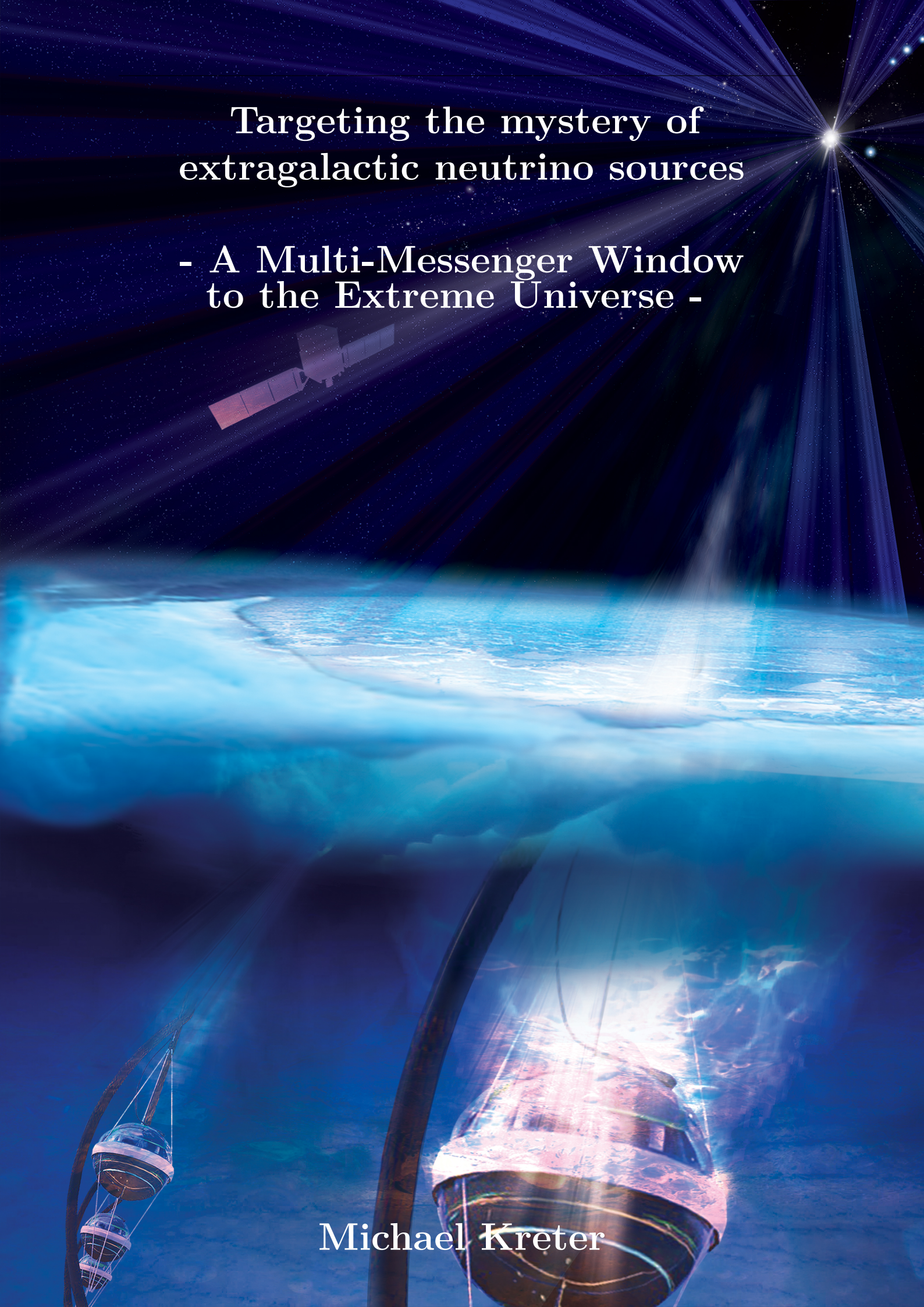

Michael Kreter

Targeting the mystery of extragalactic neutrino sources

- A Multi-Messenger Window to the Extreme Universe -

Dissertation zur Erlangung
des naturwissenschaftlichen Doktorgrades
der Julius-Maximilians-Universität Würzburg

vorgelegt von
Michael Kreter

aus Karaganda

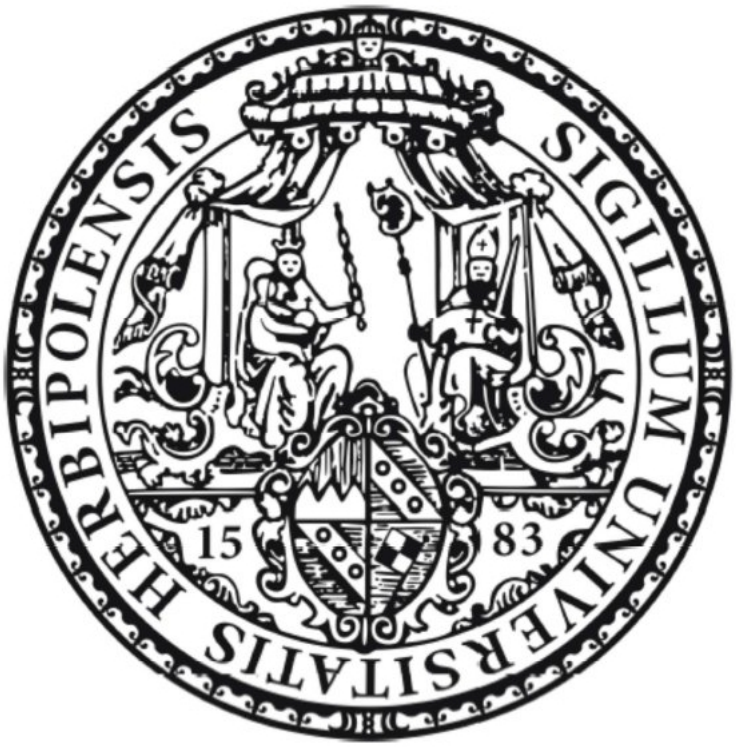

Würzburg 2018

Eingereicht am: 29.10.2018
bei der Fakultät für Physik und Astronomie.

1. Gutachter:	Prof. Dr. Matthias Kadler	(Universität Würzburg)
2. Gutachter:	Prof. Dr. Uli Katz	(FAU Erlangen-Nürnberg)
3. Gutachter:	.....	

der Dissertation

Vorsitzende(r):	Prof. Dr.Werner Porod	(Universität Würzburg)

1. Prüfer:	Prof. Dr. Matthias Kadler	(Universität Würzburg)
2. Prüfer:	Prof. Dr. Uli Katz	(FAU Erlangen-Nürnberg)
3. Prüfer:	Prof. Dr. Raimund Ströhmer	(Universität Würzburg)

im Promotionskolloquium

Tag des Promotionskolloquiums: 04.02.2019

Doktorurkunde ausgehändigt am: .....

Artist illustration:
The cover picture shows a multimessenger flaring event of a far-off galaxy which is detected in γ-rays by *Fermi*/LAT (top left) and could be the origin of a high-energy neutrino event seen by the IceCube Neutrino Observatory (sensor strings, bottom). The temporal and spatial consistent detection of both photons and neutrinos give rise to a new era of multimessenger Astronomie. Credit: NASA/Fermi and Aurore Simonnet, Sonoma State University

To my
little princess Leonie

Abstract

Active Galactic Nuclei (AGNs) are among the most powerful and most intensively studied objects in the Universe. AGNs harbor a mass accreting supermassive black hole (SMBH) in their center and emit radiation throughout the entire electromagnetic spectrum. About 10% show relativistic particle outflows, perpendicular to the so-called accretion disk, which are known as *jets*. Blazars, a subclass of AGN with jet orientations close to the line-of-sight of the observer, are highly variable sources from radio to TeV energies and dominate the γ-ray sky. The overall observed broadband emission of blazars is characterized by two distinct emission humps. While the low-energy hump is well described by synchrotron radiation of relativistic electrons, both leptonic processes such as inverse Compton scattering and hadronic processes such as pion-photoproduction can explain the radiation measured in the high-energy hump. Neutrinos, neutral, nearly massless particles, which only couple to the weak force[1] are exclusively produced in hadronic interactions of protons accelerated to relativistic energies. The detection of a high-energy neutrino from an AGN would provide an irrefutable proof of hadronic processes happening in jets. Recently, the IceCube neutrino observatory, located at the South Pole with a total instrumented volume of about one km^3, provided evidence for a diffuse high-energy neutrino flux. Since the atmospheric neutrino spectrum falls steeply with energy, individual events with the clearest signature of coming from an extraterrestrial origin are those at the highest energies. These events are uniformly distributed over the entire sky and are therefore most likely of extragalactic nature. While the neutrino event (known as "BigBird") with a reconstructed energy of $\sim 2\,\mathrm{PeV}$ has already been detected in temporal and spatial agreement with a single blazar in an active phase, still, the chance coincidence for such an association is only on the order of $\sim 5\%$. The neutrino flux at these high energies is low, so that even the brightest blazars only yield a Poisson probability clearly below unity. Such a small probability is in agreement with the observed all-sky neutrino flux otherwise, the sky would already be populated with numerous confirmed neutrino point sources.

In neutrino detectors, events are typically detected in two different signatures[2]. So-called shower-like electron neutrino events produce a large particle cascade, which leads to a precise energy measurement, but causes a large angular uncertainty. Track-like muon neutrino events, however, only produce a single trace in the detector, leading to a precise localization but poor energy reconstruction. The "BigBird" event was a shower-like neutrino event, temporally coincident with an activity phase of the blazar PKS 1424−418, lasting several months. Shower-like neutrino events typically lead to an angular resolution of $\sim 10^\circ$, while track-like events show a localization uncertainty of only $\sim 1^\circ$. Considering the potential detection of a track-like neutrino event in agreement with an activity phase of a single blazar lasting only days would significantly decrease the chance coincidence of such an association. In this thesis, a sample of bright blazars, continuously monitored by *Fermi*/LAT in the MeV to GeV regime, is considered as potential neutrino candidates. I studied the maximum possible neutrino expectation of short-term blazar flares with durations of days to weeks, based on a calorimetric argumentation. I found that the calorimetric neutrino output of most short-term blazar flares is too small to lead to a substantial neutrino detection. However, for the most extreme flares, Poisson probabilities of up to $\sim 2\%$ are reached, so that the possibility of associated neutrino detections in future data unblindings of IceCube and KM3NeT seems reasonable.

[1] Due to the small neutrino mass, gravitational coupling is also possible.

[2] A third event signature, the co-called "double-bang" event would originate from the interaction of a tau neutrino but has not been observed yet

On 22 September 2017, IceCube detected the first track-like neutrino event (named IceCube-170922A) coincident with a single blazar in an active phase. From that time on, the BL Lac object TXS 0506+056 was subject of an enormous multiwavelength campaign, revealing an enhanced flux state at the time of the neutrino arrival throughout several different wavelengths. In this thesis, I first studied the long-term flaring behavior of TXS 0506+056, using more than nine years of *Fermi*/LAT data. I found that the activity phase in the MeV to GeV regime already started in early 2017, months before the arrival of IceCube-170922A. I performed a calorimetric analysis on a 3-day period around the neutrino arrival time and found no substantial neutrino expectation from such a short time range. By computing the calorimetric neutrino prediction for the entire activity phase of TXS 0506+056 since early 2017, a possible association seems much more likely. However, the post-trial corrected chance coincidence for a long-term association between IceCube-170922A and the blazar TXS 0506+056 is on the level of $\sim 3.5\,\sigma$, establishing TXS 0506+056 as the most promising neutrino point source candidate in the scientific community.

Another way to explain a high-energy neutrino signal without an observed astronomical counterpart, would be the consideration of blazars at large cosmological distances. These high-redshift blazars are capable of generating the observed high-energy neutrino flux, while their γ-ray emission would be efficiently downscattered by *Extragalactic Background Light* (EBL), making them almost undetectable to *Fermi*/LAT. High-redshift blazars are important targets, as they serve as cosmological probes and represent one of the most powerful classes of γ-ray sources in the Universe. Unfortunately, only a small number of such objects could be detected with *Fermi*/LAT so far. In this thesis, I perform a systematic search for flaring events in high-redshift γ-ray blazars, which long-term flux is just below the sensitivity limit of *Fermi*/LAT. By considering a sample of 176 radio detected high-redshift blazars, undetected at γ-ray energies, I was able to increase the number of previously unknown γ-ray blazars by a total of seven sources. Especially the blazar 5BZQ J2219−2719, at a distance of $z = 3.63$ was found to be the most distant new γ-ray source identified within this thesis.

In the final part of this thesis, I studied the flaring behavior of bright blazars, previously considered as potential neutrino candidates. While the occurrence of flaring intervals in blazars is of purely statistical nature, I found potential differences in the observed flaring behavior of different blazar types. Blazars can be subdivided into BL Lac (BLL) objects, Flat-Spectrum Radio Quasar (FSRQ) and Blazars Candidates of Uncertain type (BCU). FSRQs are typically brighter than BL Lac or BCU type blazars, thus longer flares and more complicated substructures can be resolved. Although BL Lacs and BCUs are capable of generating significant flaring episodes, they are often identified close to the detection threshold of *Fermi*/LAT. Long-term outburst periods are exclusively observed in FSRQs, while BCUs can still contribute with flare durations of up to ten days. BL Lacs, however, are only detected in flaring states of less than four days. FSRQs are bright enough to be detected multiple times with time gaps between two subsequent flaring intervals ranging between days and months. While BL Lacs can show time gaps of more than 100 days, BCUs are only observed with gaps up to 20 days, indicating that these objects are detected only once in the considered time range of six years. The newly introduced parameter "Boxyness" describes the averaged flux in an identified flaring state and does highly depend on the shape of the considered flare. While perfectly box-like flares (flares which show a constant flux level over the entire time range) correspond to an averaged flux which is equal the maximum flare amplitude, irregular shaped flares generate a smaller averaged flux. While all blazar types show perfectly box-shaped daily

flares, BL Lacs and BCUs are typically not bright enough to be resolved for multiple days.

The work presented in this thesis illustrates the challenging state of multimessenger neutrino astronomy and the demanding hunt for the first extragalactic neutrino point sources. In this context, this work discusses the multiwavelength emission behavior of blazars as a promising class of neutrino point sources and allows for predictions of current and future source associations.

Zusammenfassung

Aktive Galaxienkerne (Active Galactic Nuclei, AGNs) zählen zu den extremsten und am intensivsten studierten Objekten im Universum. In ihrem Zentrum befindet sich ein Materie-akkretierendes supermassives schwarzes Loch. AGNs senden Strahlung im gesamten elektromagnetischen Spektrum aus, während lediglich etwa 10% dieser Galaxien Teilchen in so-genannten *Jets* auf relativistische Energien beschleunigen können. Eine Unterklasse von AGNs, bekannt als Blazare verfügt über Jets, welche unter einem geringen Sichtwinkel beobachtet werden. Diese Quellen sind höchst variabel und dominieren den beobachteten Himmel im Gammabereich. Multiwellenlängen-Beobachtungen von Blazaren zeigen eine typische Doppelhöckerstruktur. Während der niederenergetische Höcker gut durch leptonische Prozesse wie zum Beispiel Synchrotronstrahlung beschrieben werden kann, lässt sich die Emission des hochenergie-Höckers sowohl durch leptonische als auch durch hadronische Prozesse beschreiben. Neutrinos, nahezu masselose, neutrale Elementarteilchen werden ausschließlich in hadronischen Prozessen generiert. Der Nachweis eines hochenergetischen Neutrinos in Koinzidenz mit einem AGN würde somit einen unwiderlegbaren Beweis für das Vorhandensein relativistischer Protonen in diesen Quellen liefern. Die Existenz eines diffusen hochenergetischen Neutrino-Flusses konnte bereits durch das IceCube Experiment nachgewiesen werden. Bei dem IceCube Detektor handelt es sich um einen Cherenkov Detektor am Südpol mit einer gesamten instrumentierten Fläche von etwa $1 \times \mathrm{km}^3$. Hochenergetische Neutrinos sind überwiegend von extraterrestrischer Natur, da atmosphärische Neutrinos ab Energien von $> 100\,\mathrm{TeV}$ durch ihr steiles Spektrum sehr unwahrscheinlich werden. Da diese hochenergetischen Neutrinos gleichmäßig über den gesamten Himmel verteilt sind, kann von einem extragalaktischen Ursprung ausgegangen werden. Das so genannte “BigBird” Ereignis, welches mit einer Energie von $\sim 2\,\mathrm{PeV}$ rekonstruiert wurde, ist in zeitlicher und räumlicher Übereinstimmung mit einem monatelangen Ausbruch des Blazars PKS 1424−418 detektiert worden. Dennoch liegt die Wahrscheinlichkeit für eine Korrelation dieser beiden Ereignisse lediglich bei etwa 5%. Aufgrund des sehr geringen zu erwartenden Neutrino-Flusses bei diesen hohen Energien ist eine Neutrino-Erwartung individueller Quellen von deutlich unter einem Ereignis nicht verwunderlich. Anderenfalls wäre der Himmel bereits mit identifizierten Neutrino-Quellen bevölkert.

Neutrino-Detektoren weisen Neutrino-Ereignisse üblicherweise in zwei unterschiedlichen Signaturen nach. Bei dem “BigBird” Ereignis handelte es sich um ein sogenanntes “shower-like” Elektronen-Neutrino-Ereignis. Dieses erzeugt eine Teilchenkaskade innerhalb des Detektors, was zu einer Positionsunsicherheit von $\sim 10^\circ$ an Himmel führt. “Track-like” Myon-Ereignisse hingegen erzeugen lediglich eine Teilchenspur und resultieren somit in einer Positionsunsicherheit von $\sim 1^\circ$. Zur Detektion korrelierter Ereignisse wären somit ein “track-like” Neutrino-Ereignis, sowie ein Blazar Ausbruch von lediglich wenigen Tagen erforderlich. In dieser Arbeit untersuche ich eine Auswahl von 150 hellen Blazaren, welche kontinuierlich im MeV-GeV Bereich mit *Fermi*/LAT beobachtet werden. Basierend auf einem kalorimetrischen Ansatz untersuche ich die maximal zu erwartende Neutrino Anzahl kurzer Aktivitätsphasen mit einer Dauer von einigen Tagen bis Wochen. Die maximale Neutrino-Erwartung solcher kurzen Intervalle ist deutlich zu gering, um eine korrelierte Neutrino-Blazar Detektion erklären zu können. Dennoch, für die extremsten Ausbrüche sind Poisson-Wahrscheinlichkeiten von $\sim 2\%$ zu erwarten, was diese Quellen zu vielversprechenden Kandidaten in zukünftigen Neutrino-Punktquellen-Suchen macht.
Am 22. September 2017 detektierte IceCube ein hochenergetisches “track-like” Neutrino-Ereignis (bekannt als IceCube-170922A) in Übereinstimmung mit einer Phase erhöhter Aktivität des

Blazars TXS 0506+056. In dieser Arbeit untersuche ich zunächst das Langzeit-Emissionsverhalten dieser Quelle über einen Zeitraum von mehr als neun Jahren im MeV-GeV Bereich mithilfe von *Fermi*/LAT Daten. Die Aktivitätsphase dieser Quelle begann bereits Anfang 2017, Monate vor der Detektion von IceCube-170922A. Basierend auf einer kalorimetrischen Neutrino-Abschätzung konnte keine signifikante Neutrino-Erwartung in einem Zeitraum von drei Tagen um den Zeitpunkt der Neutrino-Detektion gefunden werden. Unter Berücksichtigung der gesamten Aktivitätsphase seit Anfang 2017 erscheint eine mögliche Korrelation beider Ereignisse kalorimetrisch deutlich wahrscheinlicher. Die korrigierte Zufallswahrscheinlichkeit liegt in der Größenordnung von $\sim 3.5\,\sigma$, wodurch sich TXS 0506+056 als die vielversprechendste extragalaktische Neutrino Punktquelle etabliert.

Eine weitere Möglichkeit das Auftreten hochenergetischer Neutrinos ohne Zuordnung zu einer astrophysikalischen Quelle, besteht in der Berücksichtigung von Blazaren bei hohen kosmologischen Distanzen. Solche Blazare mit hoher Rotverschiebung wären im Stande den gemessenen Neutrino-Fluss zu erzeugen, zugleich jedoch undetektiert durch *Fermi*/LAT zu bleiben. Durch die hohen kosmologischen Entfernungen dieser Blazare werden mögliche hochenergetische Photonen am extragalaktischen Hintergrundlicht (Extragalactic Background Light, EBL) hin zu kleineren Energien gestreut. Blazare bei hohen Rotverschiebungen sind überproportional relevante Quellen, da diese zu den extremsten Gamma-Quellen im Universum zählen und zudem wichtiger Bestandteil im Verständnis der Entwicklung von AGNs sind. Leider sind bisher nur sehr wenige solcher Quellen von *Fermi*/LAT detektiert worden. In dieser Arbeit führe ich eine systematische Suche nach Phasen erhöhter Gamma-Aktivität in Blazaren mit hoher Rotverschiebung durch, deren gemittelter Langzeitfluss unterhalb der Sensitivitätsgrenze von *Fermi*/LAT liegt. Basierend auf einer Auswahl von 176 im Gamma-Bereich undetektierten Blazaren mit hoher Rotverschiebung konnte die Anzahl bisher unbekannter Gamma-Quellen hoher Rotverschiebung um sieben Quellen gesteigert werden. Insbesondere der Blazar 5BZQ J2219−2719, welcher sich bei einer Rotverschiebung von $z = 3.63$ befindet, repräsentiert die am weitesten entfernte, neu identifizierte Gamma-Quelle innerhalb dieser Arbeit.

Im letztem Kapitel dieser Arbeit beschäftige ich mich mit dem Langzeit-Emissionsverhalten heller Blazare, welche zuvor als vielversprechende Neutrino-Kandidaten untersucht wurden. Während das Auftreten von Ausbrüchen von rein statistischer Natur ist, konnte ich mögliche Unterschiede im gemessenen Emissionsverhalten unterschiedlicher Blazar-Klassen feststellen. Blazare lassen sich in BL Lac (BLL) Objekte, Flat-Spectrum Radio Quasar (FSRQ) und Blazar-Kandidaten unbekannten Types (BCU) unterteilen. FSRQs sind im Allgemeinen hellere MeV-GeV Quellen als BL Lacs und BCUs, und zeigen daher häufiger und längere Ausbruch-Phasen. Während BL Lacs und BCUs zu signifikanten Ausbrüchen im Stande sind, werden diese Quellen häufig an der Detektionsschwelle von *Fermi*/LAT beobachtet. Perioden erhöhter Aktivität mit einer Dauer von mehreren Monaten können ausschließlich in FSRQs aufgelöst werden. Wobei BCUs noch Ausbrüche von etwa zehn Tagen zeigen, werden BL Lacs nicht länger als vier Tage in Folge detektiert. FSRQs werden üblicherweise in mehreren unabhängigen Ausbrüchen detektiert. Daher zeigen diese Quellen sowohl kurze Lücken von einigen Tagen zwischen der Detektion zweier aufeinanderfolgender Ausbrüche, als auch Lücken von mehr als 100 Tagen. BL Lacs werden ebenfalls in unabhängigen Ausbruchphasen identifiziert, mit Lücken von etwa 100 Tagen. BCUs hingehen zeigen lediglich eine einzelne Aktivitätsphase. Der neu definierte Parameter “Boxyness” beschreibt den mittleren Fluss innerhalb eines Ausbruchs und hängt sehr von dessen Form ab. Perfekte “boxartige”/kastenförmige Ausbrüche zeigen eine konstante Fluss-Amplitude. Irreguläre Ausbrüche hingegen führen zu

einem reduzierten mittleren Fluss. Alle Blazar-Klassen verfügen über perfekte “boxartige” Ausbrüche von lediglich einem Tag. Typischerweise sind BL Lacs und BCUs nicht hell genug um auf längeren Zeitskalen detektiert zu werden. Aufgrund der beschränkten Sensitivität von *Fermi*/LAT, können Unterstrukturen von weniger als einem Tag leider nicht aufgelöst werden.

Diese Arbeit spiegelt die Herausforderungen in der neuen Disziplin der Neutrino Astronomie, sowie die vielversprechende Jagd nach den ersten extragalaktischen Neutrino Punktquellen wieder. In diesem Zusammenhang werden Blazare als eines der vielversprechendsten Objekte möglicher zukünftiger Neutrino-Assoziationen diskutiert.

Contents

1 Introduction

In the first section of this thesis, I outline the historical evolution of astronomy from purely optical observations with the naked eye, over multiwavelength observations using different instruments to the relatively new field of multimessenger astronomy, which is based on the detection of different messengers such as photons, neutrinos and gravitational waves from astronomical objects. Then, I introduce different source candidates for the observed high energy neutrino flux and delineate the content of this work.

1.1 From Multiwavelength to Multimessenger Astronomy

For the majority of time in the history of astronomy, the night sky has only been observed by the naked eye at optical wavelengths. Electromagnetic radiation beyond the optical has been known since the early 19 th century, when Herschel (1800) and Ritter (1803) discovered infrared and ultraviolet radiation from the Sun. It was only in 1865, when Clerk Maxwell (1865) provided the first theoretical framework of electromagnetic waves, by introducing the so-called Maxwell equations. Hertz (1888, 1889) was able to detect these waves at low frequencies, by using a dipole. While radio waves are nowadays essential for modern communication, back in the 19 th century Hertz believed they were of no practical use and only a proof of the Maxwell equations (Norton 2000). In the same year, Röntgen discovered *a new kind of radiation*, which today is widely known as X-ray radiation (Röntgen 1898a,b). Gamma rays have been discovered shortly afterwards through radioactivity by Becquerel (1895), while Curie (1903) found that only a small fraction of elements are radioactive.
Astronomical sources were expected to be radio emitters. The first successful observation of the Milky Way at radio wavelengths was performed by Jansky (1932, 1933). It took until the 1960s that observations at radio wavelengths were established in the scientific community and the sky was first mapped in the Second and Third Cambridge Catalogue of radio sources (Shakeshaft et al. 1955, Edge et al. 1959). In the 1960s the first source in X-rays was found by Giacconi et al. (1962, 1964), who searched for fluorescent X-rays from the Moon. The first X-ray satellite was launched in 1970 (Jagoda et al. 1972) and discovered many new sources. These catalogs at X-ray energies were the first to contain many active galaxies (see. Sect. 2, Giacconi 2003). Gamma-ray emission from astronomical sources was predicted since the 1940s (Feenberg & Primakoff 1948; Hayakawa 1952; Morrison 1958). The first γ-ray mission *Explorer 11* (Kraushaar et al. 1965) was launched in 1961, followed by OSO-3 (launched in 1967; Kraushaar et al. 1972), OSO-7 (launched in 1971; Clark et al. 1973; Markert et al. 1977) and the Solar Maximum Mission (launched in 1980; Forrest et al. 1980). These missions were designed to study γ-ray emission from the Sun. The first missions designed to map the γ-ray sky were SAS-2 (launched in 1972; Fichtel et al. 1973) and COS-B (launched in 1975; Bignami et al. 1975), although their resolution was low. First observations with large angular and temporal resolution were possible with the Energetic Gamma Ray Experiment Telescope (EGRET, Thompson et al. 1993), onboard of the *Compton Gamma-Ray Observatory (CGRO)*, which was launched in 1991 and discovered many active galaxies. In 2008, EGRET was succeeded by the *Fermi Gamma-ray Space Telescope* (see Sect. 3.3), which provides a continuous monitoring of the entire γ-ray sky at high resolution and is still operational today. Gamma rays are believed to be first indicators for the sources of cosmic rays.
Back in the 19 th century, cosmic rays were expected to originate from the ground. Wulf (1909a) was the first to measure the intensity of (secondary) cosmic rays by the use of an electrometer and found a decrease with lower air pressure. Therefore, Wulf (1909b) concluded that these radiation needs to originate from radioactive elements in the ground. In order to pave his hypothesis, Wulf took an electrometer to the top of the Eiffel-tower and measured

a reduced intensity. This result was in contradiction to his previous findings, according to which the intensity should have vanished on the top of the Eiffel-tower (Wulf 1910). In the following years, independent studies have been performed, targeting the origin of cosmic rays. Pacini (1912) found a decrease in intensity by countersinking an electrometer into the sea, which is in disagreement to radioactivity from the crust. This was confirmed by Hess (1912) in a balloon experiment. Hess found a steady increase in radiation above a height of $\sim$ 150 m, indicating cosmic rays to be of extraterrestrial origin. Today we know that cosmic rays mainly consist of protons originating from outside the Solar System, with energies between 10^9 eV and 10^{21} eV (Blasi 2014). As cosmic rays are charged particles, they are deflected in electromagnetic fields, making it impossible to trace back their origin. Finding the sources of cosmic rays is of particular interest in astronomy, as these sources accelerate protons to extremely high energies. Describing acceleration mechanisms is a primary goal in astronomy. Active galaxies are promising candidates, as their jets (see Sect. 2.2.4) are capable of accelerating protons to the highest energies.

Neutrinos would provide an unique fingerprint of accelerated protons. As (nearly) massless neutral leptons, they do mainly couple to the weak force and can escape even dense environments, tracing back to their origin. Astronomical sources that can accelerate protons to high energies also interact with the ambient light, e.g., from stars. These seed photon field allows pion-photoproduction (see Sect. 2.3.4) to take place. High-energy protons interact with surrounding seed photons, producing both charged and neutral pions ($\pi^{\pm}, \pi^0$). These pions then decay into high energy γ-rays and neutrinos, amongst others. As neutrinos do only barely interact with matter, large instrumental volumes are required to detect them. The first underwater neutrino detectors were the Deep Underwater Muon and Neutrino Detector (DUMAND; Spiering 2012) and the Baikal Neutrino Telescope (Katz & Spiering 2012), while the Antarctic Muon and Neutrino Detector Array (AMANDA, Andres et al. 2000) was the first neutrino detector deployed in the arctic ice at the South Pole. These detectors have been succeeded by the ANTARES (see Sect. 3.5.4.1, Ageron et al. 2011) and KM3NeT (see Sect. 3.5.4.2, Löhner et al. 2013; Bruijn & van Eijk 2015) deep-sea neutrino detectors, while AMANDA has been extended to the IceCube neutrino observatory (see Sect. 3.5.4.3; Halzen & Klein 2010). The IceCube Collaboration (2013) and Aartsen et al. (2015a) have detected a neutrino signal, clearly in excess of the expected atmospheric contribution, which is likely of extraterrestrial origin. Until the year 2018, the only confirmed extraterrestrial neutrino point sources have been the Sun (Davis et al. 1968) and supernova SN1987A (Burrows & Lattimer 1987, Alexeyev et al. 1988). Recent results from the IceCube Collaboration et al. (2018); IceCube Collaboration (2018) indicate the blazar TXS 0506+056 to be a promising candidate for the first confirmed extragalactic neutrino point source.

A further multimessenger approach is the detection of gravitational waves, which are ripples in spacetime, which propagate like waves. Gravitational waves are caused by local perturbations in spacetime, which are due to the movement of massive objects. One would expect such waves from a merger of e.g. two black holes, neutron stars or inspiralling white dwarfs. Gravitational wave detectors use the concept of laser interferometry to respond on infinitesimal small variations in spacetime. With detectors on both coasts of the US (LIGO) and in Italy (VIRGO), this forms a global grid of gravitational wave detectors (Abbott et al. 2004, Accadia et al. 2012). The first direct detection of a binary black hole merger was made by the LIGO and VIRGO Collaborations (Abbott et al. 2016), while first multimessenger observations of a neutron star merger have been obtained only one year later (Abbott et al. 2017).

In this thesis, I mainly study the flaring behavior of blazars (see Sect. 2.4) and use fundamental calorimetric arguments to identify potential neutrino point source candidates which could lead to future multimessenger observations similar to TXS 0506+056.

1.2 Possible Astrophysical Sources of the Detected Neutrino Flux

Finding the sources of the detected extraterrestrial neutrino flux is one of the major challenges of modern astronomy. As neutrinos of different energy scales are produced in different processes, diverse astronomical sources can be responsible for the total detected neutrino flux. The only confirmed extraterrestrial neutrino sources for a long time have been the Sun (Davis et al. 1968) and the supernova SN1987A (Burrows & Lattimer 1987, Alexeyev et al. 1988). Only recently, the blazar TXS 0506+056 was confirmed as the first extragalactic neutrino point source (IceCube Collaboration et al. 2018; IceCube Collaboration 2018). In the following section, I will give an overview of possible neutrino point source candidates and discuss their expected contribution to the measured neutrino flux. If not labeled differently, the following sections are based on the work of Mészáros (2017) and Katz & Spiering (2012).

1.2.1 Generic Source Requirements

The isotropy of detected high energy neutrino events led to the conclusion that possible counterparts have to be mainly of extragalactic origin (Murase & Waxman 2016). Such sources could be naturally related to the sources of ultra-high energy cosmic rays (UHECRs; IceCube Collaboration et al. 2016), although these sources need only to be capable to accelerate cosmic rays to energies of $\sim 100\,\mathrm{PeV}$ to explain the detected neutrino flux. The neutrino spectrum measured in IceCube Collaboration (2013) and Aartsen et al. (2015a) can in principle be produced by a cosmic ray spectrum of $\mathrm{N}(\mathrm{E_{CR}}) \sim \mathrm{E_{CR}^{-2.5}}$, which is steeper than expected from first order Fermi acceleration (see Sect. 2.2.4.2). Extending this spectrum to $\sim 100\,\mathrm{PeV}$ for cosmic rays would result in a peak at about 6.3 PeV, the so-called Glashow resonance (e.g. Murase et al. 2013; Anchordoqui et al. 2014), which has not been observed by IceCube. The reason for this could be either a steeper single power-law neutrino spectrum, or a spectrum which contains a spectral break at a few PeV (e.g. He et al. 2013, Liu et al. 2014).
The *Fermi* diffuse isotropic γ-ray background has a major impact on possible neutrino sources, as secondary TeV to PeV γ-rays which originate from the decay of neutral pions (π^0) will be down scattered into the *Fermi* range by cascading against the extragalactic background light (EBL). A dominant fraction of the *Fermi*/LAT diffuse isotropic γ-ray background is indeed well explained by unresolved distant blazars (Ackermann et al. 2015b), γ-ray emission from which can be explained by leptonic models. While most of the typically considered neutrino candidates (see Sect. 1.2.2) are optically thin sources, which allow both neutrinos and γ-rays to escape, these sources are restricted by *Fermi*/LAT observations. For electromagnetically "hidden" sources (like e.g. Murase et al. 2016), however, such a restriction would not apply, as the produced (hadronic) γ-rays would have been absorbed or downscattered to substantial lower energies, becoming "invisible" for *Fermi*/LAT. Such "hidden" sources typically show a generic correlation between the pion formation rate in $p\gamma$ interactions and the γ-ray absorption rate, as both depend on the photon target density (Waxman & Bahcall 1997). Thus, compact sources with a high photon target density are more likely to to be degenerated, making them electromagnetically dim or effectively hidden. Another way in which neutrino candidate sources could be undetected in *Fermi*/LAT is when they are at a high redshift, leading to a more efficient absorption in the EBL (e.g Xiao et al. 2016, Ackermann et al. 2017). For a detailed study of a systematic search for high redshift-blazars with *Fermi*/LAT please refer to Sect. 6.

1.2.2 Specific Astrophysical Sources

In this section, I will discuss the neutrino prediction of specific astronomical sources, which are either of galactic or extragalactic origin.

1.2.2.1 Galactic Sources

Galactic neutrino sources are expected to be related to sources of cosmic rays (e.g. IceCube Collaboration et al. 2016). Beside the supernova SN1987A, no other galactic neutrino point source has been confirmed yet, suggesting TeV γ-ray sources to be promising candidates for hadronic interactions. These high energy γ-rays are expected to be generated following Sect. 2.3.4. Keeping in mind that high energy γ-rays can also be created by inverse Compton scattering (see Sect. 2.3.3), their detection is not a clear indication that the source accelerates hadrons rather than electrons.
The Crab nebula is a prominent γ-ray source (e.g. Aharonian et al. 2006a), which first has been detected at TeV energies in 1972 (Fazio et al. 1972). The Crab belongs to a special class of supernova remnants (SNRs), the pulsar wind nebulae (PWN), which harbor a pulsar that blasts material into the nebula. Imaging Air Cherenkov Telescopes (IACTs; see Sect. 3.4.2) have detected more than hundred TeV γ-ray sources (e.g. Hinton 2009), among which are about 30 SNRs, while unambiguous galactic sites of hadronic interaction yet have to be identified. Studying their multiwavelength behavior in the MeV−GeV energy range as well as their high-energy cutoff provides additional constraints on possible hadronic models. However, extended γ-ray sources such as the SNR Vela (Aharonian et al. 2005), the region near the Galactic Center (Aharonian et al. 2006b) and the Cygnus region (Abdo et al. 2007) remain good candidates for a neutrino detection.

1.2.2.2 Extragalactic Sources

It is much harder to predict neutrino fluxes from extragalactic rather than galactic sources. Individual source predictions are typically low, as otherwise the sky would already be filled with neutrino sources. The best-motivated candidates for the origin of the high-energy neutrino signal detected by IceCube (IceCube Collaboration 2013 and Aartsen et al. 2015a) are Active Galactic Nuclei (AGN), Gamma Ray Bursts (GRB) and Starburst Galaxies.

Starburst Galaxies:
Starburst Galaxies are sources which show an episode of large-scale star formation, lasting $10^6 - 10^7$ years. This time scale is longer than the lifetime of young massive stars, which then become supernovae. About $20 - 30\,\%$ of all star formation in the Universe occurred in such galaxies. The central region of these sources eject a galactic-scale wind, which is driven by the collective effect of supernova explosions and winds from massive stars. TeV γ-ray emission has been detected from the galaxies NGC 253 (Acero et al. 2009) and M82 (Karlsson & for the VERITAS collaboration 2009). These sources show cosmic ray densities of two or three orders of magnitude above what is measured in our own galaxy, making them possible neutrino source candidates (Loeb & Waxman 2006) for kilometer size neutrino detectors such as IceCube (see Sect. 3.5.4.3) and KM3NeT (see Sect. 3.5.4.2).

Gamma Ray Bursts:
Gamma Ray Bursts (GRBs) are among the most cataclysmic phenomena in the Universe, releasing enormous amounts of energy in γ-rays on timescales of milliseconds to minutes. Long-term bursts are caused by the collapse of a massive star into a black hole. Short-term GRB can be explained by the so-called fireball model of GRB (Piran 1999). This model assumes the central engine to eject large amounts of mass on short time scales which forms successive plasma shells and shows Lorentz factors of typically $\Gamma = 100 - 1000$. When the outer shells slow down, they get hit by the inner shells, forming internal shock fronts, where electrons and protons can be accelerated following Sect. 2.2.4.2. While electrons get cooled by

synchrotron radiation (see Sect. 2.3.2), protons can be accelerated to extremely high energies of up to 10^{21} eV (Waxman & Bahcall 1997). When the shells interact with the interstellar medium, external shocks are formed, leading to afterglow emission that is visible in different wavelengths. Neutrinos are expected to be created in three phases: the precursor phase, in which the jet is still forming and no electromagnetic radiation is observed (Razzaque et al. 2003), the "prompt" phase, where the burst of γ-rays is taking place (Waxman & Bahcall 1997) and the afterglow phase (Waxman & Bahcall 2000). Multiwavelength, direction and timing information are taken into account to search for possible neutrino-GRB coincidences, while no excess in direction and time with any known GRB has been found yet (e.g. Achterberg et al. 2008, Aartsen et al. 2016).

Active Galactic Nuclei:
Active Galactic Nuclei (AGN) are one of the most powerful objects in the Universe. The term active refers to a small fraction of galaxies, in which either the central region dominates the emission of the host galaxy, or (in addition) massive particle outflows (so-called jets, see Sect. 2.2.4) emerge from the nucleus and can be detected from radio wavelengths up to TeV energies. Luminosities on the order of $L \sim 10^{42}$ to $10^{48}\, erg\, s^{-1}$ are caused by accretion of matter towards a supermassive black hole (SMBH, see Sect. 2.2.1) with masses between $\sim 10^6\,M_\odot$ to $\sim 10^{10}\,M_\odot$. Average galaxies such as the Milky Way also harbor a SMBH in their center, while only in $\sim 30\,\%$ of these galaxies the gas accretion onto the SMBH leads to detectable radio or X-ray emission on the order of $L \sim 10^{43}\,erg\,s^{-1}$. These objects are known as *low luminosity AGN (LLAGN)*.
The multiwavelength emission behavior of AGN typically shows two distinct emission humps, where the low-energy hump is well described by synchrotron radiation (see Sect. 2.3.2). For the high-energy hump, however, both leptonic and hadronic models (see Sect. 2.2.4.3) are capable of explaining the observed high energy emission. In leptonic models, the emission is mainly caused by accelerated electrons due to inverse Compton scattering (see Sect. 2.3.3), even when protons are present. In hadronic models, accelerated protons can interact with an ambient UV photon field (see Sect. 2.3.4) generating both high energy γ-rays as well as neutrinos via the decay of neutral and charged pions. In lepto-hadronic models, typically a combination of both scenarios takes place.
Especially blazars (see Sect. 2.4), a subclass of AGN where the jet is aligned close to the light of sight, have been suspected as cosmic ray candidates. Their highly relativistic jets (bulk Lorentz factors $\Gamma_j \sim 5 - 30$) form shock fronts, which are ideal sites to accelerate protons by Fermi processes (see Sect. 3.3). Therefore, blazars are promising candidates for the observed UHECR, high energy γ-ray (Protheroe & Kazanas 1983, Biermann & Strittmatter 1987) and neutrino (Stecker & Salamon 1996) flux. Neutrino production within jets requires an adequate density of target photons and/or nuclei. In blazars, there are four main sources which can act as target photons for $p\gamma$ interactions, namely: 1) continuum photons from the accretion disc, which feed the SMBH, typically ranging between $\sim 10 - 10^5$ eV; 2) continuum infrared photons from the dusty torus, peaking around $\sim 10^{-2} - 10^{-1}$ eV; 3) line photons ($H_\alpha \sim 10$ eV) from the so-called broad line region (BLR), which also scatters continuum photons towards the jet; 4) nonthermal emission from the inner jet, which in specific AGN can be detected up to TeV energies.
Beside blazars, other classes of AGN could also contribute to the detected diffuse neutrino flux, including radio-quiet quasars (Stecker & Salamon 1996, Alvarez-Muñiz & Mészáros 2004, Pe'Er et al. 2009) and LLAGNs (Kimura et al. 2015). The proton acceleration in such models is concentrated in the nucleus, where densities are larger. Since the relative increase in proton density is much larger than for photons, *pp* interactions may become more important or even

dominant in these sources. While typical blazar models can explain the PeV neutrino data relatively well, they have problems predicting TeV neutrinos. An exception is the model by Dermer et al. (2014), which uses second order Fermi acceleration and BLR target photons to produce a neutrino spectrum with a cutoff of a few PeV. Older AGN core models have similar problems in under-predicting the TeV data. Core models for LLAGN (e.g. Kimura et al. 2015) assume an accretion flow in which *pp* interactions dominate, describing well the $10 - 100\,\mathrm{TeV}$ neutrino flux, but under estimating the PeV data. Both blazar as well as AGN core models have large astrophysical uncertainties. Although they all have difficulties in predicting the observed neutrino spectrum over several energy decades, they may not necessarily be ruled out. In addition, even fainter γ-ray sources such as radio galaxies have been considered as neutrino sources (Becker Tjus et al. 2014).

1.3 Plan of this Thesis

In this thesis I study the origin of the measured high energy neutrino flux, which is most likely of extragalactic nature. Neutrinos are elementary particles with no electric charge and a half-integer spin. As they are almost massless, neutrinos primarily couple to the weak force and can escape even dense environments. While cosmic rays and photons can either be deflected or absorbed before being detected, neutrinos can pass cosmological distances nearly undeflected, pointing back to their origin. This makes neutrinos unique messengers to study some of the most extreme environments in the Universe. As the high energy emission of astronomical sources can be equally well explained by either accelerated electrons (so-called leptonic models) or protons (so-called hadronic models)[3], a neutrino detection from an astronomical source would be a "smoking gun[4]" signal to distinguish between both models.
In the first section, I introduce the evolution of astronomy from multiwavelength to multimessenger observations and discuss possible sources of the observed high energy neutrino flux. Blazars, a subclass of Active Galactic Nuclei are more extensively discussed in section two. Blazars are promising neutrino candidates, as they show highly relativistic jets aligned close to the line of sight of the observer. These jets are capable of accelerating both electrons as well as protons, which are detected from radio wavelengths up to TeV energies and show variability on timescales of minutes to months. Their multiwavelength emission is characterized by two distinct emission humps, of which the low-energy one is well explained by synchrotron radiation, while the high-energy hump can be fitted by either leptonic or hadronic models. In the third section, I discuss relevant instruments and their detection principles, while analysis techniques necessary to obtain the used multimessenger data are introduced in section four.
In section five, a systematic search for possible neutrino candidates is performed using a sample of bright γ-ray blazars, which are characterized by bright flares on the order of days to weeks. Potential blazar candidates and caveats of the method used are discussed. Recently, a neutrino track-like event with a good angular resolution of less than $1\,\mathrm{deg}^2$ was found to be temporally and spatially consistent with increased γ-ray activity from the blazar TXS 0506+056. I perform a calorimetric analysis and calculate the chance coincidences of a correlated detection between both events. In the sixth section, I discuss flare characteristics of bright blazars, previously considered in the neutrino analysis. In the seventh section, a systematic search for γ-ray unknown high-redshift ($z \geq 2.5$) blazars is performed. These blazars are too faint to be detected on longer time periods on the order of years, but show up as significant detections on monthly time scales. High-redshift blazars are disproportionately

[3] Or a combination of both, so-called lepto-hadronic models
[4] In this context the term "smoking gun" corresponds to the final proof that indubitable distinguishes between both models

important targets because they serve as cosmological probes and represent the most powerful class of γ-ray sources in the Universe. In addition, high-redshift blazars could contribute to the detected diffuse neutrino flux. In the final section, I conclude and present an outlook in as to how the presented work can be extended and improved.
During this thesis, I was involved in other projects, including the study of PMN J1603−4904 as a likely member of the rare class of γ-ray emitting young radio galaxies. These objects, which may transition into larger radio galaxies, are a stepping stone to understanding AGN evolution. It is not completely clear how these young galaxies, seen edge-on, can produce high-energy γ-rays. The goal of this project was to investigate the possibility of other X-ray bright sources in the vicinity of PMN J1603−4904 that could be counterparts to the γ-ray emission. In this sense, I was responsible for the analysis of the *Fermi*/LAT data, which included a precise localization of the γ-ray source as well as a complicated spectral analysis. For further details, please refer to App. I.

2 Active Galactic Nuclei

Active Galactic Nuclei (AGNs) are one of the most powerful objects in the Universe. These objects harbor a Supermassive Black Hole (SMBH) in their center with masses between $\sim 10^6\,M_\odot$ to $\sim 10^{10}\,M_\odot$ and emit radiation with a luminosity of $L \sim 10^{42}$ to $10^{48}\,erg\,s^{-1}$, outshining the host galaxy by up to four orders of magnitude. The term "active" refers to the inner center of the galaxy, where powerful, non-thermal broadband emission is produced which can not be explained by the thermal processes happening in stars. While the low-energy emission is well described by relativistic electrons interacting in electric and magnetic fields, the high-energy emission can either be explained by electron or proton interactions, resulting in the production of high-energy γ-rays as well as neutrinos.
In the following section, an overview of AGN phenomenology and related emission processes is given. More detailed information can be found in Beckmann (2012), Krolik (1999) and Stanev (2004).

2.1 From Galactic Nebulae to Supermassive Black Holes: A Historical View

The dawn of extragalactic astronomy can be ascribed to Thomas Wright, who in the year 1750 speculated that some of the nebulae observed in the sky were not part of our own galaxy, but rather own galaxies by themselves (Wright 1750). A few years later, Immanuel Kant introduced the name "Welteninseln" (island universes) for these specific objects (Kant 1755). It took about a century until 1854, when François Arago established the extragalactic hypothesis in the scientific community, although it was still not accepted as true. One main difficulty was the fact that some of the nebulae were indeed of galactic origin, such as as planetary nebula and globular clusters. It was Heber Curtis who finally revealed the extragalactic origin of these nebulae by proving that the Andromeda Nebula M31 shows doppler shifts, similar to our own galaxy (Curtis 1920).
The concept of massive "black stars" whose gravitation would even trap light was first suggested by Michell (1784) and Laplace (1796) but largely ignored until Einstein's General Theory of Relativity in the early 20th century. Einstein suggested that light could be bent by massive objects (Einstein 1915a,b), which was proven only four years later by Eddington (1919) using a total solar eclipse. Schwarzschild (1916) found a solution to Einstein's field equations, suggesting that a star above a certain mass would form a singularity at the end of its life. This was believed to be a mathematical concept with no known physical realization, until Oppenheimer & Snyder (1939) showed that this is indeed happening in stars. Only two years after the theoretical framework for black holes was established, Cyg X-1 (Oda et al. 1971), the first black hole candidate was found. Many galactic black hole detections, which originate from a solar collapse, have been made since then. In the same year, Lynden-Bell & Rees (1971) suggested that the Milky Way contains a Supermassive Black Hole (SMBH), which is today known as Sagittarius A*. Due to the work of Kormendy & Richstone (1995) and King (2003), it is now believed that all galaxies harbor a SMBH.
Back in 1918, Heber Curtis noticed a "curious straight ray $[\cdots]$ apparently connected with the nucleus by a thin line of matter" from M87 (Curtis 1918), which was the first detection of a so-called "jet" - a highly relativistic outflow of matter from the central region of a galaxy. Seyfert (1942) found that several galaxies hosted some kind of additional emitting component in their center, which has to be concentrated within the central 100 pc of the galaxy and require a mass of $\sim 10^8\,M_\odot$, much higher than Woltjer (1959) predicted for a normal mass to light ratio. These particular galaxies have been found since the 1970s by searching for sources with a high energy output. While most of these sources show a power law spectrum at X-rays energies associated with the inner part of the galaxy, only a fraction shows relativistic out-

flows and non-thermal emission from radio to X-ray energies. In the 1990s, it was established that these particular galaxies are part of a common phenomenon, a so-called active galactic nucleus.

2.2 Building an Active Galactic Nucleus

"Building" an AGN requires a set of specific "ingredients" which all influence each other and together form the standard model of active galactic nuclei. In the following section, a brief introduction of the physical processes forming these "ingredients" is given, while the processes behind the observed radiation are described in Sect. 2.3.

2.2.1 Supermassive Black Hole (SMBH)

An active galactic nucleus is "powered" by a *Supermassive Black Hole* (SMBH), which is located in the center of the host galaxy. Only a humble fraction of 3 % of all identified galaxies are known to host an AGN in their center (Terzian et al. 1999). The mass of a black hole can span a wide range, from several solar masses for regular star collapse black holes to several billion solar masses for SMBHs. As not even photons can escape a black hole, these objects are difficult to find and can only be identified by indirect detection methods based on their gravitational interaction. Mass orbiting an unknown attractor can indicate the existence of a black hole. Gravitational lensing, which describes the bending of light around a huge collection of (undetectable) mass is a more direct detection method. Misner et al. (1973) proposed the so-called "No-hair theorem", according to which no information can leave the singularity and in accordance to which a black hole can be characterized by only two classical parameters, its mass and angular momentum. A black hole has an event horizon (Schwarzschild 1916) which can be understood as the redshifting surface of the collapsed star and defines an observable boundary. Hawking (1975) predicted that radiation can be observed from the event horizon, but so far, no direct evidence of this so-called Hawking radiation has been found. The information paradox, which can be derived from quantum field theory (QFT), states that at the event horizon, one of the general tenets of QFT (Locality or Unitarity) must break down. Locality (causality) requires that information can't travel faster than light while Unitarity states that information is conserved and all processes (including quantum mechanics) have to be deterministic. AGN harbor a SMBH in their center, though it is still highly debated how such massive black holes form. The Event Horizon Telescope (EHT) aims to provide first direct observational evidence of Sagittarius A* and therefore direct evidence for a SMBH in the heart of our own galaxy (Falcke et al. 2000).

2.2.2 Mass Accretion and Accretion Disks

The process of mass accretion is generally accepted to fuel an AGN by pulling matter into the SMBH (Salpeter 1964). Different velocities that are caused by friction and turbulence of the orbiting matter cause a transport of angular momentum outwards, while a stream of matter is attracted to the black hole. Material which moves to the center transfers potential energy of the gravitational field into kinetic and thermal energy. The Eddington Limit approximates the maximum accretion rate by balancing the radiation pressure and the accreting material, leading to a maximum Eddington Luminosity of

$$L_{\mathrm{Edd}} = \frac{4\pi G M_\odot m_p c}{\sigma_T} \propto 1.3 \times 10^{38} \left(\frac{M}{M_\odot}\right) \frac{\mathrm{erg}}{\mathrm{s}}\,, \tag{2.1}$$

where G represents the gravitational constant, c the speed of light, m_p the proton mass, σ_T the Thomson cross section, $M_\odot$ the solar mass and M the mass of the accreting black hole.

It is important to note that the Eddington approximation assumes spherically symmetric accretion of hydrogen gas, a simplification that is likely not true. As a direct consequence of the preservation of angular momentum of infalling material, an *accretion disk* surrounding the SMBH is formed. Assuming a geometrically thin-disk model, the spectrum of the accretion disk emits multi-temperature black-body radiation with a characteristic temperature of $T \sim 76000\,\mathrm{K}$ for a SMBH with a mass of $\sim 8.87 \times 10^8\,\mathrm{M}_\odot$ and a luminosity of $L = 3.356\,L_{\mathrm{Edd}}$ (Lawrence 2012). For $L \sim L_{\mathrm{Edd}}$, disks become geometrically thick. For geometrically thick accretion disk models, the height of the accretion disk is determined by a hydrostatic pressure equilibrium

$$\frac{1}{\rho}\frac{\partial P}{\partial z} = g_z^{\mathrm{grav}}, \tag{2.2}$$

where ρ indicates the density of matter within the accretion disk and P the pressure. The z-component of the gravitational attraction can be expressed as

$$g_z^{\mathrm{grav}} = \frac{z}{(r^2 + z^2)^{3/2}} \approx \frac{z}{r^3}, \tag{2.3}$$

while the radial component is balanced out by the centrifugal force. Paczyński & Wiita (1980) showed that thick accretion disks form when the accretion rate becomes high, reaching luminosities significantly above the Eddington limit. This behavior is caused by geometric effects such as the formation of cusps in the inner edges which depend on the angular momentum distribution. Such high luminosities produce high radiation fields in the cusp region, leading to the formation of well collimated beams of relativistic particle outflows perpendicular to the accretion disk - the so-called *jets*.

2.2.3 From Broad Emission Lines over Narrow Emission Lines to the Dust Torus

The *Broad Line Region* (BLR) is located close to the SMBH at distances of about 0.1 pc to 1 pc. Broad emission lines are observed from AGN in the optical and UV range and indicate regions of dense material above the accretion disk close to the black hole (Done & Krolik 1996). Matter in these regions has to be concentrated into clouds, as otherwise Thomson scattering would make these regions optically thick. The occurrence of the broad line region is believed to be caused by in- and outflowing material from the accretion disk or torus, while the broadening is caused by a turbulent motion of the clouds at high velocities.
At distances of about 100 pc, the *Narrow Line Region* (NLR) is characterized by the observation of narrow (forbidden) lines in a low-density environment. Based on the work of Cracco (2011), it is still unclear why the narrow line region forms. The velocities of orbiting matter are believed to be lower compared to the BLR.
Further out, the broad line region is surrounded by a dusty *torus*, preventing the observation of line broadening when observed edge-on. Liu & Zhang (2011) suggested that the formation of the torus is caused by radiative pressure from the accretion disk. This is in agreement with the model of Lawrence (1991), which suggests that the torus consists of shells of gas, surrounded by an outer dusty layer.

2.2.4 Jets - Collimated Relativistic Particle Outflows

Relativistic outflows of matter perpendicular to the accretion disk - so-called *jets* are observed in only a fraction of AGN. These outflows can form in objects that accrete matter and reach dimensions of up to Mpc-scales. AGN that show jets are called radio-loud, while AGN that do not harbor such outflows are known as radio-quiet. A morphological classification of radio-loud AGN is given by Fanaroff & Riley (1974) (see also Sect. 2.2.5).

2.2.4.1 Jet Formation and Structure

Blandford & Znajek (1977) showed that angular momentum can be extracted from the black hole, forming a so-called Blandford-Znajek jet. Within this jet, magnetic field lines are restricted by the accretion disk. The spinning black hole twists the magnetic field lines (under certain conditions) helically, collimating the particle outflow. If angular momentum is removed magnetically, this process is called the Blandford-Payne process (Blandford & Payne 1982). While the process of jet formation is still not fully understood, jet launching may be possible by transferring angular momentum to the disk, which drives a transient wind or a relativistic outflow from the magnetosphere. Variability in the observed multiwavelength flux of jets is suggested to be correlated to changing accretion rates (see Meier (2012) and Sect. 2.4.2). Various simulations of jet launching, collimation and propagation have been performed, ranging from magnetized jet models (Gaibler et al. 2009) to relativistic shock propagations on large scales (Tchekhovskoy et al. 2012; McKinney et al. 2012). High resolution radio observations indicate that AGN jets are already highly collimated at sub-parsec scales (Müller et al. 2011) and can stay collimated on Mpc scales, which is ten orders of magnitude larger than the SMBH. While the processes that confine the jet are highly debated, there is evidence that magnetic field lines and the ambient pressure play a leading role, while the acceleration of plasma can be explained by adiabatic expansion (Lyubarsky 2011). Blandford & Rees (1978) first suggested the formation and propagation of shocks in the collimated relativistic plasma of jets due to enhanced mass-injection. These shocks travel downstream and can explain the bright moving "blobs" visible in radio interferometry observations which propagate with apparent superluminal velocities (see Sect. 2.4). The creation of shocks is caused by a perturbation of the jet flow - an inhomogeneous injection of plasma or an interaction of plasma with material from the environment. The propagation of such a perturbation along the jet axis forms a shock front. When particles pass through this barrier, an acceleration increased their kinetic energy (Fermi 1949, see also Sect. 2.2.4.2).

2.2.4.2 Particle Acceleration within Jets

High energy observations of photons up to TeV energies indicate efficient particle acceleration mechanisms within jets. Theoretical models need to explain the observed spectra of AGN jets up to energies of $\sim 10^{20}\,eV$, similar to what has been observed from cosmic rays.

Fermi (1949) first described the stochastic acceleration of charged particles in interstellar clouds in order to explain the acceleration of cosmic rays. In the following description, a simplified description of this process is given.
A relativistic particle with an energy E_0 encounters a turbulent magnetic plasma cloud which moves with a velocity v_{cl}. Inside the cloud, the particle undergoes several elastic (energy and momentum conserved) scattering processes. The total energy of the particle after leaving the cloud is proportional to v_{cl} in the restframe of the cloud. When the energy of the particle at the point of exit is given by E_1, the total gain in energy can be written as:

$$\frac{\Delta E}{E} = \frac{E_1 - E_0}{E_0} = \gamma_{cl}^2 \left(1 + \beta_{cl}\right)^2 - 1 \equiv \zeta, \tag{2.4}$$

where $\beta_{cl} = \frac{v_{cl}}{c}$ and $\gamma_{cl} = \left(1 - \beta_{cl}^2\right)^{-1/2}$. For particles entering or leaving the cloud at any arbitrary angle θ, Eq. 2.4 will contain a term proportional to $\cos\theta\beta_{cl}$. Thus, the particle gains energy when it exits the cloud opposite to its initial direction ($\theta = \pi$), while the total energy gain is zero for particles moving in the same direction as the cloud ($\theta = 0$). There are also configurations in which the particle can lose energy, e.g. if it enters the cloud along the

cloud velocity. Since the particle direction inside the cloud is fully isotropic due to multiple scattering process, the exit angle θ_2 is random $\langle \cos\theta_2 \rangle = 0$. The entry angle θ_1, on the other hand, depends on the cloud velocity $\langle \cos\theta_1 \rangle = -\beta_{cl}/3$. The average energy gain per cloud encounter then becomes $\zeta \simeq 4/3\beta_{cl}^2$. It is important to notice that the energy gain per encounter in a stochastic acceleration process is constant, thus the particle energy E_n after n encounters is given by

$$E_n = E_0 \, (1+\zeta)^n \, . \tag{2.5}$$

To reach the energy E_n,

$$n = \ln\left(\frac{E_n}{E_0}\right) \, / \, \ln\,(1+\zeta) \tag{2.6}$$

encounters are necessary. During each scattering process the particle can escape the cloud with a probability P_{esc} and will stay at the energy reached in this moment. Consequently, the probability that a particle has reached an energy of E_n, so that it stays in the cloud long enough to undergo n scattering processes, is $(1-P_{esc})^n$. The number of particles with an energy larger or equal to E_n is proportional to the number of particles that remain in the acceleration regain long enough to undergo more than n encounters

$$N\,(>E_n) = N_0 \sum_n^\infty (1-P_{esc})^m \propto A \left(\frac{E_n}{E_0}\right)^{-\gamma}, \tag{2.7}$$

with $\gamma = \frac{P_{esc}}{\zeta}$. Stochastic acceleration thus generates power law spectra. As in this particular case, the power law index depends on β_{cl}^2. This process is called *second order Fermi acceleration*. In its raw form, this process has difficulties explaining the acceleration of particles within AGN jets, as the differential energy gain per time is given by

$$\frac{dE}{dt} = \frac{\zeta\, E}{T_{enc}}. \tag{2.8}$$

T_{enc} is the typical time per encounter. Thus, the acceleration time depends on the energy of the particle and reaching higher energies will take longer. To put this into context, the mean free path between two encounters is not shorter than $\sim 1\,pc$.
A more efficient acceleration mechanism can be achieved by the so-called *first order Fermi acceleration*, in which consequently the energy gain is directly proportional to the velocity of the shock $\zeta \propto \beta_S$. In this model, shocks are formed because of a discrepancy of the expansion velocity of a plasma that is larger than its sound velocity. According to Longair (2011), high energy particles with a velocity close to the speed of light are assumed to be present on both sides of the shock front. The shock itself propagates with the velocity β_S which is smaller than the particle velocity but much larger than the speed of sound in the ambient medium, resulting in a Mach number $\gg 1$. The advantage of this kind of acceleration principle is the small but constant energy gain a particle receives by crossing the shock either upstream or downstream. This energy gain is proportional to the velocity of the shock and is more efficient compared to *second order Fermi acceleration*, as no energy loss occurs. It can be shown that the average energy gain is proportional to the particle velocity and the velocity of the shock for a particle crossing the shock upstream to downstream, and vise versa. After crossing the shock the second time, the energy gain is doubled. After several shock interactions, Eq. 2.7 can be modified according to

$$N\,(E)\,dE \propto E^{-1+\left(\frac{\ln P_{esc}}{\ln \beta_S}\right)} dE, \tag{2.9}$$

with $-1+\frac{\ln P_{esc}}{\ln \beta_S} \approx -2$. Thus, non-relativistic shocks with magnetic fields parallel to the shock front and Mach numbers $\gg 1$ lead to power-law spectra with a spectral index of ≈ -2. These conditions are certainly not fulfilled in AGN. The maximum energy that can be achieved in the process of first order Fermi acceleration is given by

$$E_{max} \propto B\,\beta_S\,L, \tag{2.10}$$

where B indicates the magnetic flux density and L the scale of the shock front. The described principle is only valid for strong non-relativistic shocks and parallel magnetic field orientations. The acceleration of particles in ultra-relativistic shocks is described in e.g. Kirk et al. (2000) and Reville & Bell (2014).

2.2.4.3 Leptonic and (Lepto-) Hadronic Models

The multiwavelength emission of AGN typically shows two distinct emission humps (see Fig. 2.5), the origin of which can be explained by radiation processes such as synchrotron radiation or inverse Compton scattering described in Sect. 2.3 and 2.4.1. This characteristic emission pattern is used to further subclassify AGN into low-, intermediate- and high-peaked objects, based on the peak frequency of the low-energy component (Fossati et al. 1998). Changes in the spectral shape are often correlated to the strong variability observed in jets (see Sect.2.4.2). Such correlations provide important insights into the underlying physical process happening in jets. The low-energy hump is well explained by synchrotron emission of relativistic electrons (Sec .2.3.2), while to model the high energy emission, both leptonic and hadronic models can be used.
Pure leptonic models are successful in describing the variable emission of jets down to timescales of minutes. This fast variability and high bolometric luminosity indicates that the non-thermal emission is produced in a compact region, for which multiple-zone synchrotron models are necessary to describe the rapid change in luminosity (Krawczynski et al. 2004). Synchrotron Self-Compton (SSC) models use the synchrotron emission of relativistic electrons to scatter these photons up to higher energies by the inverse Compton effect (see Sect. 2.3.3), explaining the emission of the high-energy hump (Marscher & Gear 1985). In-jet shock models simulate the dynamics of electrons in shock fronts and are therefore capable of explaining the variability and the correlation between different wavelengths (Spada et al. 2001; Boettcher & Dermer 2010; Marscher & Gear 1985).
Hadronic models such as Mannheim (1993) and Mannheim (1995) are based on the acceleration of protons together with electrons within a jet. While the low-energy hump is still produced by synchrotron radiation of relativistic electrons, hadronic interactions lead to the production of pions via pγ interactions, resulting in a hadronic particle cascade (see Sec 2.3.4). Within these cascades, high-energy gamma-rays are produced. Furthermore, the interaction of charged pions leads to the generation of neutrinos. It can be shown that the maximum amount of expected neutrinos is correlated to the amount of photons produced at high energies (Mücke et al. 2003). Krauß et al. (2014) showed that the extragalactic neutrino flux measured by the IceCube Collaboration (2013) can be explained by blazars, a subclass of AGN (see.Sect. 2.4), while Kadler et al. (2016) indicated that the blazar PKS 1424−418 shows hints of correlation to the detection of an individual PeV neutrino event measured by IceCube (see Sect. 5).

2.2.5 Creating an Unified Picture

Historically speaking, AGN have been observed with various properties over the last century (see Sect. 2.1). Originally, properties like the strength of certain emission lines (Baldwin et al.

1981; Veilleux & Osterbrock 1987) resulted in different classification schemes. In general, Kellermann et al. (1989) showed that AGN can be divided into radio-loud and radio-quiet objects, based on their ratio of radio to optical flux. Radio-loud objects typically host relativistic jets (see Sect. 2.2.4), which are not observed in radio-quiet objects. Seyfert (1943) showed that these class of radio-quiet AGN, which are mostly found in spiral galaxies, can further be subdivided into two subclasses of so-called Seyfert galaxies based on their spectral properties and optical emission lines. As the work in this thesis is focused on radio-loud AGN, which are mainly found in elliptical galaxies, please refer to Longair (2011) for an overview of radio-quiet sources. In the following, a review of certain types of radio-loud AGN is given following Lawrence (1987), while the subclass of blazars will be discussed in more detail in Sect. 2.4.

Radio galaxies: Radio galaxies can be divided into *Broad Line Radio Galaxies* (BLRG) and *Narrow Line Radio Galaxies* (NLRG). A characteristic feature of radio galaxies is their extended radio emission, which can reach up to megaparsecs away from the central nucleus. Fanaroff & Riley (1974) defined a classification scheme that is based on the radio morphology, rather than on the optical properties of the galaxy. *Fanaroff-Riley Type 1* (FR1) galaxies are characterized by a dominant bright core and two jets, emanating from the core on both sides. The luminosity decreases along the jets with increasing distance. On the other hand, *Fanaroff-Riley Type 2* (FR2) galaxies are dominated by bright radio lobes, which are formed by the interaction of relativistic plasma from the jet with the intergalactic medium, and show a less bright central engine. The luminosity increases along the jets with increasing distance to the black hole. FR2 galaxies usually show a single-sided jet, which is relatively weak compared to FR1 galaxies.

Quasars: Quasars (Quasi Stellar Objects) or QSOs are strong radio sources with unresolved (star-like) optical counterparts. Schmidt (1963) demonstrated that quasars can be found at high redshifts. Large surveys indicate that they belong to the most luminous and distant AGN. Quasars are classified as compact objects, with a Seyfert-like optical spectrum and a point-like morphology. Schmidt & Green (1983) showed that these objects can be further categorized based on on their optical magnitude and typically exhibit either radio-loud or radio-quiet properties.

Antonucci & Miller (1985); Lawrence (1987) and Urry & Padovani (1995) introduced the idea that all the individually discovered classes of AGN are actually the same kind of objects observed under various circumstances. According to this model, all types of AGN consist of the same components such as a *supermassive black hole, accretion disk, broad line emission region, narrow line emission region, dust torus and jets*, while the broad population of objects can be explained by a projection effect based on the two parameters of radio-loudness and viewing-angle. Radio-loud AGN are characterized by the observation of a relativistic jet, while in radio-quiet objects, no jet is present. Depending on the viewing-angle, different parts of an AGN are observable. Figure 2.1 displays a schematic sketch of this projection effect. In Type 2 objects (Seyfert 2, NLRG, type 2 Quasars), which are seen at large viewing-angles, the emission from the central engine and the BLR is absorbed by the dust torus. Polarization measurements by Bianchi et al. (2012) confirmed the obscuring properties of a dusty torus. Type 1 AGN (Seyfert 1, BLRG, type 1 Quasars), on the other hand, are seen under a smaller viewing-angle, preventing obscuration by the dust torus, which makes the BLR visible. For even smaller viewing-angles, the highly beamed emission of blazars is explained by a quasi-alignment of the jet-axis with the line-of-sight of the observer and can outshine the other

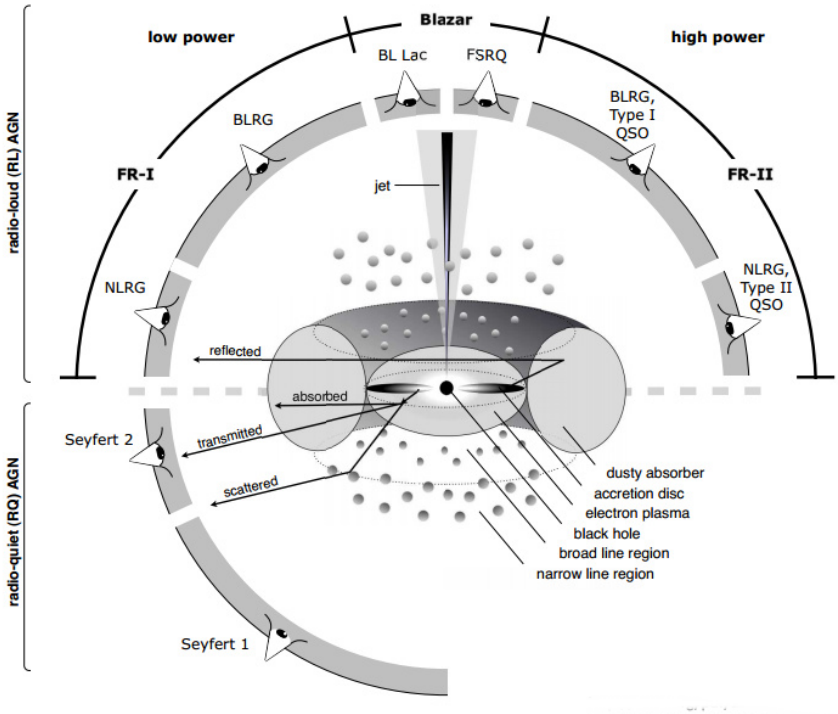

Figure 2.1: Schematic sketch of the unification model of Urry & Padovani (1995). According to the inclination angle and source luminosity, an AGN consisting of the standard components of a SMBH, accretion disk and jets, different classes of objects can be defined. Credit: Beckmann (2012)

components so that only a bright, star-like object is resolved. A summary of the unification scheme introduced by Urry & Padovani (1995) can be seen in Table 1., which today is widely accepted as the standard model of AGN.
While an orientation-based unification provides a basic model, it can't explain the difficulties in describing the discrepancy between radio-loud and radio-quiet sources, as well as the occurence of so-called radio-loud narrow-line Seyfert 1 galaxies (RL-NLS1). As a consequence, the standard model has to be extended by several additional parameters such as the black hole mass, luminosity, black hole spin and the accretion efficiency (Falcke & Biermann 1995; Laor 2000 and Meier 2002). Other unification schemes rather focus on the central absorber, differences in the AGN population and galaxy evolution (Heckman & Best 2014; Netzer 2015).

	radio-quiet	**radio-loud**
Type 1	Seyfert 1 radio-quiet Quasar	BLRG radio-loud Quasar (type 1)
Type 2	Seyfert 2 radio-quiet Quasar	NLRG (FR I & II) radio-loud Quasar (type 2)

Table 1: Unification scheme according to Urry & Padovani (1995).
The inclination angle increases from type 1 to type 2 galaxies.

2.3 Broadband Emission Processes

A detailed understanding of the underlying physical radiation and absorption process happening in AGN is crucial to model the observed broadband emission from the radio to γ-ray regime. This is rather complicated, as the observed radiation often consists of a superposition of different radiation processes, including several parts of the AGN such as the jets, accretion disk and host galaxy. Radiative processes can be differentiated into thermal and non-thermal processes based on whether or not the particle distribution is described by a Maxwell-Boltzman distribution. Especially for blazars (see Sect. 2.4), non-thermal processes dominate. Most of the emission processes have already been discussed in my Master's thesis (Kreter 2015). For completeness, important aspects will be presented again, using some of the parts verbatim.

2.3.1 Bremsstrahlung

When a charged particle is accelerated in an electric field of another charged particle, it emits radiation known as *free-free radiation* or *bremsstrahlung*. Let us assume an electron of charge $-e$ is accelerated in the electric field of a positive charged ion of charge Ze. As both particles are not bound before and after scattering, the appellation free-free radiation is used for this kind of emission. The second derivation of the dipole moment of this configuration is

$$\ddot{\vec{d}} = -e\dot{\vec{v}} \tag{2.11}$$

where the dipole moment is given as $\vec{d} = -e\vec{R}$, $\vec{R}$ is the distance between the electron and the ion and $\vec{v}$ the velocity of the electron. After taking the Fourier transformation of Eq. 2.11, one gets:

$$-\omega^2 d(\vec{\omega}) = -\frac{e}{2\pi}\int_{-\infty}^{\infty} \dot{\vec{v}} e^{i\omega t} dt \tag{2.12}$$

Please note that the Fourier transformation of $\ddot{\vec{d}}$ is $-\omega^2 d(\vec{\omega})$.
In order to simplify these calculations it may be useful to consider asymptotic limits of large and small frequencies. The electron is in close interaction with the ion over a time interval, which is of the order

$$\tau = \frac{b}{v} \tag{2.13}$$

the so-called *collision time*. Here, b is the impact parameter of the scattering process. The emitted energy per frequency ω is given by:

$$\frac{dE}{d\omega} = \begin{cases} \frac{2e^2}{3\pi c^3}\,|\Delta\vec{v}|^2 & \text{for } \omega\tau \ll 1 \\ 0 & \text{for } \omega\tau \gg 1 \end{cases} \tag{2.14}$$

For $\omega\tau \gg 1$, the exponential function in 2.12 oscillates rapidly, so the integral is small. For $\omega\tau \ll 1$, the exponential becomes unity. The change in velocity of the electron $\Delta\vec{v}$ is predominantly normal to its path, as the path is almost linear. Integrating the component of the acceleration normal to the path gives:

$$\Delta\vec{v} = \frac{Ze^2}{m}\int_{-\infty}^{\infty} \frac{b}{(b^2+v^2t^2)^{3/2}} dt = \frac{2Ze^2}{mbv} \tag{2.15}$$

For small angle scattering, the emitted energy from a single collision becomes:

$$\frac{dE(b)}{d\omega} = \begin{cases} \frac{8Z^2e^6}{3\pi c^3 m^2 v^2 b^2} & \text{for } b \ll \frac{v}{\omega} \\ 0 & \text{for } b \gg \frac{v}{\omega} \end{cases} \tag{2.16}$$

If one now expands the system to a medium with ion density n_i, electron density n_e and fixed electron velocity v, the total emitted energy per unit time per unit volume and per unit frequency interval is given by:

$$\frac{dE}{d\omega dV dt} = n_e n_i 2\pi v \int_{b_{min}}^{\infty} \frac{dE(b)}{d\omega} b \; db \tag{2.17}$$

where b_{min} is the minimum impact parameter. Please note that the infinitesimal area of a single ion is given by $2\pi b \; db$ and the electron flux (electrons per unit area per unit time) by $n_e v$. Finally, the exact result of this derivation can be expressed as:

$$\frac{dE}{d\omega dV dt} = \frac{16\pi e^6}{3\sqrt{3}c^2 m^2 v} n_e n_i Z^2 g_{ff}(v, \omega) \tag{2.18}$$

Here, $g_{ff}(v, \omega)$ is a correction factor or *Gaunt factor*, which depends on the frequency of the radiated photon and the energy of the electron (for a more detailed derivation, please refer to G.B. Rybicki 1985).
For relativistic velocities, this problem can be treated using the so-called *method of virtual quanta*. With no loss of generality, one can transform the previous calculations into the rest frame of the electron. In this new frame, the electron is at rest, while the ion is moving towards the electron. The electrostatic field of the ion is transformed into a mainly transverse pulse with $|B| \propto |E|$. This pulsed radiation then Compton scatters off the electron, which itself emits radiation. Transforming back to the rest frame of the ion, one obtains the emitted bremsstrahlung of the electron.
The opposite process to free-free radiation is *free-free absorption*. Here, an unbound electron absorbs a photon, previously emitted by bremsstrahlung. This absorption process can be characterized via a free-free absorption coefficient:

$$a_{ff} = \frac{4e^6}{3mhc}\left(\frac{2\pi}{3km}\right)^{1/2} T^{-1/2} Z^2 n_e n_i \nu^{-3} \left(1 - e^{\frac{-h\nu}{kT}}\right) \bar{g_{ff}} \tag{2.19}$$

where $\bar{g_{ff}}$ is the velocity averaged Gaunt factor. For $h\nu \gg kT$, the exponential factor is negligible, so $a_{ff} \propto \nu^{-3}$. For $h\nu \ll kT$ the Rayleigh-Jeans regime becomes important, so

$$a_{ff} = \begin{cases} \frac{4e^6}{3mhc}\left(\frac{2\pi}{3km}\right)^{1/2} T^{-1/2} Z^2 n_e n_i \nu^{-3} \bar{g_{ff}} & \text{for } h\nu \gg kT \\ \frac{4e^6}{3mhc}\left(\frac{2\pi}{3km}\right)^{1/2} T^{-3/2} Z^2 n_e n_i \nu^{-2} \bar{g_{ff}} & \text{for } h\nu \ll kT \end{cases} \tag{2.20}$$

2.3.2 Synchrotron Radiation

When charged particles are accelerated by the Lorentz force in a magnetic field $\vec{B}$, they emit radiation. The radiation of non-relativistic particles is known as *cyclotron radiation*, while for relativistic velocities this process is called *synchrotron radiation*. The Lorentz force is given by:

$$m\gamma\dot{\vec{v}} = \frac{q}{c}\left(\vec{v} \times \vec{B}\right) \tag{2.21}$$

where m is the mass of the electron, $\gamma = \left(1 - \frac{v^2}{c^2}\right)^{-1/2}$ the Lorentz factor, $\vec{v}$ the velocity of the charged particle, $\vec{B}$ the magnetic field and q the charge of the particle. Figure 2.2 illustrates the emission of synchrotron radiation cones of a charged particle moving on a helical path through a magnetic field. A characteristic frequency of the helical motion is the gyration frequency ω_g

$$\omega_g = \frac{qB}{\gamma mc} \tag{2.22}$$

where B and v stand for the absolute value of the vectors $\left(\text{e.g. } \left|\vec{B}\right|\right)$. Synchrotron emission shows a dipole characteristic in the electron rest frame.
The total energy loss of a charged particle getting accelerated in a magnetic field is:

$$\frac{dE}{dt} = -\frac{e^4 B^2}{6\pi\epsilon_0 m^2 c}\frac{v^2}{c^2}\gamma^2 \sin^2\alpha \tag{2.23}$$

where α is the *pitch angle* between the vectors of velocity and magnetic field. Finally, the radiation power of an electron in a magnetic field is given as:

$$P = \frac{4}{3}\sigma_T c\beta^2\gamma^2\frac{B^2}{8\pi} \tag{2.24}$$

where $\beta = \frac{v}{c}$. For high relativistic electrons, one can generally assume $\beta \approx 1$. Using the relation $E = \gamma mc^2$, one can show that the radiated energy of a single particle (Eq. 2.23) is proportional to m^{-4}, so synchrotron radiation of a massive particle like e.g. a proton is either low or negligible.
Non-thermal synchrotron radiation can be explained by electrons, following a power law spectrum according to:

$$n(\lambda)d\lambda = n_0\gamma^{-p}d\lambda \tag{2.25}$$

where $n(\lambda)$ is a non-thermal electron distribution and p the particle distribution index.
The total emission power is achieved by integrating over the electron distribution n

$$P_\nu = \int_1^\infty P_\nu(\gamma)n(\gamma)d\gamma. \tag{2.26}$$

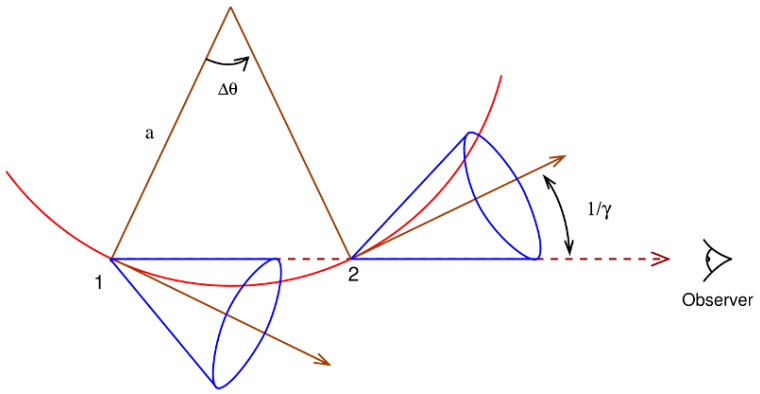

Figure 2.2: A Charged particle on its helical path through a magnetic field is emitting synchrotron radiation in a cone. Credit: G.B. Rybicki (1985)

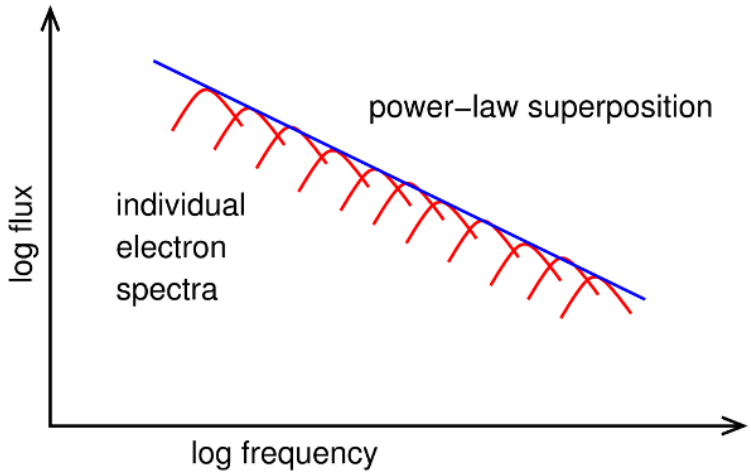

Figure 2.3: Superposition of single electron synchrotron spectra, resulting in a power law ($P_\nu \propto \nu^\alpha$). Credit: Shu (1991)

This equation shows that the integral of an electron power law distribution is again a power law (see Fig. 2.3):

$$P_\nu \propto \nu^\alpha \tag{2.27}$$

$$\text{where } \alpha = -\frac{p-1}{2}. \tag{2.28}$$

At low energies, *synchrotron self-absorption* becomes important. A photon emitted by a low energetic electron can be absorbed again by the same electron. Therefore, this changes the proportionality of the total emitted power for low frequencies:

$$P_\nu \propto B^{-\frac{1}{2}} \nu^{\frac{5}{2}} \tag{2.29}$$

Finally, synchrotron self-absorption is characterized by the self-absorption coefficient a_S

$$a_S \propto \nu^{-\frac{p+4}{2}} \tag{2.30}$$

To understand this broken power-law spectrum of synchrotron radiation, the optical depth τ_ν has to be defined:

$$\tau_\nu = \int_{s_0}^{s} a_S(s_1) ds_1 \tag{2.31}$$

where ds_1 is an infinitesimal distance the electron travels. If $\tau_\nu > 1$, the medium is called *optically thick*, while for $\tau_\nu < 1$ it is *optically thin*. The frequency near $\tau_\nu = 1$ is called the turnover frequency ν_t, as it defines the kink of the broken power law spectrum:

$$P_\nu \propto \begin{cases} \nu^{\frac{5}{2}} & \text{for } \nu < \nu_t, \\ \nu^{-\frac{p-1}{2}} & \text{for } \nu > \nu_t. \end{cases} \tag{2.32}$$

Please note that the slope of the optically thick part of the spectrum does not depend on the energy distribution of the electron, while the optically thin part is a function of the particle distribution index p.

2.3.3 Inverse Compton Scattering

At non-relativistic energies, Compton scattering transfers energy form the photon to the electron. In the case of highly relativistic electrons, *inverse Compton scattering* can lead to the opposite effect: a low frequency photon gains energy. In this case, the Thomson cross section can be applied. If one assumes the laboratory frame to be L and the rest frame of the electron to to be L', the energy of the photon in the rest frame of the electron will be small, compared to the rest energy of the electron $h\nu \ll mc^2$. Thus, the energy of the photon in L' is given by the relativistic Doppler shift formula:

$$h\nu = \gamma h\nu \left(1 + \frac{v_e}{c}\cos(\theta)\right) \tag{2.33}$$

where v_e is the velocity of the relativistic electron and θ is the angle between the direction of the photon and the incoming electron in the laboratory frame L. In the electron's rest frame L', this angle becomes small according to

$$\sin\theta = \frac{\sin\theta}{\gamma\left(1 + \frac{v_e}{c}\cos(\theta)\right)}. \tag{2.34}$$

As already mentioned, inverse Compton scattering can be treated as Thomson scattering in the electron rest frame, so one has elastic scattering with $E_2 \approx E_1$. Transferring this into the laboratory frame reads:

$$E_2 \approx \gamma^2 E_1. \tag{2.35}$$

The maximum energy gain of a photon is achieved by calculating the energy conservation in the laboratory frame L:

$$E_2 \leq E_1 + \gamma m_e c^2 \tag{2.36}$$

where the maximum change in the photon frequency is:

$$\Delta\nu \leq \gamma m_e c^2 h^{-1} \tag{2.37}$$

Finally, the total power of the inverse Compton scattering (also-called the Luminosity L_{IC}) depends on the density of photons n_{ph} available for scattering:

$$L_{\mathrm{IC}} \propto n_{\mathrm{ph}}\gamma^2 E_1. \tag{2.38}$$

If one then considers a more complex and detailed description (compared to Eq. 2.38), which includes the energy density function of the photon field U_{ph}, as well as a relativistic Doppler shift, the luminosity becomes:

$$L_{\mathrm{IC}} = \frac{4}{3}\frac{v_e^2}{c}\sigma_T\gamma^2 U_{\mathrm{ph.}} \tag{2.39}$$

In case the condition $h\nu \ll mc^2$ is not fulfilled in the electron rest frame, the assumed elastic Thomson scattering can no longer be assumed. Consequently, Klein-Nishina effects have to be considered, which include a dependency on the photon energy and scattering angle. Further information about this extended model can be found in Blumenthal & Gould (1970).

2.3.4 Hadronic Radiation Processes

Mannheim & Biermann (1989, 1992) showed that the high energy emission observed from jets can be explained by hadronic processes, which require the presence of protons within the jet. Due to the high rest mass of the proton, an efficient shock-front acceleration mechanism is needed (see Sect. 2.2.4.2). Accelerated protons can interact with the ambient matter or UV seed photon field from the accretion disk, torus, or BLR (Bednarek & Protheroe 1999; Atoyan & Dermer 2003), producing hadronic showers in the process of *pion photoproduction* such as:

$$p + \gamma \rightarrow \Delta^+ \rightarrow \begin{cases} \pi^0 + p \\ \pi^+ + n. \end{cases} \tag{2.40}$$

The resulting decay products further decay into:

$$\begin{aligned} \pi^0 &\rightarrow \gamma + \gamma \\ \pi^\pm &\rightarrow \mu^\pm + \nu_\mu \ (\text{ or } \bar{\nu_\mu}) \\ \mu^+ &\rightarrow e^+ + \bar{\nu_\mu} + \nu_e \\ \mu^- &\rightarrow e^- + \nu_\mu + \bar{\nu_e}. \end{aligned} \tag{2.41}$$

Both leptonic and hadronic processes are capable of modeling the high energy emission observed from jets (see Sect. 2.2.4.3). The expected neutrinos would be an unambiguous tracer for hadronic processes happening in jets, and further prove that AGN contribute to the flux of cosmic rays (Hillas 1984). To estimate the contribution of generated neutrinos, the ratio of cross sections $\sigma_{\pi^0 p}$ and $\sigma_{\pi^+ n}$ has to be calculated (B. Povh 1999). If one assumes a system $|JM\rangle$ of coupled isospins j_1 and j_2, the probability for the states $|j_1 m_1\rangle$ and $|j_2 m_2\rangle$ is given by the square of the Clebsch Gordan coefficients. For the decay of the Δ^+, this reads:

$$\frac{\Delta^+ \rightarrow \pi^0 + p}{\Delta^+ \rightarrow \pi^+ + n} = 2. \tag{2.42}$$

Neutral pions are two times more likely than charged pions (assuming only decays of leading order). The neutrino flux produced via pion photoproduction is expected to be correlated to the bolometric high-energy electromagnetic flux. In the case of isospin symmetry (equal amount of neutral and charged pions), it is possible to estimate the maximum neutrino flux according to Kadler et al. (2016) to $F_\nu \leqq F_\gamma$. Monte-Carlo simulations by Mücke et al. (2000) confirm this simplified approach. Details of the expected neutrino spectrum, however, are highly dependent on the assumed model parameters, typically covering an energy range of 100 TeV to 10 PeV.
Proton-proton interactions, on the other hand, lead to a fraction of generated pions of:

$$p + p \rightarrow \begin{cases} p + p + \pi^0 & \text{fraction } \frac{2}{3} \\ p + n + \pi^+ & \text{fraction } \frac{1}{3}. \end{cases} \tag{2.43}$$

At high energies, charged kaons (K^+, K^-) start to contribute to the neutrino production, decaying into either charged pions (28%) or directly into muons (64%). In addition, next to leading order decays contribute to the neutrino production channels. For more information, please refer to B. Povh (1999).

2.4 Blazars

The subclass of radio-loud AGN exhibit highly relativistic particle outflows perpendicular to the accretion disk, the so-called jets (see Sect. 2.2.4). Objects in which the viewing angle (the angle between the line of sight and the jet) is small are called *blazars* and are of specific interest in this work. Blazars are characterized by their high luminosity, caused by Doppler boosting, as well as their non-thermal emission ranging from the radio to γ-ray regime and rapid variability. Significant flux changes can occur on timescales of minutes to months or even decades. The word blazar was introduced by Ed Spiegel as a joke at the Pittsburgh Conference on BL Lac Objects in 1978, combining the words quasar and 'blazing' to emphasize the strong, boosted emission and variable nature of this class of sources.
Blazars can be further subdivided into BL Lac objects, as well as Flat-Spectrum Radio Quasars (FSRQ). While typical BL Lac spectra are dominated by a featureless non-thermal continuum, FSRQs are known for broad emission lines at optical wavelengths and a flat radio spectrum. The source BL Lacertae, first discovered by Hoffmeister (1929) as an irregular variable star in the Milky Way, the extragalactic origin of which was later confirmed by Oke & Gunn (1974), became the prototype and namesake of the corresponding blazar subclass.
In addition, blazars can be classified into low, intermediate and high peaked blazars (LSP, ISP, HSP), based on their synchrotron peak frequency in the νF_ν space (Padovani & Giommi 1995; Abdo et al. 2010a).

2.4.1 Broadband Spectral Energy Distribution

The overall observed broadband emission of blazars is made up of the different radiating components such as the accretion disk, the dust torus, the broad and narrow line region, and the jets. Due to orientation and relativistic beaming effects (see Sect. 2.2.5), not all components are equally represented in the observed spectrum. However, in radio-loud objects, the synchrotron emission (see Sect. 2.3.2) and inverse Compton radiation (see Sect. 2.3.3) from the jet are clearly dominant. Multiwavelength observations yield broadband spectra and help to disentangle different spectral components in order to study the corresponding emission mechanisms (see Sect. 2.3).
Gubbay et al. (1969) first measured an *apparent superluminal motion* in an AGN jet, which was later confirmed by e.g. Cohen et al. (1977); Jorstad et al. (2001), giving evidence of the relativistic nature of extragalactic jets. The effect of apparent superluminal motion can be explained by a projection effect of a constant and finite light evolution (see Fig. 2.4). Let's consider a bright feature propagating along the jet axis with velocity $\vec{v}$, which is seen under the small viewing-angle ϕ. Two distinct light signals are emitted from the feature at times t_0 and t_1, while propagating along the jet axis. The observer detects the signals separated by:

$$\Delta t = \left(1 - \frac{v}{c}\cos\phi\right)\Delta t_{\text{emit}} \tag{2.44}$$

where Δt_{emit} is the time interval between the emission of both light signals. If one considers the observed distance to be $\Delta x = v\Delta t_{\text{emit}}\sin\phi$, the observed velocity is given by

$$v_{\text{obs}} = \frac{v\sin\phi}{1 - \frac{v}{c}\cos\phi}. \tag{2.45}$$

The observed velocity strongly depends on the viewing-angle ϕ and can reach velocities of $v_{\text{obs}} > c$ for small angles ϕ. To derive the real velocity, this angle has to be known.
The Doppler factor D:

$$D = \frac{v_{\text{obs}}}{v_{\text{emit}}} = \frac{1}{1 + \frac{v_{\text{obs}}}{c}\cos\phi} \tag{2.46}$$

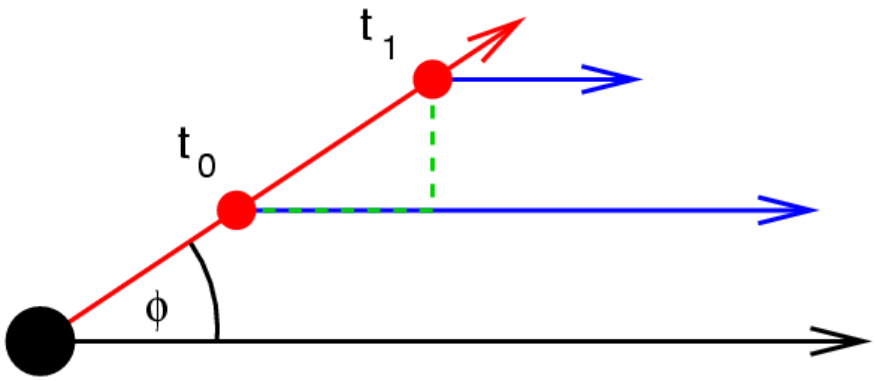

Figure 2.4: Sketch of the projection effect of superluminal motion. A bright feature propagates along the jet axis (red) with velocity $\vec{v}$. The jet is seen under the viewing-angle ϕ. The observer only takes projection images of the jet. Credit: M. Kadler

is an important quantity in the description of jet behavior. The effect of Doppler boosting describes the increase/decrease of an observed flux density due to an emitting feature moving at relativistic velocities close to the line of sight. The non-thermal continuum of blazars is often described by a power-law spectrum. It can be shown that for a flux density $F_\nu \propto \nu^{-\alpha}$, the quantity $F_\nu \nu^3$ is Lorentz invariant (G.B. Rybicki 1985), while Lind & Blandford (1985) showed that the observed intensity is given by:

$$F_\nu^{\text{obs}} = D^{3-\alpha} F_\nu^{\text{emit}}. \tag{2.47}$$

This so-called jet one-sidedness is typically seen in high resolution radio observations. The opposite, often fainter jet is known as the "counterjet".
The spectral energy distribution (SED) of blazars (see Fig. 2.5) shows a characteristic double-humped structure in the νF_ν representation with maximums in the optical and between the hard X-ray or γ-rays (Chang 2010). It is well established that the low-energy hump is due to synchrotron radiation of relativistic electrons (see Sect. 2.3.2). Both leptonic processes such as inverse Compton scattering (see Sect. 2.3.3) and hadronic processes like pion photoproduction (see Sect. 2.3.4) can explain the radiation measured in the high-energy hump, while their exact contributions still remain an open question (e.g. Abdo et al. 2011b; Böttcher et al. 2013; Finke et al. 2008; Mücke et al. 2003).
Fossati et al. (1998) studied a complete sample of blazar SEDs and found a correlation between the source luminosity and the shape of the SED (see Fig. 2.5 and Ghisellini et al. 1998). Less luminous sources tend to have a higher synchrotron peak than brighter sources. Furthermore, a correlation between both peaks has been found, resulting in a shifting in frequency of the double-humped shape. This shifting seems to depend on the source bolometric luminosity, where a brighter source is linked to a smaller synchrotron peak frequency. The exact mechanisms responsible for this blazar sequence are still a matter of actual research, assuming two distinct source populations (Meyer et al. 2011).

2.4.2 Variability of Blazars

Blazars are highly variable sources, the emissions from which are mutable over the entire electromagnetic spectrum. The variability timescales range from fast variability on the order of minutes to days to long outburst periods that can last several months, depending on the observing wavelength. Flaring models assume a change in the polarization angle, which is due

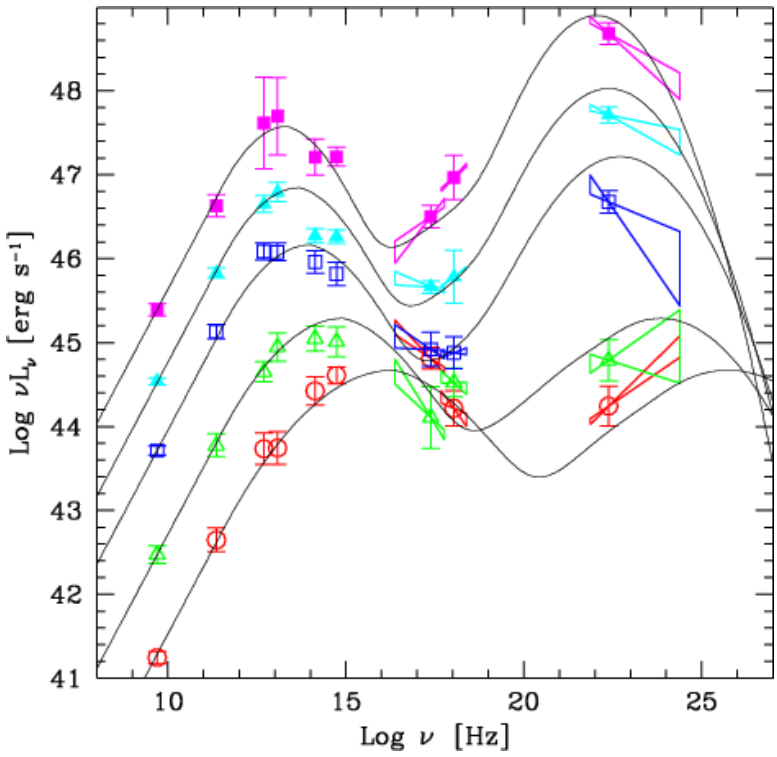

Figure 2.5: Blazar spectral energy distribution (SED) and blazar sequence. A correlated between bolometric luminosities and peak frequencies can be seen. Credit: Fossati et al. (1998)

to highly ordered magnetic fields (Abdo et al. 2010c) or the ejection of a radio component. Other models compare the variability observed in AGN to the transitions seen in galactic black holes, where disk instabilities lead to a growth of matter of the central accreting disk, which then can be injected into the jet.
The broadband emission processes are still not fully understood. While the low-energy hump of a stationary broadband blazar SED is relatively well explained by synchrotron radiation (see Sect. 2.3.2), both purely leptonic models such as the Synchrotron Self-Compton (SSC) (Ghisellini et al. 2010b and references therein) and lepto-hadronic models (see Sect. 2.2.4.3, Sect. 2.3.4) and references therein) can explain the high energy emission measured from blazars. As the modulation of stationary spectral energy distributions is degenerated, studying the variability patterns of these sources can provide strong constraints on the radiative processes happening in blazars (see e.g. Spanier & Weidinger 2012).
In SSC models, the high energy emission is produced by inverse Compton scattering (see Sect. 2.3.3) of synchrotron photons, responsible for the low-energy hump. Since the same electron population is responsible for both emission humps, a strong correlation between simultaneous observations in different wavelengths is expected (see e.g. Weidinger & Spanier 2011). In lepto-hadronic models, the high energy emission can either be dominated by proton-synchrotron emission or hadronic interactions (see Sect. 2.3.4), depending on the ratio of electron and proton luminosities (Mücke et al. 2000).

So-called "orphan flares" occur when there is no correlation of the observed flux increase to other energy ranges. In the case of Neronov et al. (2012), an orphan γ-ray flare was observed, while a lack in radio observations could be explained by an optically thick emission

regain (see Sec 2.3.2). Some quasi-periodic oscillations have been traced back to binary black hole systems (Rieger & Mannheim 2003). First hints of periodic modulations in high energies were observed in PG 1553+113 and Mrk 501 (Ackermann et al. 2015a; Kranich 2001 and Osone 2006), while optical periodicity with a period of 12 years has been measured from OJ 287 (Sillanpaa et al. 1988). Since no clear detection of periodic behavior could be achieved so far, long-term monitoring programs are needed to clarify the binary nature of these kind of sources and to study the physical processes that cause these modulations and formation of sources in the first place. In the following sections, the flaring characteristics of blazars on different time scales is discussed based on the sources Mrk 421 and 4C +01.28.

2.4.2.1 A Multiwavelength View of the HSP Blazar Mrk 421

The HSP target Mrk 421 is one of the closest and best studied blazars in the sky. Numerous multiwavelength campaigns (e.g. Abdo et al. 2011b,a, Fossati et al. 2008, Aleksić et al. 2015, Baloković et al. 2016) have targeted the broadband emission and variability behavior for more than a decade. Both flaring and quiescent states are well described by leptonic and lepto-hadronic models. Such broadband studies provide intense investigations and insights on the emission processes responsible for different flaring states. However, a detailed study of the spectral evolution of the broadband spectrum using simultaneous multiwavelength data during a flaring state has not been performed yet. Fig 2.6 displays three simultaneous light curves of Mrk 421 taken from December 2015 until mid June 2016, using *Swift*/XRT, *Fermi*/LAT and FACT[5] data. The source is highly variable, showing flares on timescales of days to weeks. Intervals of enhanced emission throughout different wavelengths have been reported to a broad astronomy community (e.g. Biland et al. 2016). The strongest variability is seen in the TeV and X-ray light curve, with flares in the order of days, while the γ-ray emission varies on longer timescales. In addition to the longterm variation, daily flares with much smaller flux amplitude are visible in the γ-ray light curve.
Several flares in the TeV regime are accompanied by activity in the X-ray and γ-rays, which may suggest correlated emission. Kreikenbohm (2018) performed a systematic correlation analysis using discrete correlation function (DCF) according to Edelson & Krolik (1988). During the entire monitoring campaign, the X-ray and TeV emission as well as the X-ray and γ-ray flux seems to be correlated (at a $3\,\sigma$ level), which suggests an underlying longterm variation in these energy ranges. The γ-ray and TeV emissions do not correlate during the 2015 TeV flare seen in Fig. 2.6, but shows hints of correlation during the rest of the monitoring time. The missing correlation in the 2015 flare indicates that the γ-ray emission is additionally effected by another process, not visible at TeV energies. This lag of correlation further strengthens the stochastic nature of flares and outbursts and provides further evidence for a disentanglement between different emission regions.
To study the spectral behavior of blazars, simultaneous broadband SEDs are crucial to distinguish between different emission models, especially in the context of neutrino associations. Such simultaneous SEDs have been used to calculate the neutrino expectation of bright blazar flares, performed in Sect. 5.1.

2.4.2.2 IntraDay Variability (IDV) of the Source 4C +01.28

The blazar 4C +01.28 is a strong high energy emitter, showing a large number of very short periods of activity in the *Fermi*/LAT γ-ray regime (see e.g. Krauss & Carpenter 2014). With

[5]The First G-APD Cherenkov Telescope (FACT) is a very high energy (VHE) gamma-ray telescope located on the Canary Island of La Palma, Spain. It is optimized for long-term monitoring of AGN at TeV energies for already more than six years. For further details please refer to Anderhub et al. (2013).

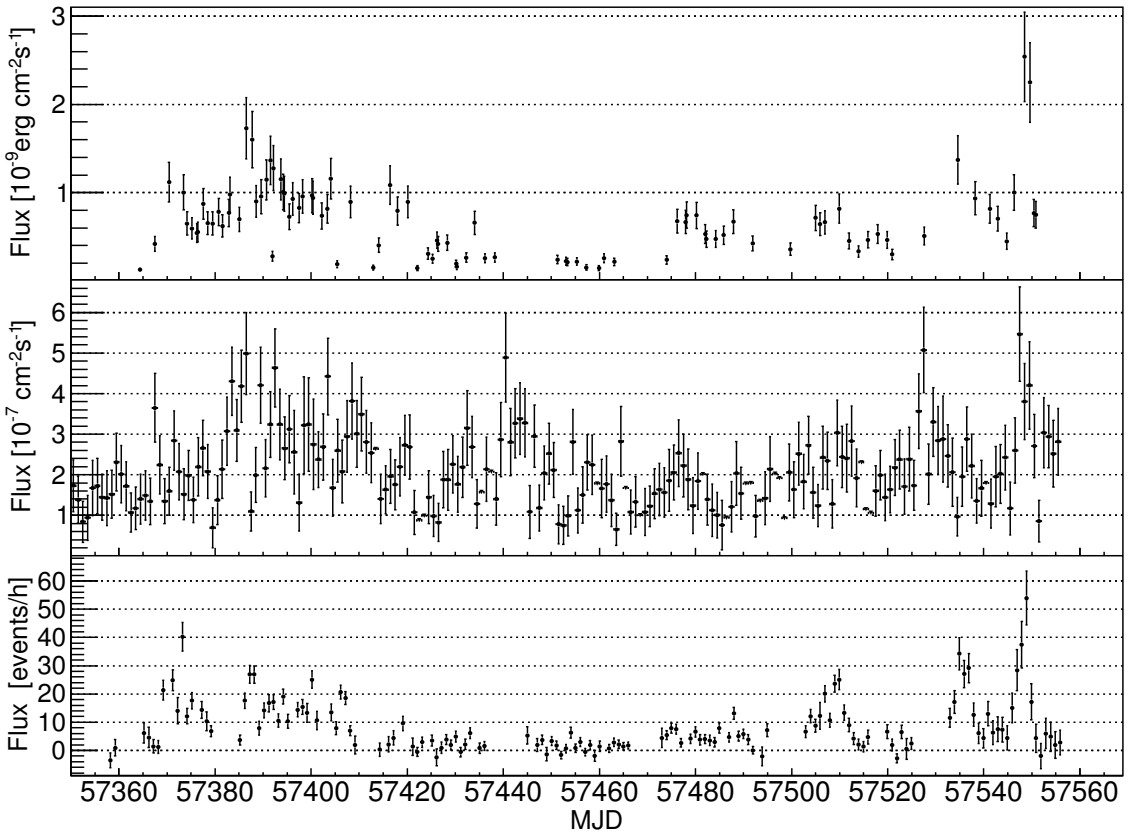

Figure 2.6: *Swift*/XRT (Top), *Fermi*/LAT (Middle) and FACT (Bottom) light curve of Mrk 421 taken in a time from December 2015 until mid June 2016. The TeV and X-ray emission exhibits variability on the daily time scales, while the γ-ray light curve varies over much longer durations. Credit: Dorner (2016)

variability timescales of less than a day, this source is of particular interest as such fast flux variations indicate a very compact emission region in addition to the steady long-term variability. Variation in blazars can be in generally divided into three classes. *IntraDay Variability (IDV)*, also known as intra-night-variability or micro-variability (Wagner & Witzel 1995), occurs on timescales of several minutes up to the course of less than a day. *Short Term Variability (STV)* can range from days to several months, while *Long Term Variability (LTV)* can show timescales of up to years (Gupta et al. 2004).
Models to explain the IDV range from jet based models which assume either helical instabilities in the jet (Marscher & Gear 1985) or turbulences behind the shock (Marscher et al. 1992) over accretion disk based models (e.g. Zhang & Bao 1991) to plasma instabilities within the jet that result in a highly polarized spine-sheath structure of the innermost region in the close vicinity of the SMBH (e.g. Blandford & Payne 1982; Blandford & Znajek 1977). Since the launch of *Fermi* in 2008, IDV has been detected in several blazars (see e.g. Foschini et al. 2011; Ackermann et al. 2016b).

3 Multiwavelength and Multimessenger Observations

Besides the model predictions introduced in Sect. 2, it is necessary to study the universe as an astrophysical laboratory in order to understand the fundamental physical principles from the accretion of matter, over the formation of jets, up to the existence of high energy cosmic-rays and neutrinos. As AGN emit throughout the entire electromagnetic spectrum, which covers many orders of magnitude, multiwavelength and essentially multimessenger observations are crucial to draw a complete picture. The opacity of Earth's atmosphere is not constant across the spectrum. While optical light reaches the surface of the Earth and allows life to evolve, high energy photons in the X-ray or γ-ray regime are absorbed by the atmosphere. High-energy astronomy therefore requires space-based observations (see Sect. 3.2 and 3.3). Apart from Imaging Air Cherenkov Telescopes (IACTs) (see Sect. 3.4) such as e.g. MAGIC, VERITAS, H.E.S.S. and the planned Cherenkov Telescope Array (CTA) these instruments detect high energy cosmic-rays ($\gtrsim 100\,\mathrm{GeV}$) indirectly via particle cascades forming in the atmosphere. Particles within these cascades travel faster than the speed of light in the ambient medium, emitting optical Cherenkov light (see Sect. 3.5.3.1) which can be detected by the IACTs. Water Cherenkov Telescopes such as HAWC, however, are based on the same indirect detection principle, but use large water tanks as an ambient medium for the detection of particle cascades.

As AGN are variable sources throughout different wavelengths, one of the largest challenges are simultaneous observations at several different wavelengths. A set of different instruments, including ground-based and space based facilities, is mandatory to achieve broadband observations of AGN. This can become difficult, as different instruments rely on completely different observation techniques and often do not observe the entire sky simultaneously. While the sample of possible targets in a satellite mission is often constrained by the vicinity of the Sun, Moon or Earth to the target of interest, IACTs and optical telescopes highly depend on the local environment conditions, for example bad weather and daylight. On the other hand, water cherenkov, as well as radio telescopes can even observe during rainy daytime. Organizing broadband multiwavelength observations requires an enormous effort and has therefore only been done for a limited number of sources such as e.g. Mrk 421, Mrk 501 and 3C 279 (Tagliaferri et al. 2008; Abdo et al. 2011b; Hayashida et al. 2015; Aleksić et al. 2013).

While "traditional" astronomy detects photons, the field of multimessenger astronomy induces the traces of additional messengers. Neutrino astronomy, especially, determines the interactions of high energy neutrinos in large fields ($\sim \mathrm{km}^3$) of instrumented volume (see Sec 3.5). As neutrinos only couple to the weak force, their interaction cross section is low, and thus large volumes are needed to increase the chance of interaction. When high energy neutrinos, which are believed to originate from hadronic interactions (see Sec 2.3.4 and 3.5.2), interact with matter, they form secondary particles such as electrons, muons or taus (depending on the initial neutrino flavor). These secondary particles travel faster than light in the ambient medium, which leads to the emission of Cherenkov light. Neutrino detectors, such as KM3NeT (see Sec 3.5.4.2) or IceCube (see Sect. 3.5.4.3) use photomultipliers to catch these optical photons and reconstruct the trajectory and energy of the secondary particle and the neutrino. The IceCube Collaboration (2013) gave evidence for the existence of an extragalactic high energy neutrino flux, while its origin and potential counterparts are still unknown and a topic of current research and this thesis.

The existence of gravitational waves was predicted by Einstein (1918) as a direct consequence of his general theory of relativity. Gravitational waves are caused by local perturbations in spacetime and can at most propagate with the speed of light. Gravitational wave detectors use the concept of laser interferometry to respond on infinitesimal small variations in space-

time. With detectors on both coasts of the US (LIGO) and in Italy (VIRGO), which are basically Michelson interferometers with arm lengths of several km, this forms a global grid of gravitational wave detectors that can even resolve time delays in the propagation of gravitational waves between different detectors. Gravitational waves are caused by accelerating masses such as binary systems, merger events or supernovae. The first direct detection of a binary black hole merger was made by Abbott et al. (2016), while the first multimessenger observations of a neutron star merger have been obtained only one year later in 2017 (Abbott et al. 2017).
In this section, I will give an overview of different instruments used to obtain multiwavelength as well as multimessenger data relevant to this work. Many of the instruments presented here have already been used in my Master's thesis (Kreter 2015). For completeness, important aspects will be discussed again, using some of the parts in verbatim.

3.1 The TANAMI Program

The TANAMI program (Tracking Active Galactic Nuclei with Austral Milliarcsecond Interferometry) is a multiwavelength program to monitor relativistic jets in AGN of the southern sky[6], complementary to the MOJAVE project on the northern hemisphere (Lister & Homan 2005). TANAMI monitors more than 90 sources, most of them are blazars (Ojha et al. 2010; Kadler et al. 2015) from the radio to γ-ray regime. Very Long Baseline Interferometry (VLBI) radio observations are performed every ~ 4 months at 8.4 GHz and 22.3 GHz, complemented by monitoring at frequencies between 4.8 GHz and 40 GHz with the Australian Telescope Compact Array (ATCA) and the Ceduna telescope (see Fig. 3.1). Multiwavelength data are obtained by virtue of several successful proposals with REM (optical), *Swift* (optical/UV and X-ray), *Fermi*/LAT and other instruments. Multimessenger projects with ANTARES, KM3NeT and IceCube are ongoing (see e.g. Krauß et al. (2014); Kadler et al. (2016) and Sect. 5).
The heart of the TANAMI program targets the parsec-scale structure of AGN ($< 30°$ declination) in the milli-arc-second-regime. High resolution radio observations are only possible by using VLBI. One of the core properties of a radio telescope is its angular resolution. According to the Rayleigh criterion, this is given by:

$$\sin(\alpha) \approx 1.22 \frac{\lambda}{d}. \tag{3.1}$$

Here, α is the angular resolution, λ the wavelength at which the observation is performed and d the diameter of the radio telescope. In the case of VLBI, d corresponds to the baseline of the array, which is the longest distance between two telescopes. For the use of VLBI, it is important for all telescopes to observe simultaneously. Roughly spoken, a VLBI image is generated by measuring the source brightness, in the first step using each telescope individually. Due to Earth's rotation and a discrepancy in the distance to the source for each individual antenna, an instrumental delay has to be corrected. Then, the VLBI image is obtained by applying a deconvolution of a complex visibility function in the so-called (u,v)-plane. For further information, please refer to Burke & Graham-Smith (2009).

3.2 X-Ray Astronomy

Earth's atmosphere is opaque to photons above UV energies, as photoabsorption by oxygen molecules takes place. This property is beneficial for life to evolve, but requires space-based observatories in order to study the universe at these energies. The first X-ray source *Scorpius*

[6] http://pulsar.sternwarte.uni-erlangen.de/tanami

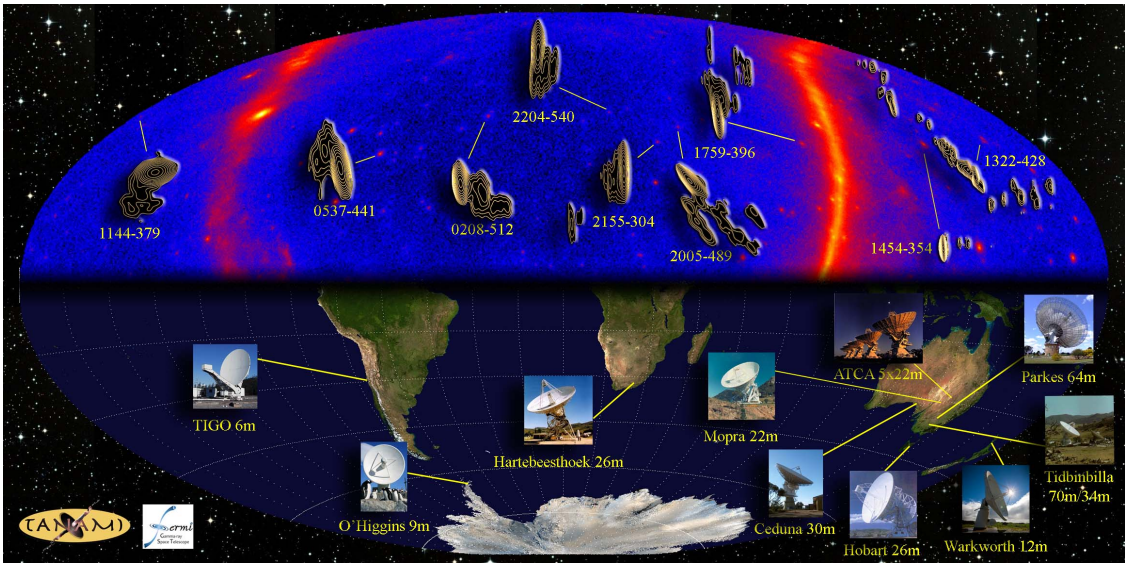

Figure 3.1: Collage to illustrate the TANAMI source sample and the VLBI monitoring program. Top: Southern-Hemisphere γ-ray skymap observed by *Fermi*/LAT (in celestial coordinates). One clearly sees the galactic plane and several extragalactic sources, which are associated with radio observations by TANAMI. Bottom: TANAMI telescopes located on Earth's southern Hemisphere. Credit: M. Kadler

X-1 was accidentally discovered by Giacconi et al. (1962, 1964), while searching for fluorescent X-rays from the Moon. *UHURU*, the first X-ray satellite launched in 1970, discovered many new X-ray sources (Jagoda et al. 1972) and opened a window to the by that time unknown high energy universe. Many missions followed afterwards. Today, there are several satellites including *Swift* (Gehrels et al. 2004), the X-ray Multi-Mirror Mission-Newton (*XMM-Newton*, Jansen et al. 2001), *Suzaku* (Mitsuda et al. 2007) and the *Chandra* X-ray observatory (Weisskopf et al. 2000) successfully operating. In this section, an overview of the detection principle of X-rays and one of the major missions in X-ray astronomy is given, following Bradt (2004); Janesick (2001) and Aschenbach (1985).

3.2.1 Wolter Telescopes

Optical telescopes focus incoming light to a focal point by the reflection on parabolic mirrors. Snell's law states that the ratio of the angles of incidence and refraction is equivalent to the ratio of refractive indexes of two media, according to

$$\frac{\sin \alpha_1}{\sin \alpha_2} = \frac{n_2}{n_1}. \tag{3.2}$$

Total reflection ($\alpha_2 = 90°$) can happen when light propagates from a medium with a higher refractive index to a medium with a lower refractive index ($n_1 > n_2$). The refractive index $n = \frac{c}{v}$ describes how light propagates through a medium with phase velocity v. One can also express the refractive index $n = \sqrt{\varepsilon\mu}$ in terms of the dielectricity constant ε and permeability of the material μ, while for most materials $\mu \sim 1$. In the field of X-ray astronomy, the complex refractive index

$$\bar{n} = 1 - \delta - i\beta \tag{3.3}$$

usually is only slightly below unity. The real part δ indicates the refractive index, which depends on the classical phase velocity, while the complex part β is called extinction coefficient

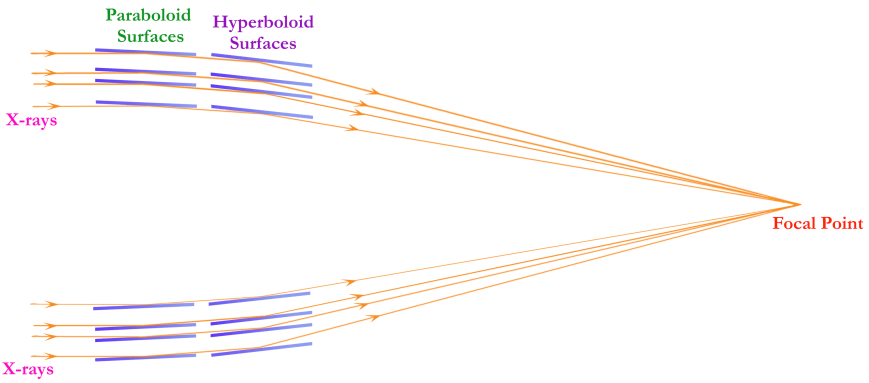

Figure 3.2: Sketch of a Wolter type I mirror configuration which illustrates the concept of grazing, the incidence reflection and focusing of X-rays. Reflection on both parabolic and hyperbolic mirrors is required to make an image. To increase the effective area of the instrument, several mirror shells are nested. Credit: http://chandra.harvard.edu

and introduces an attenuation to the propagating wave in the medium. The critical angle for X-ray reflection therefore is given as

$$\Theta_c = \sqrt{2\delta} = \sqrt{\frac{r_0 \lambda^2 n_e}{\pi}} \sim 1^\circ, \tag{3.4}$$

with the classical electron radius $r_0 \sim 10^{-15}\,\mathrm{m}$, the electron density n_e and $\lambda \sim 1\,\mathrm{nm}$ is the wavelength of the incoming X-ray light. As the dielectricity constant depends on the atomic number Z, the refraction index can be increased by using materials with a higher density. "Grazing incidence telescopes" typically use gold and iridium to achieve the reflection of photons at small angles. The Chandra mirrors, for example, have been coated with iridium, while the XMM-Newton mirrors use gold instead. X-rays can be reflected by parabolic mirrors, while for space-based observatories, the focal length sets a limiting factor due to restricted rocket lengths. Wolter telescopes (Wolter 1952a,b) combine both parabolic and hyperbolic mirrors to shorten the focal length to $\sim 10\,\mathrm{m}$, due to a double reflection of X-ray photons. In order to increase the effective area of the instrument, several mirror shells are nested (see Fig. 3.2). The Nuclear Spectroscopic Telescope Array (NuSTAR), launched in 2012, uses a stowed mast to extend to its full length of $\sim 10\,\mathrm{m}$ after reaching space. After the telescope has been successfully focused, X-ray photons can be detected by a specific charge-coupled device (CCD).

3.2.2 X-Ray Charge-Coupled Device (CCD)

In principle, X-Ray Charge-Coupled Devices (CCDs) work similarly to optical CCD sensors, but they require a larger volume due to the higher energy of X-ray photons and the larger penetration length. CCDs are solid state devices with diameters in the order of μm. They consist of a pn-junction of doped semiconductors, coated by an isolating layer, often silicon dioxide. On top, electrodes made of polysilicon are placed to make them conductive. The base material is usually silicon, often doped with phosphorus and boron. When an X-ray photon incidents the device, it passes through the electrodes and isolating layer and is absorbed in the silicon, creating a cascade of $\sim$ 1000 secondary electrons. This allows for a significantly better energy resolution compared to proportional counters, which produce less secondary

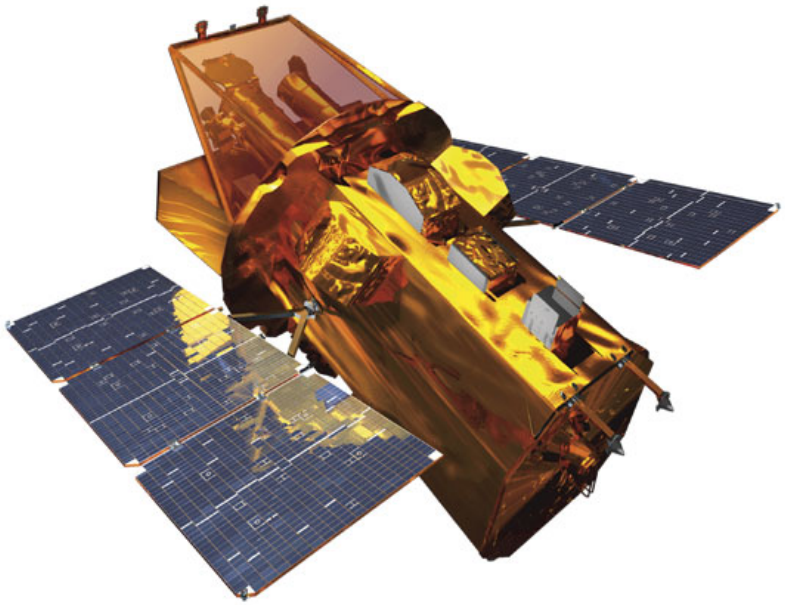

Figure 3.3: The Neil Gehrels Swift Observatory
Credit: NASA E/PO, Sonoma State University, Aurore Simonnet

electrons for a single X-ray photon. When a given CCD pixel is read out before another photon arrives, the measured charge in that pixel approximately represents the energy of the incident X-ray. In contrast to optical CCDs, devices used in X-ray astronomy generate images that account for the spectral distribution of measured X-ray photons. When several photons hit a pixel before readout, pile-up occurs. In this case, the combined energy of all photons is read out. Several satellite missions have invented different techniques to prevent pile-up from happening, like the "windowed timing mode" on board of *Swift*. In general, during pile-up, the CCD is only read out partially over a longer time. For further details, please refer to Bradt (2004).

3.2.3 The Neil Gehrels Swift Observatory

The Neil Gehrels Swift Observatory (former Swift Gamma-Ray Burst mission) post mortem named after Dr. Neil Gehrels to honor his outstanding contributions to the mission and the field of X-ray astronomy, was launched in November 2004. Operated by the NASA Goddard Space Flight Center, *Swift's* main mission is to search for Gamma-Ray Bursts (GRBs) and to perform follow-up observations at optical, ultraviolet and X-ray wavelengths (Gehrels et al. 2004). By observing $\sim$ 80 to 90 GRBs per year[7], *Swift* spends the majority of time in observing non-GRB sources such as blazars, pulsars and supernovae. Observational time can be requested via a Guest Investigator (GI) program, a Target of Opportunity (ToO) program and a Fill-In program. The GI program allows a wide scientific community to apply for observational time to perform a dedicated project, including financial resources. The ToO program has a limited amount of time to observe non-GRB sources, while observations can be performed on short notice once the target is in an active state. The Fill-In program is used to request time for a larger sample of sources which then are used to fill gaps between scheduled observations or large slewing angles. TANAMI sources are often observed by *Swift*, following the Fill-In program. *Swift* is equipped with the *Ultraviolet and Optical Telescope (UVOT)*,

[7] http://swift.gsfc.nasa.gov/archive/grb_table/

the *X-ray Telescope (XRT)* and the *Burst Alert Telescope (BAT)*, which in the following will be discussed in more detail.

3.2.3.1 The Ultraviolet and Optical Telescope (UVOT)

The Ultraviolet and Optical Telescope (UVOT) is a diffraction-limited 30 cm Ritchey-Chrétien reflector, equipped with two micro-channel plate intensified CCD detectors which were originally developed for the XMM-Newton mission. It consists of a filter wheel, allowing for simultaneous optical observations with different filters as well as ultraviolet data taking. As optical afterglows of GRBs tend to fade rapidly, UVOT telemeters first images within 50 seconds to the ground, which are then automatically posted on the Gamma-ray Coordinates Network (GCN) by the *Swift* Operations Center. This allows for a fast ground-based identification of the optical counterpart and follow-up observations of the selected region in the sky. For sources with a redshift between $\sim 1.3 < z < 5$, measurements of the photometric redshift are provided by UVOT. For more details, please refer to Roming et al. (2005).

3.2.3.2 The X-ray Telescope (XRT)

The X-ray Telescope (XRT) is designed to study the X-ray afterglow of GRBs by measuring light curves, spectra and fluxes in an energy range of $0.2 - 10\,\mathrm{keV}$. The XRT consists of a grazing Wolter type I mirror (see Sect. 3.2.1) with 12 concentric gold-coated mirrors and an X-ray CCD (see Sect. 3.2.2) in the focal plane. The CCD contains a three-phase frame-transfer device, using high resistivity silicon and an open-electrode structure (Holland et al. 1996). Data taking is possible within $20 - 70$ seconds from burst discovery and can continue for weeks. The XRT is capable of automatically choosing between two read out modes to ensure data taking over a wide energy range of variable X-ray sources. In the Imaging Mode, an integrated image of the total deposited energy per pixel is produced, locating the position of bright sources. No spectroscopic measurements are possible, however, the photon-counting mode uses sub-array windows to determine source fluxes, taking full spectral and spatial information into account. For further details, please refer to Burrows et al. (2000) and Hill et al. (2000). An overview of the XRT data extraction and analysis is given in Sect. 4.1.

3.2.3.3 The Burst Alert Telescope (BAT)

The main purpose of the Burst Alert Telescope (BAT) is to detect and localize GRBs by constantly monitoring one third of the sky with arcminute accuracy. A detection by BAT triggers an automatized pointing of the spacecraft on the position of the transient event for follow-up observations, interrupting ongoing observations. BAT consists of a coded aperture mask detector and a large area solid state detector array to detect weak bursts, with a total detection area of $52000\,\mathrm{cm}^2$ and a field-of-view (FoV) of 1.4 sr. Since the BAT field of view includes the FoVs of UVOT and XRT, long duration multiwavelength data can be taken simultaneously. In between trigger events of GRBs, BAT performs an all-sky survey at hard X-rays in an energy range of $14 - 195\,\mathrm{keV}$ (Oh et al. 2018). For further details, please refer to Barthelmy et al. (2005).

3.3 Gamma-Ray Astronomy

High energy γ-rays are produced in extreme environments like the vicinity of black holes. As opposed to charged particles such as cosmic-rays, γ-rays are not affected by magnetic fields and thus point back to their origin. Absorption by the extragalactic background light (EBL),

however, reduces the amount of high energy γ-rays from distant sources (H.E.S.S. Collaboration et al. 2013). Space-based missions are required, due the the shielding properties of Earth's atmosphere at high energies. Since the launch of the first γ-ray mission *Explorer 11* in 1961, several satellites with improved detection techniques have followed and opened a new window to the extreme universe. The Energetic Gamma Ray Experiment Telescope (EGRET, Thompson et al. (1993)), onboard the *Compton Gamma-Ray Observatory (CGRO)*, observed in an energy range from 30 keV to 30 GeV and made several major discoveries as highlighted in Gehrels & Shrader (2001). EGRET's all-sky survey revealed the highly dynamic and variable nature of the γ-ray sky and established blazars as the largest subsample of γ-ray emitting sources but also raised further questions on the nature of most detected but unidentified γ-ray emitters and the origin of this emission. Therefore, a more efficient instrument was requested in order to investigate the γ-ray sky. The *Fermi Gamma-ray Space Telescope* (see Fig. 3.4) was launched in June 2008 from Cape Canaveral and is still operational today. In the following section, an overview of the Fermi mission, its instruments and the properties of the γ-ray sky is given. Details on the data reduction and analysis techniques are given in Sect. 4.2.
Originally named *Gamma-ray Large Area Telescope (GLAST)*, the *Fermi Gamma-ray Space Telescope* was renamed shortly after launch in order to honor the work of Enrico Fermi. The instruments on board *Fermi* are the Large Area Telescope (LAT) and the Gamma-ray Burst Monitor (GBM). The main purpose of Fermi is to answer some of the long-standing questions about the γ-ray sky, such as the acceleration and formation of jets, the processes which cause GRBs, the composition of dark matter and the longterm evolution of γ-ray sources.
The aim of the GBM is to study Gamma Ray Bursts and transient sources in an energy range of 10 keV to 20 MeV, complemented by the LAT at higher energies. With a larger field of view than the LAT and a trigger time on the order of minutes, the GBM processor automatically calculates preliminary spatial and spectral information, which is transferred to the ground station for follow-up observations. For more details about the detector properties and operation of the GBM, please refer to Meegan et al. (2009).

3.3.1 The *Fermi* Large Area Telescope (*Fermi*/LAT)

The Large Area Telescope (LAT) is the primary instrument on board of *Fermi*, monitoring the entire γ-ray sky in an energy range from $\sim$ 20 MeV to $\sim$ 300 GeV every three hours (Atwood et al. 2009). Preliminary light curves of the brightest blazars are publicly available[8]. The LAT is an electron-positron pair conversion detector, as pair creation is the dominant energy loss mechanism at these energies. Incident photons first pass through an anticoincidence detector (ACD), which rejects charged particles such as the cosmic-ray background. Due to conservation of momentum, pair conversion requires heavy nuclei. Photons therefore have to pass through a thin conversion layer made of a high-Z material such as tungsten. The trajectories of the resulting electron-positron pairs are then measured by a tracker which consists of silicon strips placed between the conversion layers to optimize for angular resolution and conversion efficiency. The energy of the penetrating electron-positron pairs is measured in the calorimeter, which has to be large enough to contain the entire resulting electromagnetic shower. The LAT consists of 16 towers in a 4×4 array, each equipped with a tracker, calorimeter and data acquisition module, covered by the anticoincidence shield. In the following section, an introduction of the installed detector components will be given based on Atwood et al. (2009).

[8] http://fermi.gsfc.nasa.gov/ssc/data/access/lat/msl_lc/

Figure 3.4: Top: Artist illustration of the Fermi Gamma-ray Space Telescope.
Bottom: The satellite shortly before launch with the Large Area Telescope (LAT) on the top, the Gamma-ray Burst Monitor (GBM) at the bottom left side and the solar panels folded on the bottom right side of the instrument. Credit: Top: NASA/Sonoma State University, Aurore Simonnet, Bottom: NASA, DOE

3.3.1.1 Anticoincidence Detector (ACD):

As the cosmic-ray flux exceeds the γ-ray signal by several orders of magnitude, the primary purpose of the ACD is to provide an efficient background rejection. For this reason, charged particles entering the field of view of the LAT from any direction are identified by the ACD with an (area averaged) efficiency of 0.9997. The ACD consists of plastic scintillators, chosen as the simplest, most reliable and well-understood detector technology, which also provides much experience in space operation. The ACD is divided into segments (so-called "tiles") in order to reduce false positive detections and covers the top and four sides of the LAT with a total active area of $\sim 8.3\,\mathrm{m}^2$. Unfortunately, it is not possible to reject all events reconstructed in the calorimeter and trigger, which in addition also create a signal in the ACD. Incident γ-rays can cause a major signature within the ACD due to a backsplash effect. In this case, isotropically distributed secondary particles (with an energy of $\sim 100 - 1000\,\mathrm{keV}$) created in the electromagnetic shower of the incident γ-ray can Compton scatter in the ACD, leading to a false positive detection. On the other hand, hadronic cosmic-ray interactions in an inactive part of the ACD can cause a signal in the calorimeter and tracker without an ACD signature. For further details about the ACD, please refer to Moiseev et al. (2007).

3.3.1.2 Precision converter-tracker:

The aim of the tracker unit is to convert incident γ-ray photons into electron-positron pairs and to track their trajectories. Within each tower, the converter-tracker consists of 18 x,y tracking planes, arranged along the z-axis, measuring the position of charged particles passing through the detector. Each tracking plane consists of two electron-positron sensitive detectors which record the passage of charged particles in both directions. Two layers of silicon strips are used, each capable of determining the penetration point within the plane, allowing for a three dimensional track reconstruction. A conversion-foil made of the high-Z material tungsten is placed on top of each tracking unit, increasing the chance of pair conversion before entering the silicon strips. Using four-vector notation, the conservation of energy-momentum before and after the interaction reads:

$$p_\gamma = p_{e^-} + p_{e^+} + p_R. \tag{3.5}$$

Here, p_R indicates the recoil of the nucleus. In a semi-classical approximation, the energy-momentum of an electron is given by $(p_{e^-})^2 = -m_e^2 c^2$, while for the massless photon $(p_\gamma)^2 = 0$. This leads to:

$$0 = (p_{e^-} + p_{e^+} + p_R)^2 \tag{3.6}$$

However, for high-Z materials, the nucleus recoil is negligible ($p_R \approx 0$), so that Eq. 3.5 becomes

$$2\left(\gamma^2 - 1\right) m_e^2 c^2 \left(1 - \cos\theta_e\right) = 0. \tag{3.7}$$

This approximation requires the electron-positron pair to be emitted in the same direction ($\theta_e \approx 0$).
Based on the penetration points throughout different tracking planes, the trajectory of electron-position pairs in the detector can be reconstructed. By taking the orientation of the satellite into account, which is saved in the spacecraft file, the original direction of the incident γ-ray can be determined. The uncertainty of the reconstructed direction is characterized by the instrument's point spread function (PSF). The PSF describes the detector response to a perfect point source. Several effects, such as multiple scattering events or Bremsstrahlung, can have a negative impact on the PSF, while the detector design tries to compensate for these

contributions by e.g. minimizing the gap between the conversion foils and the photo sensitive silicon strips. Thin conversion foils are used to reduce multiple scatter events, while on the other hand also limits the pair conversion efficiency. To provide a large enough effective area for γ-ray photons, the converter-tracker is split into a "front" and a "back" region. The "front" region contains the first twelve tracking planes which are equipped with thin conversion foils to optimize the PSF for low energies. The "back" region, consists of the last four tracking planes and is instrumented with ~ 6 times thicker conversion foils to maximize the effective area of high-energy photons ($> 1\,\mathrm{GeV}$), while only reducing the angular resolution by less than a factor of two. Gamma-ray emission from a typical blazer is balanced between the "front" and "back" tracker regions, although this clearly depends on the individual source characteristics. For further details of the precision converter-tracker, please refer to Atwood et al. (2009) or Atwood et al. (2007).

3.3.1.3 Calorimeter:

Each precision converter-tracker is followed by a calorimeter unit, which consists of 96 CsI(Tl) crystals. The crystals are arranged horizontally in eight layers of twelve crystals each and each crystal is optically isolated. In the vertical direction, each layer is orientated orthogonal in respect to the previous layer, forming a total depth of 8.6 radiation lengths. The primary purpose of the calorimeter is to measure the energy deposit caused by electromagnetic showers due to resulting electron-positron pairs and to image the shower development profile. The monitoring of the shower profile provides an important background discriminator. For a measured shower, each CsI(Tl) crystal measures three spatial coordinates, two due to its physical location within the unit, while the third (more precise) coordinate is determined by measuring the light yield asymmetry at the ends of each crystal along its long dimension. This segmentation allows for a sufficient spatial imaging of the shower and determination of this direction, leading to a positional resolution within the detector from several millimeters (for low-energy deposits of $\sim 10\,\mathrm{GeV}$) to to a fraction of a millimeter (for large energy deposits of $> 1\,\mathrm{GeV}$). Although the calorimeter is only equipped with a depth of 8.6 radiation lengths, its longitudinal segmentation allows energy measurements up to a TeV. The initial energy of an electron-positron pair is derived by fitting the measurement to an energy dependent analytical description of the mean longitudinal shower profile. The resulting energy resolution is limited by fluctuations in the shower. For further details, please refer to Atwood et al. (2009) and Johnson et al. (2001); Ferreira et al. (2004).

3.3.1.4 Long-term operation:

After almost 10 years of operation, *Fermi*/LAT has provided a unique view of the variable γ-ray sky. Thanks to its continuous monitoring, *Fermi*/LAT has discovered hundreds of new γ-ray sources and enabled the study of flaring activity of already detected sources. Due to its wide coverage, *Fermi*/LAT can monitor a large amount of different source classes, such as galaxies and AGN, pulsars and neutron stars, the Sun and Moon, while also providing long-term observations of the galactic and extragalactic diffuse emission. Continuous observations and a rapid analysis are guaranteed by the *Fermi* Flare Advocate service (also known as Gamma-ray Sky Watcher, FA-GSW) (Ciprini et al. 2013). The FA-GSW service provides a quick look analysis and review of the γ-ray sky observed daily by the LAT. Potential new gamma-ray sources, interesting transients and source flares that exceed a flux threshold of $10^{-6}\,\mathrm{ph\ cm^{-2}s^{-1}}$ are communicated to the external scientific community (e.g. Kreter & Buson 2016; Kreter 2018). *Fermi*/LAT observations are crucial in the field of multimessenger astronomy, contributing to some of the major discoveries in the current century, such as the

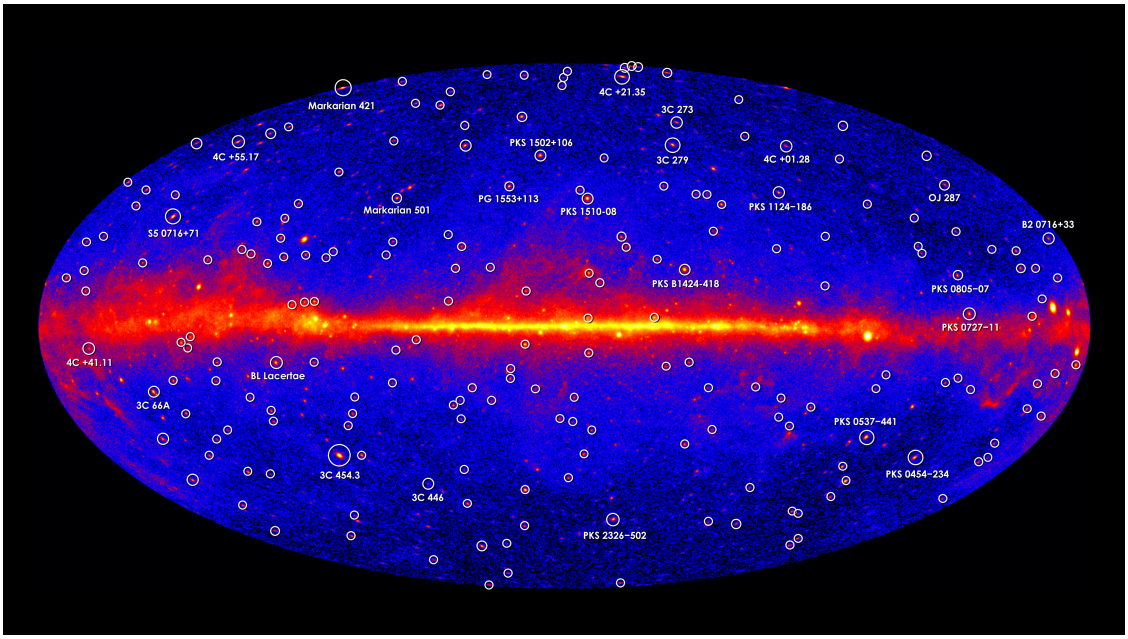

Figure 3.5: *Fermi*/LAT all-sky γ-ray survey after five years of operation in galactic coordinates. Data are shown with an energy $\geq$ 1 GeV, where light colors indicate higher flux. The γ-ray sky is dominated by emission from the galactic plane, which is composed of of a point source component and diffuse emission. Off the plane, blazars (marked with circles) clearly dominate. Credit: NASA, DOE; Fermi/LAT Collaboration

first direct detection of a neutron star merger (Abbott et al. 2017) and the detection of the first neutrino point source (IceCube Collaboration et al. 2018; IceCube Collaboration 2018). A more complete overview of the science performed by *Fermi*/LAT can be found online[9].

3.3.2 *Fermi*/LAT Performance

In order to achieve the best performance of the LAT, the design was optimized before launch and tested with beams at various accelerator facilities. Monte Carlo simulations were performed to estimate and optimize detector response, sensitivity, background rejection and other properties. In addition to a detailed understanding of the installed hardware, new instrument response functions are provided regularly, allowing for an improvement of e.g. the event classification, background rejection and energy and angular resolution. With a field of view of $\sim 20\,\%$ of the sky and an (energy dependent, see Fig. 14 and 15 in Atwood et al. 2009) effective area of $\sim 8000\,\mathrm{cm}^2$, *Fermi*/LAT mainly operates in all-sky survey mode, covering the entire sky every three hours. This results in a nearly uniform coverage of the γ-ray sky and a continuous monitoring of individual sources. The *Fermi*/LAT γ-ray all-sky map after five years of operation is shown in Fig. 3.5 in galactic coordinates. The angular resolution of LAT is both energy and direction dependent (see Fig. 17 and 18 in Atwood et al. 2009). The $1\,\sigma$ containment radius for the reconstruction of a single photon is $3.5\,^\circ$ at 100 MeV, going down to $0.15\,^\circ$ at 10 GeV. The latest instrument performance information can be found online[10].

[10] http://www.slac.stanford.edu/exp/glast/groups/canda/lat_Performance.htm

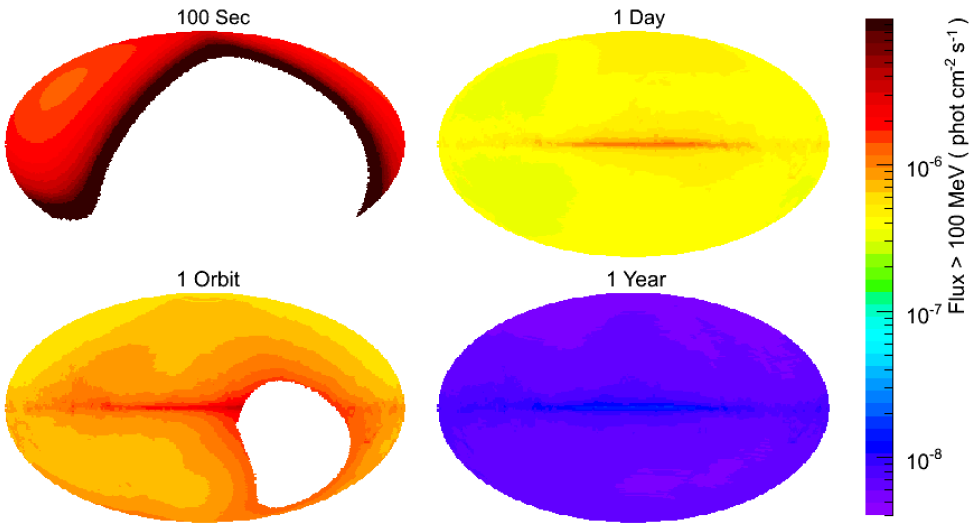

Figure 3.6: *Fermi*/LAT sensitivity for different exposure times in Galactic coordinates. In all-sky survey scanning mode, almost uniform exposure is achieved after about two orbits ($\sim 3\,\mathrm{h}$). Credit: Atwood et al. (2009)

3.3.3 *Fermi*/LAT Observation Modes

One of the main challenges of the LAT is the observation of the entire sky in a uniform way within short time scales. To achieve this goal, beside the large field of view, the LAT is mostly operated in an all-sky scanning mode, using rocking movements of the telescope[11]. Orbiting at an altitude of about 565 km with an inclination of about 25.5°, one circumnavigation takes about one and a half hours. In two subsequent orbits, the pointing positions of the instrument alters between 35° from the zenith towards north and south, respectively. In this way, uniform coverage of the entire sky is achieved after only about three hours. In this time interval, each point in the sky achieves an instrument exposure of about thirty min. Figure 3.6 shows the all-sky sensitivity for different exposure times. When requested, ToO pointing observations are possible as well.

3.3.4 *Fermi*/LAT Data Processing

Fermi/LAT data is processed both onboard and ground-based. The primary objective of onboard processing is to provide a rapid detection and localization of a γ-ray candidate such as a GRB, transient source or flaring blazar, and to encourage further follow up observations. The onboard science analysis pipeline consists of algorithms to select γ-ray events, reconstruct the direction and localize the origin of these events. While the onboard analysis uses a simplified algorithm with pre-defined parameters to search for γ-ray candidates, the efficiency for successfully reconstructing event directions is about 25 % of what can be achieved by dedicated ground-based processing. Triggered source candidates are posted on the GCN[12] to encourage rapid follow-up observations of other instruments.
For the automatized ground-based analysis pipeline, LAT science data are transfered to the Instrument Science Operations Center (ISOC) every $\sim$ three hours (two orbits), 24 hours per

[11] On 16 March 2018, a failure in the solar panel drive caused *Fermi*/LAT observations to be interrupted for about three weeks. From 4 April 2018, *Fermi*/LAT is taking data with an adjusted rocking strategy.
[12] https://gcn.gsfc.nasa.gov/

day in approximately 1.5 GB data packages. Pattern recognition and reconstruction algorithms are used for background rejection and to determine the direction, arrival time and energy of detected γ-ray events. Efficient data processing is achieved by parallel processing of events on more than 100 computing cores, finishing one data set in about one to two hours, before the next downlink arrives. In this way, keeping all events processed requires about 150 TB of disk space per year. These *level-1* data are then transfered to the *Fermi* Science Support Center (FSSC)[13] and made publicly available typically within three to four hours after the arrival of unprocessed data at the ISOC.
Time critical analysis tasks, such as the detection and characterization of transients, GRBs or AGN flares, are performed on level-1 data by the *Automated Science Processing (ASP)* pipeline. Blazars and other transient sources are monitored for flaring activity on daily and weekly time scales. The flux and upper limit evaluation uses an unbinned likelihood analysis with a simplified model file (see Sect. 4.2.4 for more details of the exact analysis) for a defined list of monitored sources[14]. This list is not static, as new transients or flaring sources will be added once found and reported via GCN notices or Astronomers Telegrams[15] (ATELs). The latency of updating daily light curves of monitored sources is typically less than six hours after level-1 data are available. For further details, please refer to Atwood et al. (2009).

3.4 TeV - Cherenkov Astronomy

Earth's atmosphere is opaque to radiation of most wavelengths. Ground-based instruments are therefore restricted to the radio and optical regime. High energy (HE) γ-ray photons in an energy range of $\sim$ 20 MeV to $\sim$ 300 GeV are monitored by space-based missions like *Fermi*/LAT. Very high energy (VHE) photons at energies between $\sim$ 50 GeV to $\sim$ 50 TeV can be measured indirectly by ground-based *Cherenkov telescopes*, which use the atmosphere as part of the detector. The underlying concept of Imaging Air Cherenkov telescopes (IACTs) will be introduced, following Weekes (2003).

3.4.1 Air Shower Development

Within the atmosphere, γ-rays can suffer different energy loss mechanisms (see Sec 2.3). From MeV energies onwards, electron-positron pair conversion clearly dominates. After approximately one radiation length, secondary electron-position pairs are produced by Bremsstrahlung due to the interaction with molecules in the atmosphere. After one more radiation length, the resulting secondary electron-positron pairs each produce another radiation pair, resulting in the formation of an electromagnetic cascade. This process continues until the averaged energy of the particles reaches a limit at which energy losses through ionization and Bremsstrahlung are equal. At this point, the air shower has reached its maximum expansion.
Showers initiated by cosmic-rays (e.g. protons) form the dominant background of ground-based Cherenkov telescopes, which require Monte Carlo simulations to model the expected TeV emission from a given source. Hadronic showers consist of a combination of electromagnetic showers and pion decays (see Sect. 2.3.4), typically forming a much wider air shower. When the primary particle is energetic enough, the resulting secondary particles in both kind of showers can travel faster the speed of light in air, resulting in the emission of Cherenkov radiation (see Sect. 3.5.3.1), upon which the fundamental detection principle of IACTs is based.

[13] https://fermi.gsfc.nasa.gov/ssc/
[14] http://fermi.gsfc.nasa.gov/ssc/data/access/lat/msl_lc/
[15] http://www.astronomerstelegram.org/

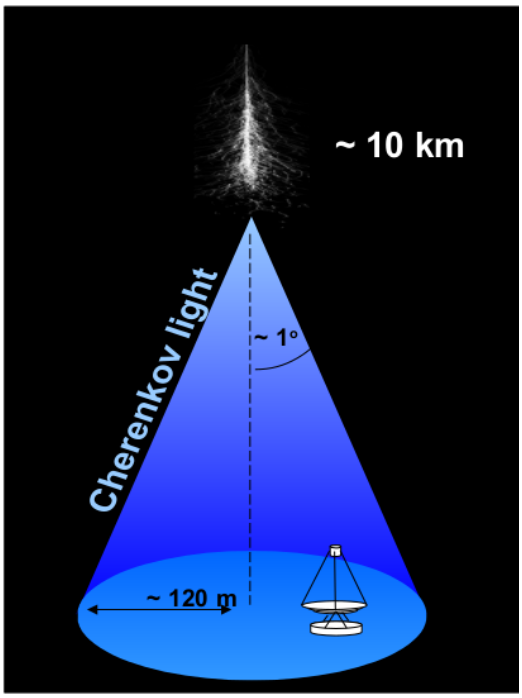

Figure 3.7: Schematic diagram of the detection principle of IACTs. A γ-ray photon enters the atmosphere and produces an electromagnetic shower, which reaches its maximum at about 10 km height. Secondary particles cause Cherenkov light flashes, that develop into a cone with radius of $\sim$ 120 m. IACTs placed inside this light pool can detect these flashes and reconstruct the direction and energy of the primary particle. Credit: University of Durham, Centre for Advanced Instrumentation.

3.4.2 Imaging Air Cherenkov Telescopes (IACTs)

An Imaging Air Cherenkov Telescope detects Cherenkov light produced by energetic particles in the atmosphere. Thus, the atmosphere is an essential part of the instrument. IACTs consist of light collecting mirrors which focus optical light onto a camera connected to a fast readout system. A schematic diagram of this detection principle is shown in Fig. 3.7. The mirrors are typically made of glass, coated with anodized aluminum to prevent degeneration over time, and are arranged in a parabolic tessellated array, the so-called Davis-Cotton design (Davies & Cotton 1957) to maximize the light collecting area. Due to the large Cherenkov light pool of $\sim$ 120 m, several telescopes can be placed within this pool, limiting the light collecting area only to the dimensions and number of telescopes. In order to detect faint and short Cherenkov flashes in the atmosphere, sensitive and fast cameras are required. Photomultipliers (PMTs) are widely used, as they are sensitive enough to detect even single photons, but require dark environments to function properly. Geiger-mode avalanche photodiodes (G-APDs), introduced by the FACT project (Anderhub et al. 2013), provide more stable detector performance and allow for observations during bright light conditions like the full moon. However, IACTs sites are typically in dark and remote places.

Photon and hadron induced showers cause different event signatures in the camera. While leptonic showers created by photons generally show single elliptical shapes, hadronic showers are more irregular and randomly orientated. Ring-like structures are created by muons in hadronic showers close to the ground. Using a pair or an array of Cherenkov telescopes significantly reduces the muon background, which usually only triggers one telescope. Stereo-

scopic observations allow for a three-dimensional reconstruction of the shower and thus, an improved flux sensitivity and better energy and angular resolution. Currently, there are four IACTs globally in operation: the Major Atmospheric Gamma-Ray Imaging Cherenkov Telescope (MAGIC) at La Palma in Spain (Aleksić et al. 2012), the High Energy Stereoscopic System (H.E.S.S.) located near the Gamsberg mountain in Namibia (Aharonian et al. 2006a), the Very Energetic Radiation Imaging Telescope Array System (VERITAS) on Mount Hopkins in Arizona in the US (Krennrich et al. 2004) and the First G-APD Cherenkov Telescope (FACT) on La Palma in Spain next to the MAGIC telescopes (Biland et al. 2014). With the Cherenkov Telescope Array (CTA), the next generation of ground-based IACTs is currently under construction and will be located on La Palma in Spain and close to Paranal in Chile (Acharya et al. 2013).

3.5 Neutrino Astronomy

The first evidence of a high energetic neutrino flux at PeV energies was found by IceCube Collaboration (2013); Aartsen et al. (2013a, 2015a). Since then, only a handful of such extremely energetic neutrinos have been found and, due to their high rareness, nicknamed "Ernie" and "Bert". These events are spatially consistent with six TANAMI blazars (see Sect.3.1) which represent the brightest γ-ray sources in the corresponding neutrino fields. By studying their multiwavelength properties, Krauß et al. (2014) found that these blazars are able to explain the measured flux of PeV neutrino events. A third extremely high energy neutrino event called "BigBird" was recorded in three years of IceCube data on 4 December 2012 (Aartsen et al. 2014a). While all of the previous mentioned events were of shower-like signature with a large angular uncertainty (see Sect. 3.5.3), Kadler et al. (2016) realized that the calorimetric output of the "BigBird" field was dominated by a single source, the FSRQ PKS B1424−418. Even if this neutrino detection seemed to be spatially and temporally consistent with a major outburst of PKS B1424−418, Kadler et al. (2016) showed that the chance coincidence for a correlated neutrino and γ-ray detection from this particular blazar is on the order of $\sim 5\,\%$. Although the neutrino fluence (the integrated flux density over time) is reduced for shorter periods of activity, the significance, however, is increased due to an effective background rejection. A systematic analysis of the neutrino expectation from short blazar flares is given in Sect. 5.1.
Neutrino events with a track-like signature (see Sect. 3.5.3) provide a much better angular uncertainty and thus significantly reduce the trial factor for possible source associations, which increases the significance. So far, only a single track-like neutrino event with an energy of 290 TeV was found to be in agreement with enhanced γ-ray activity from the source TXS 0506-056 (IceCube Collaboration et al. 2018). Even after these encouraging multimessenger detections have been made, the origin of this neutrino event is still highly debated and will be addressed in more detail in Sect. 5.2. In the following section, an overview of the basic concepts in neutrino astronomy is given, ranging from neutrino properties, over the detection principle of neutrino events to currently operating neutrino detectors.

3.5.1 Neutrino Properties

Neutrinos are elementary particles with no electric charge and a half-integer spin. The existence of (electron) neutrinos was postulated by Pauli (1930) (English translation by Brown 1978) and later proved by Cowan et al. (1956). In the following years, two other kinds of neutrinos were identified, namely the muon neutrino (Danby et al. 1962) and the tau neutrino (DONUT Collaboration et al. 2001). Each of these neutrino flavors is associated with a charged partner, the electron e, muon μ and tau τ. Within the Standard Model of elementary

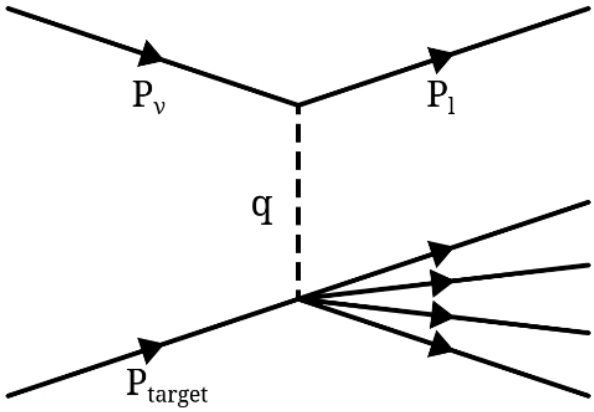

Figure 3.8: Schematic diagram of a generic neutrino ν scattering process with a *target*, a generated (charged or neutral) lepton ℓ and an unspecified amount of other outgoing particles. Credit: Scully, (2013)

particle physics (see Halzen & Martin (1984); Griffiths (2008) for an overview), these particles are grouped into three fermion flavors, corresponding to three quark generations. For each fermion, a corresponding antiparticle exists. Within the Standard Model, neutrinos are assumed to be massless. The observation of neutrino oscillation (Fukuda et al. 1998), however, implies a non-zero neutrino mass which required concepts beyond the Standard Model. Neutrino oscillation describes the change of flavor while propagating over macroscopic distances. This process requires the mass-eigenstates of the three flavors to be different.
As neutrinos are electrically neutral and do not carry any color information like quarks, they only couple to the weak force. This makes neutrinos unique messengers, as they can escape dense environments like the inner regions of AGN while putting constraints on their interaction with matter. Neutrinos are therefore difficult to detect and large instrumented volumes are required to achieve a reasonable detection probability.

3.5.2 Neutrino Interaction with Matter

In this section, an overview of possible neutrino interactions with regular matter is given, mainly based on Griffiths (2008).

3.5.2.1 Scattering Kinematics:

In the context of this thesis, it is useful to introduce the basic notations used to describe neutrino scattering kinematics. A generic neutrino interaction is displayed in Fig. 3.8. An incoming neutrino interacts with a target, producing a final-state lepton and a system of other unspecified outgoing particles. The lepton can either be charged or neutral, depending on the involved weak interaction current (either neutral current NC or charged current CC interactions can occur). If the four-momenta of the neutrino p_ν, the lepton p_ℓ and the target p_{target} are known, the following Lorentz invariant quantities can be constructed:

$$s = (p_\nu + p_{\text{target}})^2 \qquad \text{center of mass energy} \tag{3.8}$$

$$Q^2 = -q^2 = -\,(p_\nu - p_\ell)^2 \qquad \text{four-momentum transfer} \tag{3.9}$$

$$y = \frac{q \times p_{\text{target}}}{p_\nu \times p_{\text{target}}} \qquad \text{inelasticity} \tag{3.10}$$

$$x = \frac{Q^2}{2 \times p_{\text{target}} \times q} \qquad \text{Bjorken scaling variable} \tag{3.11}$$

$$W^2 = (q + p_{\text{target}})^2 \qquad \text{invariant hadronic mass} \tag{3.12}$$

Within the laboratory frame, in which the target is at rest, the inelasticity can be expressed as the fraction of neutrino energy transferred to the target system:

$$y = \frac{E_\nu - E_\ell}{E_\nu}. \tag{3.13}$$

The Bjorken scaling variable x, commonly used to describe deep inelastic scattering, can be understood as a fraction of the target's four-momentum carried by the struck quark.

3.5.2.2 Weak Neutrino-Lepton Interactions

The weak force has two interaction channels which are the charged current (CC) and neutral current (NC), both mediated by the massive vector bosons $W^\pm$ and Z^0, respectively. Figure 3.9 displays possible interactions within these channels. While the neutrino remains untouched in a NC interaction (no change in flavor and lepton), the CC interaction turns the neutrino into a charged lepton. The flavor of the charged lepton corresponds to the flavor of the neutrino.
The neutrino-lepton cross section depends on the initial spin configuration. CC interactions select only a given type of spin, so-called left-handed particles and right-handed antiparticles (Wu et al. 1957). In the case of NC interactions, a left-handed neutrino can scatter off a right-handed charged lepton. The cross section in this case is given in terms of the weak and electromagnetic interaction by the electroweak unification theory. For sufficiently high energies, this is a good approximation for deep inelastic scattering, in which a neutrino scatters off a quark within a nucleus.

3.5.2.3 Deep Inelastic Scattering

Neutrino-nucleus scattering typically provides a much larger cross section compared to neutrino-lepton interactions. Only at energies of $\sim 6\,\text{PeV}$, at the so-called "Glashow resonance" (Glashow 1960), $\bar{\nu}_e - e$ interactions dominate. Therefore, nuclei are the dominant interaction targets for the detection of neutrinos. In deep inelastic scattering processes, the neutrino hits a(an) (anti)quark within a nucleus. The nucleus is effectively broken up, while the recoiled quark and nucleus produce a spray of other hadrons. This process of hadron generation is called *hadronisation*. For further details, please refer to e.g. Olive & Particle Data Group (2014).
According to Gandhi et al. (1996), the differential cross section for a deep inelastic scattering on a nucleus is given by

$$\frac{d^2\sigma}{dxdy} = \frac{2G_F^2 M E_\nu}{\pi} \left(\frac{M_W^2}{Q^2 + M_W^2}\right)^2 \left[xq(x,Q^2) + x\bar{q}(x,Q^2)(1-y)^2\right], \tag{3.14}$$

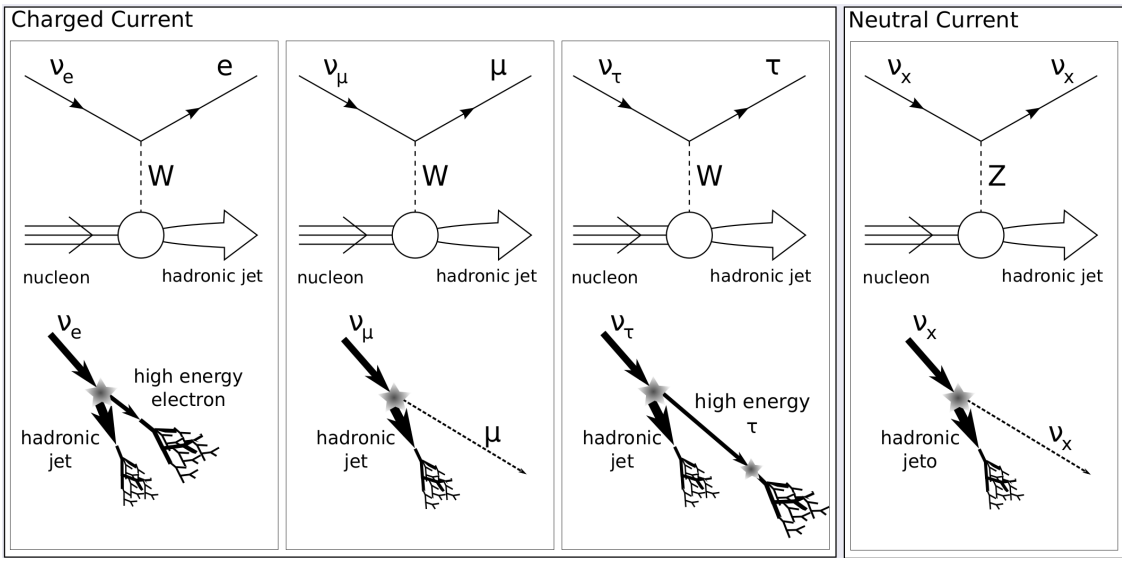

Figure 3.9: Top: Feynman diagrams of neutral current (NC) and charged current (CC) interactions. Bottom: corresponding schematic sketch. Credit: Tiffenberg, (2011)

where G_F is the Fermi constant, M the mass of the target nucleon, M_W the mass of the W-boson, E_ν the energy of the incident neutrino, x and y are the Bjorken scaling variables, $\nu = E_\nu - E_\mu$ is the energy loss in the laboratory (target) frame and E_μ the energy of the outgoing muon. The quark distribution functions can be written as

$$q(x,Q^2) = \frac{1}{2}(u_v(x,Q^2) + d_v(x,Q^2)) + \frac{1}{2}(u_s(x,Q^2) + d_s(x,Q^2)) + s_s(x,Q^2) + b_s(x,Q^2) \tag{3.15}$$

and

$$\overline{q}(x,Q^2) = \frac{1}{2}(u_s(x,Q^2) + d_s(x,Q^2)) + c_s(x,Q^2) + t_s(x,Q^2), \tag{3.16}$$

where u, d, c, s, t, b denote on the different quark flavors in a nucleus and the indices v, s label valence and sea quark contributions. Figure 3.10 shows the total cross section for the processes discussed in this section, as well as the contributions from the neutral current and charged current interactions. For neutrino energies in the range of 10^6 GeV $< E_\nu < 10^{12}$ GeV, Eq. 3.14 can be approximated by a simple power law according to:

$$\sigma_{CC}(\nu N) = 2.69 \times 10^{36} cm^2 \left(\frac{E_\nu}{1\ \text{GeV}}\right)^{0.402} \tag{3.17}$$

$$\sigma_{NC}(\nu N) = 1.06 \times 10^{36} cm^2 \left(\frac{E_\nu}{1\ \text{GeV}}\right)^{0.408} \tag{3.18}$$

$$\sigma_{CC}(\overline{\nu} N) = 2.53 \times 10^{36} cm^2 \left(\frac{E_\nu}{1\ \text{GeV}}\right)^{0.404} \tag{3.19}$$

$$\sigma_{NC}(\overline{\nu} N) = 0.98 \times 10^{36} cm^2 \left(\frac{E_\nu}{1\ \text{GeV}}\right)^{0.410}. \tag{3.20}$$

For more detailed information, e.g. for the calculation of the cross section for low energetic atmospheric neutrinos, please refer to Formaggio & Zeller (2012).

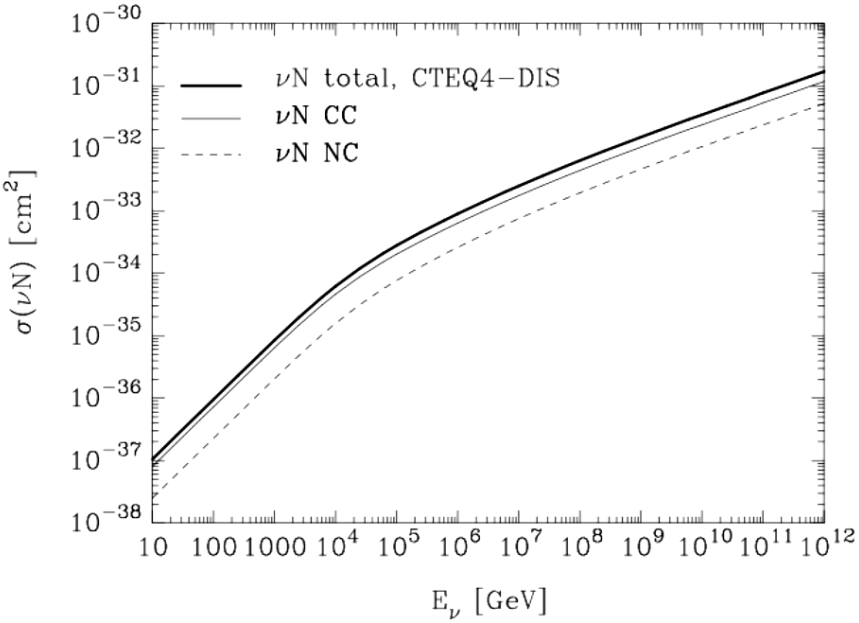

Figure 3.10: Neutrino cross section for the process of Eq. 3.14. Dotted line: neutral current contribution $\sigma(\nu N \to \nu + X)$. Thin line: charged current contribution $\sigma(\nu N \to \mu^- + X)$. Thick line: total (charged-current plus neutral-current) cross section. Credit: Gandhi et al. (1996)

3.5.3 Neutrino Detection and Event Signature

Neutrino detectors use photomultipliers to measure optical light emitted by charged leptons that form during the interaction of neutrinos with matter (see Sect. 3.5.2). These leptons emit Cherenkov radiation while propagating faster than the speed of light in the surrounding medium. In sea water, this emission peaks at a characteristic angle of 42.5°. Two main topologies of neutrino interactions can be reconstructed within a neutrino detector (see Fig. 3.11). Track-like events typically originate from the interaction of a ν_μ or $\bar{\nu_\mu}$ and result in the propagation of a high-energy $\mu^\pm$ throughout the detector. Due to the minimum deposited energy of the muon, this causes a track like signature with a good angular resolution of $\sim 0.1°$, while leading to a poor energy resolution, as a significant amount of energy is deposited outside the detector or carried away by the muon.
Shower-like events are typically caused by the interaction of a ν_e or $\bar{\nu_e}$ and result in the propagation of an electron or positron. While propagating, these leptons suffer energy losses by Bremsstrahlung and pair production (see Sect. 2.3), forming a shower cascade. While most of the secondary particles are contained within the detector, the energy resolution is much better compared to track-like events, however, due to the wide spread of the evolving shower, the angular resolution is on the order of $\sim 10°$.

Neutrino detectors use the Earth to shield against atmospheric background contamination. While classical telescopes observe the night sky above them, neutrino detectors are optimized for neutrinos penetrating Earth and therefore entering the detector from the ground. Therefore, neutrino telescopes monitor the hemisphere opposite to its location. As the ANTARES and KM3NeT detectors are located in the Mediterranean Sea, they are most sensitive to the southern sky and vice versa for the IceCube detector which is located at the South Pole. Cosmic-ray induced atmospheric showers are essential in the field of Cherenkov astronomy

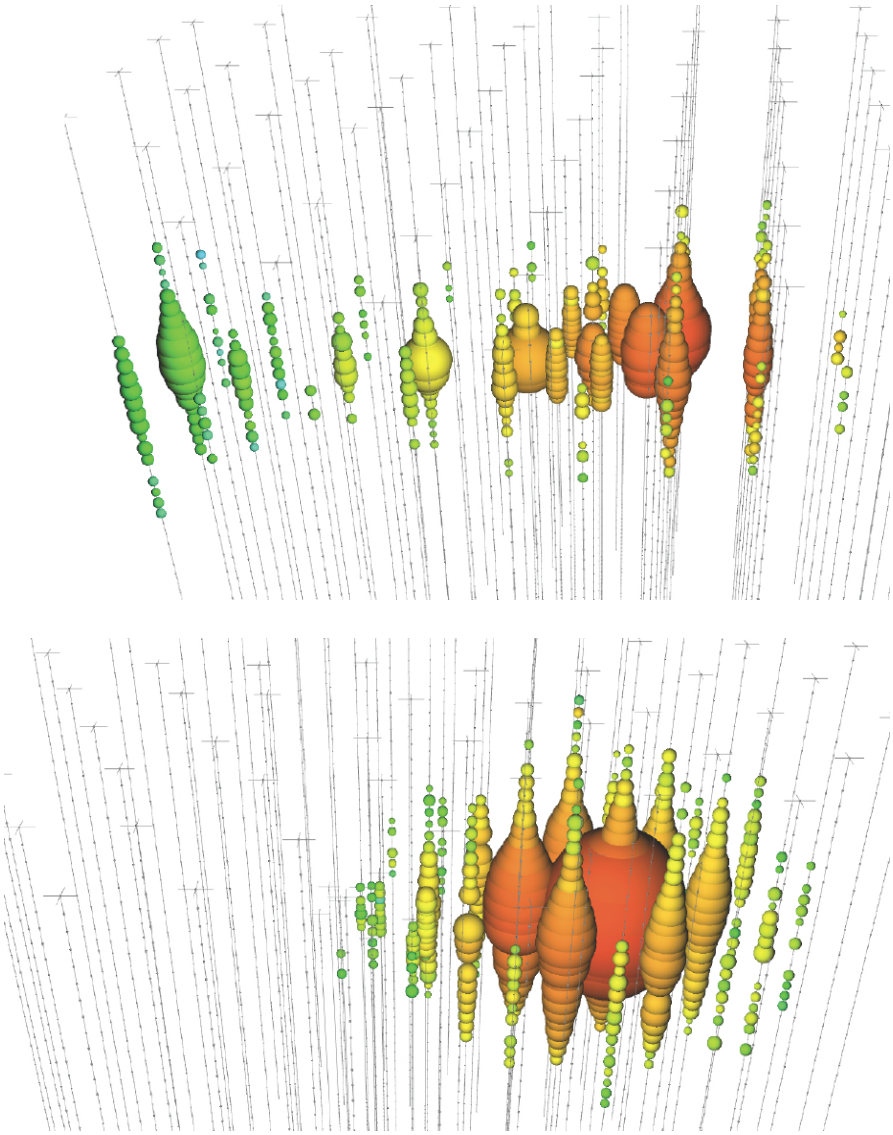

Figure 3.11: IceCube event display showing the deposited energy within the detector for a track-like (Top) and shower-like (Bottom) event. Colors indicate the arrival time from early (red) to late (green). Due to the minimum ionization of the muon, the deposited energy of a track-like event is small, leading to a good angular resolution of $\sim 0.1^\circ$ but poor energy reconstruction. As the shower cascade of a shower-like event is mainly contained within the detector, this results in a good energy reconstruction but causes angular uncertainties of $\sim 10^\circ$. Credit: IceCube Collaboration

(see Sect. 3.4), while in neutrino detectors, these air showers contribute to a large fraction of background events. Muons produced in the atmosphere can penetrate up to several kilometers of sea water or ice, triggering a neutrino event in the detector. These down-going events, entering the detector from above ($\cos\theta > 0$), are the dominant fraction of detected events and exceed neutrino induced down-going muons by several orders of magnitude (Okada 1994). Neutrinos produced in the atmosphere can penetrate Earth and therefore contribute as an irreducible background to the flux of up-going ($\cos\theta < 0$) triggered events. As it is difficult to distinguish between an atmospheric or extragalactic induced neutrino event at a fixed energy, only high-energy events ($\mathcal{O}(\mathrm{TeV}) - \mathcal{O}(\mathrm{PeV})$) are considered as purely extragalactic, due to the steeply falling atmosphere neutrino spectrum of $\frac{dN}{dE} \propto E^{-3.6}$ (Carminati 2007).

3.5.3.1 Cherenkov Radiation

Cherenkov radiation is emitted whenever a highly energetic charged particle traverses a transparent medium with a velocity faster than the speed of light in the medium. In an atomic description, the charged particle causes a local disturbance at the surrounding atoms, which leads to an electric polarization of the medium. While the particle travels faster than the medium needs to elastically relax, this causes the medium to radiate a coherent shock wave. The Cherenkov radiation is emitted with a characteristic angle with respect to the track of the particle which reads:

$$\theta_C = \arccos\left(\frac{1}{\beta n}\right), \tag{3.21}$$

in which θ_C is the so-called Cherenkov angle, β is the velocity of the particle with respect to the speed of light in vacuum c and n is the refractive index of the medium. If one assumes a highly relativistic muon ($\beta \approx 1$) traveling through either sea water ($n_{\mathrm{sea}} \approx 1.35$) or ice ($n_{\mathrm{ice}} \approx 1.32$), the Cherenkov angles become:

$$\begin{aligned} \theta_C^{\mathrm{sea}} &\approx 42.5^\circ \\ \theta_C^{\mathrm{ice}} &\approx 41^\circ. \end{aligned} \tag{3.22}$$

The number of Cherenkov photons emitted at a specific wavelength λ is given by the Frank-Tamm formula:

$$\frac{d^2 N_\gamma}{dx d\lambda} = \frac{2\pi\alpha}{\lambda^2}\left(1 - \frac{1}{\beta^2 n^2}\right), \tag{3.23}$$

in which α is the fine structure constant. This means that at characteristic wavelengths of $300\ \mathrm{nm} < \lambda < 600\ \mathrm{nm}$, about

$$\begin{aligned} \left.\frac{dN}{dx}\right|_{\mathrm{sea}} &= 340\,\mathrm{cm}^{-1} \\ \left.\frac{dN}{dx}\right|_{\mathrm{ice}} &= 325\,\mathrm{cm}^{-1} \end{aligned} \tag{3.24}$$

Cherenkov photons are emitted per particle path length. While propagating, the photons can either be absorbed or scattered. The number of photons at a given distance r from the track is:

$$N(r) = N_0 \cdot \frac{1}{r} \cdot e^{\frac{-r}{\lambda_{abs}}}, \tag{3.25}$$

in which $r = \frac{k}{\sin(\theta)}$ is the length of the photon path,

λ_{abs} is the effective absorption length
N_0 the number of photons produced at the track, and
k the wave vector of the photon.

The arrival time t at an optical module depends on the travel time of the muon, as well as the propagation time of the Cherenkov photon and is given as:

$$t = t_\mu + t_\gamma = \left[t_0 + \frac{1}{v}\left(l - \frac{k}{\tan(\theta)}\right)\right] + \left[\frac{1}{v_g}\left(\frac{k}{\sin(\theta)}\right)\right], \tag{3.26}$$

in which t_0 is the time until the generation of the muon,
k the shortest distance between the muon track and the optical module,
l the distance on the muon track to the position k,
v the velocity of the muon, and
v_g the group velocity of photons in water.

In order to allow for a detection of Cherenkov photons in the detector, the propagation path of the photons has to be shorter than the absorption length.
Since sea water and ice both mostly consist of H_2O, the physics of the primary neutrino interaction and Cherenkov light propagation are pretty similar (see Eq. 3.22 and 3.24). Hence, the main differences between sea water and ice detectors are due to different optical properties in both media. For more detailed information, please refer to Čerenkov (1937) or Kremers & Chigrin (2009).

3.5.4 Current Neutrino Detectors

In this section, an overview of currently operating neutrino telescopes is given. This includes the two deep sea neutrino detectors on the Northern hemisphere ANTARES and KM3NeT, as well as the IceCube detector, deployed in the ice sheets of Antarctica at the South Pole. A comparison of Cherenkov light properties in sea water and ice is discussed in Sect. 3.5.3.1. As it is of no relevance to this thesis, the Baikal detector deployed at the bottom of lake Baikal in eastern Siberia will not be discussed in detail. For further information, please refer to Bagduev et al. (1999).
Details about the event reconstruction, trigger algorithms and dominant background sources in these detectors can be found in Sect. 4.3, together with the concept of a neutrino point source analysis.

3.5.4.1 ANTARES

ANTARES (*Astronomy with a Neutrino Telescope and Abyss Environment RESearch*) is a large volume deep-sea water Cherenkov telescope in the Mediterranean Sea located 42 km from Toulon in France at 42°47.935 N, 6°09.942 E. ANTARES is optimized for the detection of neutrino events, which can either originate from cosmic-rays interacting in the atmosphere or from galactic and extragalactic sources. The primary purpose of ANTARES is the detection of extragalactic neutrino point sources in the southern hemisphere, to perform multimessenger analysis as well as to search for neutrinos from exotic physical processes, such as dark matter annihilation.
The ANTARES detector is located in the Mediterranean Sea at about 2.5 km below sea level. It consists of a three-dimensional array of 885 optical sensors, arranged on 12 vertical strings. Each string of about 480 m hosts 75 optical modules (OMs), which are grouped to 25 storeys

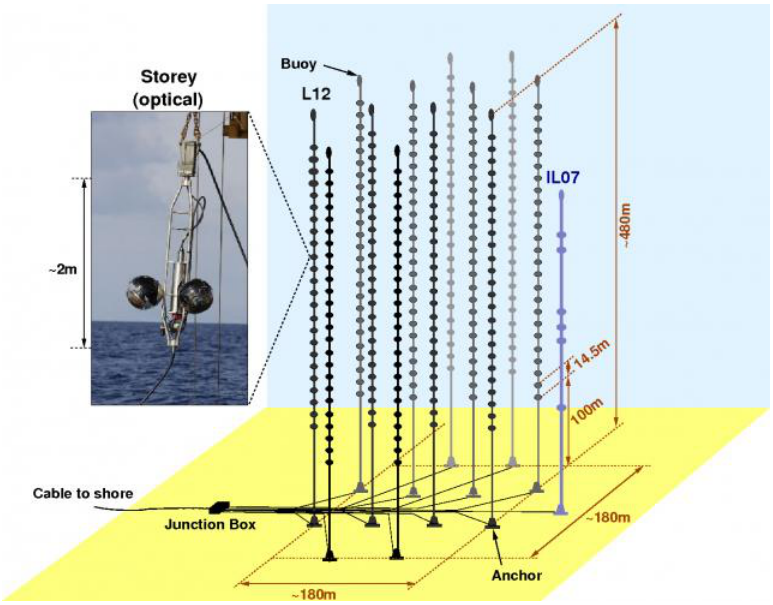

Figure 3.12: Schematic view of the ANTARES detector, which consists of 12 strings, carrying 25 detection storeys with 885 optical sensors in total. An inset of a storey, carrying three optical modules is given as a photograph. Credit: Katz & Spiering (2012)

equipped with three OMs each. The spacing between storeys is 14.5 m and the strings are separated by about 70 m. Therefore, ANTARES is equipped with a total instrumented volume about 0.03 km^3. An additional string, the Instrumentation Line (IL07), carries devices for environmental monitoring, which makes ANTARES a multidisciplinary instrument. All strings are anchored to the sea floor and kept tight by using buoys at the top of each string. The detector as displayed in Fig. 3.12 was fully deployed in May 2008. Electro-optical cables connect strings at the seabed with a junction box, which provides the main connection to the shore. The primary detection units are optical modules, which consist of a 17-inch glass sphere, housing a 10-inch PMT. Additionally, the glass sphere also contains the electronics for the high-voltage power supply as well as an optical gel for positional stabilization of all components. The PMTs are surrounded by a mu-metal cage which provides a shielding against Earth's magnetic field of approximately 46 μT. An intrinsic timing resolution (transit time spread) of about $\sigma_{\mathrm{TTS}} = 1.3$ ns is achieved, allowing for a precise measurement of the Cherenkov photon arrival time. In order to minimize atmospheric background from down-going events, the OMs are oriented downwards at an angle of 45°. Figure 3.13 shows an artist's impression of a high energetic muon moving through the ANTARES detector and producing a cone of Cherenkov light.

In order to provide track reconstruction precisions of about 0.4° for energies above 1 TeV, a reasonable detector calibration is mandatory. To calibrate for time delays caused by different optical path lengths between the OMs of each string, the relative time needed to reach different parts of the detector is measured. Flashing Light Emitting Diodes (LEDs) located inside optical modules are used for calibration. To calibrate the whole detector, each string contains four storeys which are equipped with an additional optical beacon. These beacons can be used to emit a set of pulsed LED flashes which illuminate a given number of OMs in their local surrounding. For a more global flash, a powerful pulsed laser is located at the seabed which is able to illuminate a large part of the detector with a timing precision of 0.5 ns. The correlation between a measured hit in the PMTs and the corresponding time information is achieved via

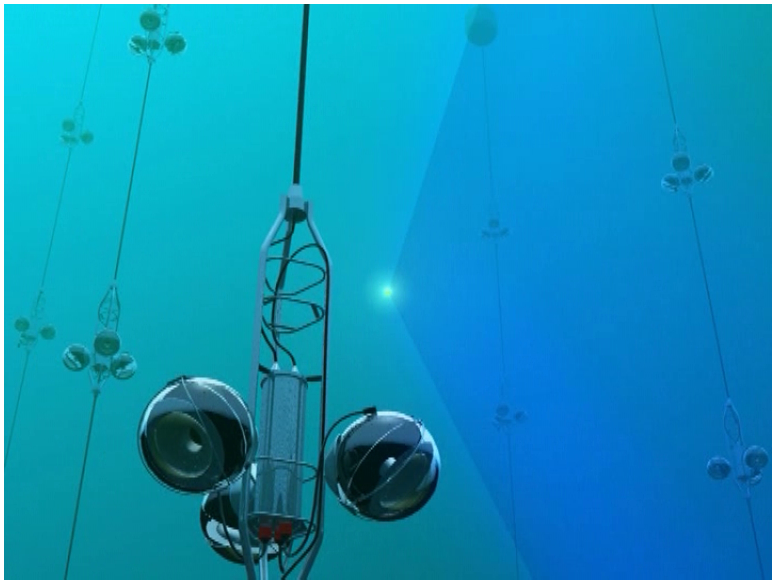

Figure 3.13: An artist's impression of a highly energetic muon moving through the ANTARES detector and producing a cone of Cherenkov light that can be detected by the three OMs on a storey. Credit: A.Kappes, Physics Institute Erlangen University

a Time to Voltage Converter (TVC). By using time ranges of 25 ns, the TVC measures the arrival time of the electrical signal within this time range with a precision of about 2 ns. The amplitude of the signal is measured using the Amplitude to Voltage Converter (AVC). Due to the low number of photons reaching the OMs during normal data tacking, the amplitude is expressed in units of photoelectrons (pe). After a threshold of 0.3 pe is reached, the AVC starts to integrate the signal for a time range of 25 ns. After this time, 250 ns are needed for the AVC to recover. Two AVCs are installed in order to minimize deadtime.

One of the major problems for a precise positioning is the flexibility of the single lines. Their position and orientation is influenced by the sea current and therefore has to be monitored continuously. A compass and tiltmeter measures the orientation of each storey. The positions of the OMs with respect to each other are measured via an acoustic detection system. Hydrophones employed on five storeys per string detect the running times of acoustic pulses generated at transmitters on the sea floor. In addition, AMADEUS is used to study the feasibility of an acoustic neutrino detection. More detailed information can be found at Ageron et al. (2011) or Katz & Spiering (2012).

3.5.4.2 KM3NeT

The Cubic Kilometre Neutrino Telescope (KM3NeT) is the next generation of deep sea neutrino telescopes currently under construction in the Mediterranean Sea (KM3NeT Collaboration 2008; Bagley et al. 2009; Adrián-Martínez et al. 2016). After an extended testing phase of the newly developed multi-PMT digital optical module provided a proof of concept, the first finalized string was deployed in December 2015. Upon completion, KM3NeT will span over three sites in the Mediterranean Sea, with a total instrumented volume of several km^3. Preliminary sites include locations close to Toulon (France), Capo Passero (Italy) and Pylos (Greece). To cover a wide field of physics, an extension of detectable neutrinos toward higher as well as lower energies in respect to ANTARES is planned.

The low energy extension *Oscillation Research with Cosmics in the Abyss (ORCA)*, located

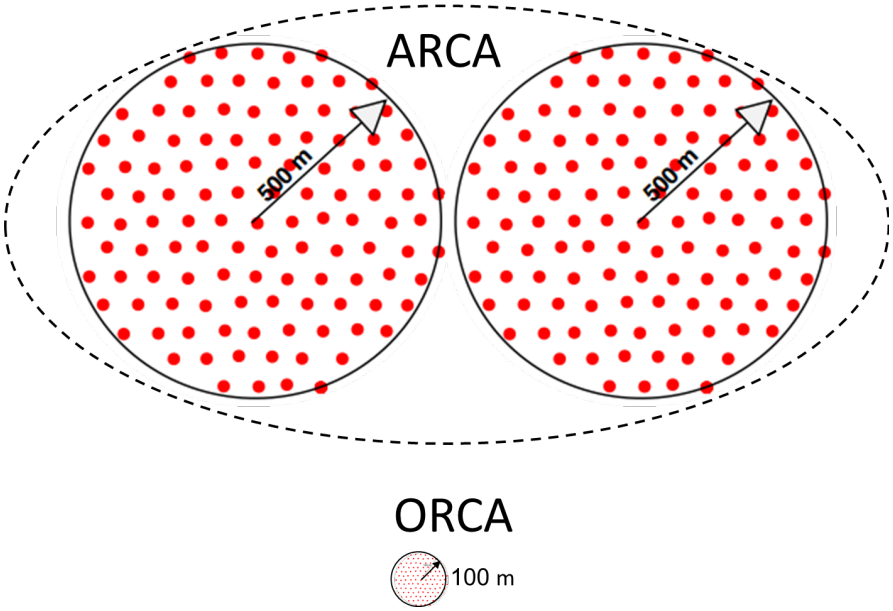

Figure 3.14: Top: Footprint and dimensions of the two sub-detectors ORCA and ARCA of the KM3NeT project. Red dots mark the position of vertical strings. Credit: https://www.km3net.org/km3net-2-0-the-next-phase-arca-and-orca/ Bottom: KM3NeT multi-PMT optical module, containing 31 PMTs as well as all necessary electronics in a 17-inch spherical pressure vessel, mounted between two dyneema ropes. Credit: Adrián-Martínez et al. (2016)

at the French site, is meant to study the neutrino mass hierarchy and neutrino oscillation. In the final configuration, this "building block" will consist of 115 instrumentation strings with 18 modules per string, each carrying 31 PMTs. In this configuration, the building block will span a vertical distance of 9 m. With an averaged string separation of 20 m, this detector will be sensitive to study neutrinos in the few-GeV range. For the high energy extension *Astroparticle Research with Cosmics in the Abyss (ARCA)*, two large volumes at the Italian site will each be equipped in a wide instrumentation building block configuration. These blocks will have a module-to-module separation of 36 m, with a distance of $\sim$ 95 m between the strings. In this configuration, the ARCA detector will be sensitive to TeV - PeV neutrino events, mainly searching for high energy extragalactic point sources of the southern sky. A footprint of the total detector layout is shown in Fig. 3.14 top.
With the development of the new multi-PMT optical module layout (see Fig. 3.14 bottom), containing 31 PMTs and all necessary electronics in a 17-inch spherical pressure vessel, KM3NeT introduces the next generation of deep sea data taking devices. For further details please refer to Löhner et al. (2013); Bruijn & van Eijk (2015) and Adrián-Martínez et al. (2016).

3.5.4.3 IceCube

The IceCube detector, with an instrumented volume of about one km^3 is currently the largest existing neutrino detector in the world, located 2450 m below the South Pole (Halzen & Klein 2010; Aartsen et al. 2017b). IceCube uses the Antarctic ice as medium for neutrino detections. In addition to the *Antarctic Muon And Neutrino Detection Array (AMANDA)* (Andres et al. 2000), IceCube started data taking in reduced configurations from 2005 on, reaching its full extension by the end of 2010. In the final configuration, IceCube consists of 86 vertical strings with a length of 1 km, distributed over one square km. With a vertical module separation of 17 m and a string distance of 125 m, IceCube is made of a total of 5160 deployed optical modules. Each module consists of a 13-inch glass sphere, hosting a single PMT and digital read-out system. With this detector layout, IceCube is sensitive to study neutrinos in the GeV to PeV regime. A schematic illustration if the IceCube detector is shown in Fig. 3.15.
Six additional strings in a compact configuration with a vertical module distance of 7 m and a horizontal string separation of 72 m have been deployed in the central region of the array in 2010. This sub-detector named *DeepCore* aims to be sensitive to neutrinos in the low-energy regime of $\sim$ 10 GeV (Wiebusch & for the IceCube Collaboration 2009; Abbasi et al. 2012). At the surface, an array of 81 ice tanks, each equipped with two optical modules, named *IceTop* provides a simultaneous veto against down-going atmospheric muons.
Furthermore, IceTop can be operated as an independent air shower detector in an energy range of 100 TeV to 1 EeV (Waldenmaier 2008). For an efficient atmospheric muon reduction, *High-Energy Starting Events (HESE)* (also known as contained-vertex events), which use the outer strings of the detector as a veto to select events having their origin inside the detector are used (Aartsen et al. 2013a).
Primary goals of IceCube include the search for sources of high-energy neutrinos (point sources as well as transient sources), the search for exotic particles (e.g dark matter and magnetic monopoles) as well as the monitoring of MeV neutrinos from supernovae and multimessenger observations. *Extreme high energy (EHE)* neutrinos with an energy between 1 PeV to 10 EeV are an unique tool for a direct survey of the ultra-high energy universe, as photons at these energies are highly attenuated by the cosmic microwave background (CMB). In addition, neutrinos observed at these energies provide constraints on the origin of extreme high energy cosmic-rays as well as the cosmological evolution of their sources (Aartsen et al. 2013b).
The greatest break-through of IceCube so far was the proof of evidence of a high-energy

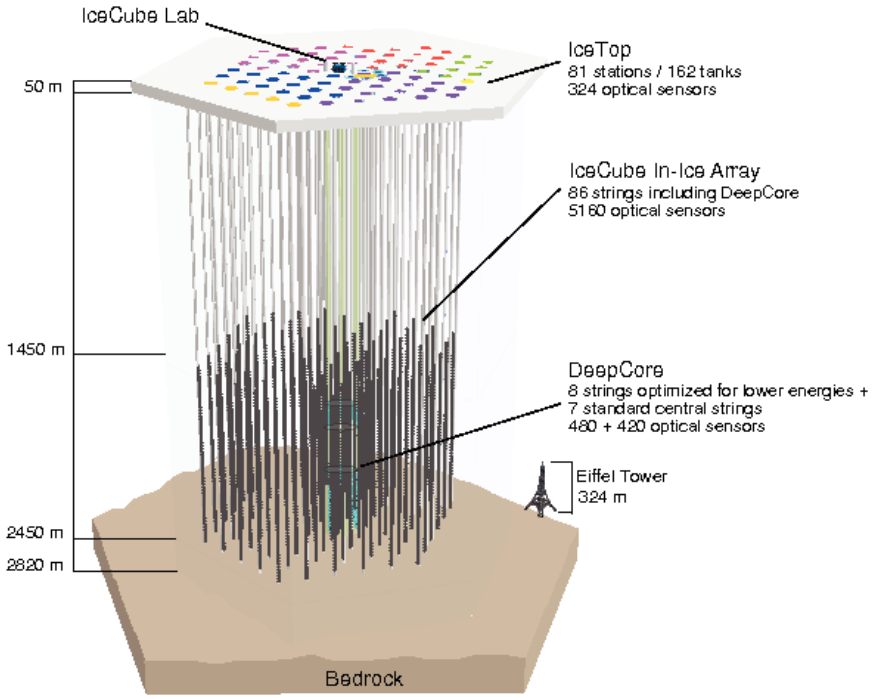

Figure 3.15: Schematic overview of the IceCube detector including the sub-array *DeepCore* and the cosmic-ray air shower array *IceTop*. Different string/station colors indicate different deployment seasons. The Eiffel tower is shown for comparison. Credit: Aartsen et al. (2017b)

extraterrestrial neutrino signal (IceCube Collaboration 2013; Aartsen et al. 2015a). As for now, more than 60 high-energy neutrino candidates with an energy between 30 TeV and 2 PeV have been detected. The measured flux fits best with an $E^{-2.2}$ neutrino energy spectrum, rejecting an atmospheric origin with more than $5\,\sigma$ (Aartsen et al. 2014a). With the detection of the first track-like high energy neutrino event, consistent with enhanced γ-ray activity from the source TXS 0506+056 (IceCube Collaboration et al. 2018), IceCube has driven another break-through by identifying the most promising neutrino point source candidate so far. For further details about a calorimetric neutrino expectation please refer to Sect. 5.1.3.

3.5.5 Towards a Global Neutrino Network

Initiated in 2013, the *Global Neutrino Network (GNN)*[16] aims to provide a general framework for a closer collaboration between the existing neutrino telescopes. Goals of the GNN include the coordination of alerts and multi-messenger projects, cross-checks of results of different instruments, a common base of public documents and software tools as well as the exchange and interaction within the field of neutrino astronomy by e.g. the organizing of joint scientific meetings. Members of the GNN include all major neutrino collaborations, namely the

[16] http://www.globalneutrinonetwork.org/

ANTARES and KM3NeT collaboration, the IceCube collaboration as well as the Baikal collaboration, working together to provide a unified global neutrino observatory.
In addition to the GNN, an *Astrophysical Multimessenger Observatory Network (AMON)*[17] is currently under development at the Pennsylvania State University (Smith et al. 2013; Keivani et al. 2017). AMON seeks to provide a real-time correlation system for the analysis of high-energy signals across all known astronomical messengers – photons, neutrinos, cosmic-rays, and gravitational waves, in order to allow for rapid follow-up observations of all collaborating instruments. Including instruments within all messengers and many parts of the electromagnetic spectrum, AMON has triggered some of the major multimessenger observations so far, including the observation of a neutron star merger (Abbott et al. 2017) and correlated neutrino γ-ray detections of a single blazar (IceCube Collaboration et al. 2018; IceCube Collaboration 2018).

[17] https://www.amon.psu.edu/

4 Analysis Techniques

Data reduction and analysis of various instruments requires targeted and optimized analysis techniques and software environments. Observations in different wavelengths use distinct data formats to store their information efficiently, while each instrument uses its own analysis pipeline for data processing/reduction. Neutrino detectors are taking data 24 h long, seven days per week, while pointed instruments like, *Swift*/XRT, only observe the target for a limited time. Typically, intensive Monte Carlo simulations are necessary to distinguish between astrophysical and background events. Performing multiwavelength and multimessenger studies requires a detailed understanding of each corresponding instrument and a huge effort in the analysis of these data. The Multi-Mission Maximum Likelihood framework (3ML) aims to provide a plug-in block-like framework, that allows a wide community of scientists to easily analyze multiwavelength data of several different instruments (Vianello et al. 2015). Individual analysis packages are provided by experts of the corresponding instrument and can uniformly be used in a python environment. In contrast, 3ML is an open source software[18], the framework is still under development and so far only standardized analysis of a limited amount of instruments are available. In this section, I will give an overview of the analysis and data reduction techniques of instruments relevant to the work presented in this thesis.

4.1 *Swift*/XRT Data Analysis

In this section, all relevant data reduction and analysis steps to obtain *Swift*/XRT spectra and light curves are introduced, mainly following Burrows et al. (2000, 2005) and Flanagan & Siegmund (2004).

4.1.1 Data Reduction

Reduction of *Swift*/XRT data was done using scripts written by Laura Barragán and Jörn Wilms. The individual steps of the extraction pipeline will be discussed briefly. For a more detailed description, please refer to the *Swift* User's guide[19].
The extraction of data taken in Photon Counting (pc) mode starts from images and event files, the so-called Level 1 data. In the next step, data have to be calibrated by transforming raw data values to actual coordinates in the detector or sky frame. For this transformation, the orientation and altitude of the satellite has to be known. Standard sources used for calibration, bad pixels and anomalous pixels are flagged and events are sorted into different classes. In the final calibration step, Good Time Intervals (GTI) are calculated, in which the telescope was taking scientific data, which is not contaminated by background frames. After calibration, source and background counts are extracted and stored into event files. In the next step, an *Ancillary Response Function* (ARF), sometimes called the effective area of a given source region is calculated. The ARF depends on the mirror area, the quantum efficiency of the CCD, the filter transmission and the energy of the detected photons. At energies of $> 10\,\mathrm{keV}$ the effective area is reduced due to a decreasing reflectivity of the mirrors, while the quantum efficiency of the CCD limits the effective area for energies $< 0.5\,\mathrm{keV}$. Additional features of the effective area are caused by atomic properties of the used materials (Fraser et al. 1994; Owens et al. 1996). In order to understand the intrinsic source spectrum, not the spectrum detected by the instrument, a *Redistribution Matrix Function* (RMF) is crucial to describe the expected detector response. The RMF is a matrix that compares the detected photon energies (in an ideal case) to the energy a photon had before arriving in the detector.

[18] https://threeml.readthedocs.io/en/latest/index.html
[19] https://swift.gsfc.nasa.gov/analysis/xrt_swguide_v1_2.pdf

Typically, the detected energy matches well with the input energy, while for energies below 2 keV detector properties can causes a mismatch.
To measure source properties such as fluxes, spectral shape and absorption, event and background counts are used together with the ARF and RMF. A fit model is folded through the detector response and fit to the data, which allows for a source and model independent calibration and a simple identification of source or calibration related features in the obtained spectrum. For further details about the calculation of fluxes and different models, please refer to Sect. 4.1.3 and Sect. 4.2.2.

4.1.2 Detector Performance

Depending on the observed target, different readout modes of the CCD can be used to ensure stable and efficient data taking. In the following, a brief overview of possible modes is given, mainly based on Burrows et al. (2000, 2005) and Flanagan & Siegmund (2004).

Image Long and Short Mode (IM):
This mode rapidly obtains an image, which is used to localize, e.g. a new GRB target. The image is generated on board, while no event recognition is performed. As the CCD most likely will be saturated, this image just serves a precise positioning and rough flux estimation.

Low rate (LR) and Piled-up Photodiode (PU):
This mode is used for bright sources and a high time resolution. In this mode, the CCD is read out constantly, even before a given frame has finished. This leads to a very fast read out and an increase in the charge uncertainty of a single pixel, as deposited charge from other pixels and previous measured photons is included in the read out signal.

Windowed Timing (WT):
In this mode, only the inner part of the CCD is read out, covering the central 8 arcmin of the field of view and allowing for a one dimensional image calculation

Photon Counting (PC):
In this mode, the CCD operates in a "frame-transfer" configuration. Each frame is read out by storing it one raw at a time in a serial register on board. Events are reconstructed and a detector bias is corrected. This is done by defining a 3×3 matrix and testing, whether the central pixel is the local maximum. In addition, the charge value of the central pixel needs to be in a certain interval. This procedure is repeated for a 5×5 matrix, providing a precise cosmic-ray rejection and bad pixel identification.

After a new GRB is triggered, the XRT automatically changes modes. The first step is to take an image (IM) for a precise localization of the source. Depending on the brightness of the GRB, the XRT continues to observe in one of the other modes. Only for Pre-Planned Targets (PPT), no image mode is required (Flanagan & Siegmund 2004). For the analysis on AGN targets in this work, only data during WT and PC modes is used.

4.1.3 Calculation of Fluxes

The XRT, in the ideal case, is sensitive to individual incident photons. The observed spectrum strongly depends on the response of the CCD, as well as on energy and direction. To study the spectral properties of a target source, it is necessary to obtain the source spectrum $s(E)$, which is related to the observed counts spectrum $C(h)$ as described in Gorenstein et al. (1968)

and Davis (2001b,a)

$$C(h) = N\tau \int dE\ R(h,E)\ A(E)\ s(E) + B(h). \tag{4.1}$$

Here, h describes the pulse-height channel, $N\tau$ corresponds to the effective exposure time, $A(E)$ to the effective area and $R(h,E)$ is the redistribution matrix. This matrix describes how much energy is deposited within each channel h, while this result can be influenced by surrounding channels. The term $B(h)$ corresponds to the expected instrumental and physical background rate, which includes X-ray and softer photons as well as thermal contributions from the CCD. Unfolding Eq. 4.1 according to Nowak et al. (2005) leads to:

$$s(E) = \frac{[C(h) - B(h)]\,/\Delta t}{\int [R(h,E)\ A(E)\ dE]}. \tag{4.2}$$

Δt indicates the total integrated observation time. Within each infinitesimal energy interval dE, the source count and background rates are assumed to be constant. This assumption obviously is not valid for strongly energy dependent spectra, as those observed in blazars, where an alternative forward-folding approach (see Sect. 4.2.2) should be used.

4.2 *Fermi*/LAT Data Analysis

In this section, an introduction to the reduction and analysis of *Fermi*/LAT data is given, while a detailed documentation of each analysis step can be found online[20]. Software tools and calibration are provided by the *Fermi*/LAT collaboration.

4.2.1 Data Preparation

For the analysis of *Fermi*/LAT data an *event file*, a *spacecraft file* and a *model file* are necessary. The event file contains information of reconstructed electron-positron pairs, like the trajectories through the detector, arrival time and deposited energy. To associate these events to a given position in the sky, a spacecraft file is needed, which stores information about the absolute orientation of the satellite like the coordinates of the current viewing direction or the rock angle (orientation of the spacecraft in z-direction from the zenith).
First of all, events need to be filtered in a given *Region of Interest* (ROI) and time range. The ROI has to be large enough to include sources in the vicinity, but small enough to keep the computing effort at a reasonable level (see Sect. 4.2.4 for the used values). The selected time range is filtered for GTIs, in which the LAT was taking science data. The model contains all known γ-ray point sources from the latest general *Fermi*/LAT source catalog (currently the 3FGL, Acero et al. (2015), while an updated catalog is in preparation[21]), as well as templates for the extragalactic and the galactic diffuse emission (Acero et al. 2016). The model also includes extended γ-ray sources, like e.g. the lobes of Centaurus A (Abdo et al. 2010a). As the LAT all-sky coverage is not uniformly and the measured count rate depends on the time LAT observes a given region in the sky, a livetime cube and exposure map have to be calculated. A maximum likelihood method is used to calculate the chance that the observed photons originate from the target source. This likelihood is then maximized, under the assumption that the used model is correct.
In the following, a detailed overview of the individual analysis steps necessary to prepare and analyze *Fermi*/LAT data is given.

[20] https://fermi.gsfc.nasa.gov/ssc/data/analysis/
[21] A preliminary point source list of 8 years of *Fermi*/LAT data (FL8Y) is publicly available at https://fermi.gsfc.nasa.gov/ssc/data/access/lat/fl8y/

4.2.1.1 Event Reconstruction

Before a dedicated analysis can be performed, both astrophysical and background events have to be reconstructed based on individual hits in various sections of the LAT. At these level, characteristic event parameters such as the direction or energy are obtained. Over the course of the mission, the event reconstruction algorithms have been updated regularly to take advantage of improvements in the understanding of the LAT and its orbital environment. Four major data releases (so-called *Passes*) have been developed over the past 10 years. The current data release (Pass 8; Atwood et al. (2013)), introduces significant improvements to the first level event reconstruction, such as a new pattern recognition algorithm in the tracker or an improved energy reconstruction. Pass 8 also benefits from an improved handling of energy leakage and crystal saturation. While the total amount of reconstructed background events (in a specific time range) increased compared to previous passes, the signal to background ratio also increases, which leads to a total gain in sensitivity over the whole LAT energy range. In addition, the Pass 8 release introduced a new event classification scheme, which is based on four hierarchical classes and several subclasses that allow for a precise event selection based on the performed analysis.

4.2.1.2 Photon Classification

As part of the first level reconstruction, LAT groups events into different classes based on their photon probability and quality of their reconstruction. Each event class places certain requirements on a reconstructed event and is characterized by its own set of instrument response functions. Within each class, events are further subdivided into event types which use topologies such as a separation into front or back events, based on whether an event converted in the front or back section of the tracker. The current Pass 8 event classes are a nested hierarchy, in which a higher class is fully contained in all previous classes. Events in a higher class have a larger proton probability, smaller effective areas, narrower point spread function and lower background contamination. The current event classes are named "TRANSIENT", "SOURCE", "CLEAN" and "ULTRACLEAN".
The lowest level event class TRANSIENT is designed for short-duration events, such as γ-ray bursts, transient sources and timing studies. Due to the typical small time ranges this event class is used for, it benefits from an enhanced photon statistic, while tolerating a higher background fraction and broader PSF. An intermediate selection between increased signal events and reduced background is provided by the SOURCE class. This class is favorable for studying point sources or moderate extended sources on medium to long time scales. To study weak sources or large regions of the sky for a long time, the ULTRACLEAN class is ideal as it provides the best background rejection rate and is less sensitive to spectral features caused by instrumental effects. The reconstruction algorithms and event classes have evolved over the past 10 years of operation and are likely to continue to do so due to an intensive support from the LAT team.

4.2.1.3 Source Model File

Due to the large FoV, the detected count rate of the LAT can not be directly converted into a source flux. Neighbouring sources around the target source, as well as diffuse photons can contribute to the measured count rate, making it impossible to identify certain photons from the target source. Similar as in X-ray astronomy (see Sect. 4.1), the "true" source flux is derived from a source model, which describes the expected γ-ray sky in a given region around the target source. The source model then is folded with the detector response, compared to

the measured data and varied to achieve the best agreement. The all-sky density distribution $S(E, \hat{x}, t)$, which is given by

$$S\left(E, \hat{x}, t\right) = \sum_i s_i\left(E, t\right) \delta\left(x - \hat{x}\right) + S_G\left(E, \hat{x}\right) + S_{EG}\left(E, \hat{x}\right) + \sum_k S_k\left(E, \hat{x}, t\right) \tag{4.3}$$

is both energy and direction dependent and can also vary over time. The model consists of all known γ-ray point sources $s_i\left(E, t\right)$ from the latest general *Fermi*/LAT source catalog, extended γ-ray emitters $S_k(E, \hat{x}, t)$ such as the lobes of Centaurus A, the Sun or Moon and both the extragalactic and galactic diffuse emission $S_{EG}(E, \hat{x})$ and $S_G(E, \hat{x})$ (see Acero et al. (2016) or Moskalenko et al. (2004) for an overview). The diffuse background is assumed to be constant over the observed time range. In a standard LAT point source analysis, all sources are assumed to be constant in the selected time range. For this purpose the time dependence is neglected and all model parameters, such as the spectral shape are averaged over the selected time interval. To study the variability behavior of γ-ray sources, e.g. by calculating a light curve, the total time range is split into smaller time bins, in which the spectral properties and intensity again are assumed to be constant. (see Sect. 4.2.3).
Models to describe known extended sources as well as the diffuse background are provided by the the *Fermi*/LAT team. Positions and spectral properties of catalog sources have been obtained in an iterative process by putting sources at the position of the highest count rates and repeating this process until the final model converges. Although sources in the *Fermi*/LAT catalogs are averaged over a certain time range, these models provide an excellent starting point for user contributed software[22] (see Sect. 4.2.3 and Sect. 4.2.4 for a detailed description of the used light curve and spectra scripts). Tools to generate a source model for any region of interest (ROI) in the sky are an example for such user contributed software. All sources of the third LAT source catalog (Acero et al. (2015)) within the pre-defined ROI are left variable, as they can influence the result of the target source due to the large PSF of the LAT. Sources outside the ROI are also considered in a given radius, while their spectral properties are fixed as their influence on the central position is much smaller. This analysis technique is a compromise between taking surrounding sources into account (which in the ideal case would be the entire sky), and keeping the computing effort at a reasonable level.

4.2.1.4 Lifetime Cube and Exposure Map

As the measured detector response depends on the time LAT observes a given region of the sky, the corresponding count rate strongly depends on this "lifetime". The lifetime is derived for every position in the sky, using the orientation information stored in the spacecraft file. In order to optimize computing aspects, the lifetime calculation is binned in a three-dimensional grid, the so-called *lifetime cube*. As this grid is computed for the entire sky, this effort only has to be performed once for a given time range. For the analysis of any other sources in the same time interval, the same lifetime cube can be reused, which increases the computing efficiency. Furthermore, lifetime cubes are additive.
By using the total response function of *Fermi*/LAT, an *exposure map* specific for the selected ROI can be calculated. Please note that the type of exposure map used within the LAT Collaboration differs from the usual way of calculating an exposure, typically being time integrals over the effective area. Here, the exposure is calculated by integrating over the total response function within a given ROI according to

$$\epsilon\left(E, \hat{x}\right) = \int_{ROI} R\left(E', \hat{x}'; E, \hat{x}, t\right) dE' d\hat{x}' dt. \tag{4.4}$$

[22] A list of user contributed LAT software is available at https://fermi.gsfc.nasa.gov/ssc/data/analysis/user/

Here, the primed parameters indicate the measured energy E' and direction $\hat{x}'$, while the parameters E and $\hat{x}$ correspond to the incident photon, respectively. Therefore, for a given position in the sky and time interval, the exposure map describes the total instrument response (see above mentioned references for more information). Using the exposure map, together with a source model (see Eq. 4.3), the predicted count rate for a given ROI can be calculated via

$$N_{pred} = \int dE \int_{ROI} d\hat{x}\ S\left(E, \hat{x}\right) \epsilon\left(E, \hat{x}\right). \tag{4.5}$$

4.2.1.5 Likelihood Analysis

The analysis of *Fermi*/LAT data is based on the maximum-likelihood method in order to get the best estimation of the target source properties from the measured events. Giving a particular source model (see Sect. 4.2.1.3), the likelihood $\mathcal{L}$ describes the probability to obtain the measured data. Assuming Poisson distributed data and following Cash (1979), the likelihood can be expressed as

$$\mathcal{L} = \prod_{i=1}^{N} \frac{m_i^{n_i} \cdot e^{-m_i}}{n_i!} = e^{-N_{pred}} \prod_{i=1}^{N} \frac{m_i^{n_i}}{n_i!}, \tag{4.6}$$

where N represents the total number of counts within the ROI, n_i are the number of counts detected within bin i, and m_i, corresponds to the expected counts in bin i. Please note that the expected count rate strongly depends on the selected model. N_{pred} indicates the total predicted number of photons within the ROI (see. Eq. 4.5). The set of parameters that maximizes Eq. 4.6 represents the maximum likelihood estimation of the target source.
The parameter used to calculate the significance of a detected source, is the test statistic (TS), which is given by

$$\mathrm{TS} = -2 \ln \left(\frac{\mathcal{L}_{max,0}}{\mathcal{L}_{max}} \right). \tag{4.7}$$

Here, $\mathcal{L}_{max,0}$ indicates the maximum likelihood for the so-called null hypothesis (model without the target source), while $\mathcal{L}_{max}$ is the likelihood for the used model, which includes the target. The significance of a detection is given by $\sigma = \sqrt{\mathrm{TS}}$, assuming normal distributed data. Since this analysis is based on a maximum likelihood approach, resulting fluxes are corrected for instrumental effects like background events and different exposure times.
Scripts used to calculate light curves (see Sect. 4.2.3) and spectra (in an unbinned likelihood analysis) have been written by W. McConville, C. Müller and A. Schooley. Software[23] developed by T. Johnson is used to generate a source model file based on the current *Fermi* catalog. Additional scripts have been written in the context of this thesis, including a (binned likelihood) spectrum, TS map calculation and source localization. Further details on the specific likelihood analysis performed in this thesis are given in the subsequent sections of this section, while a dedicated description on the maximum likelihood method is provided by the Fermi Science Support Center[24].

4.2.2 Calculation of Fluxes

As the *Fermi*/LAT energy range spans three orders of magnitude, an accurate modeling of the source spectrum is necessary. In a forward-folding approach, one uses a spectral model and

[23] These script is publicly available at https://fermi.gsfc.nasa.gov/ssc/data/analysis/user/
[24] Tutorials to perform an unbinned and binned maximum likelihood analysis are available at https://fermi.gsfc.nasa.gov/ssc/data/analysis/scitools/likelihood_tutorial.html and https://fermi.gsfc.nasa.gov/ssc/data/analysis/scitools/binned_likelihood_tutorial.html

a set of parameters to characterize the observed emission and estimate (based on the model) the corresponding flux value. For most blazar spectra, a simple power-law fit already provides a good parametrization. However, especially the brightest blazars seem to exhibit a curvature (Acero et al. 2015). A broken power law model or log-parabola often provides a more accurate description of the spectral properties of bright blazars. In order to decide whether a simple power-law or curved model better fits the data, a likelihood analysis according to

$$\mathrm{TS}_{curve} = 2\left(\log \mathcal{L}_{curved-spectrum} - \log \mathcal{L}_{power-law}\right) \tag{4.8}$$

is performed, including the curvature significance as the parameter $\textit{Signif-Curve} = \sqrt{\mathrm{TS}_{curve}\ \mathrm{R}_{syst}}$ in the 3FGL catalog. The parameter R_{syst} introduces a systematic uncertainty on the effective area. A spectrum is considered significantly curved for $\mathrm{TS}_{curve} > 16$ or $\textit{Signif-Curve} > 4$ (Acero et al. 2015).
This type of likelihood analysis uses a step-by-step approach by first performing a fit over the entire energy range (for a given time interval), which is then used as a starting value for the analysis of several energy sub-bands. In this way, the convergence of the individual sub-bands is supported. To characterize the goodness of the fit, a chi-squared minimization test is performed, where χ^2 is defined as

$$\chi^2 = \sum_i \frac{(d_i - m_i)^2}{\sigma_i}. \tag{4.9}$$

Here, $d_i \pm \sigma_i$ corresponds to the observed data, while m_i indicates the model values. The application of a χ^2-test requires Gaussian distributed data. For missions such as *Swift* and *Fermi*, which are sensitive to individual counts, this assumption is not valid. Poisson distributed data instead has to be treated with Cash statistics (Cash 1979), according to which the goodness of the fit is defined as

$$C = 2\sum_{i=1}^{n} t\cdot m_i - d_i + d_i \ln\left(\frac{d_i}{t\cdot m_i}\right). \tag{4.10}$$

The parameter t introduces an exposure time of the instrument, while the index i runs over all events reconstructed in the ROI. In the forward-folding approach, the flux is only extracted (in the ideal case) when a "good" model has been found. This modeling of the observed spectrum is necessary to distinguish predicted events originating from the target source $\mathrm{N}_{\mathrm{pred}}$, against other events reconstructed within the ROI. Note that the forward-folding approach is not unique, as different physical models can describe the data with the same accuracy.
Fitting of the γ-ray spectrum introduces a systematic uncertainty on the extracted flux, which depends on the spectral shape of the used model. Additional uncertainties originate from the used Instrumental Response Function (IRFs), Point Spread Function (PSF) and effective area. Therefore, a systematic uncertainty of $\sim 5\,\%$ is included in the extracted flux values.
In case of no significant detection, an upper limit analysis is performed following the likelihood analysis of Cash (1979) outlined in this section. To derive an upper limit, the flux is increased until a given uncertainty $\Delta \ln \mathcal{L}_{max}$ is obtained. For extreme faint sources with a $\mathrm{TS} < 1$, the upper limit can be underestimated (see Acero et al. (2015) Sect. 3.5) and thus a Bayesian method following Helene (1983) is applied.

4.2.3 Light Curve Calculation

The default way of studying the variability of a source is the calculation of a time series of fluxes, also-called light curve. For this purpose, the total time range is split into n intervals,

in which the flux density is assumed to be constant. For each interval, a likelihood analysis is performed resulting in an individual flux or upper limit estimate during that time. As the spectral shape and flux are strongly correlated (Abdo et al. 2010a), the uncertainty in the flux estimation can become large when fitting both parameters. Therefore, the light curve calculation assumes a constant spectral shape within each interval, fixing it for all sources within the ROI (including the target source) to the value obtained in a long-term study (currently the 3FGL, Acero et al. 2015). Note that with this approach, one rather detects variability than characteristics in the spectral shape. Additional spectra (where both parameters are kept free) need to be calculated to study the spectral properties of blazars. However, variability in blazars does not show a huge change in spectral shape, despite large variability in flux (Abdo et al. 2010c).
Light curve scripts used in this thesis are fully automatized and can perform a variability analysis for any given target, based on only a handful of input parameters, following the analysis chain described in these section. For further details of the exact input parameters, please refer to Sect. 4.2.4.

4.2.4 Point Source Analysis

If not explicitly indicated, the analysis of *Fermi*/LAT γ-ray data in this thesis uses the Fermi Science Tools (v10r0p5) with the reprocessed Pass 8 data and the $P8R2\_SOURCE\_V6$ instrument response functions. Within this thesis, I performed an unbinned likelihood analysis in a region of interest (ROI) of 10° around the target source, in an energy range of 100 MeV to 300 GeV. I used a zenith angle cut of 90° and the LAT event selection parameter GTMKTIME cut DATA_QUAL==1 && LAT_CONFIG==1 together with the LAT event class = 128 and the LAT event type = 3. For the modeling of the diffuse components I used the galactic diffuse emission model gll_iem_v06.fits and the isotropic diffuse model iso_P8R2_SOURCE_V6_v06.txt (Acero et al. 2016). The used xml model contains all sources of the third LAT source catalog (Acero et al. (2015)) within a source radius of 20 deg (ROI+10 deg). Variable sources (with a variability index > 72.44) are fitted even outside the ROI radius. I used a free spectral index during the spectra calculation, while it was fixed for the light curve analysis. In case no significant *Fermi*/LAT detection can be made, the upper limit calculation uses a threshold in test statistic of TS = 25 for spectra and TS = 9 for light curves and is based on the method of Feldman & Cousins (1998) and Helene (1983).

4.3 Neutrino Data Analysis

In this section, an overview of the event reconstruction and analysis techniques of neutrino data with deep sea and ice based neutrino detectors, relevant to this thesis, is given. Some aspects have already been outlined in Kreter (2015), and are partially taken in verbatim for completeness reasons.

4.3.1 Background

Several types of background sources can falsify the neutrino signal measured in Cherenkov detectors. Two main classes can be distinguished: optical background and atmospheric particles.

4.3.1.1 Optical Background

Cherenkov detectors are optimized for the detection of optical light. Noise at these wavelengths is dominant and originates mainly from three sources.

^{40}K decay:
Potassium-40 (^{40}K), which naturally occurs in the environment can decay to ^{40}Ca via β-decay (branching ratio 89.3%) or ^{40}Ar via electron capture (branching ratio 10.7%). The resulting electron from the β-decay has a maximum energy of 1.33 MeV, which is sufficient to emit Cherenkov radiation. The excited ^{40}Ar atom can emit a photon with an energy of 1.46 MeV, which is capable to produce Cherenkov photons by the generation of Compton electrons. The decay of ^{40}K provides a steady, isotropic background, which strongly depends on the optical properties of the surrounding medium, like e.g. the absorption length λ_a. For deep sea neutrino detectors, this optical background can build up to rates of ~ 100 Hz per cm^2 (Bagley et al. 2009; KM3NeT Collaboration 2008).

Dark Count Rate:
This rate is detected by the PMTs in the absence of external light sources. It is caused by radioactive decays (mainly ^{40}K) in the optical module close to the photomultiplier. Thermal generated noise within the PMT also contributes to the measured dark current. However, this continuous and steady noise rate is typically small, compared to other background sources.

Bioluminescence:
Deep sea neutrino detectors are exposed to an additional source of background, caused by bioluminescent organisms (e.g. bacteria, plankton, or jellyfish), which inhabit the deep sea. These organisms produce light at wavelengths of $\lambda = 450 - 490$ nm as a result of chemical reactions (Herring 1983; Haddock et al. 2010). Bioluminescent emission typically occurs as a slowly changing steady emission, which overlays the rates measured from ^{40}K decays and dark current throughout the entire detector. On top of this baseline rate, fast light flashes with durations of several seconds are measured on neighbouring PMTs. These bursts are typically triggered by mechanical stimulations, like the collision of organisms with the detector structure. In addition, bioluminescent rates are strongly correlated to environmental conditions, like changes in sea current and seasonal variations. These changes are due to regional or seasonal nourishment fluctuations in sea water, which correlates to bacteria populations and therefore to the entire ecosystem.

4.3.1.2 Atmospheric Background

Secondary particles produced in interactions of cosmic-rays in the atmosphere can reach the detector and leave a characteristic event signature. So-called *atmospheric muons* are typically stopped in the overburden above the detector, which is one reason why neutrino detectors are built deep underground. However, muons with sufficient energy can reach the detector from above, causing a characteristic down-going track signature. IceTop (see Sect. 3.5.4.3) was constructed to efficiently reject these background events and study the cosmic-ray spectrum in the atmosphere. Deep sea neutrino detectors, which do not feature an additional veto layer on the top, have to focus on up-going events which exclusively originate from neutrinos interacting close to the instrumented volume. *Atmospheric neutrinos*, which are also produced by cosmic-ray interactions in the atmosphere can penetrate through Earth and contribute to the flux of measured up-going neutrino events. Specific constraints regarding the reconstructed energy of the neutrino can be used to eliminate this background contribution (see Sect. 4.3.3). Misreconstructed atmospheric muons, however, can still contaminate the flux of reconstructed up-going events. An accurate event selection is necessary in order to reduce this background.

4.3.2 Triggers

Due to the huge amount of detected hits throughout the entire detector, interesting data have to be pre-selected before permanently stored for science analysis. As the majority of hits is caused by background events, effective trigger algorithms need to be implemented either in hardware or software. The basic idea of all trigger algorithms is to look for causally connected hits, while background is expected to be uncorrelated. To be causally connected, two hits i and j need to fulfill

$$|t_i - t_j| \leq \frac{|\vec{x_i} - \vec{x_j}|}{v_{medium}} + T_{extra}, \tag{4.11}$$

where, $t_{i,(j)}$ and $x_{i,(j)}$ correspond to the detection time and position of the hits, respectively, and $v_{medium} = \frac{n}{c}$ is the speed of light within the surrounding medium (see Sect. 3.5.3.1 for a comparison between sea water and ice). The time T_{extra} accounts for a time uncertainty as well as photon scattering of the detected hits and is typically on the order of $10 - 20\,\text{ns}$. By requiring clusters of causal connected hits, the amount of optical background can be reduced significantly, while keeping most of the neutrino induced events in the relevant energy range. These pre-selected events are still mainly dominated by atmospheric background and additional (analysis specific) event selections have to be applied.
Deep sea neutrino detectors like ANTARES and KM3NeT group hits into different categories labeled as hit levels. *Level 0 (L0)* hits refer to a single digitalized hit above a given threshold. *Level 1 (L1)* hits correspond to a coincidence of two (or more) L0 hits within the same module and time window. This time window can be on the order of $T \approx 10\,\text{ns}$, due to light scattering properties of deep sea water. Noise levels can be reduced significantly by requiring *Level 2 (L2)* hits, which refer to L1 hits with an additional orientation demand between different PMTs, as coincident events are expected to travel unscattered on straight lines though the detector. For more details about the reconstruction of deep sea neutrino events, please refer to Bagley et al. (2009).
The IceCube trigger software first searches for optical modules that have triggered an event. In the next step, clusters of local-coincidence hits (so-called *HLC hits*) are identified, using both spatial and timing correlations, as well as known module positions. Different trigger algorithms are applied, like a simple multiplicity trigger which counts the number of HLC hits in a given time range. Topological triggers, on the other hand, count the number of HLC hits in a given volume or along a specific string. Several detector sub-sets can be combined to identify events that trigger PMTs in different parts of the detector (see Sect. 3.5.4.3), while a global trigger reduced overlapping events by merging individual trigger windows. For further details about the IceCube event triggering, please refer to Kelley (2014).

4.3.3 Point Source Analysis

Due to the huge amount of background events in neutrino detectors (see Sect. 4.3.1) it is not a priori clear where a reconstructed event originates from. In a neutrino point source analysis, signal events are expected to originate from a potential point source like e.g. a blazar (see Sect. 2.4), while specific assumptions on the nature of the underlaying emission mechanisms (see Sect. 2.2.4.3 and Sect. 2.3.4) have to be made. To distinguish signal from background events, parameters like the angle, energy and arrival time can be reconstructed. The most obvious assumption on signal events is that they point back to their origin, so the reconstructed angle has to be small. In regard to the reconstructed energy, one expects that the energy spectrum differs for signal events and background events produced in the atmosphere. While neutrinos originating from blazar jets are assumed to follow a flat spectrum of $\frac{dN}{dE} \propto E^{-1.25}$

(Mücke et al. 2003), atmospheric neutrinos typically show a much steeper spectrum of $\frac{dN}{dE} \propto E^{-3.6}$ (Gaisser & Honda 2002; Abbasi et al. 2011) Based on the hadronic models of Mannheim (1993) and Mannheim (1995), the amount of produced neutrinos is proposed to be correlated to the number of high energetic γ-rays.
For a total number of N detected events, the contribution n_s of signal events is unknown. Therefore, an unbinned maximum likelihood method according to

$$L(n_s) = \prod_{i=1}^{N} \left[\frac{n_s}{N} S_i + (1 - \frac{n_s}{N}) B_i \right] \tag{4.12}$$

is applied. Then, this likelihood function is maximized with respect to n_s, as a higher likelihood value corresponds to a more signal-like observation. Here, n_s stands for the unknown contribution of signal events, $\frac{n_s}{N}$ and $(1 - \frac{n_s}{N})$ are the fraction of signal and background events, while the terms S_i and B_i correspond to the signal and background probability densities. These densities typically depend on an directional and energy dependent term. Fehn (2015) and Kreter (2015) showed that an additional time dependent term, which introduces a spatial and temporal correlation between expected neutrino events and observed γ-rays, significantly increased the detection potential of single point sources. For a more detailed discussion about each individual factor and the likelihood calculation, please refer to Kreter (2015) and Aartsen et al. (2017a).
While there is evidence of a high-energy neutrino flux (IceCube Collaboration 2013), no individual point sources could be identified by any of the existing neutrino facilities over the last decade, placing strong constraints on the total high-energy neutrino expectation. The next generation of neutrino observatories like the KM3NeT detector (see Sect. 3.5.4.2), which is currently under construction in the Mediterranean Sea, as well as the IceCube-Gen2 extension (IceCube-Gen2 Collaboration et al. 2014), which will provide an instrumented volume of several km^3, leading to a substantial increase in sensitivity. Detectors of this size will have a rich scientific objective, from the resolution of single neutrino point sources, over the discovery of the exact neutrino mass hierarchy, to become a leading observatory in future multimessenger programs.

5 Searching for Possible High Energy Neutrino Point Sources

Based on the analysis techniques introduced in Sect. 4, this section focuses on the results obtained in the search for possible high energy neutrino point sources. Blazars as promising neutrino source candidates (see Sect. 1.2.2) show a complex flaring behavior (see Sect. 2.4.2) in the high energy regime and are therefore targeted within this work. Here, I want to test the expected individual neutrino excess rates of promising neutrino source candidates for current neutrino observatories like IceCube (see Sect. 3.5.4.3). A systematic search for promising short-term flare neutrino associations on a daily to weekly time scale has been performed for a sample of bright γ-ray blazars. The γ-ray variability and neutrino prediction of the first confirmed neutrino point source (IceCube Collaboration et al. 2018) TXS 0505+056 have been studied on different time scales from short-term flaring periods on the order of days to long-term outbursts that last multiple months. Further details on the particular analysis results will be discussed in the following parts of this section.

5.1 A Systematic Search of Blazar Flare Neutrino Associations with IceCube

Jets from Active Galactic Nuclei (AGN) are among the best candidates (see Sect. 1.2.2, 2.2.4.3) for the recently detected extraterrestrial neutrino flux (IceCube Collaboration 2013, Aartsen et al. 2015a, IceCube Collaboration et al. 2018). Hadronic AGN jet-emission models (e.g. Mannheim 1993, 1995) predict a tight correlation between the neutrino flux and the (time-variable) γ-ray emission, while model calculations (see Krauß et al. 2014, Kadler et al. 2016) for the integrated signal of all γ-ray blazars are predicting a cumulative neutrino signal exceeding the atmospheric background above energies of 100 TeV. Since the background neutrino spectrum falls steeply with energy, the individual events with the clearest signature of being of an extraterrestrial origin are those at the highest energies. However, the neutrino flux at these highest energies is low and the long-term-average brightest blazars in the sky yield only a small Poisson probability for the detection of one event while at the same time the probability for a chance coincidence is not negligible. For this reason, an association of a high-energy neutrino with a long-term bright blazar even if coinciding with a major high-fluence outburst, can not be considered an unambiguous source identification.

5.1.1 Introduction

High-confidence associations of individual neutrinos with individual blazars could be achieved via spatially and temporally coincident detections of photons and neutrinos from short-term blazar flares. Here, I refer to the term flare for a period of enhanced activity with a duration of days to weeks, while the expression outburst is used for long-lasting periods on the order of months to years. Additionally, short-flares indicate a flaring period of only several days, often only a single day. The IceCube neutrino detector is sufficiently sensitive to detect neutrinos from such short-term flares (see e.g. Halzen & Klein 2010, Aartsen et al. 2017b). In this section, I want to test this by calculating the expected number of neutrino events produced in the IceCube detector for the brightest blazar flares of the past six years. By using *Fermi* γ-ray light curves and multiwavelength measurements of the highly dynamic spectral energy distribution of blazars, I applied fundamental calorimetric arguments to calculate the maximum-possible neutrino numbers for individual blazar flares. I used the method introduced in Krauß et al. (2014) and Kadler et al. (2016) to scale these maximum-possible values down to realistic predicted numbers taking into account their fluence, duration and position in the sky. I studied the detection potential for flare-associated neutrino searches, defined as the neutrino prediction value divided by the flare duration, and performed a systematic analysis of the 50

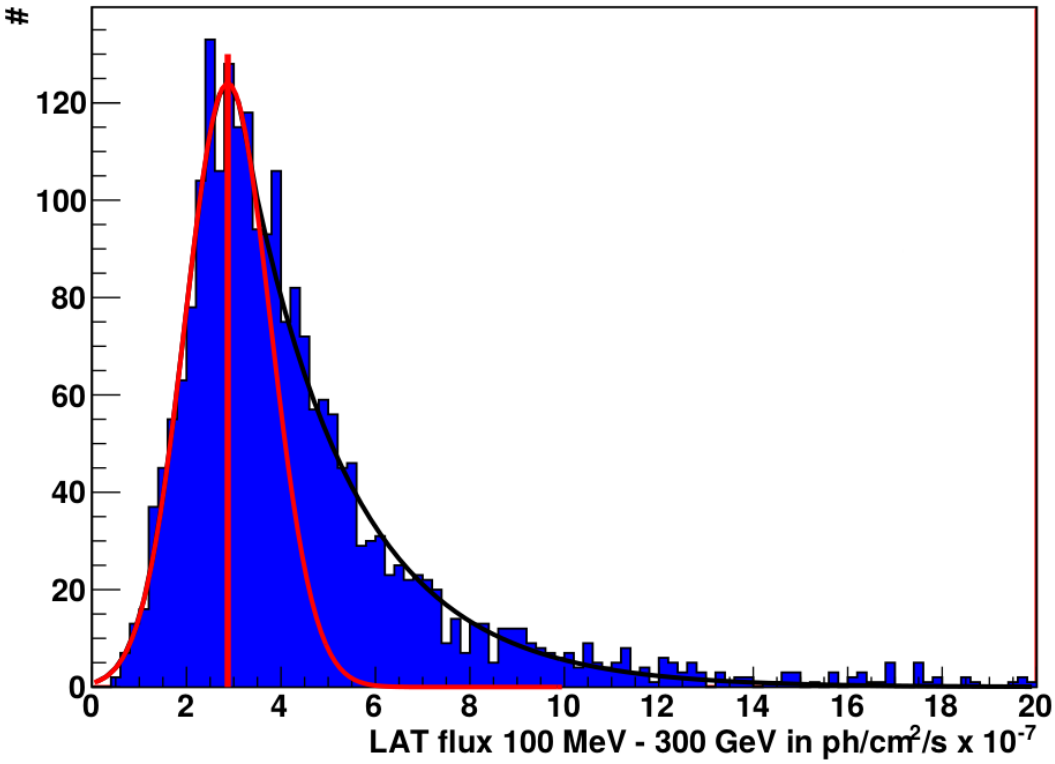

Figure 5.1: Histogram of the *Fermi*/LAT γ-ray flux of 3C 279 in an energy range of 100 MeV - 300 GeV and a time range of 55317 MJD (2010-05-01) - 57662 MJD (2016-10-01), using daily binning. The histogram is fitted with a Gaussian and exponential function. The red line represents the mean of the Gaussian fit that serves as ground level flux G while the standard deviation is used as ground level uncertainty σ in Eq. 5.1. The black curve indicates the combined fit, while the Gaussian component is fitted in red.

best-ranked flares with the highest detection potential for IceCube.

5.1.2 Flare identification

High-confidence associations of individual neutrinos with individual blazars could be achieved via spatially and temporally coincident detections of photons and neutrinos from short-term blazar flares. I used daily binned *Fermi*/LAT γ-ray light curves of a sample of 150 bright blazars monitored daily by the LAT[25], to identify periods of enhanced activity according to:

$$\sigma_{\text{indi}} = [(\text{Flux} - 3 \times \text{Flux}_{\text{err}}) - \text{G}] \times \text{A}_{\text{Eff}} \qquad (5.1)$$
$$\sigma_{\text{indi}} \geq 3\sigma \times \text{A}_{\text{Eff}}.$$

The parameters Flux and Flux_{err} indicate the LAT photon flux and 1σ flux uncertainty in an energy range of 100 MeV - 300 GeV. A_{Eff} stands for the zenith and energy dependent IceCube effective area, while G corresponds to a non-flaring quiescent ground level state of

[25] All these light curves are publicly available at http://fermi.gsfc.nasa.gov/ssc/data/access/lat/msl_lc/

the corresponding blazar. The quantity σ_{indi} defines the individual difference of each flux value to the ground level state G, while σ corresponds to the uncertainty in the ground level calculation. The ground level G and error σ are derived from a Gaussian fit of the LAT flux distribution seen in Fig. 5.1. The red line represents the mean of the Gaussian fit, which indicates the ground level flux, while the standard deviation of the Gaussian fit serves as ground level uncertainty σ. Therefore, Eq. 5.1 introduces a 3σ $(99,73\%)$ flare identification criteria above the ground level flux. The IceCube effective area A_{Eff} for a shower-like neutrino event at 2 PeV ensures a weighting of identified flares according to the IceCube sensitivity. This neutrino energy and flavor have been selected to search for similar events as studied in Kadler et al. (2016), while reducing the integration time significantly. Such a detection would lead to a higher chance coincidence, as only several days of IceCube data have to be considered. In order to select only flares that are capable to be detected in IceCube, data before 55317 MJD (2010-05-01) has been rejected, as before that date IceCube was still under construction. Please refer to App. A for a full list of identified flaring periods.
This flare identification is optimized to select bright blazar flares above a certain (source specific) threshold. Short flares on daily to weekly time scales are favored, as no additional assumption about the flaring behavior is required. Longer outburst periods, which are interrupted by non-detections are therefore split into several individual flares, as in this selection a flare corresponds to an uninterrupted period of activity. For further limitations of the used method, please refer to Sect. 5.1.5.3.

5.1.3 Neutrino Expectation

While neutrinos are exclusively created in hadronic interactions, high energy γ-rays can originate from both leptonic and hadronic interactions (see Sect. 2.2.4.3, 2.3.4). I used a calorimetric approach following Krauß et al. (2014) and Kadler et al. (2016) in order to estimate the maximum amount of high energy neutrino events, a particular flare identified in Sect. 5.1.2 would be capable to produce in a $p\gamma$-interaction (see. Sect. 2.3.4). This leads to a balance between γ-rays F_γ and neutrinos F_ν[26]:

$$\begin{aligned} F_\gamma &= \frac{1}{3}F_\pi + \frac{1}{4}\cdot\frac{2}{3}F_\pi = \frac{1}{2}F_\pi \\ F_\nu &= \frac{2}{3}\cdot\frac{3}{4}F_\pi = \frac{1}{2}F_\pi \\ F_\nu &\leq F_\gamma \end{aligned} \tag{5.2}$$

Here, in the electromagnetic energy flux, the first factor of $\frac{1}{3}$ represents the fraction of neutral pions that are expected to be generated. The second factor of $\frac{1}{4}\frac{2}{3}$ takes electromagnetic cascades into account, which are generated in the interaction of charged pions. For the neutrino flux, the factor of $\frac{2}{3}$ indicates the fraction of charged pions, while the term $\frac{3}{4}$ represents the amount of neutrinos that are produced in the interaction chain of a charged pion. In this maximal case, the integrated keV-to-GeV γ-ray fluence yields the maximum-possible neutrino output and has been confirmed by Monte Carlo simulations (Mücke et al. 2000). The maximum number of neutrino events a flare can create is given by:

$$N_\nu^{\text{max}} = \text{A}_{\text{Eff}} \times \left(\frac{F_\nu}{E_\nu}\right) \cdot \Delta t. \tag{5.3}$$

Here A_{Eff} represents the zenith and energy-dependent IceCube effective area for electron neutrinos at 2 PeV, F_ν the maximum neutrino fluence, E_ν the energy of the neutrino and

[26] This approximation is only valid in case of energy flux.

Δt the integrated time of the neutrino analysis. This time is equal to the duration of the selected flare. To get a more realistic estimation of how many electron neutrino events this model would predict to be detected in the IceCube detector, one can compute the predicted neutrino number according to:

$$N_\nu^{\mathrm{pred}} = f \times N_\nu^{\mathrm{max}}. \tag{5.4}$$

f is a scaling factor which can be factorized into a flavor factor f_I , a factor accounting for the different classes of blazars f_{II}, and a spectrum factor f_{III}:

$$f = f_I \times f_{II} \times f_{III} \tag{5.5}$$

Based on Kadler et al. (2016), I used $f_I = 0.5$, taking into account oscillation from different neutrino flavors and a neutrino power-law spectrum with slope 2.3, as measured by IceCube Collaboration (2013). $f_{II} = 1$ is chosen as only a single active source is considered within the error ellipse of a PeV neutrino event. For the spectrum factor f_{III}, unity would indicate a perfectly peaked neutrino spectrum, which is due to photopion production from monoenergetic UV photons. However, in a more realistic scenario, the actual neutrino spectrum is broader due to different Doppler shifts and source redshifts, so that $f_{III} = 0.05$ is estimated. This leads to a total scaling factor of

$$f = 0.025. \tag{5.6}$$

To account for the maximum neutrino fluence F_ν a given flare can generate, it is necessary to integrate over its entire high energy emission. An energy range of 10 keV to 20 GeV is used, as it covers the entire high energy hump of the blazar SED. See Sect. 5.1.5.3 for a more detailed discussion about the used energy range. Simultaneous *Swift*/XRT and *Fermi*/LAT observations of each flare are used to build SEDs, whose high energy hump can be parameterized by a log-parabola model. Intrinsic absorption in the X-ray is included in the parametrization to account for gamma-thick sources. Figure 5.2 displays a typical SED of a bright flare from 3C 279 (flare number 1 in Table 2), together with the fitted log-parabola and integration range. SEDs of all studied flares can be found in App. B.

5.1.4 A Sample of 50 Promising Blazar Flares

Table 2 lists the results of the neutrino expectation for the 50 best-ranked flares. These flares have been selected from all flares identified in Sect. 5.1.2 according to their averaged neutrino flux, which is defined as:

$$\sigma_{\mathrm{flare}} = \frac{F_\nu}{\Delta t}. \tag{5.7}$$

Here, Δt indicates the duration of the flare, while $\mathrm{t_{min}}$ and $\mathrm{t_{max}}$ mark the start and stop times of a flare given in Modified Julian Day (MJD). Selected flares are highlighted in blue in the light curves shown in App. C, while all other flares identified by Eq. 5.1 are marked in gray. As N_ν^{max} (Eq. 5.3) is directly correlated to the flare duration Δt, longer flares with constant brightness lead to higher neutrino expectations. In order to compare the neutrino detection potential of flares with varied durations, it is necessary to normalize flares according to their duration. The neutrino detection potential σ_ν for a given flare is given by:

$$\sigma_\nu = \frac{\mathrm{N}_\nu^{\mathrm{pred}}}{\Delta t}. \tag{5.8}$$

Figure 5.3 displays the predicted neutrino expectation $\mathrm{N}_\nu^{\mathrm{pred}}$ (Eq. 5.4) for various values of the averaged flux σ_{flare} (Eq. 5.7). Blue points represent flares with simultaneous *Fermi*/LAT and *Swift*/XRT data, while green points show flares where no simultaneous X-ray data are

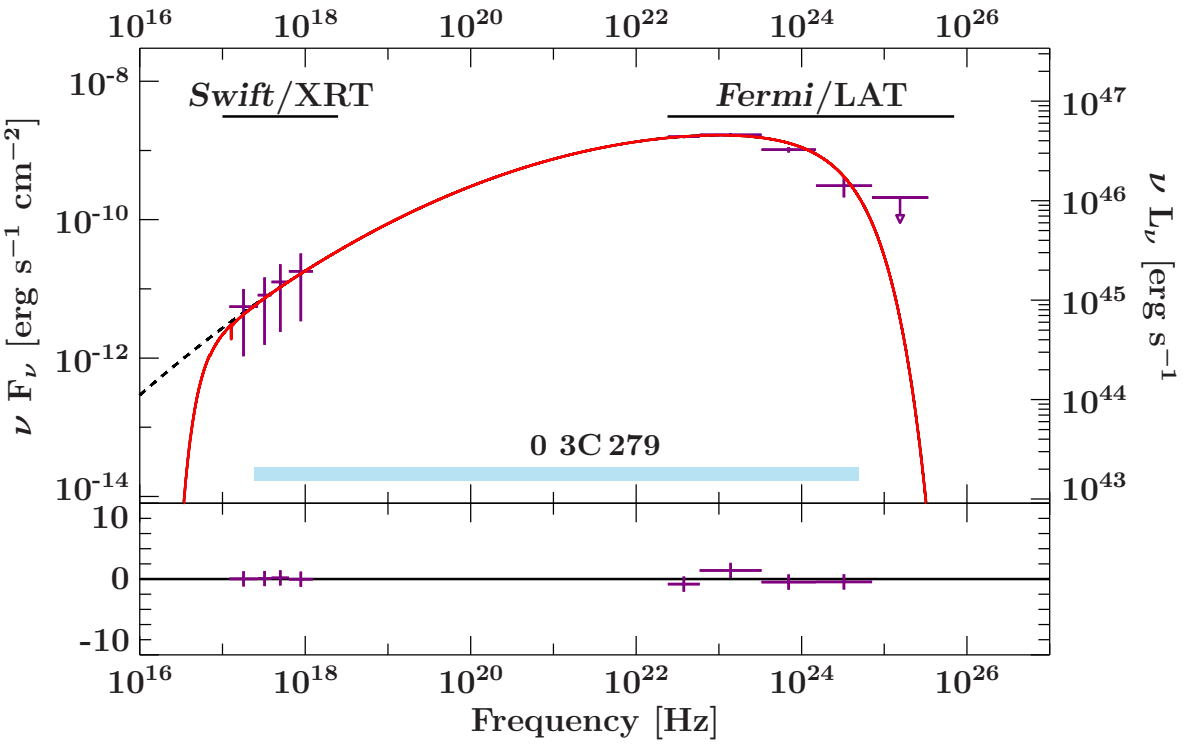

Figure 5.2: Simultaneous spectral energy distribution (SED) of the bright flare of 3C 279 in 2015 (flare 1 in Table2; Cutini (2015a)). The red line indicates a log-parabola parametrization, including intrinsic absorption in the X-ray. The black line shows the same parametrization without the absorption. The shadowed area represents the integration range from 10 keV to 20 GeV.

available. In this case, an averaged *Swift*/XRT spectrum over the entire six year period was used. No direct correlation between the predicted neutrino number and the averaged flux can be seen. Thus, even short-term flares on timescales of days can contribute with a substantial neutrino prediction, if they are bright enough to generate a competitive fluence on a relatively short time scale. This behavior can be seen in Fig. 5.4, where the neutrino prediction (Eq. 5.4) is plotted for different flare durations. Flares with a similar flare duration vary in brightness and thus can produce different neutrino expectations. The majority of flares shows a duration of less than five days, which can be explained by the used flare selection criteria (see Eq. 5.1). The neutrino detection potential σ_ν (Eq. 5.8) is displayed in Fig. 5.5, depending on the averaged flux σ_{flare} (Eq. 5.7). This plot can be interpreted as a neutrino detection power per flare, as it indicates which neutrino prediction a flare would generate normalized on a one day timescale. While the majority of flares seem to have similar detection powers, unaffected from their individual durations, flare 1 in Table 2 clearly dominates the sample by producing the highest averaged neutrino flux as well as the best daily neutrino prediction. This clearly makes flare 1 the best short-term flare candidate for a neutrino flare association, based on the selection criteria introduced in this section.

5.1.5 Discussion

The detection potential for associated neutrino searches drops steeply with increasing flare number in Table 2. The two blazars 3C 279, and PKS 1510−089 alone account for a majority of 42 flares, while the 50 highest-ranked flares are produced by a group of only seven differ-

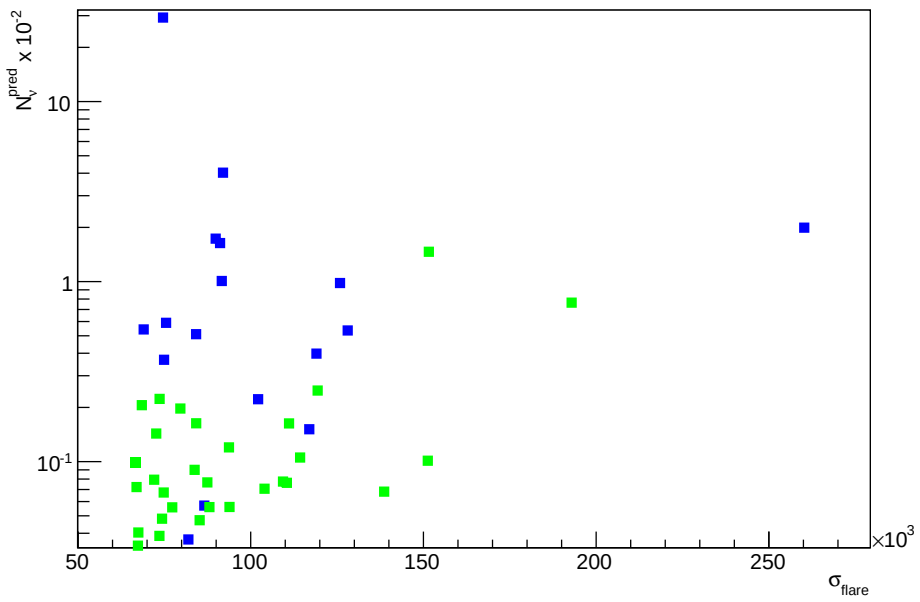

Figure 5.3: Predicted number of neutrino events N_ν^{pred} depending on the averaged flux σ_{flare}. Blue points show flares with simultaneous *Fermi*/LAT and *Swift*/XRT data, while green points show flares with an averaged *Swift*/XRT spectrum. No direct correlation between both parameters can be seen.

ent sources: 3C 279 (10 flares), PKS 1510−089 (32 flares), PKS 0402−362 (1 flare), CTA 102 (1 flare), 3C 454.3 (1 flare), PKS 1424−418 (3 flares), and PKS 1329−049 (2 flares). While long-term outbursts like flare 38 clearly provide the largest neutrino predictions due to their brightness and duration of multiple months, the individual neutrino prediction of shorter flares, whose duration is typically on the order of days, is rather small. However, individual extremely bright flares can provide a substantial neutrino detection power, if they produce enough fluence on this relatively short time range. Thus, I can at least partially confirm the results from Halzen & Kheirandish (2016), identifying flare 1 as the most promising short-term flare neutrino source candidate. Nevertheless, based on the calorimetric argumentation introduced in Sect. 5.1.3, the predicted number of 2 PeV shower-like neutrino events this particular flare would induce within the IceCube detector is only on the order of $N_\nu^{pred} \approx 0.02$ and therefore significantly smaller than suggested by Halzen & Kheirandish (2016). While Halzen & Kheirandish (2016) do consider different neutrino spectral energy ranges and interaction processes, they overestimate the expected neutrino flux by not taking into account flavor variations due to neutrino oscillation and contributions from the keV to MeV regime.
To study the total detection potential of all 50 flares in this sample, Fig. 5.6 displays the stacked neutrino expectation depending on the number of flares added to the stack. The rapid increase in the beginning is due to flares that last several weeks, while the saturating tendency originates from the rather small contribution of shorter flares with duration going down to a single day. To parameterize this behavior, a Taylor series is used. The integrated fluence of the 50 highest-ranked flares together yields only about 50 % of Poisson probability for the detection of a single coincident high-energy neutrino, consistent with the non-detection of any such events in the first six years of IceCube unblinded data. Extending this sample to e.g. 100 flares therefore would only marginally increases the total detection power, as no sub-

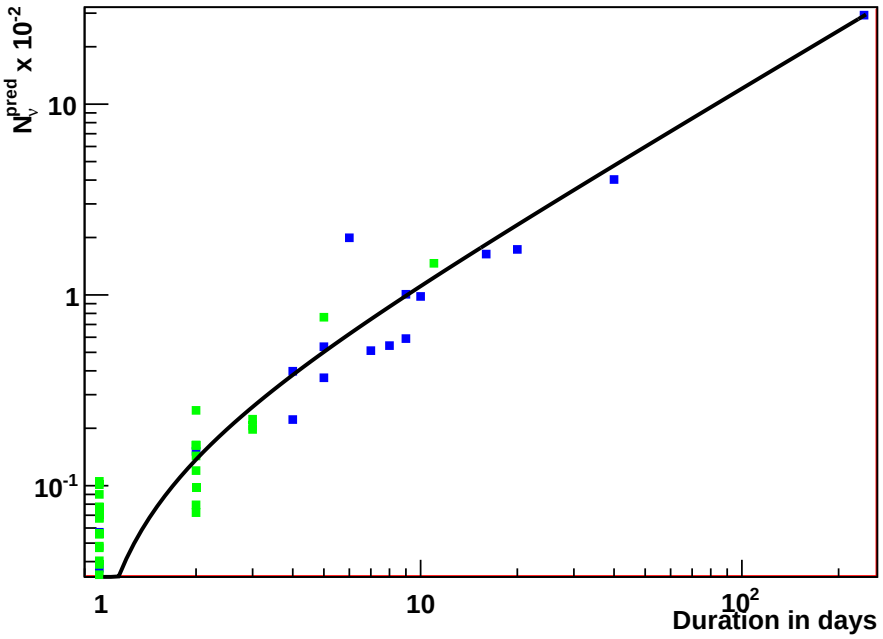

Figure 5.4: Predicted number of neutrino events N_ν^{pred} depending on the flare duration. Blue points show flares with simultaneous *Fermi*/LAT and *Swift*/XRT data, while green points show flares with an averaged *Swift*/XRT spectrum. The black line indicates a linear fit of the data, as expected from Eq.5.3.

stantial increase is given by adding more, fainter short-term flares. For the most spectacular short-term blazar flares, however, Poisson probabilities of up to $\sim 2\,\%$ are calculated, meaning the possibility of associated neutrino detections in future data unblindings of IceCube and KM3NeT seems reasonable.
In the following, the flaring behavior of the two FSRQs PKS 1510−089 and 3C 279, which dominate the selected sample will be discussed in more detail.

5.1.5.1 PKS 1510−089

The blazar PKS 1510−089 (z = 0.360; Thompson et al. (1990)) is one of a handful of flat spectrum radio quasars being active in the TeV regime and has first been observed at these high energies in 2009 by H.E.S.S. Collaboration et al. (2013). Being a particular active source in many wavelengths, this target is regularly monitored by several instruments, revealing a complex multiwavelength behavior with changing emission patterns between different energy bands. (Saito et al. 2013, 2015, Brown 2013). For further details about the VHE emission behavior of this source, please refer to e.g. Zacharias et al. (2017a,b).
At GeV energies, this source is one of the most active blazars, monitored daily by the LAT[27]. Figure 5.7 shows the six-year-long (55317 MJD to 57662 MJD) daily *Fermi*/LAT γ-ray light curve, as used for the flare identification in Sect. 5.1.2. With a total of 42 flares, PKS 1510−089 clearly dominates the selected flare sample in Table 2. Given the fact that the flare identification is biased towards higher photon fluxes ($> 10^{-6}\,\mathrm{ph\,cm^{-2}\,s^{-1}}$) and flare durations on

[27] https://fermi.gsfc.nasa.gov/FTP/glast/data/lat/catalogs/asp/current/lightcurves/1510-089_86400.png

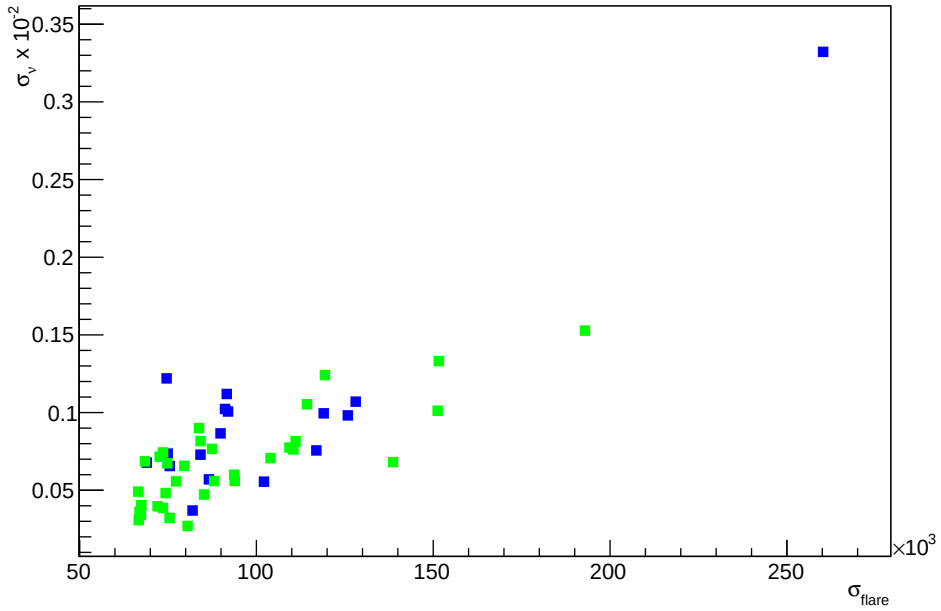

Figure 5.5: Neutrino detection power σ_ν depending on the averaged flux. Blue points show flares with simultaneous *Fermi*/LAT and *Swift*/XRT data, while green points show flares with an averaged *Swift*/XRT spectrum. Flare 1 in Table 2 clearly dominated the sample.

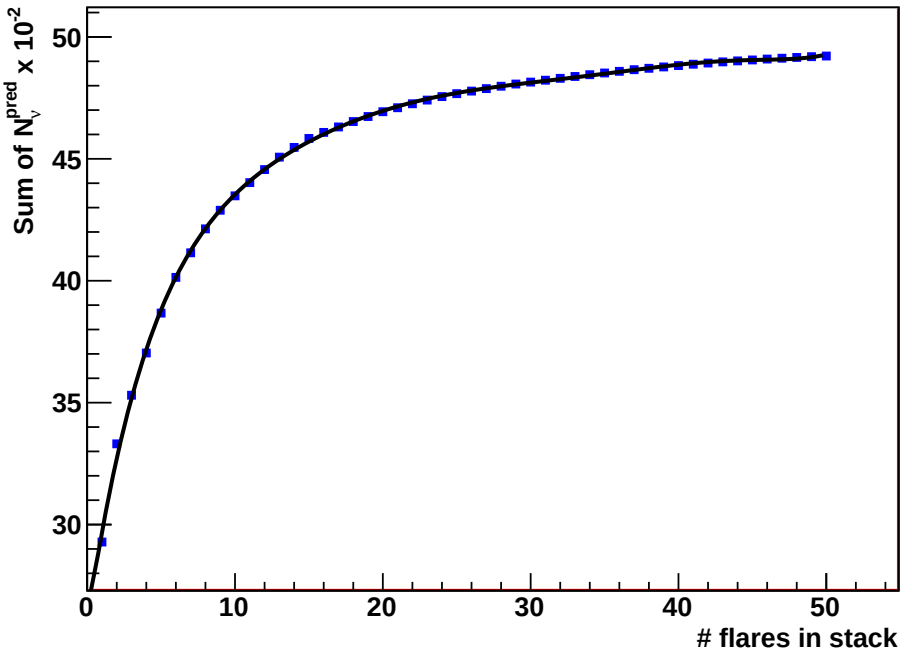

Figure 5.6: Stacked neutrino analysis, showing the sum of the predicted number of neutrino events N_ν^{pred} depending on the number of flares added to the stack. The black line represents a parametrization of the curvature. The saturating tendency is caused by the rather small contribution of short-term blazar flares.

Table 2: Neutrino expectation for the 50 best-ranked flares, selected and sorted according to their averaged flux σ_{flare} (see Eq. 5.7). t_{min} and t_{max} indicate the start and stop time of a flare in Modified Julian Day (MJD). Neutrino expectations are calculated following Sect. 5.1.3. The full list of selected flares in available in App. A

Source	Flare Number	σ_{flare}	t_{min} [MJD]	t_{max} [MJD]	N_ν^{max}	$N_\nu^{\text{pred}} \times 10^{-2}$	Duration [Days]	$\sigma_\nu \times 10^{-3}$
3C 279	1	260238	57186	57192	0.797	1.99	6	3.32
PKS 1510−089	2	192902	55849	55854	0.306	0.764	5	1.53
PKS 1510−089	3	151569	55866	55877	0.586	1.46	11	1.33
PKS 1510−089	4	151262	55856	55857	0.0405	0.101	1	1.01
3C 279	5	138636	56717	56718	0.0272	0.0681	1	0.681
3C 279	6	128078	56749	56754	0.214	0.535	5	1.07
PKS 1510−089	7	125857	57241	57251	0.393	0.982	10	0.982
3C 279	8	119379	56866	56868	0.0993	0.248	2	1.24
PKS 1510−089	9	119033	56553	56557	0.159	0.398	4	0.995
PKS 1510−089	10	116956.	55766	55768	0.0605	0.151	2	0.757
PKS 1510−089	11	114301	57098	57099	0.0422	0.105	1	1.05
PKS 1510−089	12	111097	56563	56565	0.0652	0.163	2	0.815
PKS 1510−089	13	110472	55843	55844	0.0305	0.0763	1	0.763
PKS 1510−089	14	109350	57148	57149	0.0310	0.0775	1	0.775
PKS 1510−089	15	104003	56542	56543	0.0283	0.0707	1	0.707
PKS 1510−089	16	102145	55742	55746	0.0889	0.222	4	0.555
PKS 1510−089	17	93862	56610	56611	0.0223	0.0560	1	0.560
PKS 1510−089	18	93711	55738	55740	0.0480	0.120	2	0.600
PKS 1510−089	19	91983.	55954	55994	1.61	4.03	40	1.01
PKS 1510−089	20	91625	55997	56006	0.403	1.01	9	1.12
PKS 1510−089	21	91131	57113	57129	0.655	1.64	16	1.02
PKS 1510−089	22	89860	57152	57172	0.693	1.73	20	0.866
PKS 1510−089	23	88048	57609	57610	0.0224	0.0559	1	0.559
PKS 1510−089	24	87449	57201	57202	0.0307	0.0767	1	0.767
PKS 1510−089	25	86571	55790	55791	0.0228	0.0570	1	0.570
PKS 1510−089	26	85220	57101	57102	0.0189	0.0473	1	0.473
3C 279	27	84223	57153	57155	0.0653	0.163	2	0.816
PKS 0402−362	28	84194	55824	55831	0.204	0.510	7	0.729
PKS 1510−089	29	83764	57131	57132	0.0360	0.0900	1	0.900
PKS 1510−089	30	81956	57198	57199	0.0148	0.0370	1	0.370
CTA 102	31	80537	57558	57559	0.0108	0.0270	1	0.270
3C 279	32	79636	57212	57215	0.0789	0.197	3	0.657
PKS 1510−089	33	77287	56832	56833	0.0223	0.0557	1	0.557
3C 279	34	75503	56646	56655	0.236	0.590	9	0.656
3C 279	35	75455	56757	56758	0.0129	0.0322	1	0.322
3C 279	36	74919	56742	56747	0.147	0.368	5	0.736
PKS 1510−089	37	74815	57055	57056	0.0269	0.0674	1	0.674
3C 454.3	38	74620	55408	55648	11.71	29.28	240	1.22
PKS 1510−089	39	74337	56571	56572	0.0193	0.0482	1	0.482
PKS 1510−089	40	73629	57210	57213	0.0892	0.223	3	0.744
PKS 1424−41	41	73574	56435	56436	0.0154	0.0387	1	0.387
3C 279	42	72654	55466	55468	0.0573	0.143	2	0.716
PKS 1424−41	43	72058	56394	56396	0.0317	0.0794	2	0.397
PKS 1510−089	44	69019	57215	57223	0.217	0.542	8	0.678
PKS 1510−089	45	68479	56536	56539	0.0823	0.206	3	0.686
PKS 1510−089	46	67473	56954	56955	0.0162	0.0404	1	0.404
PKS 1329−049	47	67355	55467	55468	0.0137	0.0341	1	0.341
PKS 1329−049	48	66954	55445	55447	0.0289	0.0722	2	0.361
PKS 1424−41	49	66732	57385	57386	0.0123	0.0308	1	0.308
PKS 1510−089	50	66603	56567	56569	0.0393	0.0983	2	0.491

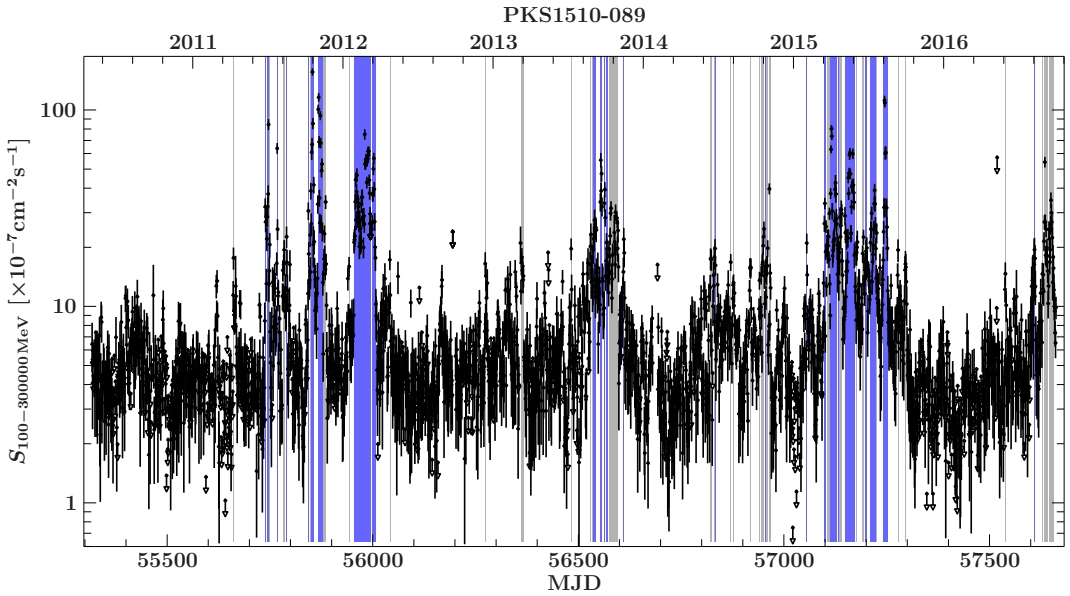

Figure 5.7: *Fermi*/LAT γ-ray light curve for PKS 1510−089 in an energy range of 100 MeV - 300 GeV and a time range of 55317 MJD - 57662 MJD using daily binning. Highlighted flares (both in blue and gray) correspond to selected time intervals following Sect. 5.1.2, while blue intervals indicate selected flares listed in Table 2. Please note the logarithmic y-axis.

the order of days to weeks, no preference on any region in the sky is included in the analysis. Based on the all-sky search for neutrino source candidates presented in this thesis, this makes PKS 1510−089 a promising neutrino point source candidate for future neutrino detections, even if the fluence of most flares is far to small to generate a subsequent neutrino prediction on daily timescales.

5.1.5.2 3C 279

The FSRQ 3C 279 (z = 0.536; Marziani et al. 1996) is one of the most prominent γ-ray sources in the sky. Regularly detected above 100 MeV by EGRET (Hartman et al. 1992,Kniffen et al. 1993), AGILE (Giuliani et al. 2009) and *Fermi*/LAT[28] (e.g. Hayashida et al. 2012, 2015), this blazar is also one of the few FSRQs active at TeV energies (e.g. MAGIC Collaboration et al. 2008). In 2015, 3C 279 underwent a remarkable bright flaring state (Cutini 2015b), becoming one of the brightest flares ever detected by the LAT. While this flare was also observed in X-rays (Pittori et al. 2015a,b, Bottacini et al. 2015), no TeV activity has been measured. The total γ-ray activity observed in the 2015 flare showed rapid variations even on two minute timescales with flare doubling times of less than five minutes (Ackermann et al. 2016b). Such a fast variability indicates a compact emission region (see Sect. 2.4.2.2) in a conical jet model as well as high Lorentz factors to avoid γ-ray absorption within the jet.
Figure 5.8 displays the six-year-long (55317 MJD to 57662 MJD) *Fermi*/LAT γ-ray light curve using daily binning. A period of six days around the massive flare in 2015 has been identified. Halzen & Kheirandish (2016) suggested this flare to be the most promising candidate for a direct neutrino point source association. Following the calorimetric argumentation presented in this section, I clearly can confirm the 2015 flare of 3C 279 as the best-ranked neutrino can-

[28] https://fermi.gsfc.nasa.gov/FTP/glast/data/lat/catalogs/asp/current/lightcurves/3C279_86400.png

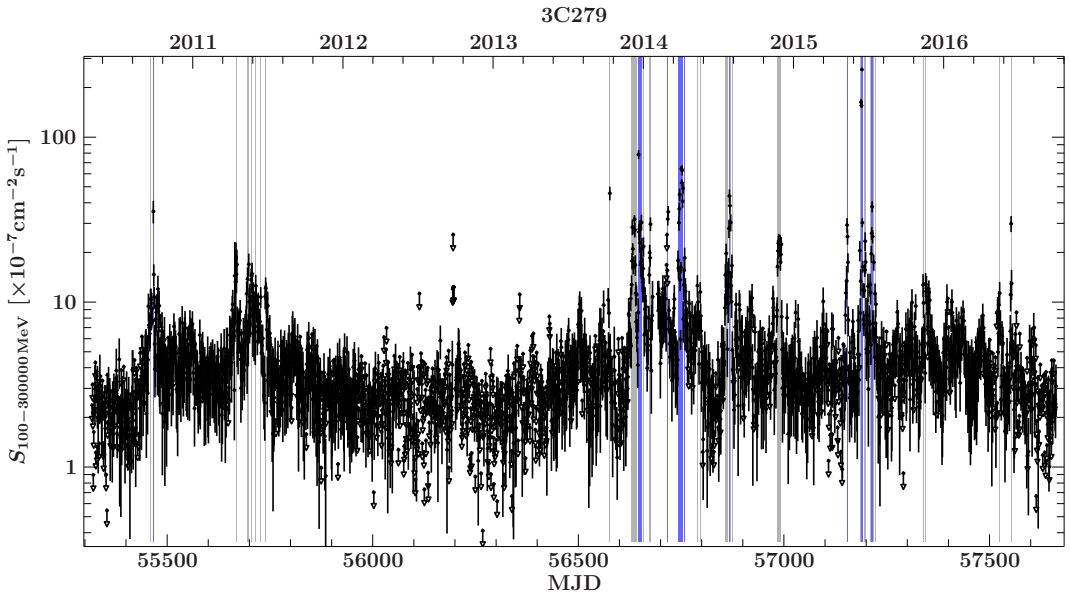

Figure 5.8: *Fermi*/LAT γ-ray light curve for 3C 279 in an energy range of 100 MeV - 300 GeV and a time range of 55317 MJD - 57662 MJD using daily binning. Highlighted flares (both in blue and gray) correspond to selected time intervals following Sect. 5.1.2, while blue intervals indicate selected flares listed in Table 2. Please note the logarithmic y-axis.

didate, based on its normalized neutrino expectation σ_ν (see Eq. 5.8). However, its individual neutrino prediction N_ν^{pred} (see Eq. 5.4) within the IceCube detector is only on the order of 0.02, lowering the expectations of Halzen & Kheirandish (2016) significantly. Compared to the 50 flares with the highest normalized neutrino expectation in Table 2, the 2015 flare of 3C 279 is still the best candidate for a 2 PeV neutrino association with a blazar flare that only lasted several days.

5.1.5.3 Limitations of the Used Method

In this section, I focus on limitations of the used method and other caveats regarding the neutrino expectation.

Calorimetric Neutrino Output

The neutrino calculation presented in this work is based on a purely hadronic origin of the observed high energy radiation. Furthermore, only photo pionproduction following Eq. 2.40 and Eq. 2.42 is taken into account, neglecting other processes such as proton-proton or Bethe-Heitler interactions in the jet (Petropoulou & Mastichiadis 2015), which would also contribute to the observed high energy emission and produce neutrinos.
FSRQs are favored against BL Lac objects due to their strong optical and UV components, which serve as target for $p\gamma$ interactions (Krauß et al. 2014). Some authors (Righi et al. 2017), however, consider BL Lac type objects as promising neutrino candidates, though it is unclear how the absence of optical seed photons in these sources can be solved.

Neutrino Spectrum

A power-law spectrum is assumed for the extragalactic neutrino flux, which could be a wrong assumption. Furthermore, Eq. 5.3 assumes all neutrinos to be produced with a given energy, following a δ-distribution. The neutrino expectation listed in Table 2 therefore only takes neutrinos generated exclusively with an energy of 2 PeV into account, neglecting contributions from lower energies as well as energy uncertainties. Eq. 5.5 includes a factor to scale the maximum neutrino expectation down, assuming the neutrino energy distribution to be smeared out between about 0.03 PeV to 10 PeV. However, this reduces the amount of predicted neutrinos, while ignoring contributions from other energies. Depending on the spectral shape or selected neutrino energy, one can easily vary the amount of predicted neutrino events by about an order of magnitude. Therefore, I consider this as one of the largest systematic uncertainties of this study.

Multiwavelength Coverage

The multiwavelength coverage is far from ideal. In fact, many of the flares listed in Table 2 are only observed by either a single *Swift*/XRT pointing or no X-ray observation at all during the duration of the flare. In the case of no detection, an averaged X-ray spectrum over the entire six year period is used. Several flares show upper limits in the *Fermi*/LAT spectrum, being significantly (TS$>$ 25) detected only in two to three energy bands. Achieving (quasi-)simultaneous data within different energy bands for most of the flares is highly challenging, as data taking cycles of different instruments are only barely synchronized and pointed instruments such as *Swift*/XRT have a given reaction time to observe new targets. For further details about the *Fermi*/LAT observation strategy please refer to Sect. 3.3.3, while in Sect. 3.2.3 details about the Neil Gehrels Swift Observatory can be found.
This sparse multiwavelength coverage leads to an inaccurate calculation of the total high energy fluence and therefore to an additional uncertainty on the neutrino expectation. However, the integrated flux varies only by less than an order of magnitude for the selected sample of flares, while the influence on the neutrino expectation is rather small.

Fluence Integration Range

The maximum number of neutrino events expected from a specific flare depends on several factors, such as the neutrino spectrum or flare duration. However, the primary ingredient in Eq. 5.3 is the total integrated high energy emission (assuming purely hadronic processes). The exact energy interval of 1 keV to 20 GeV does not affect the neutrino expectation significantly, as long as the peak of the high energy hump is covered. This clearly indicates that the maximum neutrino expectation depends on the total high energy fluence, instead of the emission in some energy bands like e.g. the *Fermi*/LAT flux. Please refer to Sect. 5.1.4 for further details regarding the connection between γ-ray fluence and neutrino expectation.

Faint Sources

As the cross section of neutrino interactions with matter is low compared to other leptons, one could detect neutrinos from sources that are too faint to be resolved with current instruments. Therefore, it is necessary to estimate additional neutrino events from fainter unresolved blazars that lie in the vicinity of our target source and could further reduce the number of predicted neutrino events from the target. A rough estimation about this unresolved blazar population can be obtained from the extragalactic γ-ray background (EGB). About 50 % to 80 % of the

EGB is expected to originate from blazars (Inoue & Totani 2009, Ackermann et al. 2015b). However, this even strengthens the result of this thesis, according to which blazar flares with durations of days are unlikely capable of explaining the detected high energy neutrino flux.

Flare Identification

The flare identification described in Sect. 5.1.2 is optimized for bright flares with durations on the order of days to weeks. Intra Day Variability (IDV, see Sect. 2.4.2.2) can not be resolved due to the selected daily time binning of the used light curves. While for each source an individual ground level flux is calculated, no variation in time is included in the ground state calculation. This mostly effects sources with a steady increase in flux over several years (e.g. PKS 1424−418), while in the presented analysis this results in a larger ground state flux uncertainty. Short-term flares are preferred selected, as the flare duration sharply is defined by the number of successive light curve bins that fulfill Eq. 5.1.
Longer periods of enhanced activity with varying flux levels or even non-detections are split into multiple (short-term) flares, which in the total ranking are all treated independently. A first approach of introducing an equivalent selection criteria for longer outburst periods on the order of weeks to years could be achieved by allowing some flux values within a longer outburst period to violate Eq. 5.1. On the one hand this modification would reduce the number of short-term flares in which a long-term outburst period is divided into, while on the other hand it would introduce a systematic offset on the duration of short-term flaring states, which would also affect the neutrino expectation.

5.2 TXS 0506+056: The First Identified Neutrino Point Source

On 22 September 2017, IceCube detected a $\sim$ 290 TeV neutrino-induced, track-like event (called IceCube-170922A) from a direction spatially and temporally consistent with enhanced γ-ray activity from the blazar TXS 0506+056. This event is of particular interest, since for the first time, a high energy track-like neutrino event with an angular uncertainty of only $\sim 1^\circ$ was found from the direction of a flaring blazar[29]. On 12 July 2018, after a huge effort of several international Collaborations, the IceCube Collaboration et al. (2018) announced the detection of the first neutrino point source, opening the window for the new field of neutrino multimessenger astronomy.
In this section, I present the results of my calorimetric analysis of TXS 0506+056, following the method introduced in Sect. 5.1.3. A *Fermi*/LAT light curve analysis (see Sect. 4.2.3) is performed to identify periods of enhanced activity at GeV energies. Based on a statistical analysis of a high number of known γ-ray sources I calculate the chance coincidence for a correlated detection of both messengers.

5.2.1 Introduction

An AMON alert[30] (see Sect. 3.5.5) was automatically triggered and distributed within one min after the detection of IceCube-170922A by the IceCube Collaboration. This alert was followed by a GCN circular[31], which applied a more sophisticated reconstruction algorithm to constrain the direction of the neutrino event. On 28 September 2017, the *Fermi*/LAT Collaboration reported enhanced γ-ray activity from the catalog source TXS 0506+056, which is $\sim 0.1^\circ$

[29] see Kadler et al. (2016) for comparison, where a PeV shower-like neutrino event was found to be consistent with an outburst period of the blazar PKS 1424−418
[30] https://gcn.gsfc.nasa.gov/notices_amon/50579430_130033.amon
[31] https://gcn.gsfc.nasa.gov/gcn3/21916.gcn3

off the neutrino direction (Tanaka et al. 2017). Observations by the Major Atmospheric Gamma Imaging Cherenkov (MAGIC) telescopes (see Sect. 3.4 and 3.5.3.1) in the time form 28 September 2017 till 3 October 2017 revealed increased activity in an energy range of above 100 GeV (Mirzoyan 2017). Follow up observations have been performed at X-ray (Keivani et al. 2017; Negoro et al. 2017), optical (Franckowiak et al. 2017; Steele 2017) and radio (Tetarenko et al. 2017) wavelengths. These observations have confirmed the variable nature of the blazar ranging from radio to γ-ray energies, clearly indicating that the source was in a flaring state at the time of the neutrino arrival. Optical observations with the Gran Telescopio Canarias (GTC) at the Roque de Los Muchachos yield the redshift of TXS 0506+056 to be $z = 0.3365 \pm 0.0010$ (Paiano et al. 2018), which was previously unknown. On 12 July 2018, after an intensive multiwavelength campaign, the IceCube Collaboration et al. (2018) announced the detection of TXS 0506+056 as the first neutrino point source with a significance at the level of $3\,\sigma$ (standard deviations). A follow up analysis by the ANTARES Collaboration (see Sect. 3.5.4.1) searched for neutrino candidates in a $\pm$ one day interval around the arrival time of IceCube-170922A and found no events from the direction of TXS 0506+056. This is in agreement with the about ten times smaller sensitivity of ANTARES for that region of the sky compared to the IceCube detector (Dornic & Coleiro 2017; Albert et al. 2018). In the following, I will use the calorimetric approach introduced in Sect. 5.1.3 to calculate the significance of this multimessenger event and put this result into context to previous studies mentioned in this section.

5.2.2 Long-term γ-ray Flaring Behavior

A long-term variability analysis has been performed in a time interval of nine years ranging from the start of the *Fermi* mission in August 2008 until the arrival of IceCube-170922A in September 2017, following Sect. 4.2.3. Figure 5.9 shows the *Fermi*/LAT γ-ray light curve in an energy range of 100MeV to 300GeV using monthly time bins. For most of the time, TXS 0506+056 was in a low-state with flux levels fluctuating around $0.7 \times 10^{-7}\,\mathrm{ph\,cm^{-2}\,s^{-1}}$. From the beginning of 2017 on, this source went into a major outburst period, brightening up to six times of its averaged flux level. After several months of increased activity, IceCube-170922A was detected in positional and temporal agreement with this major outburst period. It is worth mentioning that, compared to the bright blazar flares typically studied by Fermi and in Sect. 5.1.4, such an outburst is not unusual for a BL Lac object and would not have been followed up as extensively if the neutrino event was not detected.
Contradictory to the approach of searching for neutrino γ-ray correlations in narrow time windows around the arrival time of the neutrino event as applied by most neutrino point source studies (e.g. Aartsen et al. 2015b; The ANTARES Collaboration 2015), no short-term flaring period on the order of days is identified in September 2017, following the selection criteria introduced in Sect. 5.1.2. Based on the calorimetric argumentation introduced in Sect. 5.1.3 and the results from the short-term flare neutrino analysis seen in Table 2, this already puts first doubt against a short-term flare neutrino association, which will be addressed in the subsequent section in more detail.

5.2.3 Calorimetric Neutrino Output

No short-term flaring period has been identified according to Sect. 5.1.2 around the arrival time of IceCube-170922A in September 2017. In the following, I will compare the calorimetric neutrino output of this source in an arbitrary defined three day short-term flaring period around the neutrino detection time and a long lasting outburst covering the time of enhanced activity in 2017 seen in Fig. 5.9. A neutrino energy of $E_\nu = 290\,\mathrm{TeV}$, together

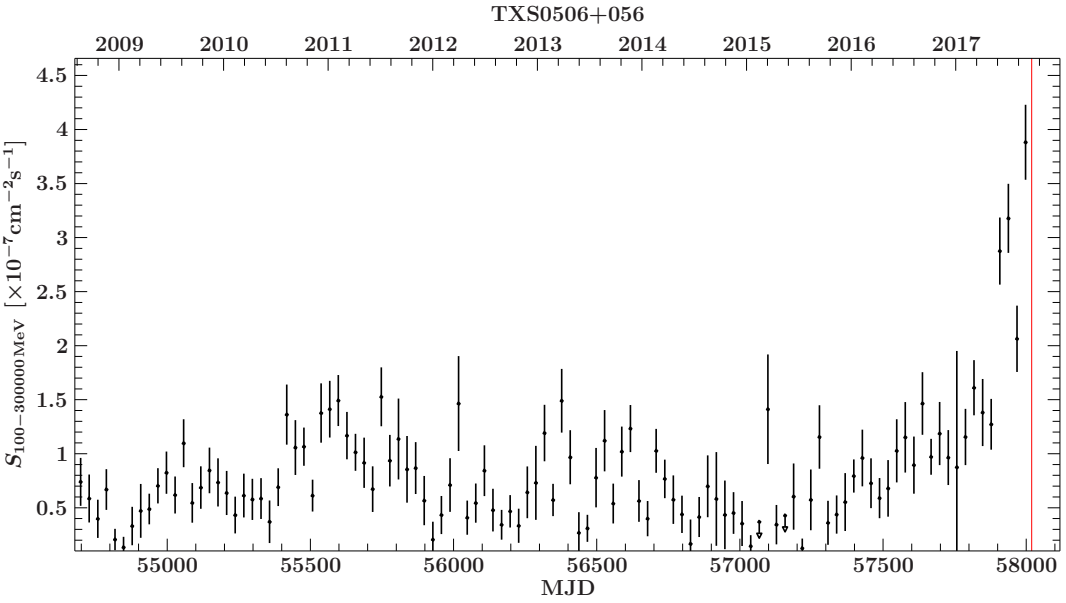

Figure 5.9: *Fermi*/LAT γ-ray light curve of TXS 0506+056 in an energy range of 100 MeV - 300 GeV and a time range of 54682.65 MJD - 58027 MJD using monthly binning. Increased γ-ray activity is seen since the beginning of 2017. The arrival time of IceCube-170922A is indicated by a red line, which is consistent with a several months long-term outburst period.

with the corresponding energy and zenith dependent effective area A_{Eff} for a muon neutrino induced track-like event is used to calculate the neutrino expectation according to Eq. 5.3. To estimate the maximum fluence, *Swift*/XRT and *Fermi*/LAT spectra have been calculated. The extraction of the *Swift*/XRT data followed the standard pipeline introduced in Sect. 4.1, while the *Fermi*/LAT spectra were calculated as described in Sect. 4.2.

5.2.3.1 Short-term Three Day Period

A time interval of three days ranging from 58017 MJD - 58020 MJD is arbitrary defined around the arrival time of the neutrino event. Figure 5.10 displays the high energy hump of the blazar SED, using simultaneous *Swift*/XRT and *Fermi*/LAT data in the selected time interval. Following the calorimetric argumentation in Sect. 5.1.4, one can estimate the maximum neutrino output that could be detectable by IceCube under the most optimistic and certainly over-optimistic conditions of a monoenergetic, single flavor (ν_μ) neutrino signal at 290 TeV to be:

$$N_\nu^{\mathrm{max}} = 0.0035. \tag{5.9}$$

Scaling[32] these number down, according to Eq. 5.5, leads to a predicted neutrino number of:

$$N_\nu^{\mathrm{pred}} \approx 9 \times 10^{-5}. \tag{5.10}$$

These numbers are small, even compared to the results found in Table 2 for flares with similar duration. This is due to the fainter nature of this source at X-ray to GeV energies, which is about one to two orders of magnitude below the flares studies in Sect. 5.1.4 and also translates

[32] While for the previous scaling an electron neutrino with an energy of 2 PeV is used, I do not expect the scaling factor to vary significantly for a 290 TeV muon neutrino. While the total number may change by a small factor, this does not affect the drawn conclusions.

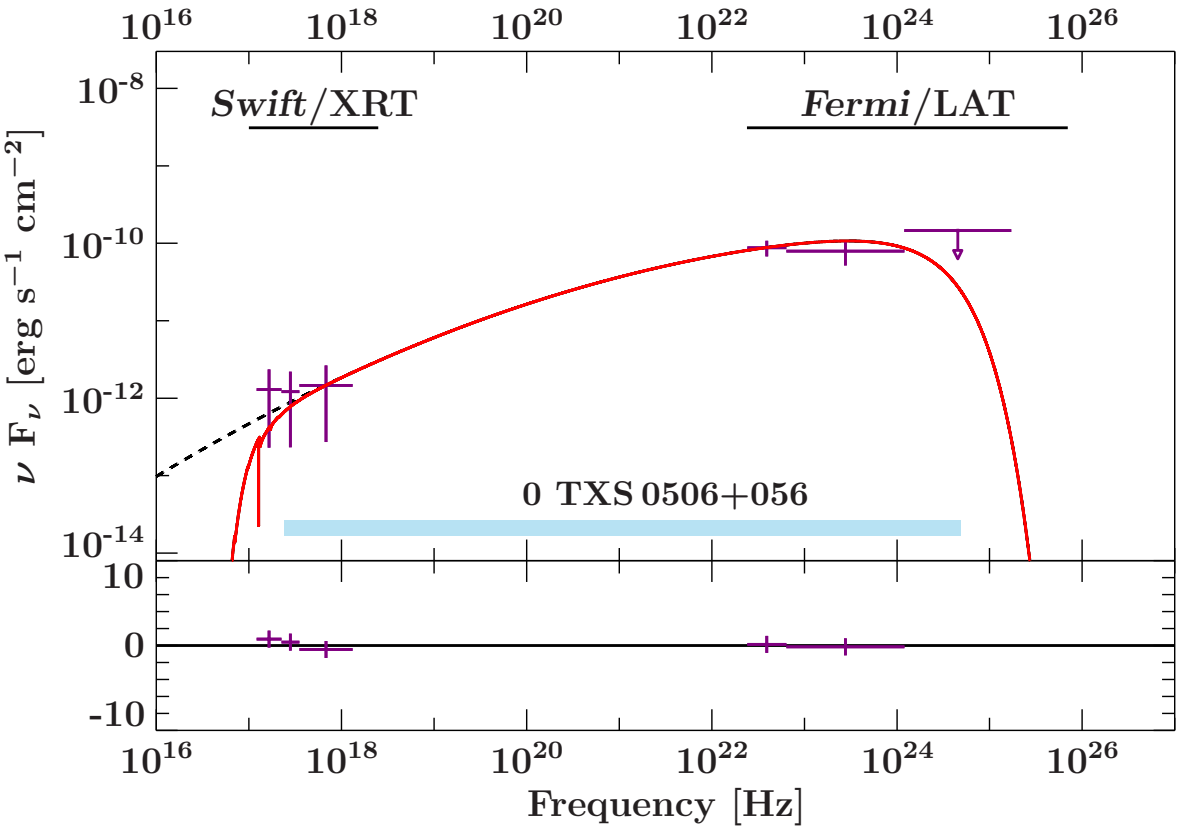

Figure 5.10: Simultaneous spectral energy distribution (SED) of TXS 0506+056 in an arbitrary defined 3-day period around the arrival time of IceCube-170922A ranging from 58017 MJD - 58020 MJD. The red line indicates a log-parabola parametrization, including intrinsic absorption in the X-ray. The black line shows the same parametrization without the absorption. The shadowed area represents the integration range from 1 keV to 20 GeV.

to a smaller integrated γ-ray fluence. From a calorimetric point of view, it thusly seems unrealistic to associate the event IceCube-170922A with a three day flare period of the blazar TXS 0506+056.

5.2.3.2 Long-term Outburst Period

The outburst period at GeV energies, during which IceCube-170922A occurred already started in April 2016, as can be seen in Fig. 5.9. Following the calorimetric argumentation of the previous sections, the neutrino output of this long-term outburst period is calculated in a time range of of 57479 MJD - 58027 MJD. Figure 5.11 shows the corresponding SED, using simultaneous *Swift*/XRT and *Fermi*/LAT data. For the maximum muon neutrino output at an energy of 290 TeV one gets:

$$N_\nu^{\max} = 1.19. \tag{5.11}$$

Scaling[33] these number down to a more realistic neutrino expectation by using Eq. 5.5, one derives

$$N_\nu^{\text{pred}} = 0.029, \tag{5.12}$$

[33] See scaling in Sect. 5.2.3.1.

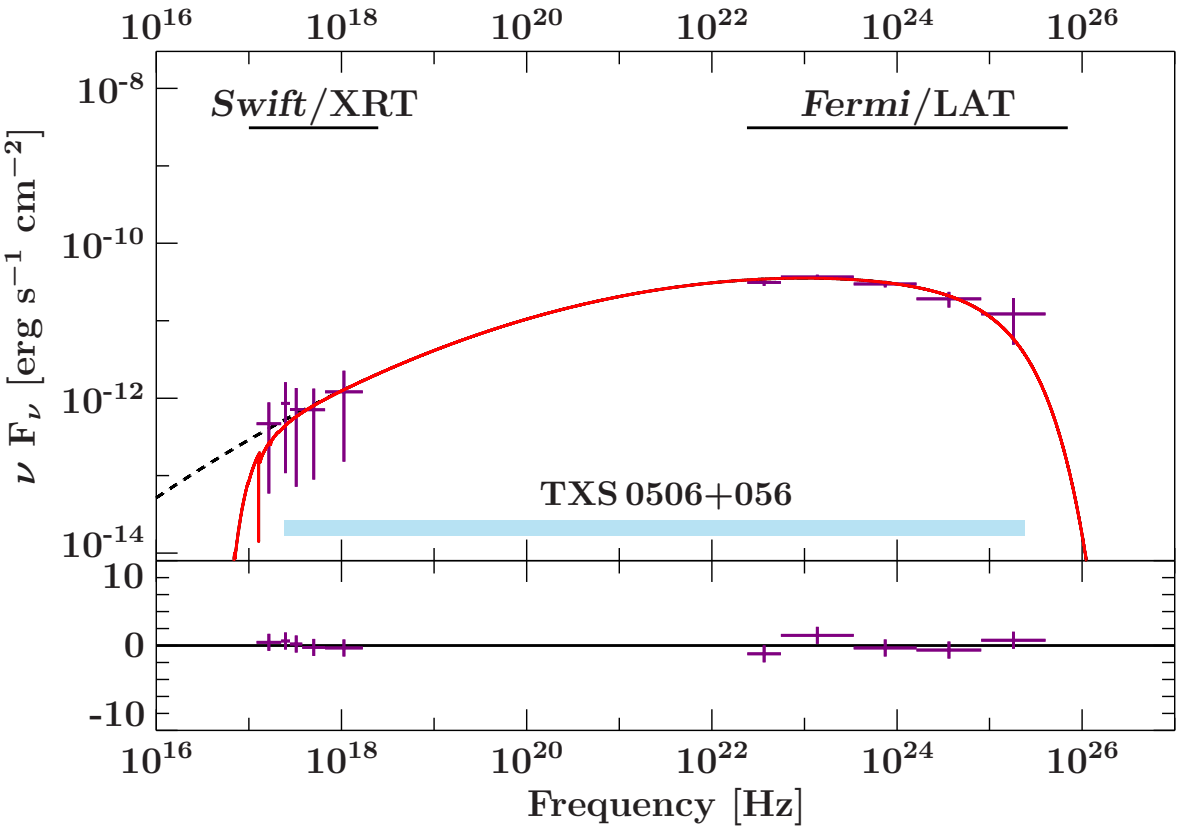

Figure 5.11: Simultaneous spectral energy distribution (SED) of the long-term outburst of TXS 0506+056 in a time range of 57479 MJD - 58027 MJD. For further details please refer to Fig. 5.10

corresponding to a Poisson probability of about 3% for a dedicated neutrino correlation with a blazar of similar fluence as TXS 0506+056. For the interpretation of this value, it is important to remember that a considerable number of other blazars has produced outbursts with similar fluence, which did not coincide with the detection of a high energy neutrino due to the small Poisson probability. Thus, it is not surprising that the neutrino prediction for the first confirmed association with a flaring blazar is well below unity. Similar values from short-term blazar flares can only be achieved by producing a much higher fluence on relatively short time scales (see e.g. flare 1 in Table 2). Thus, based on the calorimetric approach used in this thesis, an association of the high energy neutrino event IceCube-170922A with the blazar TXS 0506+056 seems reasonable. However, a dedicated statistical analysis to calculate the chance coincidence of this association has to be done, comparing the long-term outburst of TXS 0506+056 to a large number of similar sources in the sky.

5.2.4 Chance Coincidence Calculation

In order to calculate the chance coincidence for a correlated association of the neutrino event IceCube-170922A with the long-term outburst period of TXS 0506+056 (see Fig. 5.9 and Sect. 5.2.3.2), it is mandatory to study the flaring behavior of a large number of sources in the sky during the outburst period of TXS 0506+056. Therefore, the energy flux of (almost) all[34] known γ-ray sources in the sky is calculated in the relevant time range of 57479 MJD -

[34]This includes all blazars in the 3FGL and 3FHL catalogs. Not included are transient sources as well as new γ-ray sources from the recently published preliminary LAT 8-year point source list (FL8Y) (see https:

58027 MJD. This results in a total of 2281 sources, for which a dedicated light curve analysis has been performed. Please refer to App. D for a detailed overview of all blazars that have been considered. Even under the most optimistic assumptions, only a small fraction of γ-ray blazars are bright enough to yield a substantial fluence for the detection of a single high-energy neutrino event. In the sample of 2281 sources studied in this analysis, TXS 0506+056 is the 19th brightest source in the sky. Considering also the sensitivity of the IceCube detector by multiplying the LAT energy flux with the corresponding energy and zenith dependent effective area for a muon neutrino induced tack-like event, the source gets pushed up to the 13th best-ranked source in the sky. TXS 0506+056 is located on the northern hemisphere close to the equator, in a region of the sky where the IceCube detector is most sensitive. Krauß et al. showed that the LAT flux is a good proxi for the maximum neutrino prediction of a source, following Sect. 5.1.3. However, for a given LAT flux, the neutrino prediction uncertainty spans over about an order of magnitude. The situation gets much better by considering the total integrated γ-ray fluence within the high-energy hump of the blazar SED (again see Krauß et al., and Sect. 5.1.3). Here, I first derive the integrated γ-ray fluence and calorimetric neutrino prediction for the best 20 sources, sorted according to their *LAT Energy Flux* · *IceCube Effective Area*. TXS 0506+056 is found to be the 13th best-ranked source, sorted by their maximum neutrino prediction. To account for GeV faint sources with a high contribution from the keV band, which would result in a small LAT flux while at the same time causing an increase in the integrated γ-ray fluence, I extend the size of the studied subsample to a total of 50 sources. TXS 0506+056 is now ranked as the 14th best neutrino source candidate in the sky. This is due to the fact, that the blazar PKS 2155−304 creates a larger integrated γ-ray fluence compared to TXS 0506+056. In order to find the final ranking of TXS 0506+056 within the total sample of 2281 sources, this subsample has been extended to 70 sources for which an integrated γ-ray fluence and calorimetric neutrino prediction is calculated. No additional source is ranked better than TXS 0506+056, thus I can conclude that none of the remaining sources will produce an equivalent or greater maximum neutrino prediction. Table 3 lists the results of the final subsample of 70 sources, sorted by their maximum neutrino prediction. SEDs of all 70 sources are listed in App. E.

The pre-trial corrected p-value of a $\sim$ 290 TeV EHE neutrino track-like event to be detected in a radius of 0.1° (the offset of the IC170922A neutrino from the catalog position of TXS 0506+056) around a blazar of rank 14 is given by:

$$p_{pre} = 2281 \times \frac{\Omega_\nu}{4\pi} \times \frac{N_{\mathrm{rank}}}{2281}. \tag{5.13}$$

Here 2281 corresponds to the trails of all considered extragalactic γ-ray sources that have been taken into account. With $\Omega_\nu = 0.031\,\mathrm{deg}^2$ one derives:

$$p_{pre} = 1.1 \cdot 10^{-5} \approx 4.4\,\sigma, \tag{5.14}$$

This value represents the probability of a single EHE neutrino track-like event to be consistent within Ω_ν with a source ranked as high or higher as TXS 0506+056 in Table 3. By considering the number of neutrino alerts $N_{\mathrm{Alert}} = 10$, distributed during the past $\sim$ 2 years since the first publicly distributed HESE event (see Sec 3.5.4.3) by IceCube in April 2016, one can calculate the post-trial corrected chance coincide for a HESE or EHE neutrino event with a blazar that is calorimetrically capable of producing a similar or higher fluence than TXS 0506+056 according to

$$p_{post} = N_{\mathrm{Alert}} \times \frac{\Omega_\nu}{4\pi} \times N_{\mathrm{rank}}. \tag{5.15}$$

//fermi.gsfc.nasa.gov/ssc/data/access/lat/fl8y/)

This results in a post-trail corrected chance coincidence of

$$p_{post} = 1.1 \cdot 10^{-4} \approx 3.9\,\sigma. \tag{5.16}$$

To make this chance coincidence compatible to other results derived in e.g. IceCube Collaboration et al. (2018), I extend the consideration to additional 41 historical EHE events that have not been published as AMON alerts, as at that time no real-time follow-up program was available. None of these historical events did coincide with a blazar comparable in energy flux to TXS 0506+056, so that with $N_{\mathrm{Alert}} = 51$ I derive

$$p_{global} = 5.4 \cdot 10^{-4} \approx 3.5\,\sigma, \tag{5.17}$$

which is compatible to the analysis of IceCube Collaboration et al. (2018). One can therefore conclude that an association between the $\sim$ 290 TeV track-like neutrino event IceCube-170922A and the long-term outburst of the BL Lac TXS 0506+056 seems calorimetrically plausible with a significance of $\sim 3.5\,\sigma$.

5.2.5 Discussion

In this section, I have shown that an association between the $\sim$ 290 TeV track-like neutrino event IceCube-170922A and a short-term flaring period of three days around the neutrino arrival time of the blazar TXS 0506+056 is calorimetrically unlikely. From the beginning of 2017 on, this blazar underwent an enhanced phase of activity. A correlation to this long-term outburst period seems calorimetrically much more realistic. The post-trail corrected chance coincidence for this association can be calculated following an a-priori defined model (see Sect. 5.1.3) and is on the level of $\sim 3.9\,\sigma$. Taking also historical IceCube HESE and EHE events, which have been reported before the start of the real-time follow-up program into account, the final chance coincidence reduces to a $\sim 3.5\,\sigma$ detection. While the blazar TXS 0506+056 is the most promising candidate of an extragalactic neutrino point source, a clear source association, at least from the calorimetric prospective, can not be confirmed. Independently, in a time range between September 2014 and March 2015 the IceCube Collaboration (2018) found an excess of high-energy neutrino events, with respect to atmospheric background, providing an additional $\sim 3.5\,\sigma$ evidence for neutrino emission from the direction of TXS 0506+056. This further suggests blazars to be identifiable sources of the extragalactic high-energy neutrino flux, and especially the source TXS 0506+056 to be the best candidate for the first high-energy neutrino point source.
More associations are expected to follow in the future. Neutrino predictions for individual sources are small (well below unity), such that the Poisson probability for a direct association also has to be small, even for the most promising source candidates listed in Table 3. From an empirical prospective, this fits well to the observed high-energy neutrino flux, as otherwise the sky would already be full of confirmed neutrino sources. Furthermore, the calorimetric method introduced in this section can be applied for future neutrino searches, as the considered time range is variable and can easily be adapted to future flaring intervals. Monitoring in the MeV range would provide an important ingredient to study the broadband emission processes of blazars and develop future model predictions. The All-sky Medium Energy Gamma-ray Observatory (AMEGO; Perkins et al. 2018) will survey the entire sky every three hours in an energy range of 200 keV to 10 GeV. It's prime mission will be the continuous study of AGN in the MeV regime, which will provide crucial information to determine the emission mechanisms underlying these extreme objects. AMEGO is currently in a consideration phase for the NASA 2020 Astrophysics Decadal review.
The detection of a high-energy neutrino event from the BL Lac object TXS 0506+056 was

Table 3: Properties of the 70 sources selected from the total sample seen in App. D, according to their maximum calorimetric neutrino output. The energy flux is derived from a light curve analysis, while the integrated γ-ray fluence and maximum neutrino expectation are calculated following Sect. 5.1.4. The energy and zenith dependent area for a neutrino induced track-like muon event with energy of ~ 290 TeV is provided by Aartsen et al. (2014b). Sorted by the maximum neutrino output, TXS 0506+056 is the 14th best source in the sky.

Rank	Source	Energy Flux $\left[\mathrm{erg\ cm^{-2}\ s^{-1}}\right]$	Integrated γ-ray Fluence $\left[\mathrm{erg\ cm^{-2}}\right]$	Effective Area $\left[\mathrm{cm^2}\right]$	Energy Flux × Effective Area $\left[\mathrm{erg\ s^{-1}}\right]$	$N_\nu^{\max}$
1	3C 454.3	1.36×10^{-4}	$3.25 \pm 0.15 \times 10^{-9}$	40328	5.48	13.10
2	CTA 102	5.25×10^{-4}	$3.11 \pm 0.15 \times 10^{-9}$	40328	21.18	11.67
3	3C 279	9.95×10^{-5}	$1.44 \pm 0.07 \times 10^{-9}$	48787	4.85	7.20
4	PKS 1510−089	6.17×10^{-5}	$1.05 \pm 0.05 \times 10^{-9}$	48787	3.01	5.19
5	4C +01.02	5.59×10^{-5}	$8.5 \pm 0.5 \times 10^{-10}$	50288	2.80	4.36
6	PKS B1424−418	8.48×10^{-5}	$7.5 \pm 0.4 \times 10^{-10}$	48102	4.07	3.65
7	NGC 1275	1.71×10^{-4}	$1.22 \pm 0.07 \times 10^{-9}$	24368	4.17	3.02
8	PKS 0426−380	1.03×10^{-4}	$4.74 \pm 0.27 \times 10^{-10}$	48102	4.95	2.32
9	PKS 1502+106	6.06×10^{-5}	$4.45 \pm 0.26 \times 10^{-10}$	45635	2.76	2.06
10	PKS 2023−07	3.48×10^{-5}	$3.49 \pm 0.21 \times 10^{-10}$	48787	1.69	1.73
11	BL Lacertae	1.02×10^{-4}	$6.2 \pm 0.4 \times 10^{-10}$	24368	2.48	1.55
12	PKS 0447−439	1.05×10^{-4}	$3.03 \pm 0.20 \times 10^{-10}$	48102	5.05	1.48
13	PKS 2155−304	1.46×10^{-4}	$2.66 \pm 0.17 \times 10^{-10}$	47196	6.89	1.27
14	**TXS 0506+056**	$\mathbf{5.81 \times 10^{-5}}$	$\mathbf{2.63 \pm 0.18 \times 10^{-10}}$	**50288**	**2.92**	**1.19**
15	PKS 0208−512	1.82×10^{-5}	$2.57 \pm 0.24 \times 10^{-10}$	47204	0.85	1.18
16	PKS 0454−234	3.28×10^{-5}	$2.42 \pm 0.17 \times 10^{-10}$	48687	1.59	1.18
17	PKS 0336−01	2.34×10^{-5}	$2.29 \pm 0.17 \times 10^{-10}$	50176	1.17	1.17
18	4C +28.07	5.21×10^{-5}	$3.58 \pm 0.22 \times 10^{-10}$	32092	1.67	1.17
19	PKS 0727−11	2.36×10^{-5}	$2.35 \pm 0.20 \times 10^{-10}$	47981	1.13	1.14
20	3FGL J2253.1−1237	2.47×10^{-5}	$2.34 \pm 0.17 \times 10^{-10}$	47981	1.18	1.14
21	OT 081	3.92×10^{-5}	$2.43 \pm 0.18 \times 10^{-10}$	45635	1.78	1.12
22	PG 1553+113	1.60×10^{-4}	$2.36 \pm 0.17 \times 10^{-10}$	45635	7.30	1.09
23	Mkn 421	1.86×10^{-4}	$4.10 \pm 0.24 \times 10^{-10}$	24368	4.53	1.01
24	AP Librae	3.07×10^{-5}	$2.05 \pm 0.19 \times 10^{-10}$	48724	1.49	1.01
25	AO 0235+164	4.10×10^{-5}	$2.31 \pm 0.17 \times 10^{-10}$	40328	1.65	0.94
26	Ton 599	2.61×10^{-5}	$2.67 \pm 0.19 \times 10^{-10}$	32092	0.83	0.87
27	4C +01.28	1.61×10^{-5}	$1.41 \pm 0.14 \times 10^{-10}$	50288	0.81	0.72
28	TXS 2241+406	6.48×10^{-5}	$2.72 \pm 0.18 \times 10^{-10}$	24368	1.58	0.67
29	TXS 0518+211	5.66×10^{-5}	$1.76 \pm 0.16 \times 10^{-10}$	35068	1.98	0.62
30	PKS 0537−441	1.96×10^{-5}	$1.23 \pm 0.11 \times 10^{-10}$	48102	0.94	0.60
31	PKS 0524−485	2.66×10^{-5}	$1.23 \pm 0.10 \times 10^{-10}$	47204	1.25	0.59
32	PMN J1603−4904	4.19×10^{-5}	$1.19 \pm 0.16 \times 10^{-10}$	47204	1.971	0.57
33	1ES 1215+303	1.14×10^{-4}	$1.86 \pm 0.13 \times 10^{-10}$	27239	3.11	0.51
34	MH 2136−428	3.99×10^{-5}	$1.01 \pm 0.09 \times 10^{-10}$	48102	1.91	0.49
35	1H 1720+117	3.40×10^{-5}	$1.16 \pm 0.15 \times 10^{-10}$	40328	1.37	0.47
36	PKS 1424+240	6.54×10^{-5}	$1.41 \pm 0.12 \times 10^{-10}$	32092	2.09	0.46
37	3C 66A	5.78×10^{-5}	$1.82 \pm 0.14 \times 10^{-10}$	24368	1.40	0.45
38	OJ 014	2.38×10^{-5}	$8.4 \pm 0.9 \times 10^{-11}$	50288	1.19	0.42
39	PKS 0735+17	3.06×10^{-5}	$1.20 \pm 0.11 \times 10^{-10}$	35068	1.07	0.42
40	PKS 0700−661	2.06×10^{-5}	$8.7 \pm 1.0 \times 10^{-11}$	47225	0.97	0.41
41	TXS 0628−240	5.72×10^{-5}	$7.9 \pm 0.6 \times 10^{-11}$	48724	2.78	0.39
42	TXS 0141+268	2.74×10^{-5}	$1.14 \pm 0.10 \times 10^{-10}$	32092	0.87	0.37
43	PKS 0823−223	1.65×10^{-5}	$7.2 \pm 1.0 \times 10^{-11}$	48687	0.80	0.35
44	Mkn 501	4.28×10^{-5}	$1.37 \pm 0.13 \times 10^{-10}$	24368	1.04	0.34
45	PKS 0048−09	2.16×10^{-5}	$6.5 \pm 0.8 \times 10^{-11}$	48787	1.05	0.32
46	1ES 0647+250	5.69×10^{-5}	$9.0 \pm 1.0 \times 10^{-11}$	32092	1.82	0.29
47	1ES 1959+650	1.59×10^{-4}	$3.30 \pm 0.20 \times 10^{-10}$	7706	1.22	0.25
48	7C 2010+4619	4.19×10^{-5}	$1.26 \pm 0.14 \times 10^{-10}$	19924	0.83	0.25
49	PKS 1440−389	1.81×10^{-5}	$5.1 \pm 0.4 \times 10^{-11}$	48102	0.87	0.25
50	PMN J0622−2605	2.04×10^{-5}	$5.1 \pm 0.8 \times 10^{-11}$	48724	0.99	0.25
51	1RXS J194246.3+103339	1.87×10^{-5}	$5.4 \pm 0.6 \times 10^{-11}$	45635	0.85	0.25
52	PKS 0301−243	2.19×10^{-5}	$4.8 \pm 0.6 \times 10^{-11}$	48724	1.06	0.23
53	RGB J2243+203	2.40×10^{-5}	$6.6 \pm 0.5 \times 10^{-11}$	35068	0.84	0.23
54	MG1 J021114+1051	1.98×10^{-5}	$4.9 \pm 0.6 \times 10^{-11}$	45635	0.90	0.22
55	PKS 1309−216	2.50×10^{-5}	$4.1 \pm 0.6 \times 10^{-11}$	48687	1.22	0.20
56	PKS 2005−489	1.89×10^{-5}	$4.2 \pm 0.4 \times 10^{-11}$	47204	0.89	0.20
57	1RXS J020922.2-522920	1.68×10^{-5}	$3.9 \pm 0.4 \times 10^{-11}$	47204	0.79	0.18
58	3FHL J1944.9−2143	1.76×10^{-5}	$3.38 \pm 0.19 \times 10^{-11}$	48687	0.85	0.16
59	PMN J1610−6649	2.43×10^{-5}	$3.4 \pm 0.6 \times 10^{-11}$	47225	1.14	0.16
60	KUV 00311−1938	2.42×10^{-5}	$3.09 \pm 0.18 \times 10^{-11}$	48687	1.17	0.15
61	NVSS J182338−345412	2.94×10^{-5}	$3.0 \pm 0.7 \times 10^{-11}$	47196	1.38	0.14
62	1RXS J005117.7−624154	2.98×10^{-5}	$2.85 \pm 0.21 \times 10^{-11}$	49360	1.47	0.14
63	PG 1218+304	4.37×10^{-5}	$5.0 \pm 0.4 \times 10^{-11}$	27239	1.19	0.13
64	1H 1914−194	1.81×10^{-5}	$2.7 \pm 0.5 \times 10^{-11}$	48687	0.88	0.13
65	NVSS J214637−134359	1.82×10^{-5}	$2.68 \pm 0.21 \times 10^{-11}$	47981	0.87	0.13
66	1H 1013+498	4.02×10^{-5}	$6.3 \pm 0.7 \times 10^{-11}$	19924	0.80	0.12
67	PKS 0118−272	1.97×10^{-5}	$2.5 \pm 0.4 \times 10^{-11}$	48724	0.96	0.12
68	RX J1931.1+0937	1.92×10^{-5}	$2.6 \pm 0.8 \times 10^{-11}$	45635	0.87	0.12
69	RX J0115.7+2519	2.84×10^{-5}	$3.1 \pm 0.4 \times 10^{-11}$	32092	0.91	0.10
70	RX J0338.4+1302	2.61×10^{-5}	$2.1 \pm 0.6 \times 10^{-11}$	40328	1.05	0.087

unexpected, as most models (e.g. Mannheim 1993, 1995) would predict such an association form a FSRQ. Murase et al. (2014) and Dermer et al. (2014) estimated the neutrino emission of blazars through photo-meson reactions and found that the total neutrino output is dominated by the most powerful blazars (FSRQs), while weak blazars (BL Lacs) account only for a marginal contribution. In FSRQs, the underlying $p\gamma$ interactions are much more efficient (see Sect. 2.3.4), due to the undoubted presence of an UV seed photon field. In BL Lacs, however, it is unclear where these UV photons are coming from. The possibility of efficient high-energy neutrino production in BL LAC objects could be given by so-called structured jets. In such models (e.g. Tavecchio et al. 2014, Righi et al. 2017, Ansoldi et al. 2018), an inner fast moving spine of relativistic plasma is surrounded by a slower sheath layer. This results in an enhancement of inverse Compton emission, caused by radiative coupling of the two zones. In addition, such a velocity structure would result in a boosting of $p\gamma$ reactions, due to the scattering of high-energy protons from the spine off an amplified soft target photon field in the sheath layer. Such models could explain the occurrence of high-energy neutrinos in BL Lac objects, while high resolution observations of the inner jet structure have already shown a spine-sheath segmentation of the inner jet (e.g. Laing 1996, Attridge et al. 1999).
Recent preliminary studies indicate that the neutrino emission from $p\gamma$ interactions can be best described by a lepto-hadronic model (see Sect. 2.2.4.3) with a weak hadronic component. Such models require protons to be accelerated to $\sim$ PeV energies in order to produce neutrinos which are detectable by IceCube. In addition, an external co-moving[35] field of target photons in the UV to X-ray regime is required. The most awakening consequence of such a model would be a decoupling of the observed high-energy γ-ray and neutrino emission. Such a result would be in contradiction to the widely accepted correlation between high-energy γ-rays and neutrinos generated in $p\gamma$ interactions, while on the other hand an indication that the new field of neutrino astronomy is still highly debated and rapidly evolving.

5.3 Summary

In the first part of this section, I studied the calorimetric neutrino expectation of individual blazar flares on different time scales. Following the conclusions from Krauß et al. (2014) and Kadler et al. (2016), blazars flares, which provide the highest keV to GeV fluence, would be the best candidates for a neutrino association. The fluence is achieved by integrating over the peak of the high-energy hump of the blazar SED, taken only simultaneous data during a flaring period into account. I showed that the 50 short-term flares ($\sim$ days) with the highest probability for an associated neutrino detection are generated by a group of only seven different sources: 3C 279 (10 flares), PKS 1510−089 (32 flares), PKS 0402−362 (1 flare), CTA 102 (1 flare), 3C 454.3 (1 flare), PKS 1424−418 (3 flares), and PKS 1329−049 (2 flares). I found that the individual fluence of most short-term flares is way to small to lead to a substantial neutrino prediction. While long-term outbursts ($\sim$ weeks) provide a much better calorimetric neutrino prediction, their chance coincidence typically is only on the order of a few percent (see e.g. Kadler et al. 2016). However, for the brightest short-term blazar flares, Poisson probabilities of up to $\sim 2\,\%$ are calculated, so that the possibility of associated neutrino detections in future data unblindings of IceCube and KM3NeT seems reasonable.
In the second part of this section, I studied a possible calorimetric association between the $\sim$ 290 TeV track-like neutrino event IceCube-170922A and the blazar TXS 0506+056. I found that an association of this blazar to a three day period around the arrival time of the neutrino event is calorimetrically unlikely, while a correlation to a long-term outburst period of TXS 0506+056, starting early 2016 can be calculated to be at a $\sim 3.5\,\sigma$ level. Other studies

[35] Co-moving to the jet

(e.g. IceCube Collaboration et al. 2018) have derived similar significance levels. Independent from the neutrino event IceCube-170922A, the IceCube Collaboration (2018) has detected an excess of high-energy neutrino events from the direction of TXS 0506+056, providing an additional $\sim 3.5\,\sigma$ evidence for this source to the the first confirmed origin of high-energy neutrinos. However, recent preliminary studies in the field of neutrino astronomy indicate that the connection between high-energy γ-rays and neutrino may not be as strong as widely expected and further studies are required to describe the origin of these high-energy neutrino events.

To conclude, I have shown that the individual neutrino prediction of short-term blazar flares is typically way too small to be detected with current neutrino facilities like IceCube and KM3NeT. A short-term association between the neutrino event IceCube-170922A and the blazar TXS 0506+056 is calorimetrically unlikely. The sample of possible sources, which have the highest probability to be associated to a short-term blazar flare is limited to only seven different sources. While the calorimetric chance coincidence for a long-term association between IceCube-170922A and the blazar TXS 0506+056 is only on the level of $\sim 3.5\,\sigma$, independent studies came to the same conclusion, establishing TXS 0506+056 as the most promising source candidate of high-energy neutrinos in the scientific community. However, neutrino predictions from individual sources have to be below unity, as otherwise the sky would already be filled with plenty of confirmed neutrino point sources, leaving an enormous detection potential for future associations in the evolving field of neutrino astronomy.

6 Search for High-Redshift Blazars with *Fermi*/LAT

High-redshift blazars are difficult to study with *Fermi*/LAT, as their emission peaks are often downshifted to energies below the GeV band and at their large distances, only the very brightest objects are detectable. On the other hand, high-redshift blazars are disproportionately important targets, because they serve as cosmological probes and represent the most powerful class of γ-ray emitting sources in the Universe. Unfortunately, only a small number of high-redshift blazars could be detected with *Fermi*/LAT so far. In this section, I developed a strategy to increase the detection statistic at redshift $z \geq 2.5$ via a search for flaring events in high-redshift γ-ray blazars which long-term flux is just below the sensitivity limit of *Fermi*/LAT.

6.1 Introduction

Blazars (see Sect. 2.4), as a subclass of AGN are among the most powerful objects in the Universe. Their broadband emission (see Sect. 2.3) is dominated by relativistic jets, especially at γ-rays where the high-energy hump of the blazar SED (see Sect. 2.4.1) peaks in the MeV to GeV regime. The Large Area Telescope (LAT) onboard the Fermi satellite (see Sect. 3.3) has detected thousands of blazars, confirming that they are dominating the γ-ray sky (see e.g. Fig. 3.5). However, high-redshift[36] blazars are mostly missing in *Fermi* catalogs. This is due to a shift of the high-energy emission towards energies below the LAT band, both because of cosmological redshift and following the blazar sequence (see Sect. 2.4.1). In addition, absorption in the EBL leads to an efficient degrading of high-energy γ-rays below the detection threshold of *Fermi*/LAT (e.g. Ackermann et al. 2017, H.E.S.S. Collaboration et al. 2013). Although commonly represented in the radio and X-ray regime (Condon et al. 1998, Gehrels et al. 2004), these blazars are rare γ-ray emitters, accounting only for less than 10 % of the total AGN population observed by *Fermi*/LAT.
High-redshift blazars are of particular interest in the field of γ-ray Astronomy, as they are the most powerful (non-transient) astrophysical sources ever detected by *Fermi*/LAT. These sources possess the highest jet powers and accretion luminosities and have black-hole masses often in excess of $10^9\,M_\odot$ (Bloemen et al. 1995, Ghisellini et al. 2010a). They are important as cosmological probes and serve as test objects for blazar evolution models (e.g. Volonteri et al. 2011, Ghisellini et al. 2015). This directly implies, that the detection of new high-redshift blazars would test the hypotheses of blazar evolution, as the extreme distance would limit the available time for these objects to grow to such enormous black hole masses. In fact, only a small number of high-redshift blazars has been detected by *Fermi*/LAT, some of them only because of bright flaring states. Recently, five new high-redshift blazars have been identified by *Fermi*/LAT (Ackermann et al. 2017), making NVSS J151002+570243 the most distant known γ-ray emitting blazar at $z = 4.31$. These detections were made possible by the recent upgrade of *Fermi*/LAT to the Pass 8 analysis (see Atwood et al. (2009) and Sect. 4.2) and a systematic analysis of a large blazar sample.
In the following, I will introduce a new method to search for hitherto undetected high-redshift γ-ray emitting blazars, which are too faint to be detected significantly (TS $\geq$ 25, see Eq. 4.7) on long time periods typically considered for *Fermi* catalogs, but can show up as significant sources during shorter ($\sim$ monthly) periods of increased activity.

[36] In the following, the term high-redshift blazar is used as a synonym for $z \geq 2.5$

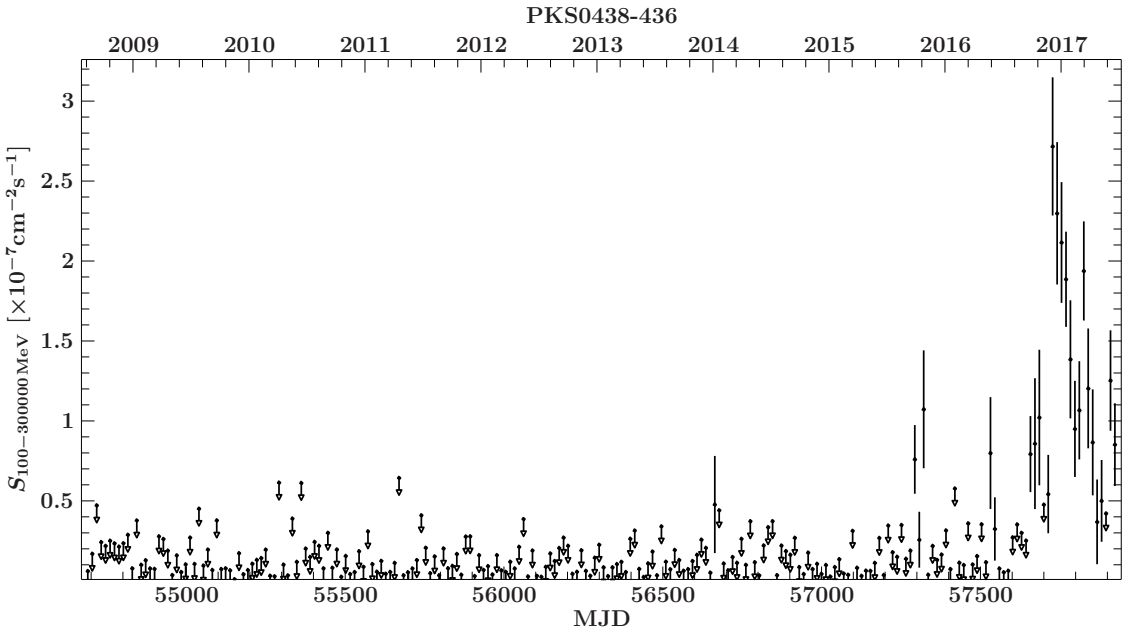

Figure 6.1: 14 day binned Pass 8 *Fermi*/LAT γ-ray light curve of PKS 0438−43 over $\sim$ nine years from 2008 August 4 to 2017 July 1. The light curve is shown for an energy range of 100 MeV to 300 GeV. This source has been detected in December 2016 by the FA-GSW service (Cheung 2016) during a bright flare, while still being unknown to any published *Fermi* catalog.

6.2 Detection Strategy and Sample Selection

Flaring states from previously γ-ray unknown high-redshift blazars have been detected several times (Cheung 2016, 2017, Angioni & Cheung 2018) by the *Fermi* Flare Advocate service (see Sect. 3.3.1). Such periods of enhanced activity typically only last for several days, leading to a significant detection (TS $\geq$ 25) due to a drastic background reduction, compared to long-term averaged fluxes used in catalogs. Figure 6.1 shows a 9+ years *Fermi*/LAT Pass 8, γ-ray light curve of the high-redshift (z = 2.83) FSRQ PKS 0438−43 in an energy range of 100 MeV to 300 GeV using a two week binning. This source had been undetected in any *Fermi* catalog and was identified by the *Fermi* Flare Advocate service (Cheung 2016) only due to its bright flare in 2016.

In this section, I perform a systematic search for γ-ray undetected high-redshift blazars, by targeting a sample of 176 blazars with a redshift of $z \geq 2.5$ and a radio flux density of more than 50 mJy, taken from the Roma BZCAT Multifrequency Catalogue of Blazars[37] and the SHAO list of high-redshift radio-loud quasars[38]. These sources were selected because of the known correlation between radio and γ-ray fluxes (e.g. Ackermann et al. 2011, Ghirlanda et al. 2010). The total sample consists of 169 BZCAT blazars, as well as seven SHAO sources, fitting the selection criteria mentioned before. Please refer to App. F for a full list of considered blazars. Monthly binned *Fermi*/LAT γ-ray light curves (see Sect. 4.2.3) are calculated for the entire sample, while the time binning of 30 days has been chosen to identify periods the FA-GSW service would have missed[39] and keep the computing effort at a reasonable level.

[37] http://www.asdc.asi.it/bzcat/

[38] http://202.127.29.4/CRATIV/en/high_z.html

[39] The FA-GSW service is designed to study the entire variable γ-ray sky. A simplified source model (see Sect.4.2.1.3) is used, including just the diffuse emission.

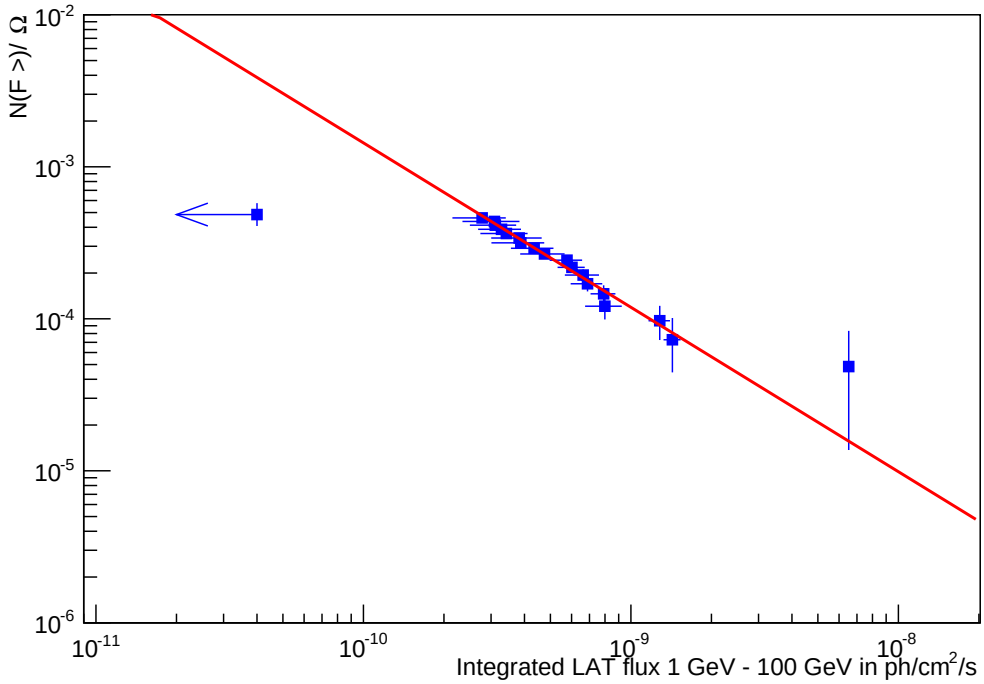

Figure 6.2: $logN - logS_{max}$ digram of blazars taken from the third catalog of active galactic nuclei detected by *Fermi*/LAT (3LAC). The plot shows the cumulative number of sources normalized per square degree with a redshift z $\geq$ 2.5, using statistical uncertainties only. The power-law fit ($N = (1.92 \pm 0.68) \times 10^{-14} \times S^{-1.079 \pm 0.097}$) is used for parametrization.

Studying a large sample of γ-ray unknown high-redshift blazars on time scales of months would significantly increase their statistic in the MeV to GeV regime and fill the deficit of those objects still present in more then nine years of *Fermi*/LAT data.

6.2.1 Detection Potential

In order to estimate the number of high-redshift blazars potentially detectable by this approach, a $logN - logS_{max}$ diagram has been created for known high-redshift γ-ray blazars. Figure 6.2 displays the cumulative number of sources, with a redshift $z \geq 2.5$, normalized per square degree , taken from the third catalog of active galactic nuclei detected by *Fermi*/LAT (3LAC; Ackermann et al. 2015c). A power-law fit is used for parametrization, allowing to extrapolate the number of expected high-redshift blazars towards lower fluxes in the energy range 1 GeV - 100 GeV[40]. For PKS 0438−43, which was not detected in the 3LAC, I calculate the corresponding upper limit (following Sect. 4.2.2), which is shown in the $logN - logS_{max}$ diagram at 4×10^{-11} ph /cm^2 /s. Based on the power-law fit, the $logN - logS_{max}$ distribution predicts $\approx$ 140 high-redshift blazars at similar or higher γ-ray flux levels, of which only 19 are known in the 3LAC. Five additional high-redshift blazars have been detected after the publication of the 3LAC (Ackermann et al. 2017), mainly due to the improved sensitivity of the Pass 8 analysis and two blazars have been detected because of flaring activity on the level detectable by the FA-GSW as described above.

[40]These energy range has been used in the 3LAC

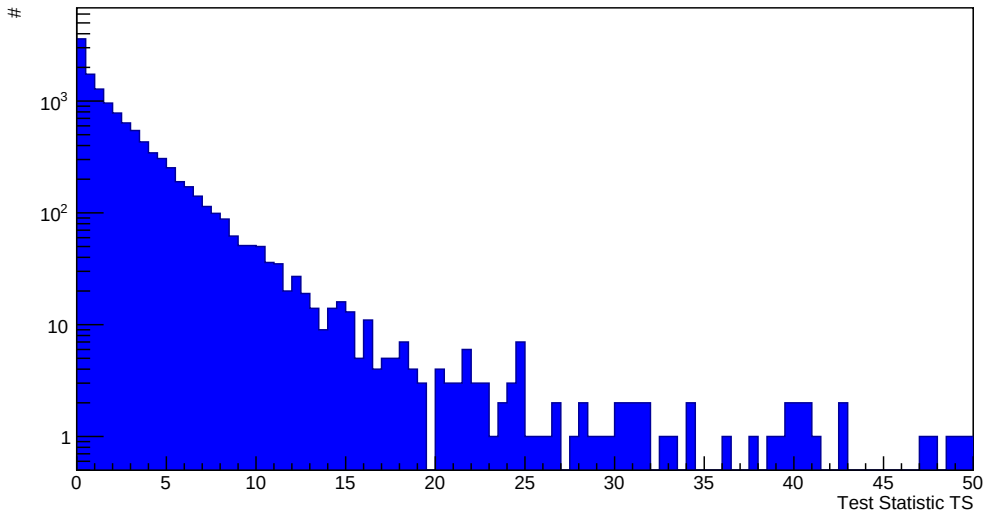

Figure 6.3: Test statistic distribution of the total $\sim$ 20000 monthly time intervals from the entire source sample listed in App. F. 51 monthly intervals are identified with a significance of TS $\geq$ 25, while at a TS $\geq$ 9 level 481 months are detected.

Since the increase in sensitivity from longer time baselines is only marginal ($\propto \sqrt{T}$), this approach searches for flares below the FA-GSW level. Therefore, I estimate the number of such flares from the fraction of detected flares in the sample of 19 known high-redshift 3LAC blazars. three out of 19 sources showed bright γ-ray flares in the past 9+ years, which were reported as Astronomer's Telegrams: TXS 0536+145 (Orienti & D'Ammand 2012), PKS 0537−286 (Cheung 2017), and B3 1343+451 (Buehler 2009). Somewhat fainter flares, which have not led to Astronomer's Telegrams are likely more frequent so that a fraction of 3/19, i.e., about 16 % can be considered a conservative lower limit. I thus conclude, that this approach should be capable to detect about 22 γ-ray flares of hitherto unknown high-redshift blazars in the MeV to GeV regime, using the previously described sample listed in App. F.

6.2.2 Detected Monthly Intervals

A total of 51 monthly intervals have been identified with a test statistic of TS $\geq$ 25 from the sample of γ-ray unknown high-redshift blazars listed in App. F. For reference, the source PKS 0537−286 has been included in the sample as sanity check of the proposed method and led to the detection of ten monthly intervals (included in the total number mentioned before). The first significant (TS $\geq$ 25) detection of these source happened already in 2012, about five years before getting picked up by the FA-GSW service, which is due to limitations in the FA-GSW method as mentioned before. This clearly proofs the capability of the introduced method to identify even faint high-redshift blazars from the selected sample. Figure 6.3 shows the total test statistic distribution, including all $\sim$ 20000 monthly time intervals from the entire sample of studied sources. While the majority of intervals is well below TS $\leq$ 9 and thus likely just of accidental nature, these TS $\geq$ 25 intervals can be considered as a significant source identification caused by eleven different blazars. Table 4 lists the properties of these identified γ-ray sources, together with their redshift and number of TS $\geq$ 25 monthly intervals. Light curves of all blazars, considered in this analysis are listed in App. G

Table 4: Identified high-redshift blazars selected from App. F, which were at least detected in a single monthly interval with a TS $\geq$ 25. Sources listed in the FL8Y are marked by a star.

Source Number	Source Name	RA J2000	DEC J2000	z	Detections TS $\geq$ 25
2	5BZQ J0009+0625	2.32	6.43	2.69	1
21⋆	5BZQ J0225+1846	36.27	18.78	2.69	4
30	5BZQ J0339−0133	54.75	-1.55	3.20	4
36	5BZQ J0434−4355	68.51	-43.93	2.65	4
43	PKS 0537−286	84.98	-28.67	3.10	10
52⋆	5BZQ J0733+0456	113.49	4.94	3.01	6
86⋆	5BZQ J1127+5650	171.92	56.84	2.89	1
113	5BZQ J1441−1523	220.44	-15.39	2.64	2
136	5BZQ J1837−5848	279.47	-58.80	3.04	15
161	5BZQ J2219−2719	334.90	-27.32	3.63	1
167	5BZQ J2321−0827	350.33	-8.46	3.16	3

6.3 Discussion and Outlook

In this section, I identified eleven high-redshift blazars, which were too faint to be detected on long-term time scales of several years, but showed significant γ-ray activity at a $\geq 5\,\sigma$ significance level on monthly time scales. The blazar PKS 0537−286 was included in the sample to test the capability of the introduced method to detect such distant blazar on monthly time scales. Here, I was able to identify seven previously unknown *Fermi*/LAT high-redshift blazars in numerous monthly intervals and thus significantly increase the sample of these rare class of γ-ray emitting galaxies. While still being closer than the most distant blazar identified in Ackermann et al. (2017), the source 5BZQ J2219−2719 at a redshift of $z = 3.63$ represents the farthest new γ-ray blazar identified within this thesis. Three blazars marked with a star in Table 4, were unidentified in the third catalog of active galactic nuclei detected by *Fermi*/LAT (Ackermann et al. 2015c), but showed activity in the past years, resulting in more than ten identified monthly intervals per source. Thus, these blazars were bright enough to be included in the preliminary LAT eight year point source list (FL8Y)[41]. Therefore, these sources are not considered as new γ-ray blazars identified within this thesis.

Still, these sources represent only a small fraction of potentially detectable high-redshift blazars. Some sources showed monthly intervals, detected slightly below the $\geq 5\,\sigma$ threshold and thus, are not included in Table 4. In addition, a total of 481 monthly intervals have been detected at a significance level of TS $\geq$ 9, with several sources showing multiple detections at these significance level, as seen in App. G. While such an individual detection would not be significant enough to claim the detection of a new γ-ray source, multiple detections from a single source could lead to a robust source identification. However, such an analysis requires a detailed understanding of the expected false positive rate of monthly intervals. These rate of expected background intervals can be estimated by performing the same analysis chain used in this section on a large number of blank sky positions, while comparing their test statistic distribution to the observed distribution of measured intervals seen in Fig. 6.3. Such an anal-

[41] See https://fermi.gsfc.nasa.gov/ssc/data/access/lat/fl8y/ for the complete eight year sample.

ysis does require a huge amount of computing time, and was still ongoing at the time of the submission of this thesis.
Nevertheless, the new identified γ-ray blazars will need to be studied in detail. A dedicated maximum likelihood analysis (following Sect. 4.2) will have to be performed in order to study their spectral properties in the MeV to GeV regime. Furthermore, blazar evolution models like e.g. Volonteri et al. (2011) and Ghisellini et al. (2015) do benefit from the increased statistic of blazars at these distances. However, such an analysis will be the content of a separate follow-up project.
This analysis has only be performed on a rather limited sample of radio detected high-redshift blazars. Following Sect. 6.2.1, the detection potential of hitherto unknown high-redshift blazars, which showed periods of increased activity in the past 9+ years of *Fermi*/LAT data is not negligible. Monthly time intervals have been considered in this analysis, mainly due to computing limitations, while on the other hand ignoring activity on shorter time scales. In addition, the detection potential of high-redshift blazars can be increased by evaluating a possible γ-ray detection for all $z \geq 2.5$ blazars in the Roma BZCAT Multifrequency Catalogue and the SHAO list of high-redshift loud quasars, instead of just focusing on the radio brightest sources. Finally, this method could be used to search for hitherto unknown γ-ray sources, which are also undetected in other wavelengths, by using randomized source positions. While there are plenty of possible ways to increase the detection potential of this method, the primary purpose of this work was to increase the statistic of high-redshift blazars detected by *Fermi*/LAT, based on a sample of radio and optical candidate sources.

7 Characterizing the Flaring Behavior of Bright Blazars

Blazars, a subclass of Active Galactic Nuclei (see Sect. 2.4) are highly variable sources (see Sect. 2.4.2) which account for the majority of extragalactic γ-ray emitters detected by *Fermi*/LAT (Ackermann et al. 2015c). Blazars can be further subdivided into BL Lac (BLL) objects, Flat-Spectrum Radio Quasars (FSRQ) and blazars of uncertain type (BCU). While typical BL Lac spectra are dominated by a featureless non-thermal continuum, FSRQs are known for broad emission lines at optical wavelengths and a flat radio spectrum. BCUs are identified as blazars, as they show a typical two-humped, blazar-like spectral energy distribution (see e.g. Böttcher (2007) for a review), while the optical spectrum is either lacking or not sensitive enough to distinguish between BL Lacs or FSRQs. The occurrence of flaring intervals is of purely statistical nature. However, several studies have tried to characterize the overall behavior of individual blazars (e.g. Abdo et al. 2010a,c,b, Vercellone et al. 2010, Ackermann et al. 2012, Hayashida et al. 2012). Unfortunately, the results of these studies vary widely, revealing relatively few consistent patterns to describe the underlying physics of relativistic jets.
In this section, I study the flaring characteristics of bright blazars monitored by *Fermi*/LAT over a period of about six years. A sample of bright blazars has already been introduced in Sect. 5.1. Here, I define the expression of a "flare" in the context this work and study specific characteristics unique to each flare, while comparing the overall flaring behavior of different blazar types.

7.1 Flare Definition

A flare is defined similar to Sect. 5.1.2 as a continuous, uninterrupted time interval a blazar spends in a given or brighter flux state. Following Eq. 5.1, periods of enhanced activity have to fulfill:

$$\begin{aligned} \sigma_{\mathrm{indi}} &= (\mathrm{Flux} - 3 \times \mathrm{Flux}_{\mathrm{err}}) - \mathrm{G} \\ \sigma_{\mathrm{indi}} &\geq 3\sigma. \end{aligned} \tag{7.1}$$

Similar to Eq. 5.1, the parameters Flux and $\mathrm{Flux}_{\mathrm{err}}$ indicate the LAT photon flux and 1σ flux uncertainty in an energy range of 100 MeV − 300 GeV. The quantity G corresponds to a non-flaring quiescent ground level state of the considered blazar. Therefore, the parameter σ_{indi} defines the individual difference of each flux value to the ground level state G, while σ indicates the uncertainty in the ground level calculation. The ground level G and error σ are derived from the median and variance of the LAT flux distribution, which provide a good estimate of the most common flux level and it's variation. Figure 7.1 shows the ground level distribution of all considered blazars. While upper limits act as a strong cut on identified flares, they have to be considered in order to derive a physical meaningful quiescent state. Please refer to App. H for a complete list of identified flares. Most blazars show ground levels between $1 \times 10^{-7}\,\mathrm{ph\,/cm^2\,/s} \leq \mathrm{G} \leq 5 \times 10^{-7}\,\mathrm{ph\,/cm^2\,/s}$. This range is mainly influenced by a selection effect due to the used blazar sample, which only includes blazars, that at least once showed a photon flux level exceeding $> 10^{-6}\,\mathrm{ph\,/cm^2\,/s}$. This introduces a bias towards the brightest γ-ray blazars in the sky and does also explain the sharp cut at $1 \times 10^{-7}\,\mathrm{ph\,/cm^2\,/s}$, as fainter blazars are not included in the *Fermi*/LAT public light curve list. Only a handful of blazars show a ground level of $> 5 \times 10^{-7}\,\mathrm{ph\,cm^{-2}\,s^{-1}}$. As the flare definition in Eq. 7.1 requires a flux level to exceed the ground level by at least three times the 1σ flux uncertainty, these bright blazars do only barely show significant flaring periods. However, $\sim$ 500 flares have been identified from a total of 80 sources[42], most of them are FSRQs. The final flare sample

[42]The considered sample consists of 150 blazars

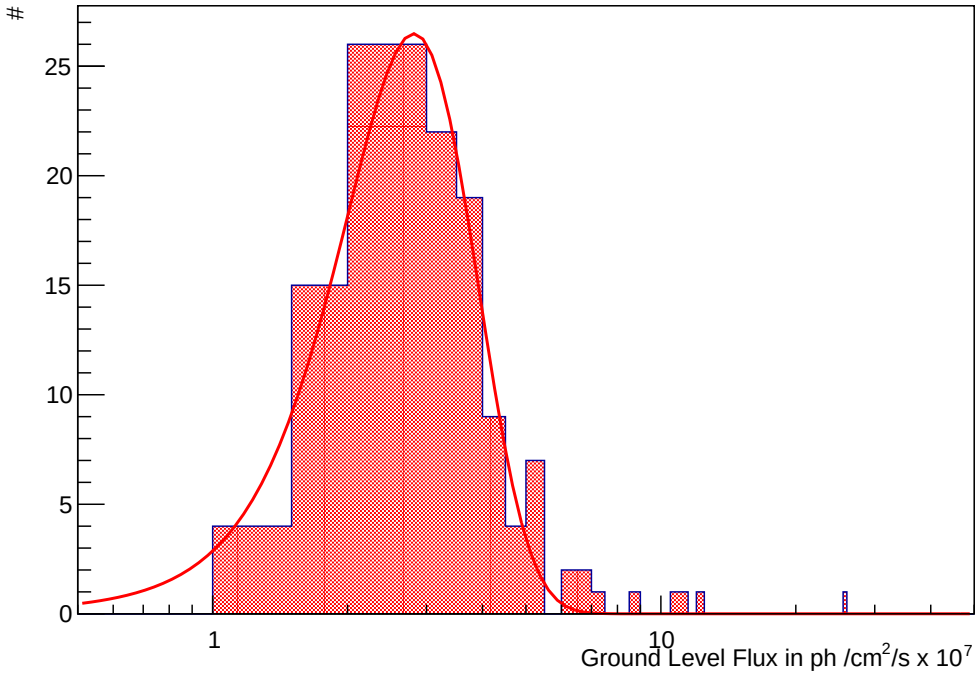

Figure 7.1: Histogram of the ground level flux G used to identify flares according to Eq. 7.1. The distribution is well described by a Poisson fit.

consists of the following blazar types: FSRQs (85 %), BL Lacs (8 %), BCUs (5 %), other kind of AGN[43] (2 %). In the following only different types of blazars will be considered, as the primary purpose of this section is to characterize their flaring behavior. A comparison to other γ-ray source classes would introduce an additional bias to an already highly focused analysis. The dominance of FSRQs can be explained by the selected flare sample, as FSRQs typically are more luminous than BL Lac and BCU objects and thus get identified by *Fermi*/LAT more frequently.

7.2 Flare Characteristics

In the following, I will introduce different flare characteristics of the selected sample and compare their properties between the above mentioned blazar types.

7.2.1 Flare Duration

Figure 7.2 displays the duration of identified flares. One clearly can see a clustering at small durations of only a few days, which can be explained by the definition of a flare in Sect. 7.1 as an uninterrupted period of enhanced activity. Upper limits and flux variations can validate this requirement, leading to a high number of flares with durations of only a few days. While BL Lacs are only detected with durations of maximum three days, BCUs can cause flares lasting up to ten days. For the longest outburst periods, however, only FSRQs are responsible, which is in agreement with previous studies (e.g. Ackermann et al. 2015c).

[43] This includes narrow line Seyfert I galaxies, radio galaxies and unknown γ-ray sources, which has been identified by the *Fermi* Flare Advocate service, introduced in Sect. 5.1.2.

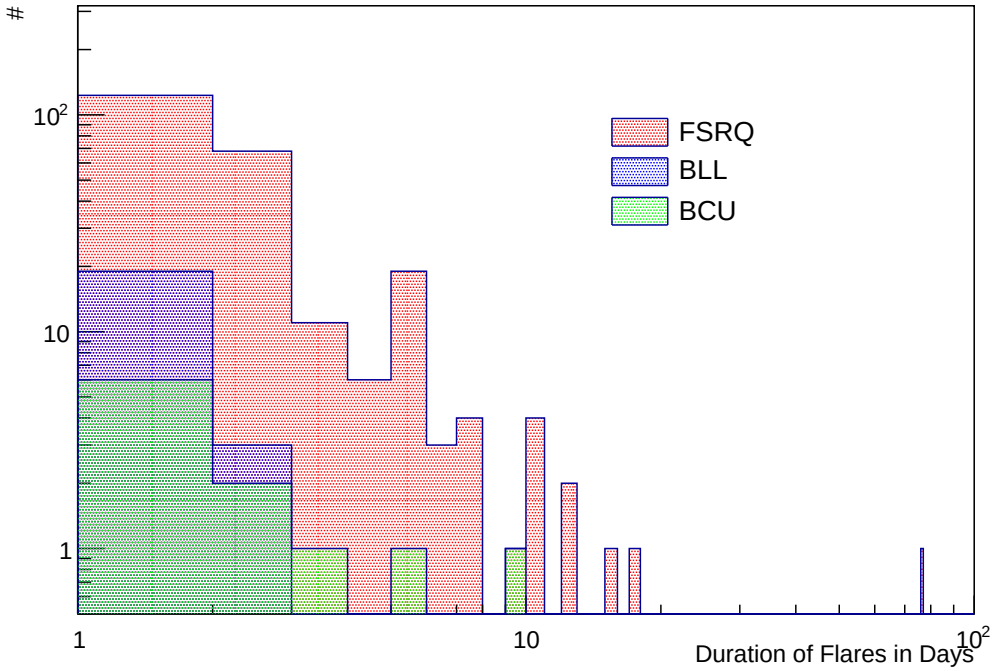

Figure 7.2: Histogram of the flare duration according to Eq. 7.1 for different blazar types. While the clustering at short durations is mainly caused by the definition of a flare in Sect. 7.1, only FSRQs show long outburst periods of more than ten days.

7.2.2 Maximum Flare Amplitude

Figure 7.3 shows two histograms of the maximum flare amplitude for different blazar types. While the top histogram only considers flares with a duration of exactly one day, the bottom histogram includes only periods of enhanced activity longer than a single day. FSRQs are detected in a wide range of different maximum flare amplitudes, both in only one day flares as well as longer activity phases. As BL Lacs and BCUs are typically much fainter in their γ-ray emission, their flares cluster around the trigger threshold of the *Fermi* Flare Advocate service, which is at $10^{-6}\,\mathrm{ph\,/cm^2\,/s}$. However, for the most extreme flares, BL Lacs can also reach flux states of up to $3 \times 10^{-6}\,\mathrm{ph\,/cm^2\,/s}$. In addition, one can see that both BL Lacs and BCUs are typically detected on daily time scales.

7.2.3 Time Gaps between Flares

In case a source is detected in at least two flaring periods, the time between the occurrence of there periods can be calculated. Short time gaps of only a few days indicate, that a longer phase of activity has been cut into smaller independent flares, which is again due to the definition of a flare introduced in Sect. 7.1. Long gaps between two successive flares, on the other hand, represent independent flaring periods, detected at the beginning and end of the considered time range. All blazar types show a wide distribution of gaps between two successive flares. While BCUs cluster at at short gaps of less than 20 days, FSRQs and BL Lacs do in addition also show gaps of more than 100 days. As FSRQs dominate this flare sample and their overall flaring behavior typically shows longer and brighter flares compared to BL Lac and BCUs, they provide more possible activity phases that can be either identified

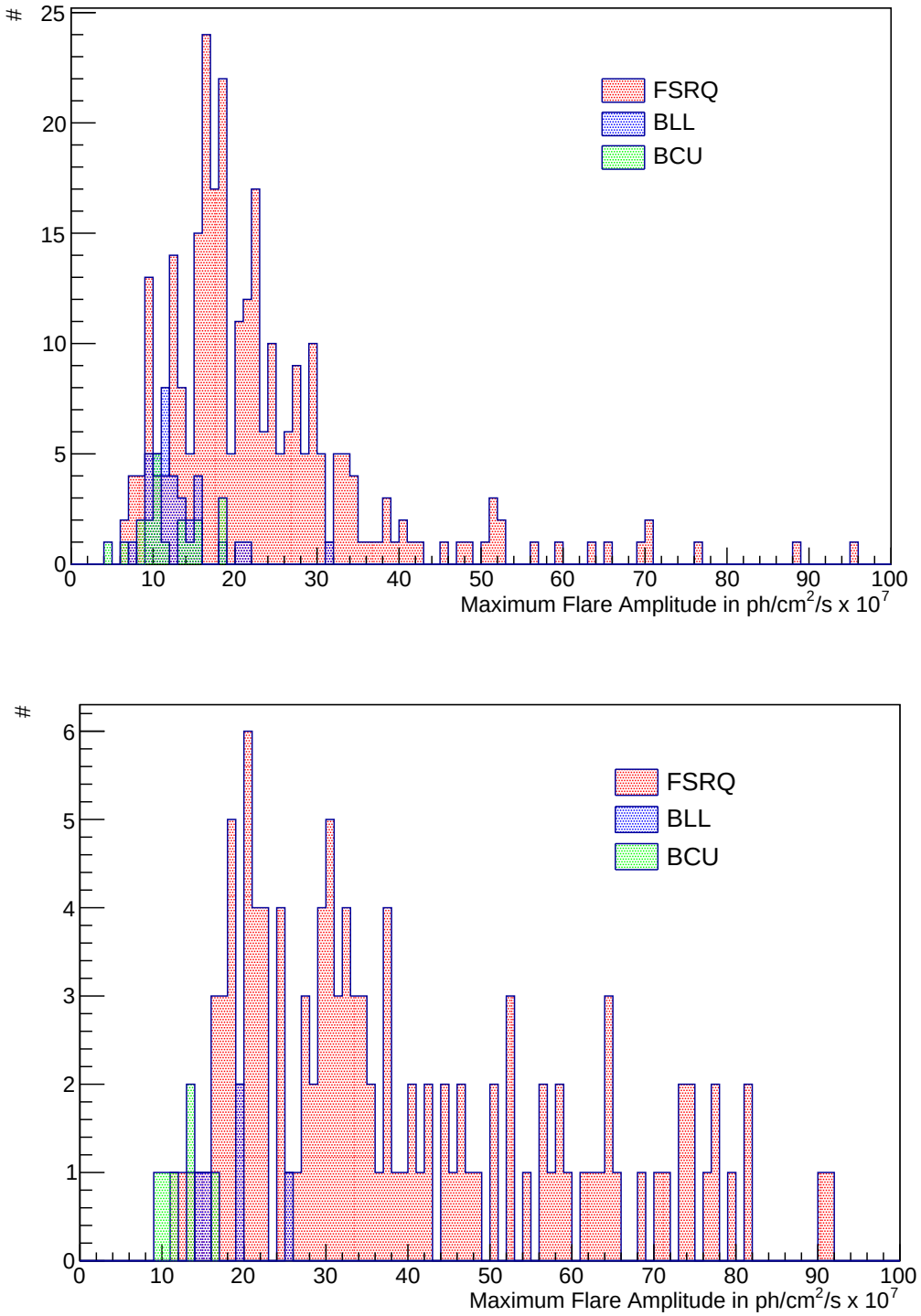

Figure 7.3: Histograms of the maximum flare amplitude for different blazar types. Top: Considering only flares with a duration of one day. Bottom: Considering only periods of enhanced activity with a duration of more than one day. While FSRQs exhibit both "faint" and bright flares, BL Lacs and BCUs typically show fainter flares which cluster around the trigger threshold of $10^{-6}\,\mathrm{ph\,/cm^2\,/s}$

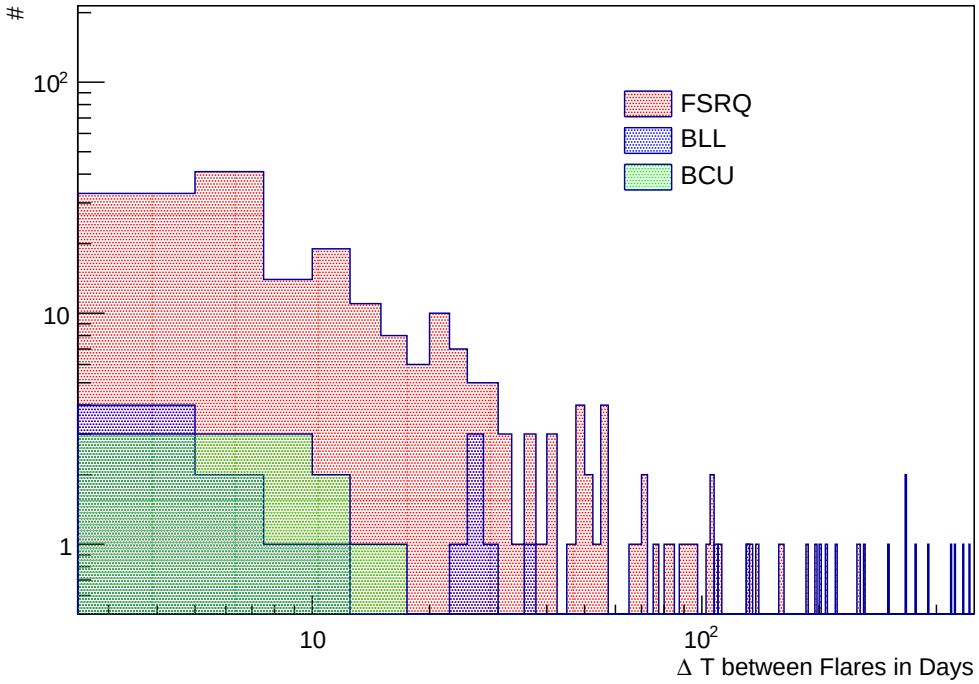

Figure 7.4: Histogram of the time between the detection of two successive flares from a given blazar. While short time gaps of only a few days indicate that a longer phase of activity has been cut into independent flares, long time gaps represent independent flares detected at the beginning and end of the considered time range. While all blazar types show gaps of only a few days, only FSRQ and BL Lac objects are identified in multiple independent activity phases.

or cut into smaller intervals. However, BCUs seem to be too faint to be detected in multiple independent activity phases, resulting in only short time gaps.

7.2.4 Flaring Power

In order to study how significant a flare is detected according to Eq. 7.1, I introduce the new parameter "Flaring Power" which is defined as the maximum flare amplitude divided by the ground level flux G. Sources with a high flaring power show more luminous flare amplitudes, clearly exceeding the ground level flux. While flaring powers of around unity would indicate a flare detection right at the ground level, higher values correspond to more significant flares. All blazar types emit flares discovered slightly above the detection threshold of *Fermi*/LAT, together with flares clearly exceeding the ground level state. The cut around a flaring power value of ~ 2 is caused by the requirement of an identified flare to exceed the ground level flux by three times the $1\,\sigma$ flux uncertainty (see Eq. 7.1). While flares from BCUs seem to be slightly more significant than flares from BL Lacs, FSRQs do still account for the most significant detections.

7.2.5 Boxyness

To study the shape of identified flares, I introduce the new parameter "Boxyness", which is defined as the integrated γ-ray fluence divided by the duration of the considered flaring

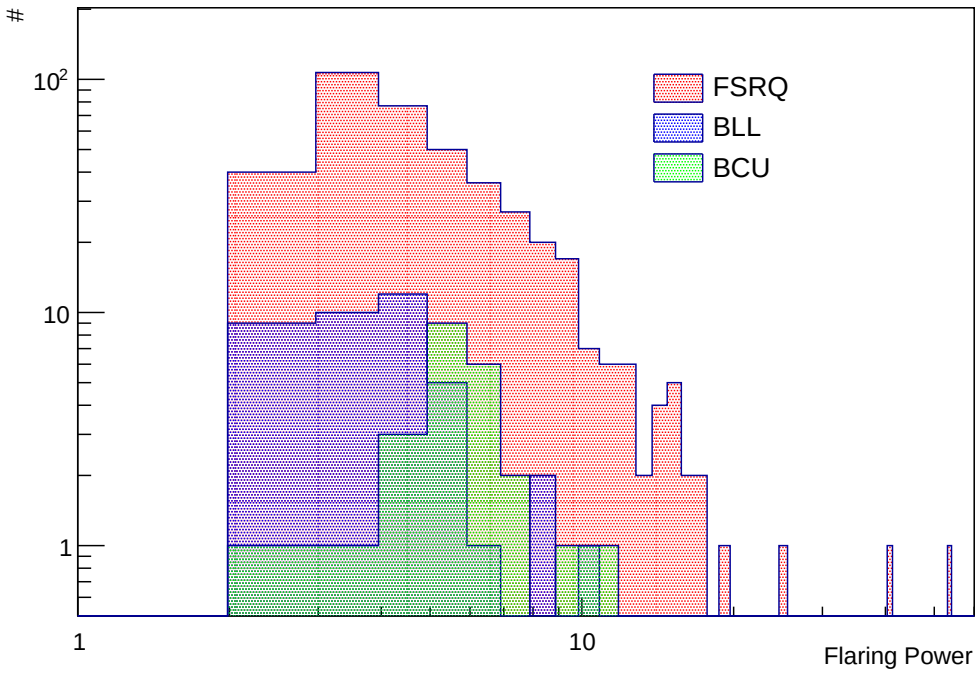

Figure 7.5: Histogram of the parameter flaring power, indicating how significant identified flares exceed the ground level flux. All blazar types show significant flares, as well as phases of activity right at the identification threshold. However, the most significant flares are caused by FSRQs.

interval. This quantity corresponds to an averaged flux in the selected time range. The shape of the flaring interval influences this averaged flux level. While perfectly box-like flares (flares, which show a constant flux level over the entire time range), correspond to an averaged flux, which is equal to the maximum flare amplitude, irregular shaped flares generate a smaller averaged flux. Figure 7.6 visualizes a basic sketch of this behavior. In order to study the shapes of the selected flare sample, Fig. 7.7 displays the boxyness depending on the maximum flare amplitude. The red line indicates an upper boundary condition in the possible parameter space of this quantity, which is given by perfectly box-shaped flares. Following the definition of this parameter, flares with a duration of only one day are perfectly box-shaped and lay on this maximum line. With increasing difference to the maximum line, flaring shapes get more irregular. Only two flares with a duration of two days show perfectly box-shaped flares, while for the majority of flares with a duration of more than one day, at least some kind of substructure seems to be present. It is worth mentioning that the shape of a flare seems not directly correlated to it's duration. While longer flares are more likely to develop substructure, Fig. 7.7 indicates that flares with durations of several days can also be nearly box-like.
Considering different blazar types, perfectly box-shaped daily flares are shown by all blazars. More irregular phases of enhanced activity, however, are dominated by FSRQs. While BL Lacs and BCUs do also show flares with durations of up to a few days, they are typically not bright enough to supply the detection of longer uninterrupted periods, which can evolve into a more complicated substructure. Furthermore, as in agreement with Sect. 7.2.2, BL Lacs

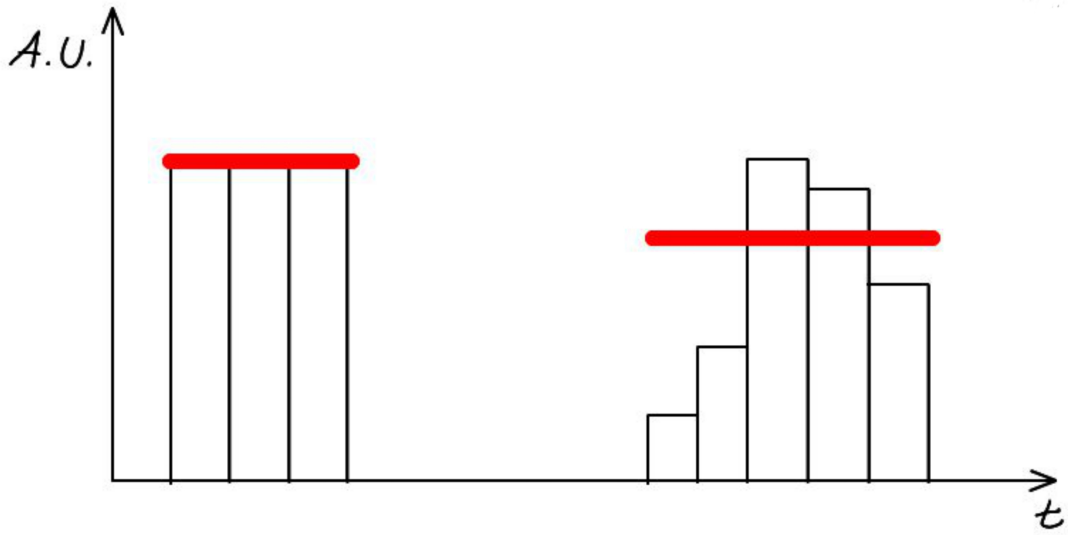

Figure 7.6: Basic sketch (in arbitrary units), showing the influence of the flare shape on the averaged flux level (marked as a red line). While perfect box-like flares (left) show an averaged flux level equal the maximum flare amplitude, more irregular flares (right) lead to a reduced averaged flux.

and BCUs are often detected close to the detection threshold or even below[44], which favors daily detections. The three BCU outliers, detected around the trigger threshold, belong to a longer phase of activity of the source B2 0619+33, which has been detected with a maximum amplitude of $\sim 1 \times 10^{-6}\,\mathrm{ph\,/cm^2\,/s}$ and shows several flux states below that level, which explains their low averaged flux. Due to the low flux level, this interval includes upper limits, which divides it into the three detected flaring periods shown in Fig. 7.7.

7.3 Discussion and Outlook

In this section, a sample of $\sim$ 500 flares, created by 80 blazars has been studied. These sources are selected from a sample of 150 bright blazars monitored by *Fermi*/LAT (see App. H). Following the selection criteria of Eq. 7.1, these periods are uninterrupted high state intervals, favoring daily flares. A dedicated analysis targeting the flaring behavior of different blazar types has been performed by studying their specific flare characteristics. As expected, FSRQs are found to be more luminous than BL Lacs and BCUs, which is in agreement with previous results (e.g. Ackermann et al. 2015c), leading to longer flaring periods and more irregular shapes on time scales of multiple days. As FSRQs are bright enough to trigger periods of enhanced activity lasting up to several months, they are detected more frequently, leading to time gaps between the detection of two successive flares from days to several months or years. While short gaps on the order of a few days can be explained by a longer phase of activity, that is cut into shorter flare due the the used flare definition of Eq. 7.1, longer gaps on the order of months correlated to multiple independent activity phases. All blazar types show flares detected right at the identification threshold of Eq. 7.1, as well as highly significant detections. However, the most significant and most luminous flaring periods are generated exclusively by FSRQs, which is expected due to their spectral shape. As BL Lacs and BCUs are in general fainter sources (again see e.g. Ackermann et al. 2015c), with maximum flare amplitudes of up

[44] This can happen, because a source is included in the *Fermi*/LAT bright blazar list by showing at least once a flux exceeding the trigger threshold of $> 10^{-6}\,\mathrm{ph\,/cm^2\,/s}$

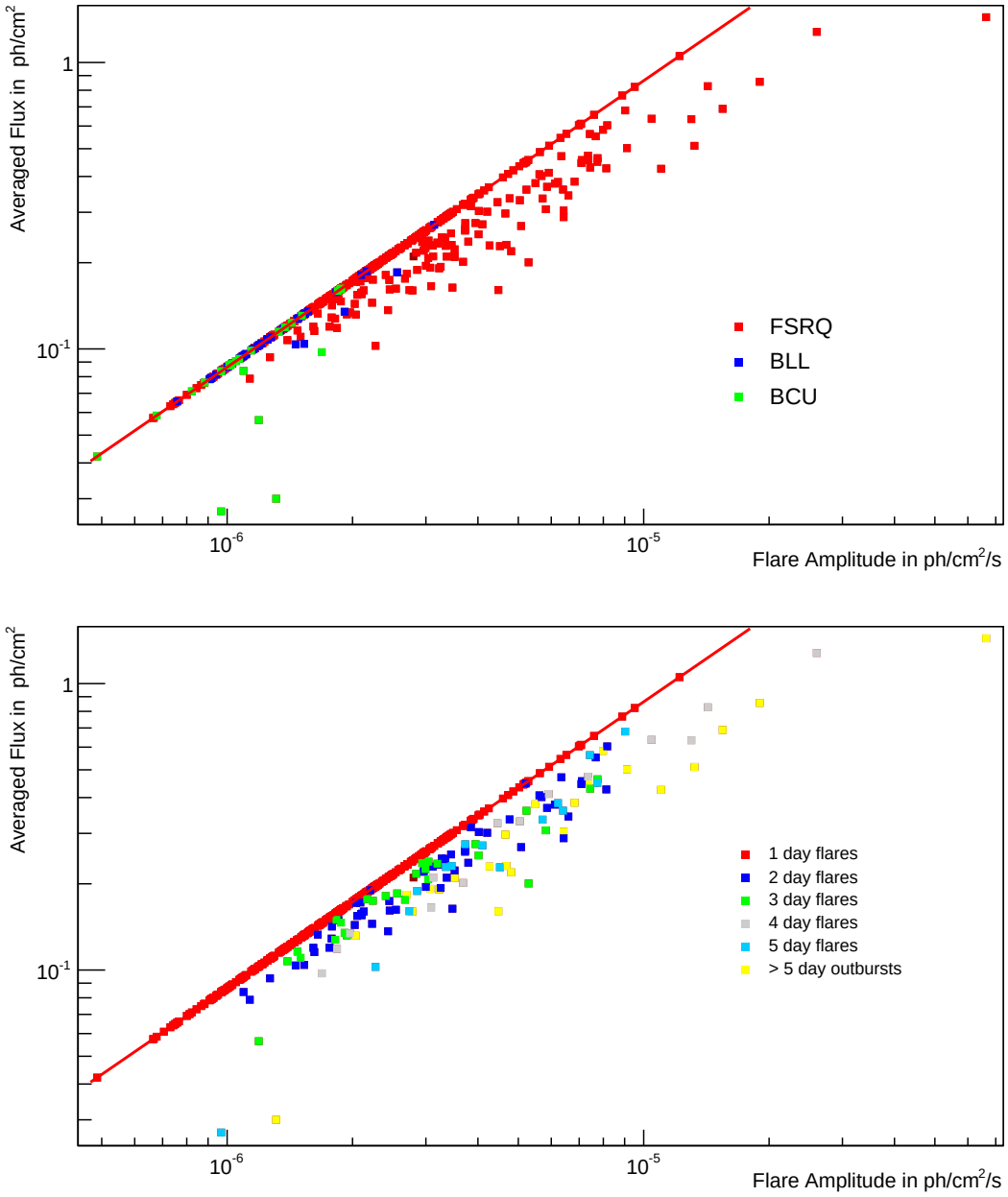

Figure 7.7: Averaged flux (boxyness) depending on the maximum flare amplitude. The red line indicates perfectly box-shaped flares, which correspond to an averaged flux being equal the maximum flare amplitude. Top: Boxyness for different types of blazars. Bottom: Boxyness for different flare durations

to $\sim 3 \times 10^{-6}$ ph /cm^2 /s, they are primary detected on daily time scales, close the the *Fermi* Flare Advocate trigger threshold. BL Lacs are too faint to be detected on time scales longer than $\sim$ three days, while BCUs on the other hand can show flaring periods of up to ten days. These longer periods in BCUs are caused by flux levels close or below the trigger threshold. Longer periods of enhanced activity in BL Lac and BCU objects are, similar as in FSRQs, cut into shorter periods with a gap of only a few days between successive flares. In addition, BL Lacs and FSRQs show time gaps of more than 100 days, indicating the detection of two independent periods of enhanced activity. BCUs, on the other hand, do only show time gaps of less than 20 days, which indicates a longer period (most likely around or below the trigger threshold) being cut into these shorter flares. Furthermore, this indicates that BCUs do not show multiple independent activity phases, which would result in larger gaps.
In this thesis, I have shown differences in the overall observed flaring behavior of different blazar types. It is not a-priori clear, whether the observed flaring behavior is caused by different processes happening within the jets of different blazar types. Furthermore, the limited sensitivity of *Fermi*/LAT, as well as shifted spectral shapes of different blazar types can be responsible for the measured differences. While both leptonic as well as hadronic processes can be responsible for the observed γ-ray emission (see Sect. 2.3), a hadronic origin cannot be immediately excluded for daily flares or even intraday variability on time scale of hours to minutes (see Sect. 2.4.2.2). Hadronic cascades (Mannheim & Biermann 1992) as well as proton-synchrotron mechanism (Aharonian 2000) can become enhanced, due to very strong magnetic fields ($\geq$ kG) and very dense target radiation fields. However, a careful analysis of these mechanisms requires a dedicated study.

This analysis is based on the publicly available list[45] of bright blazars, monitored by *Fermi*/LAT. In order to take full advantage of the current Pass 8 data release, a dedicated light curve analysis for all the 150 considered blazars (see Sect. 4.2.3) needs to be performed in the future. Furthermore, the used ground level calculation, which is based on the Median of the *Fermi*/LAT flux distribution, introduces a systematic uncertainty to the identification of flaring periods. A Gaussian fit (similar to Sect. 5.1.2) would lead to a more robust ground level estimate. However, as this fit would have to be performed for the entire sample of 150 sources, this will be addressed in a follow-up publication.
A clear difference between daily flares of all blazar types and longer identified periods has been seen. A dedicated spectral analysis (see Sect. 4.2.4) would be necessary, in order to study the spectral properties of flares with different durations. Such an analysis would be crucial to target the underlying spectral properties responsible for the observed γ-ray emission and distinguish whether there are fundamental differences in blazar flares with different durations or shapes. Unfortunately, this kind of analysis requires an enormous amount of computing time, which again will be included in a follow-up project.
Finally, the limitation to the bright blazar list of *Fermi*/LAT introduces a bias towards bright sources, which flaring characteristic could be different from the one of fainter blazars. An extension to a more general list of blazars like e.g. the third catalog of active galactic nuclei detected by *Fermi*/LAT (3LAC; Ackermann et al. 2015c) would only be a logical consequence. Furthermore, only short and uninterrupted periods of enhanced activity are considered by Eq. 7.1. A more general definition, allowing e.g. for fluctuations below the detection threshold or upper limits to be included within an identified interval, would certainly reduce some of the observed biases discussed in Sect. 7.2.

[45] http://fermi.gsfc.nasa.gov/ssc/data/access/lat/msl_lc/

8 Conclusion and Outlook

In this thesis, I studied blazars as a promising class of the observed high-energy neutrino flux. Blazars are characterized by their high luminosity and rapid variability. This subclass of active galactic nuclei shows jet orientations close to the line-of-sight of the observer and can accelerate particles to relativistic energies. The high-energy broadband emission can be explained by either leptonic or hadronic models, or a combination of both. Multiwavelength and especially multimessenger observations are crucial to draw a complete picture of the physical processes which happen in jets. Recently detected high-energy neutrino events, originating from the direction of bright blazars, give first hints of protons, which may be accelerated within jets. The detection of a high-energy neutrino from a blazar would be an irrefutable evidence of hadronic processes. However, even for a temporally and spatially consistent detection of a high-energy neutrino and a phase of enhanced activity of a single blazar, the chance coincidence is only $\sim 5\,\%$. This so-called "BigBird" event produced a large particle cascade within the IceCube detector, resulting in a positional uncertainty of $\sim 10^{\circ}$. Furthermore, the outburst period of the blazar PKS 1424−418 lasted several months, which also contributes to a lower significance of a possible association. Such a small probability is in agreement with the observed all-sky neutrino flux, as otherwise, the sky would already be populated with numerous confirmed neutrino point sources.

In this work, I studied flares on time scales of days to weeks, based on a sample of bright blazars continuously monitored by *Fermi*/LAT. Following a calorimetric approach, I estimated the maximum amount of expected neutrino events in the most optimistic scenario and used a physically motivated scaling factor to scale these numbers down to a more realistic neutrino expectation. The calorimetric approach assumes the entire high-energy emission to be produced in the process of photo-pionproduction, resulting in an equal amount of high-energy photons and neutrinos. Therefore, the integrated fluence of a blazar flare plays an essential role in the amount of expected high-energy neutrino events. I found that short-term blazar flares with durations of days to weeks typically do not generate enough fluence to lead to a substantial neutrino prediction to be detectable for IceCube. However, for the brightest short-term flares, Poisson probabilities of up to $\sim 2\%$ are reached, so that the possibility of associated neutrino detections in future data unblindings seems likely. This result indicates that the neutrino prediction of the majority of short-term blazar flares is negligible, so future neutrino point source searches should therefore concentrate on periods of maximum fluence rather than short-term temporal and spatial associations.
On 22 September 2017, IceCube detected a $\sim$ 290 TeV neutrino induced track-like event (called IceCube-170922A), consistent with an active phase of the blazar TXS 0506+056. An intense multiwavelength and multimessenger campaign followed, studying the broadband emission behavior of this specific blazar and potential correlations to other messengers. In this thesis, however, I first studied the long-term flaring behavior of this source, using more than nine years of *Fermi*/LAT data. I found that the considered activity phase had already been ongoing since the beginning of 2017, months before the detection of IceCube-170922A. I performed a calorimetric neutrino analysis on a three day short-term period around the neutrino arrival time. No substantial neutrino output, even under the most optimistic assumptions, could be obtained. Therefore, an association between the neutrino event IceCube-170922A and a three day flaring period of the blazar TXS 0506+056 is calorimetrically unlikely. Considering the long-term period since early 2017, a chance coincidence of the order of $\sim 3.5\,\sigma$ is obtained. This result is in agreement with other independent studies, clearly indicating the blazar TXS 0506+056 to be the most promising extragalactic neutrino point source so far.

The calorimetric analysis presented in this thesis focuses on a specific kind of flaring event (short and bright) or a specific source (TXS 0506+056). A broader approach, also considering a systematic search for long-term periods of enhanced activity, would be the content of a new study. While TXS 0506+056 is the first active blazar which is temporally and spatially consistent with a track-like high-energy neutrino event, more such events are expected in the future. Long-term multiwavelength and multimessenger monitoring of the entire sky is crucial for future neutrino-blazar associations. While the presented work is based on a correlation of photons and neutrinos originating from the process of photo-pionproduction, considering also fainter/undetected γ-ray sources such as high-z blazars would open the field to a huge number of potential new neutrino point-source candidates. Additional processes, such as proton-proton interactions, lepto-hadronic models with a varying hadronic contribution or multizone SED models, are also important to consider in the future.

Blazars undetected by *Fermi*/LAT could be responsible for the observed high-energy neutrino flux. Especially blazars at large cosmological distances account for one of the most extreme objects in the Universe. Due to their large redshift, they efficiently interact with the extragalactic background light, making them almost undetectable to *Fermi*/LAT. In addition, these blazars are important targets, as they serve as cosmological probes for blazar evolution models. In this work, I studied a sample of 176 *Fermi*/LAT undetected blazars which have been observed at radio and/or optical wavelengths. These blazars are undetected in their averaged flux on long-term time scales on the order of years, but can still lead to significant monthly detections in the MeV-GeV regime, during a flaring state. In total, I have studied more than 20,000 monthly intervals in a time range of about nine years and was able to identify seven previously undetected γ-ray sources which showed at least one monthly interval detected at a $5\,\sigma$ level. Especially the blazar 5BZQ J2219−2719, at a distance of $z = 3.63$ was found to be the most distant new γ-ray source identified in the context of this thesis. These new γ-ray sources will have to be studied in detail. A dedicated analysis studying the spectral properties of these new γ-ray sources is necessary. At the same time, more blazars could be identified by considering a larger target sample and/or a smaller time integration of less than a month.

The sources considered in this work offer a unique opportunity to study the overall flaring behavior of bright γ-ray blazars. In the last part of this thesis, I performed a systematic analysis of the long-term flaring behavior of bright blazars observed by *Fermi*/LAT. As expected, FSRQs are more luminous than BL Lacs and BCUs and thus are detected more frequently, show longer and brighter flares and can be resolved by *Fermi*/LAT in a more complex flare substructure on the order of several days. As BL Lacs and BCUs are typically detected close to the detection threshold of *Fermi*/LAT, these blazars are less luminous and show mostly daily flares. While the occurrence of flares is of a purely statistical nature, their observed distribution by *Fermi*/LAT clearly is influenced by the sensitivity of the detector. Even after certain differences in the overall flaring behavior of bright blazars have been seen, it is not a-priori clear whether these differences and caused by different properties of the studied source sample, or just a selection effect due the the limited sensitivity of *Fermi*/LAT. However, the flare selection introduced in this work is optimized on uninterrupted bright periods of enhanced activity. Long-term periods are often cut into independent shorter flares, introducing a large systematic uncertainty to the presented study. Similar to the search for high-z blazars, this systematic analysis of blazar flaring properties would benefit from a more general flare definition, as well as a larger target sample which also includes fainter blazars.

The identification of blazars as sources of high-energy neutrinos would provide conclusive evidence of hadronic processes in jets and would prove that active galactic nuclei do indeed contribute to the observed cosmic-ray spectrum. Studying the properties of these sources is crucial for a better understanding of e.g. jet physics and particle acceleration in order to draw a more complete picture of the Universe.

Appendices

A Full List of Flares Considered in Sec. 5.1

Table 5: Full list of flares identified by Equ. 5.1. This selection is based on the public list of bright blazars monitored by *Fermi*/LAT, and is available at http://fermi.gsfc.nasa.gov/ssc/data/access/lat/msl_lc/. Listed are identified flares, together with their source name, start and stop time of the flaring period and duration.

Flare Number	Source	t_{min} [MJD]	t_{max} [MJD]	Duration [Days]	Flare Number	Source	t_{min} [MJD]	t_{max} [MJD]	Duration [Days]
1	3C 279	57186	57192	6	41	PKS 1424−418	56435	56436	1
2	PKS 1510−089	55849	55854	5	42	3C 279	55466	55468	2
3	PKS 1510−089	55866	55877	11	43	PKS 1424−418	56394	56396	2
4	PKS 1510−089	55856	55857	1	44	PKS 1510−089	57215	57223	8
5	3C 279	56717	56718	1	45	PKS 1510−089	56536	56539	3
6	3C 279	56749	56754	5	46	PKS 1510−089	56954	56955	1
7	PKS 1510−089	57241	57251	10	47	PKS 1329−049	55467	55468	1
8	3C 279	56866	56868	2	48	PKS 1329−049	55445	55447	2
9	PKS 1510−089	56553	56557	4	49	PKS 1424−418	57385	57386	1
10	PKS 1510−089	55766	55768	2	50	PKS 1510−089	56567	56569	2
11	PKS 1510−089	57098	57099	1	51	PKS 1510−089	57644	57652	8
12	PKS 1510−089	56563	56565	2	52	PKS 1510−089	57134	57141	7
13	PKS 1510−089	55843	55844	1	53	PKS 1510−089	57632	57641	9
14	PKS 1510−089	57148	57149	1	54	PKS 1510−089	57176	57178	2
15	PKS 1510−089	56542	56543	1	55	PKS 1424−418	56490	56491	1
16	PKS 1510−089	55742	55746	4	56	PKS 1510−089	56588	56596	8
17	PKS 1510−089	56610	56611	1	57	PKS 1329−049	55457	55462	5
18	PKS 1510−089	55738	55740	2	58	PKS 1424−418	56286	56287	1
19	PKS 1510−089	55954	55994	40	59	PKS 1424−418	56237	56238	1
20	PKS 1510−089	55997	56006	9	60	PKS 1510−089	57193	57195	2
21	PKS 1510−089	57113	57129	16	61	PKS 1424−418	56149	56150	1
22	PKS 1510−089	57152	57172	20	62	3C 454.3	57551	57571	20
23	PKS 1510−089	57609	57610	1	63	PKS 1830−21	55483	55487	4
24	PKS 1510−089	57201	57202	1	64	PKS 1510−089	56528	56530	2
25	PKS 1510−089	55790	55791	1	65	PKS 0402−362	57018	57020	2
26	PKS 1510−089	57101	57102	1	66	PKS 1424−418	57365	57366	1
27	3C 279	57153	57155	2	67	3C 279	56657	56659	2
28	PKS 0402−362	55824	55831	7	68	3C 279	56576	56577	1
29	PKS 1510−089	57131	57132	1	69	PKS 1510−089	56574	56580	6
30	PKS 1510−089	57198	57199	1	70	PKS 1510−089	56876	56877	1
31	CTA 102	57558	57559	1	71	PKS 1424−418	56138	56139	1
32	3C 279	57212	57215	3	72	PKS 1510−089	55783	55785	2
33	PKS 1510−089	56832	56833	1	73	3C 279	56672	56675	3
34	3C 279	56646	56655	9	74	PKS 1510−089	57104	57110	6
35	3C 279	56757	56758	1	75	PKS 1510−089	56964	56965	1
36	3C 279	56742	56747	5	76	PKS 1329−049	55454	55455	1
37	PKS 1510−089	57055	57056	1	77	PKS 1510−089	56947	56951	4
38	3C 454.3	55408	55648	240	78	PKS 1510−089	56917	56919	2
39	PKS 1510−089	56571	56572	1	79	3C 279	56629	56639	10
40	PKS 1510−089	57210	57213	3	80	3C 279	56984	56993	9

Full List of Flares Considered in Sec. 5.1

Flare Number	Source	t_{min} [MJD]	t_{max} [MJD]	Duration [Days]
81	PKS 0402−362	57100	57103	3
82	PKS 1510−089	55880	55886	6
83	CTA 102	57421	57452	31
84	3C 279	57209	57210	1
85	PKS 1424−418	56353	56355	2
86	PKS 0402−362	57318	57320	2
87	PKS 1424−418	56398	56425	27
88	PKS 1222+216	56539	56540	1
89	PKS 1424−418	56483	56486	3
90	PKS 1424−418	55323	55330	7
91	3C 279	56870	56871	1
92	PKS 1510−089	56361	56364	3
93	3C 279	57195	57198	3
94	PKS 1424−418	56289	56291	2
95	PKS 1830−21	56064	56065	1
96	PKS 1510−089	56957	56960	3
97	3C 279	57344	57345	1
98	3C 279	57552	57553	1
99	CTA 102	57381	57386	5
100	CTA 102	56188	56203	15
101	3C 279	55704	55706	2
102	3C 454.3	57242	57260	18
103	PKS 1424−418	56241	56244	3
104	PKS 1424−418	56362	56364	2
105	PKS 1510−089	57225	57226	1
106	3C 454.3	56796	56903	107
107	PKS 1424−418	56225	56229	4
108	PKS 1510−089	55847	55848	1
109	CTA 102	57619	57635	16
110	PKS 1510−089	55749	55750	1
111	3C 454.3	56907	56921	14
112	PKS 1424−418	56293	56350	57
113	CTA 102	56952	56956	4
114	PKS 0402−362	57296	57297	1
115	PKS 1222+216	56981	56982	1
116	3C 454.3	56972	56973	1
117	PKS 1329−049	55504	55507	3
118	3C 454.3	57105	57107	2
119	CTA 102	57454	57455	1
120	PKS 1424−418	56465	56469	4
121	PKS 1510−089	57277	57278	1
122	PKS 1830−21	55498	55499	1
123	CTA 102	56690	56691	1
124	PKS 1424−418	56374	56392	18
125	PKS 1510−089	56533	56534	1
126	PKS 0402−362	57072	57073	1
127	CTA 102	56387	56393	6
128	CTA 102	57088	57090	2
129	PKS 1830−21	56147	56148	1
130	PKS 1424−418	56366	56372	6
131	3C 279	55667	55668	1
132	CTA 102	57641	57642	1
133	PKS 1510−089	57295	57296	1
134	3C 454.3	57589	57602	13
135	PKS 1222+216	56701	56703	2
136	CTA 102	57407	57419	12
137	PKS 1424−418	56459	56463	4
138	PKS 1510−089	57654	57655	1
139	CTA 102	57490	57492	2
140	CTA 102	55719	55723	4
141	CTA 102	57586	57587	1
142	CTA 102	57486	57487	1
143	3C 454.3	57190	57210	20
144	PKS 1510−089	56830	56831	1
145	3C 454.3	56984	56991	7
146	CTA 102	57542	57548	6
147	CTA 102	57359	57361	2
148	3C 279	56859	56860	1
149	PKS 1424−418	56476	56481	5
150	PKS 1510−089	56821	56822	1
151	CTA 102	57638	57639	1
152	PKS 1222+216	55355	55393	38
153	CTA 102	57515	57516	1
154	PKS 0402−362	57290	57292	2
155	PKS 1222+216	56691	56692	1
156	PKS 1222+216	56972	56979	7
157	PKS 1830−21	55502	55504	2
158	PKS 1510−089	55661	55662	1
159	PKS 1222+216	55543	55544	1
160	3C 454.3	55317	55371	54
161	PKS 1510−089	56482	56483	1
162	PKS 0402−362	56872	56875	3
163	PKS 1329−049	55450	55451	1
164	PKS 1510−089	56366	56367	1
165	PKS 0402−362	57047	57052	5
166	CTA 102	56458	56460	2
167	PKS 1510−089	57538	57539	1
168	PKS 1424−418	56739	56740	1
169	3C 279	56873	56874	1
170	PKS 1510−089	56041	56042	1
171	PKS 1510−089	55781	55782	1
172	3C 279	56861	56862	1
173	PKS 1830−21	56088	56094	6
174	PKS 1830−21	56081	56086	5
175	PKS 1510−089	57191	57192	1
176	3C 454.3	55380	55381	1
177	PKS 1424−418	56488	56489	1
178	3C 454.3	56959	56969	10
179	CTA 102	56237	56239	2
180	CTA 102	57055	57058	3
181	CTA 102	56383	56384	1
182	CTA 102	57287	57290	3
183	CTA 102	57564	57568	4
184	3C 454.3	57382	57434	52
185	PKS 1830−21	55558	55565	7
186	3C 279	57184	57185	1
187	PKS 1329−049	55480	55481	1
188	3C 454.3	57455	57466	11
189	CTA 102	57615	57617	2
190	3C 454.3	56924	56933	9
191	PKS 1424−418	56233	56234	1
192	PKS 1424−418	55333	55334	1
193	3C 454.3	56321	56322	1
194	PKS 1510−089	55942	55943	1
195	PKS 1424−418	56444	56445	1
196	PKS 2023−08	57487	57497	10
197	CTA 102	57464	57480	16
198	3C 454.3	56751	56756	5
199	PKS 1510−089	56823	56824	1
200	3C 279	57218	57219	1
201	PKS 1510−089	56944	56945	1
202	3C 454.3	57054	57077	23
203	3C 454.3	57151	57156	5
204	CTA 102	56205	56209	4
205	PKS 1510−089	56273	56274	1
206	3C 279	56857	56858	1
207	PKS 1424−418	56455	56456	1
208	CTA 102	57550	57554	4
209	PKS 1424−418	56495	56496	1
210	PKS 1424−418	56474	56475	1

Full List of Flares Considered in Sec. 5.1

Flare Number	Source	t_{min} [MJD]	t_{max} [MJD]	Duration [Days]
211	PKS 1424−418	56498	56499	1
212	PKS 1424−418	56147	56148	1
213	PKS 1424−418	56774	56775	1
214	PKS 1424−418	56440	56441	1
215	PKS 1510−089	56940	56941	1
216	PKS 1222+216	56698	56699	1
217	CTA 102	57571	57574	3
218	3C 279	55698	55699	1
219	PKS 0402−362	55989	55990	1
220	3C 454.3	56995	57031	36
221	PKS 1510−089	56870	56871	1
222	PKS 1222+216	55533	55535	2
223	3C 279	55739	55740	1
224	PKS 1424−418	56217	56218	1
225	PKS 1510−089	56966	56967	1
226	3C 454.3	57264	57355	91
227	PKS 1424−418	56271	56272	1
228	3C 454.3	55657	55658	1
229	3C 454.3	57451	57452	1
230	PKS 1424−418	57368	57369	1
231	PKS 0402−362	57078	57082	4
232	PKS 1424−418	56143	56144	1
233	PKS 1424−418	56145	56146	1
234	PKS 1424−418	56789	56790	1
235	PKS 1424−418	56472	56473	1
236	PKS 1424−418	56215	56216	1
237	PKS 1510−089	57628	57629	1
238	PKS 1329−049	55482	55483	1
239	PKS 1222+216	55332	55351	19
240	3C 454.3	57573	57587	14
241	3C 454.3	55678	55679	1
242	PKS 1424−418	56779	56780	1
243	3C 454.3	57606	57635	29
244	3C 454.3	57147	57149	2
245	3C 454.3	57170	57171	1
246	PKS 1424−418	56211	56212	1
247	3C 279	56789	56790	1
248	PKS 0402−362	57312	57313	1
249	PKS 1424−418	56126	56127	1
250	PKS 0402−362	55836	55837	1
251	3C 454.3	56287	56288	1
252	PKS 1222+216	55606	55607	1
253	CTA 102	56966	56967	1
254	3C 454.3	57223	57224	1
255	3C 279	57524	57525	1
256	3C 454.3	56607	56608	1
257	PKS 1424−418	57378	57379	1
258	3C 454.3	57174	57183	9
259	CTA 102	57377	57378	1
260	3C 454.3	56603	56604	1
261	3C 279	56796	56797	1
262	3C 454.3	57185	57188	3
263	3C 454.3	56691	56692	1
264	3C 454.3	57489	57491	2
265	3C 454.3	57103	57104	1
266	3C 279	56641	56642	1
267	3C 454.3	56554	56566	12
268	3C 454.3	57079	57099	20
269	PKS 0402−362	57330	57331	1
270	PKS 0402−362	57307	57308	1
271	3C 279	55715	55716	1
272	PKS 0402−362	57031	57032	1
273	PKS 1222+216	55477	55486	9
274	PKS 1222+216	56962	56969	7
275	3C 454.3	57530	57538	8
276	3C 279	55695	55696	1
277	PKS 1830−21	56071	56072	1
278	PKS 1830−21	57391	57392	1
279	3C 279	57338	57339	1
280	3C 279	55727	55728	1
281	3C 454.3	56387	56390	3
282	PKS 1222+216	55317	55330	13
283	3C 454.3	56382	56384	2
284	PKS 0402−362	57084	57085	1
285	PKS 1830−21	55475	55476	1
286	PKS 1329−049	55342	55343	1
287	CTA 102	56245	56246	1
288	CTA 102	57533	57534	1
289	CTA 102	57401	57402	1
290	3C 279	55459	55460	1
291	PKS 1424−418	57382	57383	1
292	PKS 1830−21	56096	56097	1
293	CTA 102	57061	57062	1
294	CTA 102	57405	57406	1
295	CTA 102	56299	56300	1
296	3C 454.3	56749	56750	1
297	CTA 102	55712	55713	1
298	3C 454.3	56765	56766	1
299	PKS 0402−362	57143	57144	1
300	3C 454.3	55373	55377	4
301	PKS 0402−362	55974	55975	1
302	PKS 0402−362	57117	57118	1
303	CTA 102	57482	57483	1
304	PKS 1222+216	55441	55443	2
305	PKS 1830−21	55496	55497	1
306	3C 279	57221	57222	1
307	3C 454.3	57524	57526	2
308	CTA 102	57578	57579	1
309	PKS 1830−21	56060	56061	1
310	PKS 1830−21	56160	56161	1
311	3C 454.3	55396	55403	7
312	CTA 102	56992	56993	1
313	PKS 0402−362	55511	55512	1
314	PKS 1329−049	55476	55477	1
315	CTA 102	56440	56441	1
316	PKS 0402−362	57115	57116	1
317	3C 454.3	57357	57359	2
318	CTA 102	57531	57532	1
319	3C 454.3	55387	55392	5
320	CTA 102	56218	56219	1
321	PKS 0402−362	57287	57288	1
322	PKS 1830−21	55507	55508	1
323	CTA 102	56462	56463	1
324	3C 454.3	57236	57240	4
325	3C 454.3	57438	57446	8
326	CTA 102	57039	57040	1
327	PKS 1329−049	55519	55520	1
328	3C 454.3	56769	56770	1
329	PKS 1222+216	56564	56565	1
330	3C 454.3	56975	56976	1
331	3C 454.3	56746	56747	1
332	PKS 2023−08	57469	57473	4
333	CTA 102	57497	57498	1
334	PKS 1830−21	56145	56146	1
335	3C 454.3	57113	57114	1
336	3C 454.3	56775	56793	18
337	3C 454.3	56727	56728	1
338	3C 454.3	56938	56939	1
339	3C 454.3	56949	56950	1
340	CTA 102	55692	55693	1

Flare Number	Source	t_{min} [MJD]	t_{max} [MJD]	Duration [Days]
341	PKS 0402−362	57029	57030	1
342	3C 454.3	56763	56764	1
343	3C 454.3	57369	57370	1
344	3C 454.3	56955	56956	1
345	CTA 102	56948	56949	1
346	CTA 102	55680	55681	1
347	PKS 1222+216	55437	55438	1
348	PKS 1222+216	55522	55523	1
349	PKS 1222+216	56664	56665	1
350	PKS 1222+216	55494	55495	1
351	3C 454.3	57380	57381	1
352	3C 454.3	57262	57263	1
353	3C 454.3	56568	56569	1
354	3C 454.3	55383	55384	1
355	3C 454.3	56512	56513	1
356	PKS 1222+216	56688	56689	1
357	PKS 1222+216	55439	55440	1
358	PKS 1222+216	56573	56574	1
359	3C 454.3	57471	57472	1
360	PKS 1222+216	55496	55497	1
361	3C 454.3	55385	55386	1
362	PKS 1222+216	55546	55547	1
363	3C 454.3	56336	56337	1
364	PKS 1222+216	56646	56647	1
365	3C 454.3	55406	55407	1
366	3C 454.3	57448	57449	1
367	PKS 1222+216	56633	56634	1
368	PKS 1222+216	55488	55489	1
369	3C 454.3	57144	57145	1
370	PKS 1222+216	55397	55398	1
371	PKS 1222+216	55548	55549	1
372	3C 454.3	56738	56739	1
373	PKS 1222+216	55570	55571	1
374	3C 454.3	57119	57120	1
375	PKS 1222+216	56498	56499	1
376	PKS 1222+216	56590	56591	1
377	3C 454.3	56589	56590	1
378	3C 454.3	57487	57488	1
379	PKS 1222+216	55628	55629	1
380	3C 454.3	56536	56537	1
381	PKS 1222+216	55704	55705	1
382	3C 454.3	56469	56470	1
383	3C 454.3	56551	56552	1
384	PKS 1222+216	55411	55412	1
385	PKS 1510−089	56583	56587	4
386	3C 454.3	56324	56325	1
387	PKS 2023−08	57269	57270	1
388	3C 454.3	56522	56523	1
389	3C 454.3	57234	57235	1
390	3C 454.3	56686	56687	1
391	PKS 1222+216	56509	56510	1
392	PKS 1222+216	56686	56687	1
393	3C 454.3	57495	57496	1
394	PKS 2023−08	57511	57512	1
395	3C 454.3	56527	56528	1
396	PKS 2023−08	57513	57514	1
397	PKS 1222+216	56592	56593	1
398	PKS 1222+216	55459	55460	1
399	PKS 2023−08	57407	57408	1
400	3C 454.3	55689	55690	1

B SEDs of all Flares in Tab. 2

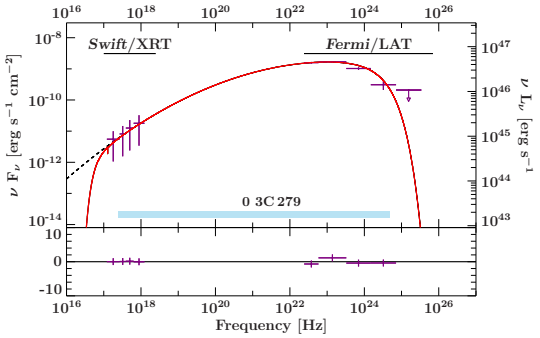

Figure B.1: Simultaneous spectral energy distribution of flare 1 from 3C 279. Please refer to Fig. 5.2 for further details.

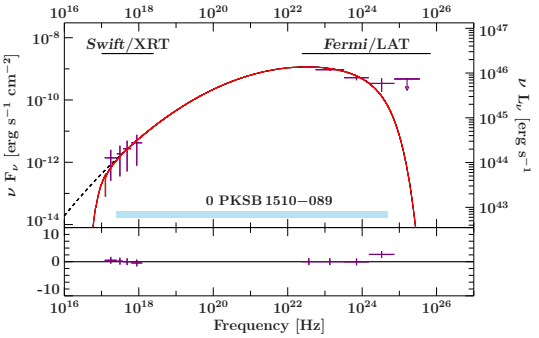

Figure B.2: Simultaneous spectral energy distribution of flare 2 from PKS 1510−089. Please refer to Fig. 5.2 for further details.

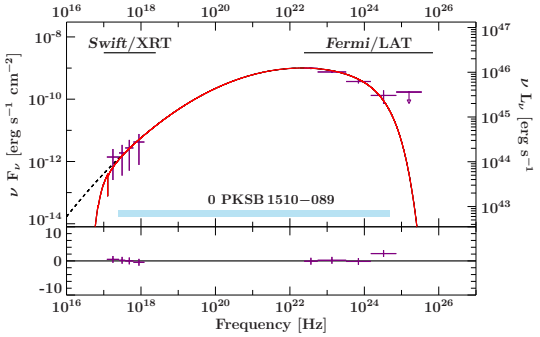

Figure B.3: Simultaneous spectral energy distribution of flare 3 from PKS 1510−089. Please refer to Fig. 5.2 for further details.

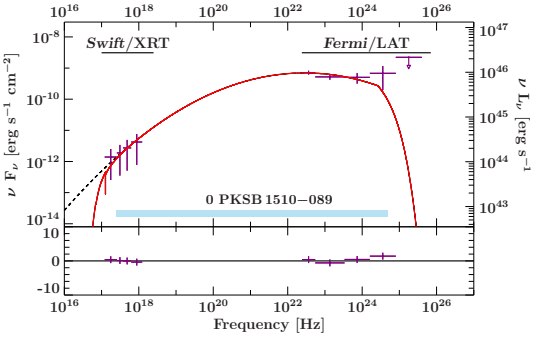

Figure B.4: Simultaneous spectral energy distribution of flare 4 from PKS 1510−089. Please refer to Fig. 5.2 for further details.

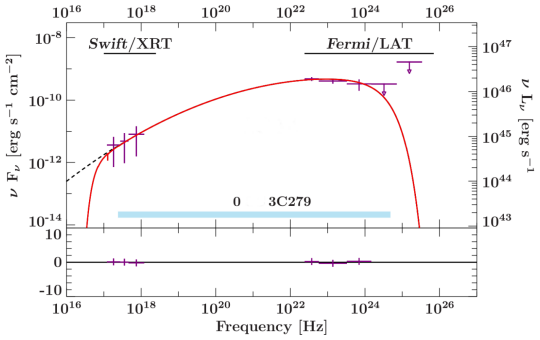

Figure B.5: Simultaneous spectral energy distribution of flare 5 from 3C 279. Please refer to Fig. 5.2 for further details.

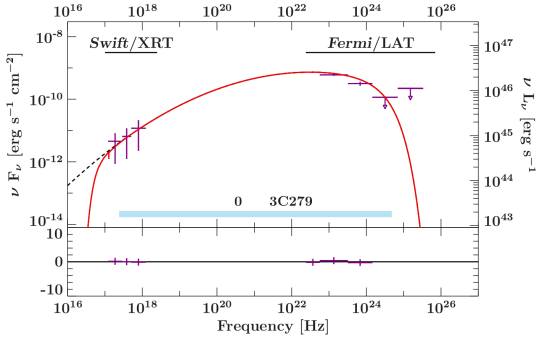

Figure B.6: Simultaneous spectral energy distribution of flare 6 from 3C 279. Please refer to Fig. 5.2 for further details.

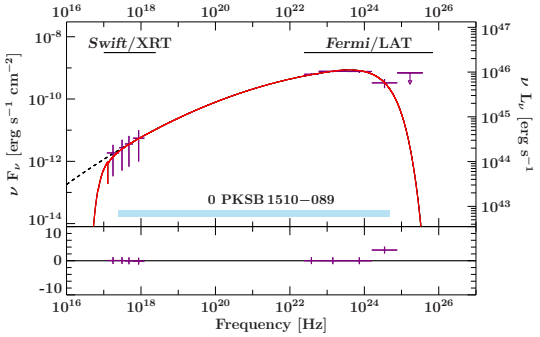

Figure B.7: Simultaneous spectral energy distribution of flare 7 from PKS 1510−089. Please refer to Fig. 5.2 for further details.

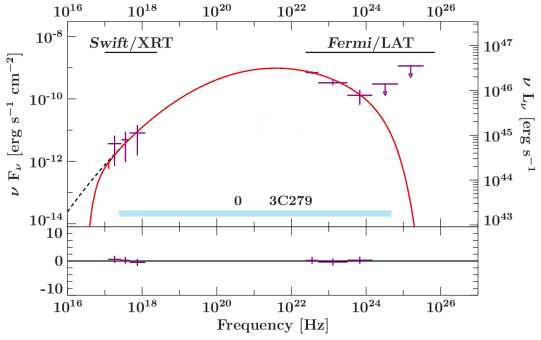

Figure B.8: Simultaneous spectral energy distribution of flare 8 from 3C 279. Please refer to Fig. 5.2 for further details.

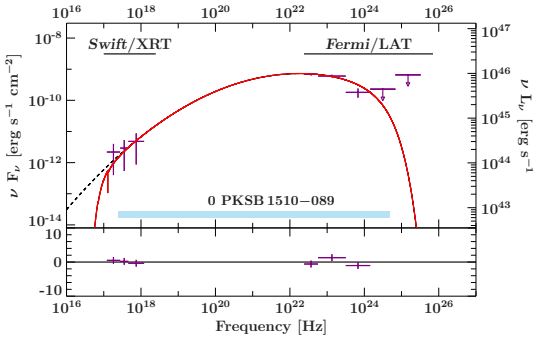

Figure B.9: Simultaneous spectral energy distribution of flare 9 from PKS 1510−089. Please refer to Fig. 5.2 for further details.

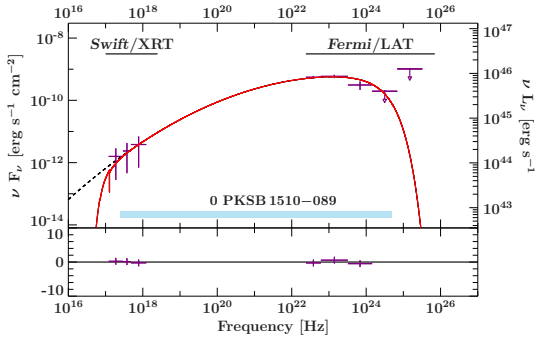

Figure B.10: Simultaneous spectral energy distribution of flare 10 from PKS 1510−089. Please refer to Fig. 5.2 for further details.

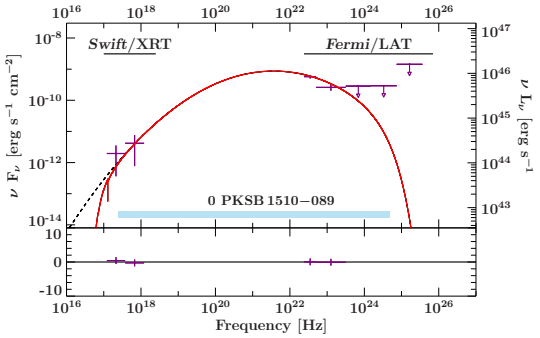

Figure B.11: Simultaneous spectral energy distribution of flare 11 from PKS 1510−089. Please refer to Fig. 5.2 for further details.

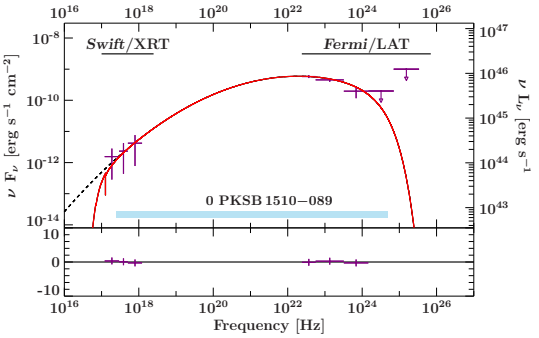

Figure B.12: Simultaneous spectral energy distribution of flare 12 from PKS 1510−089. Please refer to Fig. 5.2 for further details.

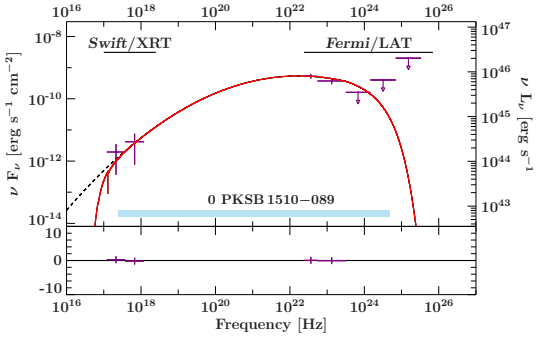

Figure B.13: Simultaneous spectral energy distribution of flare 13 from PKS 1510−089. Please refer to Fig. 5.2 for further details.

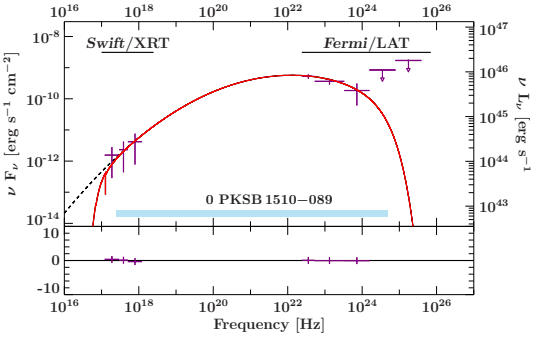

Figure B.14: Simultaneous spectral energy distribution of flare 14 from PKS 1510−089. Please refer to Fig. 5.2 for further details.

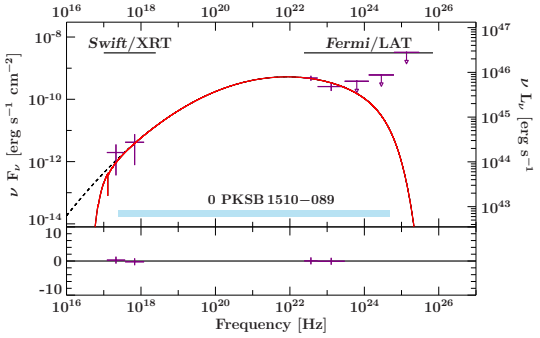

Figure B.15: Simultaneous spectral energy distribution of flare 15 from PKS 1510−089. Please refer to Fig. 5.2 for further details.

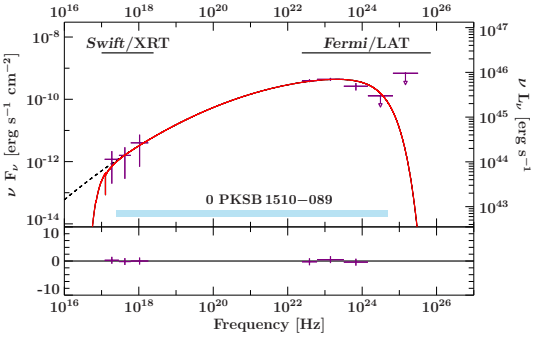

Figure B.16: Simultaneous spectral energy distribution of flare 16 from PKS 1510−089. Please refer to Fig. 5.2 for further details.

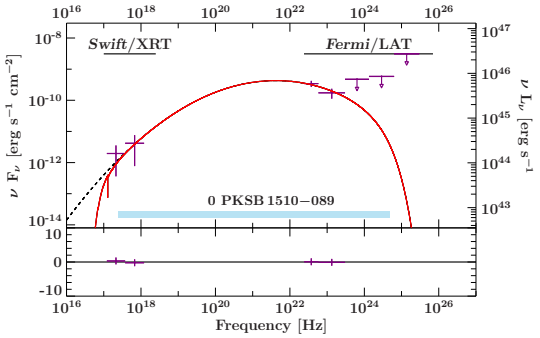

Figure B.17: Simultaneous spectral energy distribution of flare 17 from PKS 1510−089. Please refer to Fig. 5.2 for further details.

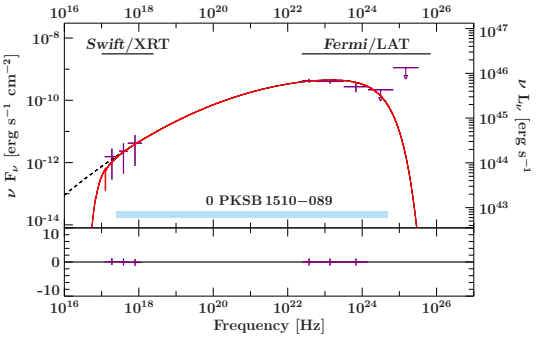

Figure B.18: Simultaneous spectral energy distribution of flare 18 from PKS 1510−089. Please refer to Fig. 5.2 for further details.

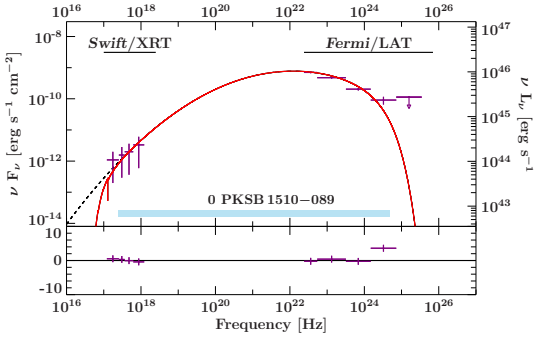

Figure B.19: Simultaneous spectral energy distribution of flare 19 from PKS 1510−089. Please refer to Fig. 5.2 for further details.

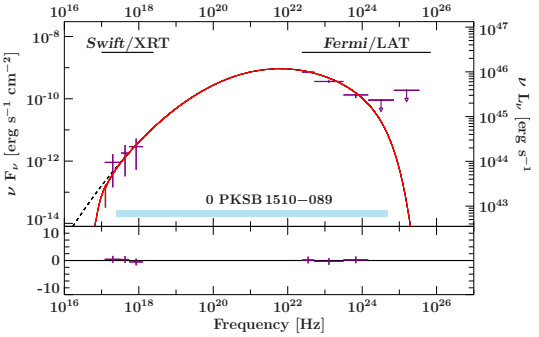

Figure B.20: Simultaneous spectral energy distribution of flare 20 from PKS 1510−089. Please refer to Fig. 5.2 for further details.

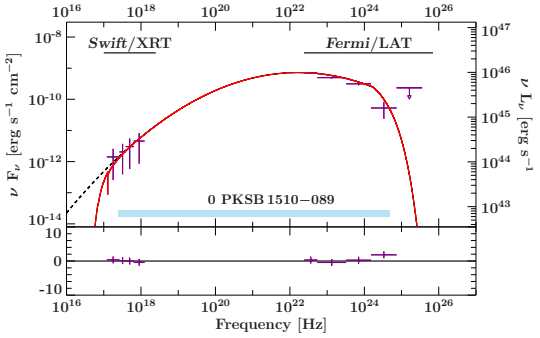

Figure B.21: Simultaneous spectral energy distribution of flare 21 from PKS 1510−089. Please refer to Fig. 5.2 for further details.

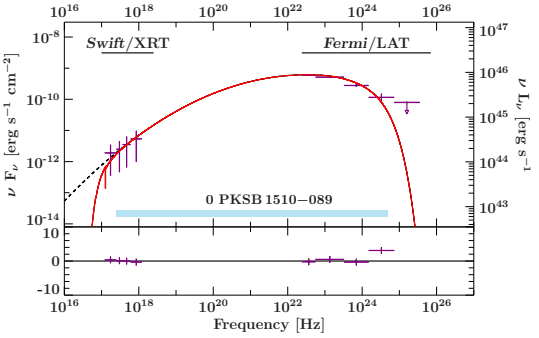

Figure B.22: Simultaneous spectral energy distribution of flare 22 from PKS 1510−089. Please refer to Fig. 5.2 for further details.

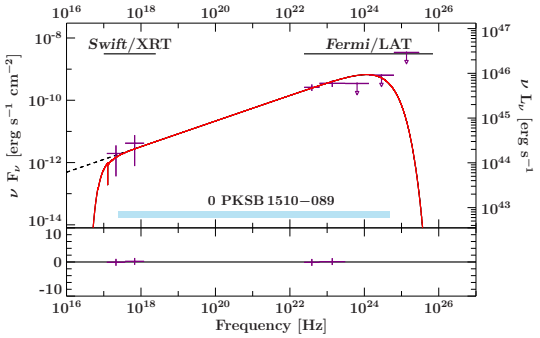

Figure B.23: Simultaneous spectral energy distribution of flare 23 from PKS 1510−089. Please refer to Fig. 5.2 for further details.

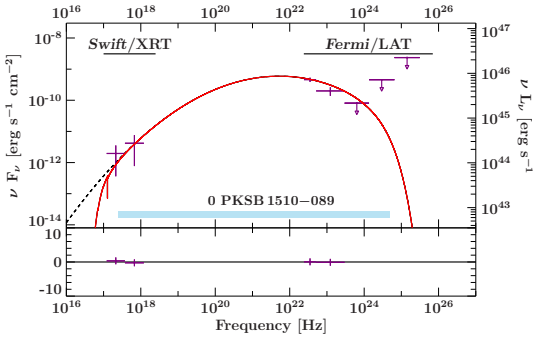

Figure B.24: Simultaneous spectral energy distribution of flare 24 from PKS 1510−089. Please refer to Fig. 5.2 for further details.

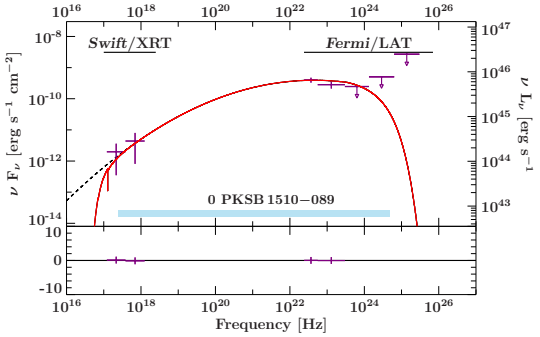

Figure B.25: Simultaneous spectral energy distribution of flare 25 from PKS 1510−089. Please refer to Fig. 5.2 for further details.

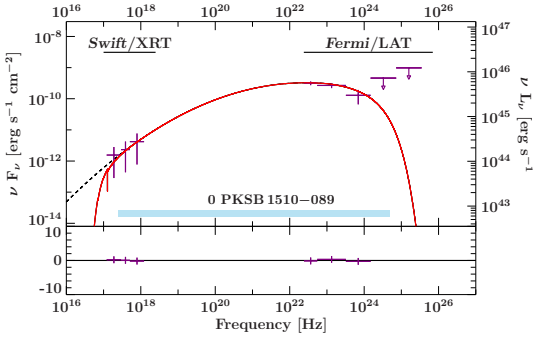

Figure B.26: Simultaneous spectral energy distribution of flare 26 from PKS 1510−089. Please refer to Fig. 5.2 for further details.

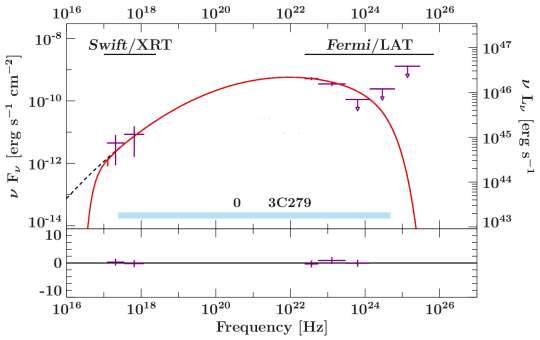

Figure B.27: Simultaneous spectral energy distribution of flare 27 from 3C 279. Please refer to Fig. 5.2 for further details.

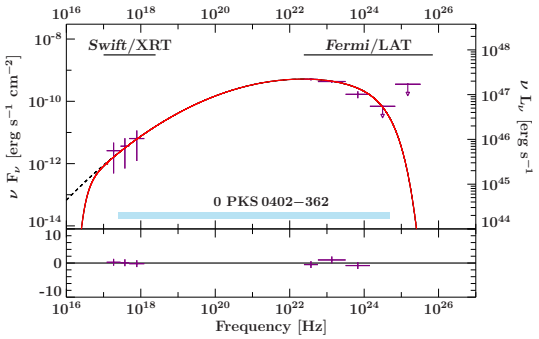

Figure B.28: Simultaneous spectral energy distribution of flare 28 from PKS 0402−362. Please refer to Fig. 5.2 for further details.

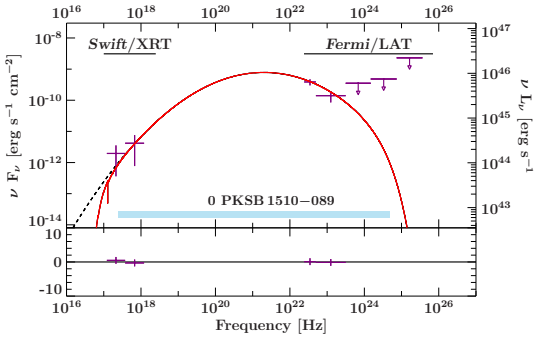

Figure B.29: Simultaneous spectral energy distribution of flare 29 from PKS 1510−089. Please refer to Fig. 5.2 for further details.

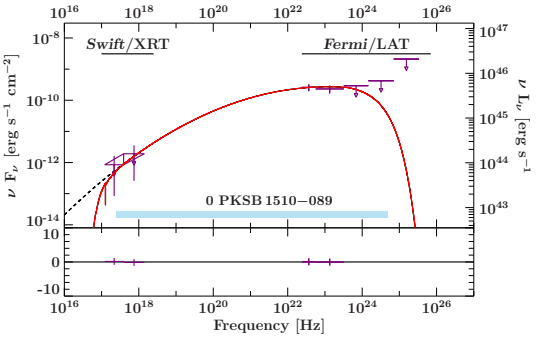

Figure B.30: Simultaneous spectral energy distribution of flare 30 from PKS 1510−089. Please refer to Fig. 5.2 for further details.

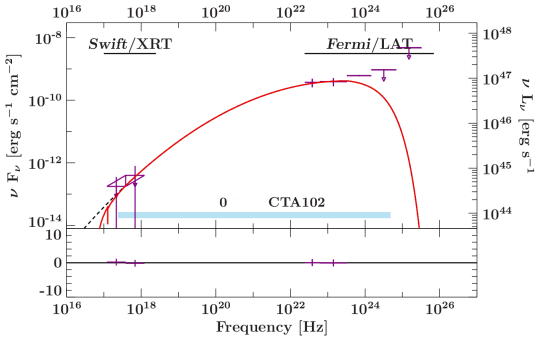

Figure B.31: Simultaneous spectral energy distribution of flare 31 from CTA 102. Please refer to Fig. 5.2 for further details.

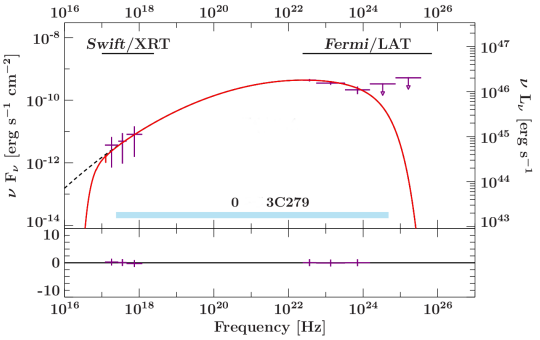

Figure B.32: Simultaneous spectral energy distribution of flare 32 from 3C 279. Please refer to Fig. 5.2 for further details.

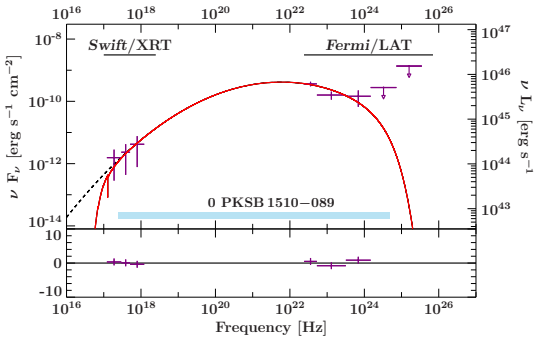

Figure B.33: Simultaneous spectral energy distribution of flare 33 from PKS 1510−089. Please refer to Fig. 5.2 for further details.

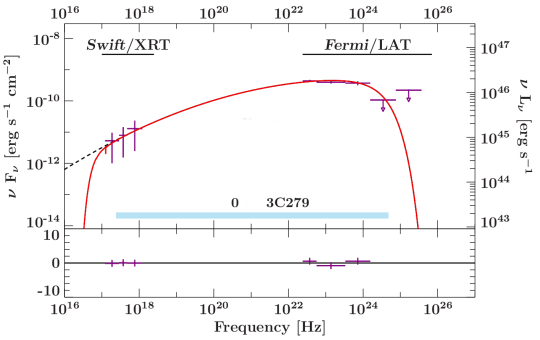

Figure B.34: Simultaneous spectral energy distribution of flare 34 from 3C 279. Please refer to Fig. 5.2 for further details.

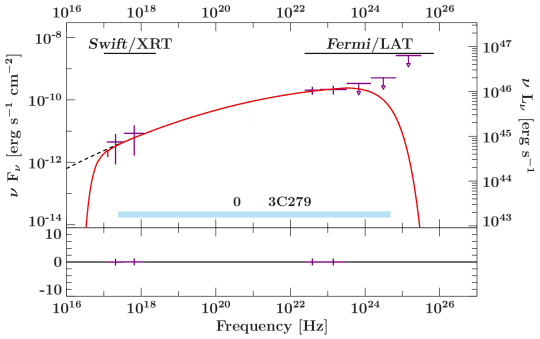

Figure B.35: Simultaneous spectral energy distribution of flare 35 from 3C 279. Please refer to Fig. 5.2 for further details.

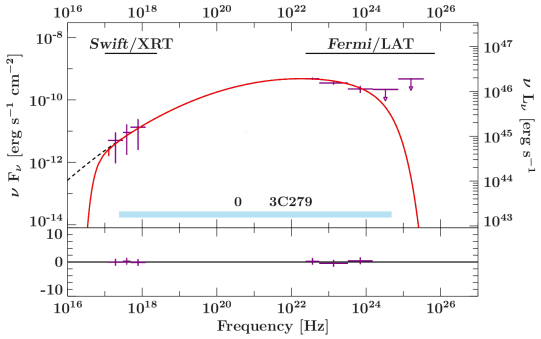

Figure B.36: Simultaneous spectral energy distribution of flare 36 from 3C 279. Please refer to Fig. 5.2 for further details.

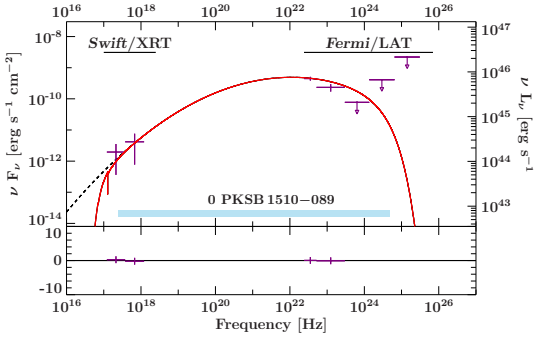

Figure B.37: Simultaneous spectral energy distribution of flare 37 from PKS 1510−089. Please refer to Fig. 5.2 for further details.

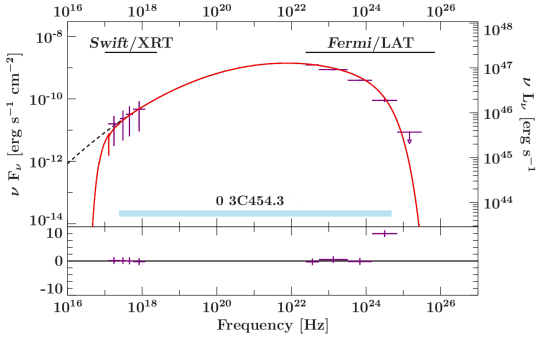

Figure B.38: Simultaneous spectral energy distribution of flare 38 from 3C 454.3. Please refer to Fig. 5.2 for further details.

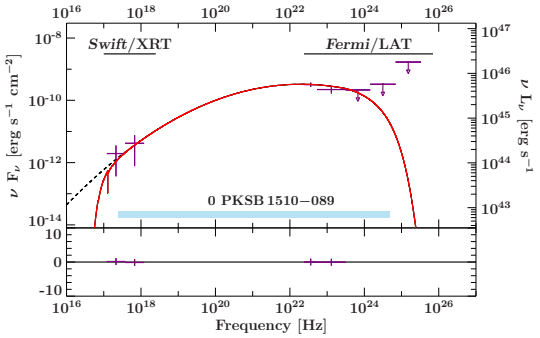

Figure B.39: Simultaneous spectral energy distribution of flare 39 from PKS 1510−089. Please refer to Fig. 5.2 for further details.

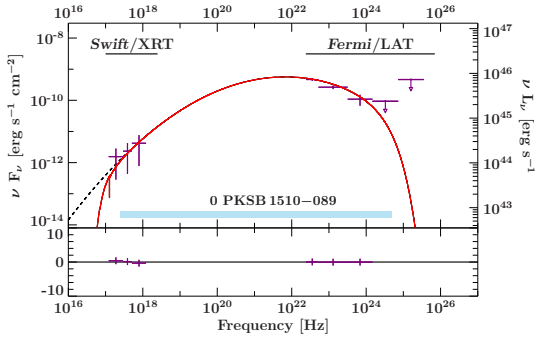

Figure B.40: Simultaneous spectral energy distribution of flare 40 from PKS 1510−089. Please refer to Fig. 5.2 for further details.

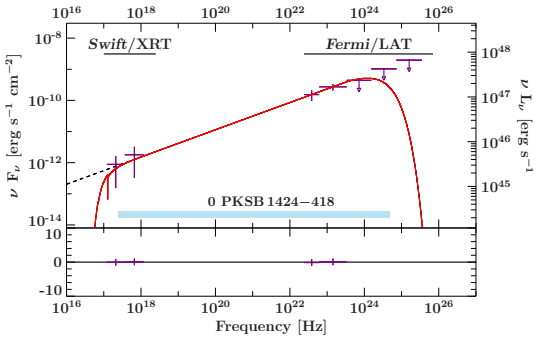

Figure B.41: Simultaneous spectral energy distribution of flare 41 from PKS 1424−418. Please refer to Fig. 5.2 for further details.

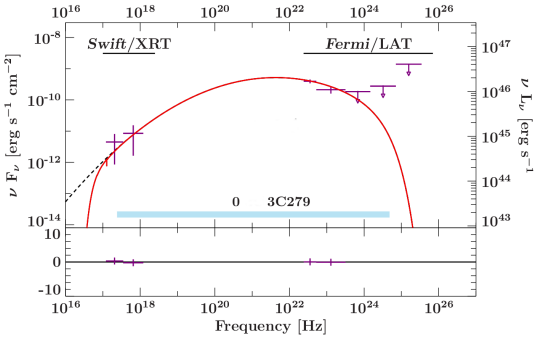

Figure B.42: Simultaneous spectral energy distribution of flare 42 from 3C 279. Please refer to Fig. 5.2 for further details.

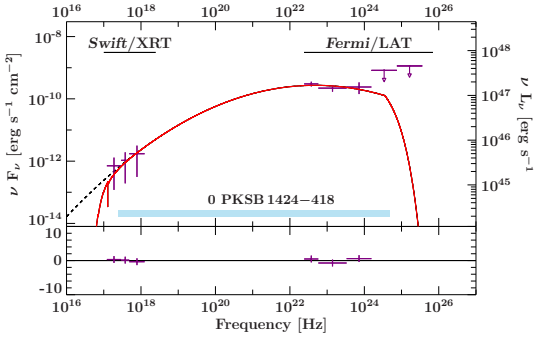

Figure B.43: Simultaneous spectral energy distribution of flare 43 from PKS 1424−418. Please refer to Fig. 5.2 for further details.

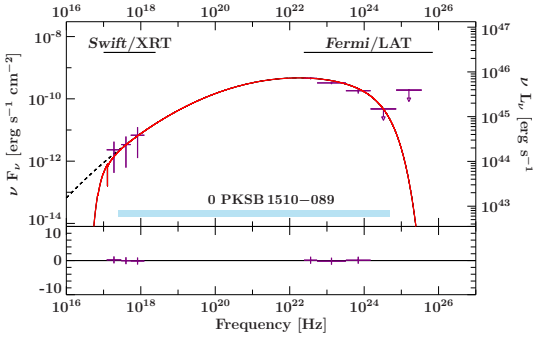

Figure B.44: Simultaneous spectral energy distribution of flare 44 from PKS 1510−089. Please refer to Fig. 5.2 for further details.

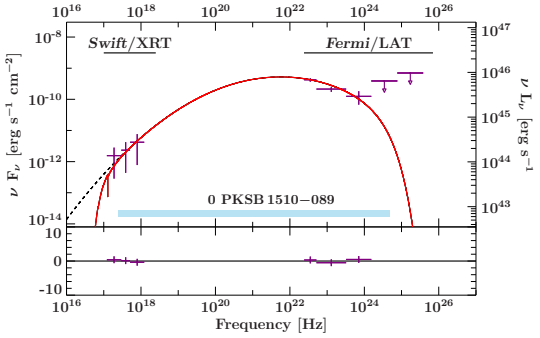

Figure B.45: Simultaneous spectral energy distribution of flare 45 from PKS 1510−089. Please refer to Fig. 5.2 for further details.

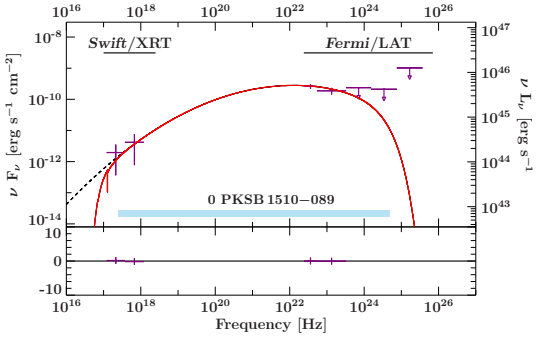

Figure B.46: Simultaneous spectral energy distribution of flare 46 from PKS 1510−089. Please refer to Fig. 5.2 for further details.

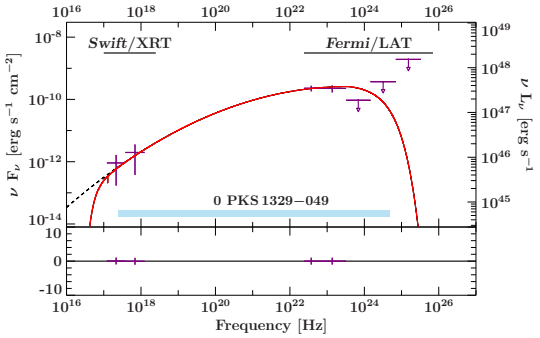

Figure B.47: Simultaneous spectral energy distribution of flare 47 from PKS 1329−049. Please refer to Fig. 5.2 for further details.

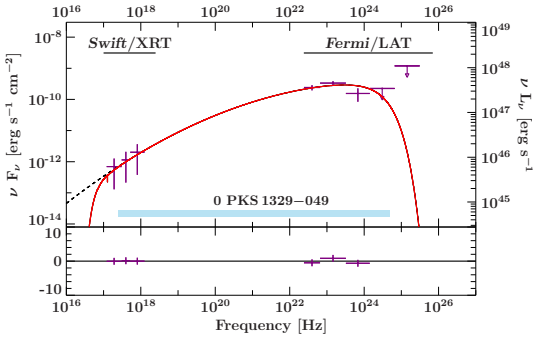

Figure B.48: Simultaneous spectral energy distribution of flare 48 from PKS 1329−049. Please refer to Fig. 5.2 for further details.

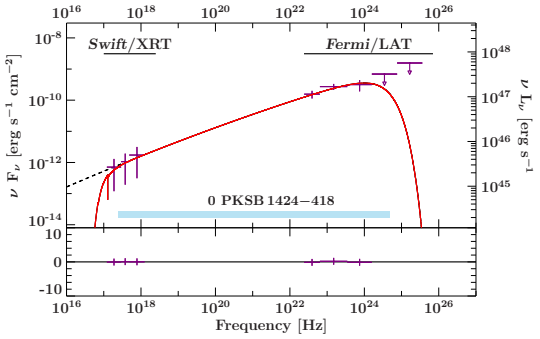

Figure B.49: Simultaneous spectral energy distribution of flare 49 from PKS 1424−418. Please refer to Fig. 5.2 for further details.

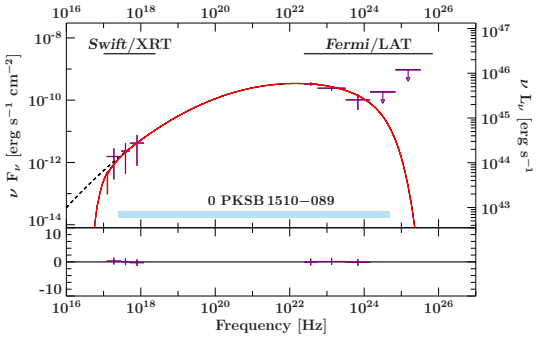

Figure B.50: Simultaneous spectral energy distribution of flare 50 from PKS 1510−089. Please refer to Fig. 5.2 for further details.

C Light Curves Used in Sec. 5.1.4

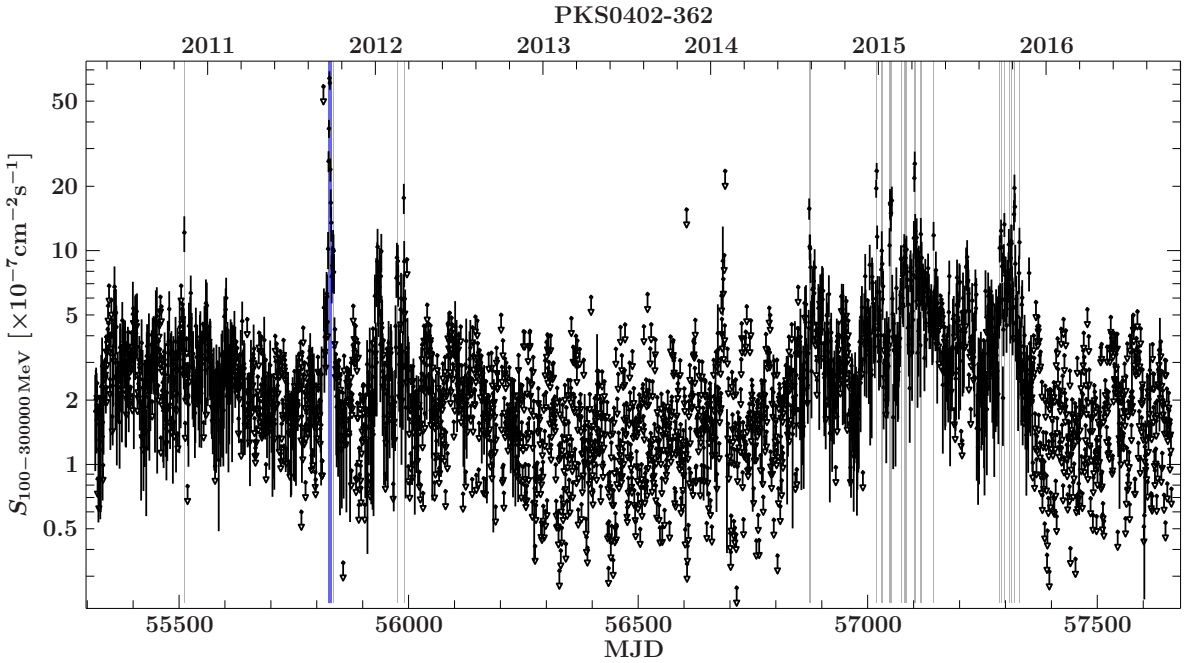

Figure C.1: *Fermi*/LAT γ-ray light curve for PKS 0402−362. Please refer to Fig. 5.7 for further details.

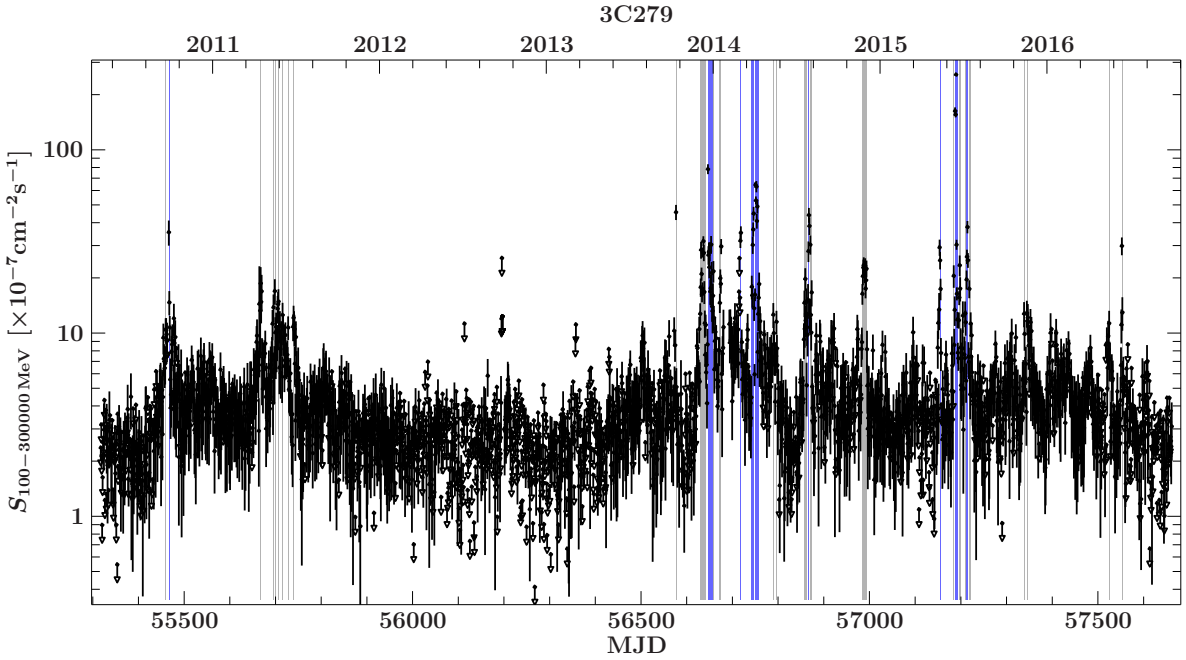

Figure C.2: *Fermi*/LAT γ-ray light curve for 3C 279. Please refer to Fig. 5.7 for further details.

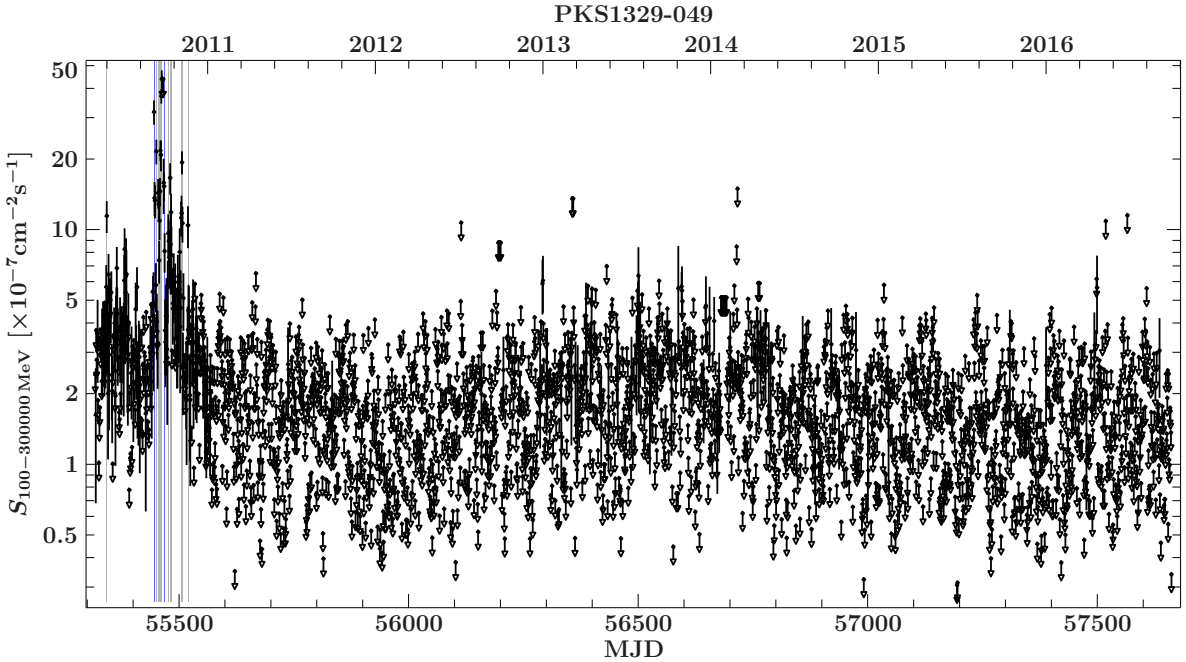

Figure C.3: *Fermi*/LAT γ-ray light curve for PKS 1329−049. Please refer to Fig. 5.7 for further details.

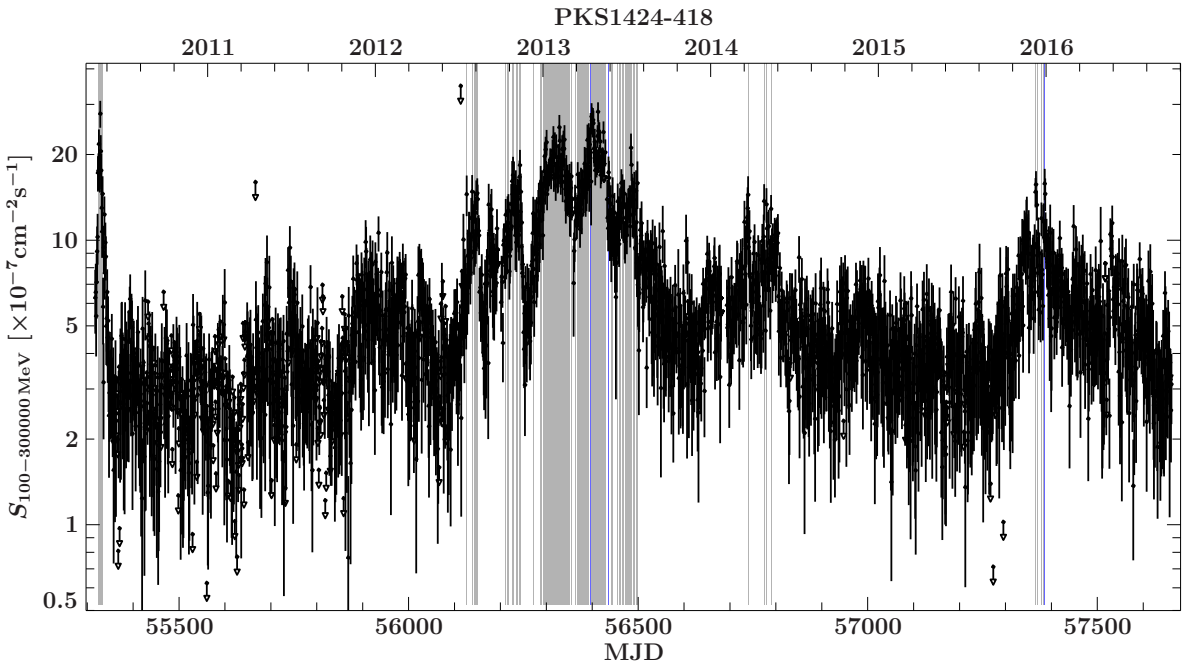

Figure C.4: *Fermi*/LAT γ-ray light curve for PKS 1424−418. Please refer to Fig. 5.7 for further details.

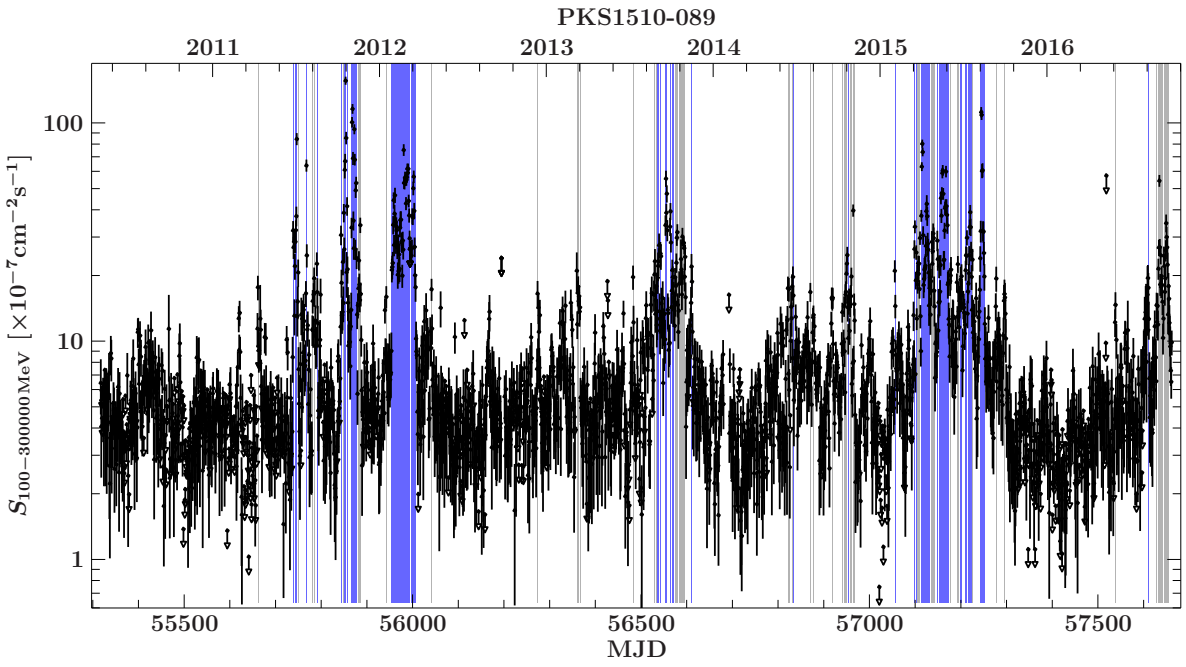

Figure C.5: *Fermi*/LAT γ-ray light curve for PKS 1510−089. Please refer to Fig. 5.7 for further details.

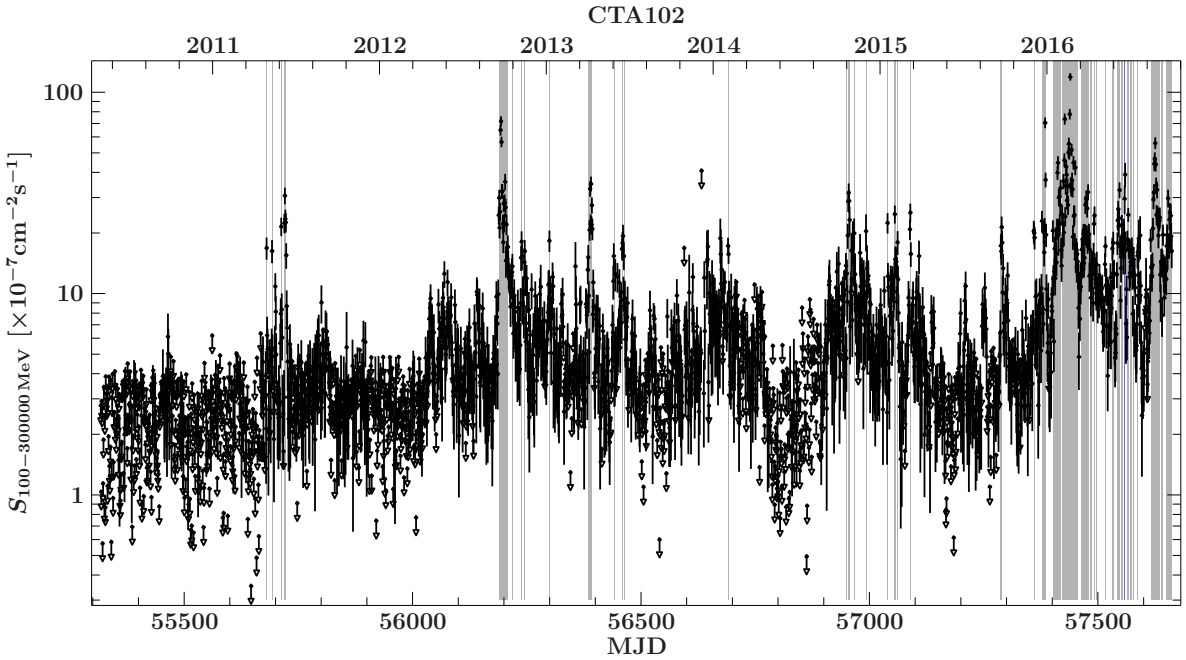

Figure C.6: *Fermi*/LAT γ-ray light curve for CTA 102. Please refer to Fig. 5.7 for further details.

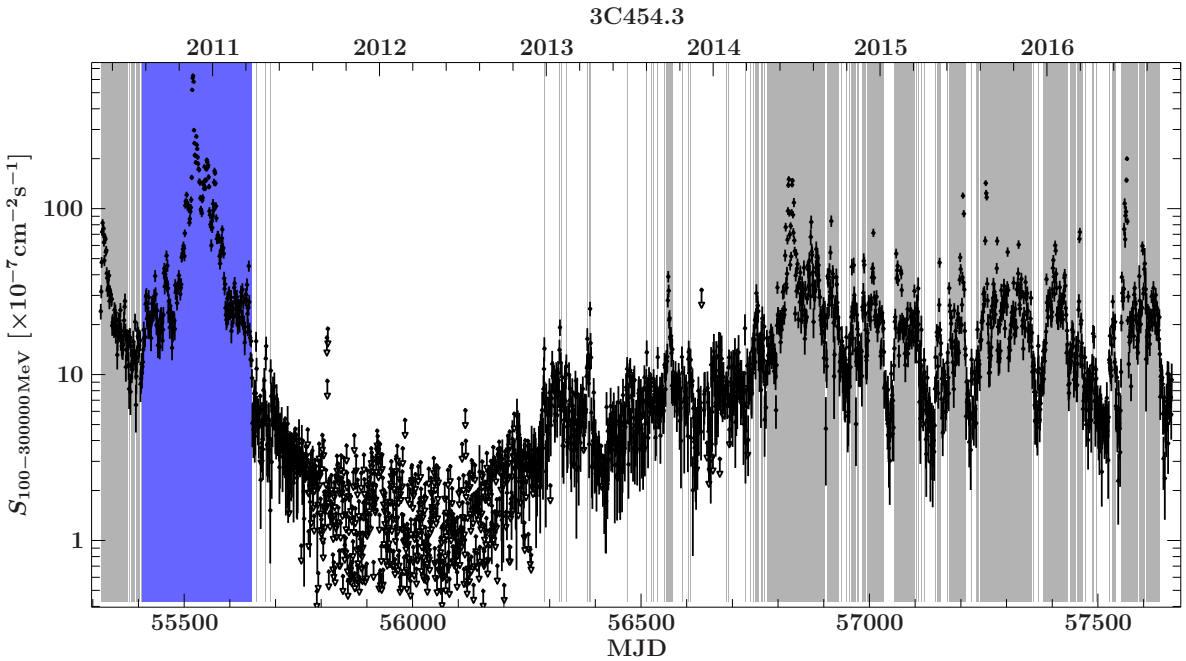

Figure C.7: *Fermi*/LAT γ-ray light curve for 3C 454.3. Please refer to Fig. 5.7 for further details.

D Sample of Blazars Considered in Sec. 5.2.4

Table 6: Full sample of blazars considered for the chance coincidence calculation in Sec. 5.2.4. This sample includes all blazars in the 3FGL and 3FHL catalogs. Not included are transient sources as well as new γ-ray sources from the recently published preliminary LAT eight year point source list (FL8Y). Sources are sorted by their averaged energy flux. TXS 0506+056 is printed in bold characters

Number	Source	Energy Flux [erg cm^{-2} s^{-1}]	Number	Source	Energy Flux [erg cm^{-2} s^{-1}]
1	3FGL J2232.5+1143	5.25×10^{-04}	39	3FGL J1248.2+5820	3.44×10^{-05}
2	3FGL J1104.4+3812	1.86×10^{-04}	40	3FGL J1725.0+1152	3.40×10^{-05}
3	3FGL J0319.8+4130	1.71×10^{-04}	41	3FGL J0457.0−2324	3.28×10^{-05}
4	3FGL J1555.7+1111	1.60×10^{-04}	42	3FGL J0136.5+3905	3.19×10^{-05}
5	3FGL J2000.0+6509	1.59×10^{-04}	43	3FGL J1037.5+5711	3.13×10^{-05}
6	3FGL J2158.8−3013	1.46×10^{-04}	44	3FGL J1517.6−2422	3.07×10^{-05}
7	3FGL J2254.0+1608	1.36×10^{-04}	45	3FGL J0738.1+1741	3.06×10^{-05}
8	3FGL J1217.8+3007	1.14×10^{-04}	46	3FGL J0051.2−6241	2.98×10^{-05}
9	3FGL J0449.4−4350	1.05×10^{-04}	47	3FGL J1823.6−3453	2.94×10^{-05}
10	3FGL J0428.6−3756	1.03×10^{-04}	48	3FGL J0115.8+2519	2.84×10^{-05}
11	3FGL J2202.7+4217	1.02×10^{-04}	49	3FGL J0144.6+2705	2.74×10^{-05}
12	3FGL J1256.1−0547	9.95×10^{-05}	50	3FGL J2116.1+3339	2.73×10^{-05}
13	3FGL J1048.4+7144	8.87×10^{-05}	51	3FGL J0526.2−4829	2.66×10^{-05}
14	3FGL J1427.9−4206	8.48×10^{-05}	52	3FGL J1159.5+2914	2.61×10^{-05}
15	3FGL J1427.0+2347	6.54×10^{-05}	53	3FGL J0338.5+1303	2.61×10^{-05}
16	3FGL J2244.1+4057	6.48×10^{-05}	54	3FGL J0809.8+5218	2.59×10^{-05}
17	3FGL J1512.8−0906	6.17×10^{-05}	55	3FGL J0035.9+5949	2.54×10^{-05}
18	3FGL J1504.4+1029	6.06×10^{-05}	56	3FGL J1120.8+4212	2.53×10^{-05}
19	**3FGL J0509.4+0541**	5.81×10^{-05}	57	3FGL J0607.4+4739	2.51×10^{-05}
20	3FGL J0222.6+4301	5.78×10^{-05}	58	3FGL J1312.5−2155	2.50×10^{-05}
21	3FGL J0630.9−2406	5.72×10^{-05}	59	3FGL J2253.1−1237	2.47×10^{-05}
22	3FGL J0650.7+2503	5.69×10^{-05}	60	3FGL J2347.0+5142	2.45×10^{-05}
23	3FGL J0521.7+2113	5.66×10^{-05}	61	3FGL J0920.9+4442	2.44×10^{-05}
24	3FGL J0108.7+0134	5.59×10^{-05}	62	3FGL J1610.8−6649	2.43×10^{-05}
25	3FGL J0237.9+2848	5.21×10^{-05}	63	3FGL J0033.6−1921	2.42×10^{-05}
26	3FGL J1221.3+3010	4.37×10^{-05}	64	3FGL J2243.9+2021	2.40×10^{-05}
27	3FGL J1653.9+3945	4.28×10^{-05}	65	3FGL J0221.1+3556	2.39×10^{-05}
28	3FGL J0721.9+7120	4.27×10^{-05}	66	3FGL J0811.3+0146	2.38×10^{-05}
29	3FGL J2012.0+4629	4.19×10^{-05}	67	3FGL J0730.2−1141	2.36×10^{-05}
30	3FGL J1603.9−4903	4.19×10^{-05}	68	3FGL J0339.5−0146	2.34×10^{-05}
31	3FGL J0238.6+1636	4.10×10^{-05}	69	3FGL J1243.1+3627	2.30×10^{-05}
32	3FGL J1015.0+4925	4.02×10^{-05}	70	3FGL J2236.3+2829	2.28×10^{-05}
33	3FGL J2139.4−4235	3.99×10^{-05}	71	3FGL J2015.6+3709	2.22×10^{-05}
34	3FGL J1751.5+0939	3.92×10^{-05}	72	3FGL J0303.4−2407	2.19×10^{-05}
35	3FGL J0957.6+5523	3.79×10^{-05}	73	3FGL J0112.1+2245	2.17×10^{-05}
36	3FGL J1454.5+5124	3.63×10^{-05}	74	3FGL J0050.6−0929	2.16×10^{-05}
37	3FGL J1542.9+6129	3.54×10^{-05}	75	3FGL J1838.8+4802	2.10×10^{-05}
38	3FGL J2025.6−0736	3.48×10^{-05}	76	3FGL J0510.0+1802	2.09×10^{-05}

Number	Source	Energy Flux [erg cm^{-2} s^{-1}]	Number	Source	Energy Flux [erg cm^{-2} s^{-1}]
77	3FGL J0700.6−6610	2.06×10^{-05}	142	3FGL J0543.9−5531	1.23×10^{-05}
78	3FGL J0854.8+2006	2.06×10^{-05}	143	3FGL J1540.1+8155	1.22×10^{-05}
79	3FGL J0622.4−2606	2.04×10^{-05}	144	3FGL J0841.3−3554	1.22×10^{-05}
80	3FGL J0211.2+1051	1.98×10^{-05}	145	3FGL J0915.8+2933	1.21×10^{-05}
81	3FGL J0120.4−2700	1.97×10^{-05}	146	3FGL J0746.6−4756	1.21×10^{-05}
82	3FGL J0538.8−4405	1.96×10^{-05}	147	3FGL J0159.4+1046	1.21×10^{-05}
83	3FGL J0113.4+4948	1.93×10^{-05}	148	3FGL J1150.5+4155	1.21×10^{-05}
84	3FGL J1230.3+2519	1.93×10^{-05}	149	3FGL J1844.3+1547	1.21×10^{-05}
85	3FGL J1931.1+0937	1.92×10^{-05}	150	3FGL J1023.9−4335	1.20×10^{-05}
86	3FGL J2009.3−4849	1.89×10^{-05}	151	3FGL J1744.9−1725	1.19×10^{-05}
87	3FGL J1942.7+1033	1.87×10^{-05}	152	3FGL J1958.2−3011	1.17×10^{-05}
88	3FGL J1903.2+5541	1.86×10^{-05}	153	3FGL J0754.8+4824	1.17×10^{-05}
89	3FGL J1748.6+7005	1.84×10^{-05}	154	3FGL J1754.1+3212	1.15×10^{-05}
90	3FGL J0612.8+4122	1.83×10^{-05}	155	3FGL J1553.3−2421	1.14×10^{-05}
91	3FGL J0210.7−5101	1.82×10^{-05}	156	3FGL J1806.7+6949	1.13×10^{-05}
92	3FGL J2143.5+1744	1.82×10^{-05}	157	3FGL J1933.4+0727	1.11×10^{-05}
93	3FGL J2146.6−1344	1.82×10^{-05}	158	3FGL J1058.6+5627	1.11×10^{-05}
94	3FGL J1917.7−1921	1.81×10^{-05}	159	3FGL J0112.8+3207	1.11×10^{-05}
95	3FGL J0131.2+6120	1.81×10^{-05}	160	3FGL J0811.2−7529	1.11×10^{-05}
96	3FGL J1444.0−3907	1.81×10^{-05}	161	3FHL J1115.0−6117	1.10×10^{-05}
97	3FGL J0423.8+4150	1.76×10^{-05}	162	3FGL J1221.4+2814	1.09×10^{-05}
98	3FHL J1944.9−2143	1.76×10^{-05}	163	3FGL J0909.8−0229	1.09×10^{-05}
99	3FGL J1033.8+6051	1.68×10^{-05}	164	3FGL J1440.4−3845	1.08×10^{-05}
100	3FGL J0209.4−5229	1.68×10^{-05}	165	3FGL J2234.1−2655	1.08×10^{-05}
101	3FGL J1734.3+3858	1.66×10^{-05}	166	3FGL J1428.5+4240	1.07×10^{-05}
102	3FGL J0921.8+6215	1.66×10^{-05}	167	3FGL J1325.4−4301	1.06×10^{-05}
103	3FGL J0825.9−2230	1.65×10^{-05}	168	3FGL J0009.3+5030	1.06×10^{-05}
104	3FGL J0508.0+6736	1.65×10^{-05}	169	3FGL J1635.2+3809	1.05×10^{-05}
105	3FGL J1031.2+5053	1.63×10^{-05}	170	3FGL J1659.7−3132	1.05×10^{-05}
106	3FGL J0334.3−3726	1.62×10^{-05}	171	3FGL J0506.9−5435	1.04×10^{-05}
107	3FGL J1058.5+0133	1.61×10^{-05}	172	3FGL J2323.5−0315	1.04×10^{-05}
108	3FGL J2115.4+2933	1.59×10^{-05}	173	3FGL J1733.0−1305	1.04×10^{-05}
109	3FGL J1553.5−3118	1.56×10^{-05}	174	3FGL J1617.7−7717	1.03×10^{-05}
110	3FGL J0348.6−2748	1.56×10^{-05}	175	3FGL J0845.1−5458	1.01×10^{-05}
111	3FGL J0505.3+0459	1.54×10^{-05}	176	3FGL J0852.6−5756	1.01×10^{-05}
112	3FGL J0818.2+4223	1.52×10^{-05}	177	3FGL J1345.6+4453	1.01×10^{-05}
113	3FGL J2345.2−1554	1.51×10^{-05}	178	3FGL J2227.8+0040	1.00×10^{-05}
114	3FGL J0856.7−1105	1.51×10^{-05}	179	3FHL J1943.9+2117	9.98×10^{-06}
115	3FGL J0102.8+5825	1.50×10^{-05}	180	3FGL J0533.2+4822	9.98×10^{-06}
116	3FGL J0953.0−0839	1.47×10^{-05}	181	3FGL J1328.9−5607	9.86×10^{-06}
117	3FGL J1833.6−2103	1.47×10^{-05}	182	3FGL J0333.9+6538	9.82×10^{-06}
118	3FGL J2005.2+7752	1.45×10^{-05}	183	3FGL J0803.3−0339	9.82×10^{-06}
119	3FGL J0453.2+6321	1.45×10^{-05}	184	3FGL J2324.7−4040	9.80×10^{-06}
120	3FHL J1747.2−2822	1.45×10^{-05}	185	3FGL J0216.6−1019	9.67×10^{-06}
121	3FGL J1926.8+6154	1.44×10^{-05}	186	3FGL J0817.8−0935	9.66×10^{-06}
122	3FGL J0501.2−0157	1.43×10^{-05}	187	3FGL J0958.6+6534	9.66×10^{-06}
123	3FGL J1218.4−0121	1.43×10^{-05}	188	3FGL J1418.4−0233	9.60×10^{-06}
124	3FGL J0718.7−4319	1.41×10^{-05}	189	3FGL J0725.8−0054	9.59×10^{-06}
125	3FGL J1941.2−6210	1.39×10^{-05}	190	3FGL J0333.6+2916	9.49×10^{-06}
126	3FGL J0322.0+2335	1.39×10^{-05}	191	3FGL J1921.9−1607	9.47×10^{-06}
127	3FGL J1353.5−6640	1.38×10^{-05}	192	3FGL J2329.2+3754	9.33×10^{-06}
128	3FGL J1448.0+3608	1.36×10^{-05}	193	3FGL J1059.2−1133	9.28×10^{-06}
129	3FGL J0043.8+3425	1.35×10^{-05}	194	3FGL J0103.4+5336	9.26×10^{-06}
130	3FGL J1800.5+7827	1.33×10^{-05}	195	3FGL J2340.7+8016	9.21×10^{-06}
131	3FGL J0904.8−5734	1.32×10^{-05}	196	3FGL J0110.2+6806	9.17×10^{-06}
132	3FGL J1132.7+0034	1.31×10^{-05}	197	3FGL J0316.2−6436	9.13×10^{-06}
133	3FGL J1558.9−6432	1.30×10^{-05}	198	3FGL J1506.6+0811	8.97×10^{-06}
134	3FGL J2056.7+4938	1.27×10^{-05}	199	3FGL J1511.8−0513	8.94×10^{-06}
135	3FGL J1253.2+5300	1.27×10^{-05}	200	3FGL J0805.4+7534	8.90×10^{-06}
136	3FGL J1230.9+1224	1.26×10^{-05}	201	3FGL J0022.5+0608	8.90×10^{-06}
137	3FGL J1258.7−2219	1.26×10^{-05}	202	3FGL J0522.9−3628	8.90×10^{-06}
138	3FGL J2323.9+4211	1.25×10^{-05}	203	3FGL J0316.1+0904	8.86×10^{-06}
139	3FGL J0141.4−0929	1.25×10^{-05}	204	3FGL J2112.5−3044	8.83×10^{-06}
140	3FGL J1304.3−4353	1.25×10^{-05}	205	3FGL J0532.7+0732	8.83×10^{-06}
141	3FGL J1332.6−1256	1.24×10^{-05}	206	3FGL J0303.6+4716	8.81×10^{-06}

Number	Source	Energy Flux [erg cm^{-2} s^{-1}]	Number	Source	Energy Flux [erg cm^{-2} s^{-1}]
207	3FGL J0008.0+4713	8.80×10^{-06}	270	3FGL J0609.4−0248	7.10×10^{-06}
208	3FGL J1824.2+5649	8.80×10^{-06}	271	3FGL J0326.2+0225	7.08×10^{-06}
209	3FGL J1532.7−1319	8.79×10^{-06}	272	3FGL J1303.0+2435	7.04×10^{-06}
210	3FGL J1642.9+3950	8.70×10^{-06}	273	3FGL J0154.0+0824	7.03×10^{-06}
211	3FGL J0905.5+1358	8.70×10^{-06}	274	3FGL J0244.8−5818	7.02×10^{-06}
212	3FGL J2024.6+0309	8.60×10^{-06}	275	3FGL J1547.1−2801	7.02×10^{-06}
213	3FGL J1653.6−0158	8.60×10^{-06}	276	3FGL J0754.4−1148	7.01×10^{-06}
214	3FGL J0910.5+3329	8.57×10^{-06}	277	3FGL J0847.1+1134	6.99×10^{-06}
215	3FGL J0248.4+5130	8.54×10^{-06}	278	3FGL J0553.5−2036	6.99×10^{-06}
216	3FGL J2348.0−1630	8.53×10^{-06}	279	3FGL J0902.4+2050	6.98×10^{-06}
217	3FGL J1959.8−4725	8.45×10^{-06}	280	3FGL J1607.0+1551	6.97×10^{-06}
218	3FGL J1136.6+7009	8.41×10^{-06}	281	3FGL J1549.7−0658	6.95×10^{-06}
219	3FGL J0912.9−2104	8.40×10^{-06}	282	3FGL J2016.4−0905	6.93×10^{-06}
220	3FGL J1625.1−0021	8.39×10^{-06}	283	3FGL J2206.9−0031	6.89×10^{-06}
221	3FGL J1443.9+2502	8.38×10^{-06}	284	3FGL J2039.5+5217	6.88×10^{-06}
222	3FGL J0809.5+5342	8.36×10^{-06}	285	3FGL J0227.2+0201	6.88×10^{-06}
223	3FGL J1657.7+4807	8.36×10^{-06}	286	3FGL J1712.6+2932	6.85×10^{-06}
224	3FGL J0137.8+5813	8.35×10^{-06}	287	3FGL J0433.6+2905	6.85×10^{-06}
225	3FGL J0814.7+6428	8.27×10^{-06}	288	3FGL J0434.6+0921	6.85×10^{-06}
226	3FGL J0100.2+0745	8.24×10^{-06}	289	3FGL J2357.4−1716	6.81×10^{-06}
227	3FGL J1918.2−4110	8.21×10^{-06}	290	3FGL J1427.6−3305	6.79×10^{-06}
228	3FGL J0238.4−3117	8.20×10^{-06}	291	3FGL J0739.4+0137	6.79×10^{-06}
229	3FGL J1522.1+3144	8.15×10^{-06}	292	3FGL J1229.1+0202	6.78×10^{-06}
230	3FGL J1103.9−5357	8.13×10^{-06}	293	3FGL J0203.6+3043	6.78×10^{-06}
231	3FGL J1312.8−0424	8.09×10^{-06}	294	3FGL J0205.0+1510	6.78×10^{-06}
232	3FGL J1518.0−2732	8.04×10^{-06}	295	3FGL J1258.1+3233	6.77×10^{-06}
233	3FGL J2258.0−2759	8.00×10^{-06}	296	3FGL J0846.9−2336	6.77×10^{-06}
234	3FGL J0132.6−1655	7.97×10^{-06}	297	3FHL J1427.9−6054	6.77×10^{-06}
235	3FGL J0831.9+0430	7.93×10^{-06}	298	3FGL J0648.8−1740	6.73×10^{-06}
236	3FGL J2022.5+7612	7.93×10^{-06}	299	3FGL J2023.2+3154	6.71×10^{-06}
237	3FGL J2121.0+1901	7.87×10^{-06}	300	3FGL J1650.2−5044	6.68×10^{-06}
238	3FGL J1649.4+5238	7.86×10^{-06}	301	3FGL J0816.4−1311	6.67×10^{-06}
239	3FGL J1147.0−3811	7.85×10^{-06}	302	3FGL J2001.1+4352	6.65×10^{-06}
240	3FGL J1146.8+3958	7.84×10^{-06}	303	3FGL J0118.8−2142	6.63×10^{-06}
241	3FGL J0525.6−6013	7.81×10^{-06}	304	3FGL J1419.5−0836	6.63×10^{-06}
242	3FGL J2103.9−6233	7.73×10^{-06}	305	3FGL J2311.0+3425	6.63×10^{-06}
243	3FGL J1624.2−4041	7.70×10^{-06}	306	3FGL J1731.8−3001	6.63×10^{-06}
244	3FGL J1445.0−0328	7.69×10^{-06}	307	3FGL J1728.3+5013	6.63×10^{-06}
245	3FGL J1307.6−4300	7.64×10^{-06}	308	3FGL J2144.2+3132	6.61×10^{-06}
246	3FGL J1314.8+2349	7.59×10^{-06}	309	3FGL J0429.8+2843	6.61×10^{-06}
247	3FGL J0947.1−2542	7.59×10^{-06}	310	3FGL J0217.2+0837	6.60×10^{-06}
248	3FGL J2030.5−1439	7.52×10^{-06}	311	3FGL J0238.3−3904	6.59×10^{-06}
249	3FGL J1630.7+5222	7.51×10^{-06}	312	3FGL J0314.3−5103	6.58×10^{-06}
250	3FGL J0206.4−1150	7.49×10^{-06}	313	3FGL J0312.7+3613	6.51×10^{-06}
251	3FGL J2250.7−2806	7.45×10^{-06}	314	3FGL J2304.6+3704	6.50×10^{-06}
252	3FGL J2141.6−6412	7.45×10^{-06}	315	3FGL J0048.0+3950	6.49×10^{-06}
253	3FGL J0049.7+0237	7.42×10^{-06}	316	3FGL J0134.5+2638	6.48×10^{-06}
254	3FGL J0318.7+2134	7.42×10^{-06}	317	3FGL J0056.3−0935	6.45×10^{-06}
255	3FGL J0115.7+0356	7.40×10^{-06}	318	3FGL J2322.9−4917	6.35×10^{-06}
256	3FGL J0753.1+5353	7.39×10^{-06}	319	3FGL J1831.0−2714	6.35×10^{-06}
257	3FGL J0143.7−5845	7.38×10^{-06}	320	3FGL J1517.6+6524	6.34×10^{-06}
258	3FGL J0308.6+0408	7.37×10^{-06}	321	3FGL J0608.0−0835	6.27×10^{-06}
259	3FGL J1117.9+5355	7.35×10^{-06}	322	3FGL J0515.8+1526	6.26×10^{-06}
260	3FGL J2001.0−1750	7.29×10^{-06}	323	3FGL J0258.9+0552	6.25×10^{-06}
261	3FGL J0038.0−2501	7.27×10^{-06}	324	3FGL J1253.7+0327	6.24×10^{-06}
262	3FGL J0602.8−4016	7.22×10^{-06}	325	3FGL J2004.8+7003	6.23×10^{-06}
263	3FGL J1911.2−2006	7.20×10^{-06}	326	3FGL J0448.6−1632	6.22×10^{-06}
264	3FGL J2236.5−1432	7.13×10^{-06}	327	3FGL J1136.6+6736	6.22×10^{-06}
265	3FGL J0420.6−3742	7.12×10^{-06}	328	3FGL J1119.9−2204	6.20×10^{-06}
266	3FGL J0001.2−0748	7.11×10^{-06}	329	3FGL J1744.1−7619	6.20×10^{-06}
267	3FGL J0843.9+5311	7.11×10^{-06}	330	3FGL J1512.2+0202	6.20×10^{-06}
268	3FGL J0853.0−3654	7.11×10^{-06}	331	3FGL J0039.0−2218	6.19×10^{-06}
269	3FGL J1035.7−6720	7.10×10^{-06}	332	3FHL J0739.7−6720	6.18×10^{-06}

Number	Source	Energy Flux [erg cm^{-2} s^{-1}]	Number	Source	Energy Flux [erg cm^{-2} s^{-1}]
333	3FGL J1249.5−0546	6.16×10^{-06}	396	3FGL J0430.1−3103	5.31×10^{-06}
334	3FGL J1503.7−1540	6.16×10^{-06}	397	3FGL J1012.2+0631	5.30×10^{-06}
335	3FHL J1033.7+3707	6.16×10^{-06}	398	3FHL J1442.5−4621	5.28×10^{-06}
336	3FGL J0259.5+0746	6.14×10^{-06}	399	3FGL J2031.0+1937	5.28×10^{-06}
337	3FGL J2346.7+0705	6.14×10^{-06}	400	3FGL J1018.4−3119	5.28×10^{-06}
338	3FGL J1539.2−3324	6.13×10^{-06}	401	3FGL J1637.6−3449	5.28×10^{-06}
339	3FGL J2039.0−1047	6.13×10^{-06}	402	3FGL J2321.9+3204	5.26×10^{-06}
340	3FGL J1745.4−0754	6.10×10^{-06}	403	3FGL J0449.0+1121	5.21×10^{-06}
341	3FGL J0909.6+0157	6.10×10^{-06}	404	3FGL J0334.3−4008	5.16×10^{-06}
342	3FGL J1032.7+3735	6.08×10^{-06}	405	3FGL J2018.5+3851	5.15×10^{-06}
343	3FGL J0340.5−2119	6.07×10^{-06}	406	3FGL J0850.2−1214	5.14×10^{-06}
344	3FGL J0440.8+2751	6.06×10^{-06}	407	3FGL J1917.1−3024	5.13×10^{-06}
345	3FGL J1813.6+3143	6.05×10^{-06}	408	3FGL J2229.7−0833	5.13×10^{-06}
346	3FGL J1204.3−0708	5.97×10^{-06}	409	3FGL J0529.1+0933	5.12×10^{-06}
347	3FGL J2035.8+4902	5.93×10^{-06}	410	3FGL J1305.4−4926	5.12×10^{-06}
348	3FGL J0946.5+1017	5.93×10^{-06}	411	3FGL J2343.7+3437	5.11×10^{-06}
349	3FGL J1346.6−6027	5.90×10^{-06}	412	3FGL J0133.2−5159	5.09×10^{-06}
350	3FGL J2109.1−6638	5.88×10^{-06}	413	3FGL J2314.0+1443	5.08×10^{-06}
351	3FGL J0620.4+2644	5.87×10^{-06}	414	3FGL J0617.6−1717	5.08×10^{-06}
352	3FGL J1314.7−4237	5.87×10^{-06}	415	3FGL J0307.3+4916	5.08×10^{-06}
353	3FHL J1109.4−6115e	5.87×10^{-06}	416	3FGL J0627.0−3529	5.07×10^{-06}
354	3FGL J1703.6−6211	5.87×10^{-06}	417	3FGL J1522.6−2730	5.07×10^{-06}
355	3FGL J0330.6+0437	5.86×10^{-06}	418	3FGL J1912.6−1223	5.06×10^{-06}
356	3FGL J1954.9−5640	5.86×10^{-06}	419	3FGL J2200.2+2139	5.06×10^{-06}
357	3FGL J1514.5−4750	5.85×10^{-06}	420	3FGL J1424.9+3615	5.02×10^{-06}
358	3FGL J1033.4−5035	5.84×10^{-06}	421	3FGL J0725.2+1425	4.98×10^{-06}
359	3FGL J0617.2+5701	5.82×10^{-06}	422	3FGL J1024.8+0105	4.94×10^{-06}
360	3FGL J1656.8−2010	5.82×10^{-06}	423	3FGL J0904.9+2739	4.93×10^{-06}
361	3FGL J0515.3−4557	5.81×10^{-06}	424	3FGL J2250.1+3825	4.92×10^{-06}
362	3FGL J0014.7+5802	5.81×10^{-06}	425	3FGL J1704.0+7646	4.91×10^{-06}
363	3FGL J1702.8−5656	5.80×10^{-06}	426	3FGL J1058.1+7010	4.91×10^{-06}
364	3FGL J1233.9−5736	5.78×10^{-06}	427	3FGL J1231.7+2847	4.87×10^{-06}
365	3FGL J0757.0+0956	5.78×10^{-06}	428	3FGL J1945.9−3115	4.87×10^{-06}
366	3FGL J1801.5+4403	5.77×10^{-06}	429	3FGL J0252.8−2218	4.86×10^{-06}
367	3FGL J0056.3−2116	5.74×10^{-06}	430	3FGL J0332.0+6308	4.85×10^{-06}
368	3FGL J1232.5−3720	5.70×10^{-06}	431	3FGL J0224.4+1615	4.84×10^{-06}
369	3FGL J0424.7+0035	5.68×10^{-06}	432	3FGL J0512.9+4038	4.84×10^{-06}
370	3FGL J2321.6−1619	5.67×10^{-06}	433	3FGL J2358.6−1809	4.83×10^{-06}
371	3FGL J0849.3+0458	5.66×10^{-06}	434	3FGL J1251.0−0203	4.82×10^{-06}
372	3FHL J0338.9−2848	5.63×10^{-06}	435	3FGL J1256.3−1146	4.79×10^{-06}
373	3FGL J2259.9−1553	5.61×10^{-06}	436	3FGL J2104.2−0211	4.78×10^{-06}
374	3FGL J0243.5+7119	5.61×10^{-06}	437	3FGL J0256.3+0335	4.78×10^{-06}
375	3FGL J2247.8+4413	5.59×10^{-06}	438	3FGL J1239.1−1158	4.77×10^{-06}
376	3FGL J0058.0−3233	5.58×10^{-06}	439	3FGL J1500.9+2238	4.76×10^{-06}
377	3FGL J1312.7−2349	5.58×10^{-06}	440	3FGL J0205.2−1700	4.73×10^{-06}
378	3FGL J2246.2+1547	5.56×10^{-06}	441	3FGL J0035.2+1513	4.72×10^{-06}
379	3FGL J0116.3−6153	5.55×10^{-06}	442	3FGL J1648.0+4230	4.72×10^{-06}
380	3FGL J1741.9−2539	5.52×10^{-06}	443	3FGL J0712.6+5033	4.70×10^{-06}
381	3FGL J1532.0+3018	5.51×10^{-06}	444	3FGL J1006.7−2159	4.70×10^{-06}
382	3FGL J0023.5+4454	5.50×10^{-06}	445	3FGL J1323.0+2942	4.70×10^{-06}
383	3FHL J1212.1−2328	5.50×10^{-06}	446	3FGL J1026.9−1750	4.69×10^{-06}
384	3FGL J2243.4−2541	5.49×10^{-06}	447	3FHL J0600.3+1245	4.69×10^{-06}
385	3FGL J1649.6−3007	5.47×10^{-06}	448	3FGL J1630.8+1047	4.68×10^{-06}
386	3FGL J1309.3+4304	5.45×10^{-06}	449	3FGL J0719.3+3307	4.66×10^{-06}
387	3FGL J1548.4+1455	5.43×10^{-06}	450	3FGL J2251.9+4031	4.66×10^{-06}
388	3FGL J2156.0+1818	5.42×10^{-06}	451	3FGL J1651.6+7219	4.65×10^{-06}
389	3FGL J2039.6−5618	5.41×10^{-06}	452	3FGL J1819.1+2134	4.65×10^{-06}
390	3FGL J1351.4+1115	5.40×10^{-06}	453	3FGL J0407.1−3825	4.64×10^{-06}
391	3FGL J0826.0+0307	5.39×10^{-06}	454	3FGL J1107.8+1502	4.62×10^{-06}
392	3FGL J1359.9−3746	5.39×10^{-06}	455	3FGL J0602.2+5314	4.62×10^{-06}
393	3FGL J0212.1+5320	5.37×10^{-06}	456	3FGL J2309.0+5428	4.62×10^{-06}
394	3FGL J0001.4+2120	5.34×10^{-06}	457	3FGL J0629.0−6248	4.61×10^{-06}
395	3FGL J2022.2−4515	5.33×10^{-06}	458	3FGL J2212.0+2355	4.59×10^{-06}

Number	Source	Energy Flux [erg cm^{-2} s^{-1}]	Number	Source	Energy Flux [erg cm^{-2} s^{-1}]
459	3FGL J0706.5+3744	4.59×10^{-06}	522	3FGL J1417.8+2540	4.08×10^{-06}
460	3FGL J0319.8+1847	4.59×10^{-06}	523	3FGL J0114.8+1326	4.07×10^{-06}
461	3FGL J1124.9+4932	4.57×10^{-06}	524	3FGL J2255.1+2411	4.06×10^{-06}
462	3FGL J2130.8−2745	4.57×10^{-06}	525	3FGL J2213.1−2532	4.06×10^{-06}
463	3FGL J0422.1−0642	4.57×10^{-06}	526	3FGL J1348.5−7150	4.05×10^{-06}
464	3FGL J0002.2−4152	4.56×10^{-06}	527	3FGL J0503.4+4522	4.04×10^{-06}
465	3FGL J1704.4−0528	4.56×10^{-06}	528	3FHL J0411.0+4217	4.04×10^{-06}
466	3FGL J0936.3−2114	4.55×10^{-06}	529	3FGL J0702.7−1952	4.02×10^{-06}
467	3FGL J1246.7−2547	4.54×10^{-06}	530	3FGL J0442.6−0017	4.01×10^{-06}
468	3FGL J0509.3+1012	4.53×10^{-06}	531	3FGL J1946.4−5403	4.01×10^{-06}
469	3FHL J1848.5+3243	4.53×10^{-06}	532	3FGL J0336.1+7500	4.00×10^{-06}
470	3FGL J1604.6+5714	4.52×10^{-06}	533	3FGL J0425.2+6319	4.00×10^{-06}
471	3FGL J1404.8+6554	4.51×10^{-06}	534	3FGL J0929.4+5013	4.00×10^{-06}
472	3FGL J0550.6−3217	4.51×10^{-06}	535	3FGL J0601.0+3837	4.00×10^{-06}
473	3FGL J1936.9−4719	4.50×10^{-06}	536	3FGL J1410.4+2821	3.99×10^{-06}
474	3FGL J0528.3+1815	4.49×10^{-06}	537	3FGL J1042.0−0557	3.99×10^{-06}
475	3FGL J1354.5+3705	4.49×10^{-06}	538	3FGL J1054.5+2210	3.99×10^{-06}
476	3FGL J1233.7−0145	4.48×10^{-06}	539	3FGL J0316.1−2611	3.99×10^{-06}
477	3FGL J1141.6−1406	4.47×10^{-06}	540	3FGL J1406.0−2508	3.98×10^{-06}
478	3FGL J1151.4+5858	4.44×10^{-06}	541	3FGL J1718.1−3056	3.98×10^{-06}
479	3FGL J0505.9+6114	4.44×10^{-06}	542	3FGL J1016.6−4244	3.98×10^{-06}
480	3FGL J1351.8−1524	4.44×10^{-06}	543	3FGL J0648.8+1516	3.98×10^{-06}
481	3FGL J1559.7+8512	4.42×10^{-06}	544	3FGL J0516.7−6207	3.98×10^{-06}
482	3FGL J2108.0+3654	4.42×10^{-06}	545	3FGL J1406.6+1644	3.97×10^{-06}
483	3FGL J1845.5−2524	4.41×10^{-06}	546	3FGL J0829.3+0901	3.96×10^{-06}
484	3FGL J2325.2+3957	4.39×10^{-06}	547	3FGL J1316.0−3338	3.95×10^{-06}
485	3FGL J0747.2−3311	4.38×10^{-06}	548	3FGL J0629.4−1959	3.95×10^{-06}
486	3FGL J0650.5+2055	4.38×10^{-06}	549	3FGL J0331.3−6155	3.95×10^{-06}
487	3FGL J1042.1−4126	4.36×10^{-06}	550	3FGL J2213.6−4755	3.94×10^{-06}
488	3FGL J1520.8−0348	4.35×10^{-06}	551	3FGL J1548.8−2250	3.94×10^{-06}
489	3FGL J1103.5−2329	4.35×10^{-06}	552	3FGL J1238.2−1958	3.93×10^{-06}
490	3FGL J2311.0+0204	4.34×10^{-06}	553	3FGL J0843.4+6713	3.93×10^{-06}
491	3FGL J0122.8+3423	4.32×10^{-06}	554	3FGL J1802.6−3940	3.93×10^{-06}
492	3FGL J1902.9−6745	4.32×10^{-06}	555	3FGL J0118.9−1457	3.93×10^{-06}
493	3FGL J1126.7−3834	4.31×10^{-06}	556	3FGL J0942.1−0756	3.92×10^{-06}
494	3FGL J1717.8−3342	4.28×10^{-06}	557	3FGL J1318.7−1232	3.91×10^{-06}
495	3FHL J0420.2+4011	4.26×10^{-06}	558	3FGL J0028.6+7507	3.91×10^{-06}
496	3FGL J2325.4−4758	4.25×10^{-06}	559	3FGL J1159.2−2141	3.90×10^{-06}
497	3FGL J2251.5−4928	4.24×10^{-06}	560	3FGL J0312.7−2222	3.90×10^{-06}
498	3FGL J1224.9+2122	4.23×10^{-06}	561	3FGL J0339.2−1738	3.90×10^{-06}
499	3FGL J0109.8+6132	4.23×10^{-06}	562	3FGL J0955.4+6940	3.89×10^{-06}
500	3FGL J1756.3+5523	4.22×10^{-06}	563	3FGL J1023.1+3952	3.89×10^{-06}
501	3FGL J0808.2−0751	4.22×10^{-06}	564	3FGL J2014.5+0648	3.88×10^{-06}
502	3FGL J1346.9−2958	4.21×10^{-06}	565	3FGL J0605.0−0000	3.87×10^{-06}
503	3FGL J1239.5+0443	4.20×10^{-06}	566	3FGL J2040.2−7115	3.87×10^{-06}
504	3FHL J2207.1+4315	4.19×10^{-06}	567	3FGL J0556.0−4353	3.86×10^{-06}
505	3FGL J1451.2+6355	4.19×10^{-06}	568	3FGL J1321.0+2215	3.85×10^{-06}
506	3FGL J1400.7−5605	4.19×10^{-06}	569	3FGL J1636.7+2624	3.85×10^{-06}
507	3FGL J0625.2+4440	4.18×10^{-06}	570	3FGL J1127.8+3618	3.84×10^{-06}
508	3FGL J0230.6−5757	4.17×10^{-06}	571	3FHL J0540.2+0654	3.84×10^{-06}
509	3FGL J1315.1−5329	4.17×10^{-06}	572	3FGL J2321.9+2732	3.83×10^{-06}
510	3FGL J1510.9−0542	4.17×10^{-06}	573	3FGL J0723.2−0728	3.82×10^{-06}
511	3FGL J1254.1+6240	4.16×10^{-06}	574	3FGL J1107.5+0223	3.82×10^{-06}
512	3FGL J0957.4+4728	4.15×10^{-06}	575	3FGL J1027.0+0609	3.81×10^{-06}
513	3FGL J0014.6+6119	4.14×10^{-06}	576	3FGL J0623.3+3043	3.80×10^{-06}
514	3FGL J0935.1−1736	4.11×10^{-06}	577	3FGL J0059.2−0152	3.80×10^{-06}
515	3FGL J0231.0+1302	4.11×10^{-06}	578	3FGL J1626.0−2951	3.79×10^{-06}
516	3FGL J1012.6+2439	4.10×10^{-06}	579	3FHL J0207.6−2402	3.78×10^{-06}
517	3FGL J1849.2+6705	4.09×10^{-06}	580	3FGL J0018.9−8152	3.77×10^{-06}
518	3FHL J1427.4−1824	4.09×10^{-06}	581	3FGL J1604.4−4442	3.76×10^{-06}
519	3FGL J1026.4−8542	4.09×10^{-06}	582	3FGL J1240.3−7149	3.76×10^{-06}
520	3FGL J1224.5+2436	4.09×10^{-06}	583	3FGL J0217.8+0143	3.75×10^{-06}
521	3FGL J2035.3+1055	4.08×10^{-06}	584	3FGL J1225.9+2953	3.75×10^{-06}

Number	Source	Energy Flux [erg cm^{-2} s^{-1}]	Number	Source	Energy Flux [erg cm^{-2} s^{-1}]
585	3FGL J1315.4+1130	3.75×10^{-06}	648	3FGL J2051.8−5535	3.36×10^{-06}
586	3FGL J1725.0−0513	3.74×10^{-06}	649	3FGL J0232.8+2016	3.36×10^{-06}
587	3FGL J0720.0−4010	3.74×10^{-06}	650	3FGL J1944.1+3919	3.36×10^{-06}
588	3FGL J0816.5+2049	3.74×10^{-06}	651	3FGL J1458.7+3719	3.35×10^{-06}
589	3FGL J0440.3−2500	3.73×10^{-06}	652	3FGL J0017.2−0643	3.35×10^{-06}
590	3FGL J0234.2−0629	3.73×10^{-06}	653	3FGL J0335.3−4459	3.35×10^{-06}
591	3FGL J1150.3+2417	3.71×10^{-06}	654	3FGL J0858.1−3130	3.34×10^{-06}
592	3FHL J1542.1−2915	3.71×10^{-06}	655	3FGL J1813.6+0614	3.33×10^{-06}
593	3FGL J0700.2+1304	3.70×10^{-06}	656	3FGL J0723.7+2050	3.33×10^{-06}
594	3FGL J1259.8−3749	3.69×10^{-06}	657	3FGL J1911.4−1908	3.33×10^{-06}
595	3FGL J0325.2−5634	3.69×10^{-06}	658	3FGL J0439.9−1859	3.33×10^{-06}
596	3FGL J0654.4+5042	3.69×10^{-06}	659	3FHL J1848.4+6538	3.32×10^{-06}
597	3FGL J2056.2−4714	3.68×10^{-06}	660	3FGL J2023.6−1139	3.32×10^{-06}
598	3FGL J2221.6−5225	3.67×10^{-06}	661	3FGL J0305.2−1607	3.31×10^{-06}
599	3FGL J0113.0−3554	3.67×10^{-06}	662	3FGL J0954.8−3948	3.31×10^{-06}
600	3FGL J2217.8+3207	3.65×10^{-06}	663	3FGL J0148.3+5200	3.30×10^{-06}
601	3FGL J1904.5+3627	3.64×10^{-06}	664	3FGL J0152.6+0148	3.30×10^{-06}
602	3FGL J0322.5−3721	3.64×10^{-06}	665	3FGL J0250.6+5630	3.30×10^{-06}
603	3FGL J1259.0−2310	3.64×10^{-06}	666	3FGL J0203.1−0227	3.30×10^{-06}
604	3FGL J2131.8−2516	3.63×10^{-06}	667	3FGL J0609.7−1841	3.30×10^{-06}
605	3FGL J0558.1−3838	3.62×10^{-06}	668	3FGL J1027.7+6316	3.30×10^{-06}
606	3FGL J1310.6+2446	3.62×10^{-06}	669	3FGL J1714.1−2029	3.29×10^{-06}
607	3FGL J1722.7+1014	3.62×10^{-06}	670	3FGL J2147.2+0929	3.27×10^{-06}
608	3FGL J0156.9−4742	3.61×10^{-06}	671	3FGL J0540.4+5823	3.27×10^{-06}
609	3FGL J0731.8−3010	3.61×10^{-06}	672	3FGL J2049.0−6801	3.27×10^{-06}
610	3FGL J0838.8−2829	3.60×10^{-06}	673	3FGL J1749.1+4322	3.26×10^{-06}
611	3FGL J1419.5+0449	3.58×10^{-06}	674	3FGL J0407.5+0740	3.25×10^{-06}
612	3FGL J0030.3−4223	3.58×10^{-06}	675	3FGL J0651.3+4014	3.25×10^{-06}
613	3FGL J1046.9−2531	3.57×10^{-06}	676	3FGL J0721.4+0404	3.24×10^{-06}
614	3FGL J2347.9+5436	3.56×10^{-06}	677	3FGL J0849.5−2912	3.24×10^{-06}
615	3FGL J1849.3−1645	3.56×10^{-06}	678	3FGL J1335.1−5655	3.24×10^{-06}
616	3FGL J1558.9+5625	3.56×10^{-06}	679	3FGL J0814.1−1012	3.24×10^{-06}
617	3FGL J2047.9−3119	3.55×10^{-06}	680	3FGL J1716.7−8112	3.23×10^{-06}
618	3FGL J1007.9+0621	3.55×10^{-06}	681	3FGL J1317.8+3429	3.23×10^{-06}
619	3FGL J1743.9+1934	3.55×10^{-06}	682	3FGL J0737.8−8245	3.23×10^{-06}
620	3FGL J1852.4+4856	3.55×10^{-06}	683	3FGL J1323.9+1405	3.22×10^{-06}
621	3FGL J1223.3−3028	3.55×10^{-06}	684	3FGL J1109.4+2411	3.21×10^{-06}
622	3FGL J0806.6+5933	3.54×10^{-06}	685	3FGL J1641.8−0619	3.21×10^{-06}
623	3FGL J1730.5+0023	3.52×10^{-06}	686	3FGL J1640.6+3945	3.20×10^{-06}
624	3FGL J1222.7+8041	3.52×10^{-06}	687	3FGL J1209.4+4119	3.20×10^{-06}
625	3FGL J0816.7+5739	3.52×10^{-06}	688	3FGL J1209.8+1810	3.20×10^{-06}
626	3FGL J0748.5+7910	3.51×10^{-06}	689	3FGL J0545.6+6019	3.20×10^{-06}
627	3FHL J0442.6+6142	3.51×10^{-06}	690	3FGL J1827.7+1141	3.20×10^{-06}
628	3FGL J0109.1+1816	3.49×10^{-06}	691	3FGL J1829.6+4844	3.20×10^{-06}
629	3FGL J0112.9−7506	3.49×10^{-06}	692	3FGL J0438.8−4519	3.20×10^{-06}
630	3FGL J0251.1−1829	3.49×10^{-06}	693	3FGL J1727.1+4531	3.19×10^{-06}
631	3FGL J1836.3+3137	3.49×10^{-06}	694	3FGL J1220.2+3434	3.19×10^{-06}
632	3FGL J1927.7+6118	3.48×10^{-06}	695	3FGL J1842.2+2742	3.19×10^{-06}
633	3FGL J1944.1−4523	3.48×10^{-06}	696	3FGL J0644.6−2853	3.19×10^{-06}
634	3FGL J1505.1+0326	3.47×10^{-06}	697	3FGL J0242.7−0001	3.19×10^{-06}
635	3FGL J1747.3+0324	3.46×10^{-06}	698	3FGL J0007.9+4006	3.17×10^{-06}
636	3FGL J1820.3+3625	3.45×10^{-06}	699	3FGL J0910.7+3858	3.17×10^{-06}
637	3FHL J2105.9+7508	3.44×10^{-06}	700	3FGL J2127.7+3612	3.17×10^{-06}
638	3FGL J0022.1−5141	3.42×10^{-06}	701	3FGL J0245.9−4651	3.16×10^{-06}
639	3FGL J0856.5+2057	3.42×10^{-06}	702	3FGL J0334.2+3915	3.16×10^{-06}
640	3FGL J2300.3+3136	3.42×10^{-06}	703	3FGL J0253.8+5104	3.14×10^{-06}
641	3FGL J1723.7−7713	3.41×10^{-06}	704	3FGL J1030.4−2030	3.13×10^{-06}
642	3FGL J2024.4−0848	3.39×10^{-06}	705	3FGL J1838.5−6006	3.13×10^{-06}
643	3FGL J0850.2+3500	3.39×10^{-06}	706	3FHL J1949.5+0906	3.12×10^{-06}
644	3FGL J1424.3+0434	3.38×10^{-06}	707	3FHL J0302.6+3354	3.12×10^{-06}
645	3FHL J1550.8−0822	3.38×10^{-06}	708	3FGL J1628.2+7703	3.10×10^{-06}
646	3FGL J1053.7+4929	3.38×10^{-06}	709	3FHL J2026.7+3449	3.10×10^{-06}
647	3FGL J1345.8+0704	3.38×10^{-06}	710	3FGL J0138.5−4612	3.10×10^{-06}

Number	Source	Energy Flux [erg cm^{-2} s^{-1}]	Number	Source	Energy Flux [erg cm^{-2} s^{-1}]
711	3FGL J1306.8−4031	3.09×10^{-06}	774	3FGL J2233.1+6542	2.82×10^{-06}
712	3FGL J1417.5−4402	3.09×10^{-06}	775	3FGL J2256.7−2011	2.81×10^{-06}
713	3FGL J0701.4−4634	3.08×10^{-06}	776	3FGL J0426.3+6827	2.80×10^{-06}
714	3FGL J0839.5+0102	3.08×10^{-06}	777	3FGL J1117.3+2546	2.80×10^{-06}
715	3FGL J1457.4−3539	3.08×10^{-06}	778	3FGL J1809.7+2909	2.79×10^{-06}
716	3FGL J1415.2+4832	3.03×10^{-06}	779	3FGL J1722.7−0415	2.78×10^{-06}
717	3FGL J0253.1−5438	3.03×10^{-06}	780	3FHL J0709.7−3008	2.78×10^{-06}
718	3FGL J0656.4+4232	3.03×10^{-06}	781	3FGL J1739.4+4955	2.78×10^{-06}
719	3FGL J0824.1+2434	3.03×10^{-06}	782	3FGL J1203.2+3847	2.76×10^{-06}
720	3FGL J0710.3+5908	3.02×10^{-06}	783	3FGL J1241.6−1456	2.76×10^{-06}
721	3FHL J1849.3−6448	3.02×10^{-06}	784	3FGL J2232.9−2021	2.76×10^{-06}
722	3FGL J0238.0+5237	3.02×10^{-06}	785	3FGL J1106.4−3643	2.76×10^{-06}
723	3FGL J2134.1−0152	3.02×10^{-06}	786	3FGL J1619.1+7538	2.76×10^{-06}
724	3FHL J2110.2+0404	3.01×10^{-06}	787	3FGL J2235.3−4835	2.76×10^{-06}
725	3FGL J0041.9+3639	3.01×10^{-06}	788	3FGL J2324.7+0801	2.75×10^{-06}
726	3FGL J1037.5−2821	3.00×10^{-06}	789	3FGL J0812.0+0237	2.75×10^{-06}
727	3FGL J1630.6+8232	2.99×10^{-06}	790	3FGL J0509.7−6418	2.75×10^{-06}
728	3FGL J1730.6−0357	2.99×10^{-06}	791	3FGL J0123.7−2312	2.74×10^{-06}
729	3FGL J0304.3−2836	2.98×10^{-06}	792	3FGL J0157.0−5301	2.74×10^{-06}
730	3FGL J1740.3+4736	2.98×10^{-06}	793	3FGL J0940.6−7609	2.73×10^{-06}
731	3FGL J2157.5+3126	2.98×10^{-06}	794	3FGL J1816.2−2726	2.73×10^{-06}
732	3FGL J1146.1−0640	2.98×10^{-06}	795	3FGL J0827.2−0711	2.73×10^{-06}
733	3FGL J2328.4−4034	2.98×10^{-06}	796	3FGL J0228.3−5545	2.72×10^{-06}
734	3FGL J1231.8+1421	2.97×10^{-06}	797	3FGL J0826.3−6400	2.72×10^{-06}
735	3FGL J1249.1−2808	2.97×10^{-06}	798	3FGL J1753.5−5010	2.72×10^{-06}
736	3FGL J2050.2+0409	2.96×10^{-06}	799	3FHL J1440.2−2343	2.72×10^{-06}
737	3FGL J2319.2−4207	2.95×10^{-06}	800	3FGL J1828.9−2417	2.71×10^{-06}
738	3FGL J1155.4−3417	2.95×10^{-06}	801	3FGL J0653.6+2817	2.71×10^{-06}
739	3FGL J1203.5−3925	2.95×10^{-06}	802	3FGL J0353.0−6831	2.70×10^{-06}
740	3FGL J2159.2−2841	2.94×10^{-06}	803	3FGL J1955.0−1605	2.70×10^{-06}
741	3FGL J1208.7+5442	2.94×10^{-06}	804	3FGL J1924.8−2914	2.70×10^{-06}
742	3FGL J0626.6−4259	2.93×10^{-06}	805	3FGL J2339.0+2122	2.70×10^{-06}
743	3FGL J0032.3−5522	2.93×10^{-06}	806	3FGL J0219.0+2440	2.70×10^{-06}
744	3FGL J1613.8+3410	2.92×10^{-06}	807	3FGL J1824.4+4310	2.69×10^{-06}
745	3FGL J0519.3+2746	2.91×10^{-06}	808	3FGL J1533.5+3416	2.69×10^{-06}
746	3FGL J1120.6+0713	2.91×10^{-06}	809	3FGL J0818.8+2751	2.68×10^{-06}
747	3FGL J1943.2−3510	2.91×10^{-06}	810	3FGL J0323.6−0109	2.67×10^{-06}
748	3FGL J1955.9+0212	2.90×10^{-06}	811	3FHL J0659.5−6743	2.67×10^{-06}
749	3FGL J1753.6−4447	2.89×10^{-06}	812	3FGL J1544.1−2555	2.67×10^{-06}
750	3FGL J1059.3+0224	2.89×10^{-06}	813	3FGL J1040.4+0615	2.67×10^{-06}
751	3FGL J2354.4−6612	2.89×10^{-06}	814	3FGL J1949.0+1312	2.66×10^{-06}
752	3FGL J1832.4−5659	2.88×10^{-06}	815	3FGL J0325.6−1648	2.65×10^{-06}
753	3FGL J2336.5+2356	2.88×10^{-06}	816	3FGL J0043.5−0444	2.65×10^{-06}
754	3FGL J1506.1+3728	2.88×10^{-06}	817	3FGL J1322.9+0435	2.65×10^{-06}
755	3FGL J1735.4−1118	2.88×10^{-06}	818	3FGL J1048.6+2338	2.65×10^{-06}
756	3FGL J0910.9+2248	2.87×10^{-06}	819	3FGL J0648.1+1606	2.65×10^{-06}
757	3FGL J1119.8−2647	2.87×10^{-06}	820	3FGL J0127.9+2551	2.65×10^{-06}
758	3FGL J0018.4+2947	2.87×10^{-06}	821	3FGL J2212.5+0703	2.65×10^{-06}
759	3FGL J1010.2−3120	2.87×10^{-06}	822	3FHL J0701.5+2512	2.64×10^{-06}
760	3FGL J1440.9+0610	2.87×10^{-06}	823	3FGL J1759.2−3848	2.64×10^{-06}
761	3FGL J0054.8−2455	2.87×10^{-06}	824	3FGL J1219.7−0314	2.62×10^{-06}
762	3FGL J1151.4−1346	2.86×10^{-06}	825	3FGL J1912.9−8008	2.62×10^{-06}
763	3FHL J0507.4−3347	2.86×10^{-06}	826	3FGL J1625.6−2058	2.61×10^{-06}
764	3FGL J1142.0+1546	2.86×10^{-06}	827	3FGL J0746.4−0225	2.60×10^{-06}
765	3FGL J0921.0−2258	2.85×10^{-06}	828	3FGL J0700.3−6310	2.60×10^{-06}
766	3FGL J1841.2+2910	2.85×10^{-06}	829	3FGL J2219.2+1806	2.60×10^{-06}
767	3FGL J1700.1+6829	2.84×10^{-06}	830	3FGL J1944.0−0535	2.59×10^{-06}
768	3FGL J1101.5+4106	2.84×10^{-06}	831	3FGL J0131.3+5548	2.59×10^{-06}
769	3FGL J0839.6+1803	2.83×10^{-06}	832	3FGL J1809.0+3517	2.59×10^{-06}
770	3FGL J1310.2−1159	2.83×10^{-06}	833	3FGL J1340.6+4412	2.59×10^{-06}
771	3FGL J1830.1+0617	2.83×10^{-06}	834	3FGL J1438.7+3710	2.59×10^{-06}
772	3FGL J2325.6+1650	2.82×10^{-06}	835	3FGL J1543.5+0451	2.59×10^{-06}
773	3FGL J1416.0+1325	2.82×10^{-06}	836	3FGL J0304.9+6817	2.59×10^{-06}

Number	Source	Energy Flux [erg cm^{-2} s^{-1}]	Number	Source	Energy Flux [erg cm^{-2} s^{-1}]
837	3FGL J1007.4−3334	2.59×10^{-06}	900	3FGL J1221.5−0632	2.41×10^{-06}
838	3FGL J2021.9+0630	2.59×10^{-06}	901	3FGL J0611.2+4323	2.41×10^{-06}
839	3FGL J1647.1−6438	2.58×10^{-06}	902	3FGL J1610.6−3956	2.41×10^{-06}
840	3FGL J1213.1−2619	2.58×10^{-06}	903	3FGL J1302.6+5748	2.40×10^{-06}
841	3FGL J0807.1−0541	2.57×10^{-06}	904	3FGL J1626.4−7640	2.40×10^{-06}
842	3FGL J1647.4+4950	2.57×10^{-06}	905	3FGL J1740.4+5347	2.40×10^{-06}
843	3FGL J0924.0+2816	2.57×10^{-06}	906	3FGL J0318.1+0252	2.39×10^{-06}
844	3FGL J1057.6−2754	2.56×10^{-06}	907	3FGL J0412.0+0229	2.39×10^{-06}
845	3FGL J2103.7−1113	2.56×10^{-06}	908	3FGL J1304.2−2411	2.39×10^{-06}
846	3FGL J0707.0+7741	2.56×10^{-06}	909	3FGL J0758.6−1451	2.39×10^{-06}
847	3FHL J1850.4+2631	2.56×10^{-06}	910	3FHL J1514.7−0949	2.39×10^{-06}
848	3FGL J0953.7−1510	2.56×10^{-06}	911	3FGL J1645.9+6336	2.38×10^{-06}
849	3FGL J0040.3+4049	2.55×10^{-06}	912	3FGL J1204.0+1144	2.38×10^{-06}
850	3FGL J2359.5−2052	2.54×10^{-06}	913	3FHL J1523.2+0533	2.38×10^{-06}
851	3FGL J1540.8+1449	2.54×10^{-06}	914	3FGL J1934.2+6002	2.38×10^{-06}
852	3FGL J1549.4+0237	2.53×10^{-06}	915	3FGL J0708.9+2239	2.38×10^{-06}
853	3FGL J1650.8+0830	2.53×10^{-06}	916	3FGL J0236.7−6136	2.37×10^{-06}
854	3FGL J0909.0+2310	2.53×10^{-06}	917	3FGL J2142.7+1957	2.36×10^{-06}
855	3FHL J0057.9+6325	2.53×10^{-06}	918	3FGL J2356.0+4037	2.36×10^{-06}
856	3FGL J1935.5+8355	2.53×10^{-06}	919	3FGL J2350.4−3004	2.35×10^{-06}
857	3FGL J0158.6−3931	2.52×10^{-06}	920	3FGL J1803.3−6706	2.35×10^{-06}
858	3FGL J0015.7+5552	2.52×10^{-06}	921	3FGL J0912.7+1556	2.35×10^{-06}
859	3FGL J1256.9+3649	2.52×10^{-06}	922	3FGL J0312.1−0921	2.34×10^{-06}
860	3FGL J1258.4+2123	2.52×10^{-06}	923	3FGL J1036.4−4348	2.34×10^{-06}
861	3FGL J0146.4−6746	2.51×10^{-06}	924	3FGL J1335.4−2949	2.34×10^{-06}
862	3FGL J1335.2−4056	2.51×10^{-06}	925	3FGL J1238.3−4543	2.34×10^{-06}
863	3FGL J1552.1+0852	2.50×10^{-06}	926	3FGL J0127.4+5433	2.34×10^{-06}
864	3FGL J0505.5+0416	2.50×10^{-06}	927	3FGL J0829.6−1137	2.34×10^{-06}
865	3FGL J2158.0−1501	2.50×10^{-06}	928	3FGL J1923.2−7452	2.33×10^{-06}
866	3FGL J2207.8−5345	2.50×10^{-06}	929	3FGL J2006.6+0150	2.33×10^{-06}
867	3FGL J2236.0−3629	2.50×10^{-06}	930	3FGL J0127.1−0818	2.32×10^{-06}
868	3FGL J0152.8+7517	2.49×10^{-06}	931	3FGL J2243.6−1230	2.32×10^{-06}
869	3FGL J2150.2−1411	2.48×10^{-06}	932	3FGL J0402.1−2618	2.32×10^{-06}
870	3FGL J1424.6−6807	2.48×10^{-06}	933	3FGL J1503.7+4759	2.31×10^{-06}
871	3FGL J2359.3−3038	2.48×10^{-06}	934	3FGL J1342.7+0945	2.31×10^{-06}
872	3FGL J1226.8+0638	2.48×10^{-06}	935	3FGL J1818.6+0903	2.31×10^{-06}
873	3FGL J0606.4−4729	2.48×10^{-06}	936	3FGL J2237.5−8326	2.31×10^{-06}
874	3FGL J2351.9−7601	2.47×10^{-06}	937	3FGL J1338.6−2403	2.31×10^{-06}
875	3FHL J1042.8+0055	2.47×10^{-06}	938	3FGL J1049.8+1425	2.31×10^{-06}
876	3FGL J1439.2+3931	2.47×10^{-06}	939	3FGL J0558.6−7459	2.31×10^{-06}
877	3FGL J2240.9+4121	2.47×10^{-06}	940	3FGL J1615.8+4712	2.31×10^{-06}
878	3FGL J1020.0+6323	2.47×10^{-06}	941	3FGL J0022.1−1855	2.29×10^{-06}
879	3FGL J0941.0+6151	2.46×10^{-06}	942	3FGL J0244.4−8224	2.28×10^{-06}
880	3FGL J1830.8−3136	2.46×10^{-06}	943	3FGL J1224.5+4957	2.28×10^{-06}
881	3FHL J0933.5−5240	2.46×10^{-06}	944	3FGL J1436.8+2322	2.28×10^{-06}
882	3FGL J0737.2−3233	2.46×10^{-06}	945	3FGL J1334.3−4152	2.28×10^{-06}
883	3FGL J1125.9+2007	2.46×10^{-06}	946	3FGL J0045.7+1217	2.27×10^{-06}
884	3FGL J0603.8+2155	2.45×10^{-06}	947	3FGL J1958.0−3847	2.27×10^{-06}
885	3FGL J1109.6+3734	2.45×10^{-06}	948	3FGL J1600.3−5810	2.26×10^{-06}
886	3FGL J0948.8+0021	2.45×10^{-06}	949	3FGL J0038.0+0012	2.26×10^{-06}
887	3FGL J2300.0+4053	2.45×10^{-06}	950	3FGL J0133.0−4413	2.26×10^{-06}
888	3FHL J1623.4+0858	2.45×10^{-06}	951	3FGL J1022.8−0113	2.26×10^{-06}
889	3FGL J0747.4+0904	2.45×10^{-06}	952	3FGL J2334.8+1432	2.26×10^{-06}
890	3FGL J1743.9−1310	2.44×10^{-06}	953	3FGL J0800.9+4401	2.26×10^{-06}
891	3FGL J1158.8+0941	2.44×10^{-06}	954	3FGL J0802.0+1005	2.26×10^{-06}
892	3FGL J1125.0−2101	2.44×10^{-06}	955	3FGL J0730.5−6606	2.26×10^{-06}
893	3FGL J0912.4+2800	2.44×10^{-06}	956	3FGL J1110.4−1835	2.25×10^{-06}
894	3FGL J0333.4+7853	2.43×10^{-06}	957	3FGL J0154.9+4433	2.25×10^{-06}
895	3FGL J0744.3+7434	2.43×10^{-06}	958	3FGL J2131.1−6625	2.25×10^{-06}
896	3FGL J0526.4+2247	2.43×10^{-06}	959	3FGL J1319.6+7759	2.24×10^{-06}
897	3FGL J1740.3+5211	2.42×10^{-06}	960	3FGL J1213.9−4412	2.23×10^{-06}
898	3FGL J1912.7+4610	2.42×10^{-06}	961	3FGL J0217.0−6635	2.23×10^{-06}
899	3FGL J2247.2−0004	2.41×10^{-06}	962	3FGL J1754.3−6424	2.23×10^{-06}

Number	Source	Energy Flux [erg cm^{-2} s^{-1}]	Number	Source	Energy Flux [erg cm^{-2} s^{-1}]
963	3FGL J0834.7+4403	2.22×10^{-06}	1026	3FHL J2142.3+3659	2.03×10^{-06}
964	3FGL J2322.5+3436	2.22×10^{-06}	1027	3FHL J1950.5+3457	2.03×10^{-06}
965	3FGL J1154.0−3243	2.22×10^{-06}	1028	3FGL J2330.8−2144	2.02×10^{-06}
966	3FHL J0753.9+0452	2.21×10^{-06}	1029	3FGL J2144.9−3356	2.02×10^{-06}
967	3FGL J0032.3−2852	2.21×10^{-06}	1030	3FGL J2026.3+1430	2.02×10^{-06}
968	3FGL J2014.3−0047	2.21×10^{-06}	1031	3FGL J0431.6+7403	2.02×10^{-06}
969	3FGL J1402.7−3240	2.21×10^{-06}	1032	3FGL J1326.6−5256	2.01×10^{-06}
970	3FGL J2036.4+6551	2.20×10^{-06}	1033	3FGL J0726.6−4727	2.01×10^{-06}
971	3FGL J1646.9−1332	2.20×10^{-06}	1034	3FGL J1910.8+2855	2.01×10^{-06}
972	3FGL J1849.4−4312	2.19×10^{-06}	1035	3FHL J0357.3−0316	2.01×10^{-06}
973	3FHL J2002.1−5736	2.18×10^{-06}	1036	3FGL J2112.7+0819	2.01×10^{-06}
974	3FGL J2336.5−4116	2.17×10^{-06}	1037	3FGL J0430.5+1655	2.01×10^{-06}
975	3FGL J0703.4−3914	2.17×10^{-06}	1038	3FGL J1145.1+1935	2.01×10^{-06}
976	3FGL J1450.9+5200	2.17×10^{-06}	1039	3FGL J1611.9+1404	2.00×10^{-06}
977	3FGL J0712.2−6436	2.16×10^{-06}	1040	3FGL J2015.2−0138	2.00×10^{-06}
978	3FGL J1527.0−3804	2.16×10^{-06}	1041	3FGL J1130.7−7800	2.00×10^{-06}
979	3FHL J2239.5−2439	2.16×10^{-06}	1042	3FGL J1404.3−5241	2.00×10^{-06}
980	3FGL J0748.3+2401	2.15×10^{-06}	1043	3FGL J0125.4−2548	1.99×10^{-06}
981	3FGL J2309.6−3633	2.15×10^{-06}	1044	3FGL J0348.7−1606	1.99×10^{-06}
982	3FGL J0805.2−0112	2.15×10^{-06}	1045	3FGL J1818.5+1320	1.99×10^{-06}
983	3FGL J2228.5−1636	2.15×10^{-06}	1046	3FHL J1716.1+2308	1.99×10^{-06}
984	3FHL J0301.4−5618	2.15×10^{-06}	1047	3FGL J1728.5+0428	1.99×10^{-06}
985	3FGL J2318.6−3829	2.14×10^{-06}	1048	3FGL J1304.9−2109	1.99×10^{-06}
986	3FGL J2115.2+1215	2.13×10^{-06}	1049	3FGL J1016.0−0635	1.98×10^{-06}
987	3FHL J1800.2+2813	2.13×10^{-06}	1050	3FGL J0911.8+3351	1.98×10^{-06}
988	3FGL J1353.2+1435	2.13×10^{-06}	1051	3FGL J0521.7+0103	1.98×10^{-06}
989	3FGL J1228.4−0317	2.13×10^{-06}	1052	3FGL J0758.9+2705	1.98×10^{-06}
990	3FGL J1535.0+3721	2.12×10^{-06}	1053	3FGL J0730.5−0537	1.98×10^{-06}
991	3FGL J0557.7−0720	2.12×10^{-06}	1054	3FGL J2108.6−0250	1.97×10^{-06}
992	3FGL J1719.2+1744	2.12×10^{-06}	1055	3FGL J1125.5−3558	1.97×10^{-06}
993	3FGL J1848.4+3216	2.12×10^{-06}	1056	3FGL J0343.3−6443	1.97×10^{-06}
994	3FGL J1824.2−5427	2.12×10^{-06}	1057	3FGL J1247.0+4421	1.97×10^{-06}
995	3FHL J2027.0+3343	2.11×10^{-06}	1058	3FGL J2317.3−4534	1.97×10^{-06}
996	3FGL J2022.2−7220	2.11×10^{-06}	1059	3FHL J0233.0+3742	1.96×10^{-06}
997	3FGL J0749.0+4459	2.11×10^{-06}	1060	3FGL J0532.0−4827	1.96×10^{-06}
998	3FGL J1052.0+0816	2.11×10^{-06}	1061	3FGL J0954.2+4913	1.96×10^{-06}
999	3FGL J0004.7−4740	2.10×10^{-06}	1062	3FGL J1829.4+5402	1.95×10^{-06}
1000	3FGL J1153.4+4033	2.10×10^{-06}	1063	3FGL J0242.3+1059	1.95×10^{-06}
1001	3FGL J0147.0−5204	2.10×10^{-06}	1064	3FGL J2049.7+1002	1.95×10^{-06}
1002	3FGL J1058.4+8112	2.09×10^{-06}	1065	3FGL J2046.7−1011	1.95×10^{-06}
1003	3FGL J1950.2+1215	2.09×10^{-06}	1066	3FGL J0937.9−1435	1.95×10^{-06}
1004	3FGL J1232.3+1701	2.09×10^{-06}	1067	3FGL J2028.7+1012	1.95×10^{-06}
1005	3FGL J2026.3+7644	2.09×10^{-06}	1068	3FGL J1758.8−4108	1.94×10^{-06}
1006	3FGL J1537.8−8000	2.09×10^{-06}	1069	3FHL J0029.4+2052	1.94×10^{-06}
1007	3FGL J1359.0+5544	2.08×10^{-06}	1070	3FHL J1455.4−7559	1.94×10^{-06}
1008	3FGL J0013.9−1853	2.08×10^{-06}	1071	3FGL J0050.4−0449	1.94×10^{-06}
1009	3FGL J0654.4+4514	2.08×10^{-06}	1072	3FGL J1337.6−1257	1.94×10^{-06}
1010	3FGL J2001.8+7041	2.07×10^{-06}	1073	3FHL J1441.3−1934	1.94×10^{-06}
1011	3FGL J1332.8+2723	2.07×10^{-06}	1074	3FGL J0249.1+8438	1.94×10^{-06}
1012	3FGL J2217.0+2421	2.06×10^{-06}	1075	3FGL J1058.5−8003	1.94×10^{-06}
1013	3FGL J1231.6−5113	2.06×10^{-06}	1076	3FHL J0737.5+6534	1.93×10^{-06}
1014	3FGL J0706.1−4849	2.05×10^{-06}	1077	3FGL J1051.5−6517	1.93×10^{-06}
1015	3FGL J1442.8+1200	2.05×10^{-06}	1078	3FGL J0303.7−6211	1.93×10^{-06}
1016	3FGL J2055.6+1609	2.04×10^{-06}	1079	3FGL J1220.2+7105	1.93×10^{-06}
1017	3FGL J0008.3+1456	2.04×10^{-06}	1080	3FGL J0342.8+1321	1.93×10^{-06}
1018	3FGL J1756.9+7032	2.04×10^{-06}	1081	3FGL J0030.2−1646	1.92×10^{-06}
1019	3FGL J2042.1+2428	2.04×10^{-06}	1082	3FHL J1640.3+6850	1.92×10^{-06}
1020	3FGL J1151.5+0957	2.04×10^{-06}	1083	3FGL J2225.8−0454	1.92×10^{-06}
1021	3FGL J0729.5−3127	2.04×10^{-06}	1084	3FGL J1426.2+3402	1.91×10^{-06}
1022	3FGL J1440.2−1538	2.03×10^{-06}	1085	3FGL J1534.5+0128	1.91×10^{-06}
1023	3FGL J1745.4+4721	2.03×10^{-06}	1086	3FGL J0216.4+0507	1.91×10^{-06}
1024	3FGL J0849.9+5108	2.03×10^{-06}	1087	3FGL J1535.7+3920	1.91×10^{-06}
1025	3FGL J0733.8+5021	2.03×10^{-06}	1088	3FGL J0159.8−2741	1.91×10^{-06}

Number	Source	Energy Flux [erg cm^{-2} s^{-1}]	Number	Source	Energy Flux [erg cm^{-2} s^{-1}]
1089	3FGL J1128.0+5921	1.90×10^{-06}	1152	3FGL J2152.9−0045	1.76×10^{-06}
1090	3FGL J2203.4+1725	1.90×10^{-06}	1153	3FGL J1254.9−4423	1.76×10^{-06}
1091	3FGL J1736.0+2033	1.90×10^{-06}	1154	3FGL J2149.7+0323	1.76×10^{-06}
1092	3FGL J1353.1−4414	1.90×10^{-06}	1155	3FHL J1412.0+3835	1.76×10^{-06}
1093	3FHL J1946.0+0937	1.89×10^{-06}	1156	3FGL J1006.7+3453	1.76×10^{-06}
1094	3FGL J0433.1+3228	1.88×10^{-06}	1157	3FGL J1844.1+5709	1.76×10^{-06}
1095	3FGL J2053.4−4052	1.88×10^{-06}	1158	3FGL J1018.8+5913	1.75×10^{-06}
1096	3FGL J2055.2−0019	1.88×10^{-06}	1159	3FGL J2325.3−3557	1.75×10^{-06}
1097	3FGL J1546.0+0818	1.88×10^{-06}	1160	3FGL J1344.5−3655	1.75×10^{-06}
1098	3FGL J0223.3+6820	1.87×10^{-06}	1161	3FGL J0416.8+0104	1.75×10^{-06}
1099	3FGL J1113.1−4515	1.87×10^{-06}	1162	3FGL J1118.2−0411	1.75×10^{-06}
1100	3FGL J0433.7−6028	1.87×10^{-06}	1163	3FGL J2104.7+2113	1.74×10^{-06}
1101	3FGL J2356.9+6812	1.87×10^{-06}	1164	3FGL J2224.6−1122	1.74×10^{-06}
1102	3FHL J1834.2+3136	1.87×10^{-06}	1165	3FGL J0349.2−1158	1.73×10^{-06}
1103	3FGL J0656.2−0323	1.87×10^{-06}	1166	3FHL J0550.4−4356	1.73×10^{-06}
1104	3FGL J1422.4+3227	1.87×10^{-06}	1167	3FGL J0456.3−3131	1.73×10^{-06}
1105	3FGL J2151.6+4154	1.87×10^{-06}	1168	3FGL J2353.6−3037	1.73×10^{-06}
1106	3FGL J2340.7+3847	1.87×10^{-06}	1169	3FGL J2327.7+0941	1.72×10^{-06}
1107	3FGL J1923.5−2104	1.86×10^{-06}	1170	3FGL J0309.0+1029	1.72×10^{-06}
1108	3FGL J0045.3+2126	1.86×10^{-06}	1171	3FGL J0930.0+4951	1.72×10^{-06}
1109	3FGL J1310.6+3222	1.86×10^{-06}	1172	3FGL J0648.1−3045	1.72×10^{-06}
1110	3FHL J2138.7−2055	1.86×10^{-06}	1173	3FGL J0802.3−5610	1.72×10^{-06}
1111	3FGL J1559.9+2319	1.86×10^{-06}	1174	3FGL J0526.0+4253	1.72×10^{-06}
1112	3FGL J1720.7+0711	1.86×10^{-06}	1175	3FHL J0557.3−0616	1.71×10^{-06}
1113	3FGL J1913.9+4441	1.85×10^{-06}	1176	3FGL J2358.5+3827	1.71×10^{-06}
1114	3FGL J0804.4+0418	1.85×10^{-06}	1177	3FGL J0353.0−3622	1.71×10^{-06}
1115	3FGL J0212.8−3504	1.85×10^{-06}	1178	3FGL J1544.6−1125	1.71×10^{-06}
1116	3FGL J1440.0−3955	1.85×10^{-06}	1179	3FGL J0401.0−5359	1.70×10^{-06}
1117	3FGL J0832.6+4914	1.84×10^{-06}	1180	3FGL J1539.8−1128	1.70×10^{-06}
1118	3FGL J0730.5+3307	1.84×10^{-06}	1181	3FGL J1224.6−8312	1.70×10^{-06}
1119	3FGL J0525.3−4558	1.84×10^{-06}	1182	3FGL J0047.5−2516	1.70×10^{-06}
1120	3FGL J0209.5+4449	1.84×10^{-06}	1183	3FGL J0003.2−5246	1.70×10^{-06}
1121	3FGL J0110.9−1254	1.83×10^{-06}	1184	3FGL J2133.0−6433	1.70×10^{-06}
1122	3FGL J1002.3+2220	1.83×10^{-06}	1185	3FGL J1509.7+5556	1.69×10^{-06}
1123	3FGL J1607.9−2040	1.83×10^{-06}	1186	3FGL J1446.8−1831	1.69×10^{-06}
1124	3FGL J2248.6−3235	1.83×10^{-06}	1187	3FGL J1823.4+6857	1.69×10^{-06}
1125	3FGL J1025.1+2333	1.83×10^{-06}	1188	3FGL J0533.0−3939	1.68×10^{-06}
1126	3FGL J1616.8+4111	1.83×10^{-06}	1189	3FGL J1357.5+0125	1.68×10^{-06}
1127	3FGL J1858.0−5423	1.83×10^{-06}	1190	3FGL J1954.8−1122	1.68×10^{-06}
1128	3FGL J1630.2−1052	1.82×10^{-06}	1191	3FGL J1258.6−1800	1.68×10^{-06}
1129	3FGL J2353.7−3911	1.82×10^{-06}	1192	3FGL J1043.1+2407	1.68×10^{-06}
1130	3FGL J1203.1+6029	1.82×10^{-06}	1193	3FGL J0809.6+3456	1.68×10^{-06}
1131	3FGL J1841.7+3218	1.81×10^{-06}	1194	3FGL J2118.0−3241	1.68×10^{-06}
1132	3FGL J0824.9+5551	1.81×10^{-06}	1195	3FGL J1153.4+4932	1.68×10^{-06}
1133	3FGL J1744.3−0353	1.81×10^{-06}	1196	3FGL J1309.0+0347	1.68×10^{-06}
1134	3FGL J0401.4+2109	1.81×10^{-06}	1197	3FGL J1349.6−1133	1.68×10^{-06}
1135	3FGL J1434.6+6640	1.81×10^{-06}	1198	3FHL J1934.2−2419	1.67×10^{-06}
1136	3FGL J0912.6−2757	1.81×10^{-06}	1199	3FHL J0528.4+3851	1.67×10^{-06}
1137	3FGL J2310.1−0557	1.81×10^{-06}	1200	3FGL J0839.6+3538	1.67×10^{-06}
1138	3FGL J1717.4−5157	1.80×10^{-06}	1201	3FGL J0644.3−6713	1.67×10^{-06}
1139	3FGL J1637.7+4715	1.80×10^{-06}	1202	3FGL J0153.4+7114	1.67×10^{-06}
1140	3FGL J1721.4−5253	1.80×10^{-06}	1203	3FGL J0121.8−3917	1.67×10^{-06}
1141	3FGL J1440.1+4955	1.80×10^{-06}	1204	3FHL J0041.5+3759	1.67×10^{-06}
1142	3FHL J1451.8−4145	1.80×10^{-06}	1205	3FGL J0609.6−2851	1.66×10^{-06}
1143	3FGL J0848.5+7018	1.80×10^{-06}	1206	3FHL J1605.0−1140	1.66×10^{-06}
1144	3FHL J0852.5−3124	1.80×10^{-06}	1207	3FGL J0658.3−5832	1.66×10^{-06}
1145	3FGL J0453.2−2808	1.79×10^{-06}	1208	3FGL J1858.4−2509	1.66×10^{-06}
1146	3FGL J1322.6−1619	1.79×10^{-06}	1209	3FGL J1513.3−3719	1.66×10^{-06}
1147	3FGL J0309.9−6057	1.79×10^{-06}	1210	3FGL J0250.6+1713	1.66×10^{-06}
1148	3FHL J1705.3+5434	1.79×10^{-06}	1211	3FGL J0401.8−3144	1.65×10^{-06}
1149	3FGL J0854.2+4408	1.78×10^{-06}	1212	3FHL J1503.3+1651	1.65×10^{-06}
1150	3FGL J1554.4+2010	1.77×10^{-06}	1213	3FHL J1927.5+0153	1.64×10^{-06}
1151	3FGL J0301.8−2721	1.77×10^{-06}	1214	3FGL J1254.1−2203	1.64×10^{-06}

Number	Source	Energy Flux [erg cm^{-2} s^{-1}]	Number	Source	Energy Flux [erg cm^{-2} s^{-1}]
1215	3FHL J1208.1+6120	1.64×10^{-06}	1278	3FGL J0006.6+4618	1.52×10^{-06}
1216	3FGL J0849.1+6607	1.63×10^{-06}	1279	3FGL J1039.5+7324	1.52×10^{-06}
1217	3FGL J1617.4−5846	1.63×10^{-06}	1280	3FGL J0922.4−0529	1.52×10^{-06}
1218	3FGL J1953.3+3847	1.63×10^{-06}	1281	3FGL J0427.9−6704	1.52×10^{-06}
1219	3FGL J2336.5−7620	1.62×10^{-06}	1282	3FGL J1033.2+4116	1.51×10^{-06}
1220	3FGL J1330.0+4437	1.62×10^{-06}	1283	3FGL J2220.6−6833	1.51×10^{-06}
1221	3FGL J1200.8+1228	1.62×10^{-06}	1284	3FGL J0302.5−7915	1.51×10^{-06}
1222	3FGL J1250.5+0217	1.62×10^{-06}	1285	3FGL J1052.8−3741	1.51×10^{-06}
1223	3FGL J1051.8+0105	1.62×10^{-06}	1286	3FGL J0940.9−1337	1.51×10^{-06}
1224	3FGL J2203.7+3143	1.62×10^{-06}	1287	3FGL J0019.4+2021	1.51×10^{-06}
1225	3FGL J2338.7−7401	1.62×10^{-06}	1288	3FGL J0312.7+0133	1.51×10^{-06}
1226	3FGL J1508.6+2709	1.62×10^{-06}	1289	3FGL J0356.3−6948	1.51×10^{-06}
1227	3FGL J0241.3+6542	1.61×10^{-06}	1290	3FHL J2030.4+2236	1.51×10^{-06}
1228	3FGL J1159.6−0723	1.61×10^{-06}	1291	3FGL J2119.2−3313	1.50×10^{-06}
1229	3FGL J1129.9−1446	1.61×10^{-06}	1292	3FGL J0533.2+5944	1.50×10^{-06}
1230	3FGL J1944.8+4300	1.61×10^{-06}	1293	3FGL J1808.4−3519	1.50×10^{-06}
1231	3FGL J1543.5−0244	1.61×10^{-06}	1294	3FGL J1211.8+6413	1.50×10^{-06}
1232	3FHL J0751.3−0424	1.61×10^{-06}	1295	3FHL J0501.0+2425	1.50×10^{-06}
1233	3FGL J2034.6−4202	1.61×10^{-06}	1296	3FGL J1757.7−6030	1.50×10^{-06}
1234	3FGL J1825.2−5230	1.60×10^{-06}	1297	3FGL J0820.4+3640	1.50×10^{-06}
1235	3FGL J1829.8+1328	1.60×10^{-06}	1298	3FGL J1333.7+5057	1.50×10^{-06}
1236	3FGL J1715.7+6837	1.59×10^{-06}	1299	3FGL J0657.6−4701	1.49×10^{-06}
1237	3FGL J1304.3−5535	1.59×10^{-06}	1300	3FHL J1640.1+0629	1.49×10^{-06}
1238	3FGL J0930.2+8612	1.59×10^{-06}	1301	3FGL J2041.7−3732	1.49×10^{-06}
1239	3FHL J0458.0+1151	1.59×10^{-06}	1302	3FGL J1047.8−3737	1.48×10^{-06}
1240	3FGL J0418.0−0251	1.59×10^{-06}	1303	3FGL J1224.6+4332	1.48×10^{-06}
1241	3FGL J2039.7+1237	1.59×10^{-06}	1304	3FGL J0432.5+0539	1.48×10^{-06}
1242	3FGL J2133.3+2533	1.59×10^{-06}	1305	3FGL J1419.9+5425	1.48×10^{-06}
1243	3FGL J2333.0−5525	1.59×10^{-06}	1306	3FGL J0608.2−2306	1.48×10^{-06}
1244	3FGL J2036.8−2830	1.59×10^{-06}	1307	3FGL J0521.4−1740	1.48×10^{-06}
1245	3FGL J2010.0−2120	1.58×10^{-06}	1308	3FGL J1725.3+5853	1.47×10^{-06}
1246	3FGL J1023.7+3000	1.57×10^{-06}	1309	3FHL J0259.5+5453	1.47×10^{-06}
1247	3FGL J2110.0+0442	1.57×10^{-06}	1310	3FGL J1031.0+7440	1.47×10^{-06}
1248	3FGL J1810.7+5335	1.57×10^{-06}	1311	3FGL J1404.8+0401	1.47×10^{-06}
1249	3FGL J2038.8−3613	1.57×10^{-06}	1312	3FGL J1325.2−5411	1.47×10^{-06}
1250	3FGL J2153.9+6626	1.57×10^{-06}	1313	3FGL J0434.0−5726	1.47×10^{-06}
1251	3FGL J1416.1−2417	1.57×10^{-06}	1314	3FGL J2056.3−5925	1.47×10^{-06}
1252	3FGL J0950.1+4554	1.57×10^{-06}	1315	3FGL J1512.2−2255	1.47×10^{-06}
1253	3FGL J1507.4+1725	1.57×10^{-06}	1316	3FHL J0954.2−2520	1.47×10^{-06}
1254	3FGL J1603.7+1106	1.57×10^{-06}	1317	3FGL J1237.9+6258	1.47×10^{-06}
1255	3FGL J1141.2+6805	1.57×10^{-06}	1318	3FGL J0904.8−3516	1.46×10^{-06}
1256	3FGL J1704.1+1234	1.56×10^{-06}	1319	3FGL J0333.6+0233	1.46×10^{-06}
1257	3FGL J1115.0−0701	1.56×10^{-06}	1320	3FGL J0049.4−5401	1.46×10^{-06}
1258	3FGL J1533.2+1852	1.56×10^{-06}	1321	3FGL J0032.5+3912	1.46×10^{-06}
1259	3FGL J0409.8−0358	1.56×10^{-06}	1322	3FHL J0531.8−6639e	1.45×10^{-06}
1260	3FGL J0013.2−3954	1.56×10^{-06}	1323	3FGL J0814.5+2943	1.45×10^{-06}
1261	3FGL J1205.8−2636	1.56×10^{-06}	1324	3FGL J1550.5+0526	1.45×10^{-06}
1262	3FGL J0349.9−2102	1.56×10^{-06}	1325	3FGL J0343.3+3622	1.45×10^{-06}
1263	3FGL J1155.9+6136	1.56×10^{-06}	1326	3FGL J1848.9+4247	1.45×10^{-06}
1264	3FGL J0855.4+7142	1.55×10^{-06}	1327	3FGL J1809.4+2040	1.45×10^{-06}
1265	3FGL J2212.6+2801	1.55×10^{-06}	1328	3FGL J0841.4+7053	1.45×10^{-06}
1266	3FGL J0245.4+2410	1.55×10^{-06}	1329	3FGL J0626.0−5436	1.44×10^{-06}
1267	3FHL J1545.7−2338	1.55×10^{-06}	1330	3FGL J1232.8+1332	1.44×10^{-06}
1268	3FGL J1436.8+5639	1.55×10^{-06}	1331	3FGL J0538.9+1646	1.44×10^{-06}
1269	3FGL J0851.8+5531	1.55×10^{-06}	1332	3FGL J1215.0+5002	1.44×10^{-06}
1270	3FGL J1932.6−4537	1.55×10^{-06}	1333	3FGL J0816.1−5044	1.44×10^{-06}
1271	3FGL J2134.5−2131	1.55×10^{-06}	1334	3FGL J0253.5+3216	1.44×10^{-06}
1272	3FGL J1625.7−2527	1.54×10^{-06}	1335	3FGL J0515.5−0123	1.44×10^{-06}
1273	3FGL J1656.0+2044	1.53×10^{-06}	1336	3FGL J2335.6−2342	1.43×10^{-06}
1274	3FGL J2321.3+5113	1.53×10^{-06}	1337	3FGL J1351.7−2913	1.43×10^{-06}
1275	3FGL J1156.7−2250	1.53×10^{-06}	1338	3FGL J1557.4−7040	1.43×10^{-06}
1276	3FGL J1639.8+4125	1.53×10^{-06}	1339	3FGL J1514.8+4446	1.43×10^{-06}
1277	3FGL J0405.5−1307	1.52×10^{-06}	1340	3FGL J1813.6+2820	1.43×10^{-06}

Number	Source	Energy Flux [erg cm^{-2} s^{-1}]	Number	Source	Energy Flux [erg cm^{-2} s^{-1}]
1341	3FGL J2348.4−5100	1.42×10^{-06}	1404	3FHL J1401.0−3716	1.32×10^{-06}
1342	3FGL J0345.1−2353	1.42×10^{-06}	1405	3FGL J1256.1−5703	1.32×10^{-06}
1343	3FGL J0357.1−4957	1.42×10^{-06}	1406	3FGL J1049.7+1548	1.32×10^{-06}
1344	3FGL J1742.2+5947	1.42×10^{-06}	1407	3FHL J2159.6−4619	1.32×10^{-06}
1345	3FGL J0116.2−2744	1.42×10^{-06}	1408	3FGL J0525.2−6614	1.32×10^{-06}
1346	3FGL J1127.0−1857	1.42×10^{-06}	1409	3FGL J1326.8+2211	1.32×10^{-06}
1347	3FGL J0213.0+2245	1.41×10^{-06}	1410	3FGL J2041.9−7318	1.32×10^{-06}
1348	3FGL J0312.7+2011	1.41×10^{-06}	1411	3FGL J1119.7−3046	1.31×10^{-06}
1349	3FGL J1746.6+0433	1.41×10^{-06}	1412	3FHL J0820.2−2803	1.31×10^{-06}
1350	3FGL J0456.2−6924	1.41×10^{-06}	1413	3FGL J0037.9+1239	1.31×10^{-06}
1351	3FGL J1955.7−7019	1.41×10^{-06}	1414	3FGL J1152.3−0841	1.31×10^{-06}
1352	3FGL J0014.0−5025	1.41×10^{-06}	1415	3FGL J1719.3+1206	1.31×10^{-06}
1353	3FHL J0929.2−4110	1.41×10^{-06}	1416	3FGL J0725.4−5007	1.31×10^{-06}
1354	3FGL J1248.0+5130	1.40×10^{-06}	1417	3FGL J1100.5+4020	1.31×10^{-06}
1355	3FGL J1612.4−3100	1.40×10^{-06}	1418	3FGL J0540.0−2837	1.30×10^{-06}
1356	3FGL J2007.8−4429	1.40×10^{-06}	1419	3FGL J1158.9+0818	1.30×10^{-06}
1357	3FGL J2250.6+3308	1.40×10^{-06}	1420	3FGL J1305.5+7854	1.30×10^{-06}
1358	3FGL J0043.7−1117	1.40×10^{-06}	1421	3FGL J0020.9+0323	1.29×10^{-06}
1359	3FGL J2223.3+0103	1.40×10^{-06}	1422	3FGL J0631.2+2019	1.29×10^{-06}
1360	3FGL J1300.2+1416	1.40×10^{-06}	1423	3FGL J2230.6−4419	1.29×10^{-06}
1361	3FGL J0519.2−4542	1.39×10^{-06}	1424	3FGL J0903.1+4649	1.29×10^{-06}
1362	3FGL J0217.5+7349	1.39×10^{-06}	1425	3FGL J1745.7+3952	1.29×10^{-06}
1363	3FGL J0200.3−4108	1.38×10^{-06}	1426	3FGL J0416.6−1850	1.29×10^{-06}
1364	3FGL J1220.1−3715	1.38×10^{-06}	1427	3FGL J0708.7+1747	1.29×10^{-06}
1365	3FGL J2258.1−8248	1.38×10^{-06}	1428	3FGL J0009.1+0630	1.28×10^{-06}
1366	3FGL J0021.6−2553	1.38×10^{-06}	1429	3FGL J1435.2+2023	1.28×10^{-06}
1367	3FGL J0325.5+2223	1.38×10^{-06}	1430	3FGL J1936.6−4215	1.28×10^{-06}
1368	3FGL J0805.0−0622	1.38×10^{-06}	1431	3FGL J0207.9−3846	1.28×10^{-06}
1369	3FGL J1720.3−0428	1.37×10^{-06}	1432	3FGL J1059.9+2056	1.28×10^{-06}
1370	3FGL J1640.9+1142	1.37×10^{-06}	1433	3FGL J1444.0−7033	1.28×10^{-06}
1371	3FGL J0950.4+7550	1.37×10^{-06}	1434	3FGL J1222.4+0414	1.28×10^{-06}
1372	3FGL J2024.4−3254	1.37×10^{-06}	1435	3FGL J0003.8−1151	1.28×10^{-06}
1373	3FGL J1251.0−4943	1.37×10^{-06}	1436	3FGL J0116.0−1134	1.27×10^{-06}
1374	3FGL J1124.1+2337	1.37×10^{-06}	1437	3FGL J0427.3−3900	1.27×10^{-06}
1375	3FGL J1129.0+3705	1.37×10^{-06}	1438	3FGL J1332.0−0508	1.27×10^{-06}
1376	3FGL J0813.3+6509	1.37×10^{-06}	1439	3FGL J2206.5+6451	1.27×10^{-06}
1377	3FGL J0253.0−0125	1.36×10^{-06}	1440	3FGL J2117.6+3725	1.27×10^{-06}
1378	3FGL J0151.6+2205	1.36×10^{-06}	1441	3FGL J0455.7−4617	1.26×10^{-06}
1379	3FGL J2321.2−6439	1.36×10^{-06}	1442	3FGL J1254.5+2210	1.26×10^{-06}
1380	3FGL J2258.2−3645	1.36×10^{-06}	1443	3FGL J0226.5−4442	1.26×10^{-06}
1381	3FGL J2354.0+2722	1.36×10^{-06}	1444	3FGL J2127.5−6001	1.26×10^{-06}
1382	3FGL J1155.3−1112	1.36×10^{-06}	1445	3FGL J1126.8−5001	1.26×10^{-06}
1383	3FGL J1207.6−4537	1.35×10^{-06}	1446	3FGL J0635.7−7517	1.26×10^{-06}
1384	3FGL J1521.1+5543	1.35×10^{-06}	1447	3FGL J2142.2−2546	1.26×10^{-06}
1385	3FGL J2123.6+0533	1.35×10^{-06}	1448	3FGL J1757.1+1533	1.25×10^{-06}
1386	3FGL J0859.1+6219	1.35×10^{-06}	1449	3FHL J0812.5+2821	1.25×10^{-06}
1387	3FGL J0733.5+5153	1.35×10^{-06}	1450	3FGL J2031.8+1223	1.25×10^{-06}
1388	3FGL J1231.5+6414	1.34×10^{-06}	1451	3FGL J2036.6−3325	1.25×10^{-06}
1389	3FGL J1829.2+3229	1.34×10^{-06}	1452	3FGL J0830.8+2629	1.24×10^{-06}
1390	3FGL J1218.0−0029	1.34×10^{-06}	1453	3FGL J0158.6+0102	1.24×10^{-06}
1391	3FGL J0750.6+1232	1.34×10^{-06}	1454	3FGL J2316.8−5209	1.24×10^{-06}
1392	3FGL J0919.4+6604	1.34×10^{-06}	1455	3FGL J2103.9−3546	1.24×10^{-06}
1393	3FGL J0516.3+7351	1.34×10^{-06}	1456	3FGL J1250.2−0233	1.24×10^{-06}
1394	3FGL J2142.6−2029	1.34×10^{-06}	1457	3FGL J1306.8−2146	1.24×10^{-06}
1395	3FGL J1215.1+1658	1.33×10^{-06}	1458	3FHL J0414.6−5339	1.24×10^{-06}
1396	3FGL J2149.6+1915	1.33×10^{-06}	1459	3FGL J1121.4−0554	1.24×10^{-06}
1397	3FGL J0928.9−3530	1.33×10^{-06}	1460	3FGL J2244.6+2503	1.23×10^{-06}
1398	3FGL J1709.6+4318	1.33×10^{-06}	1461	3FGL J1546.6+1812	1.23×10^{-06}
1399	3FGL J1503.7−6426	1.33×10^{-06}	1462	3FGL J0842.0−6055	1.23×10^{-06}
1400	3FGL J1018.3+3542	1.33×10^{-06}	1463	3FHL J1843.4−4835	1.22×10^{-06}
1401	3FGL J1154.2−0010	1.33×10^{-06}	1464	3FGL J1553.5+1256	1.22×10^{-06}
1402	3FGL J2258.3−5526	1.33×10^{-06}	1465	3FGL J2126.5−4605	1.22×10^{-06}
1403	3FGL J2154.0−1137	1.32×10^{-06}	1466	3FHL J0620.9−5033	1.22×10^{-06}

Number	Source	Energy Flux [erg cm^{-2} s^{-1}]	Number	Source	Energy Flux [erg cm^{-2} s^{-1}]
1467	3FGL J1937.0−3956	1.21×10^{-06}	1530	3FGL J1249.7+3705	1.10×10^{-06}
1468	3FGL J0849.9−3540	1.21×10^{-06}	1531	3FGL J2151.8−3025	1.10×10^{-06}
1469	3FGL J0925.6+5959	1.21×10^{-06}	1532	3FGL J0539.9−7553	1.10×10^{-06}
1470	3FGL J0925.7+3129	1.21×10^{-06}	1533	3FGL J0348.1+4431	1.10×10^{-06}
1471	3FGL J1012.7+4229	1.21×10^{-06}	1534	3FGL J0239.4+1326	1.09×10^{-06}
1472	3FGL J1040.8+1342	1.21×10^{-06}	1535	3FGL J1626.1+3512	1.09×10^{-06}
1473	3FGL J0824.9+3916	1.21×10^{-06}	1536	3FGL J0749.4+1059	1.09×10^{-06}
1474	3FGL J1112.6+1749	1.21×10^{-06}	1537	3FGL J0958.4−6752	1.09×10^{-06}
1475	3FGL J0145.6+8600	1.21×10^{-06}	1538	3FGL J2024.8−2331	1.09×10^{-06}
1476	3FGL J1545.0−6641	1.21×10^{-06}	1539	3FGL J0223.6+3927	1.09×10^{-06}
1477	3FGL J2209.8−0450	1.20×10^{-06}	1540	3FGL J1408.8−0751	1.09×10^{-06}
1478	3FGL J1939.6−4925	1.20×10^{-06}	1541	3FGL J1454.0+1622	1.09×10^{-06}
1479	3FGL J0529.2−5917	1.20×10^{-06}	1542	3FGL J0228.0+2248	1.08×10^{-06}
1480	3FGL J1740.8−1933	1.19×10^{-06}	1543	3FGL J2006.0−2311	1.08×10^{-06}
1481	3FGL J0208.6+3522	1.19×10^{-06}	1544	3FGL J1203.9−1745	1.08×10^{-06}
1482	3FGL J1345.9−3357	1.19×10^{-06}	1545	3FGL J0040.5−2339	1.08×10^{-06}
1483	3FGL J2152.4+1735	1.19×10^{-06}	1546	3FGL J2000.1+4212	1.08×10^{-06}
1484	3FGL J1103.1+1155	1.18×10^{-06}	1547	3FGL J2015.3−1431	1.08×10^{-06}
1485	3FGL J1110.0+7134	1.18×10^{-06}	1548	3FGL J0315.5−1026	1.08×10^{-06}
1486	3FGL J1259.3−8151	1.18×10^{-06}	1549	3FGL J1637.9+5719	1.07×10^{-06}
1487	3FHL J1719.0−5348	1.18×10^{-06}	1550	3FGL J1806.8+5346	1.07×10^{-06}
1488	3FHL J1808.7+2420	1.18×10^{-06}	1551	3FGL J0017.1+1445	1.07×10^{-06}
1489	3FGL J0105.1−2415	1.17×10^{-06}	1552	3FGL J1259.5−3231	1.07×10^{-06}
1490	3FGL J1421.8−7920	1.17×10^{-06}	1553	3FGL J0420.4−6013	1.07×10^{-06}
1491	3FGL J2330.4−3726	1.17×10^{-06}	1554	3FGL J1412.0+5249	1.07×10^{-06}
1492	3FGL J2331.9−1609	1.17×10^{-06}	1555	3FGL J0002.0−6722	1.07×10^{-06}
1493	3FGL J1339.8−0133	1.17×10^{-06}	1556	3FGL J2204.4+0439	1.06×10^{-06}
1494	3FGL J2145.5+1007	1.16×10^{-06}	1557	3FGL J2250.3+1747	1.06×10^{-06}
1495	3FHL J0706.1+0247	1.16×10^{-06}	1558	3FGL J1223.3+0818	1.06×10^{-06}
1496	3FGL J2338.7+0251	1.16×10^{-06}	1559	3FGL J0224.1−1846	1.05×10^{-06}
1497	3FHL J1447.0−2657	1.16×10^{-06}	1560	3FGL J0211.2−0649	1.05×10^{-06}
1498	3FGL J1602.8−1924	1.15×10^{-06}	1561	3FGL J1837.3−2403	1.05×10^{-06}
1499	3FGL J1311.0+0036	1.15×10^{-06}	1562	3FGL J0604.1−4817	1.04×10^{-06}
1500	3FGL J0127.2+0325	1.15×10^{-06}	1563	3FGL J1817.7+2530	1.04×10^{-06}
1501	3FGL J0505.5−1558	1.15×10^{-06}	1564	3FGL J1129.0+3758	1.04×10^{-06}
1502	3FGL J0048.1−6343	1.15×10^{-06}	1565	3FGL J1608.6+1029	1.03×10^{-06}
1503	3FGL J0121.7+5154	1.14×10^{-06}	1566	3FGL J0718.9−5004	1.03×10^{-06}
1504	3FGL J0820.9−1258	1.14×10^{-06}	1567	3FGL J0423.2−0119	1.03×10^{-06}
1505	3FGL J2147.3−7536	1.14×10^{-06}	1568	3FGL J0506.9+0321	1.03×10^{-06}
1506	3FGL J1339.0+1153	1.14×10^{-06}	1569	3FGL J0003.4+3100	1.03×10^{-06}
1507	3FGL J1041.8+3901	1.14×10^{-06}	1570	3FGL J2116.9+1343	1.03×10^{-06}
1508	3FHL J0402.9+6433	1.13×10^{-06}	1571	3FGL J0818.0+3237	1.03×10^{-06}
1509	3FGL J0636.7+7115	1.13×10^{-06}	1572	3FGL J0509.7−0400	1.03×10^{-06}
1510	3FHL J0414.7+5711	1.13×10^{-06}	1573	3FGL J2055.0+0016	1.03×10^{-06}
1511	3FGL J1340.6−0408	1.13×10^{-06}	1574	3FGL J0630.3+6906	1.03×10^{-06}
1512	3FGL J0734.3−7709	1.12×10^{-06}	1575	3FGL J2358.3−2853	1.03×10^{-06}
1513	3FGL J2254.0+1403	1.12×10^{-06}	1576	3FGL J1422.8−7828	1.03×10^{-06}
1514	3FGL J1331.8+4718	1.12×10^{-06}	1577	3FGL J0742.6+5444	1.03×10^{-06}
1515	3FGL J1513.5−3233	1.12×10^{-06}	1578	3FGL J0046.7−8419	1.02×10^{-06}
1516	3FHL J0359.4−0235	1.12×10^{-06}	1579	3FGL J2327.2−4130	1.02×10^{-06}
1517	3FGL J2131.5−0915	1.12×10^{-06}	1580	3FGL J0039.1−0939	1.02×10^{-06}
1518	3FGL J1442.6+5156	1.12×10^{-06}	1581	3FGL J0826.3−5056	1.02×10^{-06}
1519	3FGL J1458.7−2120	1.11×10^{-06}	1582	3FGL J1304.8−0338	1.02×10^{-06}
1520	3FGL J2000.4−2926	1.11×10^{-06}	1583	3FGL J2300.1−3547	1.02×10^{-06}
1521	3FGL J0359.7+7649	1.11×10^{-06}	1584	3FGL J0525.8−2014	1.02×10^{-06}
1522	3FGL J0505.3−0422	1.11×10^{-06}	1585	3FGL J0137.0+4752	1.02×10^{-06}
1523	3FGL J2200.0−6930	1.11×10^{-06}	1586	3FGL J0430.2−2508	1.02×10^{-06}
1524	3FHL J0353.4+8256	1.11×10^{-06}	1587	3FGL J0608.6+5328	1.02×10^{-06}
1525	3FGL J1330.9+5201	1.11×10^{-06}	1588	3FGL J1347.6−3754	1.01×10^{-06}
1526	3FGL J1741.4+0938	1.10×10^{-06}	1589	3FGL J2230.5−7817	1.01×10^{-06}
1527	3FGL J1031.6+6021	1.10×10^{-06}	1590	3FGL J0301.4−1652	1.01×10^{-06}
1528	3FGL J0529.8−7242	1.10×10^{-06}	1591	3FGL J0707.2+6101	1.01×10^{-06}
1529	3FHL J0158.8+3314	1.10×10^{-06}	1592	3FGL J2315.7−5018	1.01×10^{-06}

Number	Source	Energy Flux [erg cm^{-2} s^{-1}]	Number	Source	Energy Flux [erg cm^{-2} s^{-1}]
1593	3FGL J1205.4+0412	1.01×10^{-06}	1656	3FGL J1421.0−2431	8.90×10^{-07}
1594	3FGL J0426.3+3510	1.00×10^{-06}	1657	3FGL J0045.2−3704	8.89×10^{-07}
1595	3FGL J0906.3−0906	1.00×10^{-06}	1658	3FGL J1849.5+2751	8.89×10^{-07}
1596	3FGL J0426.6+0459	9.96×10^{-07}	1659	3FGL J1047.6+7240	8.85×10^{-07}
1597	3FGL J0130.8+1441	9.96×10^{-07}	1660	3FGL J1732.7+5914	8.81×10^{-07}
1598	3FGL J0059.6+0003	9.93×10^{-07}	1661	3FGL J1357.6+7643	8.80×10^{-07}
1599	3FGL J0747.5−4927	9.91×10^{-07}	1662	3FGL J2357.3−0150	8.77×10^{-07}
1600	3FGL J0237.5−3603	9.89×10^{-07}	1663	3FGL J0217.1−0833	8.77×10^{-07}
1601	3FGL J2352.0+1752	9.82×10^{-07}	1664	3FGL J1848.1−4230	8.76×10^{-07}
1602	3FGL J0343.2−2534	9.80×10^{-07}	1665	3FGL J1656.2−3303	8.76×10^{-07}
1603	3FGL J1355.0−1044	9.79×10^{-07}	1666	3FGL J1326.1+2931	8.76×10^{-07}
1604	3FGL J1022.3−4234	9.78×10^{-07}	1667	3FGL J0514.6−4406	8.75×10^{-07}
1605	3FGL J1808.4−3703	9.78×10^{-07}	1668	3FGL J0437.7−7330	8.75×10^{-07}
1606	3FGL J0716.0−4525	9.78×10^{-07}	1669	3FGL J1430.8−4434	8.75×10^{-07}
1607	3FGL J0644.6+6035	9.77×10^{-07}	1670	3FGL J1642.4+8045	8.73×10^{-07}
1608	3FGL J1411.4−0724	9.75×10^{-07}	1671	3FGL J0733.8+4108	8.73×10^{-07}
1609	3FGL J0652.0−4808	9.75×10^{-07}	1672	3FGL J0700.6+3557	8.71×10^{-07}
1610	3FGL J0051.0−0649	9.70×10^{-07}	1673	3FGL J0958.3−0318	8.71×10^{-07}
1611	3FGL J0049.4−4149	9.70×10^{-07}	1674	3FHL J2225.8−0803	8.67×10^{-07}
1612	3FGL J1315.7−0732	9.68×10^{-07}	1675	3FGL J1159.3−2226	8.61×10^{-07}
1613	3FGL J1346.2−2608	9.67×10^{-07}	1676	3FGL J1632.8+3838	8.61×10^{-07}
1614	3FGL J1805.9+3407	9.61×10^{-07}	1677	3FGL J0216.1−7016	8.61×10^{-07}
1615	3FGL J1514.8−3623	9.59×10^{-07}	1678	3FGL J0310.4−5015	8.57×10^{-07}
1616	3FGL J0232.9+2606	9.58×10^{-07}	1679	3FHL J0845.8−5551	8.55×10^{-07}
1617	3FGL J1326.2−4651	9.57×10^{-07}	1680	3FGL J2118.4+0013	8.55×10^{-07}
1618	3FGL J0316.6+4119	9.56×10^{-07}	1681	3FGL J1728.0+1217	8.53×10^{-07}
1619	3FGL J1505.0−3432	9.56×10^{-07}	1682	3FGL J1407.7−4256	8.53×10^{-07}
1620	3FGL J1424.3−1753	9.56×10^{-07}	1683	3FGL J2144.6+6606	8.53×10^{-07}
1621	3FGL J0921.6+2339	9.54×10^{-07}	1684	3FGL J1816.0−6407	8.52×10^{-07}
1622	3FGL J2143.1−3928	9.48×10^{-07}	1685	3FGL J0538.4−3909	8.52×10^{-07}
1623	3FGL J0539.8+1434	9.44×10^{-07}	1686	3FGL J0934.1+3933	8.48×10^{-07}
1624	3FGL J2338.1−0229	9.42×10^{-07}	1687	3FGL J1007.8+0026	8.47×10^{-07}
1625	3FGL J1241.9+0639	9.42×10^{-07}	1688	3FGL J1438.6−4209	8.46×10^{-07}
1626	3FGL J1810.8+1609	9.40×10^{-07}	1689	3FGL J2042.3−5416	8.46×10^{-07}
1627	3FHL J0243.3+1915	9.36×10^{-07}	1690	3FGL J1105.9+2814	8.46×10^{-07}
1628	3FGL J1309.5+1154	9.36×10^{-07}	1691	3FGL J1319.3+1402	8.43×10^{-07}
1629	3FGL J1705.5+7134	9.33×10^{-07}	1692	3FHL J1243.0+7316	8.38×10^{-07}
1630	3FHL J1632.2+5801	9.30×10^{-07}	1693	3FGL J0725.8+0212	8.38×10^{-07}
1631	3FHL J2016.3+4953	9.28×10^{-07}	1694	3FGL J0516.6+1012	8.37×10^{-07}
1632	3FGL J0026.2−4812	9.27×10^{-07}	1695	3FGL J0830.3−5855	8.35×10^{-07}
1633	3FGL J1553.1+5437	9.27×10^{-07}	1696	3FGL J1143.0+6123	8.34×10^{-07}
1634	3FGL J0650.4−1636	9.24×10^{-07}	1697	3FGL J1040.9−1205	8.33×10^{-07}
1635	3FGL J1644.4+2632	9.22×10^{-07}	1698	3FGL J0403.7−2442	8.33×10^{-07}
1636	3FGL J0904.3+4240	9.20×10^{-07}	1699	3FGL J1418.9+7731	8.32×10^{-07}
1637	3FGL J1308.7+3545	9.19×10^{-07}	1700	3FGL J0230.8+4032	8.30×10^{-07}
1638	3FGL J0935.2+0903	9.18×10^{-07}	1701	3FGL J0156.5−2423	8.27×10^{-07}
1639	3FGL J0923.3+4127	9.16×10^{-07}	1702	3FGL J1506.3+4332	8.26×10^{-07}
1640	3FGL J1808.0+4652	9.14×10^{-07}	1703	3FGL J0439.6−3159	8.23×10^{-07}
1641	3FGL J2358.2−1022	9.11×10^{-07}	1704	3FGL J1705.5+0948	8.21×10^{-07}
1642	3FGL J1051.4+3941	9.10×10^{-07}	1705	3FGL J0228.7−3106	8.21×10^{-07}
1643	3FGL J0802.3−0941	9.09×10^{-07}	1706	3FGL J1213.7+1306	8.19×10^{-07}
1644	3FGL J0647.1−4415	9.08×10^{-07}	1707	3FGL J0957.5−1351	8.18×10^{-07}
1645	3FGL J2133.6+2821	9.03×10^{-07}	1708	3FGL J1220.3+6055	8.16×10^{-07}
1646	3FGL J1345.1+1949	9.03×10^{-07}	1709	3FGL J1617.3−2519	8.15×10^{-07}
1647	3FGL J0008.6−2340	9.02×10^{-07}	1710	3FGL J2254.6+4253	8.15×10^{-07}
1648	3FGL J0308.4−2852	8.99×10^{-07}	1711	3FGL J0425.0−5331	8.14×10^{-07}
1649	3FGL J0403.9−3604	8.99×10^{-07}	1712	3FGL J0931.8+6739	8.14×10^{-07}
1650	3FHL J0441.6+1504	8.98×10^{-07}	1713	3FGL J0042.0+2318	8.13×10^{-07}
1651	3FGL J1356.3−4029	8.96×10^{-07}	1714	3FGL J1003.6+2608	8.12×10^{-07}
1652	3FGL J2014.5+5246	8.93×10^{-07}	1715	3FGL J1117.7−4632	8.11×10^{-07}
1653	3FGL J1434.1+4203	8.92×10^{-07}	1716	3FGL J1911.1−5318	8.10×10^{-07}
1654	3FGL J0530.8+1330	8.91×10^{-07}	1717	3FGL J1107.4−4447	8.07×10^{-07}
1655	3FGL J0338.1−2443	8.90×10^{-07}	1718	3FGL J1351.1+0030	8.05×10^{-07}

Number	Source	Energy Flux [erg cm^{-2} s^{-1}]	Number	Source	Energy Flux [erg cm^{-2} s^{-1}]
1719	3FGL J1815.1+5919	8.01×10^{-07}	1782	3FGL J1549.9−3044	7.22×10^{-07}
1720	3FGL J2007.7−7728	7.99×10^{-07}	1783	3FGL J1154.3+6023	7.20×10^{-07}
1721	3FHL J0856.8+5136	7.99×10^{-07}	1784	3FGL J1442.0+4348	7.18×10^{-07}
1722	3FGL J0204.8+3212	7.95×10^{-07}	1785	3FGL J0749.5+1320	7.17×10^{-07}
1723	3FGL J1150.7−4816	7.95×10^{-07}	1786	3FGL J1331.5+1711	7.16×10^{-07}
1724	3FGL J0649.6−3138	7.95×10^{-07}	1787	3FGL J1218.8−4827	7.16×10^{-07}
1725	3FGL J0444.5+3425	7.92×10^{-07}	1788	3FGL J2358.0−4552	7.15×10^{-07}
1726	3FGL J1549.5+1709	7.88×10^{-07}	1789	3FGL J0919.5−2200	7.15×10^{-07}
1727	3FGL J0909.1+0121	7.85×10^{-07}	1790	3FGL J2357.8−5310	7.14×10^{-07}
1728	3FGL J0647.0−5134	7.82×10^{-07}	1791	3FGL J1200.9−1432	7.12×10^{-07}
1729	3FGL J0434.0−2010	7.82×10^{-07}	1792	3FGL J0202.3+0851	7.11×10^{-07}
1730	3FGL J0952.8+0711	7.82×10^{-07}	1793	3FGL J1333.8−4417	7.08×10^{-07}
1731	3FGL J1344.2−1724	7.80×10^{-07}	1794	3FGL J2141.7−3734	7.08×10^{-07}
1732	3FGL J0928.7+7300	7.80×10^{-07}	1795	3FGL J0835.4+0930	7.08×10^{-07}
1733	3FGL J1711.6+8846	7.78×10^{-07}	1796	3FGL J2220.3+2812	7.00×10^{-07}
1734	3FGL J0252.3+3830	7.76×10^{-07}	1797	3FGL J1625.0+5651	6.97×10^{-07}
1735	3FGL J2135.3−5008	7.75×10^{-07}	1798	3FGL J2305.3−4219	6.95×10^{-07}
1736	3FGL J0905.8−2127	7.75×10^{-07}	1799	3FGL J0042.5+4117	6.92×10^{-07}
1737	3FGL J0213.1−2720	7.74×10^{-07}	1800	3FGL J1454.2−3751	6.89×10^{-07}
1738	3FGL J1304.6+1200	7.73×10^{-07}	1801	3FGL J0643.4−5358	6.88×10^{-07}
1739	3FGL J1502.2+5553	7.72×10^{-07}	1802	3FHL J1915.2−1323	6.86×10^{-07}
1740	3FGL J2110.0+0812	7.71×10^{-07}	1803	3FGL J0048.0+2236	6.86×10^{-07}
1741	3FGL J1258.7+5137	7.70×10^{-07}	1804	3FGL J0846.8−2638	6.86×10^{-07}
1742	3FGL J1220.0−2502	7.70×10^{-07}	1805	3FGL J1630.3−6126	6.83×10^{-07}
1743	3FGL J0658.8+2318	7.68×10^{-07}	1806	3FGL J2354.1+4605	6.82×10^{-07}
1744	3FGL J0615.4−3116	7.67×10^{-07}	1807	3FGL J0325.2+3410	6.81×10^{-07}
1745	3FGL J1804.1+2532	7.66×10^{-07}	1808	3FGL J0834.1+4223	6.79×10^{-07}
1746	3FGL J1228.7+4857	7.65×10^{-07}	1809	3FGL J0527.3+6647	6.79×10^{-07}
1747	3FGL J0830.7+2408	7.65×10^{-07}	1810	3FGL J1748.0+3405	6.78×10^{-07}
1748	3FGL J1528.1−2904	7.64×10^{-07}	1811	3FGL J0019.1−5645	6.76×10^{-07}
1749	3FGL J1222.7+7952	7.62×10^{-07}	1812	3FGL J0507.1−6102	6.74×10^{-07}
1750	3FGL J0813.5−0356	7.62×10^{-07}	1813	3FGL J0358.8+6002	6.74×10^{-07}
1751	3FGL J1028.0+1829	7.61×10^{-07}	1814	3FGL J2323.7+2523	6.74×10^{-07}
1752	3FGL J0503.5+6538	7.61×10^{-07}	1815	3FGL J1136.6−6826	6.72×10^{-07}
1753	3FGL J0016.5+1713	7.60×10^{-07}	1816	3FGL J0937.7+5008	6.72×10^{-07}
1754	3FGL J2156.9−0855	7.59×10^{-07}	1817	3FGL J0758.7+3747	6.71×10^{-07}
1755	3FGL J2114.7+3130	7.59×10^{-07}	1818	3FGL J1117.0+2014	6.69×10^{-07}
1756	3FGL J1637.1+1314	7.56×10^{-07}	1819	3FGL J1658.3+6149	6.68×10^{-07}
1757	3FGL J0622.9+3326	7.55×10^{-07}	1820	3FGL J1136.9+2551	6.68×10^{-07}
1758	3FGL J0840.8+1315	7.54×10^{-07}	1821	3FGL J1216.6−0557	6.67×10^{-07}
1759	3FGL J0623.1−4143	7.53×10^{-07}	1822	3FGL J1037.4−3742	6.67×10^{-07}
1760	3FGL J0132.1−5340	7.48×10^{-07}	1823	3FGL J1112.1+0500	6.63×10^{-07}
1761	3FGL J2059.9+2029	7.47×10^{-07}	1824	3FGL J1153.7−2555	6.60×10^{-07}
1762	3FGL J2043.6+0001	7.45×10^{-07}	1825	3FGL J2014.9+1623	6.60×10^{-07}
1763	3FGL J0202.5+4206	7.44×10^{-07}	1826	3FGL J1616.4+4631	6.56×10^{-07}
1764	3FGL J1239.4+0727	7.44×10^{-07}	1827	3FGL J1200.9+2010	6.53×10^{-07}
1765	3FGL J1516.9+1926	7.42×10^{-07}	1828	3FGL J2221.6+6507	6.52×10^{-07}
1766	3FGL J1301.5+3333	7.42×10^{-07}	1829	3FGL J0128.5+4430	6.51×10^{-07}
1767	3FGL J0139.9+8735	7.40×10^{-07}	1830	3FGL J1100.2−2044	6.51×10^{-07}
1768	3FGL J0941.6+2727	7.40×10^{-07}	1831	3FGL J1525.8−0834	6.48×10^{-07}
1769	3FGL J0822.9+4041	7.39×10^{-07}	1832	3FGL J2109.4+1437	6.47×10^{-07}
1770	3FGL J0533.6−8323	7.39×10^{-07}	1833	3FGL J0303.0+3150	6.46×10^{-07}
1771	3FGL J0257.8−1216	7.37×10^{-07}	1834	3FGL J1028.5−0235	6.45×10^{-07}
1772	3FGL J1112.4+3449	7.36×10^{-07}	1835	3FGL J1341.5+5517	6.44×10^{-07}
1773	3FGL J1757.4+6536	7.36×10^{-07}	1836	3FGL J0229.3−3643	6.43×10^{-07}
1774	3FGL J1419.8+3819	7.36×10^{-07}	1837	3FGL J1123.6+7231	6.43×10^{-07}
1775	3FGL J0240.0−0253	7.36×10^{-07}	1838	3FGL J2329.3−4955	6.39×10^{-07}
1776	3FGL J0855.2−0718	7.35×10^{-07}	1839	3FHL J1130.7−3137	6.38×10^{-07}
1777	3FGL J2017.6−4110	7.27×10^{-07}	1840	3FGL J0447.8−2119	6.34×10^{-07}
1778	3FGL J0214.7−5823	7.26×10^{-07}	1841	3FGL J1409.2−3743	6.30×10^{-07}
1779	3FGL J2235.6−2319	7.25×10^{-07}	1842	3FGL J0704.3−4828	6.27×10^{-07}
1780	3FGL J1117.7+0217	7.25×10^{-07}	1843	3FGL J0222.1−1616	6.26×10^{-07}
1781	3FGL J0600.9−3943	7.23×10^{-07}	1844	3FGL J2335.1−0133	6.26×10^{-07}

Number	Source	Energy Flux [erg cm^{-2} s^{-1}]	Number	Source	Energy Flux [erg cm^{-2} s^{-1}]
1845	3FGL J1427.2+1610	6.22×10^{-07}	1908	3FGL J0016.3−0013	5.05×10^{-07}
1846	3FGL J0208.0−6838	6.22×10^{-07}	1909	3FGL J1024.4−4545	5.05×10^{-07}
1847	3FGL J0550.3−4521	6.21×10^{-07}	1910	3FGL J0222.9−1117	5.04×10^{-07}
1848	3FGL J1338.9+6532	6.16×10^{-07}	1911	3FGL J1539.5+2746	5.03×10^{-07}
1849	3FGL J0000.2−3738	6.15×10^{-07}	1912	3FGL J0029.1−7045	5.02×10^{-07}
1850	3FGL J1209.9+7607	6.15×10^{-07}	1913	3FGL J0133.3+4324	5.01×10^{-07}
1851	3FGL J1628.7−8056	6.14×10^{-07}	1914	3FGL J1131.1+5810	4.95×10^{-07}
1852	3FGL J0526.6+6321	6.13×10^{-07}	1915	3FGL J0225.2−2602	4.95×10^{-07}
1853	3FGL J0216.0+0300	6.12×10^{-07}	1916	3FGL J0103.7+1323	4.92×10^{-07}
1854	3FGL J1038.0−2425	6.02×10^{-07}	1917	3FGL J1104.3+0730	4.91×10^{-07}
1855	3FGL J1244.8+5707	6.00×10^{-07}	1918	3FGL J2132.4−5420	4.91×10^{-07}
1856	3FGL J0733.3+5904	6.00×10^{-07}	1919	3FGL J0601.2−7036	4.90×10^{-07}
1857	3FGL J0031.2−2320	5.99×10^{-07}	1920	3FGL J1415.0−1001	4.89×10^{-07}
1858	3FGL J1308.1−6707	5.98×10^{-07}	1921	3FGL J0724.1+2857	4.86×10^{-07}
1859	3FGL J1021.8+8023	5.98×10^{-07}	1922	3FGL J0132.5−0802	4.84×10^{-07}
1860	3FGL J1550.4+6027	5.97×10^{-07}	1923	3FGL J0004.2+0843	4.84×10^{-07}
1861	3FGL J1013.5+3440	5.94×10^{-07}	1924	3FGL J0740.6−5230	4.83×10^{-07}
1862	3FGL J1830.0−4439	5.94×10^{-07}	1925	3FGL J1723.5−5609	4.80×10^{-07}
1863	3FGL J0006.2+0135	5.92×10^{-07}	1926	3FGL J0540.5−5416	4.69×10^{-07}
1864	3FHL J1048.4−5030	5.90×10^{-07}	1927	3FGL J0022.7+4651	4.68×10^{-07}
1865	3FGL J0812.9+5555	5.88×10^{-07}	1928	3FGL J0858.1−1951	4.67×10^{-07}
1866	3FGL J2040.0−5734	5.87×10^{-07}	1929	3FGL J0451.6+7231	4.67×10^{-07}
1867	3FGL J2250.3−4206	5.87×10^{-07}	1930	3FGL J0502.5+0612	4.60×10^{-07}
1868	3FGL J0342.2+3857	5.85×10^{-07}	1931	3FGL J0421.6+1950	4.56×10^{-07}
1869	3FGL J2318.6+1912	5.84×10^{-07}	1932	3FGL J0156.3+3913	4.55×10^{-07}
1870	3FGL J1303.7−4619	5.78×10^{-07}	1933	3FGL J0102.3+4217	4.54×10^{-07}
1871	3FGL J0746.9+8511	5.78×10^{-07}	1934	3FGL J0434.4−2341	4.53×10^{-07}
1872	3FGL J2344.4+0549	5.77×10^{-07}	1935	3FGL J1808.3−3357	4.53×10^{-07}
1873	3FGL J1417.7−5026	5.73×10^{-07}	1936	3FGL J1403.1+1304	4.53×10^{-07}
1874	3FGL J2107.7−4822	5.72×10^{-07}	1937	3FGL J1625.2−2845	4.51×10^{-07}
1875	3FGL J0133.2−4737	5.69×10^{-07}	1938	3FGL J1643.6−0642	4.44×10^{-07}
1876	3FGL J0107.0−1208	5.63×10^{-07}	1939	3FGL J1050.4+0435	4.44×10^{-07}
1877	3FGL J0628.4+2429	5.63×10^{-07}	1940	3FGL J1212.6+5135	4.43×10^{-07}
1878	3FGL J1625.9+4125	5.57×10^{-07}	1941	3FGL J0809.5+4045	4.42×10^{-07}
1879	3FGL J0049.8−5737	5.56×10^{-07}	1942	3FGL J1258.0+6120	4.38×10^{-07}
1880	3FGL J0218.9+3642	5.56×10^{-07}	1943	3FGL J0418.2+3412	4.38×10^{-07}
1881	3FGL J2243.2−3933	5.55×10^{-07}	1944	3FGL J0030.7−0209	4.38×10^{-07}
1882	3FGL J2029.5−4232	5.54×10^{-07}	1945	3FGL J1702.6+3116	4.36×10^{-07}
1883	3FGL J0324.5−1315	5.53×10^{-07}	1946	3FGL J2044.0+1035	4.34×10^{-07}
1884	3FGL J2329.9−4734	5.53×10^{-07}	1947	3FGL J0055.2−1213	4.33×10^{-07}
1885	3FGL J1147.8−0725	5.50×10^{-07}	1948	3FGL J0010.5−1425	4.33×10^{-07}
1886	3FGL J0111.5+0535	5.49×10^{-07}	1949	3FGL J0958.6−2447	4.29×10^{-07}
1887	3FGL J2100.6−7844	5.46×10^{-07}	1950	3FGL J0323.7−6038	4.29×10^{-07}
1888	3FGL J1014.2+4115	5.42×10^{-07}	1951	3FGL J1534.4+5323	4.27×10^{-07}
1889	3FGL J0945.9+5756	5.35×10^{-07}	1952	3FGL J2312.9−6923	4.26×10^{-07}
1890	3FGL J1322.3+0839	5.28×10^{-07}	1953	3FGL J1723.9+4004	4.22×10^{-07}
1891	3FGL J0109.9−4020	5.28×10^{-07}	1954	3FGL J0916.3+3857	4.20×10^{-07}
1892	3FGL J1528.7−2247	5.27×10^{-07}	1955	3FGL J1142.1−6941	4.19×10^{-07}
1893	3FGL J0521.9−3847	5.24×10^{-07}	1956	3FGL J0031.3+0724	4.17×10^{-07}
1894	3FGL J2006.5−0939	5.22×10^{-07}	1957	3FGL J1002.0−2837	4.14×10^{-07}
1895	3FGL J2353.3−4805	5.22×10^{-07}	1958	3FGL J2307.7+1449	4.10×10^{-07}
1896	3FGL J0748.8+4929	5.19×10^{-07}	1959	3FGL J1731.9+5428	4.08×10^{-07}
1897	3FGL J1855.1−6008	5.18×10^{-07}	1960	3FGL J1839.9+7646	4.06×10^{-07}
1898	3FGL J0357.1+2325	5.17×10^{-07}	1961	3FGL J0340.4−2423	4.02×10^{-07}
1899	3FGL J0309.5−0749	5.17×10^{-07}	1962	3FGL J0145.1−2732	4.01×10^{-07}
1900	3FGL J0301.8−7157	5.16×10^{-07}	1963	3FGL J2121.5−8253	3.97×10^{-07}
1901	3FGL J0456.3+2702	5.14×10^{-07}	1964	3FGL J0150.5−5447	3.97×10^{-07}
1902	3FGL J0007.4+1742	5.12×10^{-07}	1965	3FGL J0006.4+3825	3.97×10^{-07}
1903	3FGL J0444.6−6012	5.12×10^{-07}	1966	3FGL J0326.0−1842	3.94×10^{-07}
1904	3FGL J0310.8+3814	5.10×10^{-07}	1967	3FGL J1035.2+5545	3.92×10^{-07}
1905	3FGL J0747.4−0734	5.09×10^{-07}	1968	3FGL J0047.9+5447	3.88×10^{-07}
1906	3FGL J0647.6−6058	5.07×10^{-07}	1969	3FGL J1136.4+3405	3.87×10^{-07}
1907	3FGL J0351.4−3248	5.07×10^{-07}	1970	3FGL J2151.6−2744	3.83×10^{-07}

Number	Source	Energy Flux [erg cm^{-2} s^{-1}]	Number	Source	Energy Flux [erg cm^{-2} s^{-1}]
1971	3FGL J1531.8+4704	3.80×10^{-07}	2034	3FHL J1433.5−7304	2.61×10^{-07}
1972	3FGL J0333.4+4003	3.77×10^{-07}	2035	3FHL J0215.2+7555	2.61×10^{-07}
1973	3FGL J1341.0+3955	3.75×10^{-07}	2036	3FGL J2229.1+2255	2.61×10^{-07}
1974	3FGL J0336.9−1304	3.75×10^{-07}	2037	3FGL J1229.8−5305	2.56×10^{-07}
1975	3FGL J0105.3+3928	3.73×10^{-07}	2038	3FGL J0836.5−2020	2.56×10^{-07}
1976	3FGL J1722.7+6104	3.73×10^{-07}	2039	3FGL J2205.9−4704	2.55×10^{-07}
1977	3FGL J0224.1−7941	3.68×10^{-07}	2040	3FGL J1343.6+5753	2.51×10^{-07}
1978	3FGL J1312.7+4828	3.65×10^{-07}	2041	3FGL J1512.3+8005	2.41×10^{-07}
1979	3FGL J1949.4−6140	3.62×10^{-07}	2042	3FGL J2343.6+1551	2.37×10^{-07}
1980	3FGL J0211.0+1922	3.60×10^{-07}	2043	3FGL J0414.9−0840	2.37×10^{-07}
1981	3FGL J2005.7−8241	3.59×10^{-07}	2044	3FGL J0939.9−2831	2.30×10^{-07}
1982	3FGL J0336.9−3622	3.58×10^{-07}	2045	3FGL J0959.7+2124	2.27×10^{-07}
1983	3FGL J2120.4−1256	3.56×10^{-07}	2046	3FGL J2202.4−8339	2.27×10^{-07}
1984	3FGL J0447.1−2540	3.55×10^{-07}	2047	3FHL J0102.8−2001	2.23×10^{-07}
1985	3FGL J0358.7+0633	3.53×10^{-07}	2048	3FGL J1418.5+3543	2.22×10^{-07}
1986	3FGL J2236.0−1706	3.51×10^{-07}	2049	3FHL J1403.4+4319	2.21×10^{-07}
1987	3FGL J0031.6+0938	3.50×10^{-07}	2050	3FGL J1532.0−2618	2.20×10^{-07}
1988	3FGL J1027.8+8253	3.49×10^{-07}	2051	3FGL J0151.0+0537	2.19×10^{-07}
1989	3FGL J0928.5+4048	3.47×10^{-07}	2052	3FGL J2237.1−3921	2.19×10^{-07}
1990	3FGL J1038.9−5311	3.45×10^{-07}	2053	3FGL J0239.0+2555	2.12×10^{-07}
1991	3FGL J1536.6+8331	3.44×10^{-07}	2054	3FHL J1748.5−0854	2.07×10^{-07}
1992	3FGL J1001.0+2913	3.43×10^{-07}	2055	3FGL J2307.4−1208	2.07×10^{-07}
1993	3FGL J1145.8+4425	3.39×10^{-07}	2056	3FGL J1028.3−7419	2.07×10^{-07}
1994	3FGL J1739.0+8716	3.38×10^{-07}	2057	3FGL J0807.1+7744	2.00×10^{-07}
1995	3FGL J0351.1+0128	3.37×10^{-07}	2058	3FGL J1842.3−5841	1.98×10^{-07}
1996	3FGL J1330.6+7002	3.35×10^{-07}	2059	3FGL J0828.5+5217	1.97×10^{-07}
1997	3FGL J0728.0+4828	3.35×10^{-07}	2060	3FGL J0039.1+4330	1.94×10^{-07}
1998	3FGL J1018.1+1904	3.34×10^{-07}	2061	3FGL J1045.5−2335	1.93×10^{-07}
1999	3FGL J1529.5+6733	3.32×10^{-07}	2062	3FGL J1948.1−7059	1.90×10^{-07}
2000	3FGL J2222.3−3500	3.32×10^{-07}	2063	3FGL J0352.9+5655	1.89×10^{-07}
2001	3FGL J1032.5+6623	3.31×10^{-07}	2064	3FGL J0823.6−4838	1.87×10^{-07}
2002	3FGL J1327.9+2524	3.23×10^{-07}	2065	3FGL J1330.5+3023	1.85×10^{-07}
2003	3FGL J1650.0+0356	3.21×10^{-07}	2066	3FGL J1408.0−2924	1.81×10^{-07}
2004	3FGL J1016.9−2653	3.21×10^{-07}	2067	3FGL J1635.3+4257	1.81×10^{-07}
2005	3FGL J1517.0+2637	3.19×10^{-07}	2068	3FGL J1729.0+6049	1.78×10^{-07}
2006	3FGL J0508.2−1936	3.19×10^{-07}	2069	3FGL J2126.5−3926	1.76×10^{-07}
2007	3FGL J0359.3−2612	3.19×10^{-07}	2070	3FGL J1350.8+3035	1.75×10^{-07}
2008	3FGL J0017.6−0512	3.17×10^{-07}	2071	3FGL J0611.1−6100	1.73×10^{-07}
2009	3FGL J0948.1−3641	3.16×10^{-07}	2072	3FGL J1010.8−0158	1.71×10^{-07}
2010	3FGL J1236.6+3901	3.15×10^{-07}	2073	3FGL J0930.7+5133	1.71×10^{-07}
2011	3FGL J0058.3+3315	3.13×10^{-07}	2074	3FGL J1330.1−7002	1.70×10^{-07}
2012	3FGL J1606.1+5630	3.12×10^{-07}	2075	3FGL J0126.1−2227	1.67×10^{-07}
2013	3FGL J1709.9+4624	3.06×10^{-07}	2076	3FGL J0152.2+3707	1.63×10^{-07}
2014	3FGL J1123.3−2529	3.06×10^{-07}	2077	3FGL J1618.8+5520	1.62×10^{-07}
2015	3FGL J0946.2+5209	3.03×10^{-07}	2078	3FGL J1207.6−2232	1.61×10^{-07}
2016	3FGL J0939.2−1732	3.01×10^{-07}	2079	3FGL J1321.7+8312	1.51×10^{-07}
2017	3FGL J0354.6+8011	3.01×10^{-07}	2080	3FGL J1421.0−1122	1.50×10^{-07}
2018	3FGL J0127.5+5634	2.97×10^{-07}	2081	3FGL J1512.3+6622	1.48×10^{-07}
2019	3FGL J1730.6+3711	2.97×10^{-07}	2082	3FGL J0200.9−6635	1.48×10^{-07}
2020	3FGL J0725.8−3532	2.94×10^{-07}	2083	3FGL J1310.7+5515	1.46×10^{-07}
2021	3FGL J0638.6+7324	2.94×10^{-07}	2084	3FGL J0807.9+4946	1.45×10^{-07}
2022	3FGL J0108.5−0035	2.94×10^{-07}	2085	3FHL J0350.0+0640	1.43×10^{-07}
2023	3FGL J1520.3+4209	2.94×10^{-07}	2086	3FGL J1045.7−2926	1.38×10^{-07}
2024	3FGL J0137.6−2430	2.94×10^{-07}	2087	3FGL J1959.1−4245	1.36×10^{-07}
2025	3FGL J0923.1+3853	2.92×10^{-07}	2088	3FGL J0836.3+2143	1.36×10^{-07}
2026	3FGL J1918.0+3750	2.89×10^{-07}	2089	3FGL J0342.6−3006	1.33×10^{-07}
2027	3FGL J0127.6+4851	2.87×10^{-07}	2090	3FGL J0926.3+5409	1.33×10^{-07}
2028	3FGL J0255.8+0532	2.81×10^{-07}	2091	3FGL J1637.8+7325	1.29×10^{-07}
2029	3FGL J1531.0+5737	2.78×10^{-07}	2092	3FGL J1200.4+0202	1.23×10^{-07}
2030	3FGL J0125.2−0627	2.77×10^{-07}	2093	3FGL J0114.8+1917	1.19×10^{-07}
2031	3FGL J0732.2−4638	2.74×10^{-07}	2094	3FHL J0233.9+8042	1.16×10^{-07}
2032	3FHL J1726.2−1710	2.73×10^{-07}	2095	3FGL J1801.5−7825	1.16×10^{-07}
2033	3FGL J1341.9−2053	2.69×10^{-07}	2096	3FHL J1624.9+2328	1.10×10^{-07}

Number	Source	Energy Flux [erg cm^{-2} s^{-1}]	Number	Source	Energy Flux [erg cm^{-2} s^{-1}]
2097	3FGL J1807.8−5011	1.06×10^{-07}	2160	3FGL J2337.5+4108	3.21×10^{-10}
2098	3FGL J1251.3+1041	1.06×10^{-07}	2161	3FHL J1811.2−2800	3.06×10^{-10}
2099	3FHL J0709.1−1525	1.03×10^{-07}	2162	3FGL J0512.0−3737	3.05×10^{-10}
2100	3FGL J0502.6+1759	1.03×10^{-07}	2163	3FGL J1507.6−3710	2.85×10^{-10}
2101	3FGL J0915.0+5844	1.02×10^{-07}	2164	3FGL J0540.0+1208	2.76×10^{-10}
2102	3FGL J0654.5+0926	9.57×10^{-08}	2165	3FGL J1659.4+2631	2.73×10^{-10}
2103	3FHL J2317.8+2839	9.52×10^{-08}	2166	3FGL J1103.3+5239	2.35×10^{-10}
2104	3FGL J2110.3−1013	9.47×10^{-08}	2167	3FHL J1340.0−1501	2.33×10^{-10}
2105	3FHL J0213.9−6950	9.46×10^{-08}	2168	3FHL J1729.9−4148	1.75×10^{-10}
2106	3FGL J0825.4−0213	9.35×10^{-08}	2169	3FGL J2107.1+2248	1.71×10^{-10}
2107	3FHL J1923.4−2502	9.27×10^{-08}	2170	3FGL J1214.4−2315	1.68×10^{-10}
2108	3FGL J1016.1+5555	9.18×10^{-08}	2171	3FHL J0930.7−3031	1.62×10^{-10}
2109	3FGL J1813.6−6845	9.11×10^{-08}	2172	3FGL J2030.2−0622	1.60×10^{-10}
2110	3FGL J1521.8+4340	8.83×10^{-08}	2173	3FHL J1907.0+0713	1.52×10^{-10}
2111	3FHL J2030.2−5037	8.78×10^{-08}	2174	3FHL J1353.8−3936	1.45×10^{-10}
2112	3FGL J1514.1+2940	8.42×10^{-08}	2175	3FGL J1016.0+0513	1.38×10^{-10}
2113	3FGL J0102.1+4458	8.27×10^{-08}	2176	3FGL J2334.1+0732	1.28×10^{-10}
2114	3FGL J1955.1+1357	8.06×10^{-08}	2177	3FGL J2146.7−1527	1.26×10^{-10}
2115	3FGL J1835.4+1349	7.65×10^{-08}	2178	3FGL J2224.4+0351	1.26×10^{-10}
2116	3FGL J0714.7−3924	7.38×10^{-08}	2179	3FGL J1806.2+2744	1.20×10^{-10}
2117	3FGL J2150.5−1754	6.49×10^{-08}	2180	3FHL J1753.9+2442	1.12×10^{-10}
2118	3FGL J1656.9+6008	6.32×10^{-08}	2181	3FGL J1105.7+4427	1.07×10^{-10}
2119	3FGL J2249.3−5943	5.89×10^{-08}	2182	3FGL J0154.1+4642	9.78×10^{-11}
2120	3FGL J2118.3+5751	5.43×10^{-08}	2183	3FGL J0946.2+0103	8.06×10^{-11}
2121	3FHL J1917.9+0331	4.98×10^{-08}	2184	3FHL J1959.9−4606	8.04×10^{-11}
2122	3FGL J2159.8+1025	4.40×10^{-08}	2185	3FHL J0140.3+7054	7.80×10^{-11}
2123	3FGL J1024.1−3232	4.28×10^{-08}	2186	3FHL J1457.8−4642	7.55×10^{-11}
2124	3FGL J0438.3−1258	4.17×10^{-08}	2187	3FGL J0226.3+0941	7.37×10^{-11}
2125	3FGL J1617.8+5137	3.88×10^{-08}	2188	3FGL J1215.9−1926	7.27×10^{-11}
2126	3FGL J1123.2−6415	3.38×10^{-08}	2189	3FHL J1405.8−1854	6.92×10^{-11}
2127	3FGL J0537.0+0957	3.27×10^{-08}	2190	3FHL J1034.8−4645	6.15×10^{-11}
2128	3FGL J2046.7−4259	3.14×10^{-08}	2191	3FHL J1924.2−1548	5.48×10^{-11}
2129	3FHL J2109.6+3954	2.62×10^{-08}	2192	3FGL J1140.4+1529	5.37×10^{-11}
2130	3FGL J1359.2+0204	2.48×10^{-08}	2193	3FHL J0121.8+3808	5.21×10^{-11}
2131	3FGL J0710.5+4732	2.40×10^{-08}	2194	3FGL J1541.8+1105	5.00×10^{-11}
2132	3FGL J2358.9+3926	2.39×10^{-08}	2195	3FHL J1925.4+3706	4.58×10^{-11}
2133	3FGL J2236.2−5049	2.18×10^{-08}	2196	3FGL J0157.9−4615	4.46×10^{-11}
2134	3FHL J0725.5−0504	2.08×10^{-08}	2197	3FGL J0024.4+0350	4.29×10^{-11}
2135	3FHL J0549.1+3258	1.56×10^{-08}	2198	3FHL J0041.7−1608	4.12×10^{-11}
2136	3FHL J2156.4−0036	1.26×10^{-08}	2199	3FHL J2256.0−7119	3.90×10^{-11}
2137	3FGL J1759.1−4822	1.23×10^{-08}	2200	3FHL J1754.2−4334	3.86×10^{-11}
2138	3FGL J1205.9+3315	1.20×10^{-08}	2201	3FGL J1057.6−4051	3.79×10^{-11}
2139	3FGL J1807.8+6427	1.09×10^{-08}	2202	3FGL J1644.6−0911	3.77×10^{-11}
2140	3FHL J0350.4−5143	9.42×10^{-09}	2203	3FGL J1225.4−3448	3.74×10^{-11}
2141	3FHL J0842.8+6656	8.50×10^{-09}	2204	3FGL J1051.0+5332	3.72×10^{-11}
2142	3FGL J2210.2+6509	8.00×10^{-09}	2205	3FGL J0834.6+6101	3.51×10^{-11}
2143	3FHL J0559.5+6409	7.03×10^{-09}	2206	3FGL J1446.1−1628	3.46×10^{-11}
2144	3FHL J1648.1−1548	5.22×10^{-09}	2207	3FGL J0148.6+0128	3.43×10^{-11}
2145	3FGL J0901.0−6725	4.19×10^{-09}	2208	3FGL J1450.4+0911	3.31×10^{-11}
2146	3FHL J0133.1−4533	3.26×10^{-09}	2209	3FGL J2002.7+6303	3.16×10^{-11}
2147	3FHL J1528.4−6730	3.24×10^{-09}	2210	3FGL J2337.2−8425	3.04×10^{-11}
2148	3FGL J0756.3−6433	2.82×10^{-09}	2211	3FGL J0134.3−3842	2.97×10^{-11}
2149	3FHL J0550.9+5657	2.52×10^{-09}	2212	3FGL J0049.0+4224	2.90×10^{-11}
2150	3FHL J0901.5+6712	1.95×10^{-09}	2213	3FGL J0917.3−0344	2.69×10^{-11}
2151	3FGL J2212.3−7039	1.87×10^{-09}	2214	3FHL J0459.3+1921	2.52×10^{-11}
2152	3FGL J0203.6+1148	1.71×10^{-09}	2215	3FGL J0757.5−0536	2.39×10^{-11}
2153	3FHL J2002.5−7119	9.35×10^{-10}	2216	3FHL J1650.9+0430	2.33×10^{-11}
2154	3FHL J1744.5−2609	8.99×10^{-10}	2217	3FGL J1322.8−0938	2.25×10^{-11}
2155	3FHL J1439.4−2524	5.32×10^{-10}	2218	3FGL J2025.1−2858	2.16×10^{-11}
2156	3FHL J2240.3−5240	5.23×10^{-10}	2219	3FHL J0838.5+4006	2.14×10^{-11}
2157	3FHL J1421.5−1654	4.36×10^{-10}	2220	3FGL J0204.2+2420	2.12×10^{-11}
2158	3FHL J1626.4+6257	4.15×10^{-10}	2221	3FGL J0758.1+1130	2.02×10^{-11}
2159	3FHL J2042.7+1520	4.14×10^{-10}	2222	3FGL J0221.2+2518	1.99×10^{-11}

Number	Source	Energy Flux [erg cm^{-2} s^{-1}]
2223	3FHL J2058.8−1442	1.98×10^{-11}
2224	3FHL J0856.4−5308	1.97×10^{-11}
2225	3FGL J1559.8−2525	1.88×10^{-11}
2226	3FGL J1112.1+1034	1.80×10^{-11}
2227	3FHL J1547.3−1530	1.71×10^{-11}
2228	3FGL J0856.4+6429	1.67×10^{-11}
2229	3FGL J1330.0−3818	1.61×10^{-11}
2230	3FGL J1628.1+0254	1.55×10^{-11}
2231	3FHL J1643.7+3317	1.49×10^{-11}
2232	3FGL J0927.9−2037	1.42×10^{-11}
2233	3FGL J2127.1−5615	1.19×10^{-11}
2234	3FGL J1109.4−4815	1.11×10^{-11}
2235	3FGL J1541.6+1414	1.04×10^{-11}
2236	3FHL J2052.5+0810	1.02×10^{-11}
2237	3FGL J1223.2+1215	9.85×10^{-12}
2238	3FGL J2106.1+2505	8.89×10^{-12}
2239	3FGL J2330.5+1104	8.55×10^{-12}
2240	3FGL J1149.1+2815	8.28×10^{-12}
2241	3FGL J1138.2+4905	8.07×10^{-12}
2242	3FHL J2000.4−1327	7.42×10^{-12}
2243	3FGL J1506.4−0340	7.33×10^{-12}
2244	3FHL J1855.5+0142	7.26×10^{-12}
2245	3FGL J0050.0−4458	7.16×10^{-12}
2246	3FGL J1048.8−5006	7.14×10^{-12}
2247	3FGL J0805.4+6144	6.72×10^{-12}
2248	3FGL J1427.8−3215	6.62×10^{-12}
2249	3FGL J0226.7−4747	6.57×10^{-12}
2250	3FGL J1941.8+7218	6.29×10^{-12}
2251	3FGL J1516.7+3648	5.69×10^{-12}
2252	3FGL J2305.8+1658	5.37×10^{-12}
2253	3FGL J0415.7−4351	5.33×10^{-12}
2254	3FGL J2054.8−4908	5.07×10^{-12}
2255	3FGL J1821.9+6636	5.00×10^{-12}
2256	3FHL J0241.0−3037	4.96×10^{-12}
2257	3FGL J2233.5−1235	4.73×10^{-12}
2258	3FHL J2245.5−1734	4.72×10^{-12}
2259	3FGL J0251.5−5959	4.52×10^{-12}
2260	3FGL J0535.6−2749	4.29×10^{-12}
2261	3FGL J2144.6−5640	3.72×10^{-12}
2262	3FGL J0420.4+1448	3.68×10^{-12}
2263	3FGL J1727.4+0634	3.55×10^{-12}
2264	3FGL J0627.9−1517	3.05×10^{-12}
2265	3FGL J0746.4+2540	2.91×10^{-12}
2266	3FHL J0327.6+2619	2.01×10^{-12}
2267	3FHL J0950.6+6357	1.65×10^{-12}
2268	3FHL J0500.6+1903	1.63×10^{-12}
2269	3FHL J1559.1+6736	1.03×10^{-12}
2270	3FHL J0805.9+3834	5.14×10^{-13}
2271	3FHL J0319.2−7045	3.86×10^{-13}
2272	3FHL J0931.4−3559	2.41×10^{-13}
2273	3FHL J0055.8+4507	1.05×10^{-13}
2274	3FHL J0110.9+4346	8.41×10^{-14}
2275	3FHL J0541.1−4855	2.02×10^{-14}
2276	3FHL J0115.4−2916	1.45×10^{-14}
2277	3FHL J0059.4−3513	2.43×10^{-15}
2278	3FHL J1719.1+0654	2.35×10^{-15}
2279	3FHL J0343.5−6302	8.17×10^{-16}
2280	3FHL J1212.2+2439	9.52×10^{-17}
2281	3FHL J2050.2−2624	1.31×10^{-18}

E SEDs of all Blazars in Tab. 3

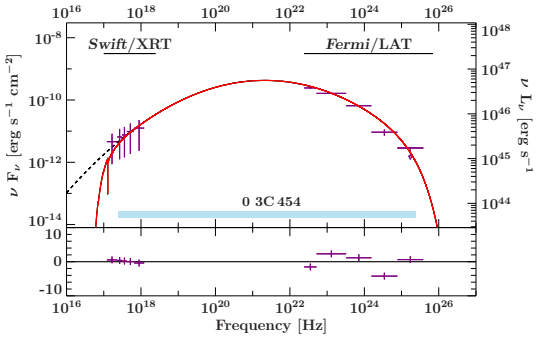

Figure E.1: Spectral energy distribution of 3C 454.3. Please refer to Fig. 5.11 for further details.

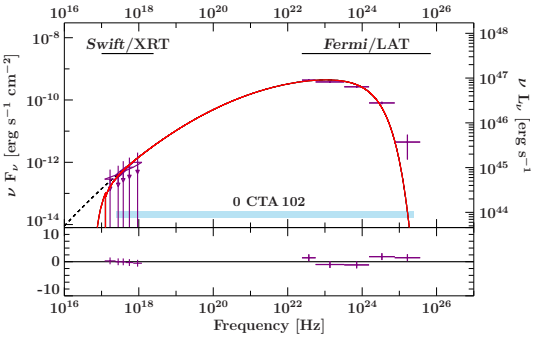

Figure E.2: Spectral energy distribution of CTA 102. Please refer to Fig. 5.11 for further details.

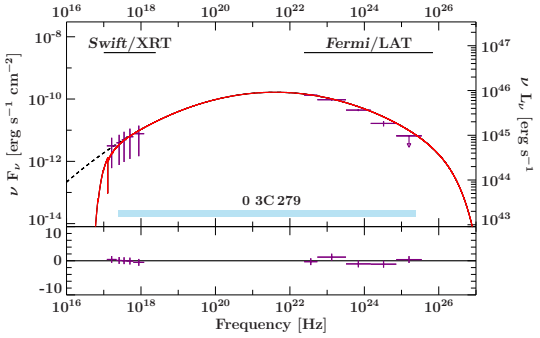

Figure E.3: Spectral energy distribution of 3C 279. Please refer to Fig. 5.11 for further details.

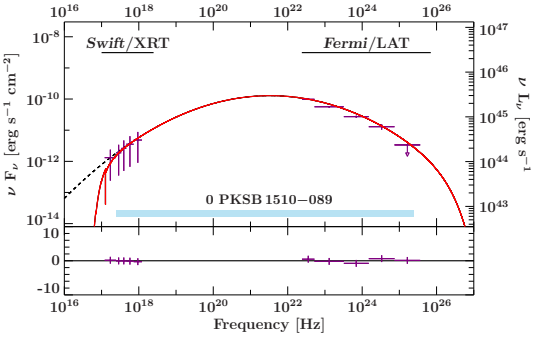

Figure E.4: Spectral energy distribution of PKS 1510−089. Please refer to Fig. 5.11 for further details.

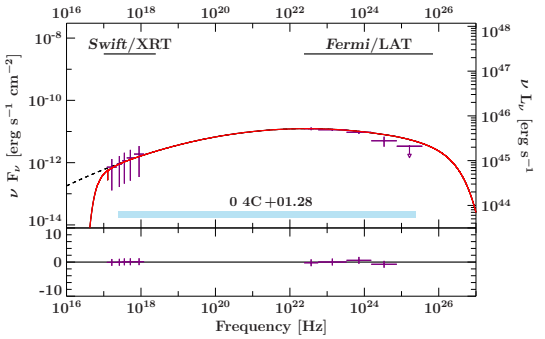

Figure E.5: Spectral energy distribution of 4C +01.02. Please refer to Fig. 5.11 for further details.

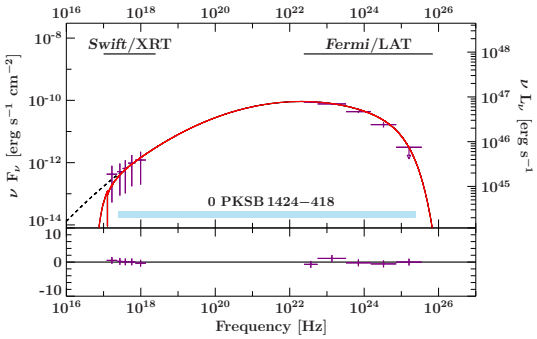

Figure E.6: Spectral energy distribution of PKS B1424−418. Please refer to Fig. 5.11 for further details.

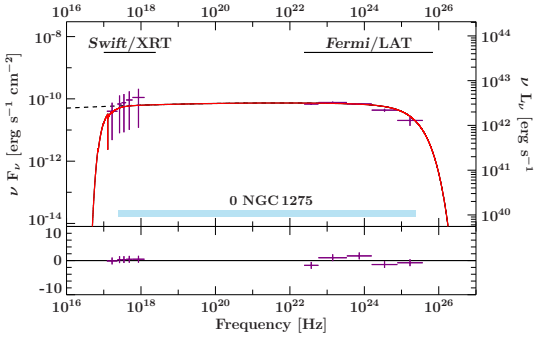

Figure E.7: Spectral energy distribution of NGC 1275. Please refer to Fig. 5.11 for further details.

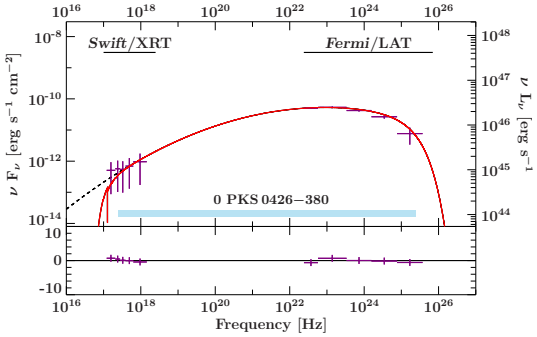

Figure E.8: Spectral energy distribution of PKS 0426−380. Please refer to Fig. 5.11 for further details.

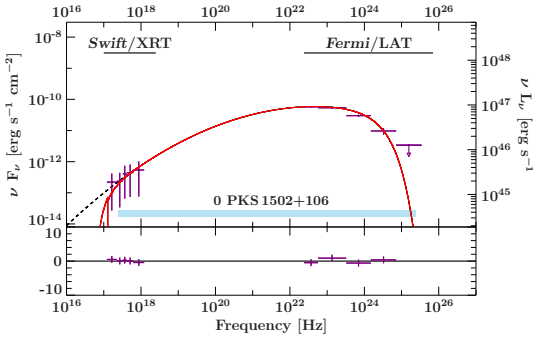

Figure E.9: Spectral energy distribution of PKS 1502+106. Please refer to Fig. 5.11 for further details.

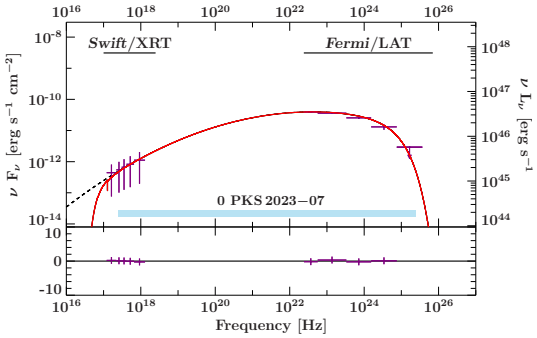

Figure E.10: Spectral energy distribution of PKS 2023−07. Please refer to Fig. 5.11 for further details.

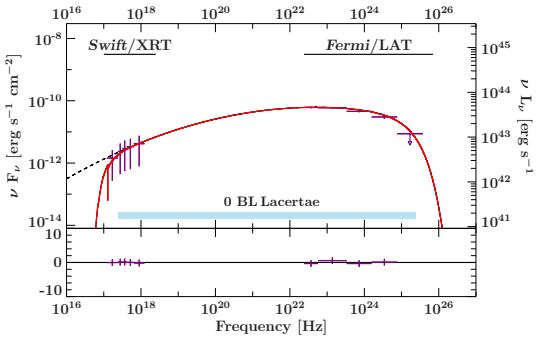

Figure E.11: Spectral energy distribution of BL Lacertae. Please refer to Fig. 5.11 for further details.

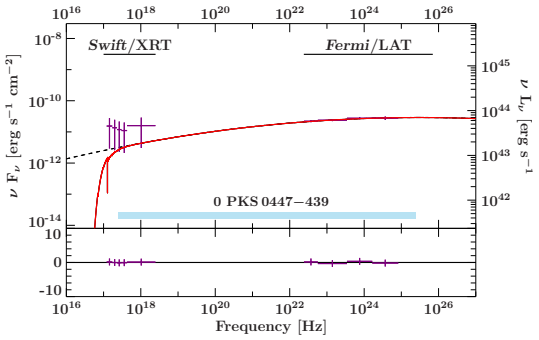

Figure E.12: Spectral energy distribution of PKS 0447−439. Please refer to Fig. 5.11 for further details.

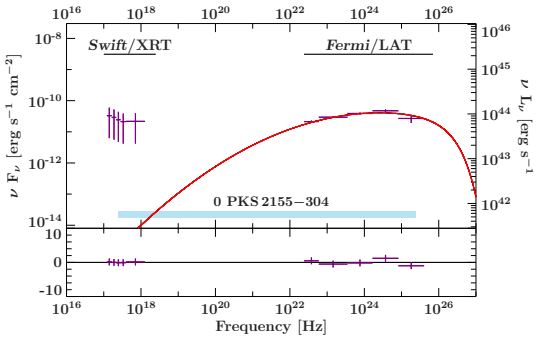

Figure E.13: Spectral energy distribution of PKS 2155−304. Please refer to Fig. 5.11 for further details.

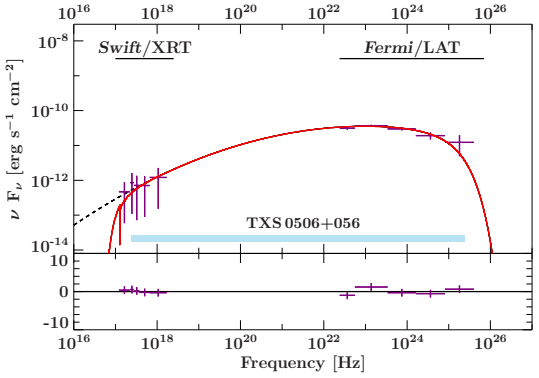

Figure E.14: Spectral energy distribution of TXS 0506+056. Please refer to Fig. 5.11 for further details.

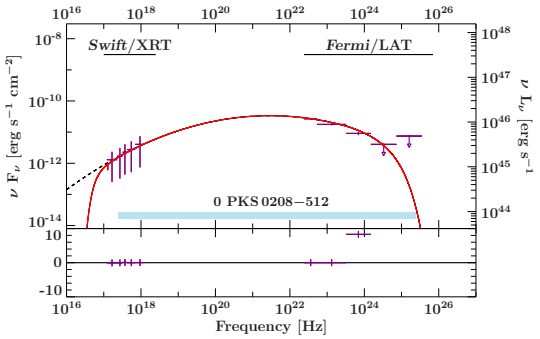

Figure E.15: Spectral energy distribution of PKS 0208−512. Please refer to Fig. 5.11 for further details.

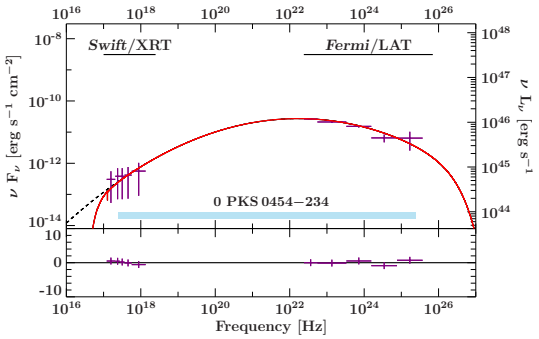

Figure E.16: Spectral energy distribution of PKS 0454−234. Please refer to Fig. 5.11 for further details.

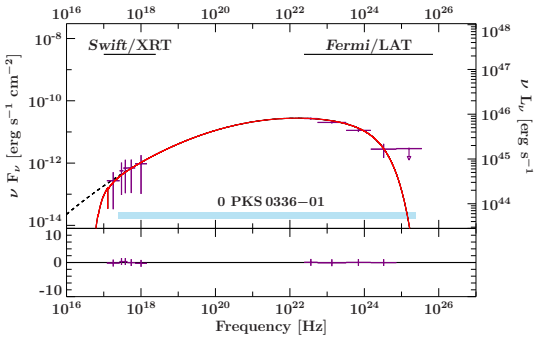

Figure E.17: Spectral energy distribution of PKS 0336−01. Please refer to Fig. 5.11 for further details.

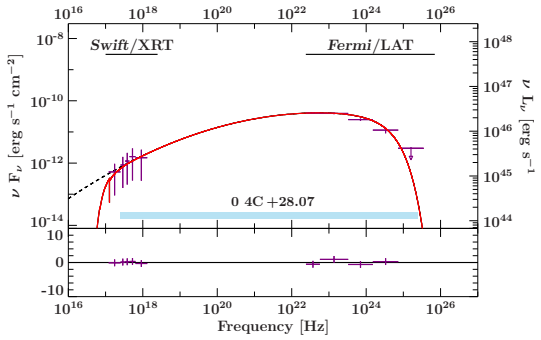

Figure E.18: Spectral energy distribution of 4C +28.07. Please refer to Fig. 5.11 for further details.

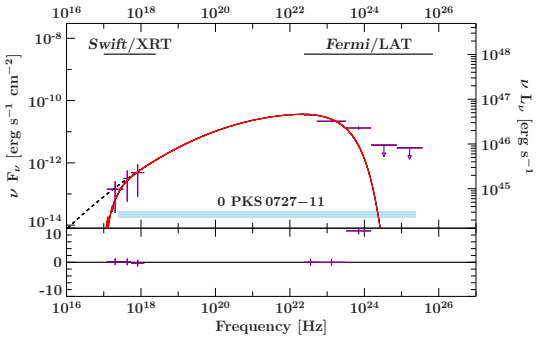

Figure E.19: Spectral energy distribution of PKS 0727−11. Please refer to Fig. 5.11 for further details.

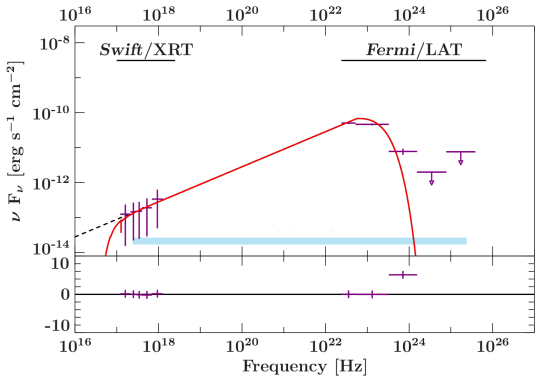

Figure E.20: Spectral energy distribution of 3FGL J2253.1−1237. Please refer to Fig. 5.11 for further details.

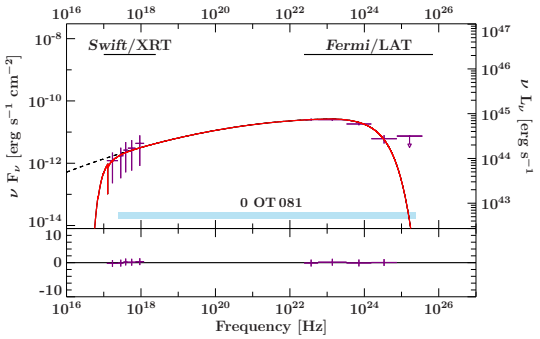

Figure E.21: Spectral energy distribution of OT 081. Please refer to Fig. 5.11 for further details.

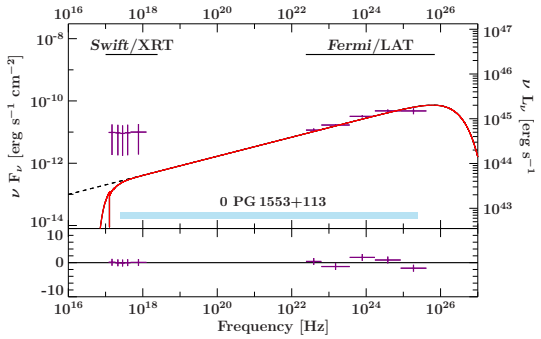

Figure E.22: Spectral energy distribution of PG 1553+113. Please refer to Fig. 5.11 for further details.

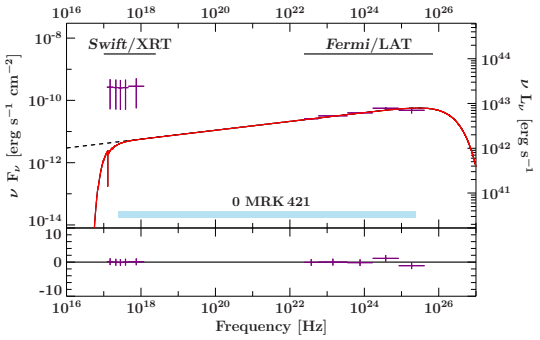

Figure E.23: Spectral energy distribution of Mkn 421. Please refer to Fig. 5.11 for further details.

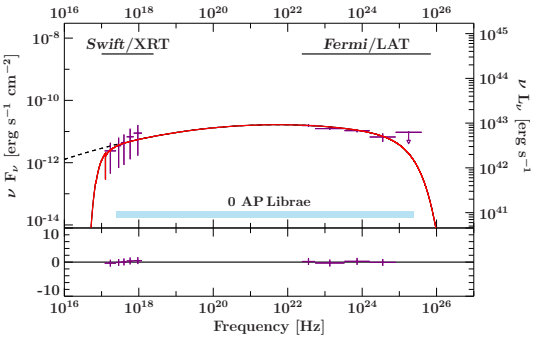

Figure E.24: Spectral energy distribution of AP Librae. Please refer to Fig. 5.11 for further details.

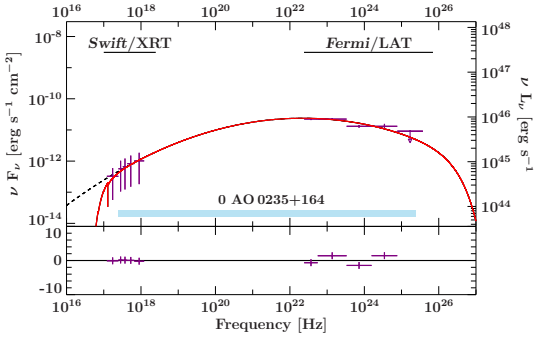

Figure E.25: Spectral energy distribution of AO 0235+164. Please refer to Fig. 5.11 for further details.

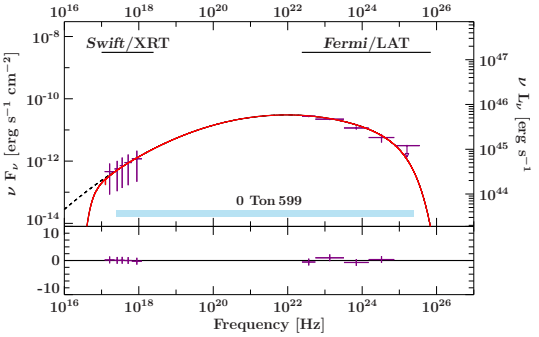

Figure E.26: Spectral energy distribution of Ton 599. Please refer to Fig. 5.11 for further details.

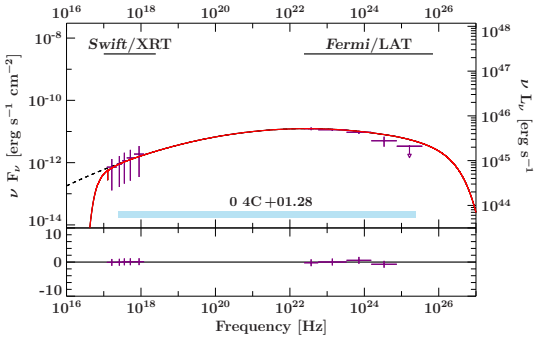

Figure E.27: Spectral energy distribution of 4C +01.28. Please refer to Fig. 5.11 for further details.

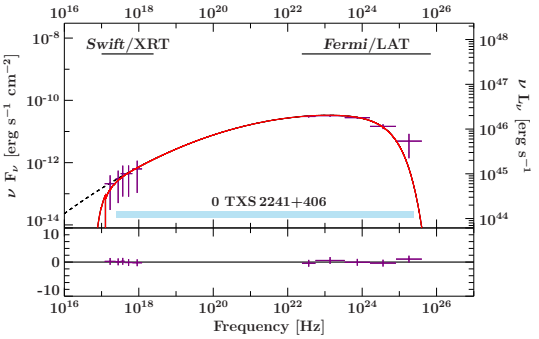

Figure E.28: Spectral energy distribution of TXS 2241+406. Please refer to Fig. 5.11 for further details.

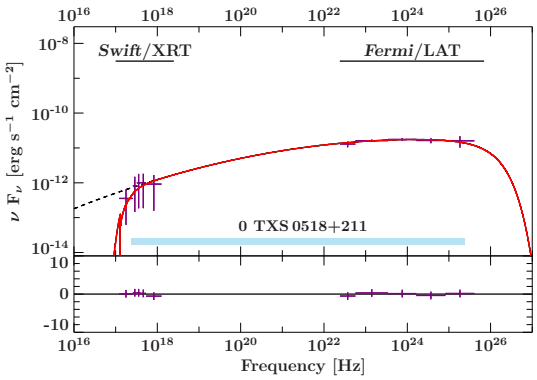

Figure E.29: Spectral energy distribution of TXS 0518+211. Please refer to Fig. 5.11 for further details.

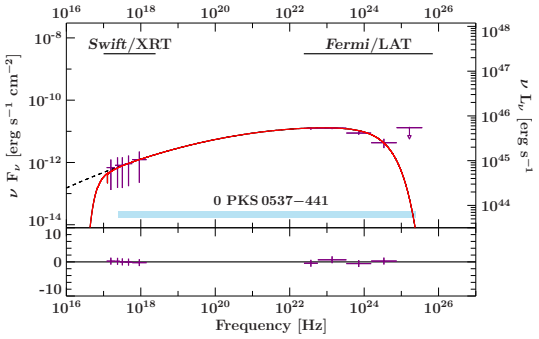

Figure E.30: Spectral energy distribution of PKS 0537−441. Please refer to Fig. 5.11 for further details.

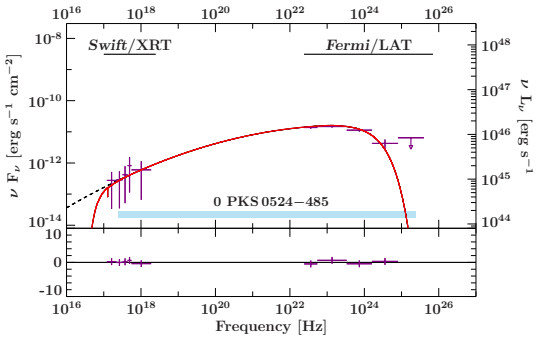

Figure E.31: Spectral energy distribution of PKS 0524−485. Please refer to Fig. 5.11 for further details.

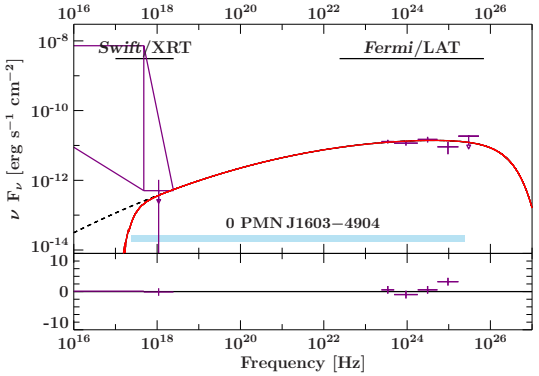

Figure E.32: Spectral energy distribution of PMN J1603−4904. Please refer to Fig. 5.11 for further details.

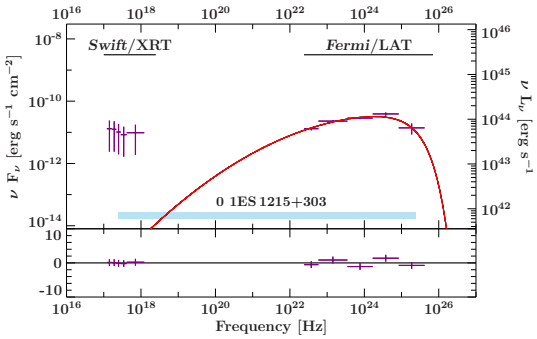

Figure E.33: Spectral energy distribution of 1ES 1215+303. Please refer to Fig. 5.11 for further details.

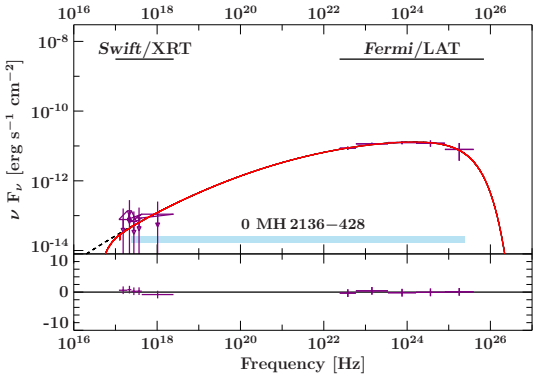

Figure E.34: Spectral energy distribution of MH 2136−428. Please refer to Fig. 5.11 for further details.

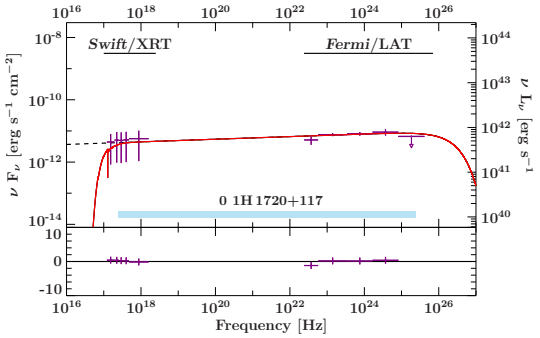

Figure E.35: Spectral energy distribution of 1H 1720+117. Please refer to Fig. 5.11 for further details.

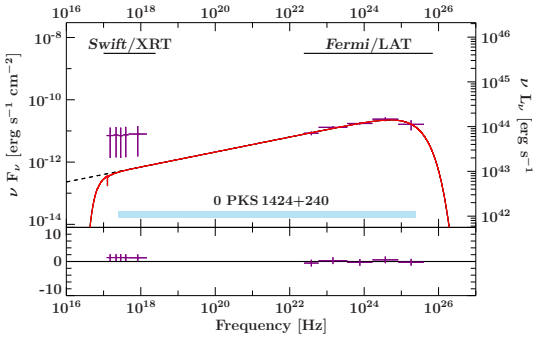

Figure E.36: Spectral energy distribution of PKS 1424+240. Please refer to Fig. 5.11 for further details.

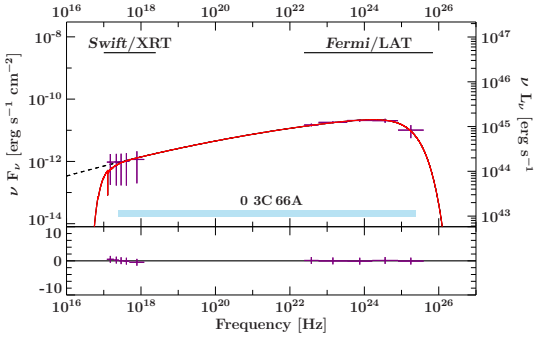

Figure E.37: Spectral energy distribution of 3C 66A. Please refer to Fig. 5.11 for further details.

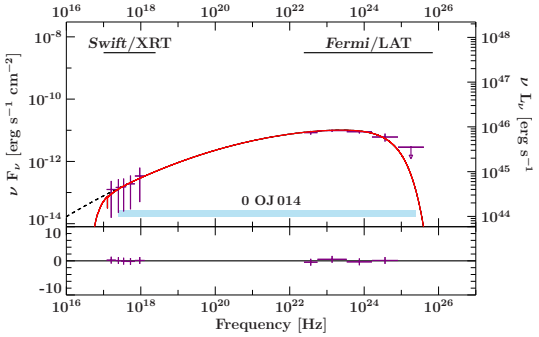

Figure E.38: Spectral energy distribution of OJ 014. Please refer to Fig. 5.11 for further details.

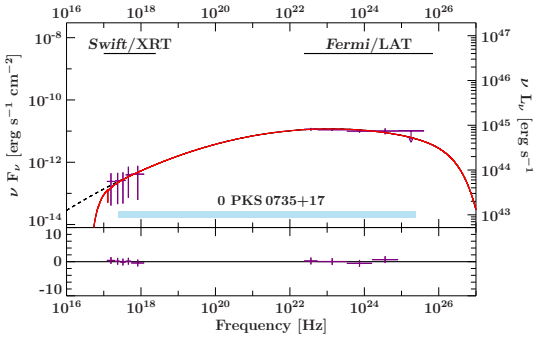

Figure E.39: Spectral energy distribution of PKS 0735+17. Please refer to Fig. 5.11 for further details.

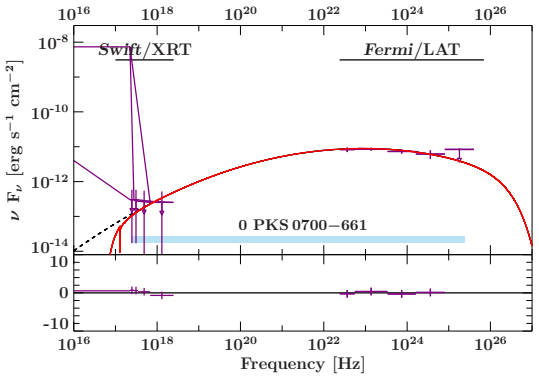

Figure E.40: Spectral energy distribution of PKS 0700−661. Please refer to Fig. 5.11 for further details.

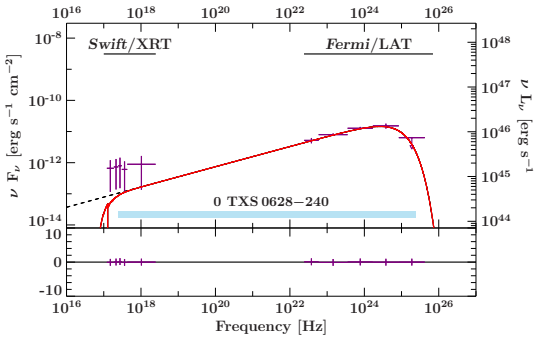

Figure E.41: Spectral energy distribution of TXS 0628−240. Please refer to Fig. 5.11 for further details.

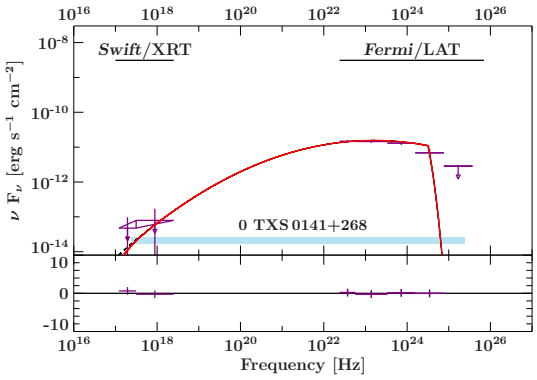

Figure E.42: Spectral energy distribution of TXS 0141+268. Please refer to Fig. 5.11 for further details.

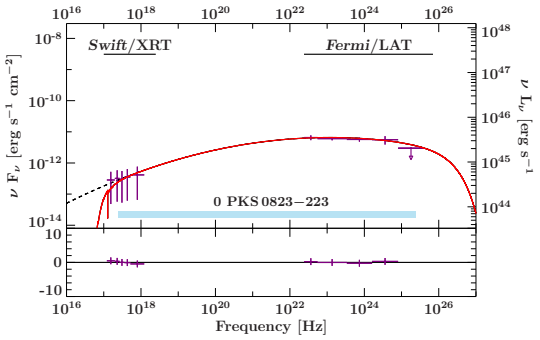

Figure E.43: Spectral energy distribution of PKS 0823−223. Please refer to Fig. 5.11 for further details.

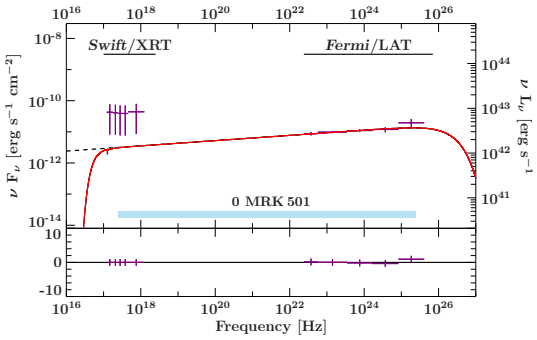

Figure E.44: Spectral energy distribution of Mkn 501. Please refer to Fig. 5.11 for further details.

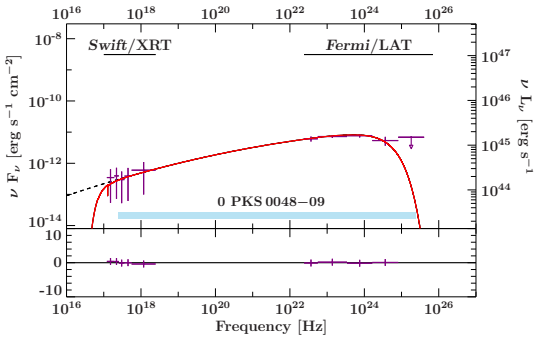

Figure E.45: Spectral energy distribution of PKS 0048−09. Please refer to Fig. 5.11 for further details.

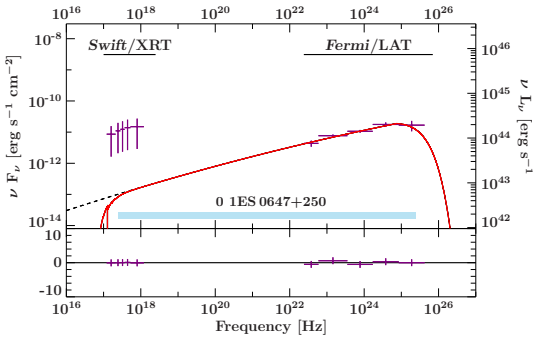

Figure E.46: Spectral energy distribution of 1ES 0647+250. Please refer to Fig. 5.11 for further details.

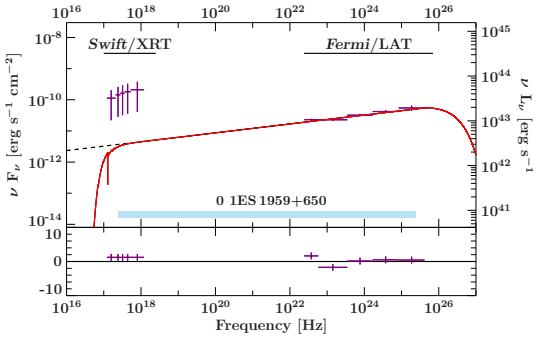

Figure E.47: Spectral energy distribution of 1ES 1959+650. Please refer to Fig. 5.11 for further details.

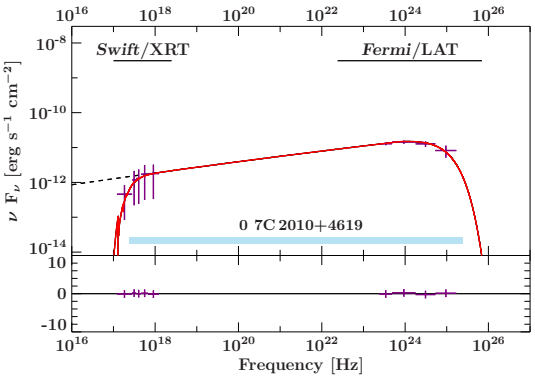

Figure E.48: Spectral energy distribution of 7C 2010+4619. Please refer to Fig. 5.11 for further details.

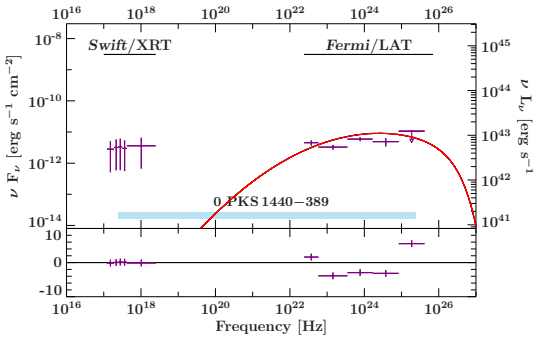

Figure E.49: Spectral energy distribution of PKS 1440−389. Please refer to Fig. 5.11 for further details.

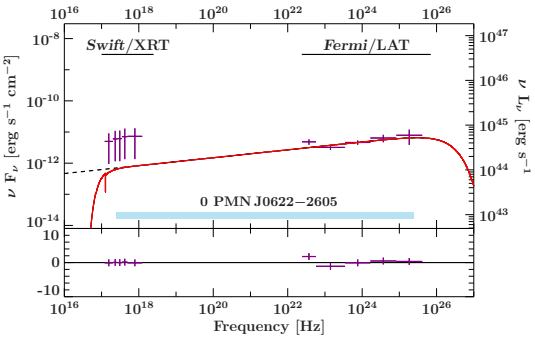

Figure E.50: Spectral energy distribution of PMN J0622−2605. Please refer to Fig. 5.11 for further details.

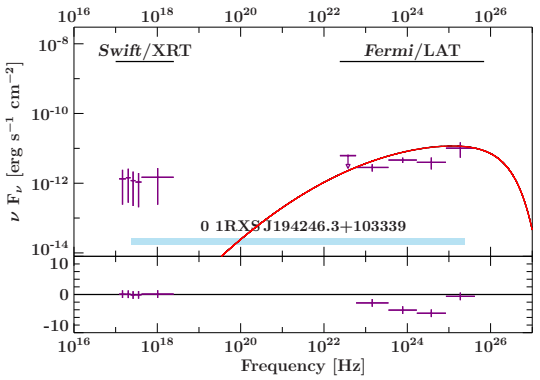

Figure E.51: Spectral energy distribution of 1RXS J194246.3+103339. Please refer to Fig. 5.11 for further details.

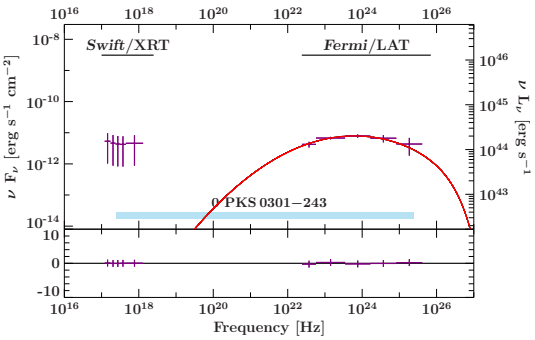

Figure E.52: Spectral energy distribution of PKS 0301−243. Please refer to Fig. 5.11 for further details.

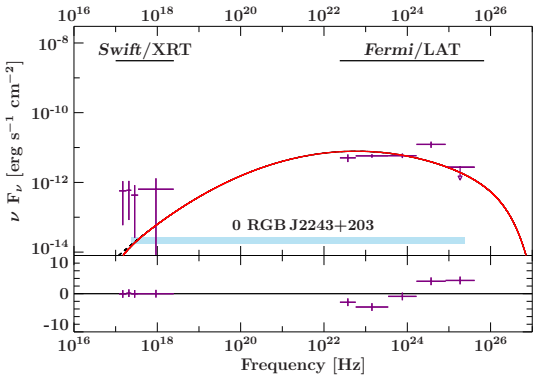

Figure E.53: Spectral energy distribution of RGB J2243+203. Please refer to Fig. 5.11 for further details.

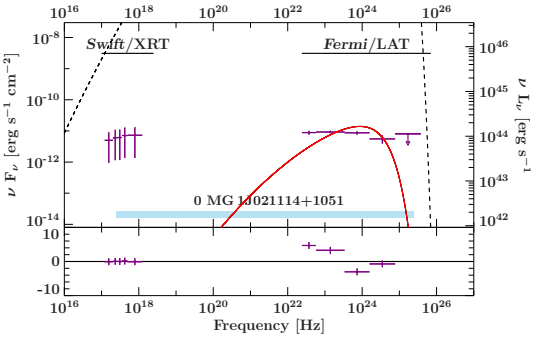

Figure E.54: Spectral energy distribution of MG1 J021114+1051. Please refer to Fig. 5.11 for further details.

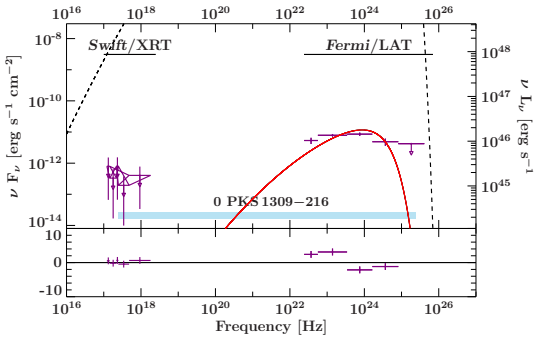

Figure E.55: Spectral energy distribution of PKS 1309−216. Please refer to Fig. 5.11 for further details.

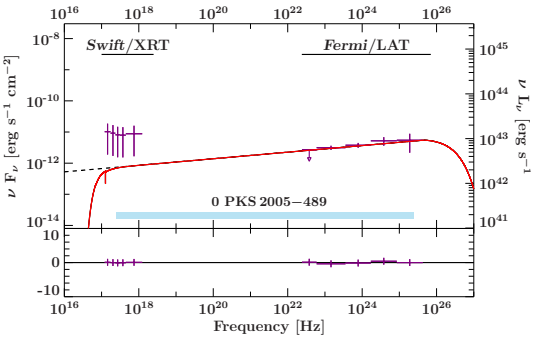

Figure E.56: Spectral energy distribution of PKS 2005−489. Please refer to Fig. 5.11 for further details.

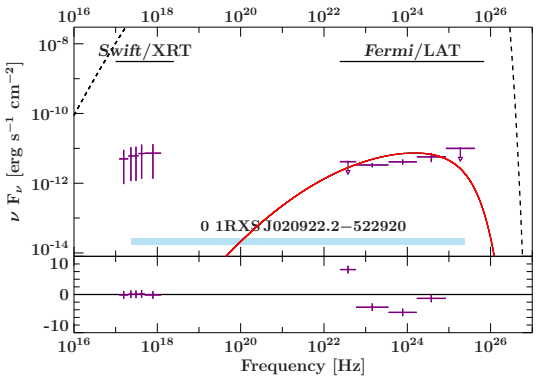

Figure E.57: Spectral energy distribution of 1RXS J020922.2−522920. Please refer to Fig. 5.11 for further details.

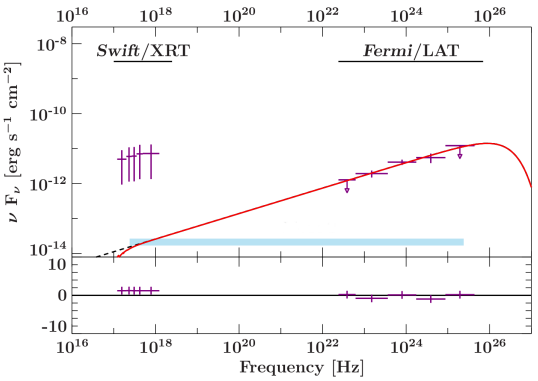

Figure E.58: Spectral energy distribution of 3FHL J1944.9−2143. Please refer to Fig. 5.11 for further details.

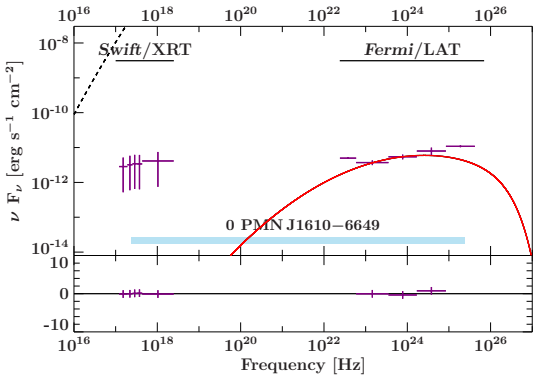

Figure E.59: Spectral energy distribution of PMN J1610−6649. Please refer to Fig. 5.11 for further details.

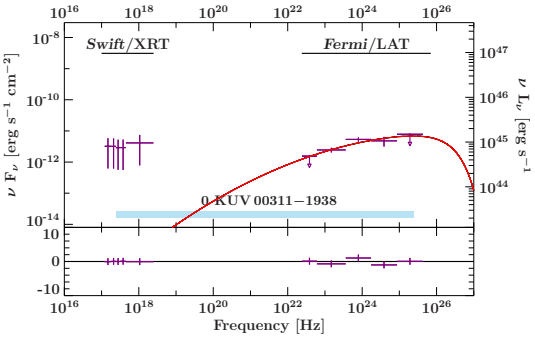

Figure E.60: Spectral energy distribution of KUV 00311−1938. Please refer to Fig. 5.11 for further details.

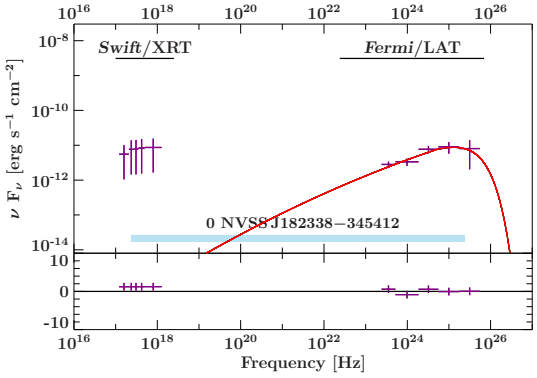

Figure E.61: Spectral energy distribution of NVSS J182338−345412. Please refer to Fig. 5.11 for further details.

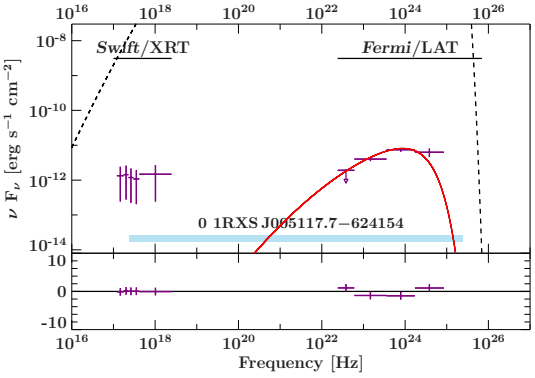

Figure E.62: Spectral energy distribution of 1RXS J005117.7−624154. Please refer to Fig. 5.11 for further details.

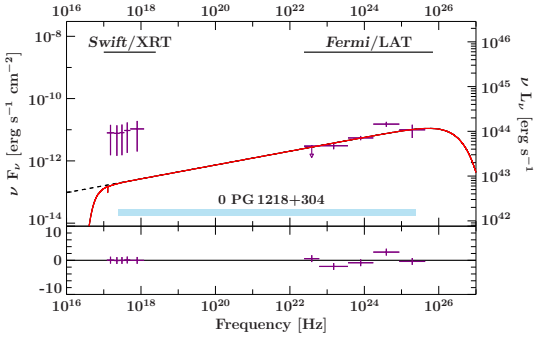

Figure E.63: Spectral energy distribution of PG 1218+304. Please refer to Fig. 5.11 for further details.

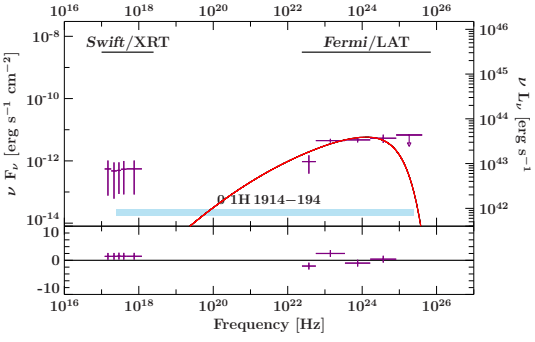

Figure E.64: Spectral energy distribution of 1H 1914−194. Please refer to Fig. 5.11 for further details.

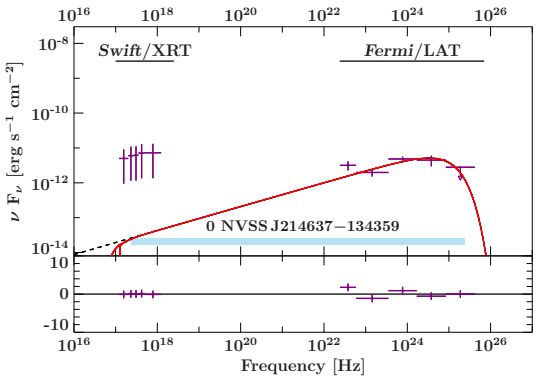

Figure E.65: Spectral energy distribution of NVSS J214637−134359. Please refer to Fig. 5.11 for further details.

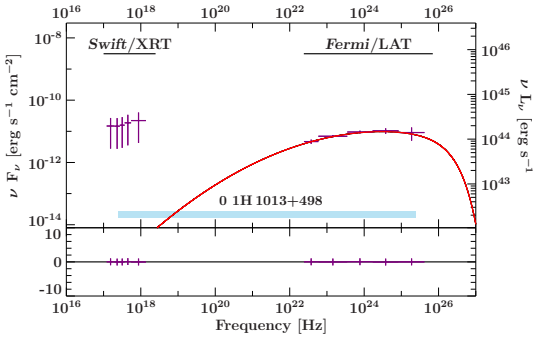

Figure E.66: Spectral energy distribution of 1H 1013+498. Please refer to Fig. 5.11 for further details.

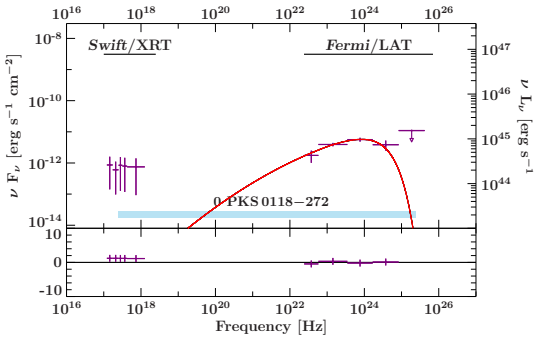

Figure E.67: Spectral energy distribution of PKS 0118−272. Please refer to Fig. 5.11 for further details.

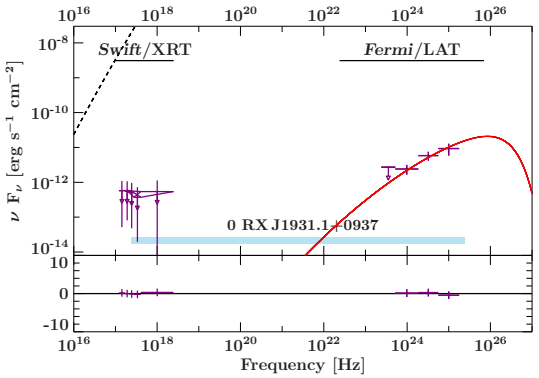

Figure E.68: Spectral energy distribution of RX J1931.1+0937. Please refer to Fig. 5.11 for further details.

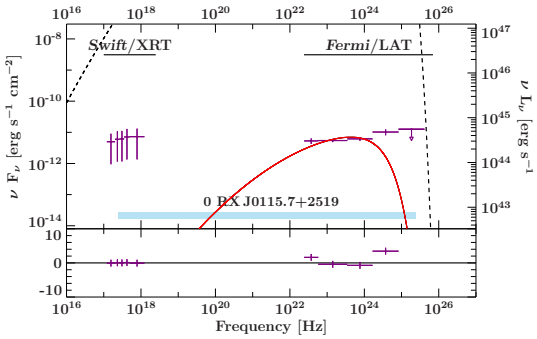

Figure E.69: Spectral energy distribution of RX J0115.7+2519. Please refer to Fig. 5.11 for further details.

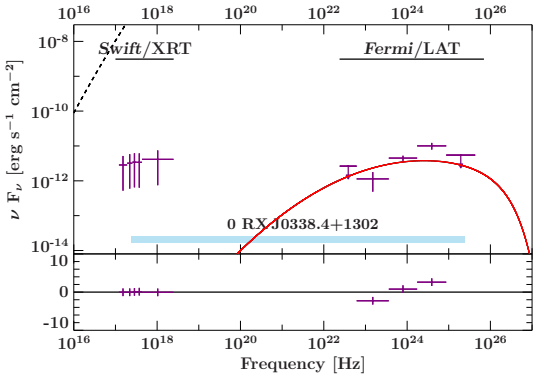

Figure E.70: Spectral energy distribution of RX J0338.4+1302. Please refer to Fig. 5.11 for further details.

F Sample of Blazars Considered in Sec. 6

Table 7: Full sample of γ-ray unknown high-redshift blazars considered in Sec. 6. These blazars with a redshift of $z \geq 2.5$ have been selected from the Roma BZCAT Multifrequency Catalogue of Blazars and the SHAO list of high-redshift loud quasars.

Number	Source		RA J2000	DEC J2000	z	Number	Source		RA J2000	DEC J2000	z
1	5BZQ	J0001+1914	0.29	19.24	3.10	51	5BZQ	J0730+4049	112.71	40.83	2.50
2	5BZQ	J0009+0625	2.32	6.43	2.69	52	5BZQ	J0733+0456	113.49	4.94	3.01
3	5BZQ	J0014−3059	3.66	-30.99	2.79	53	5BZQ	J0741+2557	115.37	25.96	2.75
4	5BZQ	J0017+8135	4.29	81.59	3.39	54	5BZQ	J0745+1011	116.39	10.19	2.62
5	5BZQ	J0019−3031	4.93	-30.52	2.68	55	5BZQ	J0810+3847	122.54	38.80	3.95
6	5BZQ	J0034+2754	8.68	27.91	2.96	56	5BZQ	J0812−1810	123.12	-18.18	2.97
7	5BZQ	J0037−2145	9.31	-21.76	2.51	57	5BZQ	J0839+5112	129.94	51.20	4.40
8	5BZQ	J0049−3116	12.35	-31.27	2.72	58	5BZQ	J0906+6930	136.63	69.51	5.47
9	5BZQ	J0052+4402	13.12	44.05	2.62	59	5BZQ	J0915+0007	138.97	0.12	3.07
10	5BZQ	J0057−0024	14.32	-0.41	2.75	60	5BZQ	J0918+0636	139.60	6.61	4.22
11	5BZQ	J0115−2804	18.85	-28.08	2.58	61	5BZQ	J0934+4908	143.57	49.14	2.58
12	5BZQ	J0121−2806	20.25	-28.11	3.12	62	5BZQ	J0935−3332	143.79	-33.54	2.91
13	5BZQ	J0122+0310	20.51	3.17	4.00	63	5BZQ	J0941−8615	145.48	-86.25	3.70
14	5BZQ	J0138−2711	24.54	-27.19	3.00	64	5BZQ	J0947−7731	146.96	-77.53	2.53
15	5BZQ	J0148+4215	27.19	42.26	3.24	65	5BZQ	J0952−2453	148.13	-24.90	2.63
16	5BZQ	J0203+1134	30.94	11.58	3.64	66	5BZQ	J0955−1845	148.81	-18.76	2.91
17	5BZQ	J0205+1444	31.30	14.74	2.85	67	5BZQ	J0958−4110	149.66	-41.18	2.93
18	5BZQ	J0216−0118	34.02	-1.30	2.80	68	5BZQ	J1007+5802	151.85	58.03	3.35
19	5BZQ	J0216−7331	34.19	-73.53	2.68	69	5BZQ	J1007+1356	151.92	13.94	2.72
20	5BZQ	J0220−2151	35.15	-21.85	2.55	70	5BZQ	J1011+4700	152.84	47.01	2.93
21	5BZQ	J0225+1846	36.27	18.78	2.69	71	5BZQ	J1012−4259	153.15	-42.98	2.95
22	5BZQ	J0246+1823	41.55	18.39	3.59	72	5BZQ	J1016+2037	154.18	20.63	3.12
23	5BZQ	J0258−3909	44.56	-39.16	3.45	73	5BZQ	J1017+6116	154.36	61.27	2.81
24	5BZQ	J0324−2918	51.18	-29.31	4.63	74	5BZQ	J1023+2649	155.80	26.83	2.79
25	5BZQ	J0325−2140	51.25	-21.68	2.83	75	5BZQ	J1026+2542	156.60	25.72	5.29
26	5BZQ	J0331−2524	52.79	-25.41	2.69	76	5BZQ	J1028−0844	157.16	-8.74	4.28
27	5BZQ	J0332−7249	53.18	-72.82	2.74	77	5BZQ	J1041−4740	160.44	-47.67	2.56
28	5BZQ	J0332−4455	53.18	-44.93	2.68	78	5BZQ	J1044+2959	161.03	29.98	2.98
29	5BZQ	J0337−1204	54.48	-12.07	3.44	79	5BZQ	J1049+3737	162.29	37.63	2.99
30	5BZQ	J0339−0133	54.75	-1.55	3.20	80	5BZQ	J1050−3517	162.72	-35.30	2.97
31	5BZQ	J0405−0739	61.25	-7.66	2.82	81	5BZQ	J1050+3430	162.74	34.50	2.52
32	5BZQ	J0407−3303	61.89	-33.06	2.56	82	5BZQ	J1058−3024	164.50	-30.42	2.52
33	5BZQ	J0422−3844	65.56	-38.75	3.11	83	5BZQ	J1100−4249	165.21	-42.82	3.56
34	5BZQ	J0424+0805	66.24	8.09	3.09	84	5BZQ	J1119+6004	169.81	60.08	2.65
35	5BZQ	J0428+1732	67.15	17.54	3.32	85	5BZQ	J1124−1501	171.01	-15.03	2.56
36	5BZQ	J0434−4355	68.51	-43.93	2.65	86	5BZQ	J1127+5650	171.92	56.84	2.89
37	5BZQ	J0437−1844	69.26	-18.75	2.70	87	5BZQ	J1139−1552	174.87	-15.88	2.63
38	5BZQ	J0513+0100	78.42	1.01	2.68	88	5BZQ	J1150+4332	177.57	43.53	3.04
39	5BZQ	J0522+0113	80.57	1.23	2.94	89	5BZQ	J1155−3107	178.76	-31.13	4.30
40	5BZU	J0525−3343	81.28	-33.72	4.41	90	5BZQ	J1215+6422	183.95	64.37	3.23
41	5BZQ	J0525−2338	81.28	-23.64	3.10	91	5BZQ	J1217+5835	184.30	58.59	2.55
42	5BZQ	J0530−2503	82.53	-25.06	2.78	92	5BZQ	J1217+3305	184.39	33.09	2.61
43	5BZQ	J0539−2839	84.98	-28.67	3.10	93	5BZQ	J1230−1139	187.73	-11.65	3.53
44	5BZQ	J0557+2413	89.27	24.23	3.23	94	5BZQ	J1253−4059	193.50	-40.99	4.46
45	5BZQ	J0603−1716	90.99	-17.27	2.71	95	5BZQ	J1306+4741	196.62	47.69	2.52
46	5BZQ	J0610−2301	92.66	-23.03	2.85	96	5BZQ	J1313+1027	198.42	10.45	2.91
47	5BZQ	J0612−4337	93.12	-43.63	3.46	97	5BZQ	J1318−0607	199.64	-6.12	2.73
48	5BZQ	J0614+6046	93.60	60.77	2.70	98	5BZQ	J1322+3912	200.73	39.20	2.99
49	5BZQ	J0624+3856	96.08	38.95	3.47	99	5BZQ	J1325+1123	201.30	11.39	4.42
50	5BZQ	J0642+6758	100.52	67.98	3.18	100	5BZQ	J1337−1319	204.31	-13.32	3.48

Number	Source	RA J2000	DEC J2000	z
101	5BZQ J1356−1101	209.20	-11.02	3.01
102	5BZQ J1357−1744	209.28	-17.73	3.15
103	5BZQ J1400+0425	210.20	4.43	2.55
104	5BZQ J1404−0130	211.19	-1.51	2.52
105	5BZQ J1405+0415	211.25	4.26	3.21
106	5BZQ J1406+3433	211.72	34.56	2.56
107	5BZQ J1413+4505	213.33	45.09	3.11
108	5BZQ J1420+1205	215.20	12.10	4.03
109	5BZQ J1421−0643	215.28	-6.73	3.69
110	5BZQ J1424+2256	216.16	22.93	3.62
111	5BZQ J1429+5406	217.34	54.10	3.01
112	5BZQ J1430+4204	217.60	42.08	4.72
113	5BZQ J1441−1523	220.44	-15.39	2.64
114	5BZQ J1445+0958	221.32	9.98	3.52
115	5BZQ J1448−1122	222.21	-11.37	2.63
116	5BZQ J1459+4442	224.90	44.70	3.40
117	5BZQ J1504+0813	226.10	8.23	2.83
118	5BZQ J1506+8319	226.60	83.32	2.58
119	5BZQ J1526+6650	231.68	66.85	3.02
120	5BZQ J1535+1954	233.82	19.91	3.60
121	5BZQ J1556+3517	239.14	35.30	6.80
122	5BZQ J1559+0304	239.88	3.08	3.90
123	5BZQ J1559−2442	239.92	-24.71	2.82
124	5BZQ J1603+5730	240.98	57.52	2.85
125	5BZQ J1608+5613	242.09	56.23	3.08
126	5BZQ J1616+0459	244.16	4.99	3.22
127	5BZQ J1624−0649	246.14	-6.83	3.31
128	5BZQ J1632−0033	248.24	-0.56	3.42
129	5BZQ J1638−0340	249.58	-3.67	2.87
130	5BZQ J1656+1826	254.14	18.44	2.55
131	5BZQ J1658−0739	254.68	-7.65	3.74
132	5BZQ J1704+0134	256.03	1.57	2.84
133	5BZQ J1707+0148	256.89	1.81	2.57
134	5BZQ J1740+4506	265.03	45.11	2.79
135	5BZQ J1832+1357	278.18	13.96	2.83
136	5BZQ J1837−5848	279.47	-58.80	3.04
137	5BZQ J1838−3427	279.62	-34.46	2.78
138	5BZQ J1840+3900	280.24	39.01	3.10
139	5BZQ J1850+2825	282.61	28.42	2.54
140	5BZQ J1913−4503	288.44	-45.05	2.56
141	5BZQ J1930−6056	292.53	-60.94	3.25
142	5BZQ J1939−1002	294.99	-10.04	3.79
143	5BZQ J1942−7015	295.69	-70.26	2.90
144	5BZQ J1949−1957	297.47	-19.95	2.65
145	5BZQ J1951+0134	297.90	1.58	4.11
146	5BZQ J2003−3251	300.85	-32.86	3.77
147	5BZQ J2007+0636	301.80	6.61	2.86
148	5BZQ J2015+6554	303.98	65.91	2.85
149	5BZQ J2020+6747	305.08	67.79	2.57
150	5BZQ J2042−2223	310.74	-22.39	3.63
151	5BZQ J2043+1255	310.79	12.92	3.28
152	5BZQ J2050+3127	312.71	31.46	3.18
153	5BZQ J2102+6015	315.67	60.25	4.58
154	5BZQ J2106+0231	316.62	2.53	2.94
155	5BZQ J2114−6851	318.56	-68.85	2.91
156	5BZQ J2130−4515	322.72	-45.26	2.71
157	5BZQ J2152−7807	328.01	-78.12	4.00
158	5BZQ J2207−5707	331.98	-57.13	2.73
159	5BZQ J2215−2944	333.82	-29.74	2.70
160	5BZQ J2217+0220	334.45	2.34	3.57
161	5BZQ J2219−2719	334.90	-27.32	3.63
162	5BZU J2248−0541	342.00	-5.69	3.30
163	5BZQ J2248−2702	342.15	-27.05	2.75
164	5BZQ J2251+2217	342.97	22.29	3.67
165	5BZQ J2258+0203	344.74	2.06	2.67
166	5BZQ J2316−3349	349.18	-33.82	2.94
167	5BZQ J2321−0827	350.33	-8.46	3.16
168	5BZQ J2354−1513	358.63	-15.22	2.68
169	5BZQ J2359+3850	359.89	38.85	2.71
170	J0813+3508	123.39	35.14	4.92
171	J1606+3124	241.54	31.41	4.56
172	J0311+0507	47.95	5.13	4.51
173	J2134−0419	323.55	-4.32	4.35
174	J1021+2209	155.28	22.16	4.24
175	J0257+4338	44.50	43.64	4.07
176	J1715+2145	258.84	21.76	4.01

G Light Curves of all Blazars Considered in Sec. 6

Table 8: *Fermi*/LAT γ-ray light curve of all sources considered in Sec. 6 in an energy range of 100 MeV - 300 GeV over a time range of $\sim$ nine years from 2008 August 4 to 2017 July 1 using monthly binning. Sources are sorted according to App. F All detection are at a level of TS ≥ 9

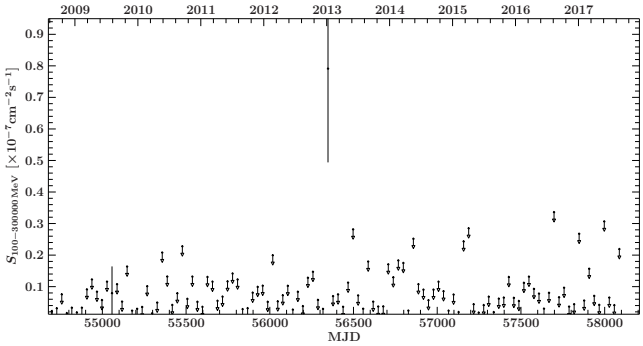

Figure G.1: *Fermi*/LAT γ-ray light curve of source 1

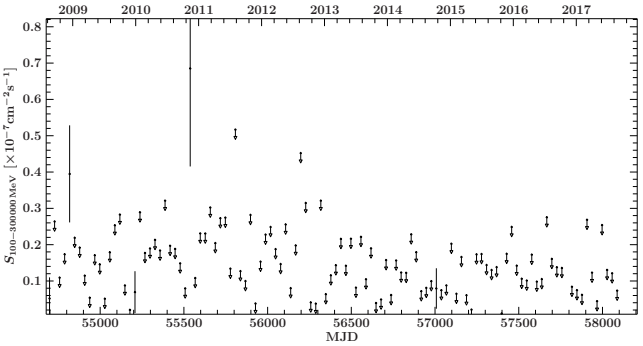

Figure G.2: *Fermi*/LAT γ-ray light curve of source 2

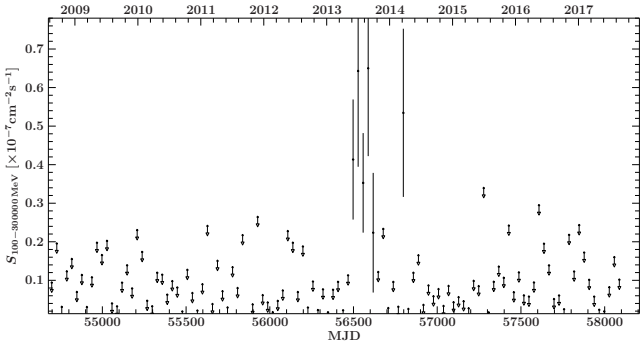

Figure G.3: *Fermi*/LAT γ-ray light curve of source 3

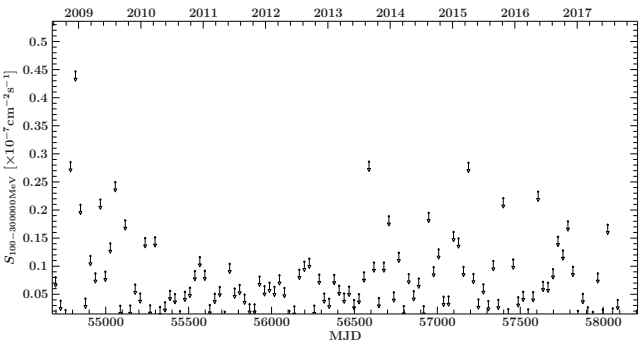

Figure G.4: *Fermi*/LAT γ-ray light curve of source 4

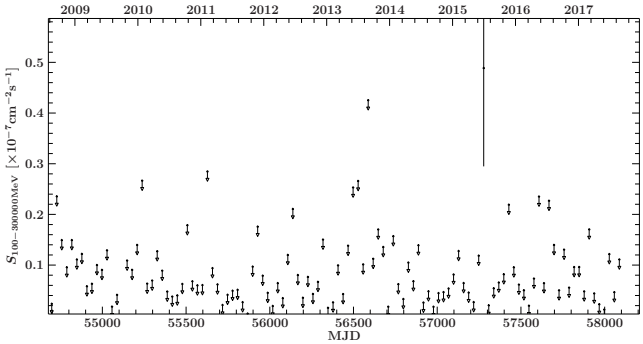

Figure G.5: *Fermi*/LAT γ-ray light curve of source 5

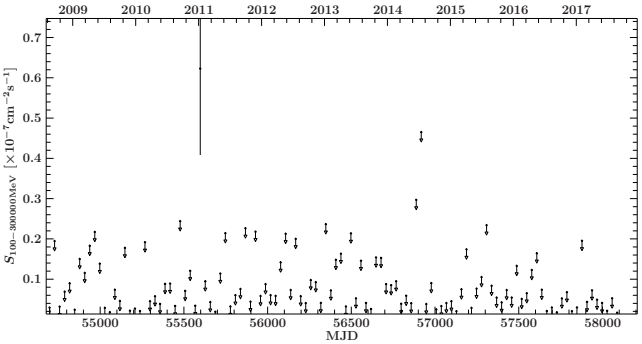

Figure G.6: *Fermi*/LAT γ-ray light curve of source 6

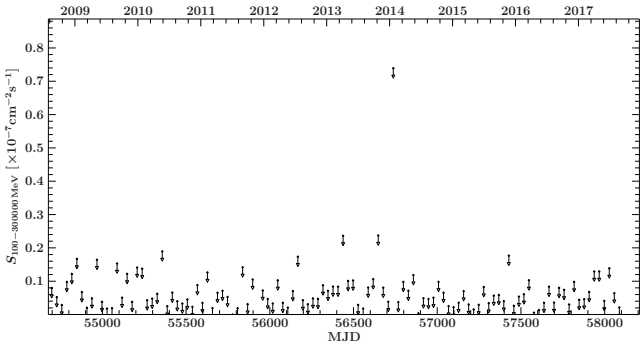

Figure G.7: *Fermi*/LAT γ-ray light curve of source 7

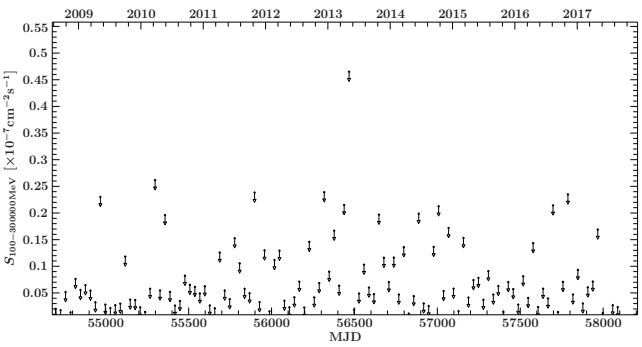

Figure G.8: *Fermi*/LAT γ-ray light curve of source 8

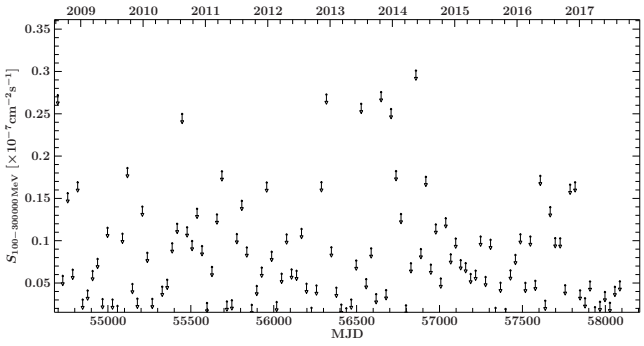

Figure G.9: *Fermi*/LAT γ-ray light curve of source 9

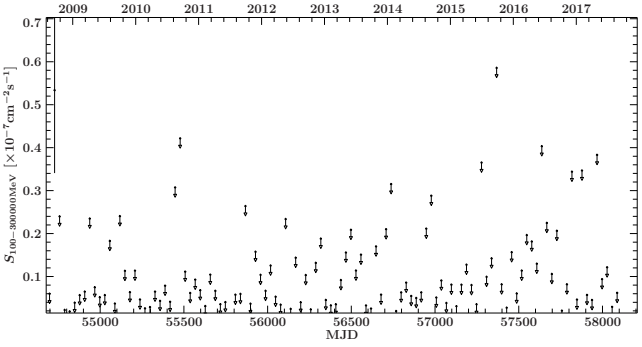

Figure G.10: *Fermi*/LAT γ-ray light curve of source 10

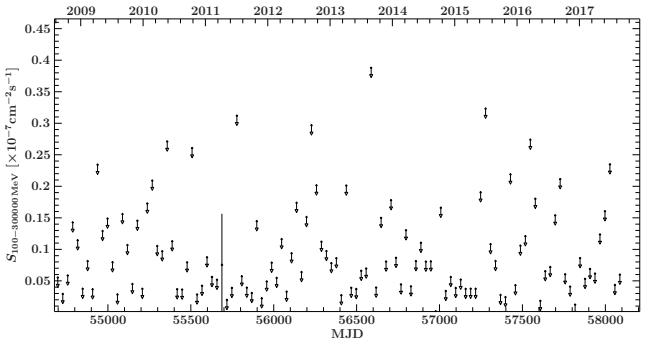

Figure G.11: *Fermi*/LAT γ-ray light curve of source 11

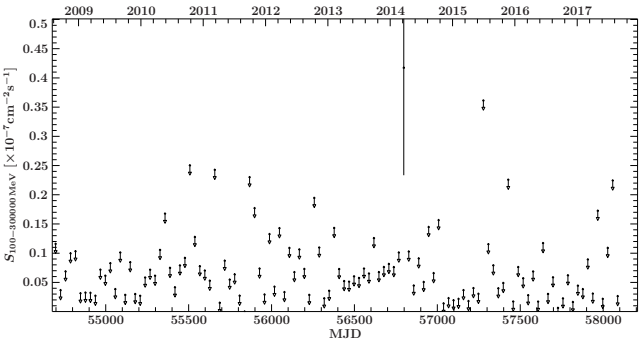

Figure G.12: *Fermi*/LAT γ-ray light curve of source 12

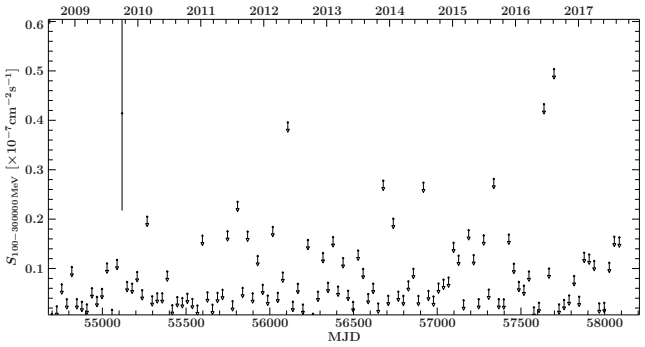

Figure G.13: *Fermi*/LAT γ-ray light curve of source 13

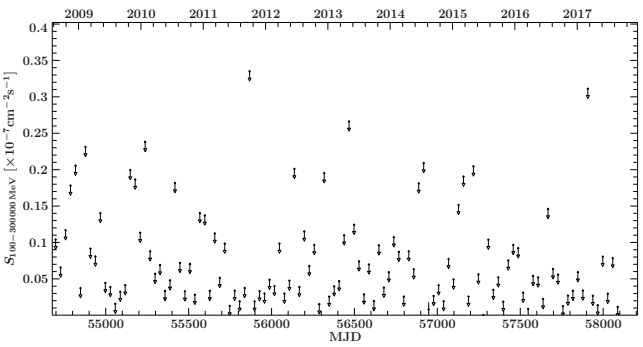

Figure G.14: *Fermi*/LAT γ-ray light curve of source 14

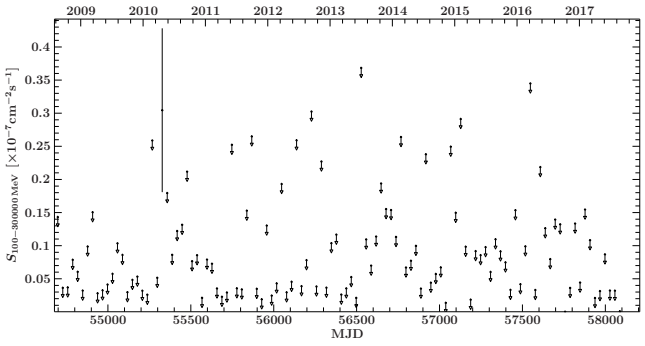

Figure G.15: *Fermi*/LAT γ-ray light curve of source 15

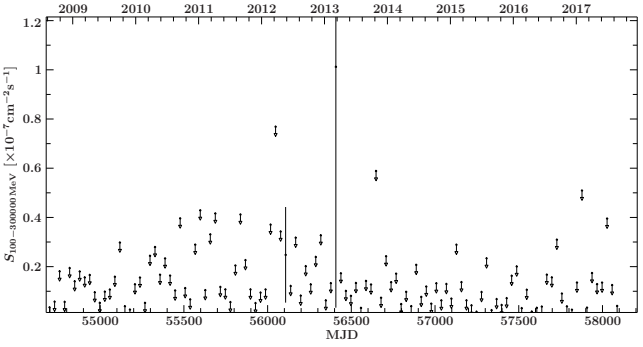

Figure G.16: *Fermi*/LAT γ-ray light curve of source 16

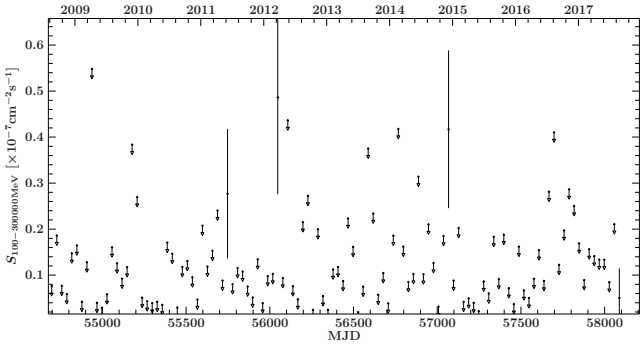

Figure G.17: *Fermi*/LAT γ-ray light curve of source 17

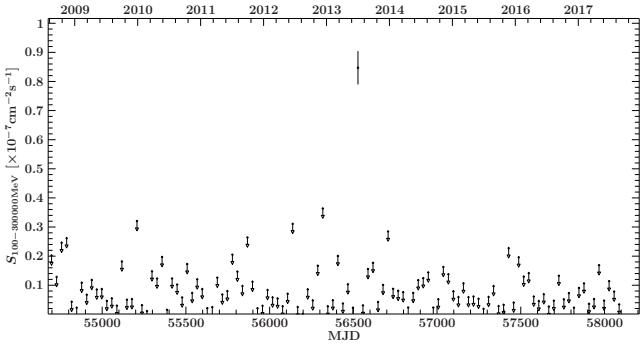

Figure G.18: *Fermi*/LAT γ-ray light curve of source 18

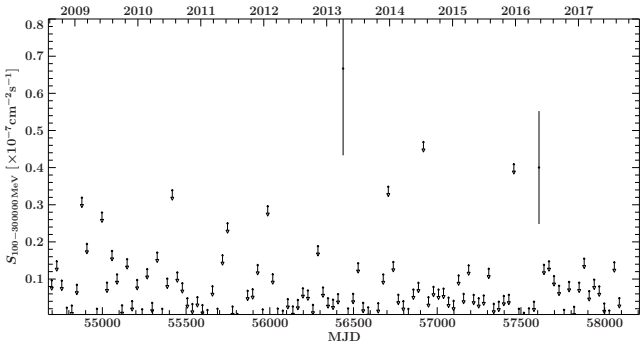

Figure G.19: *Fermi*/LAT γ-ray light curve of source 19

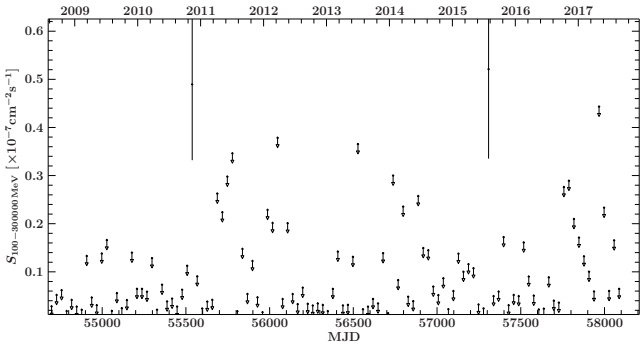

Figure G.20: *Fermi*/LAT γ-ray light curve of source 20

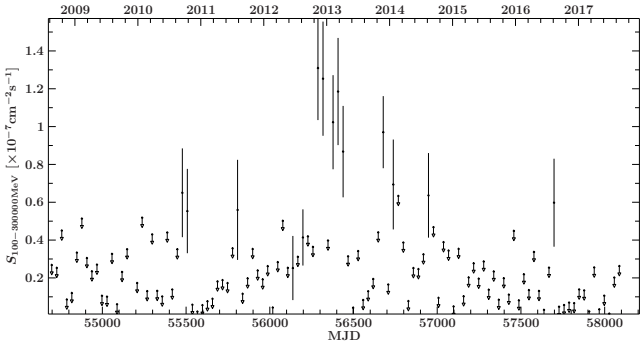

Figure G.21: *Fermi*/LAT γ-ray light curve of source 21

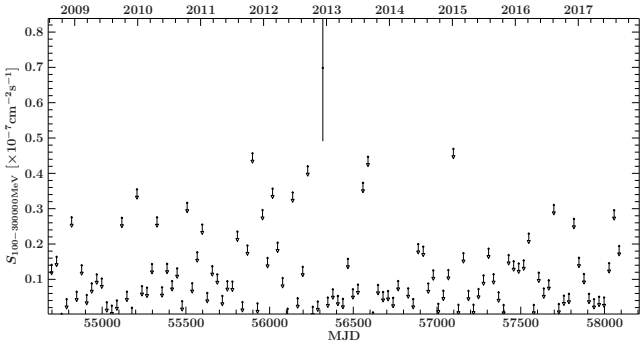

Figure G.22: *Fermi*/LAT γ-ray light curve of source 22

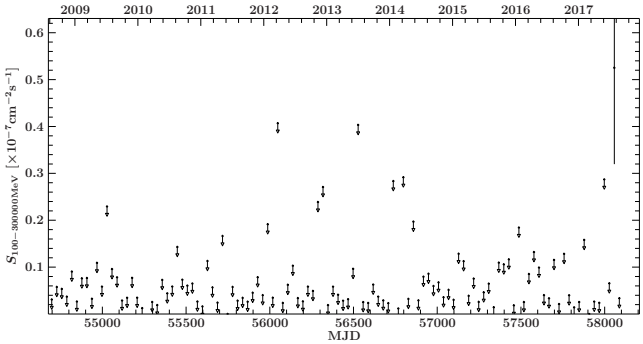

Figure G.23: *Fermi*/LAT γ-ray light curve of source 23

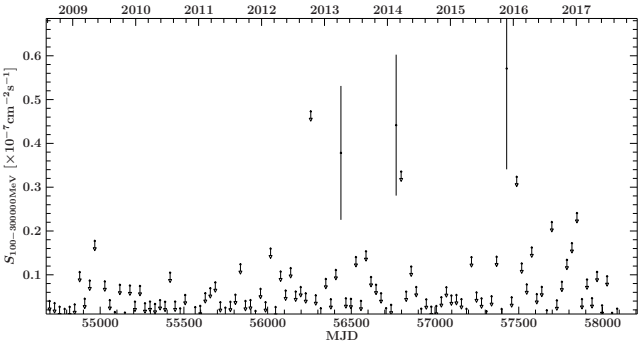

Figure G.24: *Fermi*/LAT γ-ray light curve of source 24

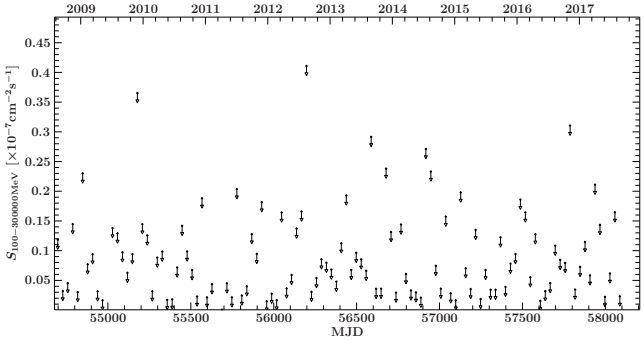

Figure G.25: *Fermi*/LAT γ-ray light curve of source 25

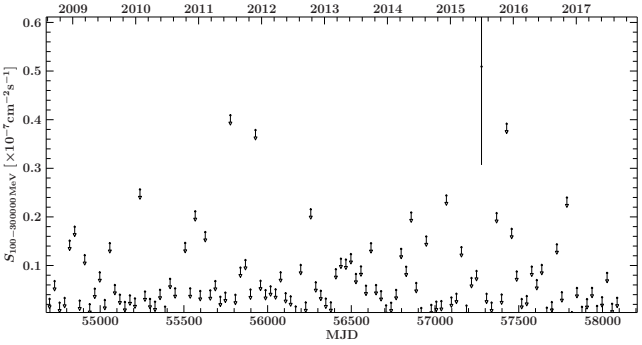

Figure G.26: *Fermi*/LAT γ-ray light curve of source 26

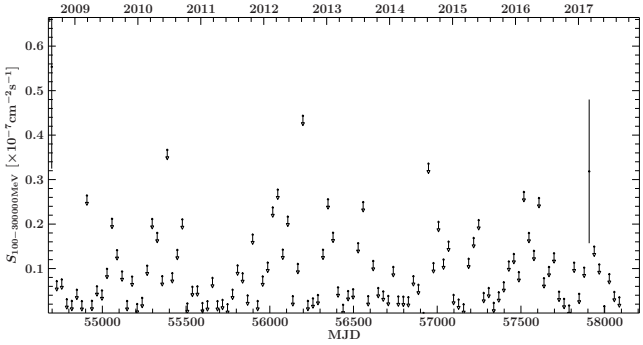

Figure G.27: *Fermi*/LAT γ-ray light curve of source 27

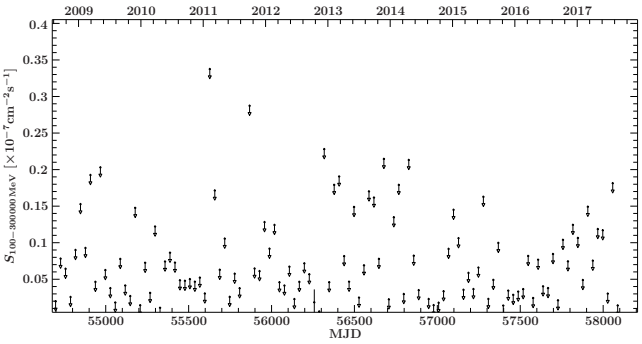

Figure G.28: *Fermi*/LAT γ-ray light curve of source 28

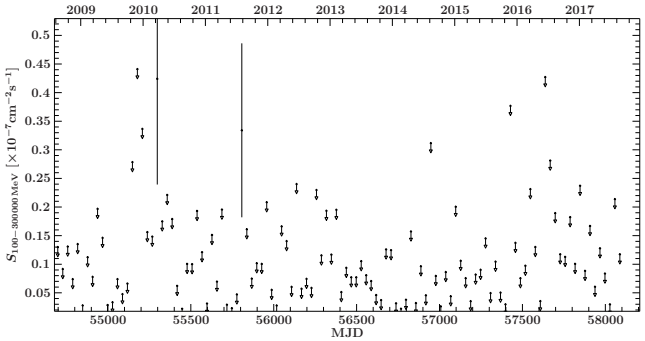

Figure G.29: *Fermi*/LAT γ-ray light curve of source 29

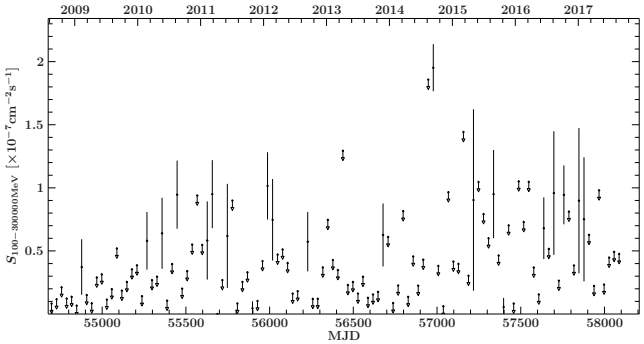

Figure G.30: *Fermi*/LAT γ-ray light curve of source 30

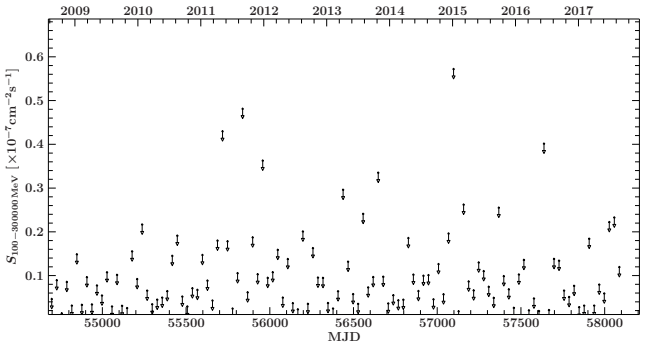

Figure G.31: *Fermi*/LAT γ-ray light curve of source 31

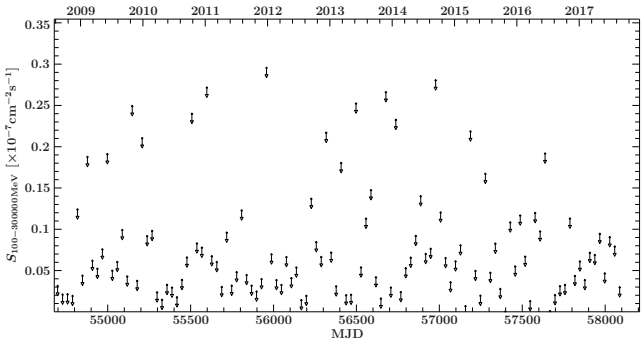

Figure G.32: *Fermi*/LAT γ-ray light curve of source 32

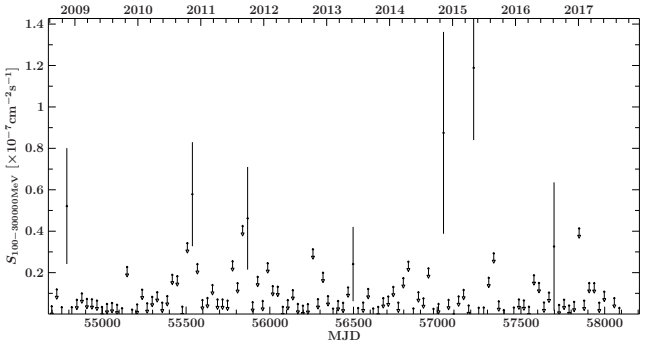

Figure G.33: *Fermi*/LAT γ-ray light curve of source 33

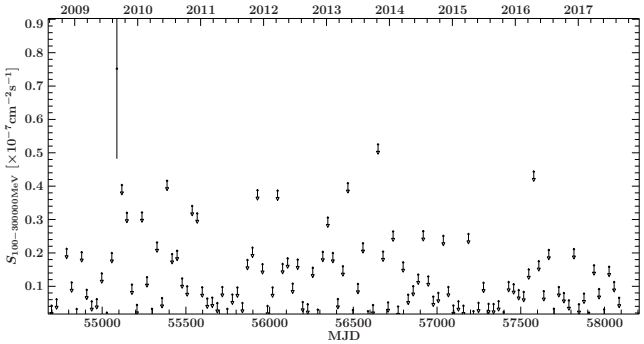

Figure G.34: *Fermi*/LAT γ-ray light curve of source 34

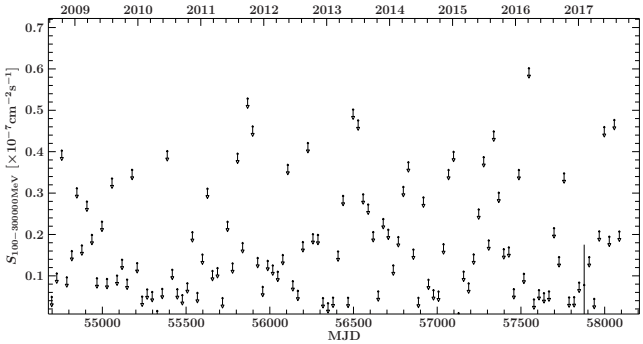

Figure G.35: *Fermi*/LAT γ-ray light curve of source 35

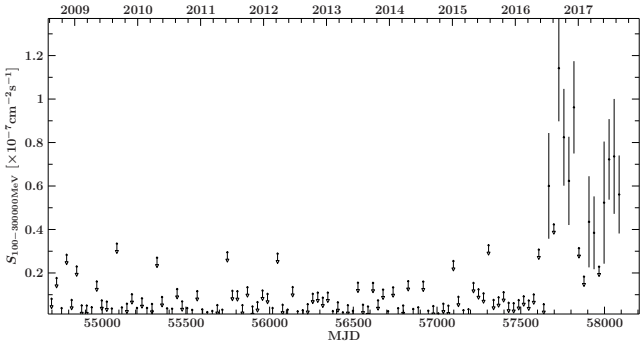

Figure G.36: *Fermi*/LAT γ-ray light curve of source 36

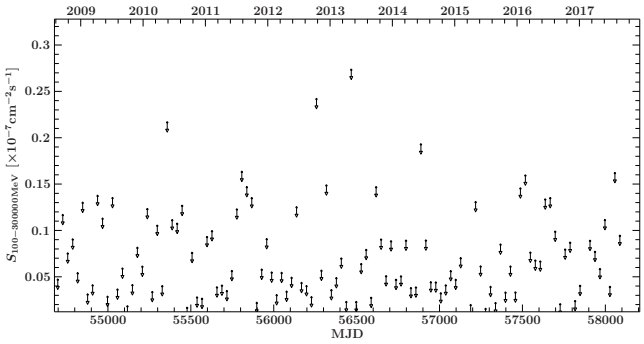

Figure G.37: *Fermi*/LAT γ-ray light curve of source 37

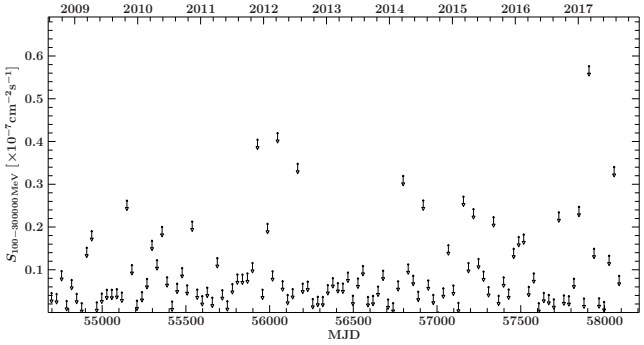

Figure G.38: *Fermi*/LAT γ-ray light curve of source 38

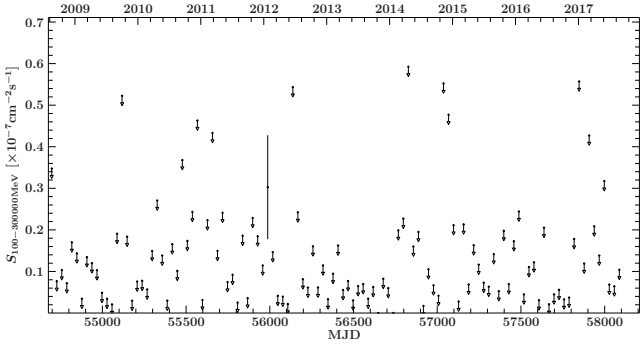

Figure G.39: *Fermi*/LAT γ-ray light curve of source 39

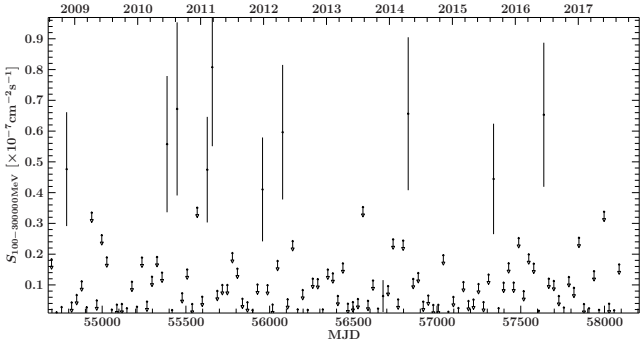

Figure G.40: *Fermi*/LAT γ-ray light curve of source 40

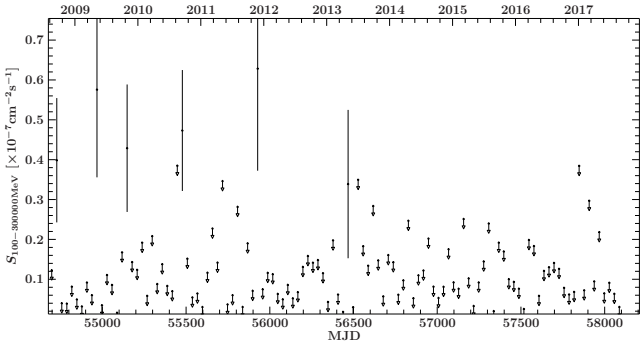

Figure G.41: *Fermi*/LAT γ-ray light curve of source 41

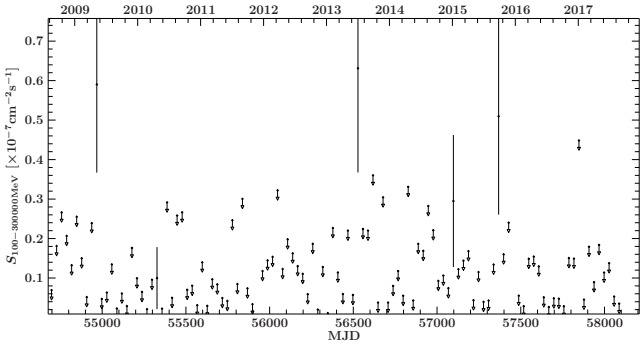

Figure G.42: *Fermi*/LAT γ-ray light curve of source 42

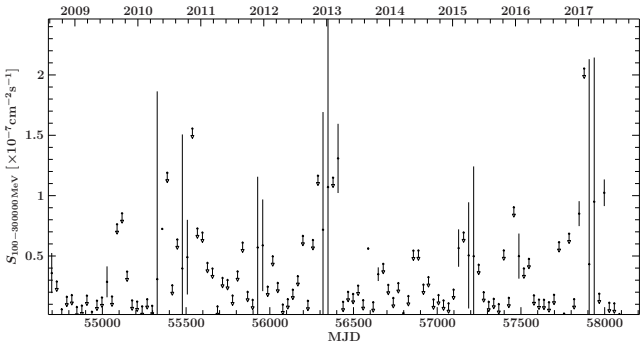

Figure G.43: *Fermi*/LAT γ-ray light curve of source 43

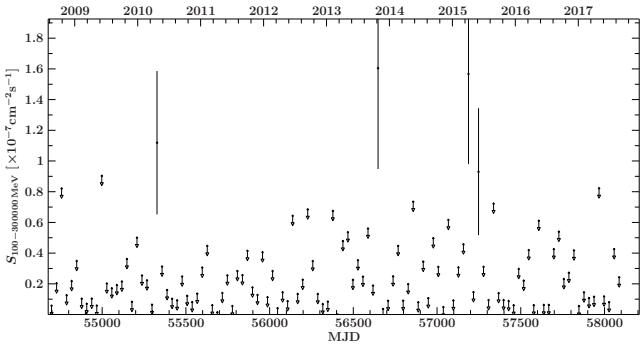

Figure G.44: *Fermi*/LAT γ-ray light curve of source 44

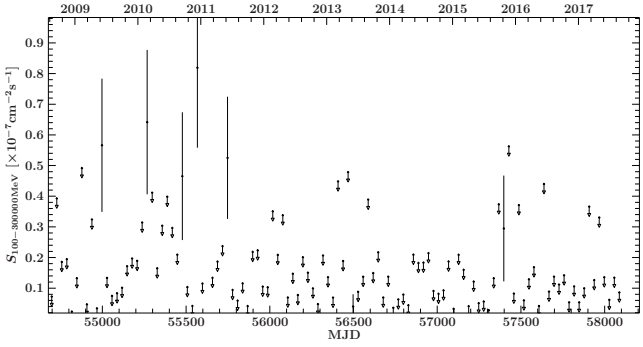

Figure G.45: *Fermi*/LAT γ-ray light curve of source 45

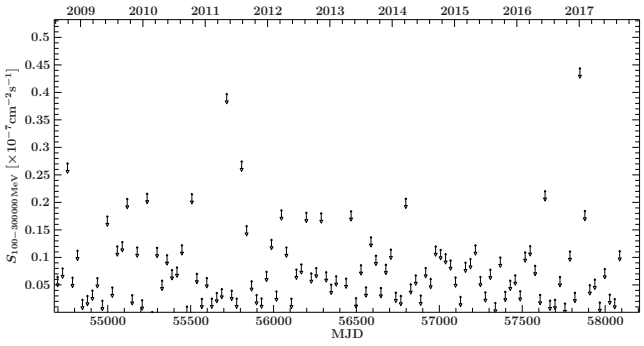

Figure G.46: *Fermi*/LAT γ-ray light curve of source 46

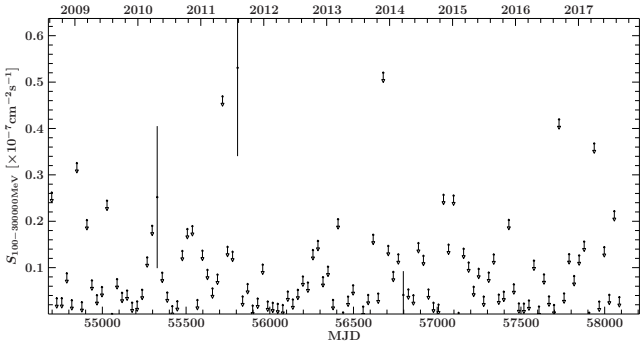

Figure G.47: *Fermi*/LAT γ-ray light curve of source 47

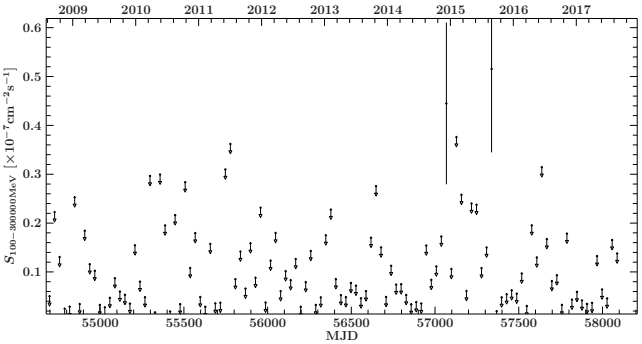

Figure G.48: *Fermi*/LAT γ-ray light curve of source 48

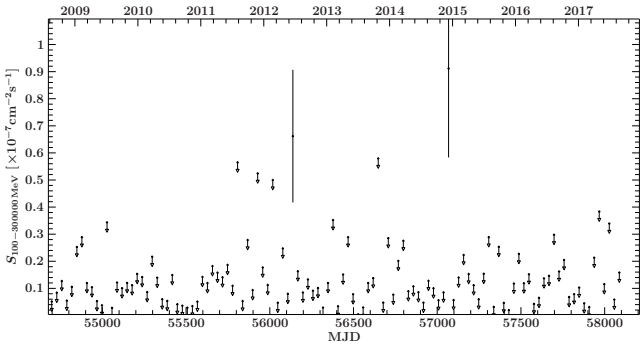

Figure G.49: *Fermi*/LAT γ-ray light curve of source 49

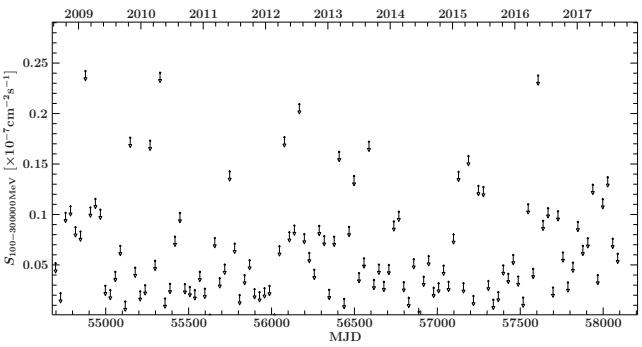

Figure G.50: *Fermi*/LAT γ-ray light curve of source 50

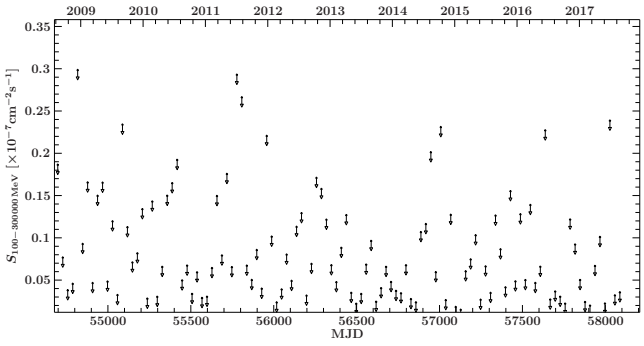

Figure G.51: *Fermi*/LAT γ-ray light curve of source 51

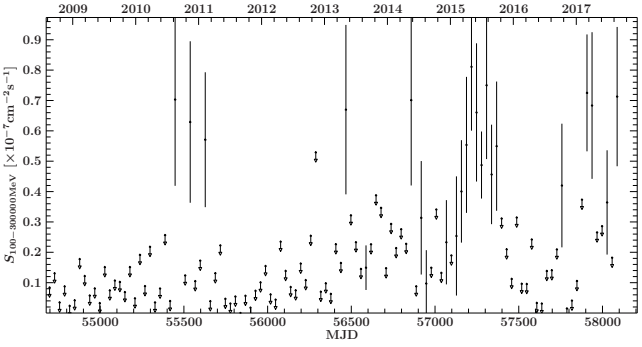

Figure G.52: *Fermi*/LAT γ-ray light curve of source 52

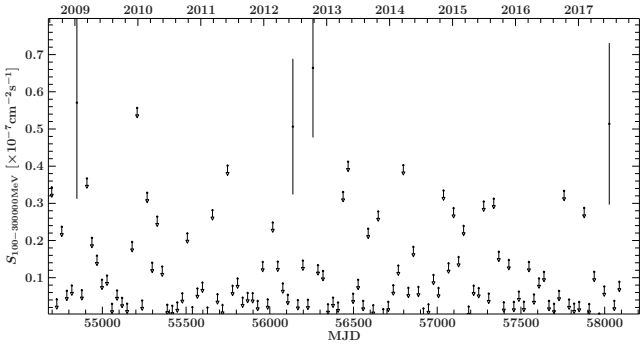

Figure G.53: *Fermi*/LAT γ-ray light curve of source 53

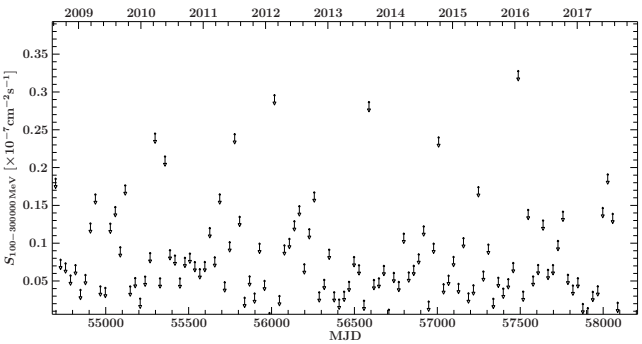

Figure G.54: *Fermi*/LAT γ-ray light curve of source 54

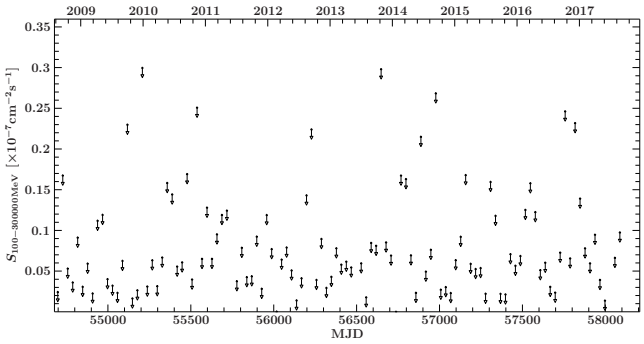

Figure G.55: *Fermi*/LAT γ-ray light curve of source 55

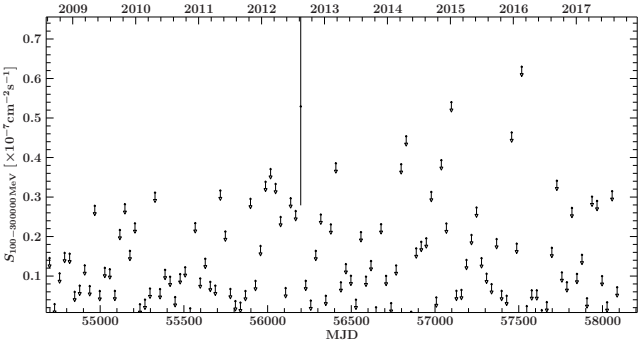

Figure G.56: *Fermi*/LAT γ-ray light curve of source 56

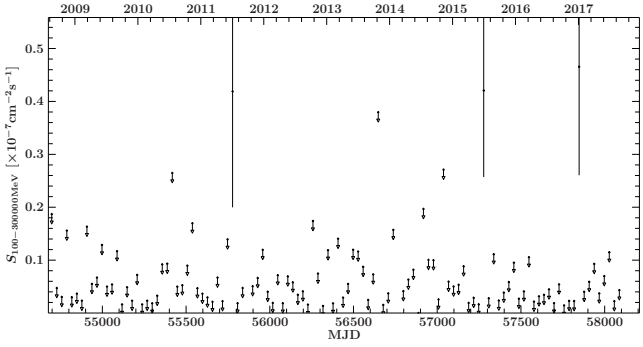

Figure G.57: *Fermi*/LAT γ-ray light curve of source 57

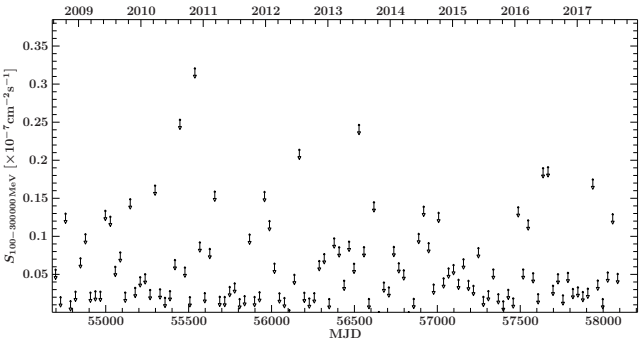

Figure G.58: *Fermi*/LAT γ-ray light curve of source 58

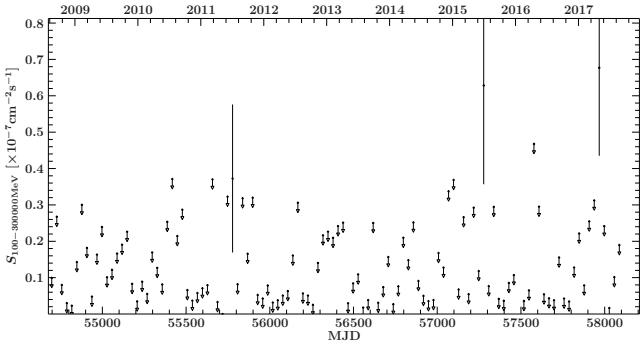

Figure G.59: *Fermi*/LAT γ-ray light curve of source 59

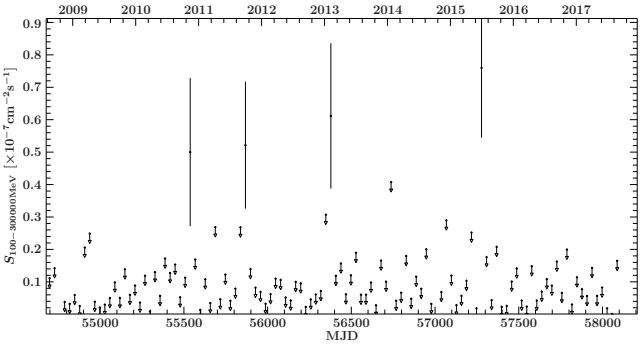

Figure G.60: *Fermi*/LAT γ-ray light curve of source 60

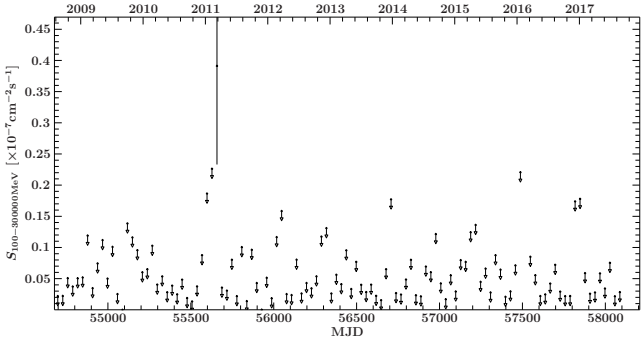

Figure G.61: *Fermi*/LAT γ-ray light curve of source 61

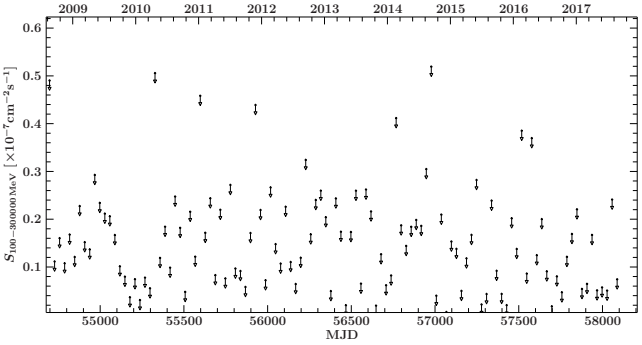

Figure G.62: *Fermi*/LAT γ-ray light curve of source 62

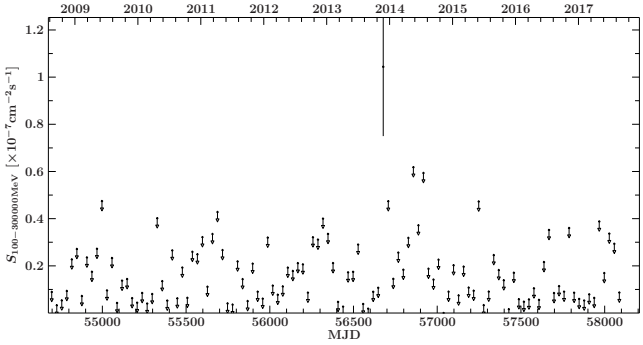

Figure G.63: *Fermi*/LAT γ-ray light curve of source 63

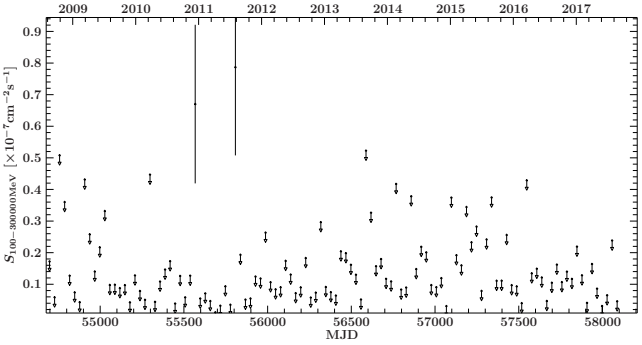

Figure G.64: *Fermi*/LAT γ-ray light curve of source 64

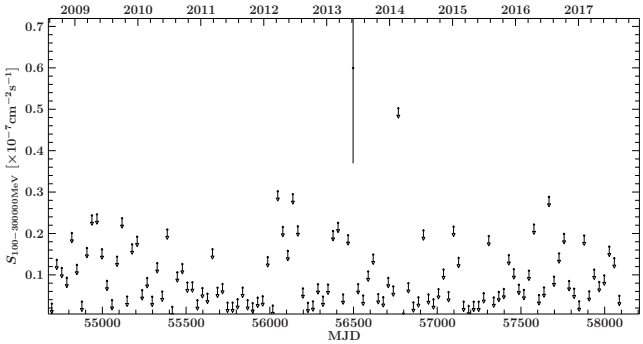

Figure G.65: *Fermi*/LAT γ-ray light curve of source 65

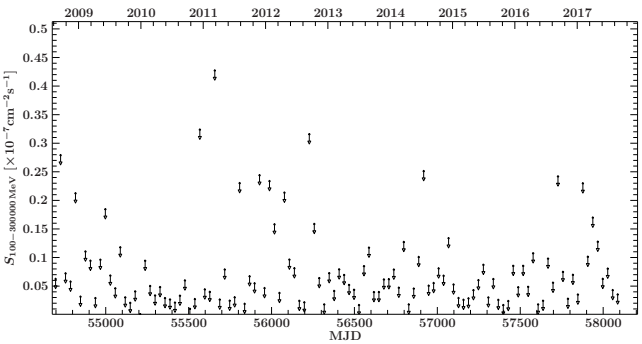

Figure G.66: *Fermi*/LAT γ-ray light curve of source 66

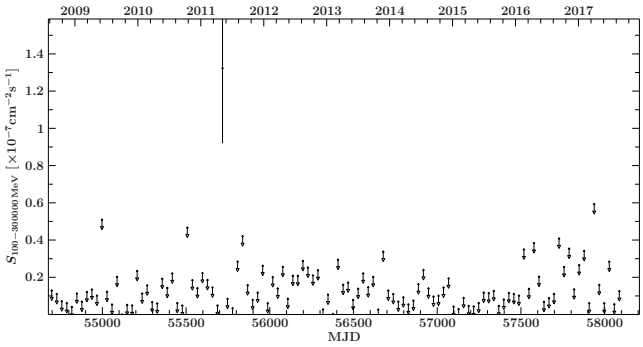

Figure G.67: *Fermi*/LAT γ-ray light curve of source 67

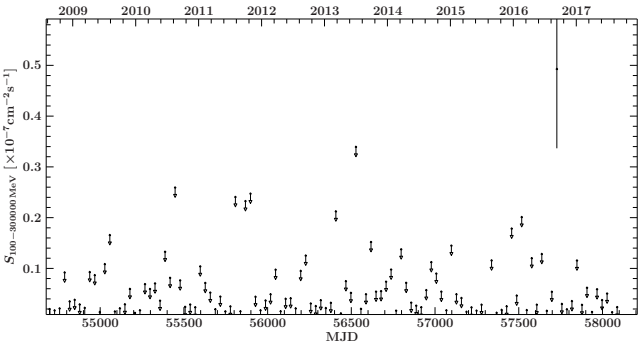

Figure G.68: *Fermi*/LAT γ-ray light curve of source 68

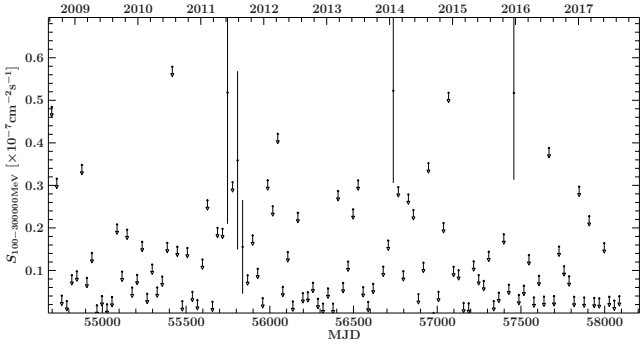

Figure G.69: *Fermi*/LAT γ-ray light curve of source 69

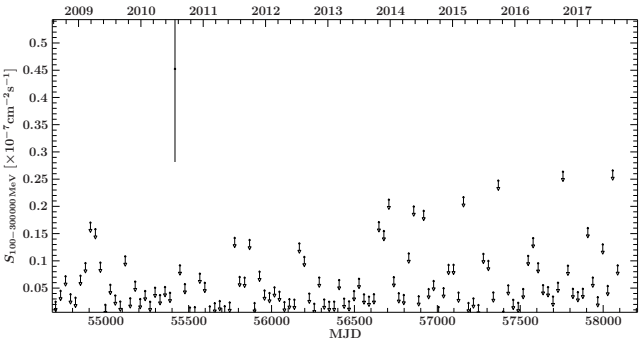

Figure G.70: *Fermi*/LAT γ-ray light curve of source 70

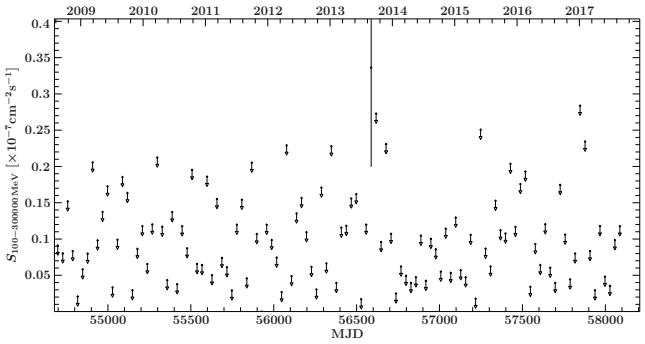

Figure G.71: *Fermi*/LAT γ-ray light curve of source 71

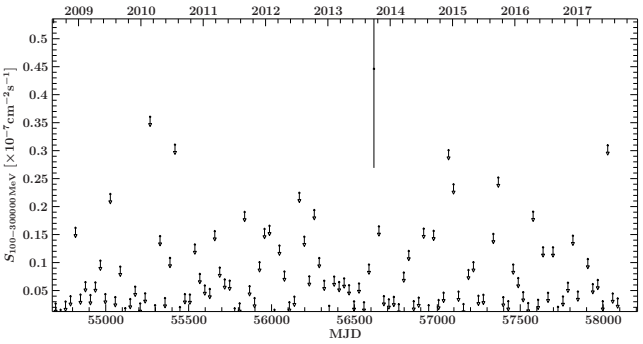

Figure G.72: *Fermi*/LAT γ-ray light curve of source 72

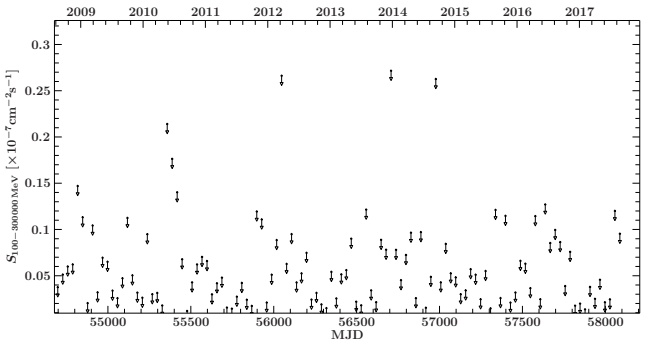

Figure G.73: *Fermi*/LAT γ-ray light curve of source 73

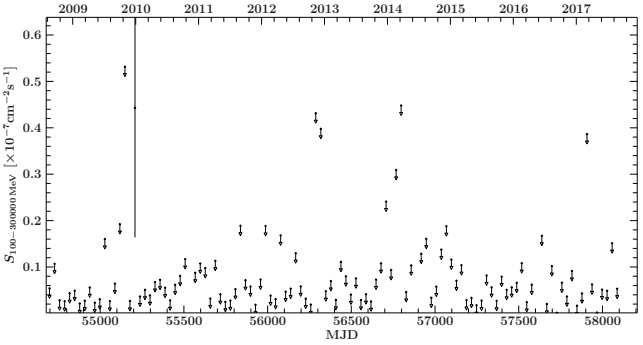

Figure G.74: *Fermi*/LAT γ-ray light curve of source 74

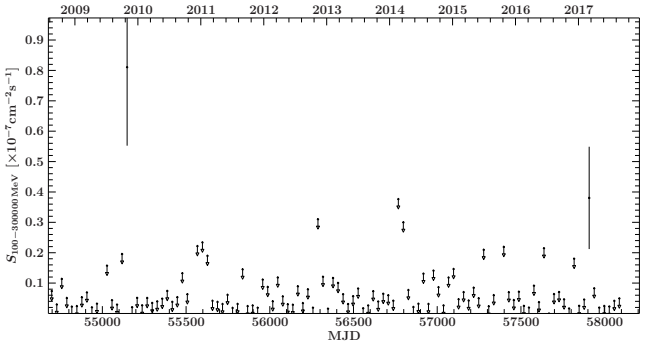

Figure G.75: *Fermi*/LAT γ-ray light curve of source 75

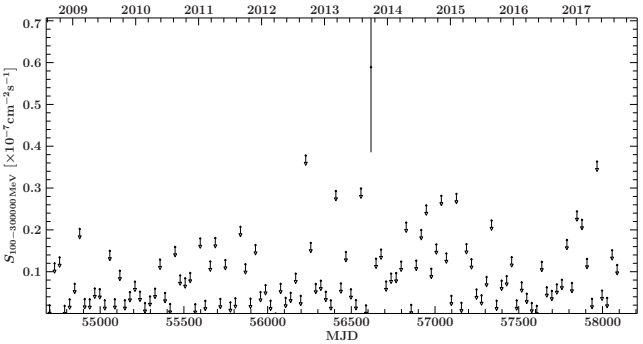

Figure G.76: *Fermi*/LAT γ-ray light curve of source 76

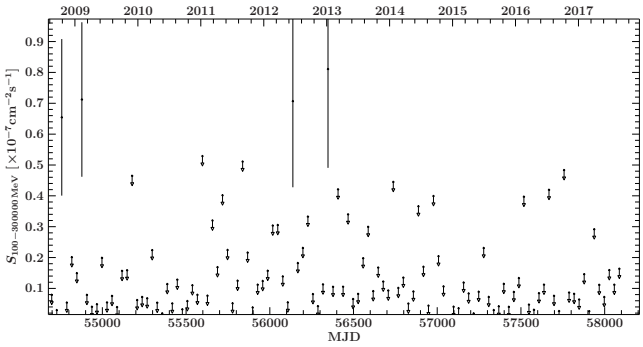

Figure G.77: *Fermi*/LAT γ-ray light curve of source 77

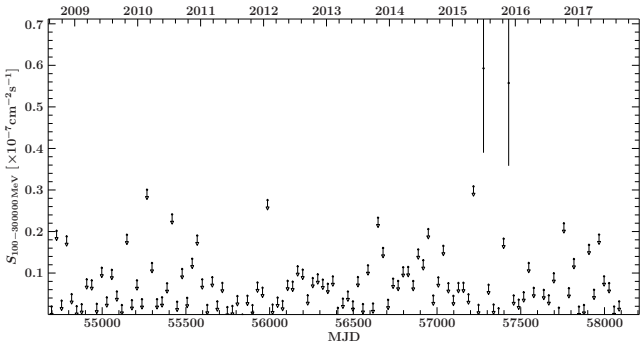

Figure G.78: *Fermi*/LAT γ-ray light curve of source 78

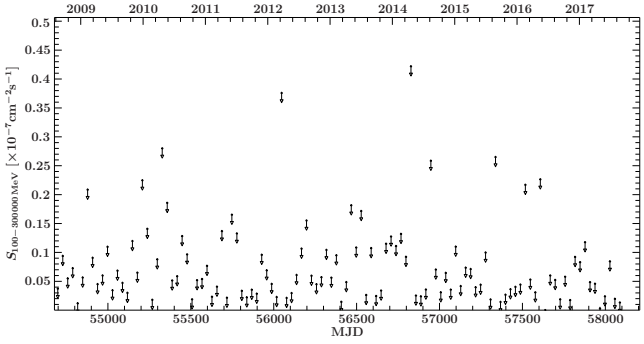

Figure G.79: *Fermi*/LAT γ-ray light curve of source 79

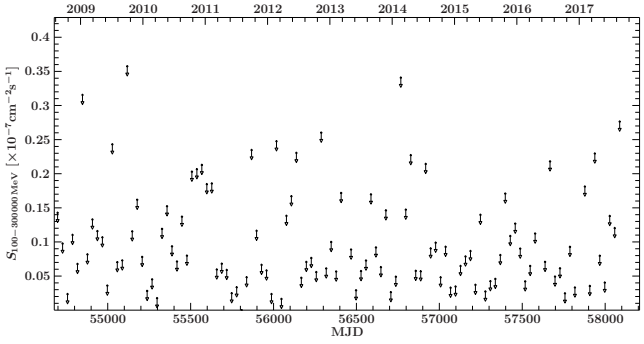

Figure G.80: *Fermi*/LAT γ-ray light curve of source 80

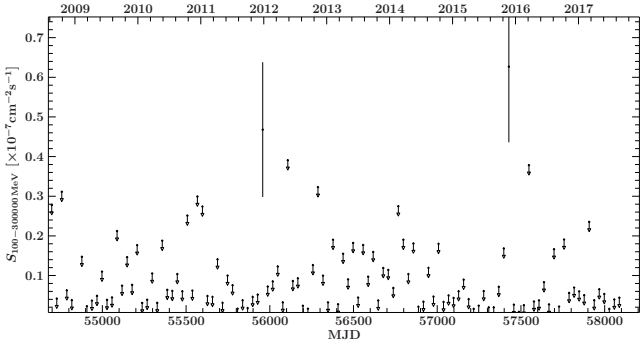

Figure G.81: *Fermi*/LAT γ-ray light curve of source 81

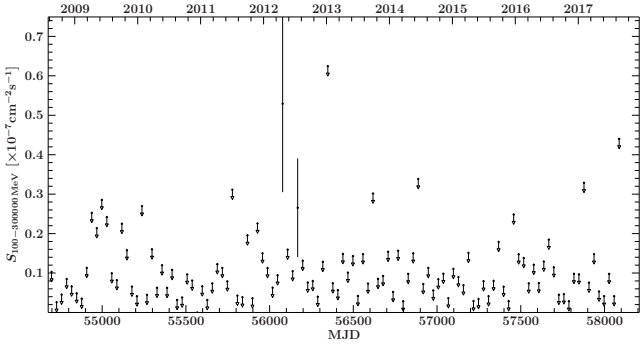

Figure G.82: *Fermi*/LAT γ-ray light curve of source 82

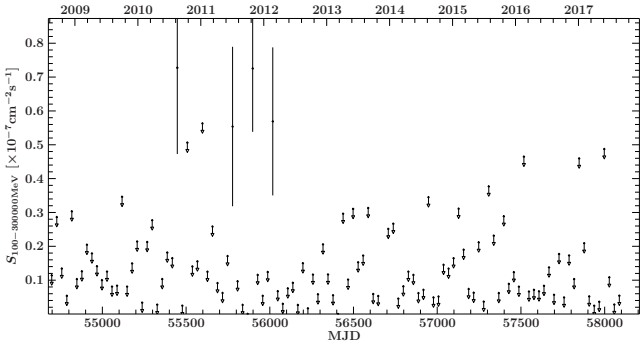

Figure G.83: *Fermi*/LAT γ-ray light curve of source 83

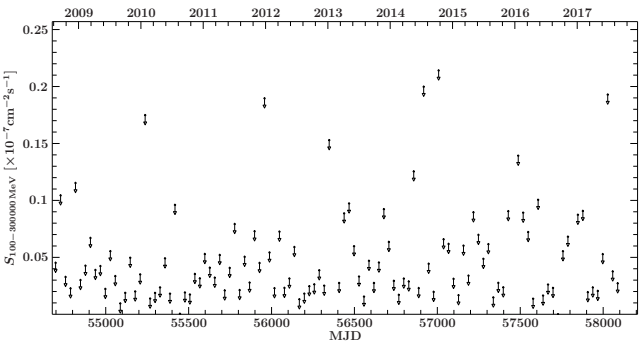

Figure G.84: *Fermi*/LAT γ-ray light curve of source 84

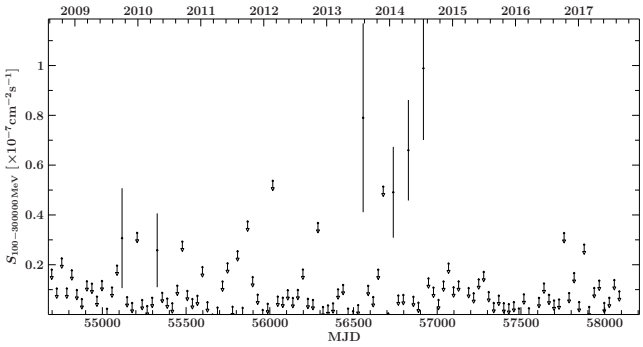

Figure G.85: *Fermi*/LAT γ-ray light curve of source 85

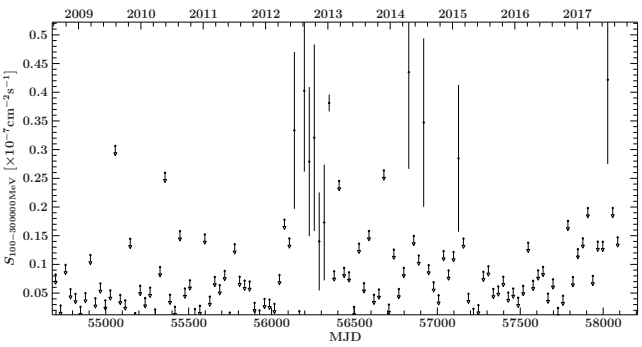

Figure G.86: *Fermi*/LAT γ-ray light curve of source 86

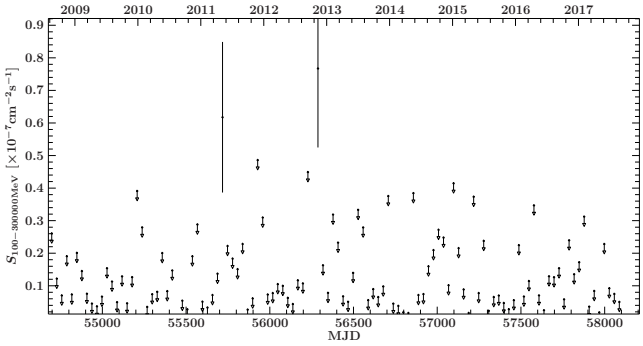

Figure G.87: *Fermi*/LAT γ-ray light curve of source 87

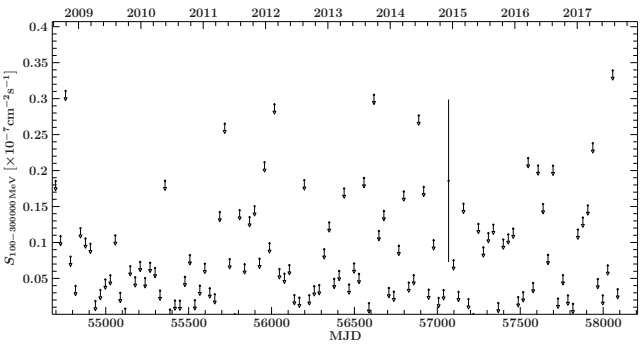

Figure G.88: *Fermi*/LAT γ-ray light curve of source 88

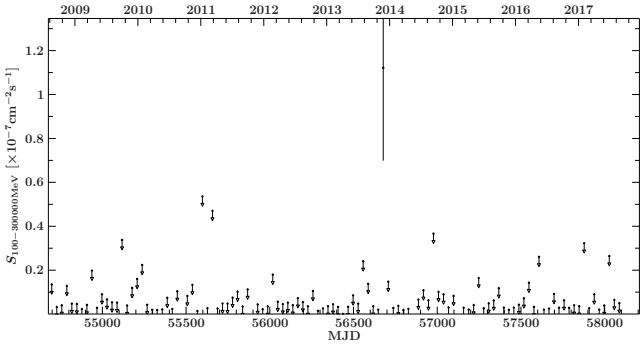

Figure G.89: *Fermi*/LAT γ-ray light curve of source 89

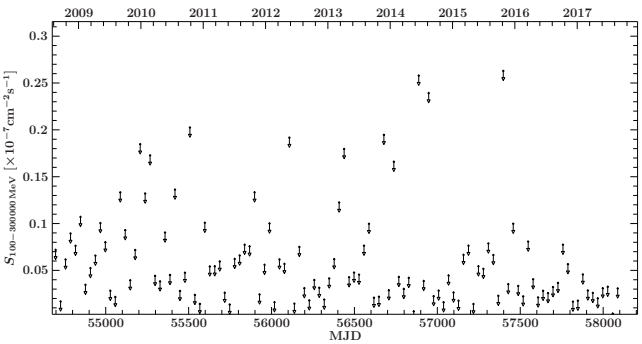

Figure G.90: *Fermi*/LAT γ-ray light curve of source 90

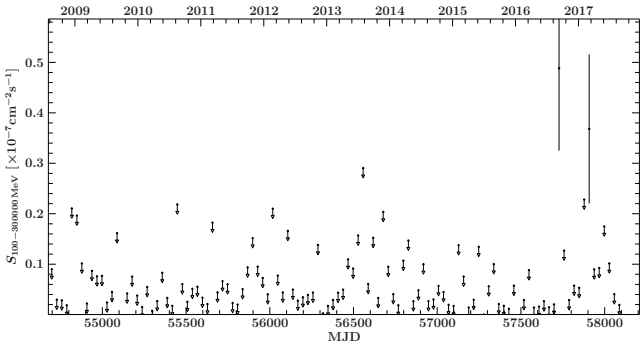

Figure G.91: *Fermi*/LAT γ-ray light curve of source 91

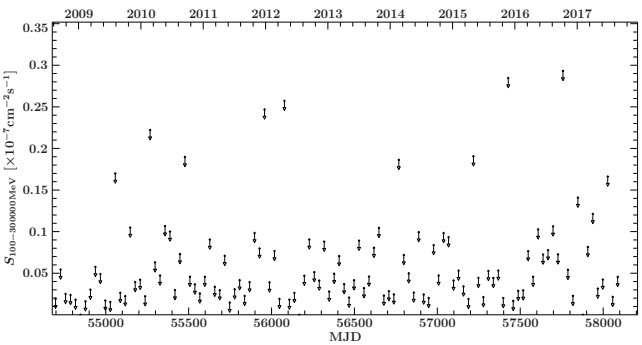

Figure G.92: *Fermi*/LAT γ-ray light curve of source 92

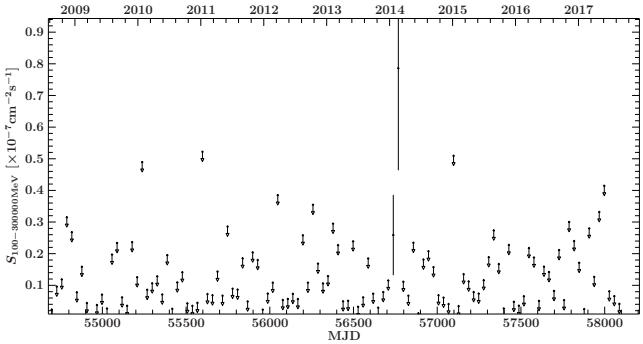

Figure G.93: *Fermi*/LAT γ-ray light curve of source 93

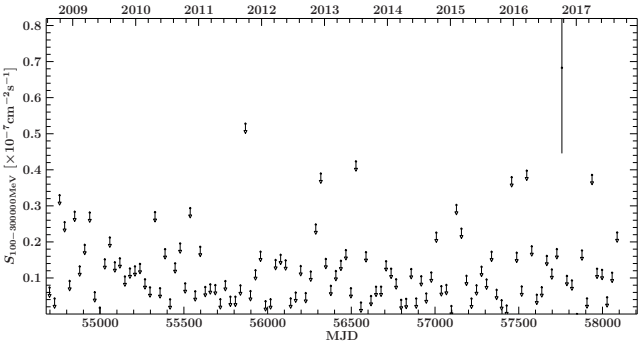

Figure G.94: *Fermi*/LAT γ-ray light curve of source 94

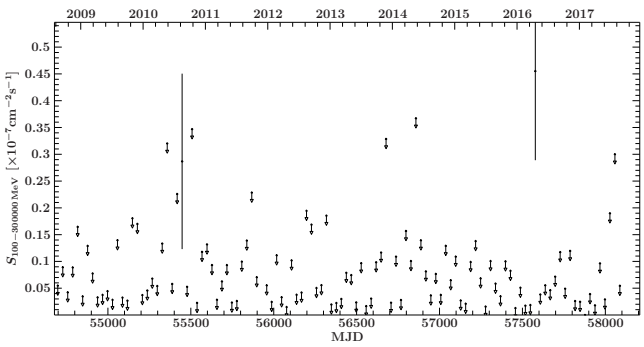

Figure G.95: *Fermi*/LAT γ-ray light curve of source 95

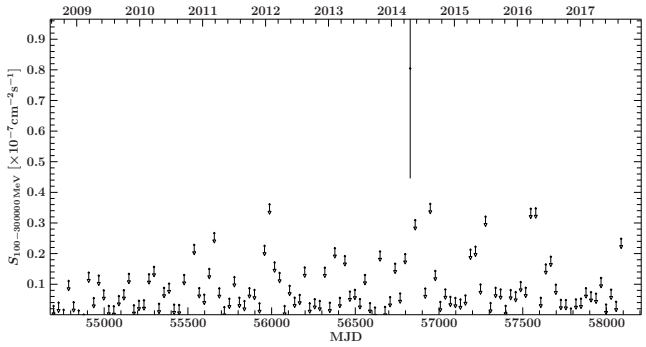

Figure G.96: *Fermi*/LAT γ-ray light curve of source 96

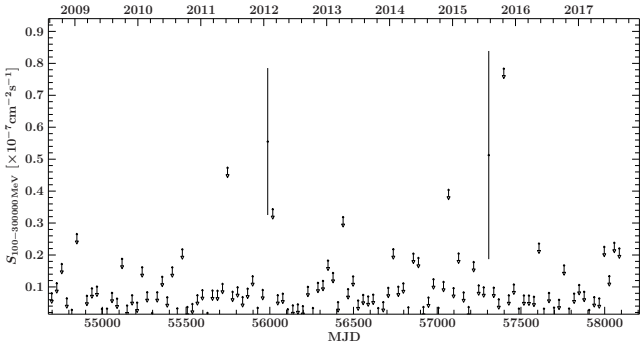

Figure G.97: *Fermi*/LAT γ-ray light curve of source 97

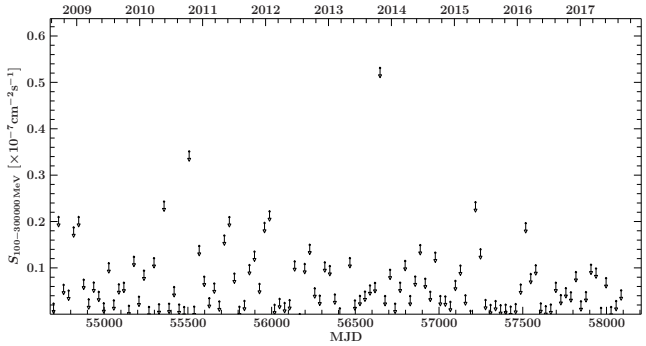

Figure G.98: *Fermi*/LAT γ-ray light curve of source 98

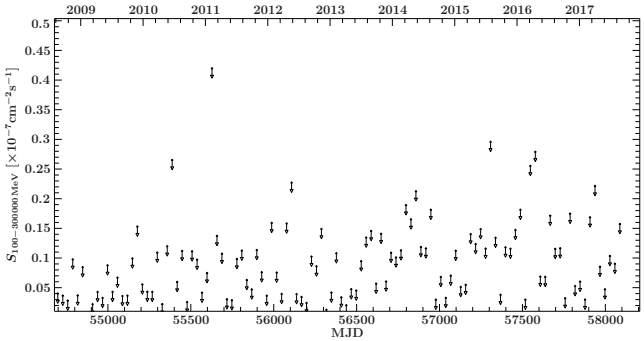

Figure G.99: *Fermi*/LAT γ-ray light curve of source 99

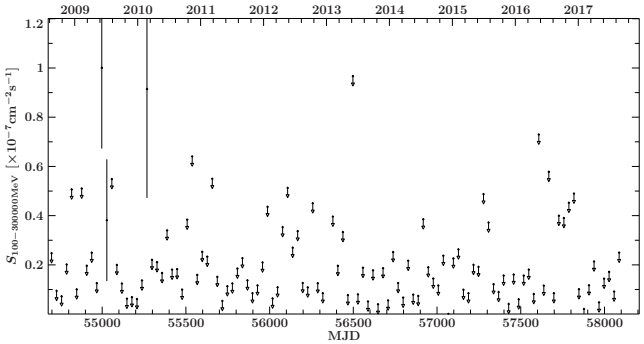

Figure G.100: *Fermi*/LAT γ-ray light curve of source 100

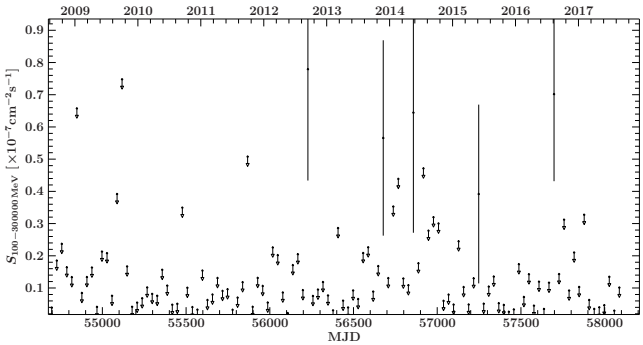

Figure G.101: *Fermi*/LAT γ-ray light curve of source 101

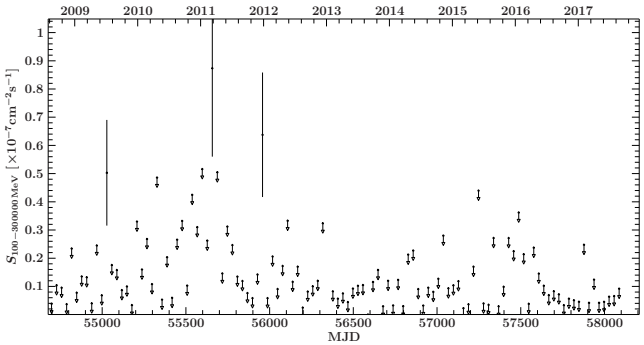

Figure G.102: *Fermi*/LAT γ-ray light curve of source 102

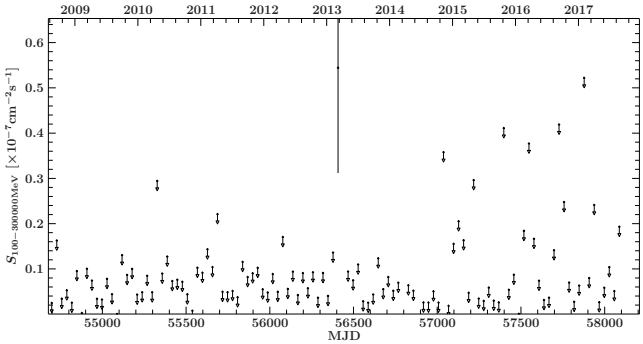

Figure G.103: *Fermi*/LAT γ-ray light curve of source 103

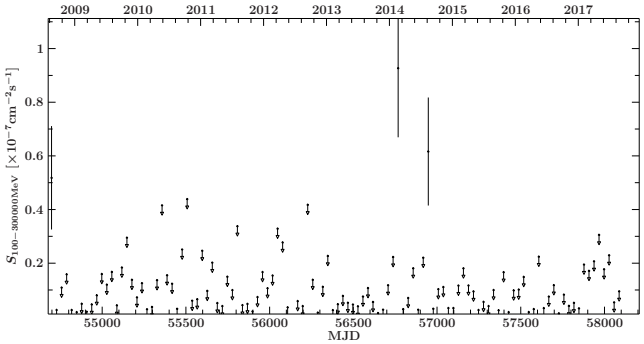

Figure G.104: *Fermi*/LAT γ-ray light curve of source 104

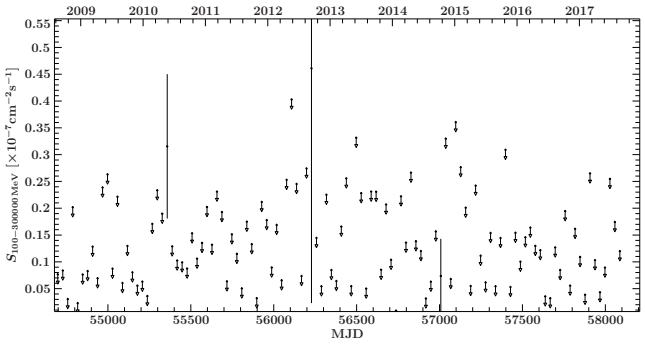

Figure G.105: *Fermi*/LAT γ-ray light curve of source 105

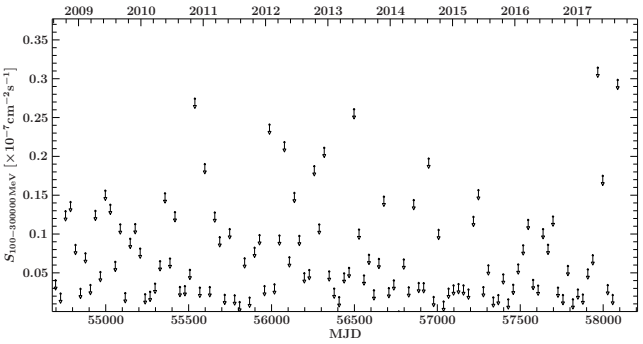

Figure G.106: *Fermi*/LAT γ-ray light curve of source 106

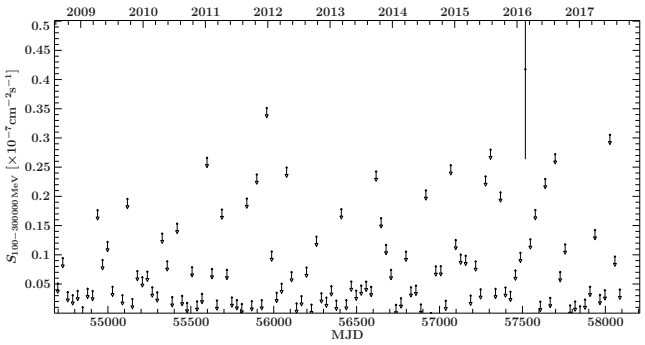

Figure G.107: *Fermi*/LAT γ-ray light curve of source 107

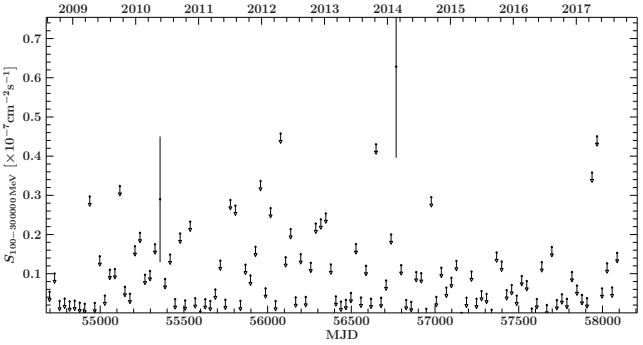

Figure G.108: *Fermi*/LAT γ-ray light curve of source 108

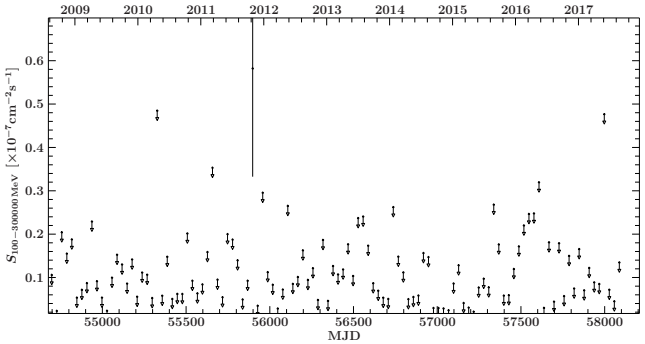

Figure G.109: *Fermi*/LAT γ-ray light curve of source 109

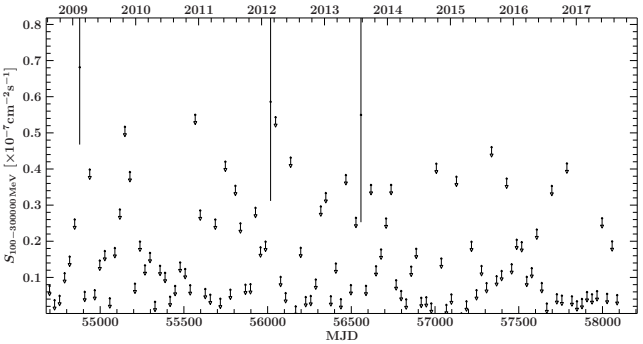

Figure G.110: *Fermi*/LAT γ-ray light curve of source 110

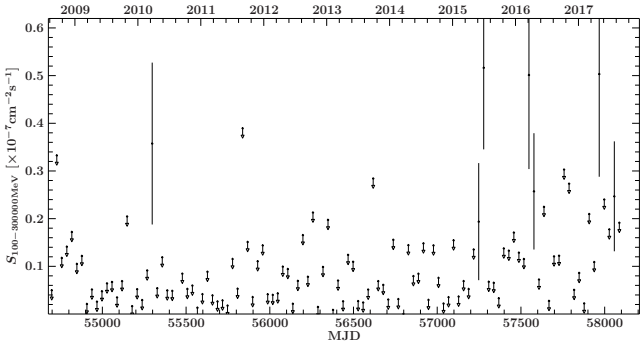

Figure G.111: *Fermi*/LAT γ-ray light curve of source 111

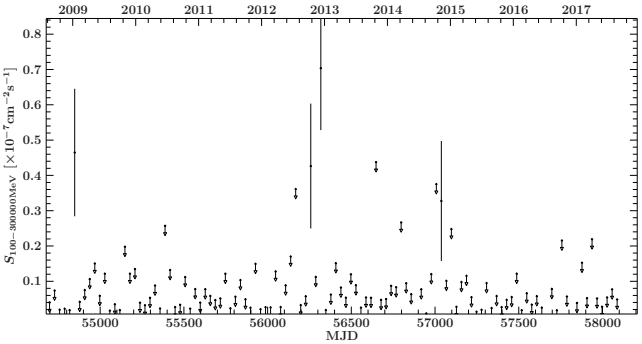

Figure G.112: *Fermi*/LAT γ-ray light curve of source 112

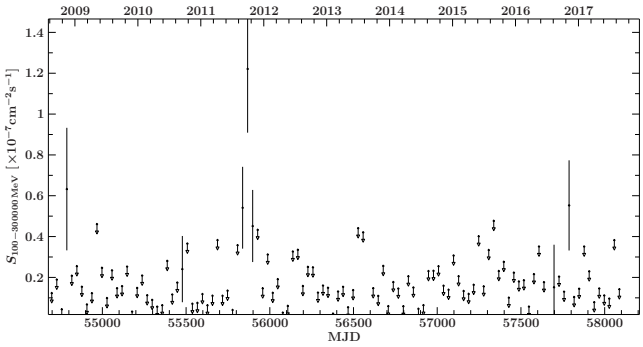

Figure G.113: *Fermi*/LAT γ-ray light curve of source 113

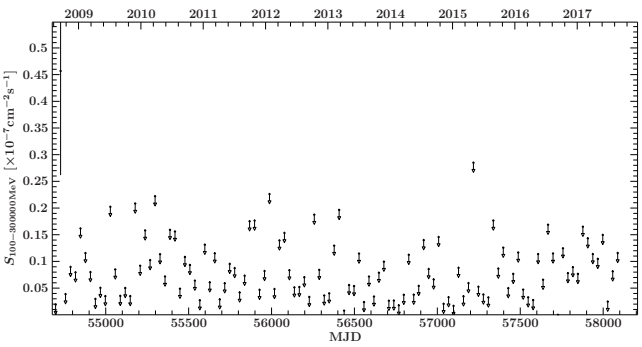

Figure G.114: *Fermi*/LAT γ-ray light curve of source 114

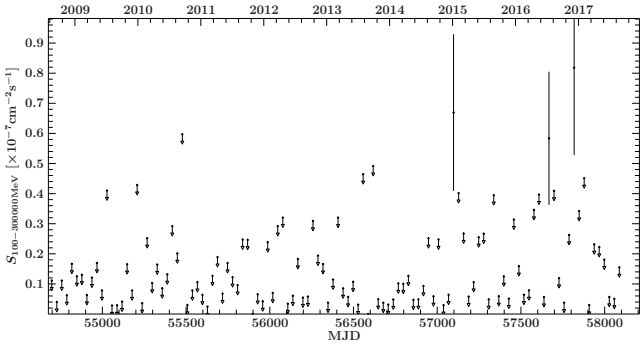

Figure G.115: *Fermi*/LAT γ-ray light curve of source 115

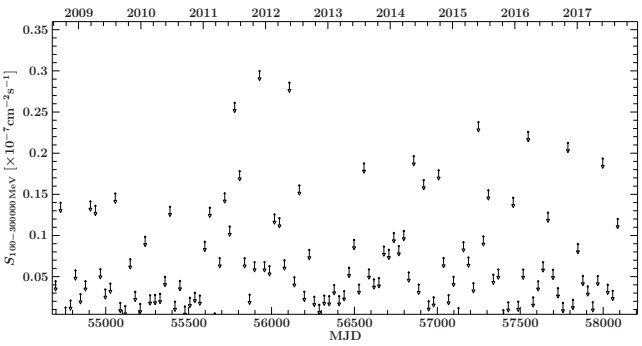

Figure G.116: *Fermi*/LAT γ-ray light curve of source 116

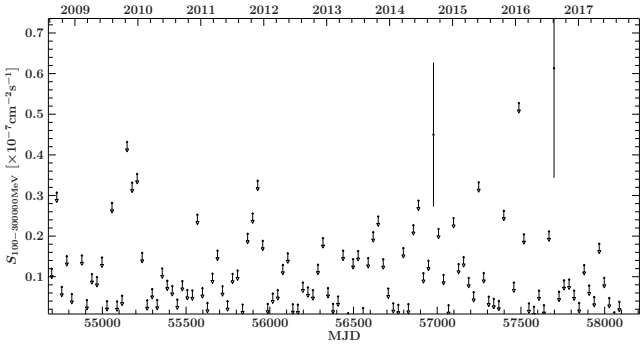

Figure G.117: *Fermi*/LAT γ-ray light curve of source 117

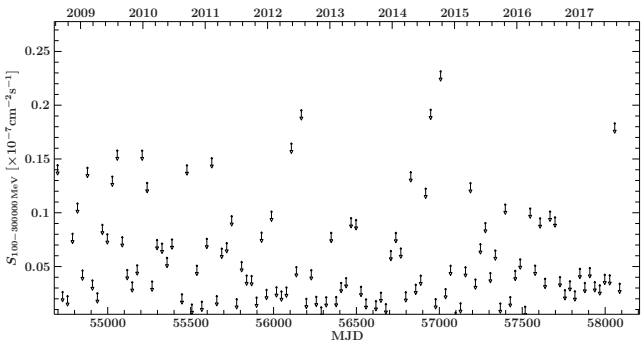

Figure G.118: *Fermi*/LAT γ-ray light curve of source 118

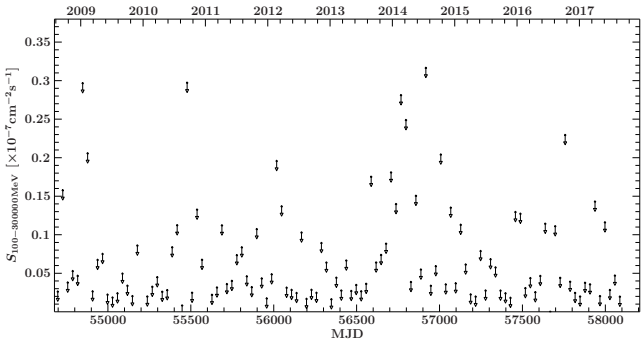

Figure G.119: *Fermi*/LAT γ-ray light curve of source 119

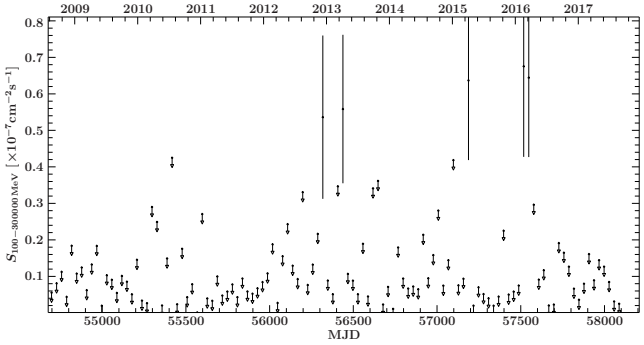

Figure G.120: *Fermi*/LAT γ-ray light curve of source 120

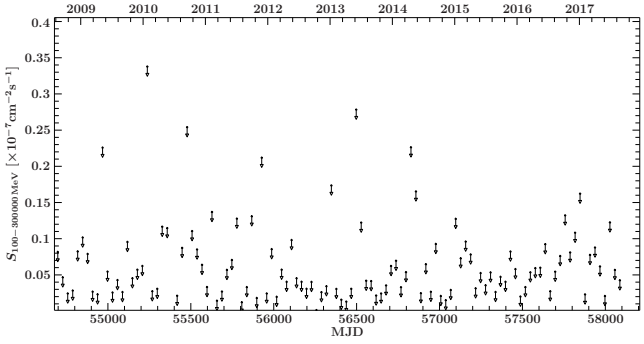

Figure G.121: *Fermi*/LAT γ-ray light curve of source 121

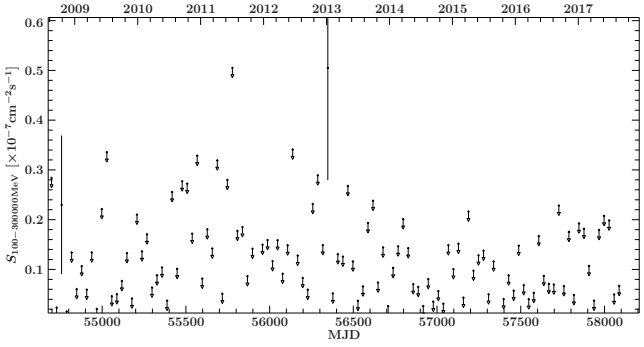

Figure G.122: *Fermi*/LAT γ-ray light curve of source 122

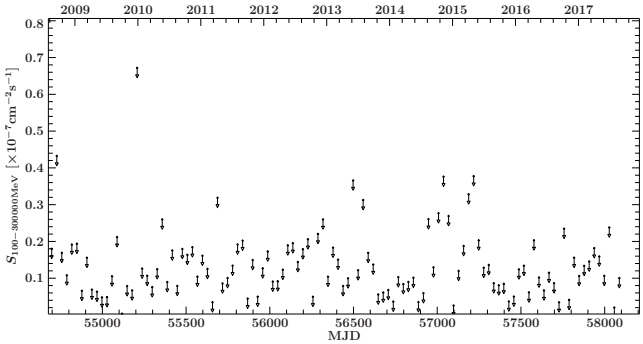

Figure G.123: *Fermi*/LAT γ-ray light curve of source 123

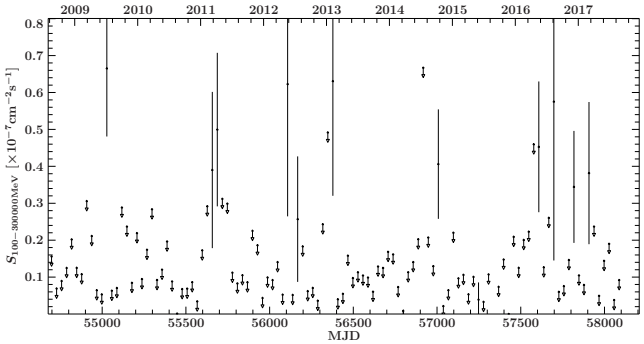

Figure G.124: *Fermi*/LAT γ-ray light curve of source 124

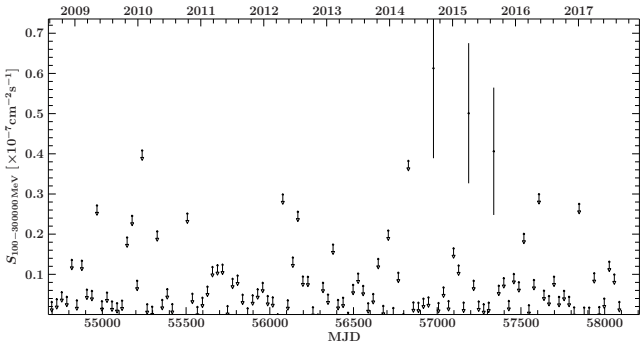

Figure G.125: *Fermi*/LAT γ-ray light curve of source 125

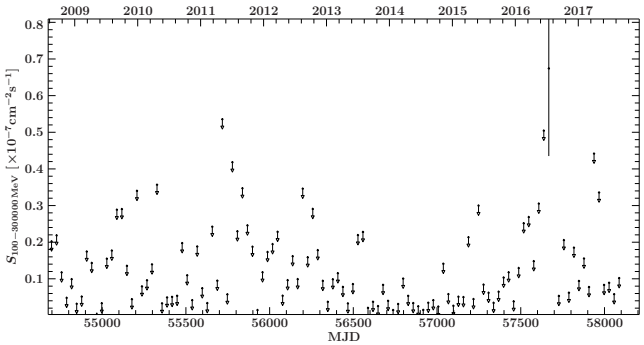

Figure G.126: *Fermi*/LAT γ-ray light curve of source 126

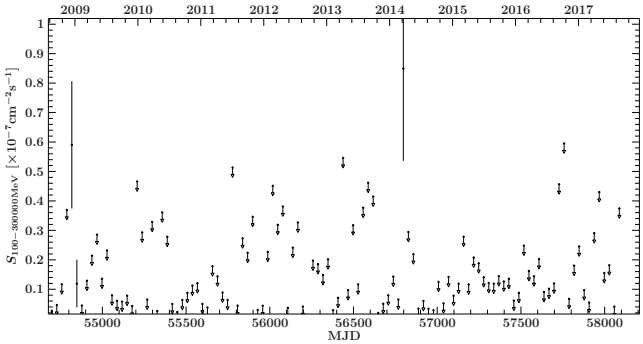

Figure G.127: *Fermi*/LAT γ-ray light curve of source 127

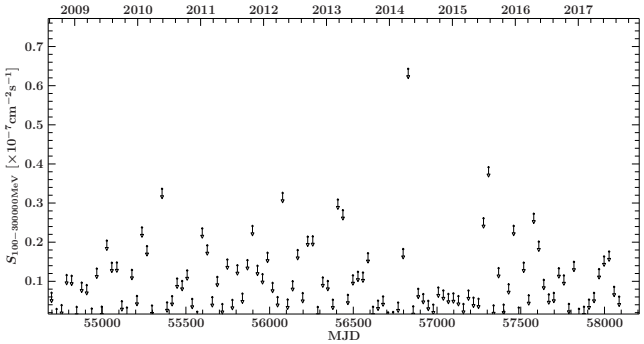

Figure G.128: *Fermi*/LAT γ-ray light curve of source 128

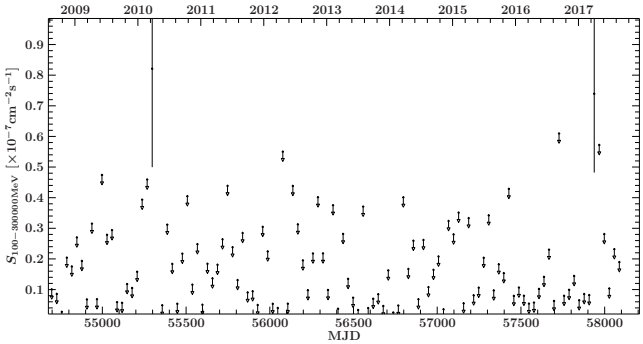

Figure G.129: *Fermi*/LAT γ-ray light curve of source 129

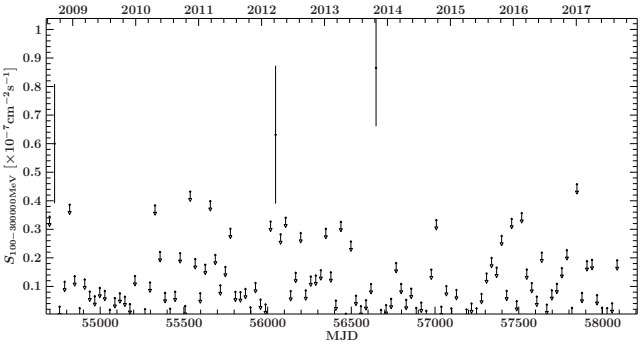

Figure G.130: *Fermi*/LAT γ-ray light curve of source 130

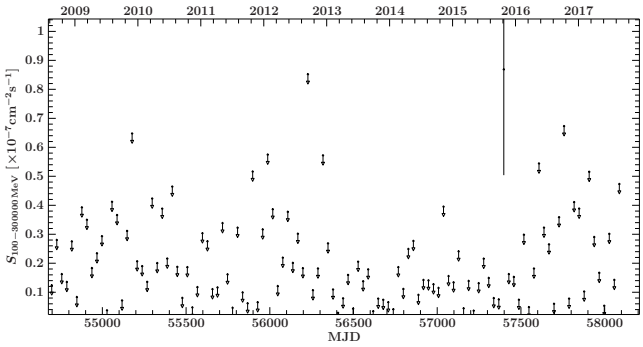

Figure G.131: *Fermi*/LAT γ-ray light curve of source 131

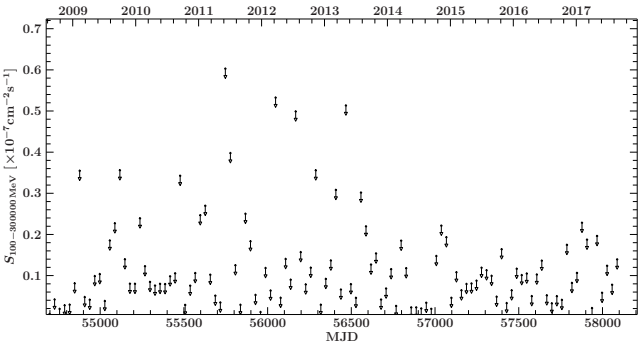

Figure G.132: *Fermi*/LAT γ-ray light curve of source 132

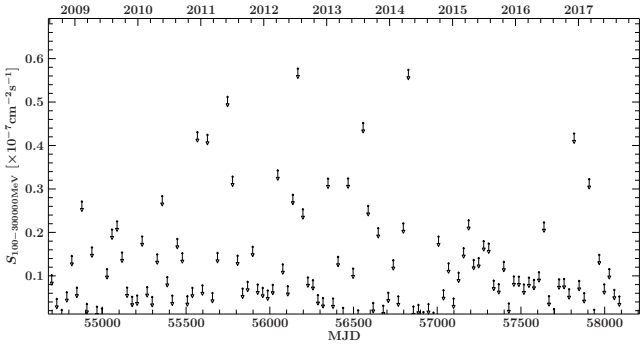

Figure G.133: *Fermi*/LAT γ-ray light curve of source 133

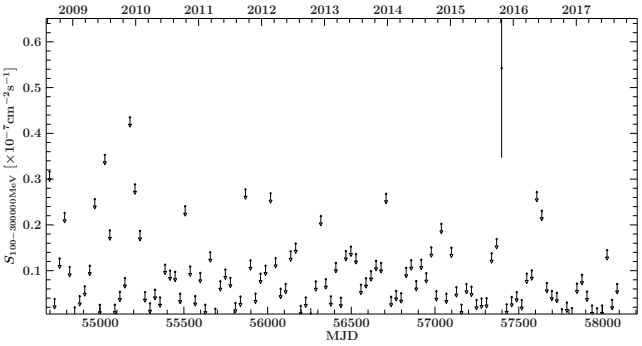

Figure G.134: *Fermi*/LAT γ-ray light curve of source 134

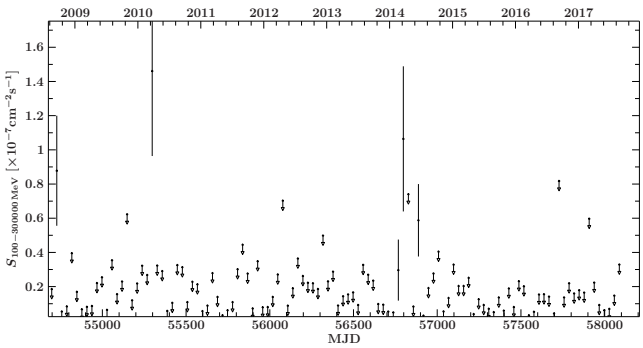

Figure G.135: *Fermi*/LAT γ-ray light curve of source 135

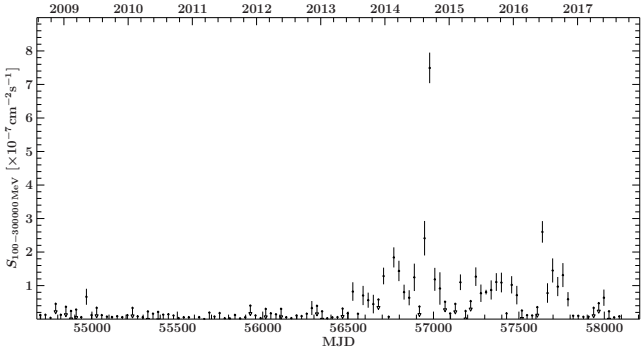

Figure G.136: *Fermi*/LAT γ-ray light curve of source 136

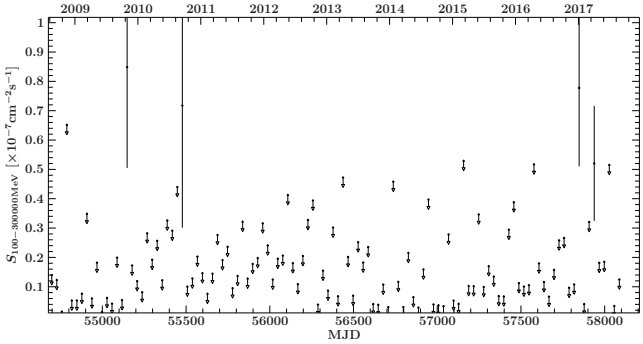

Figure G.137: *Fermi*/LAT γ-ray light curve of source 137

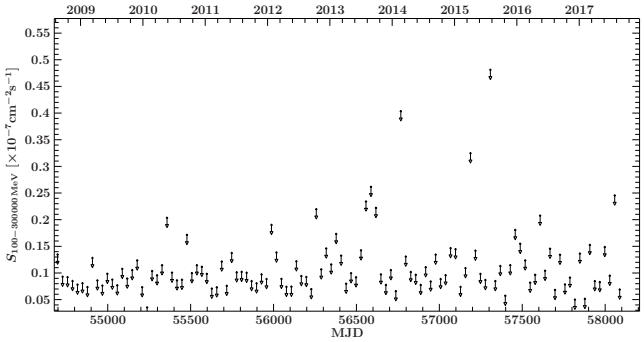

Figure G.138: *Fermi*/LAT γ-ray light curve of source 138

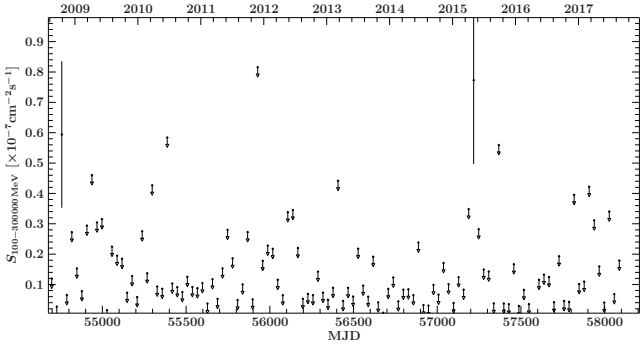

Figure G.139: *Fermi*/LAT γ-ray light curve of source 139

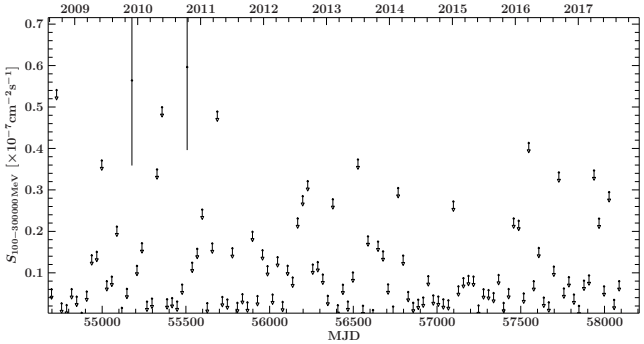

Figure G.140: *Fermi*/LAT γ-ray light curve of source 140

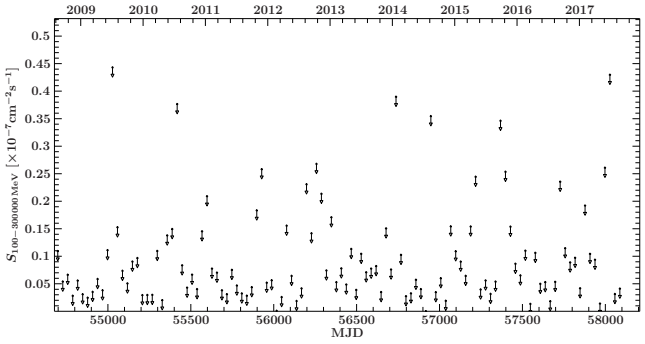

Figure G.141: *Fermi*/LAT γ-ray light curve of source 141

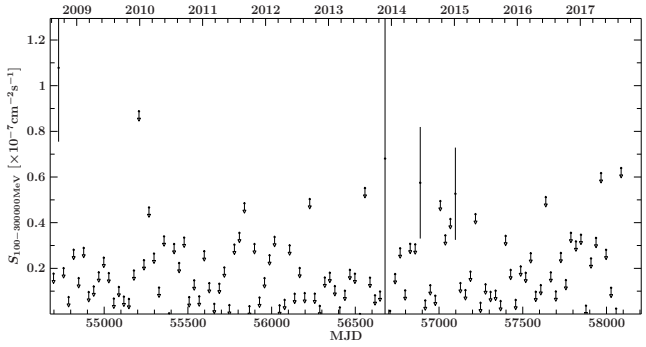

Figure G.142: *Fermi*/LAT γ-ray light curve of source 142

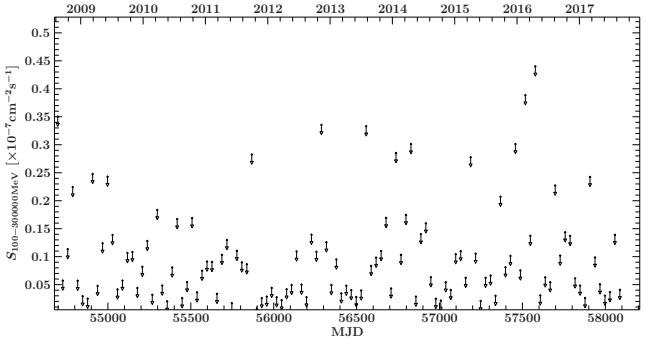

Figure G.143: *Fermi*/LAT γ-ray light curve of source 143

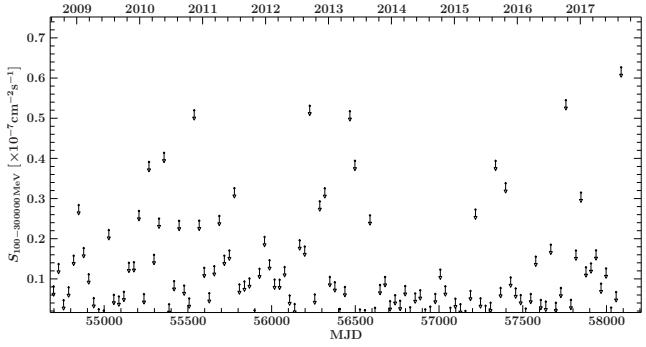

Figure G.144: *Fermi*/LAT γ-ray light curve of source 144

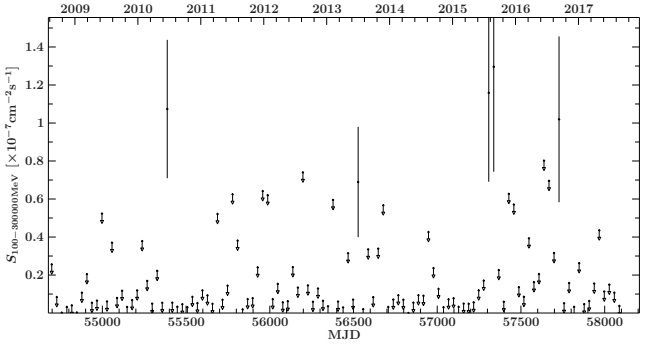

Figure G.145: *Fermi*/LAT γ-ray light curve of source 145

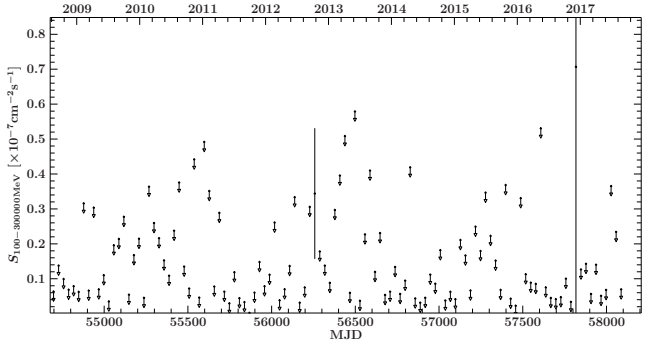

Figure G.146: *Fermi*/LAT γ-ray light curve of source 146

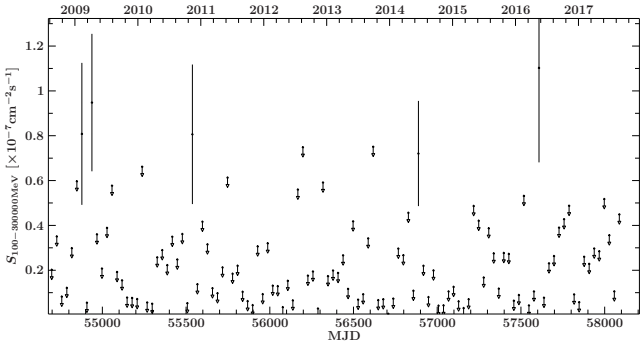

Figure G.147: *Fermi*/LAT γ-ray light curve of source 147

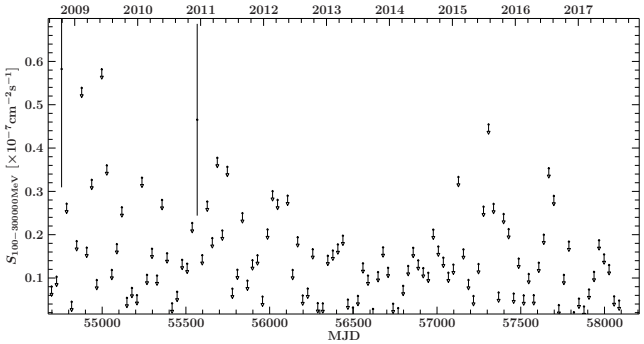

Figure G.148: *Fermi*/LAT γ-ray light curve of source 148

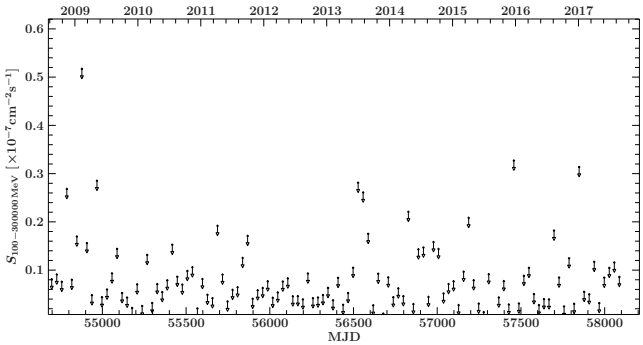

Figure G.149: *Fermi*/LAT γ-ray light curve of source 149

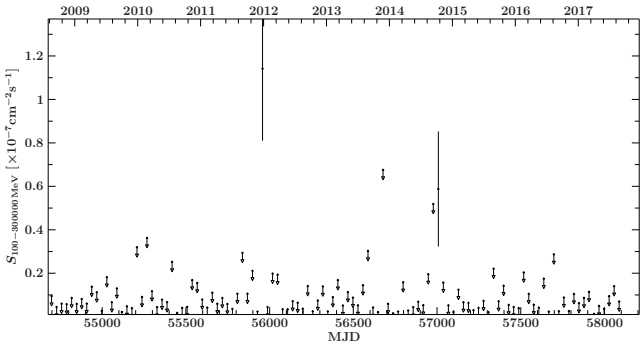

Figure G.150: *Fermi*/LAT γ-ray light curve of source 150

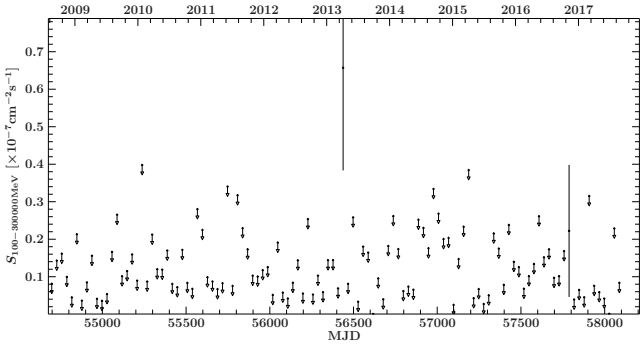

Figure G.151: *Fermi*/LAT γ-ray light curve of source 151

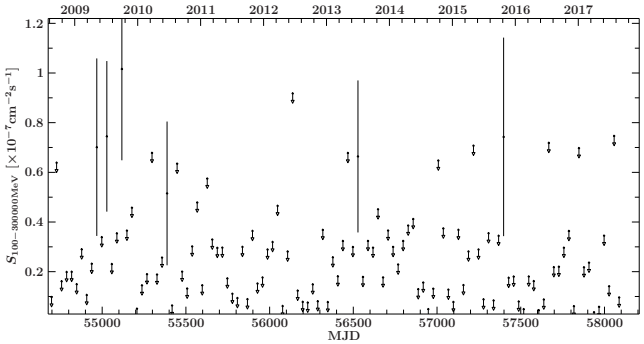

Figure G.152: *Fermi*/LAT γ-ray light curve of source 152

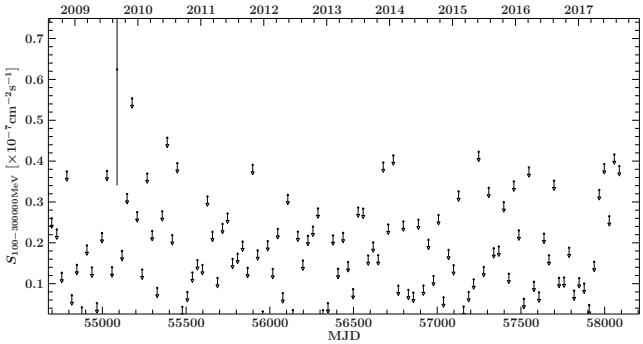

Figure G.153: *Fermi*/LAT γ-ray light curve of source 153

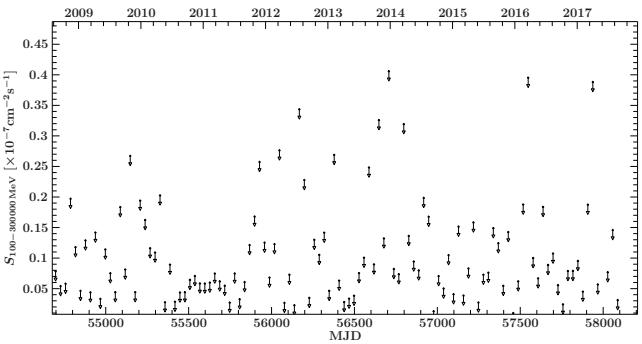

Figure G.154: *Fermi*/LAT γ-ray light curve of source 154

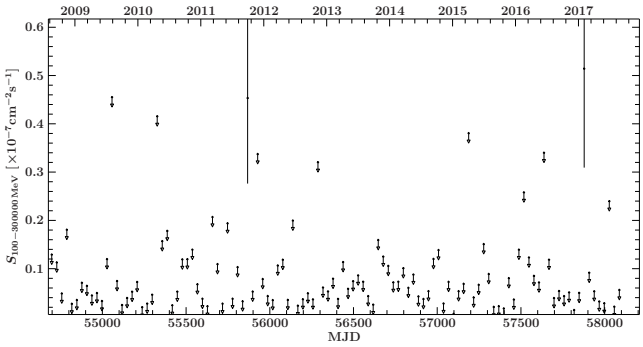

Figure G.155: *Fermi*/LAT γ-ray light curve of source 155

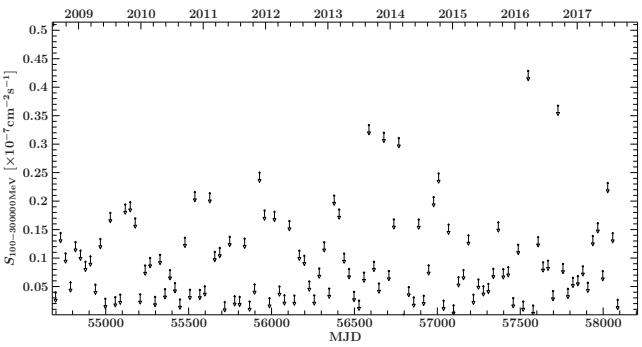

Figure G.156: *Fermi*/LAT γ-ray light curve of source 156

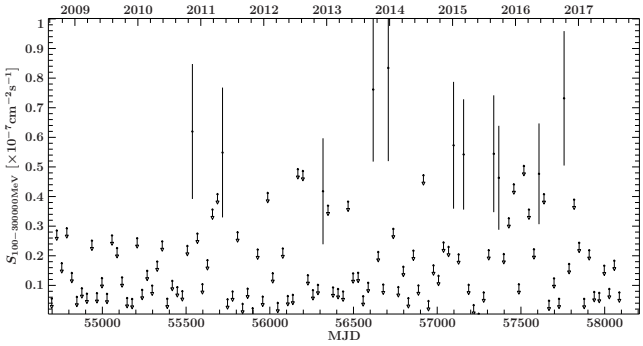

Figure G.157: *Fermi*/LAT γ-ray light curve of source 157

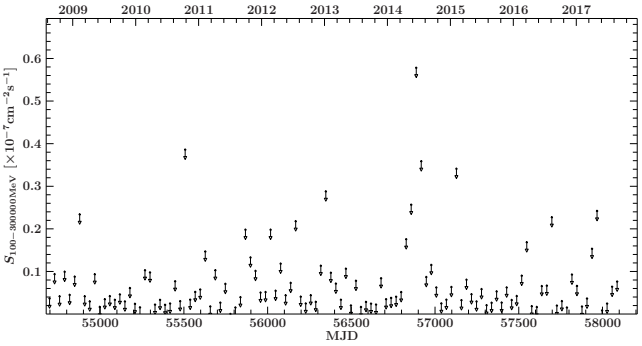

Figure G.158: *Fermi*/LAT γ-ray light curve of source 158

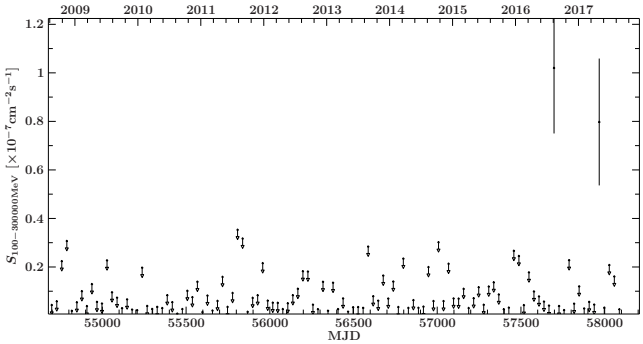

Figure G.159: *Fermi*/LAT γ-ray light curve of source 159

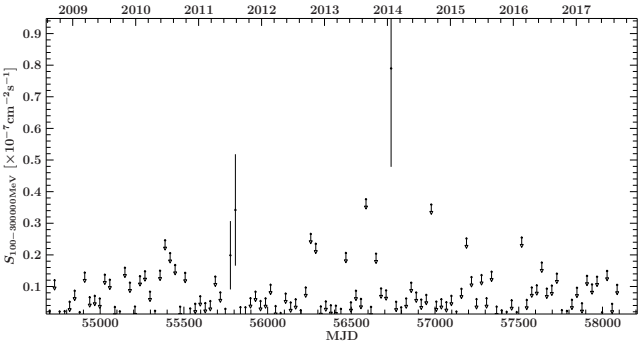

Figure G.160: *Fermi*/LAT γ-ray light curve of source 160

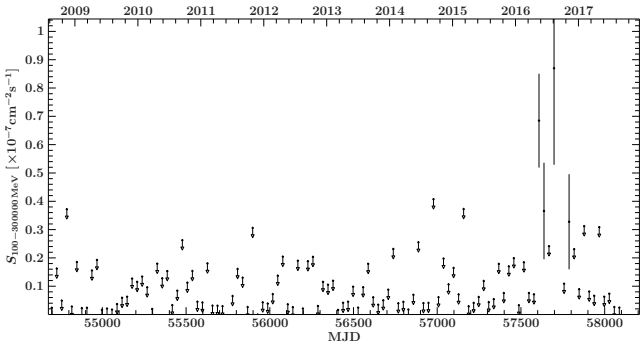

Figure G.161: *Fermi*/LAT γ-ray light curve of source 161

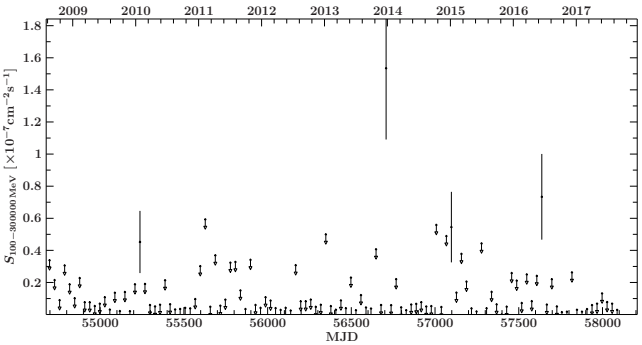

Figure G.162: *Fermi*/LAT γ-ray light curve of source 162

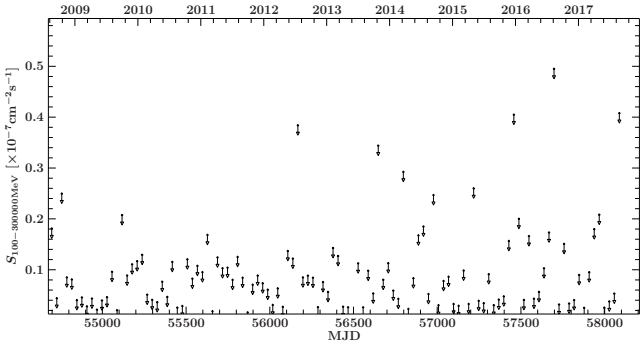

Figure G.163: *Fermi*/LAT γ-ray light curve of source 163

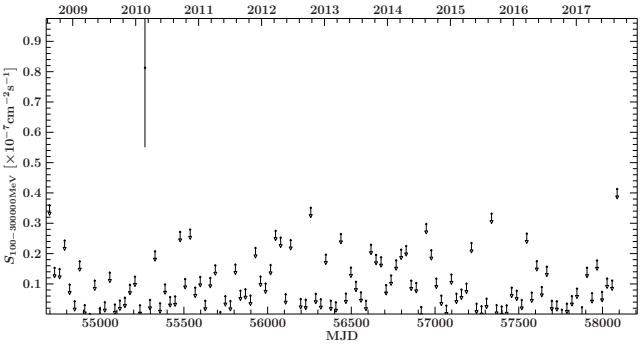

Figure G.164: *Fermi*/LAT γ-ray light curve of source 164

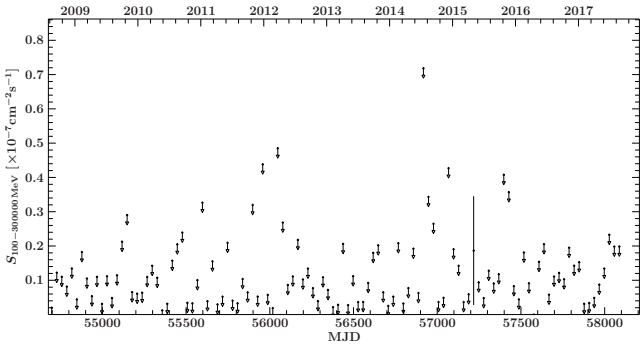

Figure G.165: *Fermi*/LAT γ-ray light curve of source 165

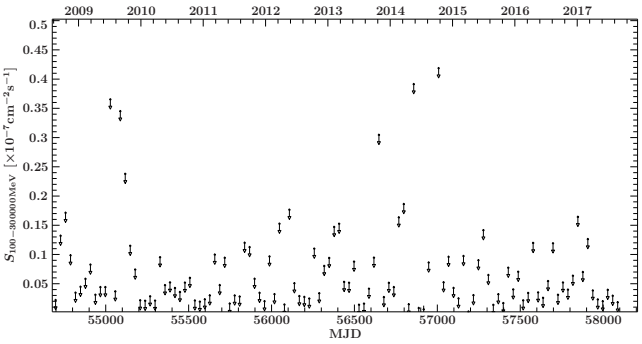

Figure G.166: *Fermi*/LAT γ-ray light curve of source 166

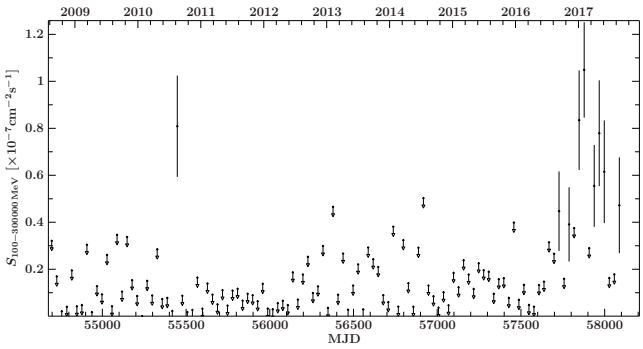

Figure G.167: *Fermi*/LAT γ-ray light curve of source 167

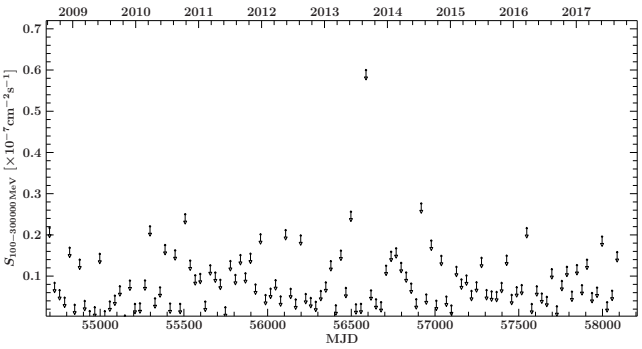

Figure G.168: *Fermi*/LAT γ-ray light curve of source 168

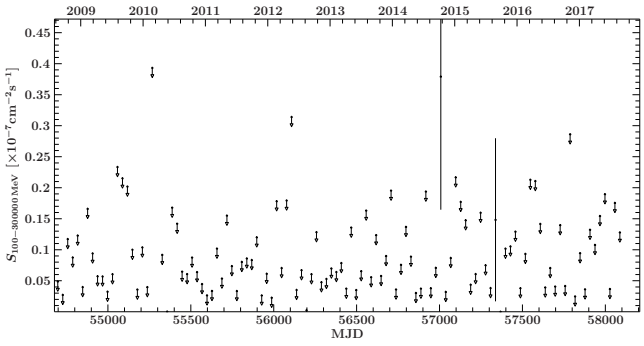

Figure G.169: *Fermi*/LAT γ-ray light curve of source 169

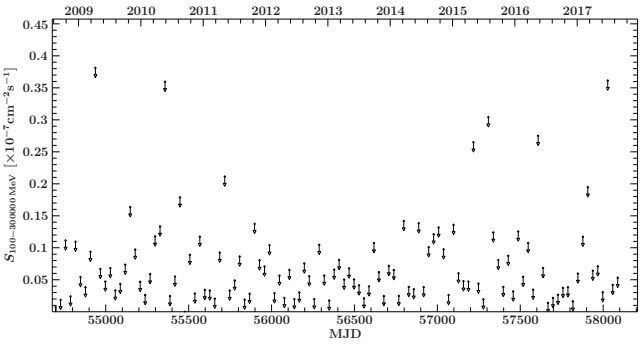

Figure G.170: *Fermi*/LAT γ-ray light curve of source 170

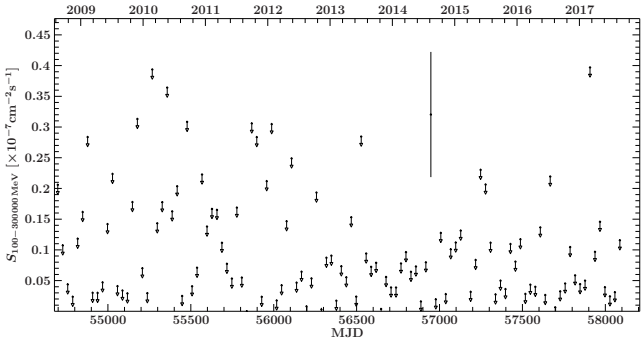

Figure G.171: *Fermi*/LAT γ-ray light curve of source 171

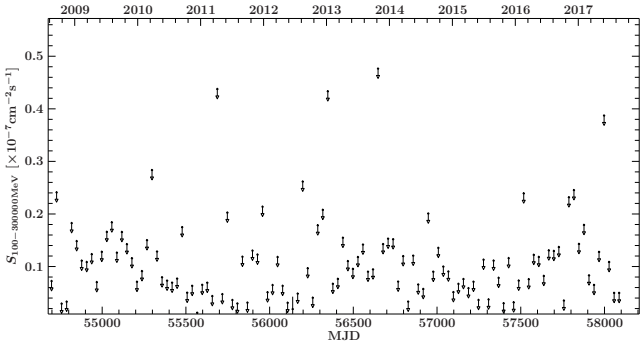

Figure G.172: *Fermi*/LAT γ-ray light curve of source 172

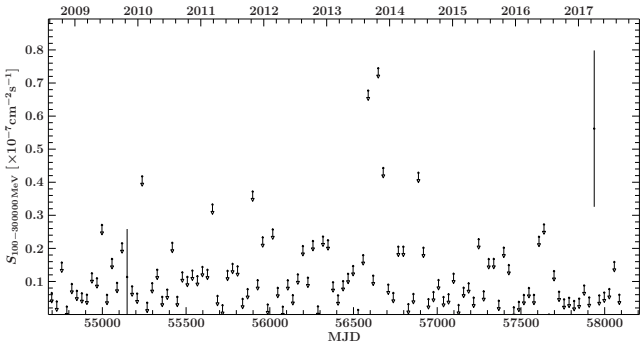

Figure G.173: *Fermi*/LAT γ-ray light curve of source 173

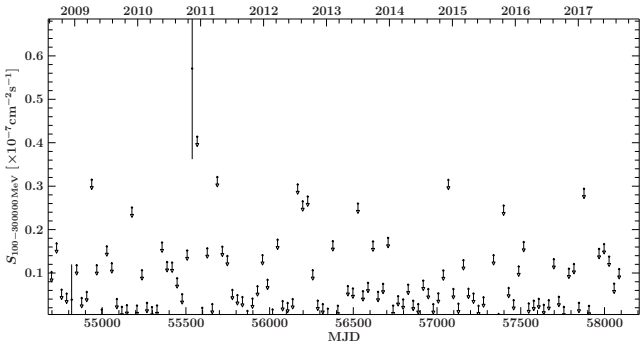

Figure G.174: *Fermi*/LAT γ-ray light curve of source 174

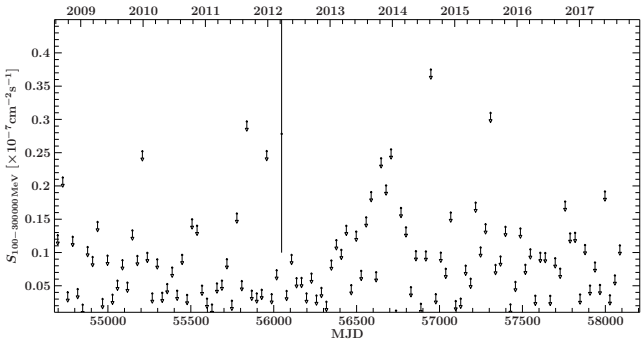

Figure G.175: *Fermi*/LAT γ-ray light curve of source 175

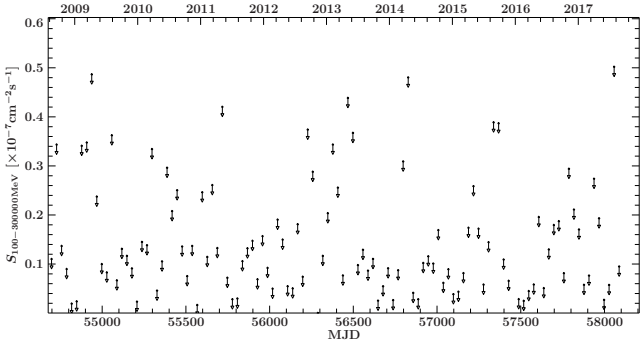

Figure G.176: *Fermi*/LAT γ-ray light curve of source 176

H Full List of Flares Considered in Sec. 7

Table 9: Full list of flares identified by Equ. 7.1. This selection is based on the public list of bright blazars monitored by *Fermi*/LAT, and is available at http://fermi.gsfc.nasa.gov/ssc/data/access/lat/msl_lc/. Listed are identified flares, together with their source name, start and stop time of the flaring period, maximum flare amplitude and duration of the flare.

Flare Number	Source	t_{min} [MJD]	t_{max} [MJD]	Flare Amplitude $\left[\text{ph cm}^{-2}\ \text{s}^{-1}\right]$	Duration [Days]
1	PKS 0235+164	57264	57265	1.18×10^{-6}	1
2	0827+243	56197	56198	1.73×10^{-6}	1
3	0827+243	56210	56211	1.08×10^{-6}	1
4	0827+243	56252	56253	9.97×10^{-7}	1
5	0827+243	56285	56286	9.51×10^{-7}	1
6	PKS 1150+497	55676	55677	1.57×10^{-6}	1
7	PKS 1150+497	55695	55697	2.43×10^{-6}	2
8	PKS 1150+497	55698	55701	1.40×10^{-6}	3
9	PKS 1150+497	55738	55739	6.64×10^{-7}	1
10	PKS 1510−089	55738	55739	3.68×10^{-6}	1
11	PKS 1510−089	55745	55747	8.13×10^{-6}	2
12	PKS 1510−089	55767	55768	7.05×10^{-6}	1
13	PKS 1510−089	55849	55850	3.56×10^{-6}	1
14	PKS 1510−089	55851	55855	1.30×10^{-5}	4
15	PKS 1510−089	55867	55871	1.04×10^{-5}	4
16	PKS 1510−089	55872	55874	7.08×10^{-6}	2
17	PKS 1510−089	55875	55877	5.86×10^{-6}	2
18	PKS 1510−089	55885	55886	3.90×10^{-6}	1
19	PKS 1510−089	55957	55959	5.08×10^{-6}	2
20	PKS 1510−089	55960	55966	4.81×10^{-6}	6
21	PKS 1510−089	55972	55976	4.46×10^{-6}	4
22	PKS 1510−089	55979	55994	7.37×10^{-6}	15
23	PKS 1510−089	55998	56000	4.21×10^{-6}	2
24	PKS 1510−089	56001	56004	7.44×10^{-6}	3
25	PKS 1510−089	56006	56007	2.61×10^{-6}	1
26	PKS 1510−089	56539	56540	2.47×10^{-6}	1
27	PKS 1510−089	56553	56555	6.42×10^{-6}	2
28	PKS 1510−089	56556	56557	5.29×10^{-6}	1
29	PKS 1510−089	56564	56565	4.59×10^{-6}	1
30	PKS 1510−089	56578	56580	3.28×10^{-6}	2
31	PKS 1510−089	56590	56591	2.67×10^{-6}	1
32	PKS 1510−089	56592	56595	2.94×10^{-6}	3
33	PKS 1510−089	56596	56597	2.47×10^{-6}	1
34	PKS 1510−089	56950	56951	2.12×10^{-6}	1
35	PKS 1510−089	56964	56965	3.84×10^{-6}	1
36	PKS 1510−089	57099	57100	3.45×10^{-6}	1
37	PKS 1510−089	57106	57107	2.42×10^{-6}	1
38	PKS 1510−089	57108	57109	2.23×10^{-6}	1
39	PKS 1510−089	57110	57111	2.92×10^{-6}	1
40	PKS 1510−089	57113	57117	7.35×10^{-6}	4
41	PKS 1510−089	57123	57124	2.94×10^{-6}	1
42	PKS 1510−089	57125	57126	4.25×10^{-6}	1
43	PKS 1510−089	57127	57129	3.85×10^{-6}	2
44	PKS 1510−089	57138	57139	2.66×10^{-6}	1
45	PKS 1510−089	57148	57149	2.78×10^{-6}	1
46	PKS 1510−089	57156	57162	5.50×10^{-6}	6
47	PKS 1510−089	57164	57165	2.76×10^{-6}	1
48	PKS 1510−089	57166	57171	5.72×10^{-6}	5
49	PKS 1510−089	57177	57178	2.58×10^{-6}	1
50	PKS 1510−089	57193	57194	2.89×10^{-6}	1

Flare Number	Source	t_{min} [MJD]	t_{max} [MJD]	Flare Amplitude [ph cm^{-2} s^{-1}]	Duration [Days]
51	PKS 1510−089	57210	57211	2.14×10^{-6}	1
52	PKS 1510−089	57212	57214	3.34×10^{-6}	2
53	PKS 1510−089	57218	57223	4.10×10^{-6}	5
54	PKS 1510−089	57225	57226	2.27×10^{-6}	1
55	PKS 1510−089	57244	57250	9.11×10^{-6}	6
56	PKS 1510−089	57632	57636	5.23×10^{-6}	4
57	PKS 1510−089	57647	57648	2.26×10^{-6}	1
58	PKS 1510−089	57649	57650	3.37×10^{-6}	1
59	PKS 1510−089	57651	57652	3.29×10^{-6}	1
60	PKS 1633+382	55689	55690	2.23×10^{-6}	1
61	PKS 1633+382	55696	55697	2.71×10^{-6}	1
62	PKS 1633+382	55745	55746	1.78×10^{-6}	1
63	PKS 1633+382	55748	55749	1.57×10^{-6}	1
64	PKS 1633+382	55752	55753	1.93×10^{-6}	1
65	PKS 1633+382	56188	56189	1.60×10^{-6}	1
66	PKS 1633+382	56208	56209	1.88×10^{-6}	1
67	PKS 1633+382	56223	56225	1.65×10^{-6}	2
68	PKS 1633+382	56241	56242	1.84×10^{-6}	1
69	PKS 1633+382	56245	56246	1.73×10^{-6}	1
70	PKS 1633+382	56442	56443	1.39×10^{-6}	1
71	PKS 1633+382	56491	56492	1.53×10^{-6}	1
72	PKS 1633+382	56498	56501	2.67×10^{-6}	3
73	PKS 1633+382	56502	56504	2.05×10^{-6}	2
74	PKS 1633+382	56510	56511	2.00×10^{-6}	1
75	PKS 1633+382	56512	56515	1.88×10^{-6}	3
76	PKS 1633+382	56532	56533	1.82×10^{-6}	1
77	PKS 1633+382	56549	56550	2.18×10^{-6}	1
78	PKS 1633+382	56564	56565	1.58×10^{-6}	1
79	3C 120	57136	57137	2.49×10^{-6}	1
80	3C 279	55668	55669	3.34×10^{-6}	1
81	3C 279	55698	55699	2.30×10^{-6}	1
82	3C 279	56631	56634	2.99×10^{-6}	3
83	3C 279	56635	56638	3.04×10^{-6}	3
84	3C 279	56646	56647	5.63×10^{-6}	1
85	3C 279	56648	56649	2.99×10^{-6}	1
86	3C 279	56650	56651	2.98×10^{-6}	1
87	3C 279	56653	56655	2.98×10^{-6}	2
88	3C 279	56675	56676	2.60×10^{-6}	1
89	3C 279	56717	56719	3.73×10^{-6}	2
90	3C 279	56742	56743	1.85×10^{-6}	1
91	3C 279	56744	56747	3.95×10^{-6}	3
92	3C 279	56749	56755	6.83×10^{-6}	6
93	3C 279	56859	56860	1.67×10^{-6}	1
94	3C 279	56865	56866	2.85×10^{-6}	1
95	3C 279	56867	56869	4.77×10^{-6}	2
96	3C 279	56871	56872	2.04×10^{-6}	1
97	3C 279	56984	56985	2.16×10^{-6}	1
98	3C 279	56986	56987	3.21×10^{-6}	1
99	3C 279	56988	56991	3.20×10^{-6}	3
100	3C 279	57153	57155	3.37×10^{-6}	2
101	3C 279	57184	57185	2.08×10^{-6}	1
102	3C 279	57187	57191	2.60×10^{-5}	4
103	3C 279	57212	57216	3.68×10^{-6}	4
104	3C 279	57218	57219	1.83×10^{-6}	1
105	3C 279	57552	57554	3.79×10^{-6}	2
106	3C 446	57263	57264	9.89×10^{-7}	1
107	3C 454.3	55320	55325	9.03×10^{-6}	5
108	3C 454.3	55326	55328	8.17×10^{-6}	2
109	3C 454.3	55329	55330	6.31×10^{-6}	1
110	3C 454.3	55461	55462	6.99×10^{-6}	1
111	3C 454.3	55464	55465	5.16×10^{-6}	1
112	3C 454.3	55495	55500	7.43×10^{-6}	5
113	3C 454.3	55501	55577	6.64×10^{-5}	76
114	3C 454.3	55579	55586	7.99×10^{-6}	7
115	3C 454.3	56816	56817	7.60×10^{-6}	1
116	3C 454.3	56820	56837	1.55×10^{-5}	17
117	3C 454.3	56864	56865	5.03×10^{-6}	1
118	3C 454.3	56868	56870	5.21×10^{-6}	2
119	3C 454.3	56872	56874	7.67×10^{-6}	2
120	3C 454.3	56914	56915	5.14×10^{-6}	1
121	3C 454.3	56916	56917	8.88×10^{-6}	1
122	3C 454.3	56988	56989	4.73×10^{-6}	1
123	3C 454.3	57008	57009	7.08×10^{-6}	1
124	3C 454.3	57058	57059	5.16×10^{-6}	1
125	3C 454.3	57198	57200	5.68×10^{-6}	2
126	3C 454.3	57204	57205	1.22×10^{-5}	1
127	3C 454.3	57206	57207	9.51×10^{-6}	1
128	3C 454.3	57253	57257	1.42×10^{-5}	4
129	3C 454.3	57279	57280	6.52×10^{-6}	1
130	3C 454.3	57302	57303	5.23×10^{-6}	1
131	3C 454.3	57326	57327	5.93×10^{-6}	1
132	3C 454.3	57403	57404	4.14×10^{-6}	1
133	3C 454.3	57406	57408	6.34×10^{-6}	2
134	3C 454.3	57459	57461	7.11×10^{-6}	2
135	3C 454.3	57557	57565	1.90×10^{-5}	8
136	3C 454.3	57597	57599	5.62×10^{-6}	2
137	4C +01.02	57347	57348	2.99×10^{-6}	1
138	4C +01.02	57368	57369	1.90×10^{-6}	1
139	4C +01.02	57577	57582	2.86×10^{-6}	5
140	4C +01.02	57583	57585	2.11×10^{-6}	2

Flare Number	Source	t_{min} [MJD]	t_{max} [MJD]	Flare Amplitude $\left[\text{ph cm}^{-2}\ \text{s}^{-1}\right]$	Duration [Days]	Flare Number	Source	t_{min} [MJD]	t_{max} [MJD]	Flare Amplitude $\left[\text{ph cm}^{-2}\ \text{s}^{-1}\right]$	Duration [Days]
141	4C +01.02	57595	57596	2.04×10^{-6}	1	186	CTA 102	55712	55713	2.51×10^{-6}	1
142	4C +01.02	57603	57604	1.76×10^{-6}	1	187	CTA 102	55720	55721	4.04×10^{-6}	1
143	4C +01.02	57616	57618	2.13×10^{-6}	2	188	CTA 102	56189	56190	2.84×10^{-6}	1
144	4C +01.02	57624	57625	2.25×10^{-6}	1	189	CTA 102	56192	56197	6.23×10^{-6}	5
145	4C +28.07	55838	55839	2.23×10^{-6}	1	190	CTA 102	56199	56201	3.20×10^{-6}	2
146	4C +28.07	55845	55846	1.28×10^{-6}	1	191	CTA 102	56202	56203	2.93×10^{-6}	1
147	4C +28.07	55869	55870	1.27×10^{-6}	1	192	CTA 102	56388	56389	3.26×10^{-6}	1
148	4C +28.07	55880	55881	1.74×10^{-6}	1	193	CTA 102	56390	56391	3.25×10^{-6}	1
149	4C +28.07	55883	55884	1.85×10^{-6}	1	194	CTA 102	56392	56393	3.39×10^{-6}	1
150	AP Lib	57630	57631	1.10×10^{-6}	1	195	CTA 102	56954	56955	3.07×10^{-6}	1
151	B2 0619+33	55405	55406	1.07×10^{-6}	1	196	CTA 102	57289	57290	2.06×10^{-6}	1
152	B2 0619+33	55411	55416	9.68×10^{-7}	5	197	CTA 102	57384	57386	6.12×10^{-6}	2
153	B2 0619+33	55424	55425	1.02×10^{-6}	1	198	CTA 102	57411	57413	3.73×10^{-6}	2
154	B2 0619+33	55426	55427	9.66×10^{-7}	1	199	CTA 102	57415	57416	2.78×10^{-6}	1
155	B2 0619+33	55435	55437	1.10×10^{-6}	2	200	CTA 102	57417	57419	3.12×10^{-6}	2
156	B2 0619+33	55450	55451	6.77×10^{-7}	1	201	CTA 102	57424	57425	2.77×10^{-6}	1
157	B2 0619+33	55455	55456	8.83×10^{-7}	1	202	CTA 102	57426	57428	6.60×10^{-6}	2
158	B2 0619+33	55464	55465	4.87×10^{-7}	1	203	CTA 102	57429	57434	3.73×10^{-6}	5
159	B2 0619+33	55470	55479	1.31×10^{-6}	9	204	CTA 102	57435	57445	1.10×10^{-5}	10
160	B2 0619+33	55482	55483	1.03×10^{-6}	1	205	CTA 102	57446	57447	3.44×10^{-6}	1
161	B2 0619+33	55485	55486	8.23×10^{-7}	1	206	CTA 102	57450	57451	3.86×10^{-6}	1
162	B2 0619+33	55492	55496	1.69×10^{-6}	4	207	CTA 102	57472	57473	2.79×10^{-6}	1
163	B2 0619+33	55499	55500	9.68×10^{-7}	1	208	CTA 102	57474	57475	2.89×10^{-6}	1
164	B2 0619+33	55512	55513	1.84×10^{-6}	1	209	CTA 102	57478	57479	2.62×10^{-6}	1
165	B2 0619+33	55523	55526	1.19×10^{-6}	3	210	CTA 102	57544	57545	2.60×10^{-6}	1
166	B2 0619+33	55543	55544	1.05×10^{-6}	1	211	CTA 102	57547	57548	3.10×10^{-6}	1
167	B2 1504+37	57061	57062	1.94×10^{-6}	1	212	CTA 102	57559	57560	3.89×10^{-6}	1
168	B2 1504+37	57071	57072	1.03×10^{-6}	1	213	CTA 102	57566	57567	2.26×10^{-6}	1
169	B2 1520+31	55519	55520	1.56×10^{-6}	1	214	CTA 102	57621	57630	4.66×10^{-6}	9
170	B2 1520+31	55523	55524	2.11×10^{-6}	1	215	CTA 102	57631	57632	2.17×10^{-6}	1
171	B2 1846+32B	55487	55488	2.54×10^{-6}	1	216	CTA 102	57633	57634	2.16×10^{-6}	1
172	B2 2308+34	55598	55599	1.28×10^{-6}	1	217	CTA 102	57653	57654	2.71×10^{-6}	1
173	B2 2308+34	56581	56582	9.19×10^{-7}	1	218	CTA 102	57657	57658	2.40×10^{-6}	1
174	B3 1343+451	56165	56166	1.21×10^{-6}	1	219	CTA 102	57659	57660	2.47×10^{-6}	1
175	B3 1708+433	55509	55510	1.17×10^{-6}	1	220	PMN J1717−5155	56025	56026	1.51×10^{-6}	1
176	B3 1708+433	55519	55520	1.00×10^{-6}	1	221	GB6 B1310+4844	55360	55361	7.05×10^{-7}	1
177	B3 1708+433	55531	55532	1.21×10^{-6}	1	222	GB6 B1310+4844	55364	55365	7.48×10^{-7}	1
178	BL Lac	56164	56165	2.10×10^{-6}	1	223	GB6 B1310+4844	55371	55372	8.12×10^{-7}	1
179	BL Lac	56296	56297	2.16×10^{-6}	1	224	LSI +61_303	55377	55378	2.42×10^{-6}	1
180	CGRaBS J1848+3219	55493	55494	2.10×10^{-6}	1	225	LSI +61_303	55569	55571	2.80×10^{-6}	2
181	CGRaBS J1848+3219	55496	55497	1.79×10^{-6}	1	226	LSI +61_303	55622	55623	2.25×10^{-6}	1
182	CGRaBS J1849+6705	55748	55749	2.29×10^{-6}	1	227	LSI +61_303	55747	55748	2.10×10^{-6}	1
183	CRATES J0531−4827	55454	55455	7.59×10^{-7}	1	228	MG2 J071354+1934	55580	55581	1.68×10^{-6}	1
184	CRATES J0531−4827	55467	55468	1.09×10^{-6}	1	229	Mrk 421	55358	55359	9.41×10^{-7}	1
185	CRATES J0531−4827	55471	55472	1.54×10^{-6}	1	230	Mrk 421	56126	56127	9.74×10^{-7}	1

Flare Number	Source	t_{min} [MJD]	t_{max} [MJD]	Flare Amplitude [ph cm^{-2} s^{-1}]	Duration [Days]
231	Mrk 421	56156	56157	1.21×10^{-6}	1
232	Mrk 421	56377	56378	9.07×10^{-7}	1
233	NGC 1275	56715	56716	2.99×10^{-6}	1
234	NGC 1275	56989	56990	1.54×10^{-6}	1
235	NGC 1275	57312	57313	1.41×10^{-6}	1
236	NGC 1275	57319	57320	1.37×10^{-6}	1
237	NRAO 190	56498	56500	1.78×10^{-6}	2
238	NRAO 190	56501	56505	3.09×10^{-6}	4
239	NRAO 676	56096	56097	1.76×10^{-6}	1
240	NRAO 676	56104	56105	2.03×10^{-6}	1
241	NRAO 676	56112	56119	4.68×10^{-6}	7
242	NRAO 676	56123	56124	2.12×10^{-6}	1
243	NRAO 676	56213	56214	2.41×10^{-6}	1
244	NRAO 676	56219	56220	2.26×10^{-6}	1
245	NRAO 676	56222	56226	1.97×10^{-6}	4
246	NRAO 676	56333	56335	2.03×10^{-6}	2
247	NRAO 676	56337	56338	2.17×10^{-6}	1
248	NRAO 676	57489	57490	1.87×10^{-6}	1
249	OJ 287	55844	55845	1.03×10^{-6}	1
250	OJ 287	55868	55870	1.53×10^{-6}	2
251	OJ 287	57427	57428	9.12×10^{-7}	1
252	ON 246	57084	57085	1.16×10^{-6}	1
253	PKS 0235−618	55752	55753	1.29×10^{-6}	1
254	PKS 0336−01	57342	57345	1.50×10^{-6}	3
255	PKS 0402−362	55825	55830	6.40×10^{-6}	5
256	PKS 0402−362	55989	55990	1.45×10^{-6}	1
257	PKS 0402−362	57019	57020	2.58×10^{-6}	1
258	PKS 0402−362	57049	57050	1.79×10^{-6}	1
259	PKS 0402−362	57101	57102	2.01×10^{-6}	1
260	PKS 0402−362	57106	57107	1.40×10^{-6}	1
261	PKS 0402−362	57307	57308	1.21×10^{-6}	1
262	PKS 0402−362	57319	57320	2.32×10^{-6}	1
263	PKS 0403−13	57580	57582	1.61×10^{-6}	2
264	PKS 0426−380	55360	55361	1.37×10^{-6}	1
265	PKS 0426−380	56417	56418	1.47×10^{-6}	1
266	PKS 0426−380	56443	56444	1.25×10^{-6}	1
267	PKS 0426−380	56453	56454	1.11×10^{-6}	1
268	PKS 0426−380	56491	56492	1.15×10^{-6}	1
269	PKS 0426−380	57531	57532	1.83×10^{-6}	1
270	PKS 0426−380	57640	57641	1.28×10^{-6}	1
271	PKS 0454−234	55890	55891	1.16×10^{-6}	1
272	PKS 0454−234	55897	55898	1.45×10^{-6}	1
273	PKS 0454−234	56589	56590	1.29×10^{-6}	1
274	PKS 0458−02	57257	57261	1.84×10^{-6}	4
275	PKS 0458−02	57265	57266	6.67×10^{-7}	1
276	PKS 0458−02	57279	57280	7.42×10^{-7}	1
277	PKS 0502+049	56897	56898	1.27×10^{-6}	1
278	PKS 0502+049	56900	56901	9.84×10^{-7}	1
279	PKS 0502+049	56908	56909	2.24×10^{-6}	1
280	PKS 0502+049	56909	56910	3.41×10^{-6}	1
281	PKS 0502+049	56910	56911	1.52×10^{-6}	1
282	PKS 0502+049	56912	56913	2.26×10^{-6}	1
283	PKS 0502+049	56913	56914	1.74×10^{-6}	1
284	PKS 0502+049	56914	56915	2.82×10^{-6}	1
285	PKS 0502+049	56915	56916	1.53×10^{-6}	1
286	PKS 0502+049	56916	56917	1.86×10^{-6}	1
287	PKS 0502+049	56918	56919	1.73×10^{-6}	1
288	PKS 0502+049	56919	56920	1.54×10^{-6}	1
289	PKS 0502+049	57026	57027	8.45×10^{-7}	1
290	PKS 0502+049	57031	57032	9.46×10^{-7}	1
291	PKS 0502+049	57060	57061	1.82×10^{-6}	1
292	PKS 0502+049	57064	57065	1.35×10^{-6}	1
293	PKS 0502+049	57065	57066	9.26×10^{-7}	1
294	PKS 0502+049	57069	57070	9.76×10^{-7}	1
295	PKS 0502+049	57078	57079	9.68×10^{-7}	1
296	PKS 0502+049	57079	57080	2.07×10^{-6}	1
297	PKS 0502+049	57093	57094	9.27×10^{-7}	1
298	PKS 0502+049	57099	57100	1.88×10^{-6}	1
299	PKS 0502+049	57100	57101	2.06×10^{-6}	1
300	PKS 0502+049	57102	57103	2.49×10^{-6}	1
301	PKS 0502+049	57103	57104	2.37×10^{-6}	1
302	PKS 0502+049	57104	57105	1.85×10^{-6}	1
303	PKS 0502+049	57105	57106	1.88×10^{-6}	1
304	PKS 0502+049	57108	57109	1.27×10^{-6}	1
305	PKS 0502+049	57555	57556	7.31×10^{-7}	1
306	PKS 0502+049	57581	57582	7.50×10^{-7}	1
307	PKS 0502+049	57585	57586	9.44×10^{-7}	1
308	PKS 0502+049	57601	57602	9.75×10^{-7}	1
309	PKS 0502+049	57602	57603	8.00×10^{-7}	1
310	PKS 0502+049	57628	57629	7.66×10^{-7}	1
311	PKS 0502+049	57641	57642	8.66×10^{-7}	1
312	PKS 0507+17	56405	56417	4.48×10^{-6}	12
313	PKS 0507+17	56420	56421	1.61×10^{-6}	1
314	PKS 0507+17	56422	56423	1.09×10^{-6}	1
315	PKS 0507+17	56431	56433	1.27×10^{-6}	2
316	PKS 0507+17	57601	57602	8.80×10^{-7}	1
317	PKS 0521−36	55377	55378	1.87×10^{-6}	1
318	PKS 0521−36	56273	56274	1.88×10^{-6}	1
319	PKS 0716+714	55854	55855	1.51×10^{-6}	1
320	PKS 0716+714	56156	56157	1.38×10^{-6}	1

Flare Number	Source	t_{min} [MJD]	t_{max} [MJD]	Flare Amplitude [ph cm^{-2} s^{-1}]	Duration [Days]
321	PKS 0716+714	57118	57119	1.48×10^{-6}	1
322	PKS 0736+01	57070	57071	1.68×10^{-6}	1
323	PKS 0736+01	57108	57109	1.47×10^{-6}	1
324	PKS 0736+01	57114	57115	2.49×10^{-6}	1
325	PKS 0736+01	57171	57172	1.59×10^{-6}	1
326	PKS 0903−57	57195	57196	1.38×10^{-6}	1
327	PKS 1313−333	57397	57398	1.30×10^{-6}	1
328	PKS 1329−049	55445	55446	3.31×10^{-6}	1
329	PKS 1329−049	55450	55451	3.20×10^{-6}	1
330	PKS 1329−049	55458	55463	4.52×10^{-6}	5
331	PKS 1329−049	55481	55482	1.76×10^{-6}	1
332	PKS 1329−049	55506	55507	2.20×10^{-6}	1
333	PKS 1346−112	55890	55891	1.17×10^{-6}	1
334	PKS 1424−418	56242	56243	1.58×10^{-6}	1
335	PKS 1424−418	56299	56301	2.21×10^{-6}	2
336	PKS 1424−418	56303	56304	1.83×10^{-6}	1
337	PKS 1424−418	56309	56316	2.70×10^{-6}	7
338	PKS 1424−418	56317	56318	1.82×10^{-6}	1
339	PKS 1424−418	56319	56321	2.09×10^{-6}	2
340	PKS 1424−418	56323	56324	1.70×10^{-6}	1
341	PKS 1424−418	56327	56328	1.77×10^{-6}	1
342	PKS 1424−418	56332	56333	1.61×10^{-6}	1
343	PKS 1424−418	56334	56335	1.67×10^{-6}	1
344	PKS 1424−418	56346	56347	1.69×10^{-6}	1
345	PKS 1424−418	56353	56354	1.59×10^{-6}	1
346	PKS 1424−418	56375	56376	1.70×10^{-6}	1
347	PKS 1424−418	56378	56379	1.91×10^{-6}	1
348	PKS 1424−418	56383	56384	1.74×10^{-6}	1
349	PKS 1424−418	56392	56393	2.21×10^{-6}	1
350	PKS 1424−418	56398	56399	2.78×10^{-6}	1
351	PKS 1424−418	56400	56403	2.84×10^{-6}	3
352	PKS 1424−418	56404	56406	2.04×10^{-6}	2
353	PKS 1424−418	56407	56410	2.24×10^{-6}	3
354	PKS 1424−418	56411	56423	3.23×10^{-6}	12
355	PKS 1424−418	56424	56429	2.27×10^{-6}	5
356	PKS 1424−418	56437	56438	1.76×10^{-6}	1
357	PKS 1424−418	56476	56477	1.41×10^{-6}	1
358	PKS 1424−418	56484	56486	2.10×10^{-6}	2
359	PKS 1424−418	56739	56740	1.89×10^{-6}	1
360	PKS 1502+106	57204	57205	1.82×10^{-6}	1
361	PKS 1502+106	57209	57210	2.04×10^{-6}	1
362	PKS 1502+106	57216	57217	3.36×10^{-6}	1
363	PKS 1622−253	55719	55722	1.82×10^{-6}	3
364	PKS 1622−253	55724	55725	1.45×10^{-6}	1
365	PKS 1622−253	55726	55727	1.68×10^{-6}	1
366	PKS 1622−253	55753	55754	2.44×10^{-6}	1
367	PKS 1622−253	56571	56572	3.08×10^{-6}	1
368	PKS 1824−582	56952	56953	2.98×10^{-6}	1
369	PKS 1824−582	56964	56965	1.25×10^{-6}	1
370	PKS 1824−582	56967	56968	3.72×10^{-6}	1
371	PKS 1824−582	56969	56975	2.04×10^{-6}	6
372	PKS 1824−582	56980	56982	2.46×10^{-6}	2
373	PKS 1824−582	57636	57638	2.23×10^{-6}	2
374	PKS 1830−211	55483	55488	7.74×10^{-6}	5
375	PKS 1830−211	55498	55499	1.88×10^{-6}	1
376	PKS 1830−211	55502	55504	1.85×10^{-6}	2
377	PKS 1830−211	55505	55506	2.27×10^{-6}	1
378	PKS 1830−211	55507	55508	1.69×10^{-6}	1
379	PKS 1830−211	55513	55514	1.65×10^{-6}	1
380	PKS 1830−211	55538	55539	1.84×10^{-6}	1
381	PKS 1830−211	55556	55557	1.66×10^{-6}	1
382	PKS 1830−211	55558	55563	3.46×10^{-6}	5
383	PKS 1830−211	55564	55566	3.45×10^{-6}	2
384	PKS 1830−211	55579	55580	2.71×10^{-6}	1
385	PKS 1830−211	56065	56066	1.57×10^{-6}	1
386	PKS 1830−211	56071	56072	1.67×10^{-6}	1
387	PKS 1830−211	56084	56087	2.40×10^{-6}	3
388	PKS 1830−211	56091	56092	2.59×10^{-6}	1
389	PKS 1830−211	56093	56095	1.79×10^{-6}	2
390	PKS 1830−211	56107	56108	2.06×10^{-6}	1
391	PKS 1830−211	56145	56146	1.53×10^{-6}	1
392	PKS 1830−211	56147	56148	1.56×10^{-6}	1
393	PKS 2023−07	57470	57473	1.48×10^{-6}	3
394	PKS 2023−07	57487	57497	3.07×10^{-6}	10
395	PKS 2032+107	57175	57176	2.96×10^{-6}	1
396	PKS 2032+107	57183	57184	1.69×10^{-6}	1
397	PKS 2032+107	57241	57243	3.47×10^{-6}	2
398	PKS 2032+107	57245	57246	1.86×10^{-6}	1
399	PKS 2032+107	57274	57275	2.35×10^{-6}	1
400	PKS 2032+107	57299	57300	1.68×10^{-6}	1
401	PKS 2142−75	56798	56800	2.45×10^{-6}	2
402	PKS 2149−306	56300	56303	1.94×10^{-6}	3
403	PKS 2149−306	56305	56306	1.38×10^{-6}	1
404	PKS 2149−306	56312	56313	2.96×10^{-6}	1
405	PKS 2155−304	56794	56795	1.34×10^{-6}	1
406	PKS 2233−148	56083	56084	1.57×10^{-6}	1
407	PKS 2233−148	56089	56092	2.56×10^{-6}	3
408	PKS 2233−148	56093	56094	1.20×10^{-6}	1
409	PKS 2233−148	56098	56099	3.14×10^{-6}	1
410	PKS 2326−502	56571	56572	1.38×10^{-6}	1

Flare Number	Source	t_{min} [MJD]	t_{max} [MJD]	Flare Amplitude $\left[\text{ph cm}^{-2}\ \text{s}^{-1}\right]$	Duration [Days]
411	PKS 2326−502	56575	56576	1.60×10^{-6}	1
412	PKS 2326−502	56598	56599	2.16×10^{-6}	1
413	PKS 2326−502	56610	56611	2.13×10^{-6}	1
414	PKS 2326−502	56633	56634	1.66×10^{-6}	1
415	PKS 2326−502	56640	56641	1.72×10^{-6}	1
416	PKS 2326−502	56642	56645	2.17×10^{-6}	3
417	PKS 2326−502	56650	56651	1.96×10^{-6}	1
418	PKS B0906+015	55516	55517	1.23×10^{-6}	1
419	PKS B1222+216	55323	55328	3.35×10^{-6}	5
420	PKS B1222+216	55341	55344	7.75×10^{-6}	3
421	PKS B1222+216	55347	55348	4.01×10^{-6}	1
422	PKS B1222+216	55358	55362	5.04×10^{-6}	4
423	PKS B1222+216	55363	55370	1.32×10^{-5}	7
424	PKS B1222+216	55371	55381	6.42×10^{-6}	10
425	PKS B1222+216	55385	55387	3.52×10^{-6}	2
426	PKS B1222+216	55389	55391	2.96×10^{-6}	2
427	PKS B1222+216	55481	55482	2.22×10^{-6}	1
428	PKS B1222+216	55483	55485	4.02×10^{-6}	2
429	PKS B1222+216	55534	55535	3.01×10^{-6}	1
430	PKS B1222+216	56539	56540	3.49×10^{-6}	1
431	PKS B1222+216	56564	56565	2.29×10^{-6}	1
432	PKS B1222+216	56633	56634	1.77×10^{-6}	1
433	PKS B1222+216	56691	56693	2.10×10^{-6}	2
434	PKS B1222+216	56701	56703	3.26×10^{-6}	2
435	PKS B1222+216	56964	56967	3.04×10^{-6}	3
436	PKS B1222+216	56972	56975	5.82×10^{-6}	3
437	PKS B1222+216	56976	56977	4.86×10^{-6}	1
438	PMN J0017−0512	56437	56438	2.31×10^{-6}	1
439	PMN J0948+0022	55731	55732	1.46×10^{-6}	1
440	PMN J1038−5311	56062	56063	1.14×10^{-6}	1
441	PMN J1913−3630	55490	55491	1.43×10^{-6}	1
442	PMN J2345−1555	56410	56411	2.44×10^{-6}	1
443	PMN J2345−1555	56413	56414	1.22×10^{-6}	1
444	S3 0218+35	56161	56162	9.75×10^{-7}	1
445	S3 0218+35	56165	56167	1.76×10^{-6}	2
446	S3 0218+35	56176	56177	2.30×10^{-6}	1
447	S3 0218+35	56185	56188	4.01×10^{-6}	3
448	S3 0218+35	56189	56193	3.12×10^{-6}	4
449	S3 0218+35	56195	56201	2.79×10^{-6}	6
450	S3 0218+35	56203	56205	2.54×10^{-6}	2
451	S3 0218+35	56212	56214	3.00×10^{-6}	2
452	S3 0218+35	56215	56216	1.67×10^{-6}	1
453	S3 0218+35	56217	56222	2.74×10^{-6}	5
454	S3 0218+35	56223	56233	4.27×10^{-6}	10
455	S3 0218+35	56234	56235	3.08×10^{-6}	1
456	S3 0218+35	56236	56243	3.52×10^{-6}	7
457	S3 0218+35	56247	56250	1.83×10^{-6}	3
458	S3 0218+35	56251	56252	1.19×10^{-6}	1
459	S3 0218+35	56265	56266	1.85×10^{-6}	1
460	S4 0954+65	57065	57066	1.00×10^{-6}	1
461	S4 0954+65	57069	57072	1.91×10^{-6}	3
462	S4 0954+65	57073	57074	1.07×10^{-6}	1
463	S4 0954+65	57078	57079	1.54×10^{-6}	1
464	S4 0954+65	57084	57085	1.25×10^{-6}	1
465	S4 1030+61	55330	55331	1.67×10^{-6}	1
466	S4 1749+70	55620	55622	1.46×10^{-6}	2
467	S4 1800+44	57460	57461	1.80×10^{-6}	1
468	S4 1800+44	57468	57469	2.96×10^{-6}	1
469	S5 0836+71	55866	55867	3.06×10^{-6}	1
470	S5 0836+71	55872	55873	2.02×10^{-6}	1
471	S5 0836+71	55885	55886	1.66×10^{-6}	1
472	S5 0836+71	55920	55921	1.74×10^{-6}	1
473	S5 0836+71	57234	57237	5.29×10^{-6}	3
474	S5 0836+71	57321	57322	1.36×10^{-6}	1
475	S5 0836+71	57325	57326	2.38×10^{-6}	1
476	S5 0836+71	57335	57339	5.92×10^{-6}	4
477	S5 0836+71	57340	57341	1.62×10^{-6}	1
478	S5 0836+71	57357	57359	1.62×10^{-6}	2
479	S5 1803+78	55683	55684	1.11×10^{-6}	1
480	S5 1803+78	55709	55710	9.17×10^{-7}	1
481	TXS 1530−131	55808	55809	1.01×10^{-6}	1
482	TXS 1530−131	56769	56770	1.33×10^{-6}	1
483	TXS 1530−131	56771	56772	1.51×10^{-6}	1
484	TXS 2241+406	57346	57347	1.15×10^{-6}	1
485	TXS 2358+209	57554	57555	1.66×10^{-6}	1
486	Ton 599	55433	55434	1.37×10^{-6}	1
487	Ton 599	57345	57347	1.13×10^{-6}	2

I Investigating source confusion in PMN J1603−4904

This section is based on the work of Krauß et al. (2018) and is taken in large parts in verbatim. I contributed with the analysis of *Fermi*/LAT data, writing of subsections and discussion of the results. Since large parts of the following text are taken in verbatim from the above mentioned publication, the text uses "we", where appropriate.

PMN J1603−4904 is a likely member of the rare class of γ-ray emitting young radio galaxies. Only one other source, PKS 1718−649, has been confirmed so far. These objects, which may transition into larger radio galaxies, are a stepping stone to understanding AGN evolution. It is not completely clear how these young galaxies, seen edge-on, can produce high-energy γ-rays. PMN J1603−4904 has been detected by TANAMI Very Long Baseline Interferometry (VLBI) observations and has been followed-up with multiwavelength observations. A *Fermi* /LAT γ-ray source has been associated with it in the LAT catalogs. We have obtained *Chandra* observations of the source in order to consider the possibility of source confusion, due to the relatively large positional uncertainty of *Fermi* /LAT. The goal was to investigate the possibility of other X-ray bright sources in the vicinity of PMN J1603−4904 that could be counterparts to the γ-ray emission. With *Chandra* /ACIS, we find no other sources in the uncertainty ellipse of *Fermi* /LAT data, which includes an improved localization analysis of 8 years of data. We further study the X-ray fluxes and spectra. We conclude that PMN J1603−4904 is indeed the second confirmed γ-ray bright young radio galaxy.

Introduction

Active Galactic Nuclei (AGN) are the most luminous persistent objects in the Universe. A subset of AGN exhibits relativistic outflows, called jets. Many questions of jet physics remain unsolved, including the details of jet launching, confinement and acceleration processes. In this context, peculiar AGN in transitory stages become relevant for addressing the key questions of AGN science. Among these objects are young radio galaxies, which exhibit shorter jets (up to a few kpc), and are also known as compact symmetric objects (CSO) due to their compactness at radio wavelengths (Phillips & Mutel, 1982; Wilkinson et al., 1994; Readhead et al., 1996; O'Dea, 1998). They are typically seen at large inclination angles to the jet(s) and have negligible Doppler boosting. While γ-ray emission from young AGN was predicted (Kino et al., 2007, 2009; Stawarz et al., 2008; Kino & Asano, 2011), a detection by the *Fermi Gamma-ray Space Telescope* Large Area Telescope (hereafter *Fermi* /LAT) remained elusive for many years (D'Ammando et al., 2016). Using the improved Pass 8 reconstruction (Atwood et al., 2013), Migliori et al. (2016) detected the first CSO at γ-ray energies, PKS 1718−649. Three other candidate sources have been proposed: 4C +55.17 (McConville et al., 2011), PKS 1413+135 (Gugliucci et al., 2005), and PMN J1603−4904 (Müller et al., 2014). The first two have not been confirmed to be young radio galaxies. It remains unclear which attributes make some young AGN γ-ray loud. A direct link between Narrow Line Seyfert 1 galaxies (NLS1) and young AGNs (Compact Symmetric Sources) has been suggested by Caccianiga et al. (2014), but seems unlikely (Orienti et al., 2015).

PMN J1603−4904 is a radio source (Wright et al., 1994). It was recently confirmed to be a compact symmetric object from MHz data, which makes it a young or frustated AGN (Müller et al., 2016). It was detected by *Fermi* /LAT and classified as a low synchrotron peaked (LSP) BL Lac object (2FGL J1603.8−4904, 3FGL J1603.9−4903; Nolan et al., 2012; Acero et al., 2015; Ackermann et al., 2015c). The first association with the γ-ray source was proposed by Kovalev (2009). It is also listed in the LAT catalogs of sources detected above 10 GeV and 50 GeV (1FHL J1603.7−4903,2FHL J1603.9−4903, 3FHL J1603.8−4903

Ackermann et al., 2013, 2016a; Ajello et al., 2017). It is reported as a variable source in the 3FGL catalog. PMN J1603−4904 was first proposed to be a γ-ray bright CSO by Müller et al. (2014), who discussed its unusual VLBI structure and spectral energy distribution (SED). We followed up on this paper with X-ray observations with *Suzaku* and *XMM-Newton* , which led to the first high S/N X-ray spectrum that also exhibited an emission line at 5.44 keV, which we interpreted as a redshifted neutral Fe Kα line (at $z = 0.18$; Müller et al., 2015). Optical data by Shaw et al. (2013), which resulted in the LSP BL Lac classification, were not sensitive enough to detect any lines. Further optical spectroscopy showed our proposed redshift to be incorrect. X-Shooter data resulted in a redshift measurement of $z = 0.2321 \pm 0.0004$ (Goldoni et al., 2016). The emission line is due to He-like Fe, emitted at a rest frame energy of 6.7 keV. This emission feature is not typically seen in AGN, where edge-on sources exhibit neutral or slightly ionized Fe Kα emission, which is expected to originate in the accretion disks. This feature seems to be common for CSO sources (Siemiginowska et al., 2016). Highly ionized Fe emission is also observed in the LINER galaxy M81 (Page et al., 2004), though the latter still exhibits neutral Fe Kα emission while PMN J1603−4904 does not. It is unclear whether this suggests a complete lack of an accretion disk, a truncated accretion disk (which could likely achieve the high temperatures to ionize Fe) or a lack of neutral Fe.

Further radio studies of PMN J1603−4904 find a low-frequency turnover in the MHz – GHz spectrum, which indicates a source extent of 1.4 kpc and confirmed its young radio source classification (Müller et al., 2016). The source is located close to the Galactic plane ($l = 332.15°$, $b = 2.57°$), which hinders optical/UV and soft X-ray observations due to extinction and photoelectric absorption. The low Galactic latitude also complicates γ-ray data analysis due to the large number of nearby sources, the Galactic diffuse emission, and the three nearby extended sources, which all have to be taken into account. The radio source is consistent with the *Fermi* /LAT 95% 2FGL positional uncertainty, but it is unclear if there are other possible counterparts within the uncertainty ellipse in either radio or X-ray wavelengths (Müller et al., 2014). Optical data are unable to solve this problem, due to the large number of nearby stars and the strong extinction. In this paper we examine recent *Chandra* /ACIS data, the highest angular resolution data available at high energies, to confirm or rule out source confusion for PMN J1603−4904 . In Section 2 we discuss the observations and analysis methods. In Section 3 we discuss the results of the observations. The final section reports our conclusions.

Observations & Methods

Chandra

We took one *Chandra* observation of PMN J1603−4904 with the Advanced CCD Imaging Spectrometer (ACIS; observation ID 17106, 10.08 ksec) on 12 May 2016. The data are not affected by pile-up, as PMN J1603−4904 is a relatively weak X-ray emitter (Müller et al., 2015). The data were extracted using the standard tools from the CIAO 4.8. The extraction radius for PMN J1603−4904 is 3.″3, while the background was extracted with annuli centered on the source position with radii of 4.″4 and 40″. The source to the east of PMN J1603−4904 (no. 1, see Fig. I.1) was extracted with an extraction radius of 4.″9, while the background annulus radii were 8.″3 and 25.″9. The source to the east is seen in archival *XMM* data as well. The source to the west is not detected in *XMM*, either due to its low flux, or it is variable. The spectral analysis was performed with the Interactive Spectral Interpretation System (ISIS, version 1.6.2-40, Houck & Denicola, 2000). The *Chandra* data were modeled with an absorbed powerlaw, which fits both PMN J1603−4904 and the eastern source (no. 1). Due to low S/N in the individual bins, we use Cash statistics (Cash, 1979) for spectral analysis. For the absorbing column we use the abundances of Wilms et al. (2000) and the

Table 10: *Chandra* positions of the three X-ray sources in the direct vicinity of PMN J1603−4904 ($\alpha_{\mathrm{J2000.0}} = 16^{\mathrm{h}}03^{\mathrm{m}}50\overset{\mathrm{s}}{.}69$, $\delta_{\mathrm{J2000.0}} = -49°04'05\overset{''}{.}49$). Positions and uncertainties have been determined using wavdetect. The position of the central source (no. 2) is consistent with the radio position of PMN J1603−4904.

No.	$\alpha_{\mathrm{J2000.0}}$	$\delta_{\mathrm{J2000.0}}$	$u(\alpha_{\mathrm{J2000.0}})$	$u(\delta_{\mathrm{J2000.0}})$
1	$16^{\mathrm{h}}04^{\mathrm{m}}01\overset{\mathrm{s}}{.}111$	$-49°04'12\overset{''}{.}00$	$0.139''$	$0.182\ ''$
2	$16^{\mathrm{h}}03^{\mathrm{m}}50\overset{\mathrm{s}}{.}687$	$-49°04'04\overset{''}{.}44$	$0.046''$	$0.035''$
3	$16^{\mathrm{h}}03^{\mathrm{m}}34\overset{\mathrm{s}}{.}280$	$-49°02'57\overset{''}{.}16$	$0.238''$	$0.130''$

cross sections of Verner et al. (1996) with the newest version of the tbnew model[46]. In order to determine the coordinates of the X-ray sources we ran the CIAO tools `mkpsfmap` (at 2 keV with 50% enclosed counts) and `wavdetect` with the default scales. For the de-reddening of the optical/UV/IR data, the best-fit absorbing column N_{H} has been converted to A_{V} from X-ray dust scattering halo measurements of Predehl & Schmitt (1995), with the update by Nowak et al. (2012) for the revised abundance of the interstellar medium (see Krauß et al., 2016, for a detailed explanation of the treatment of multiwavelength data).

Fermi /LAT γ-ray data analysis

For the analysis of the *Fermi* /LAT γ-ray data, we used the *Fermi* Science Tools (v11r0p0) with the reprocessed Pass 8 data and the P8R2_SOURCE_V6 instrument response functions. The localization of the source is tricky with `gtfindsrc` due to its position near the Galactic plane. The localization we performed is similar to that in the 3FGL catalog (Acero et al., 2015), and only data above 3.2 GeV have been used as the data have been binned 4/decade. The log-likelihood surface is assumed to be parabolic. A selection of eight points is sampled in a circle around the estimated position, which is used to estimate the five parameters for the ellipse. The center is then moved to the estimated maximum, a new circle chosen at the 2 σ radius, and the procedure is iterated until convergence. The deviation of the fit from the measured values defines a goodness-of-fit quantity. The curvature of the surface is used to determine the covariance matrix, which in turn determines the positional uncertainty ellipse. We quote the values corresponding to a 95% containment. The positions and uncertainties are then used to determine the need for systematic adjustment by comparing with a set of AGNs, which have very accurate radio positions. To account for them we multiply the 95% uncertainties by a factor of 1.05, and add $0.433'$ in quadrature. For the spectral analysis we used an unbinned likelihood analysis in a region of interest of 5° around PMN J1603−4904 in the 1–300 GeV energy range. Sources within a 15° radius of PMN J1603−4904 were included in the likelihood fitting, with their parameters fixed. A free spectral index is used, together with a detection threshold of test statistic $TS = 25$ (Wilks, 1938).

Results

We find three X-ray sources in the *Chandra* /ACIS image in the direct vicinity of the 2MASS coordinates of PMN J1603−4904 (see Fig. I.1; Skrutskie et al., 2006). The coordinates are given in Table 10. The X-ray source in the center (no. 2) matches the radio coordinates. We can exclude the western source (no. 3) as a counterpart. It is at an angular distance of $2\overset{'}{.}9$ to PMN J1603−4904 , well outside the uncertainty ellipses of our analysis and those of the

[46]available online at: http://pulsar.sternwarte.uni-erlangen.de/wilms/research/tbabs/

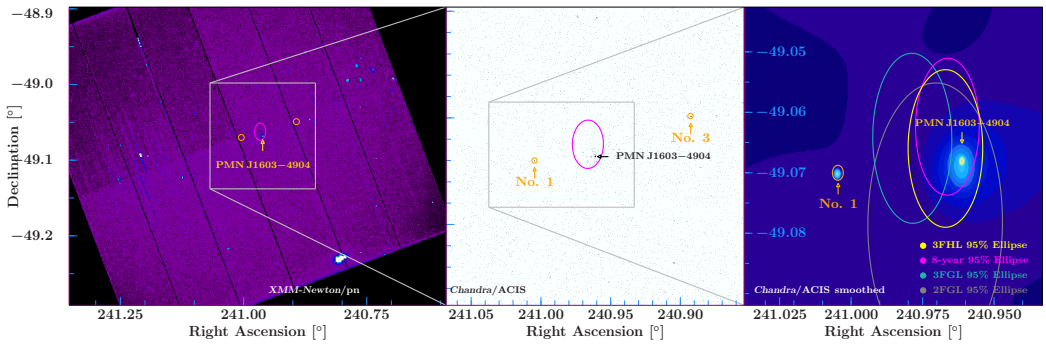

Figure I.1: *XMM-Newton* and *Chandra* /ACIS images of PMN J1603−4904 . The positions of the sources are marked with arrows. Two unknown, weak X-ray sources are marked in orange circles. The 95% uncertainty on the *Fermi* /LAT positions from the 2FGL, 3FGL, and the 3FHL catalogs are marked in gray, green, and yellow, respectively. *Left: XMM-Newton* /pn observation (ObsID 0724700101); *Middle:Chandra* /ACIS observation (ObsID 17106); *Right:* Same *Chandra* /ACIS observation, the image was smoothed with a Gaussian kernel of S/N range of 3–5.

Fermi /LAT catalogs. The eastern source (no. 1) is also outside the LAT uncertainty ellipses, but closer, being at an angular distance of 1.′7 and the 3FGL uncertainty region seems to be closer to the eastern source than any of the LAT results (see Fig. I.1, right panel). Based on this image, the γ-ray source is indeed the counterpart to the young radio source, although the radio source lies just outside the 3FGL 95% uncertainty ellipse. In the 8-year *Fermi* /LAT analysis, the source is detected at $TS = 2373$, with a photon index $\Gamma = 1.98 \pm 0.03$ and a flux $F_{1-300\,\mathrm{GeV}} = (5.57 \pm 0.22) \times 10^{-9}\,\mathrm{ph\,s^{-1}\,cm^{-2}}$. This flux is slightly lower than the fluxes reported in the LAT catalogs.

We further analyze the *Chandra* spectra of PMN J1603−4904 and of the source to the east of PMN J1603−4904 . X-ray observations by *Suzaku* and *XMM-Newton* were taken from Müller et al. (2015). The indices are consistent with the *Chandra* best fit of PMN J1603−4904 , while the flux is slightly lower (see Table 11). Due to the low S/N, particularly at energies above 5 keV, the Fe emission line is not detected with *Chandra* . We model the *Chandra* /ACIS data with an absorbed powerlaw and with an absorbed collisionally-ionized emission model (APEC) and compare the results to those of the *Suzaku* /*XMM-Newton* data from 2013 (see Table 12). It is worth noting that the eastern source has a very soft index of $\Gamma = 5.3^{+1.5}_{-2.1}$, assuming the same absorbing column as for PMN J1603−4904 . With a 21 cm derived Galactic equivalent hydrogen column of $6.32 \times 10^{21}\,\mathrm{cm^{-2}}$ (Kalberla et al., 2005) the index is much flatter and more realistic. This suggests that the source has little or no intrinsic absorption. We add the *Chandra* data to the high-energy SED, which includes the combined *Suzaku* and *XMM* data, as well as the LAT spectrum from the 3FGL catalog (see Fig. I.3). We have included both the spectrum from PMN J1603−4904 and from the eastern source (in black and pink, respectively). While it is already challenging to explain the strong γ-ray emission and the flat γ-ray index in combination with the flat X-ray index of PMN J1603−4904 (in both *Suzaku* +*XMM* and *Chandra*), it is nearly impossible to explain the soft index of the eastern source in combination with the LAT data, except by invoking different populations of particles. The high-energy SED seems to confirm that the eastern source is an extremely unlikely counterpart. Modeling the broadband SED of PMN J1603−4904 with a physical one-zone model will remain challenging with such a high Compton dominance and flat indices.

Although the optical/UV is likely non-thermal (Goldoni et al., 2016), a further possibility is thermal emission from an e.g., APEC component that would explain the He-like Fe line,

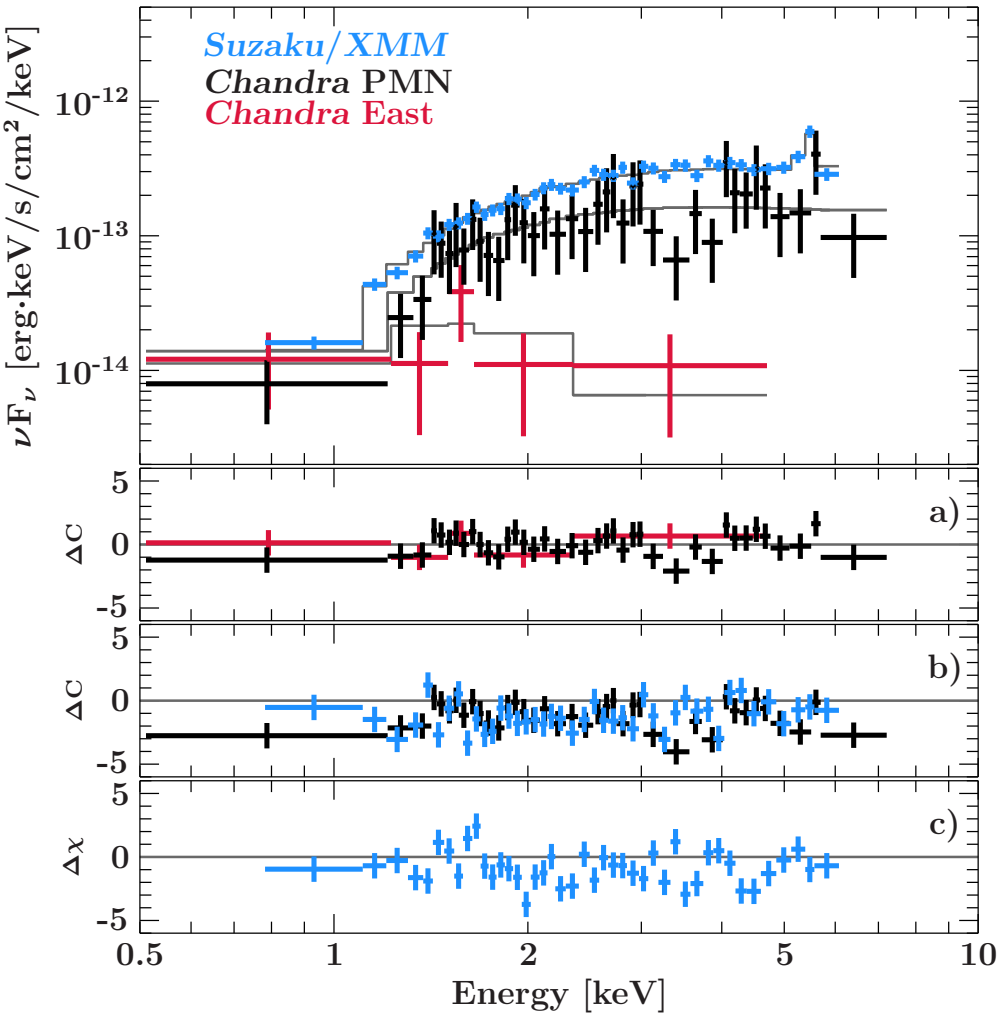

Figure I.2: X-ray spectra: Combined *Suzaku* /*XMM-Newton* spectrum of PMN J1603−4904 (blue), *Chandra* /ACIS spectrum of PMN J1603−4904 (black), *Chandra* /ACIS spectrum of the source east of PMN J1603−4904 (pink). A best-fit absorbed powerlaw is shown for the two *Chandra* spectra. The fit models shown are the best fit powerlaw models for the *Chandra* spectrum and the APEC model for the combined *Suzaku* /*XMM* data. Residuals are given for the a) best fit powerlaw spectrum, b) the combined APEC fit, and c) the *Suzaku* /*XMM* APEC fit.

which is consistent with results by Siemiginowska et al. (2016). A combined fit to the *Chandra* /ACIS and combined Suzaku and *XMM* data results in a best fit absorbing column of $(1.62 \pm 0.12) \times 10^{22}\,\mathrm{cm}^{-2}$, which can explain the absence of observed He-like S/Si. It is interesting to note that this value is smaller than the value necessary for a purely phenomenological powerlaw fit with an added gaussian line, which is $2.05^{+0.14}_{-0.12} \times 10^{22}\,\mathrm{cm}^{-2}$. This lower value is not compatible with the Galactic absorption of $6.32 \times 10^{21}\,\mathrm{cm}^{-2}$ and suggests intrinsic absorption, possibly from a dusty torus, which is in agreement with the interpretation of the blackbody feature in the infrared with a hot torus (Müller et al., 2014).

Photoionization is an alternative way to produce the He-like Fe emission line, but the low S/N of the spectra does not allow us to differentiate between the models.

Table 11: Best fit values from *Suzaku* and *XMM-Newton* data taken from Müller et al. (2015) in comparison with best fit values for *Chandra* /ACIS data for PMN J1603−4904 and two fits to the eastern source. Values without uncertainties have been frozen to the given value. Uncertainties are given at the 90% confidence level. The absorbing column is given in units of $10^{22}\,\mathrm{cm}^{-2}$, and the unabsorbed 2–10 keV flux is given in units of $10^{-13}\,\mathrm{erg\,s}^{-1}\,\mathrm{cm}^{-2}$.

Parameter	*Suzaku* & *XMM*	*Chandra*	*Chandra* East	*Chandra* East
N_H	$2.05^{+0.14}_{-0.12}$	2.05	2.05	0.632
Γ	$2.07^{+0.04}_{-0.12}$	$2.23^{+0.29}_{-0.28}$	$5.3^{+1.5}_{-2.1}$	$3.0^{+1.4}_{-1.2}$
F_{2-10}	4.39 ± 0.17	$2.8^{+0.7}_{-0.6}$	$0.08^{+0.05}_{-0.04}$	$0.14^{+0.28}_{-0.1}$
χ^2/dof	183.0/162	28.8/37	2.9/3	2.3/3

Table 12: APEC best fit values to combined fitting of *Chandra* /ACIS and *Suzaku* /*XMM* data, and only *Suzaku* /*XMM* data. Note that the fit to the combined data sets was done using Cash statistic and not χ^2 statistics, so χ^2 is the Cash statistic value in that case.

Fit	N_H $[10^{22}\,\mathrm{cm}^{-2}]$	kT [keV]	Abundance	χ^2/dof
comb.	1.62 ± 0.12	$5.9^{+0.9}_{-0.7}$	$0.46^{+0.16}_{-0.14}$	137.298/78
XMM	1.61 ± 0.13	$6.1^{+1.1}_{-0.8}$	$0.46^{+0.17}_{-0.16}$	31.816/39

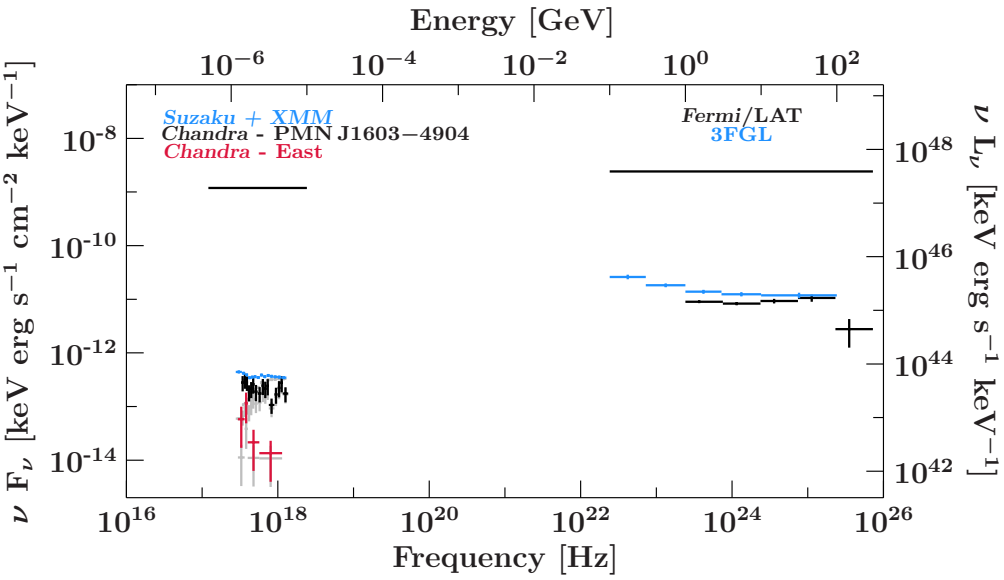

Figure I.3: High-energy SED showing the archival combined *Suzaku* and *XMM* data and the *Chandra* /ACIS data of both PMN J1603−4904 and the eastern source in X-rays. The *Fermi* /LAT spectrum of PMN J1603−4904 is shown. The absorbed X-ray spectra are shown in gray.

Conclusion

We have presented *Chandra* /ACIS and *Fermi* /LAT data of PMN J1603−4904 . We show that we can rule out source confusion between the *Fermi* /LAT source and sources at lower energies by using the high angular resolution of *Chandra* and an improved 8-year localization of the γ-ray source 3FGL J1603.9−4903. The positional uncertainty is consistent with the radio coordinates and the X-ray counterpart. An alternative X-ray counterpart at $\sim 1'$ distance to PMN J1603−4904 can be ruled out as a counterpart to the γ-ray source, based on the localization and the spectral shape. Its spectral index is further inconsistent with LAT data, as seen from the high-energy SED. Its absorbing column is consistent with Galactic absorption (although the low S/N makes a good fit of the absorbing column impossible).

Using *Chandra* /ACIS positions, fluxes, and spectra, in combination with *Fermi* /LAT data, we confirm the X-ray counterpart, rule out contributions from nearby X-ray sources, and confirm a high Compton dominance in the broadband SED of PMN J1603−4904 . We therefore conclude that PMN J1603−4904 is likely one of only two known γ-ray emitting young radio galaxies and that its emission mechanisms and strong Compton dominance warrant further research.

References

Aartsen M.G., Abbasi R., Abdou Y., et al., 2013a, Physical Review Letters 111, 021103

Aartsen M.G., Abbasi R., Ackermann M., et al., 2013b, Phys. Rev. D88, 112008

Aartsen M.G., Abraham K., Ackermann M., et al., 2017a, ApJ835, 151

Aartsen M.G., Abraham K., Ackermann M., et al., 2016, ApJ824, 115

Aartsen M.G., Abraham K., Ackermann M., et al., 2015a, Physical Review Letters 115, 081102

Aartsen M.G., Ackermann M., Adams J., et al., 2017b, Journal of Instrumentation 12, P03012

Aartsen M.G., Ackermann M., Adams J., et al., 2015b, ApJ807, 46

Aartsen M.G., Ackermann M., Adams J., et al., 2014a, Physical Review Letters 113, 101101

Aartsen M.G., Ackermann M., Adams J., et al., 2014b, ApJ796, 109

Abbasi R., Abdou Y., Abu-Zayyad T., et al., 2012, Nature484, 351

Abbasi R., Abdou Y., Abu-Zayyad T., et al., 2011, Phys. Rev. D83, 012001

Abbott B., Abbott R., Adhikari R., et al., 2004, Nuclear Instruments and Methods in Physics Research A 517, 154

Abbott B.P., Abbott R., Abbott T.D., et al., 2016, Physical Review Letters 116, 061102

Abbott B.P., Abbott R., Abbott T.D., et al., 2017, ApJ848, L12

Abdo A.A., Ackermann M., Agudo I., et al., 2010a, ApJ716, 30

Abdo A.A., Ackermann M., Ajello M., et al., 2011a, ApJ727, 129

Abdo A.A., Ackermann M., Ajello M., et al., 2010b, Science 328, 725

Abdo A.A., Ackermann M., Ajello M., et al., 2010c, Nature463, 919

Abdo A.A., Ackermann M., Ajello M., et al., 2011b, ApJ736, 131

Abdo A.A., Allen B., Berley D., et al., 2007, ApJ658, L33

Accadia T., Acernese F., Alshourbagy M., et al., 2012, Journal of Instrumentation 7, 3012

Acero F., Ackermann M., Ajello M., et al., 2015, ApJS218, 23

Acero F., Ackermann M., Ajello M., et al., 2016, ApJS223, 26

Acero F., Aharonian F., Akhperjanian A.G., et al., 2009, Science 326, 1080

Acharya B.S., Actis M., Aghajani T., et al., 2013, Astroparticle Physics 43, 3

Achterberg A., Ackermann M., Adams J., et al., 2008, ApJ674, 357

Ackermann M., Ajello M., Albert A., et al., 2015a, ApJ813, L41

Ackermann M., Ajello M., Albert A., et al., 2015b, ApJ799, 86

Ackermann M., Ajello M., Allafort A., et al., 2011, ApJ741, 30

Ackermann M., Ajello M., Allafort A., et al., 2013, ApJS209, 34

Ackermann M., Ajello M., Atwood W.B., et al., 2015c, ApJ810, 14

Ackermann M., Ajello M., Atwood W.B., et al., 2016a, ApJS222, 5

Ackermann M., Ajello M., Baldini L., et al., 2017, ApJ837, L5

Ackermann M., Ajello M., Ballet J., et al., 2012, ApJ751, 159

Ackermann M., Anantua R., Asano K., et al., 2016b, ApJ824, L20

Adrián-Martínez S., Ageron M., Aharonian F., et al., 2016, Journal of Physics G Nuclear Physics 43, 084001

Ageron M., Aguilar J.A., Al Samarai I., et al., 2011, Nuclear Instruments and Methods in Physics Research A 656, 11

Aharonian F., Akhperjanian A.G., Bazer-Bachi A.R., et al., 2006a, A&A457, 899

Aharonian F., Akhperjanian A.G., Bazer-Bachi A.R., et al., 2005, A&A437, L7

Aharonian F., Akhperjanian A.G., Bazer-Bachi A.R., et al., 2006b, Nature439, 695

Aharonian F.A., 2000, New A5, 377

Ajello M., Atwood W.B., Baldini L., et al., 2017, ApJS232, 18

Albert A., Andrè M., Anghinolfi M., et al., 2018, ArXiv e-prints

Aleksić J., Alvarez E.A., Antonelli L.A., et al., 2012, Astroparticle Physics 35, 435

Aleksić J., Ansoldi S., Antonelli L.A., et al., 2015, A&A578, A22

Aleksić J., Antonelli L.A., Antoranz P., et al., 2013, A&A556, A67

Alexeyev E.N., Alexeyeva L.N., Krivosheina I.V., Volchenko V.I., 1988, Physics Letters B 205, 209

Alvarez-Muñiz J., Mészáros P., 2004, Phys. Rev. D70, 123001

Anchordoqui L.A., Goldberg H., Lynch M.H., et al., 2014, Phys. Rev. D89, 083003

Anderhub H., Backes M., Biland A., et al., 2013, Journal of Instrumentation 8, P06008

Andres E., Askebjer P., Barwick S.W., et al., 2000, Astroparticle Physics 13, 1

Angioni R., Cheung C.C., 2018, The Astronomer's Telegram 11137

Ansoldi S., Antonelli L.A., Arcaro C., et al., 2018, ApJ863, L10

Antonucci R.R.J., Miller J.S., 1985, ApJ297, 621

Aschenbach B., 1985, Reports on Progress in Physics 48, 579

Atoyan A.M., Dermer C.D., 2003, ApJ586, 79

Attridge J.M., Roberts D.H., Wardle J.F.C., 1999, ApJ518, L87

Atwood W., Albert A., Baldini L., et al., 2013, ArXiv e-prints

Atwood W.B., Abdo A.A., Ackermann M., et al., 2009, ApJ697, 1071

Atwood W.B., Bagagli R., Baldini L., et al., 2007, Astroparticle Physics 28, 422

B. Povh, K. Rith C.S., 1999, Teilchen und Kerne, Springer

Bagduev R.I., Balkanov V., Belolaptikov I.A., et al., 1999, Nuclear Instruments and Methods in Physics Research A 420, 138

Bagley P., et al., 2009, KM3NeT: Technical Design Report http://inspirehep.net/record/1366114/files/TDRKM3NeT.pdf

Baldwin J.A., Phillips M.M., Terlevich R., 1981, PASP93, 5

Baloković M., Paneque D., Madejski G., et al., 2016, ApJ819, 156

Barthelmy S.D., Barbier L.M., Cummings J.R., et al., 2005, Space Sci. Rev.120, 143

Becker Tjus J., Eichmann B., Halzen F., et al., 2014, Phys. Rev. D89, 123005

Beckmann, V. Shrader C., 2012, Active Galactic Nuclei, Wiley-Vch

Becquerel H., 1895 122

Bednarek W., Protheroe R.J., 1999, MNRAS302, 373

Bianchi S., Maiolino R., Risaliti G., 2012, Advances in Astronomy 2012, 782030

Biermann P.L., Strittmatter P.A., 1987, ApJ322, 643

Bignami G.F., Boella G., Burger J.J., et al., 1975, Space Science Instrumentation 1, 245

Biland A., Bretz T., Buß J., et al., 2014, Journal of Instrumentation 9, P10012

Biland A., Dorner D., Lauer R., et al., 2016, The Astronomer's Telegram 9137

Blandford R.D., Payne D.G., 1982, MNRAS199, 883

Blandford R.D., Rees M.J., 1978, Phys. Scr17, 265

Blandford R.D., Znajek R.L., 1977, MNRAS179, 433

Blasi P., 2014, Comptes Rendus Physique 15, 329

Bloemen H., Bennett K., Blom J.J., et al., 1995, A&A293

Blumenthal G.R., Gould R.J., 1970, Reviews of Modern Physics 42, 237

Boettcher M., Dermer C.D., 2010, In: AAS/High Energy Astrophysics Division #11, Vol. 42. Bulletin of the American Astronomical Society, p. 706

Bottacini E., Ferrigno C., Fotopoulou S., et al., 2015, The Astronomer's Telegram 7648

Böttcher M., 2007, Ap&SS309, 95

Böttcher M., Reimer A., Sweeney K., Prakash A., 2013, ApJ768, 54

Bradt H., 2004, Astronomy Methods: A Physical Approach to Astronomical Observations

Brown A.M., 2013, MNRAS431, 824

Brown L.M., 1978, Physics Today 31, 23

Bruijn R., van Eijk D., 2015, In: 34th International Cosmic Ray Conference (ICRC2015), Vol. 34. International Cosmic Ray Conference, p. 1157

Buehler R., 2009, The Astronomer's Telegram 2217

Burke B.F., Graham-Smith F., 2009, An Introduction to Radio Astronomy

Burrows A., Lattimer J.M., 1987, ApJ318, L63

Burrows D.N., Hill J.E., Nousek J.A., et al., 2005, Space Sci. Rev.120, 165

Burrows D.N., Hill J.E., Nousek J.A., et al., 2000, In: Flanagan K.A., Siegmund O.H. (eds.) X-Ray and Gamma-Ray Instrumentation for Astronomy XI, Vol. 4140. Proc. SPIE, p.64

Caccianiga A., Antón S., Ballo L., et al., 2014, MNRAS441, 172

Carminati G., 2007, ANTARES internal note: ANTARES-Soft/2007-004

Cash W., 1979, ApJ228, 939

Chang C.S., 2010, Ph.D. thesis, Max-Planck-Institut für Radioastronomie <EMAIL>cschang@mpifr-bonn.mpg.de</EMAIL>

Cheung C.C., 2016, The Astronomer's Telegram 9854

Cheung C.C., 2017, The Astronomer's Telegram 10356

Ciprini S., Thompson D.J., on behalf of the Fermi LAT collaboration 2013, ArXiv e-prints

Clark G.W., Bradt H.V., Lewin W.H.G., et al., 1973, ApJ179, 263

Clerk Maxwell J., 1865, Philosophical Transactions of the Royal Society of London Series I 155, 459

Cohen M.H., Kellermann K.I., Shaffer D.B., et al., 1977, Nature268, 405

Condon J.J., Cotton W.D., Greisen E.W., et al., 1998, AJ115, 1693

Cowan, Jr. C.L., Reines F., Harrison F.B., et al., 1956, Science 124, 103

Cracco V., 2011, PASP123, 1133

Curie M., 1903, Recherches sur les substances radioactives

Curtis H.D., 1918, Publications of Lick Observatory 13, 9

Curtis H.D., 1920, JRASC14, 317

Cutini S., 2015a, The Astronomer's Telegram 7633

Cutini S., 2015b, The Astronomer's Telegram 7633

D'Ammando F., Orienti M., Giroletti M., Fermi Large Area Telescope Collaboration 2016, Astronomische Nachrichten 337, 59

Danby G., Gaillard J.M., Goulianos K., et al., 1962, Physical Review Letters 9, 36

Davies J.M., Cotton E.S., 1957, Solar Energy 1, 16

Davis J.E., 2001a, ApJ562, 575

Davis J.E., 2001b, ApJ548, 1010

Davis R., Harmer D.S., Hoffman K.C., 1968, Phys. Rev. Lett. 20, 1205

Dermer C.D., Murase K., Inoue Y., 2014, Journal of High Energy Astrophysics 3, 29

Done C., Krolik J.H., 1996, ApJ463, 144

DONUT CollaborationKodama K., Ushida N., et al., 2001, Physics Letters B 504, 218

Dorner D., 2016, Timeresolved View of Blazar Flares Using Longterm Monitoring - Example of a Recent Flare of Mrk 421, Gamma 16

Dornic D., Coleiro A., 2017, The Astronomer's Telegram 10773

Eddington A.S., 1919, Nature104, 372

Edelson R.A., Krolik J.H., 1988, ApJ333, 646

Edge D.O., Shakeshaft J.R., McAdam W.B., et al., 1959, MmRAS68, 37

Einstein A., 1915a, Sitzungsberichte der Königlich Preußischen Akademie der Wissenschaften (Berlin), Seite 778-786.

Einstein A., 1915b, Sitzungsberichte der Königlich Preußischen Akademie der Wissenschaften (Berlin), Seite 799-801.

Einstein A., 1918, Sitzungsberichte der Königlich Preußischen Akademie der Wissenschaften (Berlin), Seite 154-167.

Falcke H., Biermann P.L., 1995, A&A293, 665

Falcke H., Melia F., Agol E., 2000, ApJ528, L13

Fanaroff B.L., Riley J.M., 1974, MNRAS167, 31P

Fazio G.G., Helmken H.F., O'Mongain E., Weekes T.C., 1972, ApJ175, L117

Feenberg E., Primakoff H., 1948, Physical Review 73, 449

Fehn K., 2015, Ph.D. thesis, FAU Erlangen

Feldman G.J., Cousins R.D., 1998, Phys. Rev. D57, 3873

Fermi E., 1949, Physical Review 75, 1169

Ferreira O., Bogaert G., Bonnemaison A., et al., 2004, Nuclear Instruments and Methods in Physics Research A 530, 323

Fichtel C.E., Kniffen D.A., Hartman R.C., 1973, ApJ186, L99

Finke J.D., Dermer C.D., Böttcher M., 2008, ApJ686, 181

Flanagan K.A., Siegmund O.H.W., (eds.) 2004, X-Ray and Gamma-Ray Instrumentation for Astronomy XIII, Vol. 5165 of Proc. SPIE, Proc. SPIE

Formaggio J.A., Zeller G.P., 2012, Reviews of Modern Physics 84, 1307

Forrest D.J., Chupp E.L., Ryan J.M., et al., 1980, Sol. Phys.65, 15

Foschini L., Ghisellini G., Tavecchio F., et al., 2011, A&A530, A77

Fossati G., Buckley J.H., Bond I.H., et al., 2008, ApJ677, 906

Fossati G., Maraschi L., Celotti A., et al., 1998, MNRAS299, 433

Franckowiak A., Stanek K.Z., Kochanek C.S., et al., 2017, The Astronomer's Telegram 10794

Fraser G.W., Abbey A.F., Holland A., et al., 1994, Nuclear Instruments and Methods in Physics Research A 350, 368

Fukuda Y., Hayakawa T., Ichihara E., et al., 1998, Physical Review Letters 81, 1562

Gaibler V., Krause M., Camenzind M., 2009, MNRAS400, 1785

Gaisser T.K., Honda M., 2002, Annual Review of Nuclear and Particle Science 52, 153

Gandhi R., Quigg C., Hall Reno M., Sarcevic I., 1996, Astroparticle Physics 5, 81

G.B. Rybicki A.L., 1985, Radiative Processes in Astrophysics, John Wiley & Sons

Gehrels N., Chincarini G., Giommi P., et al., 2004, ApJ611, 1005

Gehrels N., Shrader C.R., 2001, In: Ritz S., Gehrels N., Shrader C.R. (eds.) Gamma 2001: Gamma-Ray Astrophysics, Vol. 587. American Institute of Physics Conference Series, p.3

Ghirlanda G., Ghisellini G., Tavecchio F., Foschini L., 2010, MNRAS407, 791

Ghisellini G., Celotti A., Fossati G., et al., 1998, MNRAS301, 451

Ghisellini G., Della Ceca R., Volonteri M., et al., 2010a, MNRAS405, 387

Ghisellini G., Haardt F., Ciardi B., et al., 2015, MNRAS452, 3457

Ghisellini G., Tavecchio F., Foschini L., et al., 2010b, MNRAS402, 497

Giacconi R., 2003, Reviews of Modern Physics 75, 995

Giacconi R., Gursky H., Paolini F.R., Rossi B.B., 1962, Physical Review Letters 9, 439

Giacconi R., Gursky H., Waters J.R., 1964, Nature204, 981

Giuliani A., D'Ammando F., Vercellone S., et al., 2009, A&A494, 509

Glashow S.L., 1960, Physical Review 118, 316

Goldoni P., Pita S., Boisson C., et al., 2016, A&A586, L2

Gorenstein P., Gursky H., Garmire G., 1968, ApJ153, 885

Griffiths D., 2008, Introduction to Elementary Particles

Gubbay J., Legg A.J., Robertson D.S., et al., 1969, Nature224, 1094

Gugliucci N.E., Taylor G.B., Peck A.B., Giroletti M., 2005, ApJ622, 136

Gupta A.C., Banerjee D.P.K., Ashok N.M., Joshi U.C., 2004, A&A422, 505

Haddock S.H.D., Moline M.A., Case J.F., 2010, Annual Review of Marine Science 2, 443

Halzen F., Kheirandish A., 2016, ApJ831, 12

Halzen F., Klein S.R., 2010, Review of Scientific Instruments 81, 081101

Halzen F., Martin A.D., 1984, Quarks and leptons : an introductory course in modern particle physics

Hartman R.C., Bertsch D.L., Fichtel C.E., et al., 1992, ApJ385, L1

Hawking S.W., 1975, Communications in Mathematical Physics 43, 199

Hayakawa S., 1952, Progress of Theoretical Physics 8, 571

Hayashida M., Madejski G.M., Nalewajko K., et al., 2012, ApJ754, 114

Hayashida M., Nalewajko K., Madejski G.M., et al., 2015, ApJ807, 79

He H.N., Wang T., Fan Y.Z., et al., 2013, Phys. Rev. D87, 063011

Heckman T.M., Best P.N., 2014, ARA&A52, 589

Helene O., 1983, Nuclear Instruments and Methods in Physics Research 212, 319

Herring P.J., 1983, Proceedings of the Royal Society of London Series B 220, 183

Herschel W., 1800, Philosophical Transactions of the Royal Society of London Series I 90, 284

Hertz H., 1888, Annalen der Physik 270, 273

Hertz H., 1889, Annalen der Physik 272, 769

Hess V., 1912, Physikalische Zeitschrift 13, 1084

H.E.S.S. CollaborationAbramowski A., Acero F., et al., 2013, A&A550, A4

Hill J.E., Zugger M.E., Shoemaker J., et al., 2000, In: Flanagan K.A., Siegmund O.H. (eds.) X-Ray and Gamma-Ray Instrumentation for Astronomy XI, Vol. 4140. Proc. SPIE, p.87

Hillas A.M., 1984, ARA&A22, 425

Hinton J., 2009, New Journal of Physics 11, 055005

Hoffmeister C., 1929, Astronomische Nachrichten 236, 233

Holland A.D., Turner M.J., Abbey A.F., Pool P.J., 1996, In: Siegmund O.H., Gummin M.A. (eds.) EUV, X-Ray, and Gamma-Ray Instrumentation for Astronomy VII, Vol. 2808. Proc. SPIE, p.414

Houck J.C., Denicola L.A., 2000, In: Manset N., Veillet C., Crabtree D. (eds.) Astronomical Data Analysis Software and Systems IX, Vol. 216. Astronomical Society of the Pacific Conference Series, p. 591

IceCube Collaboration ., Fermi-LAT Collaboration ., MAGIC ., et al., 2018, Science 361, 6398

IceCube Collaboration 2013, Science 342, 1242856

IceCube Collaboration 2018, Science 361, 147

IceCube CollaborationPierre Auger CollaborationTelescope Array Collaboration 2016, J. Cosmology Astropart. Phys.1, 037

IceCube-Gen2 Collaboration:Aartsen M.G., et al., 2014, ArXiv e-prints

Inoue Y., Totani T., 2009, ApJ702, 523

Jagoda N., Austin G., Mickiewicz S., Goddard R., 1972, IEEE Transactions on Nuclear Science 19, 579

Janesick J.R., 2001, Scientific charge-coupled devices

Jansen F., Lumb D., Altieri B., et al., 2001, A&A365, L1

Jansky K.G., 1932, Proc. IEEE, p. 1920

Jansky K.G., 1933, Proc. IEEE, p. 1387

Johnson W.N., Grove J.E., Phlips B.F., et al., 2001, IEEE Transactions on Nuclear Science 48, 1182

Jorstad S.G., Marscher A.P., Mattox J.R., et al., 2001, ApJS134, 181

Kadler M., Krauß F., Mannheim K., et al., 2016, Nature Physics 12, 807

Kadler M., Ojha R., TANAMI Collaboration 2015, Astronomische Nachrichten 336, 499

Kalberla P.M.W., Burton W.B., Hartmann D., et al., 2005, A&A440, 775

Kant I., 1755, Allgemeine Naturgeschichte und Theorie des Himmels

Karlsson N., for the VERITAS collaboration 2009, ArXiv e-prints

Katz U.F., Spiering C., 2012, Progress in Particle and Nuclear Physics 67, 651

Keivani A., Ayala H., DeLaunay J., 2017, ArXiv e-prints

Kellermann K.I., Sramek R., Schmidt M., et al., 1989, AJ98, 1195

Kelley J.L., 2014, AIP Conference Proceedings 154–157

Kimura S.S., Murase K., Toma K., 2015, ApJ806, 159

King A., 2003, ApJ596, L27

Kino M., Asano K., 2011, MNRAS412, L20

Kino M., Ito H., Kawakatu N., Nagai H., 2009, MNRAS395, L43

Kino M., Kawakatu N., Ito H., 2007, MNRAS376, 1630

Kirk J.G., Guthmann A.W., Gallant Y.A., Achterberg A., 2000, ApJ542, 235

KM3NeT Collaboration 2008, Conceptual Design Report http://www.km3net.org/CDR/CDR-KM3NeT.pdf

Kniffen D.A., Bertsch D.L., Fichtel C.E., et al., 1993, ApJ411, 133

Kormendy J., Richstone D., 1995, ARA&A33, 581

Kovalev Y.Y., 2009, ApJ707, L56

Kranich D., 2001, Ph.D. thesis, TU München

Kraushaar W., Clark G.W., Garmire G., et al., 1965, ApJ141, 845

Kraushaar W.L., Clark G.W., Garmire G.P., et al., 1972, ApJ177, 341

Krauss F., Carpenter B., 2014, The Astronomer's Telegram 5909

Krauß F., Deoskar K., Baxter C., et al., in press, A&A

Krauß F., Kadler M., Mannheim K., et al., 2014, A&A566, L7

Krauß F., Kreter M., Müller C., et al., 2018, A&A610, L8

Krauß F., Wilms J., Kadler M., et al., 2016, A&A591, A130

Krawczynski H., Hughes S.B., Horan D., et al., 2004, ApJ601, 151

Kreikenbohm A., 2018, Ph.D. thesis, Julius-Maximilians-Universität Würzburg

Kremers C., Chigrin D.N., 2009, Journal of Optics A: Pure and Applied Optics 11, 114008

Krennrich F., Bond I.H., Boyle P.J., et al., 2004, New A Rev.48, 345

Kreter M., 2015, Master's thesis, Julius-Maximilians-Universität Würzburg

Kreter M., 2018, The Astronomer's Telegram 11378

Kreter M., Buson S., 2016, The Astronomer's Telegram 9779

Krolik J., 1999, Active galactic nuclei : from the central black hole to the galactic environment, Princeton University Press

Laing R.A., 1996, In: Hardee P.E., Bridle A.H., Zensus J.A. (eds.) Energy Transport in Radio Galaxies and Quasars, Vol. 100. Astronomical Society of the Pacific Conference Series, p. 241

Laor A., 2000, ApJ543, L111

Laplace P.S., 1796, Exposition du système du monde

Lawrence A., 1987, PASP99, 309

Lawrence A., 1991, MNRAS252, 586

Lawrence A., 2012, MNRAS423, 451

Lind K.R., Blandford R.D., 1985, ApJ295, 358

Lister M.L., Homan D.C., 2005, AJ130, 1389

Liu R.Y., Wang X.Y., Inoue S., et al., 2014, Phys. Rev. D89, 083004

Liu Y., Zhang S.N., 2011, ApJ728, L44

Loeb A., Waxman E., 2006, J. Cosmology Astropart. Phys.5, 003

Löhner H., Dorosti-Hasankiadeh Q., Heine E., et al., 2013, Nuclear Instruments and Methods in Physics Research A 718, 513

Longair M.S., 2011, High Energy Astrophysics

Lynden-Bell D., Rees M.J., 1971, MNRAS152, 461

Lyubarsky Y., 2011, Phys. Rev. E83, 016302

MAGIC CollaborationAlbert J., Aliu E., et al., 2008, Science 320, 1752

Mannheim K., 1993, A&A269, 67

Mannheim K., 1995, Astroparticle Physics 3, 295

Mannheim K., Biermann P.L., 1989, A&A221, 211

Mannheim K., Biermann P.L., 1992, A&A253, L21

Markert T.H., Canizares C.R., Clark G.W., et al., 1977, ApJ218, 801

Marscher A.P., Gear W.K., 1985, ApJ298, 114

Marscher A.P., Gear W.K., Travis J.P., 1992, In: Valtaoja E., Valtonen M. (eds.) Variability of Blazars., p. 85

Marziani P., Sulentic J.W., Dultzin-Hacyan D., et al., 1996, ApJS104, 37

McConville W., Ostorero L., Moderski R., et al., 2011, ApJ738, 148

McKinney J.C., Tchekhovskoy A., Blandford R.D., 2012, MNRAS423, 3083

Meegan C., Lichti G., Bhat P.N., et al., 2009, ApJ702, 791

Meier D.L., 2002, New A Rev.46, 247

Meier D.L., 2012, Black Hole Astrophysics: The Engine Paradigm

Mészáros P., 2017, Annual Review of Nuclear and Particle Science 67, 45

Meyer E.T., Fossati G., Georganopoulos M., Lister M.L., 2011, ApJ740, 98

Michell J., 1784, Philosophical Transactions of the Royal Society of London Series I 74, 35

Migliori G., Siemiginowska A., Sobolewska M., et al., 2016, ApJ821, L31

Mirzoyan R., 2017, The Astronomer's Telegram 10817

Misner C.W., Thorne K.S., Wheeler J.A., 1973, Gravitation

Mitsuda K., Bautz M., Inoue H., et al., 2007, PASJ59, S1

Moiseev A.A., Hartman R.C., Ormes J.F., et al., 2007, Astroparticle Physics 27, 339

Morrison P., 1958, In: Vallarta M.S. (ed.) Fifth International Congress on Cosmic Radiation., p. 305

Moskalenko I.V., Strong A.W., Reimer O., 2004, In: Cheng K.S., Romero G.E. (eds.) Cosmic Gamma-Ray Sources, Vol. 304. Astrophysics and Space Science Library, p. 279

Mücke A., Engel R., Rachen J.P., et al., 2000, Computer Physics Communications 124, 290

Mücke A., Protheroe R.J., Engel R., et al., 2003, Astroparticle Physics 18, 593

Müller C., Burd P.R., Schulz R., et al., 2016, A&A593, L19

Müller C., Kadler M., Ojha R., et al., 2014, A&A562, A4

Müller C., Kadler M., Ojha R., et al., 2011, A&A530, L11

Müller C., Krauß F., Dauser T., et al., 2015, A&A574, A117

Murase K., Ahlers M., Lacki B.C., 2013, Phys. Rev. D88, 121301

Murase K., Guetta D., Ahlers M., 2016, Physical Review Letters 116, 071101

Murase K., Inoue Y., Dermer C.D., 2014, Phys. Rev. D90, 023007

Murase K., Waxman E., 2016, Phys. Rev. D94, 103006

Negoro H., Ueno S., Tomida H., et al., 2017, The Astronomer's Telegram 10838

Neronov A., Semikoz D., Taylor A.M., 2012, A&A541, A31

Netzer H., 2015, ARA&A53, 365

Nolan P.L., Abdo A.A., Ackermann M., et al., 2012, ApJS199, 31

Norton A., 2000, Dynamic fields and waves

Nowak M.A., Neilsen J., Markoff S.B., et al., 2012, ApJ759, 95

Nowak M.A., Wilms J., Heinz S., et al., 2005, ApJ626, 1006

Oda M., Gorenstein P., Gursky H., et al., 1971, ApJ166, L1

O'Dea C.P., 1998, PASP110, 493

Oh K., Koss M., Markwardt C.B., et al., 2018, ApJS235, 4

Ojha R., Kadler M., Böck M., et al., 2010, A&A519, A45

Okada A., 1994, Astroparticle Physics 2, 393

Oke J.B., Gunn J.E., 1974, ApJ189, L5

Olive K.A., Particle Data Group 2014, Chinese Physics C 38, 090001

Oppenheimer J.R., Snyder H., 1939, Physical Review 56, 455

Orienti M., D'Ammand F., 2012, The Astronomer's Telegram 3999

Orienti M., D'Ammando F., Larsson J., et al., 2015, MNRAS453, 4037

Osone S., 2006, Astroparticle Physics 26, 209

Owens A., Bayliss S.C., Durham P.J., et al., 1996, ApJ468, 451

Pacini D., 1912, Il Nuovo Cimento 3, 93

Paczyńsky B., Wiita P.J., 1980, A&A88, 23

Padovani P., Giommi P., 1995, ApJ444, 567

Page M.J., Soria R., Zane S., et al., 2004, A&A422, 77

Paiano S., Falomo R., Treves A., Scarpa R., 2018, ApJ854, L32

Pauli W., 1930, Letter to Tübingen conference participants

Pe'Er A., Murase K., Mészáros P., 2009, Phys. Rev. D80, 123018

Perkins J.S., Ajello M., Hartmann D., et al., 2018, PoS, p. 598

Petropoulou M., Mastichiadis A., 2015, MNRAS447, 36

Phillips R.B., Mutel R.L., 1982, A&A106, 21

Piran T., 1999, Phys. Rep.314, 575

Pittori C., Verrecchia F., Puccetti S., et al., 2015a, The Astronomer's Telegram 7639

Pittori C., Verrecchia F., Puccetti S., et al., 2015b, The Astronomer's Telegram 7668

Predehl P., Schmitt J.H.M.M., 1995, A&A293, 889

Protheroe R.J., Kazanas D., 1983, ApJ265, 620

Razzaque S., Mészáros P., Waxman E., 2003, Phys. Rev. D68, 083001

Readhead A.C.S., Taylor G.B., Pearson T.J., Wilkinson P.N., 1996, ApJ460, 634

Reville B., Bell A.R., 2014, MNRAS439, 2050

Rieger F.M., Mannheim K., 2003, A&A397, 121

Righi C., Tavecchio F., Guetta D., 2017, A&A598, A36

Ritter J.W., 1803, Annalen der Physik 12, 409

Roming P.W.A., Kennedy T.E., Mason K.O., et al., 2005, Space Sci. Rev.120, 95

Röntgen W.C., 1898a, Annalen der Physik 300, 1

Röntgen W.C., 1898b, Annalen der Physik 300, 12

Saito S., Stawarz Ł., Tanaka Y.T., et al., 2013, ApJ766, L11

Saito S., Stawarz Ł., Tanaka Y.T., et al., 2015, ApJ809, 171

Salpeter E.E., 1964, ApJ140, 796

Schmidt M., 1963, Nature197, 1040

Schmidt M., Green R.F., 1983, ApJ269, 352

Schwarzschild K., 1916, Abh. Konigl. Preuss. Akad. Wissenschaften Jahre 1906,92, Berlin,1907 1916

Scully, D.I., 2013, Ph.D. thesis, University of Warwick

Seyfert C.K., 1942, Leaflet of the Astronomical Society of the Pacific 4, 71

Seyfert C.K., 1943, ApJ97, 28

Shakeshaft J.R., Ryle M., Baldwin J.E., et al., 1955, MmRAS67, 106

Shaw M.S., Romani R.W., Cotter G., et al., 2013, ApJ764, 135

Shu F., 1991, The physics of astrophysics. Volume 1: Radiation, University Science Books

Siemiginowska A., Sobolewska M., Migliori G., et al., 2016, ApJ823, 57

Sillanpaa A., Haarala S., Valtonen M.J., et al., 1988, ApJ325, 628

Skrutskie M.F., Cutri R.M., Stiening R., et al., 2006, AJ131, 1163

Smith M.W.E., Fox D.B., Cowen D.F., et al., 2013, Astroparticle Physics 45, 56

Spada M., Ghisellini G., Lazzati D., Celotti A., 2001, MNRAS325, 1559

Spanier F., Weidinger M., 2012, In: International Journal of Modern Physics Conference Series, Vol. 8. International Journal of Modern Physics Conference Series, p.293

Spiering C., 2012, European Physical Journal H 37, 515

Stanev T., 2004, High energy cosmic rays

Stawarz Ł., Ostorero L., Begelman M.C., et al., 2008, ApJ680, 911

Stecker F.W., Salamon M.H., 1996, Space Sci. Rev.75, 341

Steele I.A., 2017, The Astronomer's Telegram 10799

Tagliaferri G., Foschini L., Ghisellini G., et al., 2008, ApJ679, 1029

Tanaka Y.T., Buson S., Kocevski D., 2017, The Astronomer's Telegram 10791

Tavecchio F., Ghisellini G., Guetta D., 2014, ApJ793, L18

Tchekhovskoy A., McKinney J.C., Narayan R., 2012, In: Journal of Physics Conference Series, Vol. 372. Journal of Physics Conference Series, p. 012040

Terzian Y., Khachikian E., Weedman D., (eds.) 1999, Active Galactic Nuclei and Related Phenomena, Vol. 194 of IAU Symposium, IAU Symposium

Tetarenko A.J., Sivakoff G.R., Kimball A.E., Miller-Jones J.C.A., 2017, The Astronomer's Telegram 10861

The ANTARES Collaboration 2015, J. Cosmology Astropart. Phys.12, 014

Thompson D.J., Bertsch D.L., Fichtel C.E., et al., 1993, ApJS86, 629

Thompson D.J., Djorgovski S., de Carvalho R., 1990, PASP102, 1235

Tiffenberg, J., 2011, UHE neutrino searches with the Pierre Auger neutrino observatory, NUSKY

Urry C.M., Padovani P., 1995, PASP107, 803

Čerenkov P.A., 1937, Physical Review 52, 378

Veilleux S., Osterbrock D.E., 1987, ApJS63, 295

Vercellone S., D'Ammando F., Vittorini V., et al., 2010, ApJ712, 405

Verner D.A., Ferland G.J., Korista K.T., Yakovlev D.G., 1996, ApJ465, 487

Vianello G., Lauer R.J., Younk P., et al., 2015, ArXiv e-prints

Volonteri M., Haardt F., Ghisellini G., Della Ceca R., 2011, MNRAS416, 216

Wagner S.J., Witzel A., 1995, ARA&A33, 163

Waldenmaier T., 2008, Nuclear Instruments and Methods in Physics Research A 588, 130

Waxman E., Bahcall J., 1997, Physical Review Letters 78, 2292

Waxman E., Bahcall J.N., 2000, ApJ541, 707

Weekes T.C., 2003, Very high energy gamma-ray astronomy

Weidinger M., Spanier F., 2011, ArXiv e-prints

Weisskopf M.C., Tananbaum H.D., Van Speybroeck L.P., O'Dell S.L., 2000, In: Truemper J.E., Aschenbach B. (eds.) X-Ray Optics, Instruments, and Missions III, Vol. 4012. Proc. SPIE, p.2

Wiebusch C., for the IceCube Collaboration 2009, ArXiv e-prints

Wilkinson P.N., Polatidis A.G., Readhead A.C.S., et al., 1994, ApJ432, L87

Wilks S.S., 1938, Annals Math. Statist 9, 60

Wilms J., Allen A., McCray R., 2000, ApJ542, 914

Wolter H., 1952a, Annalen der Physik 445, 94

Wolter H., 1952b, Annalen der Physik 445, 286

Woltjer L., 1959, ApJ130, 38

Wright A.E., Griffith M.R., Burke B.F., Ekers R.D., 1994, ApJS91, 111

Wright T., 1750, An original theory or new hypothesis of the universe : founded upon general phaenomena of the visible creation; and particularly the Via the laws of nature, and solving by mathematical principles : the Lactea ...compris'd in nine familiar letters from the author to his friendand : illustrated with upward of thirty graven and mezzotinto plates ...

Wu C.S., Ambler E., Hayward R.W., et al., 1957, Physical Review 105, 1413

Wulf T., 1909a 8, 251

Wulf T., 1909b 10, 997

Wulf T., 1910 11, 811

Xiao D., Mészáros P., Murase K., Dai Z.G., 2016, ApJ826, 133

Zacharias M., Jankowsky F., Mohamed M., et al., 2017a, ArXiv e-prints

Zacharias M., Sitarek J., Dominis Prester D., et al., 2017b, ArXiv e-prints

Zhang X.H., Bao G., 1991, A&A246, 21

9 Acknowledgments

At this point I would like to thank all the people who supported me during this thesis. Without them, I would not been able to write this thesis.
Firstly, I thank Prof. Dr. Matthias Kadler for giving me the opportunity to write this PhD thesis under his supervision. From my MSc. thesis on, he was drawing my interest on active galactic nuclei and neutrino Astronomy. I thank Matthias for all the fruitful discussions we had and for giving me the chance to present my work at several conferences and workshops. Furthermore, I want to thank Matthias for introducing me to colleagues at NASA Goddard space flight center in Greenbelt Maryland and giving the the chance to visit them twice during my PhD thesis.
At this point, I want to thank the head of the Astronomy chair of Würzburg Prof. Dr. Karl Mannheim for giving me the chance of performing this thesis here in Würzburg and for all his helpful comments and the nice discussions.
Many thanks also to Dr. Felicia Krauß, Dr. Sara Buson, Dr. Roopesh Ojha and Dr. Dave Thompson for all their support while getting familiar with the analysis of *Fermi*/LAT data. I want to thank them for their steady support regarding any aspect of the *Fermi*/LAT analysis during the entire time of this thesis and for the pleasant time at Goddard and several conferences. In addition, I want to tanks Dr. Felicia Krauß for the productive work we did together on PMN J1603−4904. I thank Dr. Sara Buson for generating the *Fermi*/LAT data for a huge amount of high-redshift blazar light curves considered in this thesis.
I want to express my thanks to Dr. Daniela Dorner for giving me the chance to visit Goddard for a second time. I also thank Daniela for always being available for discussions during which I learned a lot about TeV Astronomy. For fruitful discussions I also want to thank Paul Ray Burd, Dr. Dorit Glawion, Dr. Amit Shukla and Andrea Gokus. Special thanks goes also to my proof readers: Dr. Dorit Glawion, Dr. Daniela Dorner, Rosamunde Pare, Andrea Gokus, Katharina Leiter, Annika Kreikenbohm and Marcus Langejahn.
As the work within this thesis required plenty of computing time, I want to thank Prof. Dr. Joern Wilms and all the admins at the Dr. Karl Remeis observatory in Bamberg for allowing me to calculate a huge part of the used *Fermi*/LAT data there.
Lukas Schrenk I want to thank for providing a steady supply of ice cream and "Spezi' at the institute, which really helped to keep my sugar level at a stage where I can work most efficient. During lunch time, I enjoyed discussions about a large variety of topics with i.a. Florian Rösch, Stefan Lindeholz, Manuel Dörr, Lukas Schrenk, Amar Hekalo and Michael Blank. Many thanks also to the entire group at the chair of Astronomy, and especially to Katharina Leiter and Annika Kreikenbohm for the pleasant atmosphere. I really enjoyed the time I could spent ay the institute.
Finally, I deeply want to thank my entire family for always supporting me during this thesis and during my entire time at the university of Würzburg since my first semester. However, most of my thank belongs to my wife Jenny and my little princess Leonie, which give me a reason to to continue working every day. While time together was always limited and rare, I enjoy every second with my two ladies.